Anthony N. Kounadis

Emmanuel E. Gdoutos   *Editors*

Recent Advances in Mechanics

Selected Papers from the Symposium
on Recent Advances in Mechanics,
Academy of Athens, Athens, Greece,
17–19 September, 2009, organised by
the Pericles S. Theocaris Foundation
in Honour of P.S. Theocaris, on the Tenth
Anniversary of his Death

Recent Advances in Mechanics

Anthony N. Kounadis
and Emmanuel E. Gdoutos (Eds.)

Recent Advances in Mechanics

Selected Papers from the Symposium on
Recent Advances in Mechanics, Academy
of Athens, Athens, Greece, 17-19 September,
2009, Organised by the Pericles S. Theocaris
Foundation in Honour of P.S. Theocaris,
on the Tenth Anniversary of His Death

Editors

Anthony N. Kounadis
Academy of Athens
Soranou Efessiou 4
GR-115 27 Athens
Greece
E-mail: kounadis@bioacademy.gr

Emmanuel E. Gdoutos
Dept. of Civil Engineering
Democritus University of Thrace
GR-671 00 Xanthi
Greece
E-mail: egdoutos@civil.duth.gr

Pericles S. Theocaris Foundation

Symposium
On Recent Advances in Mechanics

Dedicated to P.S. Theocaris
In Commemoration of Ten Years from his Death

17-19 September 2009

Anthony N. Kounadis and Emmanuel E. Gdoutos (*Editors*)

Academy of Athens

Springer

Participants of the Theocaris Symposium in front of the Academy of Athens

Preface

This book contains 24 papers presented at the symposium on "Recent Advances in Mechanics" dedicated to the late Professor–Academician **Pericles S. Theocaris** in commemoration of the tenth anniversary of his death. The symposium was organized by the Pericles S. Theocaris Foundation. The papers were written by world renowned and recognized experts in their fields and serve as a reference and guide for future research.

P.S. Theocaris dominated the Greek and international arena of Theoretical and Applied Mechanics during the second half of the twentieth century. With his continuous presence in the scientific community, manifested by the publication of original works, he opened new paths in many areas of *Applied Mechanics* and supervised a plethora of emerging scientists and engineers. Furthermore, through the establishment of a well-equipped Laboratory of Applied Mechanics at the *National Technical University of Athens*, he made a name for himself as the father of Mechanics in Greece. The Laboratory of Applied Mechanics that he directed from 1960 until his retirement in 1989 was the nursery and heart of the contemporary Mechanics community in Greece. Furthermore, P.S. Theocaris had a particular position in the international scientific community. It is rather difficult to find a researcher in the area of Applied Mechanics worldwide who has not heard of P.S. Theocaris.

The topics covered in the book can be divided into three major themes:

- Mathematical methods in applied mechanics (nine papers)
- Experimental mechanics (nine papers)
- Fracture mechanics (six papers)

The papers appear by alphabetical order of the corresponding author in each theme. The various topics discussed within each theme are as follows:

Mathematical Methods in Applied Mechanics

"Application of Reciprocity Relations to Laser-Based Ultrasonics," by J.D. Achenbach, discusses an application of the reciprocity theorem for thermo-anisotropic elastodynamics of inhomogeneous solids. The theorem relates body forces, surface tractions, displacements, temperatures and strains of two solutions of the field equations. It is used to analyze the dynamic response to high-intensity heating of a small surface region of a half-space that is transversely isotropic and whose elastic moduli and mass density depend on the depth coordinate.

"An Asymptotic Method of Boundary-Value Problems Solution of Elasticity Theory for Thin Bodies," by L.A. Aghalovyan discusses an asymptotic method for the solution of the first, second and mixed boundary value problems of elasticity theory for layered beams, plates and shells. The method permits the solution of dynamic problems of thin bodies. General asymptotic solutions are obtained.

"Reliable Optimal Design in Contact Mechanics," by N.V. Banichuk, S. Yu. Ivanova and E.V. Makeev formulates the problem of contact pressure optimization for the case of a rigid punch interacted with an elastic medium. The shape of the punch is considered as an unknown design variable. The total forces and moments applied to the punch and the loads acted at the outside regions are given. Optimal shapes are found analytically for punches having rectangular contact domains.

"Scaling of Strength and Lifetime Distributions of Quasibrittle Structures," by Z.P. Bažant and J.-L. Le presents a refined theory on the strength distribution of quasibrittle structures, which is based on the fracture mechanics of nanocracks propagating by activation energy controlled small jumps through a nano-structure and an analytical model for the multi-scale transition of strength statistics. It is shown that the theory matches the experimentally observed systematic deviations of strength and lifetime histograms of industrial ceramics from the Weibull distribution.

"Directional Distortional Hardening in Plasticity within Thermodynamics," by Y.F. Dafalias and H.P. Feigenbaum presents a complete theory for metal plasticity that includes directional distortional hardening supplemented by the classical kinematic and isotropic hardenings. It is shown that the theory fits well experimentally found yield surfaces and can be used to simulate stress controlled biaxial ratcheting with good accuracy.

"Forced Vibrations of the System: Structure – Viscoelastic Layer," by B.V. Gusev and A. S. Faivusovich presents analytical solutions of the problem of inter-related vibrations of an elastic structure with viscoelastic layer. The investigations were made to work out the method of the dynamical computation and optimization of technological processes for forming reinforced concrete articles on the shock and vibration machines and shock machines developed by the authors were used. Numerical results and experimental data were presented.

"Extreme Instability Phenomena in Autonomous Weakly Damped Systems: Hopf Bifurcations, Double Pure Imaginary Eigenvalues, Load Discontinuity," by A.N. Kounadis reconsiders the dynamic asymptotic instability of autonomous multi-parameter discrete systems under step compressive loading (conservative or nonconservative) using the efficient - and rather forgotten - Lienard-Chipart stability criterion. Attention is focused on the interaction of nonuniform mass distribution and infinitesimal damping which may have a tremendous effect on the Jacobian eigenvalues and thereafter on the local asymptotic instability.

"Variational Approach to Static and Dynamic Elasticity Problems," by G.G. Kostin and V.V. Saurin considers the integrodifferential approach incorporated in the variational technique for linear elastic static and dynamic problems. A family of static and dynamical variational principles, in which displacement, stress, and momentum fields are varied, is proposed. A regular numerical algorithm of

constrained minimization for the initial-boundary value problem is developed. The case of an optimization problem of lateral controlled motions of a 3D rectilinear elastic prism with a rectangular cross section is investigated.

"An Accelerated Newmark Scheme for Integrating the Equation of Motion of Nonlinear Systems Comprising Restoring Elements Governed by Fractional Derivatives," by G.I. Evangelatos and Pol. D. Spanos develops a new algorithm for numerical integration of the equations of motion of a nonlinear system with damping governed by fractional derivatives in the time domain. The major advantage of this approach is that, a very small number of past terms are required and, the calculation of the effective values of mass damping and stiffness is performed only once.

Experimental Mechanics

"Photoelastic Tomography as Hybrid Mechanics," by H. Aben, L. Ainola, and A. Errapart develops a non-destructive method based on the use of equations of the theory of elasticity and hybrid algorithms for the determination of axisymmetric stress fields in arbitrary sections of test objects. The method is used for the determination of residual stresses in glass.

"Using an Electronic Speckle Interferometry for Measurement of a Stress-Deformation State of Elastic Bodies and Structures," by R.V. Goldstein, V.M. Kozintsev and A.L. Popov presents the method and related equipment of the electronic speckle pattern interferometry (ESPI) for studying stress and deformation fields in elastic bodies and structures. ESPI is used for measurement of residual stresses in welded structures, micro-displacements related to delamination of thin coatings, diagnostics of shrinkage stresses in coatings and determination of their elastic characteristics. The method is generalized for measuring displacements at the nanometer scale.

"Structural Integrity and Residual Strength of Composites Exposed to Fire," by G.A. Kardomateas studies the compressive response of an axially restrained composite column, which is exposed to a heat flux due to fire by analytical and experimental means. The column is exposed to fire from one-side and an analytical approach is outlined for the resulting heat damage, the charred layer formation and non-uniform transient temperature distribution. Due to the nonuniform stiffness and the effect of the ensuing thermal moment, the structure behaves like an imperfect column, and responds by bending rather than buckling in the classical Euler (bifurcation) sense.

"Theory and Application of Sampling Moiré Method." by Y. Morimoto and M. Fujigaki introduces the theory of sampling moiré and uses it for the measurement of the displacements of a beam and the shape and strains of a rubber structure. The method uses an image processor of a grating pattern on an object recorded by a digital camera. It has the advantage of non-contact measurement of displacements with simplicity, high accuracy, high speed, and low cost. The method can easily be applied to dynamic problems with a high-speed camera.

"Recent Advances in Microelectromechanical Systems and their Applications for Future Challenges," by R.J. Pryputniewicz presents recent advances in optoelectronic methodology for micro- and nano-scale measurements and their use is

illustrated with representative examples of microelectromechanical systems (MEMS) operating at high frequencies and used in demanding environments. Advances in emerging technologies of MEMS and nanotechnology, especially relating to the applications, constitute one of the most challenging tasks in today's micromechanics and nanomechanics. Development of miniscule devices requires sophisticated design, analysis, fabrication, testing, and characterization tools and should be based on a combined use of the analytical, computational, and experimental solutions methodology.

"Experimental Mechanics in Nano-Engineering," by C.A. Sciammarella, F.M. Sciammarella and L. Lamberti presents a new approach to studies at the nano-scale based on the use of evanescent illumination. The proposed methodology provides the means of measuring the dimensions and shapes of objects, surface topography, roughness and strains allowing the precise detection of information at the nano-scale. It is shown that evanescent illumination is the key to making experimental mechanics methodologies well suitable for nano-engineering applications. Nanometer resolutions were achieved by using experimental setups that included a conventional optical microscope.

"Advanced Cement Based Nanocomposites," by S.P. Shah, M.S. Konsta-Gdoutos and Z.S. Metaxa studies the development of high-performance cementitious nanocomposites reinforced with multiwall carbon nanotubes (CNTs). Effective dispersion was achieved by applying ultrasonic energy and with the use of a surfactant. Fracture mechanics test results indicate that the fracture properties of cement matrix increased through proper dispersion of small amounts of CNTs (0.025wt% and 0.08wt%). Nanoindentation results suggest that CNTs can modify and reinforce the cement paste matrix at the nanoscale by increasing the amount of high stiffness C-S-H and decreasing the porosity, which leads to the reduction of the autogenous shrinkage.

"Application of Digital Speckle Pattern Interferometry (DSPI) in Determination of Elastic Modulus Using Plate Vibration," by Ch. Shakher and R. Kumar presents a technique for the evaluation of the elastic modulus of materials based on the vibration analysis of a plate using digital speckle pattern interferometry and the Rayleigh method. A series of experiments were conducted on square aluminium plates with one edge fixed and other edges free. The experimental results show that a single observation of frequency at first torsional mode is sufficient to determine the elastic modulus for all practical purposes.

"The Development and Applications of Amplitude Fluctuation Electronic Speckle Pattern Interferometry Method," by W.-C. Wang and C.-H. Hwang presents the development and improvement of an amplitude fluctuation electronic speckle pattern interferometry (ESPI) method. The effects of environmental noise and vibration characteristics on the ESPI fringe pattern are investigated. Theoretical derivation of the effect of environmental noise is performed and the time varying brightness of the traditional time averaged (TA) ESPI fringe patterns is successfully explained. Furthermore, applications of the method are briefly reviewed.

Fracture Mechanics

"Piezonuclear Transmutations in Brittle Rocks under Mechanical Loading: Microchemical Analysis and Geological Confirmations," by A. Carpinteri, G. Lacidogna, A. Manuello and O. Borla reports Neutron emission measurements by means of ^{3}He devices and neutron bubble detectors during three different kinds of compression tests on brittle rocks: (i) under displacement control, (ii) under cyclic loading, and (iii) by ultrasonic vibration. It is shown that piezonuclear reactions giving rise to neutron emissions are possible in inert non-radioactive solids under loading.

"Stress Triaxiality at Crack Tips Studied by Caustics," by E.E. Gdoutos studies the three-dimensional nature of the stress field in the vicinity of the crack tip. It also analyzes the conditions that should be satisfied among the dimensions of the optical arrangement and the specimen properties and thickness in order the caustic to be generated by the light rays transmitted or reflected from the region of the specimen where plane stress conditions dominate.

"Reinforcement of a Cracked Infinite Elastic Plate with Defects," by S.M. Mkhitaryan and D.I. Bardzokas studies a series of linear elastic crack problems with reinforcements, that are classified as contact problems, and are treated by using complex analysis and singular integral equations. The optimal position of the reinforcement can be selected in order to obtain lower stress intensity factors at the crack tips.

"Some Actual Problems of Fracture Mechanics of Materials and Structures," by V.V. Panasyuk and I.M. Dmytrakh presents some theoretical and experimental results on problems of fracture mechanics of materials and on durability of structural elements. Conceptual problems of fracture mechanics and strength of cracked materials are formulated. Furthermore, actual problems of fracture mechanics and strength of materials in service environments are considered.

"Cyclic Plasticity with an Application to Extremely Low Cycle Fatigue of Structural Steel," by D. Sumarac and Z. Petrašković shows that the Preisach model has several advantages when it is applied to the problem of so called cyclic stable plasticity of axially loaded members. The model is applied to extremely low fatigue. This case is very important for design of dampers applied for reconstruction of seismically damaged structures, because the Manson-Coffin Law overestimates the number of cycles before failure.

"The Fracture Toughness of a Highly Filled Polymer Composite," by O.A. Stapountzi, M.N. Charalambides and J.G. Williams reports fracture toughness values for an ATH-PMMA composite for filler volume fractions ranging from 0.35 to 0.49 and tested over the temperature range from 0 to 90 °C. It is obtained that the toughness decreases with increasing filler content contrary to expectations. Using a toughness model it was possible to calculate the adhesion energy of the particles and the average particle size.

It is with profound sorrow to announce the unexpected death of one of the authors of the book Professor Dimos Bartzokas. Dimos was a colleague at the National Technical University of Athens, and a good friend. May his memory be eternal.

    We would like to thank the authors who accepted the editors' invitation to participate in the symposium and to contribute to this book. Thanks are also due to the Academy of Athens, the National Technical University of Athens, the Pericles S. Theocaris Foundation and Ms Eugenia Theocaris who sponsored this symposium. A special word of thanks goes to Mrs. Nathalie Jacobs of Springer for her kind and continuous collaboration and support and the esthetic appearance of this book.

    With humble respect to the memory of the late Professor and Academician P.S. Theocaris, we present this book to the mechanics community as a small tribute to his service, leadership and contributions to the mechanics community.

September 2010   *A.N. Kounadis*
                                                                                   E.E. Gdoutos

Pericles S. Theocaris
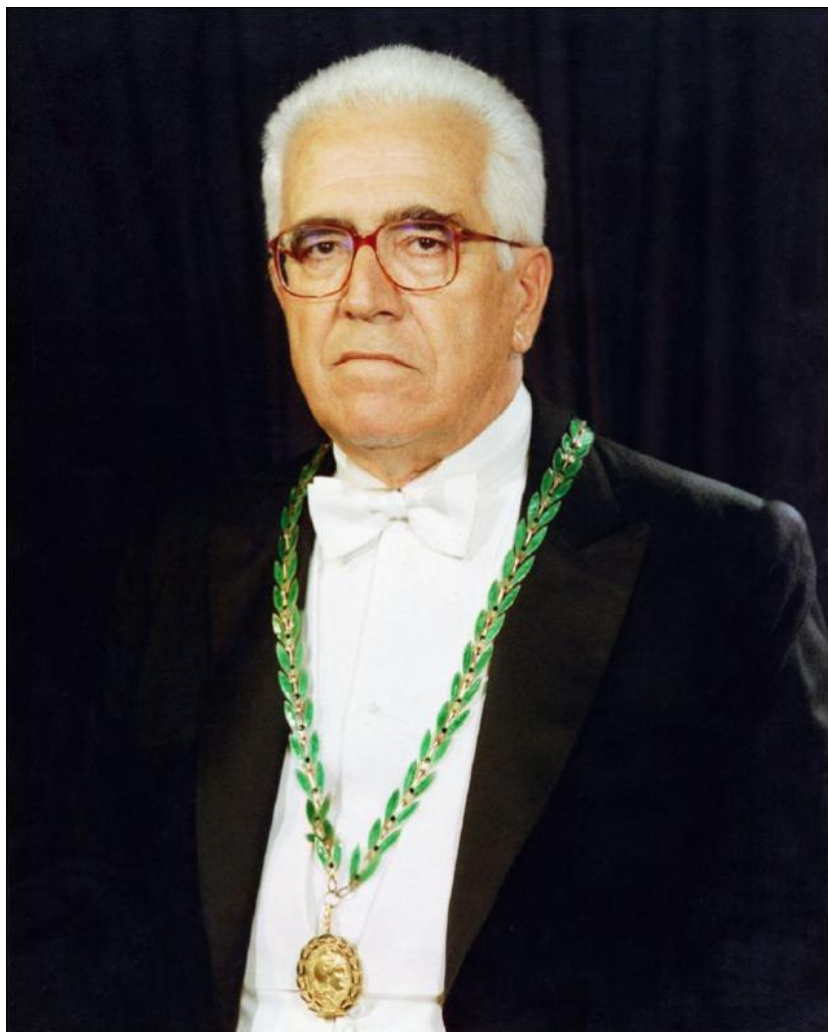
Biography

Pericles S. Theocaris
Professor - Academician

P.S. Theocaris was descendant of a noble family from the heroic town of Kalavryta of the prefecture of Patras, Greece, son of the army General Stavros Theocaris. He was born in Athens on September 24, 1921. He registered in the Hellenic Military Academy of Athens in 1938. As a junior student he participated in the Greek-Italian war of 1940 and served for six months in the Albanian front. For his heroic acts during the war he was decorated with the *Golden Medal of Bravery.*

In 1942 he registered at the National Technical University of Athens (NTUA) and graduated in 1948 with the Diploma of Mechanical-Electrical engineer, first in his class with the highest degree among all classes of all Schools of NTUA. During his studies he was awarded five prizes. From January 1949 to April 1951 he served in the Army as a captain of the Technical Corps.

In 1951 he obtained a fellowship for specialized studies at M.I.T. (U.S.A.) for six months. He was awarded a scholarship by the University of Brussels and a scholarship the French government for postgraduate studies. He obtained: a) the degree of Doctor of Applied Sciences, with Great Distinction from the University of Brussels in March 1953*, and b)* in November 1953 the degree of Doctor of Physical Sciences from the University of Paris with very honorable mention.

In September 1957 he obtained a fellowship at the National Academy of Sciences and National Research Council of the U.S.A. and he was appointed Visiting Research Fellow at the Illinois Institute of Technology, in Chicago. In 1958 he was appointed Visiting Assistant Professor at Brown University, U.S.A.

In 1960 he was elected Professor and Director of the Laboratory for Testing Materials (LTM) at the Athens National Technical University. During his directorship LTM was classified as one of the best laboratories of testing materials worldwide. He was invited by the French government to be Research Visitor at the Central Laboratory of Bridges and Roads of the Ministry of Public Works of France. In 1963 he was appointed Visiting Professor at the Department of Mechanics of Pennsylvania State University, U.S.A. In October 1965 he was a Research Visitor at the Ernst Mach Institute of the University of Freiburg, Germany.

In 1968 he was elected Professor (Full) at the Chair of Theoretical and Applied Mechanics of NTUA. In 1969 he served as Member of the Senate of NTUA. He was elected Rector of the National technical University of Athens twice in 1974 and in 1979 and contributed to the foundation of the Technical University of Crete

as President of the Board of Trustees (1974 - 1979). In 1980 he was honored with the title of "Rector Magnificus" of the National Technical University of Athens.

- In 1973 he was elected member of the National Academy of Athens (Section of Sciences).
- In 1983 he was elected President of the Academy of Athens and during the period 1989-1994 Secretary General.
- In 1974 he was appointed Vice-Minister of National Education in the caretaker government of Greece and Vice-President of the board of Trustees of the National Observatory of Athens.
- From 1989 to 1991 he was appointed Secretary General in the General Secretariat of Research and Development.
- In September 1978, he served as President of the Greek Council for the Exhibition of Greek Antiquities in Paris, New York and Moscow under the title: Greek Art of the Aegean Islands (1979).
- From 1980 to 1987 he served as Scientific Greek Representative to the International Council of Scientific Unions (ICSU).
- In October 1982 he was elected fellow of the Archeological Society of Athens.
- From 1978 until 1995 he was President of the Hellenic Society of Theoretical and Applied Mechanics.
- He was member of the following National Academies: Royal Academy of Engineering of Great Britain, Serbian Academy of Sciences and Arts, Bulgarian Academy of Sciences, Academia Tiberina of Italy, International Academy of Sciences of Germany and of Academia Europea of which he was a founding member. In March 1991 he was elected member of Academia Scientiarum et Artium Europaea.
- He was member of many scientific councils and was awarded with the following prizes: Empeirikeion Prize, 1971 (President of the Empeirikeion Foundation in 1974), Bernard Hall Prize of Great Britain (1974), Aurel Vlaicou Prize of Romania (1980)
- In 1996 the Aristotelean University of Thessaloniki and in 1999 the Democritus University of Thrace granted him the degree of Doctor of Science honoris causa.

He received the following military medals:

- Golden Medal of Bravery
- Silver Cross with Swords of the Order of King George A
- Military Cross
- Medal of Extraordinary Actions
- Medal of the Greek-Italian war

For his scientific activities, his contribution to the advancement of the science of Mechanics he was awarded the following medals:

- Golden Cross of the Order of King George A
- Commander of the Order of Phoenix

- ▪ Commander of the Order of Valour
- ▪ Grand Cross of Merit of the Patriarchate of Alexandria and all Africa
- ▪ Notable Castrinsius of the Holy See of the Patriarchate of Canstantinople
- ▪ Finally, in July 8, 1999 the President of the Hellenic Republic bestowed him the Great Brigade of the Order of Merit

His scientific work includes 948 papers and books. During the years 1988-1997 he was the author with the greatest number of published papers in Applied Mechanics, according to the journal of Applied Mechanics Reviews.

P.S. Theocaris, in addition to his above-mentioned scientific work in *Mechanics and Applied Mathematics,* published exceptional articles for the history of Hellenic Science from Homeric to Byzantine era as well as studies of purely historic nature, in general.

He started his life as a hero of the Greek-Italian war in the Albanian front, continued with an outstanding academic career to become finally adorer of the Hellenic Ideal, to a true hierophant of science, and a distinguished leader of the modern Hellenism.

P.S. Theocaris passed away on September 14, 1999.

Research Activities

General Description

Professor P.S. Theocaris published 948 books and papers. They may be grouped in the following nine main categories:

(1) *One hundred and sixty papers, which deal with problems of elasticity and plasticity by optical methods.* New theoretical methods based on the theory of complex variables and the properties of isostatics were introduced by P.S. Theocaris. The experimental solution of elastic-plastic problems by using the experimental methods of photoelastic coatings, moiré and the electrical analogies were advanced for the first time. The photoelastic method (classical and photoelastic coatings) was extended in different problems of the praxis and important applications were introduced. The matrix theory based on the Muller and Jones calculus and the Poincaré sphere were developed. These developments were included in an authoritative book published by Springer-Verlag. Closed-form solutions for solving systems of higher order differential equations and closed-form solutions to difficult problems of complicated shell-, beam- and frame-structures in civil engineering were introduced in an elegant manner.

(2) *He developed the experimental method of moiré for evaluating displacement and strain fields.* Seventy one papers deal exclusively with the method. He authored the first book on moiré fringes entitled "*Moiré Fringes in Strain Analysis*", published by Pergamon Press in 1969.

(3) *Viscoelasticity and rheology of high polymers, also including the mesophase model* was another area of his scientific activities. Ninety seven papers deal exclusively with this subject. P.S. Theocaris extended the

time-temperature superposition principle, valid for the mechanical properties of high polymers, to their optical properties and introduced important laws in this area of knowledge.

    (4)   *The optical method of caustics is an exclusive field of his research*. He published two hundred twenty five papers in this area.

    (5)   *Solutions to integral equations with singularities*. He has contributed one hundred fourteen papers. He progressed the state-of-the-art from the theoretical point of view**,** but mainly from the numerical and applications-point of view.

    (6)   *The theory of fracture takes up a large part of his research time.* Eighty-nine papers were published all over the world in this field. Theoretical and experimental studies in this domain concern the static and dynamic behavior of fracture bodies. A main contribution in this field is the introduction of a new fracture criterion, the **T-criterion** which, for the first time, takes into account, in a rational way from the point of view of physical properties of the materials, the contribution of the distortions and dilatational components of energy for initiation of fracture.

    (7)   *Dynamic and impact phenomena* have also been studied by Professor P.S. Theocaris in sixty papers mainly related to this subject.

    (8)   *Ninety-three papers deal with modern composite materials, fiber-reinforced and particulates.* New viscoelastic theories and models were introduced, especially the models taking into consideration the interphase between main phases of the composite. The theories developed in this field and especially the interphase model made his contributions well-known throughout the world. A book published by Springer-Verlag was devoted to this subject.

    (9)   *A new failure criterion based on the theory of Failure Tensor Polynomials was introduced and developed by P.S. Theocaris*. This takes into consideration in a rational way the contribution of all components of strain energy density of the materials and is convenient for any type of material, even the most anisotropic. This criterion is based on principles of the components of the strain energy and was applied to different orthotropic materials, transversely isotropic, foamy materials, as well as porous and microstructures. Forty papers dealing with applications of this criterion were published.

Books

1.   "Moiré Fringes in Strain Analysis." This is the first book dealing exclusively with applications of moiré fringes in the metrology of deformations, Pergamon Press, London, 426 pages, 1969.
2.   "Miarovsie Polos pri Isledovanii Defonnatii." The previous book was translated into Russian by Prof. B.N. Uchachov of the Polytechnic University of Moscow and published by MIR Publishing Co. of Moscow, 1971.
3.   "Experimental Mechanics of Materials," Technical University Press, 580 pages. 1970 (in Greek).
4.   "Experimental Stress Analysis," Technical University Press, 430 pages, 1974 (in Greek).
5.   "Moiré Fringes in Strain Analysis," Technical University Press, 447 pages, 1974, Translation into Greek of book No. 1.

6. "Matrix Theory in Photoelasticity," Springer-Verlag Series in Optical Sciences, Vol. 11, Springer-Verlag, 1979 (with Professor E.E. Gdoutos)
7. "Mixed Mode Crack Propagation" Edited by G. Sih and P.S. Theocaris, Sijthoff & Noordhoff, Holland, 1981.
8. "Compedium in Astronomy," Edited by E. Mariolopoulos, P.S. Theocaris and L. Mavridis, D. Reidel Publishing Co., Holland, 1982.
9. "Interrelation Between Processing, Structure and Properties of Polymeric Materials," IUPAC International Symposium, Athens 1982, J. Seferis and P.S. Theocaris, Editors, Elsevier, Netherlands, 1984.
10. "The Concept of Mesophase in Composites," Springer-Verlag, 1985.

Monographs

"Experimental Study of the Stability of Parthenon", *Transactions of the National Academy of Athens*, Vol. 44, No.4, p.116, 1979 (with E. Koroneos).

Book Chapters

1   "Studiul Cimpurilor de Tensiuni Singulare Ci Ajutorul Causticelor." (La Methode des Caustiques a L'etude de Champs des Contraintes Singuliers). Chapter VI in *Handbook on Applications of Stress Methods* (Book in Romanian, Professor D.R. Mocanu, Editor) 1977.
2   "Methods Kaustik-Nova Doswiadczaina Badania Osobliwosci Pola Naprazenia," Review paper about caustics in Polish published by the Polish Academy.
3   "Stresses in Three-Dimensional Composites with Limiting Shear Properties," *Development in Composite Materials*, Chapter 9, G.S. Holister Editor, Applied Science Publishers, England, 1977.
4   "Modern Methods in Polarization Optics," *Developments in Stress Analysis 1*, Chapter 3, G.S. Holister Editor, Applied Science Publishers, England, 1979.
5   "The Method of Caustics Applied to Elasticity Problems," *Developments in Stress Analysis 1*, Chapter 2, G.S. Holister, Editor, Applied Science Publishers, England, 1979.
6   "Elastic Stress Intensity Factors Evaluated by Caustics: Experimental Determination of Crack-Tip Stress Intensity Factors," *Mechanics of Fracture. Vol. VII,* G. Sih, Editor, 1980.
7   "The Interphase and its Influence on the Mechanical Properties of Composites," *"New Developments in the Characterization of Polymers in the Solid State - Advances in Polymer Science,"* H.H. Kausch and H.G. Zachmann Editors, Springer Publ., Germany, 1984.
8   "Crack Propagation Modes in Composites: The Influence of Mesophase," *Handbook of Advanced Materials Testing*, Vol. II., Chapter 26, N.P. Cheremisinoff, Editor, M. Dekker, Publ., N. Jersey, U.S.A., 1994.

9   "Failure Criteria for Anisotropic Bodies," *Handbook of Fatigue Crack Propagation in Metallic Structures,* Vol. 1, Chapter 1, A. Carpinteri, Editor, Elsevier Publ. Amsterdam, 1994.

10 "New Methods in Studying Fracture and Failure Mechanics," *A.A. Griffith's Memorial Volume*, C. Cherepanov Editor, Krieger Publ., U.S.A., 1996.

Participation in Societies and Congresses

Professor P.S. Theocaris was a member of the following Societies:

Society for Experimental Stress Analysis (U.S.A., from 1954, Fellow from 1987), **Groupement pour l' Avancement des Methodes d' Analyse des Contraintes** (France, from 1954), **Societe Royale Belge des Ingenieurs et des Industriels** (Belgium, from 1954), **American Society of Mechanical Engineers** (from 1955), **Society of the Sigma-Xi** (U.S.A., from 1958), **International Association for Bridges and Structural Engineering** (Switzerland, from 1962), Delegate for Greece at the **Reunion Internationale des Laboratoires d' Essais des Materiaux** (from 1961), **Optical Society of America** (from 1971), and **American Association for the Advancement of Science**.

He participated in many international and national congresses of Mechanics, Experimental Mechanics, Fracture Mechanics, Rheology, Optics, Composite Materials, etc. with paper presentations in the U.S.A., France, England, Switzerland, Germany, Italy, Poland, Romania, Russia and Japan.

Contents

Part III: Fracture Mechanics

Contributors

H. Aben,
Institute of Cybernetics,
Tallinn University of Technology,
21 Akadeemia tee,
12618 Tallinn,
Estonia

J.D. Achenbach,
Department of Mechanical
Engineering, Northwestern
University,
Evanston, IL 60208, USA

L.A. Aghalovyan,
Institute of Mechanics of
National Academy of
Sciences of Armenia,
Armenia

L. Ainola,
Institute of Cybernetics,
Tallinn University of Technology,
21 Akadeemia tee,
12618 Tallinn, Estonia

N.V. Banichuk,
A. Yu. Ishlinsky Institute for
Problems in Mechanics,
Russian Academy of Sciences,
Moscow, Russia

D.I. Bardzokas,
National Technical University of
Athens, School of Applied
Mathematical and Physical Sciences,
Department of Mechanics, Athens
Greece

Z.P. Bažant,
Department of Civil and Environmental
Engineering, Northwestern University,
Evanston, IL 60208, USA

O. Borla,
Politecnico di Torino, Department of
Structural Engineering & Geotechnics,
Corso Duca degli Abruzzi 24 – 10129
Torino, Italy, and Istituto Nazionale di
Fisica Nucleare, INFN sez. Torino, Via
Pietro Giuria 1 – 10125 Torino, Italy

A. Carpinteri,
Politecnico di Torino, Department of
Structural Engineering & Geotechnics,
Corso Duca degli Abruzzi 24 – 10129
Torino, Italy

M.N. Charalambides,
Mechanical Engineering Department,
Imperial College, London, UK

Y.F. Dafalias,
Department of Mechanics,
Faculty of Applied Mathematical and
Physical Science, National Technical,
University of Athens, Zographou,
Hellas, and Department of Civil and
Environmental Engineering, University
of California, Davis CA, USA

I. Dmytrakh,
Karpenko Physico-Mechanical Institute
of National Academy of Sciences of
Ukraine, 5 Naukova Street, 79601,
Lviv, Ukraine

A. Errapart,
Institute of Cybernetics, Tallinn
University of Technology,
21 Akadeemia tee, 12618 Tallinn,
Estonia

G.I. Evangelatos,
Rice University, Department of Civil
Engineering, Houston, Texas, USA

A.S. Faivusovich,
Lugansk National Agrarian University
91008, Lugansk, Ukraine

H.P. Feigenbaum,
Department of Mechanical Engineering,
Northern Arizona University,
Flagstaff AZ, USA

M. Fujigaki,
Department of Opto-Mechatronics,
Faculty of Systems Engineering,
Wakayama University, 930 Sakaedani,
Wakayama 640-8510, Japan

E.E. Gdoutos,
Office of Theoretical and Applied
Mechanics of the Academy of Athens,
School of Engineering, Democritus
University of Thrace,
GR-671 00 Xanthi, Greece

R.V. Goldstein,
A.Yu.Ishlinsky Institute for
Problems in Mechanics, the Russian
Academy of Sciences, 119526,
Vernadskogo 101, Moscow, Russia

B.V. Gusev,
Moscow State University of Railway
Engineering (MIIT) 125009, Moscow,
Russia

C.-H. Hwang,
Instrument Technology Research Center,
National Applied Research Laboratories,
Taiwan, Republic of China

S. Yu. Ivanova,
A. Yu. Ishlinsky Institute for Problems
in Mechanics, Russian Academy of
Sciences, Moscow, Russia

G.A. Kardomateas,
School of Aerospace Engineering,
Georgia Institute of Technology,
Atlanta, Georgia 30332-0150, USA

M.S. Konsta-Gdoutos,
School of Engineering,
Democritus University of Thrace,
GR-67100, Xanthi, Greece

G.V. Kostin,
Institute for Problems in Mechanics of
the Russian Academy of Sciences,
pr. Vernadskogo, 101-1,
119526 Moscow, Russia

A.N. Kounadis,
Academy of Athens, Soranou Efessiou
4, GR-115 27 Athens, Greece

V.M. Kozintsev,
A.Yu.Ishlinsky Institute for Problems in
Mechanics, the Russian Academy of
Sciences, 119526, Vernadskogo 101,
Moscow, Russia

R. Kumar,
Department of Mechanical Engineering,
Sant Longowal Institute of Engineering
and Technology, Longowal – 148 106
(Punjab), India

G. Lacidogna,
Politecnico di Torino, Department of
Structural Engineering & Geotechnics,
Corso Duca degli Abruzzi 24 – 10129
Torino, Italy

L. Lamberti,
Dipartimento di Ingegneria Meccanica
e Gestionale, Politecnico di Bari, Bari,
Italy

J.-L. Le,
Department of Civil and
Environmental Engineering,
Northwestern University,
Evanston, IL 60208, USA

E.V. Makeev,
A. Yu. Ishlinsky Institute for Problems
in Mechanics, Russian Academy of
Sciences, Moscow, Russia

A. Manuello,
Politecnico di Torino, Department of
Structural Engineering & Geotechnics,
Corso Duca degli Abruzzi 24 – 10129
Torino, Italy

Z.S. Metaxa,
School of Engineering, Democritus
University of Thrace, GR-67100,
Xanthi, Greece

S.M. Mkhitaryan,
Institute of Mechanics of NAS RA,
Yerevan, Armenia

Y. Morimoto,
Moire Institute Inc., 2-1-4-804,
Hagurazaki, Izumisano,
Osaka 598-0046, Japan

V. Panasyuk,
Karpenko Physico-Mechanical
Institute of National Academy of
Sciences of Ukraine, 5 Naukova
Street, 79601, Lviv, Ukraine

Z. Petrašković,
Research-productive Centre System
DC 90, 11000 Belgrade, Serbia

A.L. Popov,
A.Yu. Ishlinsky Institute for
Problems in Mechanics, the Russian
Academy of Sciences,
119526, Vernadskogo 101,
Moscow, Russia

R.J. Pryputniewicz,
NEST – NanoEngineering,
Science, and Technology,
CHSLT – Center for Holographic
Studies and Laser Micro-Mechatronics,
Mechanical Engineering Department
Professor of Electrical and
Computer Engineering,
Worcester Polytechnic Institute,
Worcester, MA 01609, USA

V.V. Saurin,
Institute for Problems in
Mechanics of the Russian
Academy of Sciences,
pr. Vernadskogo, 101-1, 119526
Moscow, Russia

C.A. Sciammarella,
College of Engineering &
Engineering Technology, Northern
Illinois University, DeKalb, USA

F.M. Sciammarella,
College of Engineering &
Engineering Technology, Northern
Illinois University, DeKalb, USA

S.P. Shah,
ACBM Center, Northwestern
University, 2145 Sheridan Road,
Suite A130, Evanston,
IL 60208, USA

Ch. Shakher,
Laser Applications and Holography
Laboratory, Instrument Design
Development Centre,
Indian Institute of Technology,
Delhi, New Delhi – 110 016,
India

Pol D. Spanos,
Rice University, Department of
Mechanical Engineering and
Materials Science, Houston, Texas,
USA

O.A. Stapountzi,
Mechanical Engineering
Department, Imperial College,
London, UK

D. Šumarac,
Faculty of Civil Engineering,
University of Belgrade,
Serbia

W.-C. Wang,
Department of Power Mechanical
Engineering, National Tsing Hua
University, Taiwan, Republic of China

J.G. Williams,
School of Aerospace, Mechanical &
Mechatronic Engineering,
University of Sydney, Australia

Part I
Mathematical Methods in Applied Mechanics

Application of Reciprocity Relations to Laser-Based Ultrasonics

Jan D. Achenbach

Department of Mechanical Engineering, Northwestern University,
Evanston, IL 60208, USA
`achenbach@northwestern.edu`

Abstract. An application of the global reciprocity theorem for thermo-anisotropic elastodynamics of inhomogeneous solids is discussed. The theorem relates body forces, surface tractions, displacements, temperatures and strains of two solutions of the field equations, states A and B, by integrals over a volume V and its bounding surface S. The difference between various anisotropies enters via the stress temperature tensor, which is different for different cases of anisotropy. The reciprocity theorem is used to analyze the dynamic response to high-intensity heating of a small surface region of a half-space that is transversely isotropic and whose elastic moduli and mass density depend on the depth coordinate.

1 Introduction

The reciprocity theorem for classical linearized elasticity has been known for more than a century. As stated in the book by Kovalenko [1], a first statement of the reciprocity theorem for isotropic thermoelasticity was presented by Maizel' [2]. Despite its long existence, the theorem was not used extensively to actually solve problems. A recent book by Achenbach [3] presents, however, novel uses of reciprocity relations for the actual determination of elastodynamic fields.

As an example, we consider the surface-wave motion generated by line-focus laser irradiation of a transversely isotropic half-space whose mechanical properties depend on the depth component z.

Due to length limitations of this paper, we are not able to elaborate as much as would be desirable, but details can be found in Refs. [4] and [5].

2 Thermo-anisotropic Elasticity

When a free cube of an anisotropic material is subjected to a uniform temperature T, the thermal strains, ε_{ks}^{T}, may be written in the general form

$$\varepsilon_{ks}^{T} = \alpha_{ks}T, \qquad \alpha_{ks} = \alpha_{sk,} \tag{1}$$

where α_{ks} are the components of the thermal expansion tensor. For a material with axes of symmetry that are aligned with the Cartesian coordinate axes, we may write

$$\alpha_{12} = \alpha_{23} = \alpha_{13} \equiv 0 \tag{2}$$

On the basis of a simple intuitive argument the thermo-anisotropic stress-strain relations may then be written as

$$\tau_{ij} = C_{ijks}(\varepsilon_{ks} - \alpha_{ks}T), \text{ or } \tau_{ij} = C_{ijks}\varepsilon_{ks} - m_{ij}T \tag{3a,b}$$

Where

$$m_{ij} = C_{ijks}\alpha_{ks} \tag{4}$$

are the components of the stress-temperature tensor. For the case that Eq.(2) holds the general stress-strain relation (6) reduces to

$$\tau_{ij} = C_{ijks}\varepsilon_{ks} - \overline{m}_{ij}T \tag{5}$$

Where

$$\overline{m}_{ij} = C_{ij11}\alpha_{11} + C_{ij22}\alpha_{22} + C_{ij33}\alpha_{33} \tag{6}$$

3 Reciprocity Theorem

For convenience of presentation we use indicial notation in this section. For the steady-state time-harmonic case, body forces, displacements, surface tractions and temperatures are defined by

$$f_i(\boldsymbol{x},t) = f_i(\boldsymbol{x})e^{-i\omega t}, \ u_i(\boldsymbol{x},t) = u_i(\boldsymbol{x})e^{-i\omega t}, \ t_i(\boldsymbol{x},t) = t_i(\boldsymbol{x})e^{-i\omega t},$$
$$T(\boldsymbol{x},t) = T(\boldsymbol{x})e^{-i\omega t} \tag{7}$$

Let us now consider a solid elastic body of volume V and bounding surface S. The two elasticodynamic states, are indicated by superscripts A and B. As shown in Ref [5] the reciprocity theorem for the two states may then by written as

$$\int_V (f_j^A u_j^B - f_j^B u_j^A)dV + \int_S (t_i^A u_i^B - t_i^B u_i^A)dS = -\overline{m}_{ij}\int_V \left(T^A \varepsilon_{ij}^B - T^B \varepsilon_{ij}^A \right)dV \tag{8}$$

The terms in the integrals, depend on x and z. For an isotropic material the reciprocity theorem in the form given here was apparently first derived by Maizel' [2].

The quantities indicated by superscripts A can be thought of as the solution of an actual problem, while B indicates an auxiliary solution, or in our terminology, a virtual wave. Let us consider the case that the disturbance for the actual problem is

generated strictly by a distribution of temperature $T^A(\mathbf{x})$, i.e., $f_j^A \equiv 0$. The virtual wave can be taken as isothermal ($T^B \equiv 0$) and with zero body forces, i.e., $f_j^B \equiv 0$. Equation (8) then reduces to

$$\int_S (t_i^A u_i^B - t_i^B u_i^A)\, dS = -\bar{m}_{ij} \int_V T^A \varepsilon_{ij}^B\, dV \tag{9}$$

4 Transverse Isotropy with Depth Dependent Properties

The stress-strain relations are referred to Cartesian coordinates, x and z. The z – axis is the axis of symmetry of the transverse isotropy. Relative to the x, z system the stress-strain relations for plane strain of the inhomogeneous transversely iso-tropic solid may be written as:

$$\tau_x = C_{11}(z)\frac{\partial u}{\partial x} + C_{13}(z)\frac{\partial w}{\partial z} - m_x T \text{ , and}$$
$$\tau_z = C_{13}(z)\frac{\partial u}{\partial x} + C_{33}(z)\frac{\partial w}{\partial z} - m_z T \tag{10a,b}$$

$$\tau_{xz} = C_{44}(z)\left(\frac{\partial u}{\partial z} + \frac{\partial w}{\partial x}\right) \tag{11}$$

It is noted that the elastic behavior depends on the depth z. Thus the material is inhomogeneous and the formulation includes functionally graded materials. In addition the mass density, $\rho(z)$ is also taken to depend on z. Here m_x and m_z are components of the stress-temperature tensor:

$$m_x = \alpha_x \left[C_{11}(z) + C_{12}(z) \right] + \alpha_z C_{13}(z) \text{ , and}$$
$$m_z = 2\alpha_x C_{13}(z) + \alpha_z C_{33}(z), \tag{12a,b}$$

Where α_x and α_z are components of the thermal expansion tensor.

5 Heating of the Boundary

Let us consider the case that thermal conductivity may be ignored, and that $T^A(x,t)$ is applied only to a boundary, which in this case is taken as the plane $z = 0$. The assumption that the thermal conductivity may be ignored, would gen-erally be a dubious one. However, if the heat is applied with a high-intensity pulse, as will be considered here, the resulting wave motion is also an intensive pulse which propagates away from the source of heat with a high velocity. The

principal pulse then comes directly from the source region. Additional wave motion due to diffusion of the heat will be of smaller magnitude and arrive later.

When T is applied on the boundary, the volume integral on the right hand side of Eq. (9) is converted into a surface integral. The vanishing of surface traction of state B, the virtual wave, has, however, implications for the form of $\bar{m}_{ij}\varepsilon_{ij}^B$. For example, for a transversely isotropic material we have at $z = 0$:

$$\tau_z^B = C_{13}\,\varepsilon_x^B + C_{33}\varepsilon_z = 0 \tag{13}$$

Hence

$$\varepsilon_z^{\;B} = -\frac{C_{13}}{C_{33}}\varepsilon_x^{\;B} \tag{14}$$

From Eqs. (5)-(6) and (11) it then follows that

$$\bar{m}_{ij}\varepsilon_{ij}^B = D_x\varepsilon_x^{\;B} - D_z\frac{C_{13}}{C_{33}}\varepsilon_x^{\;B} = -D\varepsilon_x^B \text{, where}$$

$$D = \frac{2C_{13}C_{13} - (C_{11}+C_{12})C_{33}}{C_{33}}\,\alpha_x \tag{15a,b}$$

Equation (15) is identical to the one obtained earlier by using an intuitive argument of thermal expansion of a surface element in Ref. [4].

When heat conduction is ignored, the temperature is governed by

$$\rho c_V \frac{\partial T}{\partial t} = q \,, \tag{16}$$

where ρ and c_V are the mass density and the specific heat at constant deformation, and q represents the heat deposition per unit volume and per unit time. The rate of heat production by mechanical deformation has been neglected. For the two-dimensional case of line illumination at $x = 0$, $z = 0$, a suitable expression for q is often taken as

$$q = \bar{E}(1 - R_i)\delta(x)g(t) \,, \tag{17}$$

where $\bar{E}$ is the energy of the laser pulse per unit length in the direction normal to the x,z plane, and R_i is the surface reflectivity. Integration of Eq.(15) then yields

$$T(t) = \frac{\bar{E}}{\rho c_V}(1 - R_i)\,\delta(x)\int_0^t g(s)ds \tag{18}$$

The function $g(s)$ can be represented by a Fourier integral

$$\hat{g}(\omega) = \frac{1}{2\pi}\int_{-\infty}^{\infty} g(t)\,e^{i\omega t}\,dt \tag{19}$$

In the frequency domain we write

$$\hat{T}(\omega) = -\frac{\overline{E}}{\rho c_V}(1 - R_i)\frac{1}{i\omega}\hat{g}(\omega) ,$$ (20)

For a line temperature application of the type given by Eq.(19), Eq.(9) becomes

$$\int_S (t_i^A u_i^B - t_i^B u_i^A)\,dS = D\hat{T}(\omega)\int_{-\infty}^{\infty}\delta(x)\varepsilon_x^B(x, z = 0)\,dx$$ (21)

6 Surface Waves due to Laser Irradiation

The line focus irradiation generates a two-dimensional, plane strain elastodynamic state. The corresponding radiated surface waves, which we call state A, may be written as

$$u^A(x, z) = \pm iAV(z)e^{\pm ik\,x} , \text{ and } w^A(x, z) = AW(z)e^{\pm ik\,x}$$ (22a,b)

Here the plus and minus signs apply for propagation in the positive and negative x- directions, i.e., for $x > 0$ and $x < 0$, respectively. The corresponding expressions for the stresses are

$$\tau_{11}^A(x, z) = AT_{11}(z)e^{\pm ik\,x} , \text{ and } \tau_{1z}^A(x, z) = \pm iAT_{1z}(z)e^{\pm ik\,x}$$ (23a,b)

For the special case that all elastic constants and the mass density have the same exponential dependence on z, details for these expressions are given in Ref. [6].

Following a method developed in Ref. [3], the surface waves generated by line-focus irradiation will be obtained by an application of the reciprocity theorem for time-harmonic wave motion given by Eq. (20). In the present application, State A is the system of surface waves generated by the laser illumination, as given by Eqs. (21)-(22). For State B, the virtual wave, we select a surface wave propagating in the positive x- direction:

$$u^B(x, z) = iBV(z)e^{ikx} , \text{ and } w^B(x, z) = BW(z)e^{ikx}$$ (24)

$$\tau_{11}^B(x, z) = BT_{11}(z)e^{ik\,x} , \text{ and } \tau_{1z}^B(x, z) = iBT_{1z}(z)e^{ik\,x}$$ (25)

For the problem at hand, and considering the contour shown in Fig. 1 by dashed lines, the reciprocity relation, Eq. (20), includes contributions from the lines at $x = a$, $0 \le z < \infty$, $x = b$, $0 \le z < \infty$ and from the temperature term at $x = 0$, $z = 0$. There are no other contributions from $z = 0$ and from the line $z =$ constant as $z \rightarrow \infty$. We obtain from Eq. (20)

$$-kD\hat{T}(\omega)V(0) = \int_0^{\infty} F_{AB}\mid_{x=b} dz - \int_0^{\infty} F_{AB}\mid_{x=a} dz,$$ (26)

Where

$$F_{AB}(x, z) = u^A\tau_{11}^B + w^A\tau_{1z}^B - u^B\tau_{11}^A - w^B\tau_{1z}^A$$ (27)
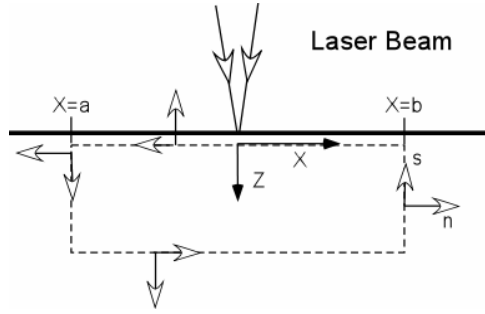
Fig. 1. Focused laser-beam irradiation of a solid body with contour for reciprocity relation

As has been noted in earlier calculations, see Ref. [3], the integration along $x = a, \quad 0 \le z < \infty$ and $x = b, \quad 0 \le z < \infty$, only yield contributions from counter-propagating waves. By the present choice of the virtual wave, State A and State B are counter-propagating at $x = a, \quad 0 \le z < \infty$. Substituting of the expressions for States A and B into Eq. (19) then yields

$$-kD\hat{T}(\omega)V(0) = 2iAI, \text{ where } I = \int_0^\infty \left[T_{11}(z)V(z) - T_{1z}(z)W(z) \right] dz \qquad \text{(28a,b)}$$

The integral involves exponential terms and can be easily evaluated, see Ref. [6].

Fourier analysis can be used to determine the surface wave displacement generated by a pulsed laser beam.

References

[1] Kovalenko, A.D.: Thermoelasticity, Wolters-Noordoff Publishing, Groningen, the Netherlands (1969)
[2] Maizel, V.M.: Generalization of the Betti-Maxwell theorem to the case of thermal stresses and some applications. In: DAN SSSR, vol. 30 (1941)
[3] Achenbach, J.D.: Reciprocity in Elastodynamics. Cambridge University Press, Cambridge (2003)
[4] Achenbach, J.D.: The Thermoelasticity of Laser-Based Ultrasonics. Journal of Thermal Stresses 28, 713–728 (2005)
[5] Achenbach, J.D.: Application of the Reciprocity Theorem to Analyze Ultrasound Generated by High-Intensity Surface Heating of Elastic Bodies. Journal of Thermal Stresses 30, 841–853 (2007)
[6] Kulkarni, S.S., Achenbach, J.D.: Application of the Reciprocity Theorem to Determine Line-Load Generated Surface Waves on an Inhomogeneous Transversely Isotropic Half-Space. Wave Motion 45, 350–360 (2008)

An Asymptotic Method of Boundary-Value Problems Solution of Elasticity Theory for Thin Bodies

Lenser A. Aghalovyan

Institute of Mechanics of National Academy of Sciences of Armenia, Armenia
`aghal@mechins.sci.am`

Abstract. By an asymptotic method the solution of boundary value problems of elasticity theory for isotropic, anisotropic, layered beams, plates and shells is built. The first, second and the mixed boundary problems for one-layered and multy-layered beams, plates and shells are solved. The asymptotic method permits us to solve effectively dynamic problems for thin bodies. Free and forced vibrations are considered. General asymptotic solutions are obtained. The conditions of resonance rise are established.

1 Introduction

Thin bodies, met in various spheres of technics are characteristic so that one of their dimensions sharply differs from the two others. For beams and bars the length is much more than the dimensions of the cross-section, and for plates and shells the thickness is much less than their tangential dimensions. Therefore, passing to dimensionless coordinates in the equations of elasticity theory and using dimensionless displacements, these equations will contain small geometrical parameter ε. It has become clear, that the equations system of elasticity theory for thin bodies is singularly perturbed by small parameter [1]. The solution of such systems is combined from the solution of the inner problem (basic solution) and the solution for the boundary layer [1-4]:

$$I = I^{\text{int}} + I_b \tag{1}$$

In the paper by an asymptotic method the solution of the inner problem for isotropic, anisotropic, layered beams and bars, for plates and shells is built.

The solution for the boundary layer of the strip-rectangle, plates and shells is built. By the asymptotic method the second and the mixed boundary problems for thin bodies are solved [1,5,6]. The method permits us to solve effectively dynamic problems for thin bodies [6,7].

2 The Asymptotic Solution of the First Boundary Value Problem of Elasticity Theory for the Orthotropic Thermoelastic Strip: The Connection with the Classical Theories of Beams and Bars

Consider a plane, correspondingly simple problem, on the example of which the clear and sequential presentation of the essence of the asymptotic method and determination of possibilities of its application for solving more complicated problems is possible.

It is required to find the solution of the plane problem of thermoelasticity for orthotropic strip-rectangle $D = \{(x,y) : 0 \leq x \leq \ell, -h \leq y \leq h, \ell >> h\}$ under the boundary conditions of the first boundary-value problem of elasticity theory at $y = \pm h$

$$\sigma_{xy}(x,\pm h) = \pm X^{\pm}(x), \quad \sigma_{yy}(x,\pm h) = \pm Y^{\pm}(x) \tag{2}$$

and under the conditions at $x = 0, \ell$ (conditions of fastening), which are for now considered to be arbitrary.

In the equations of thermoelasticity by Duhamel-Neuman model, passing to dimensionless coordinates $\xi = x/\ell$, $\zeta = y/h$ and displacements $U = u/\ell$, $V = \mathrm{v}/\ell$, we get a singularly perturbed by small parametre $\varepsilon = h/\ell$ system

$$\frac{\partial \sigma_{xx}}{\partial \xi} + \varepsilon^{-1} \frac{\partial \sigma_{xy}}{\partial \zeta} + \ell F_x(\xi, \zeta) = 0$$

$$\frac{\partial \sigma_{xy}}{\partial \xi} + \varepsilon^{-1} \frac{\partial \sigma_{yy}}{\partial \zeta} + \ell F_y(\xi, \zeta) = 0$$

$$\frac{\partial U}{\partial \xi} = a_{11}\sigma_{xx} + a_{12}\sigma_{yy} + \alpha_{11}\theta(\xi, \zeta) \tag{3}$$

$$\varepsilon^{-1} \frac{\partial V}{\partial \zeta} = a_{12}\sigma_{xx} + a_{22}\sigma_{yy} + \alpha_{22}\theta(\xi, \zeta)$$

$$\varepsilon^{-1} \frac{\partial U}{\partial \zeta} + \frac{\partial V}{\partial \xi} = a_{66}\sigma_{xy} + \alpha_{12}\theta(\xi, \zeta)$$

where σ_{ij} are the stresses tensor components, a_{ij} are the elasticity constants, $\theta = T(x, y) - T_0(x, y)$ is the change of the temperature field, α_{ij} are the coefficients of the temperature extension, $X^{\pm}(x), Y^{\pm}(x)$ are the surface loading, F_x, F_y are the volume forces, for example, the weight ($F_x = 0, F_y = -\rho g$, ρ is density) or the reduced seismic loading by Mononobe model ($F_x = k_s \beta \gamma, F_y \approx 0,75 F_x$, k_s is the coefficient of seismicness, β is the coefficient of dynamicness, γ is the specific weight). The solution of system (3) has the form of (1), I^{int} is sought in the form of

$$I^{int} = \varepsilon^{q_Q + s} Q^{(s)}, \quad s = \overline{0, N} \tag{4}$$

The notation means $s = \overline{0, N}$ summing by the umbral index from $s = 0$ up to the number of the approximations $s = N$, Q is any of the sought stresses and displacements, the values q_Q are integers, characterizing the intensity (the asymptotic order) of the given value. They should be established so, that after the substitution (4) into the equations (3) the noncontradictory system for the successive determination of the coefficients $Q^{(s)}$ could be obtained. The obtained solution should satisfy the conditions on the facial surfaces of the thin body. The values q_Q sensitively reacts on the type of the boundary conditions on the facial surfaces. These values are determined by the only way. In case of the first boundary plane problem (2) for strip (isotropic and anisotropic).

$$q = -2 \ \ for \ \ \sigma_{xx}, \ \ q = -1 \ \ for \ \ \sigma_{xy}, \ q = 0 \ \ for \ \ \sigma_{yy}$$
$$q = -2 \ \ for \ \ u, \ \ q = -3 \ \ for \ \ v \tag{5}$$

Substituting (4), (5) into system (3) and equalizing in each equation the coefficients at the same degrees of ε, we obtain a recurrent system for determining the coefficients $Q^{(s)}$. With this the contribution of the volume forces and the temperature field will be the contribution order of the surface forces, if

$$\ell F_x = \varepsilon^{-2+s} F_x^{(s)}, \ \ \ell F_y = \varepsilon^{-1+s} F_y^{(s)}, \ \ \theta = \varepsilon^{-2+s} \theta^{(s)}$$
$$F_x^{(0)} = \varepsilon^2 \ell F_x, \ F_y^{(0)} = \varepsilon \ell F_y, \ \theta^{(0)} = \varepsilon^2 \theta, \ F_x^{(s)} = F_y^{(s)} = \theta^{(s)} = 0, \ \ s \neq 0 \tag{6}$$

Having solved the recurrent system, we get

$$V^{(s)} = \mathbf{v}^{(s)}(\xi) + \mathbf{v}_*^{(s)}(\xi, \zeta)$$

$$U^{(s)} = -\frac{d\mathbf{v}^{(s)}}{d\xi}\zeta + u^{(s)}(\xi) + u_*^{(s)}(\xi, \zeta)$$

$$\sigma_{xx}^{(s)} = -\frac{1}{a_{11}}\frac{d^2\mathbf{v}^{(s)}}{d\xi^2}\zeta + \frac{1}{a_{11}}\frac{du^{(s)}}{d\xi} + \sigma_{xx*}^{(s)}(\xi, \zeta)$$

$$\sigma_{xy}^{(s)} = \frac{1}{a_{11}}\frac{d^3\mathbf{v}^{(s)}}{d\xi^3}\frac{\zeta^2}{2} - \frac{1}{a_{11}}\frac{d^2u^{(s)}}{d\xi^2}\zeta + \sigma_{xy0}^{(s)}(\xi) + \sigma_{xy*}^{(s)}(\xi, \zeta) \tag{7}$$

$$\sigma_{yy}^{(s)} = -\frac{1}{a_{11}}\frac{d^4\mathbf{v}^{(s)}}{d\xi^4}\frac{\zeta^3}{6} + \frac{1}{a_{11}}\frac{d^3u^{(s)}}{d\xi^3}\frac{\zeta^2}{2} - \frac{d\sigma_{xy0}^{(s)}(\xi)}{d\xi}\zeta + \sigma_{yy0}^{(s)}(\xi) + \sigma_{yy*}^{(s)}(\xi, \zeta)$$

where

$$\mathbf{v}_*^{(s)} = \int_0^\zeta [a_{12}\sigma_{xx}^{(s-2)} + a_{22}\sigma_{yy}^{(s-4)} + \alpha_{22}\theta^{(s-2)}]d\zeta$$

$$u_*^{(s)} = \int_0^\zeta [a_{66}\sigma_{xy}^{(s-2)} + \alpha_{12}\theta^{(s-1)} - \frac{\partial \mathbf{v}_*^{(s)}}{\partial \xi}]d\zeta$$

$$\sigma_{xx*}^{(s)} = \frac{1}{a_{11}}[\frac{\partial u_*^{(s)}}{\partial \xi} + a_{12}\sigma_{yy}^{(s-2)} - \alpha_{11}\theta^{(s)}] \tag{8}$$

$$\sigma_{xy*}^{(s)} = -\int_0^\zeta [F_x^{(s)} + \frac{\partial \sigma_{xx*}^{(s)}}{\partial \xi}]d\zeta, \quad \sigma_{yy*}^{(s)} = -\int_0^\zeta [F_y^{(s)} + \frac{\partial \sigma_{xy*}^{(s)}}{\partial \xi}]d\zeta$$

$$Q^{(m)} \equiv 0, \quad Q_*^{(m)} \equiv 0, \ when \ m < 0$$

In solution (4), (7) the functions $u^{(s)}(\xi)$, $\mathbf{v}^{(s)}(\xi)$, $\sigma_{xy0}^{(s)}$, $\sigma_{yy0}^{(o)}$ are not known yet. They should be determined from the boundary conditions.

Having satisfied boundary conditions (2), $\sigma_{xy0}^{(s)}$, $\sigma_{yy0}^{(o)}$ are expressed by $u^{(s)}, \mathbf{v}^{(s)}$ which are determined from the equations

$$\frac{2}{a_{11}}\frac{d^2u^{(s)}}{\xi^2} = q_x^{(s)} \tag{9}$$

$$q_x^{(s)} = -[X^{+(s)} + X^{-(s)}] + \sigma_{xy*}^{(s)}(\xi, 1) - \sigma_{xy*}^{(s)}(\xi, -1)$$

$$\frac{2}{3a_{11}}\frac{d^4 v^{(s)}}{\xi^4} = q^{(s)}$$

$$q^{(s)} = Y^{+(s)} + Y^{-(s)} - \sigma_{yy*}^{(s)}(\xi,1) + \sigma_{yy*}^{(s)}(\xi,-1) + \tag{10}$$

$$+ \frac{d}{d\xi}[X^{+(s)} - X^{-(s)} - \sigma_{xy*}^{(s)}(\xi,1) - \sigma_{xy*}^{(s)}(\xi,-1)]$$

$$X^{\pm(0)} = \varepsilon X^{\pm}, Y^{\pm(0)} = Y^{\pm}, \quad X^{\pm(s)} = Y^{\pm(s)} = 0, \quad s \neq 0$$

therefore

$$\frac{2}{a_{11}}u^{(s)} = \int_0^\xi d\xi \int_0^\xi q_x^{(s)} d\xi + C_1^{(s)}\xi + C_2^{(s)}$$

$$\frac{2}{3a_{11}}v^{(s)} = \int_0^\xi d\xi \int_0^\xi d\xi \int_0^\xi d\xi \int_0^\xi q^{(s)} d\xi + C_3^{(s)}\frac{\xi^3}{3!} + C_4^{(s)}\frac{\xi^2}{2} + C_5^{(s)}\xi + C_6^{(s)} \tag{11}$$

According (7) the stresses values depend on the constants $C_1^{(s)}, C_3^{(s)}, C_4^{(s)}$, and the constants $C_2^{(s)}, C_5^{(s)}, C_6^{(s)}$ will characterize the rigid displacement, which can be eliminated, fastening one point, for example $O(0,0)$:

$$U^{(s)}(0,0) = 0, \quad V^{(s)}(0,0) = 0, \quad \left(\frac{\partial U^{(s)}}{\partial \zeta} - \frac{\partial V^{(s)}}{\partial \xi}\right)_{\substack{\xi=0 \\ \zeta=0}} = 0$$

If on the edges $x = 0, \ell$ the stresses or displacements values are given, for example

$$\text{a) } \sigma_{xx}(0,\zeta) = \varphi_1(\zeta), \quad \sigma_{xy}(0,\xi) = \varphi_2(\zeta)$$

$$\text{b) } u(0,\zeta) = \psi_1(\zeta), \quad v(0,\xi) = \psi_2(\zeta) \tag{12}$$

then it is obvious that it is impossible to satisfy conditions (12) by three constants $C_i^{(s)}$ in each point of the end-wall $x = 0$ or $x = \ell$, which once again confirms that the initial boundary-value problem is singularly perturbed. For satisfying conditions (12) it is necessary to have principally a new solution too, the solution of a boundary layer type is like that.

In order to build the solution of the boundary layer type near the end-wall $x = 0$, in equations (3) without accounting the volume forces and the temperature field (they are taken into account in the solution of the inner problem) we introduce a new substitution of the variable $\gamma = \xi / \varepsilon$, we ascribe index "b" to all the unknown and the solution of the new system will be sought in the form of the functions of the boundary layer type:

$$\sigma_{ijb}(\gamma,\zeta) = \varepsilon^{-1+s}\sigma_{ijb}^{(s)}(\zeta)\exp(-\lambda\gamma), \quad s = \overline{0,N}$$

$$(U_b, V_b) = \varepsilon^s (u_b^{(s)}(\zeta), v_b^{(s)}(\zeta))\exp(-\lambda\gamma) \tag{13}$$

where λ is for now an unknown number which characterizes the velocity of the values diminution when removing from the boundary. The sought values may be expressed through $\sigma_{yyb}^{(s)}$ by formulae

$$\sigma_{xxb}^{(s)} = \frac{1}{\lambda^2}\frac{d^2\sigma_{yyb}^{(s)}}{d\zeta^2}, \quad \sigma_{xyb}^{(s)} = \frac{1}{\lambda}\frac{d\sigma_{yyb}^{(s)}}{d\zeta}$$

$$u_b^{(s)} = -\left[\frac{a_{11}}{\lambda^3}\frac{d^2\sigma_{yyb}^{(s)}}{d\zeta^2} + \frac{a_{12}}{\lambda}\sigma_{yyb}^{(s)}\right], \quad v_b^{(s)} = -\left[\frac{a_{11}}{\lambda^4}\frac{d^3\sigma_{yyb}^{(s)}}{d\zeta^3} + \frac{a_{12}+a_{66}}{\lambda^2}\frac{d\sigma_{yyb}^{(s)}}{d\zeta}\right] \tag{14}$$

where $\sigma_{yyb}^{(s)}$ is determined from the equation

$$a_{11}\frac{d^4\sigma_{yyb}^{(s)}}{d\zeta^4} + \lambda^2(a_{66}+2a_{12})\frac{d^2\sigma_{yyb}^{(s)}}{d\zeta^2} + \lambda^4 a_{22}\sigma_{yyb}^{(s)} = 0 \tag{15}$$

The solution of the boundary layer should satisfy the boundary conditions

$$\sigma_{yyb}^{(s)}(\zeta = \pm1) = 0, \quad \sigma_{xyb}^{(s)}(\zeta = \pm1) = 0 \tag{16}$$

From the correlations (14) and conditions (16) a very important property follows – the stresses σ_{xxb}, σ_{xyb} in the arbitrary cross-section $\gamma = \gamma_k$ are self-balanced

$$\int_{-1}^{+1}\sigma_{xxb}(\gamma,\zeta)d\zeta = 0, \quad \int_{-1}^{+1}\zeta\sigma_{xxb}(\gamma,\zeta)d\zeta = 0, \quad \int_{-1}^{+1}\sigma_{xyb}(\gamma,\zeta)d\zeta \neq 0, \quad \forall\gamma = \gamma_k \tag{17}$$

the displacements do not have this character, i.e.

$$\int_{-1}^{+1}u_b(\gamma,\zeta)d\zeta \neq 0, \quad \int_{-1}^{+1}\zeta u_b(\gamma,\zeta)d\zeta = 0, \quad \int_{-1}^{+1}v_b(\gamma,\zeta)d\zeta \neq 0, \quad \forall\gamma = \gamma_k \tag{18}$$

The solution of equation (15) depends on the sign of the discriminant $\Delta = (a_{66}+2a_{12})^2 - 4a_{11}a_{22}$. Determining $\sigma_{yyb}^{(s)}$ and satisfying conditions (16), we shall have

$$\sigma_{yyb}^{(s)} = A_n^{(s)}F_n(\zeta) \tag{19}$$

In the skew-symmetric problem (bend)

$$\text{a) } \Delta = 0, \quad F_n(\zeta) = \cos\beta\lambda_n \sin\beta\lambda_n\zeta - \zeta\sin\beta\lambda_n \cos\beta\lambda_n\zeta \tag{20}$$

$$\lambda_n \text{ is the root of the equation } \sin 2\beta\lambda_n - 2\beta\lambda_n = 0, \quad \beta = \sqrt[4]{\frac{E_1}{E_2}}$$

b) $\Delta > 0, \quad F_n(\zeta) = \sin\beta_2\lambda_n \sin\beta_1\lambda_n\zeta - \sin\beta_1\lambda_n \sin\beta_2\lambda_n\zeta$ (21)

$$\omega\sin z_n - \sin\omega z_n = 0, \quad z_n = (\beta_1 + \beta_2)\lambda_n, \quad \omega = \frac{\beta_2 - \beta_1}{\beta_1 + \beta_2}$$

c)

$$\Delta < 0, \quad F_n(\zeta) = \cos\beta\lambda_n \text{sh}\alpha\lambda_n \sin\beta\lambda_n\zeta \text{ch}\alpha\lambda_n\zeta - \sin\beta\lambda_n \text{ch}\alpha\lambda_n \cos\beta\lambda_n\zeta \text{sh}\alpha\lambda_n\zeta \quad (22)$$

$$\omega\sin z_n - \text{sh}\omega z_n = 0, \quad z_n = 2\beta\lambda_n, \quad \omega = \frac{\alpha}{\beta}, \quad 0 < \omega < 1$$

Parameters $\beta_1, \beta_2, \alpha, \beta$ are expressed through the constants of the elasticity by the formulae, brought in [1]. In the analogous way the solution in the symmetric (tension-compression) problem is written [1]. It is considered, that in (19) summation in correspondence with all the roots λ_n with $\text{Re}\lambda_n > 0$ of the transcendental equations takes place.

   Transcendental equations (20)-(22) have denumerable set of the complex-conjugate roots. Considering this, we write any of the stresses and displacements Q_b in the form of

$$Q_{bn}^{(s)} = A_n^{(s)}\tilde{Q}_{bn}(\zeta, \gamma), \quad \tilde{Q}_{bn}(\zeta, \gamma) = Q_{bn}(\zeta)\exp(-\lambda_n\gamma)$$ (23)

then representing $A_n^{(s)} = \frac{1}{2}(A_{1n}^{(s)} - iA_{2n}^{(s)}), \quad \lambda_n = x_n + iy_n$ we shall have

$$Q_{bn}^{(s)} = A_{1n}^{(s)}\text{Re}\tilde{Q}_{bn} + A_{2n}^{(s)}\text{Im}\tilde{Q}_{bn}, \quad n = \overline{1,k}$$ (24)

Virtue of homogeneity of the boundary layer   boundary-value problem the solution will be determined with the exactness of the arbitrary constant. Solution (24) for every s is exact. The solution corresponding to the end-wall $x = \ell$ can be obtained from solution (13) by the formal change γ into

$$\gamma_1 = \frac{1}{\varepsilon} - \gamma = (\ell - x)/h .$$

   The boundary layer values when removing from the end-wall $x = 0$ diminish as $\exp(-\text{Re}\lambda_n\gamma)$. Usually when satisfying conditions (12) is neglected by the influence of the boundary layer at $x = \ell$, which is equivalent to the condition

$$1 + \exp\left(-\operatorname{Re}\lambda_1 \frac{\ell}{h}\right) \approx 1$$

which is always fulfilled for beams from real materials and real lengths ($\ell \geq 10h$). For example, for the beams made of glassplastic STET λ_n is determined from equation (21), we have $\operatorname{Re}\lambda_1 \approx 2.297$, $\operatorname{Re}\lambda_2 \approx 3.398$, $\operatorname{Re}\lambda_3 \approx 5.622$ i.e. this condition is practically always fulfilled. As the boundary-value problem of the boundary layer is homogeneous, its solution is determined with the exactness of the constant multiplier, which is often represented as ε^χ, the value χ depends on the type of the conditions at $x = 0, \ell$.

Such approach permits us to produce the conjugation of the inner problem and the boundary layer solutions.

3 Conjugation of the Inner Problem and the Boundary Layer Solutions: Proof of Validity of Saint-Venant Principle

Consider the question of satisfaction of conditions (12). According to (1), (4), (5), (13), (23)

$$
\begin{aligned}
\sigma_{xx} &= \varepsilon^{-2+s}\sigma_{xx}^{(s)}(\xi,\zeta) + \varepsilon^{\chi-1+s}\tilde{\sigma}_{xxb}^{(s)}(\gamma,\zeta) \\
\sigma_{xy} &= \varepsilon^{-1+s}\sigma_{xy}^{(s)}(\xi,\zeta) + \varepsilon^{\chi-1+s}\tilde{\sigma}_{xyb}^{(s)}(\gamma,\zeta)
\end{aligned}
\tag{25}
$$

After the substitution (25) into (12) we obtain noncontradictory conditions only at $\chi = -1$:

$$
\begin{aligned}
\sigma_{xx}^{(s)}(0,\zeta) + \sigma_{xxb}^{(s)}(\zeta) &= \varphi_1^{(s-2)}(\zeta), \quad \varphi_i^{(0)} = \varphi_i \\
\sigma_{xy}^{(s-1)}(0,\zeta) + \sigma_{xyb}^{(s)}(\zeta) &= \varphi_2^{(s-2)}(\zeta), \quad \varphi_i^{(m)} = 0, \ m \neq 0
\end{aligned}
\tag{26}
$$

Using the self-balance property of the boundary layer stresses, from (17), (26) the conditions

$$
\int_{-1}^{+1}\sigma_{xx}^{(s)}(0,\zeta)d\zeta = \int_{-1}^{+1}\varphi_1^{(s-2)}d\zeta, \quad \int_{-1}^{+1}\zeta\sigma_{xx}^{(s)}(0,\zeta)d\zeta = \int_{-1}^{+1}\zeta\varphi_1^{(s-2)}d\zeta
$$

$$
\int_{-1}^{+1}\sigma_{xy}^{(s)}(0,\zeta)d\zeta = \int_{-1}^{+1}\varphi_2^{(s-1)}d\zeta
\tag{27}
$$

will follow.

From three conditions (27) three constants $C_1^{(s)}$, $C_3^{(s)}$, $C_4^{(s)}$ are determined in the solution of the inner problem, therefore the solution of the inner problem itself.

Returning to conditions (26), for determining the constants $A_{1n}^{(s)}$, $A_{2n}^{(s)}$ in the solution of the boundary layer we get the conditions:

$$\sigma_{xxb}^{(s)} = \varphi_1^{(s-2)}(\zeta) - \sigma_{xx}^{(s)}(0,\zeta)$$
$$\sigma_{xyb}^{(s)} = \varphi_2^{(s-2)}(\zeta) - \sigma_{xy}^{(s-1)}(0,\zeta)$$

(28)

or

$$A_{1n}^{(s)} \operatorname{Re} \tilde{\sigma}_{xxbn}(0,\zeta) + A_{2n}^{(s)} \operatorname{Im} \tilde{\sigma}_{xxbn}(0,\zeta) = \varphi_1^{(s-2)}(\zeta) - \sigma_{xx}^{(s)}(0,\zeta)$$
$$A_{1n}^{(s)} \operatorname{Re} \tilde{\sigma}_{xybn}(0,\zeta) + A_{2n}^{(s)} \operatorname{Im} \tilde{\sigma}_{xybn}(0,\zeta) = \varphi_2^{(s-2)}(\zeta) - \sigma_{xy}^{(s-1)}(0,\zeta)$$

(29)

$n = \overline{1,k}$, k is a number of selected λ_n.

   From conditions (29) $A_{1n}^{(s)}$, $A_{2n}^{(s)}$ may be determined by Fourier, collocations, least squares methods. The right parts of conditions (29) are self-balanced, therefore, the boundary layer in the first boundary-value problem of elasticity theory takes the self-balanced part of the end-wall loading on itself, it did not influence on the solution of the inner problem. This purely mathematical result proves the validity of Saint-Venant principle in the first boundary-value problem of elasticity theory.
   In the case of conditions (12,b) we have

$$\varepsilon^{-2+s}U^{(s)}(0,\zeta) + \varepsilon^{\chi+s}u_b^{(s)}(0,\zeta) = \psi_1/\ell$$
$$\varepsilon^{-3+s}V^{(s)}(0,\zeta) + \varepsilon^{\chi+s}v_b^{(s)}(0,\zeta) = \psi_2/\ell$$

(30)

Conditions (30) will be noncontradictory at $\chi = -3$, therefore

$$U^{(s-1)}(0,\zeta) + u_b^{(s)}(0,\zeta) = \psi_1^{(s-3)}, \quad \psi_i^{(0)} = \psi_i/\ell$$
$$V^{(s)}(0,\zeta) + v_b^{(s)}(0,\zeta) = \psi_2^{(s-3)}, \quad \psi_i^{(s)} = 0, m \neq 0$$

(31)

According to (18) the displacements of the boundary layer are not self-balanced, that is why we can't use the previous method as Saint-Venant principle for the displacements is not valid.
   For the cojugation of the solutions it is possible to use the method of least squares, i.e. minimization of the error integral I

$$I = \int_{-1}^{+1}[(U^{(s-1)}(0,\zeta) + u_b^{(s)}(0,\zeta) - \psi_1^{(s-3)})^2 + (V^{(s)}(0,\zeta) + v_b^{(s)}0,\zeta) - \psi_2^{(s-3)})^2]d\zeta$$

From the system of algebraic equations

$$\frac{\partial J}{\partial C_i^{(s)}} = 0 \quad i = 1,3,4$$

$$\frac{\partial J}{\partial A_{1n}^{(s)}} = 0, \quad \frac{\partial J}{\partial A_{2n}^{(s)}} = 0, \quad n = 0,1,...,k \tag{32}$$

Considering that $u_b^{(s)}(0,\zeta) = A_{1n}^{(s)} \operatorname{Re}\tilde{u}_b(0,\zeta) + A_{2n}^{(s)} \operatorname{Im}\tilde{u}_b(0,\zeta)$, (u,v) the constants $C_1^{(s)}$, $C_3^{(s)}$, $C_4^{(s)}$ of the inner problem and $A_{1n}^{(s)}$, $A_{2n}^{(s)}$ of the boundary layer are determined.

The asymptotics (4), (5) and the above described method of the solution are applicable for layered beams and bars, too. The structure of solution (1) remains in force when solving space problems of plates and shells.

For orthotropic plates $D\{(x,y,z): 0 \le x \le a, 0 \le y \le b, -h \le z \le h\}$ after the change of the variables $x = \ell\xi$, $y = \ell\eta$, $z = h\zeta$, $\ell = \min(a,b)$ and passing to dimensionless displacements $U = u/\ell, V = v/\ell, w = w/\ell$ we again come to the singularly perturbed system. In the inner problem we have asymptotics

$$q = -2 \text{ for } \sigma_{xx}, \sigma_{xy}, \sigma_{yy}, \ q = -1 \text{ for } \sigma_{xz}, \sigma_{yz}, \ q=0 \text{ for } \sigma_{zz}$$

$$q = -2 \text{ for } u,v; q = -3 \text{ for } w \tag{33}$$

The solution of the inner problem is reduced to the solution of the system

$$\ell_{11}u^{(s)} + \ell_{12}v^{(s)} = p_1^{(s)}, \quad \ell_{12}u^{(s)} + \ell_{22}v^{(s)} = p_2^{(s)}$$

$$B_{11}\frac{\partial^4 w^{(s)}}{\partial\xi^4} + 2(B_{12} + 2B_{66})\frac{\partial^4 w^{(s)}}{\partial\xi^2\partial\eta^2} + B_{22}\frac{\partial^4 w^{(s)}}{\partial\eta^4} = q^{(s)} \tag{34}$$

where

$$\ell_{11} = B_{11}\frac{\partial^2}{\partial\xi^2} + B_{66}\frac{\partial^2}{\partial\eta^2}, \quad (1,2;\xi,\eta)$$

$$\ell_{12} = (B_{12} + B_{66})\frac{\partial^2}{\partial\xi\partial\eta} \tag{35}$$

$$B_{11} = a_{22}/\Delta, \ B_{22} = a_{11}/\Delta, \ B_{12} = -a_{12}/\Delta, \ B_{66} = 1/a_{66}, \ \Delta = a_{11}a_{22} - a_{12}^2$$

At $s = 0$ the first two equations (34), written in dimensional coordinates coincide with the equations of the generalized plane problem, and the last equation coincides with the equation of the bend according to Kirchhoff-Love classical theory

of plates. The next approximations make the results according to classical theory more precise.

The boundary layer for plates and shells consists of plane and antiplane (boundary torsion) boundary layers. The structure of the generalized plane boundary layer is analogous to the structure in the plane problem, and the values of the antiplane boundary layer diminish when removing from the lateral surface $x = 0$ as

$$\exp\left(-\sqrt{\frac{G_{23}}{G_{12}}}\pi\frac{x}{h}\right) \text{ and } \exp\left(-\sqrt{\frac{G_{23}}{G_{12}}}\frac{\pi}{2}\frac{x}{h}\right) \tag{36}$$

corresponding to the symmetric (tension-compression) and antisymmetic (bend) space problems.

Kirchhoff-Love classical theory of plates does not take into account these boundary layers. E. Reissner and S.A. Ambartsumyan precise theories take into account the antiplane boundary layer and its influence on the inner stress-strain state.

4   The Solution of the Second and Mixed Space Boundary-Value Problem for Thin Bodies

Classical and precise theories of beams, plates and shells consider only one class of problems – when on the facial surfaces of a thin body the values of the corresponding stresses tensor components are given. Under other conditions on the facial surfaces, for example, when the values of displacements are given, or on one surface the values of stresses and on the opposite surface displacements are given the corresponding solutions have not been obtained yet.

It is proved that for this class of problems hypotheses of classical and precise theories are not applicable [1]. For solving these classes of problems the asymptotic method has appeared to be very effective. Principally new asymptotics for stresses and displacements, permitting to obtain solutions of not only plane but also space problems for thin bodies, including anisotropic (21 constant of elasticity) and layered problems [1,5].

Let us illustrate possibilities of the method by the solutions of the second and mixed space boundary-value problems of thermoelasticity theory for anisotropic plates.

It is required to find in the area $D = \{(x, y, z) : 0 \le x \le a, 0 \le y \le b, -h \le z \le h, \quad h << \ell, \ell = \min(a,b)\}$ busy with the plate of the thermoelasticity equations solution by Duhamel-Neuman model of an anisotropic body:

equations of equilibrium

$$\frac{\partial \sigma_{xx}}{\partial x} + \frac{\partial \sigma_{xy}}{\partial y} + \frac{\partial \sigma_{xz}}{\partial z} + F_x(x, y, z) = 0, \qquad (x, y, z) \tag{37}$$

correlations of thermoelasticity

$$\frac{\partial u}{\partial x} = a_{11}\sigma_{xx} + a_{12}\sigma_{yy} + a_{13}\sigma_{zz} + a_{14}\sigma_{yz} + a_{15}\sigma_{xz} + a_{16}\sigma_{xy} + \alpha_{11}\theta$$

$$(x, y, z; u, \text{v}, w; a_{1i}, a_{2i}, a_{3i}; a_{11}, a_{22}, a_{33})$$

$$\frac{\partial w}{\partial y} + \frac{\partial \text{v}}{\partial z} = a_{14}\sigma_{xx} + a_{24}\sigma_{yy} + a_{34}\sigma_{zz} + a_{44}\sigma_{yz} + a_{45}\sigma_{xz} + a_{46}\sigma_{xy} + \alpha_{23}\theta$$

(38)

$$(x, y, z; u, v, w; 4,5,6; \alpha_{23}, \alpha_{13}, \alpha_{12})$$

Satisfying the boundary conditions

$$u(x, y, -h) = u^-(x, y), \quad \text{v}(x, y, -h) = \text{v}^-(x, y), \quad w(x, y, -h) = w^-(x, y) \text{ (39)}$$

$$\sigma_{xz}(x, y, h) = \sigma_{xz}^+(x, y), \quad \sigma_{yz}(x, y, h) = \sigma_{yz}^+(x, y), \quad \sigma_{zz}(x, y, h) = \sigma_{zz}^+(x, y) \text{ (40)}$$

or

$$u(x, y, h) = u^+(x, y), \quad \text{v}(x, y, h) = \text{v}^+(x, y), \quad w(x, y, h) = w^+(x, y) \quad \text{(41)}$$

and the conditions on the lateral surface, which for now are considered to be arbitrary.

In the equations (37), (38) passing to dimensionless coordinates and displace-ments $\xi = x/\ell, \eta = y/\ell, \zeta = z/h, U = u/\ell, V = \text{v}/\ell, W = w/\ell$, we again obtain singularly perturbed by small parametre $\varepsilon = h/\ell$ system, the solu-tion of which has the form of (1), but, for I^{int} asymptotics (4), (33) is not admis-sible, which indicates inapplicability of the hypotheses of classical theory for the solution of the above formulated problems. For their solution asymptotics is applicable

$$q_{\sigma_{ij}} = -1, \qquad q_{u,\text{v},w} = 0 \tag{42}$$

Substituting the representation (4), (42) into transformed system (37), (38) we get a recurrent system for determining $Q^{(s)}(\xi, \eta, \zeta)$. The solution of this system will contain six arbitrary functions, which are uniquely determined from condi-tions (39), (40) or (39), (41).

This class of problems differs from classical by this, too, as the solution I^{int} becomes fully known. Rising residual on the lateral surface is removed by the so-lution for the boundary layer, which does not influence on the solution of the inner problem any more. If the functions $Q^\pm(x, y)$ entering conditions (39)-(41) are polynomials, the iteration process cuts off and we obtain a mathematically precise solution of the inner problem (solution for layer).

We derive it for the plate with general anisotropy, corresponding the problem (39), (40), when $u^- = \text{v}^- = w^- = 0, \quad \sigma_{xz}^+, \sigma_{yz}^+, \sigma_{zz}^+ = const$:

$$\sigma_{xx} = A_{13}\sigma_{zz}^+ + A_{14}\sigma_{yz}^+ + A_{15}\sigma_{xz}^+$$

$$\sigma_{yy} = A_{23}\sigma_{zz}^+ + A_{24}\sigma_{yz}^+ + A_{25}\sigma_{xz}^+$$

$$\sigma_{xy} = A_{63}\sigma_{zz}^+ + A_{64}\sigma_{yz}^+ + A_{65}\sigma_{xz}^+$$

$$\sigma_{xz} = \sigma_{xz}^+, \quad \sigma_{yz} = \sigma_{yz}^+, \quad \sigma_{zz} = \sigma_{zz}^+ \tag{43}$$

$$u = (z+h)(A_{53}\sigma_{zz}^+ + A_{54}\sigma_{yz}^+ + A_{55}\sigma_{xz}^+)$$

$$v = (z+h)(A_{43}\sigma_{zz}^+ + A_{44}\sigma_{yz}^+ + A_{45}\sigma_{xz}^+)$$

$$w = (z+h)(A_{33}\sigma_{zz}^+ + A_{34}\sigma_{yz}^+ + A_{35}\sigma_{xz}^+)$$

where

$$A_{kl} = -a_{1l}B_{k1} - a_{2l}B_{k2} - A_{6l}B_{k6}, \quad l,m = 3,4,5$$

$$A_{ml} = a_{m1}A_{1l} + a_{m2}A_{2l} + A_{m6}A_{6l} + a_{ml}$$

$$B_{ij} = (a_{ik}a_{jk} - a_{ij}a_{kk})/\Delta, \quad (i \ne j \ne k \ne i) \tag{44}$$

$$B_{kk} = (a_{ii}a_{jj} - a_{ij}^2)/\Delta, \quad i,j,k = 1,2,6$$

$$\Delta = a_{11}a_{22}a_{66} + 2a_{12}a_{16}a_{26} - a_{11}a_{26}^2 - a_{22}a_{16}^2 - a_{66}a_{12}^2$$

For orthotropic plates we have

$$\sigma_{xx} = A_{13}\sigma_{zz}^+, \quad \sigma_{yy} = A_{23}\sigma_{zz}^+, \quad \sigma_{xy} = 0$$

$$\sigma_{xz} = \sigma_{xz}^+, \quad \sigma_{yz} = \sigma_{yz}^+, \quad \sigma_{zz} = \sigma_{zz}^+ \tag{45}$$

$$u = \frac{\sigma_{xz}^+}{G_{13}}(h+z), \quad v = \frac{\sigma_{yz}^+}{G_{23}}(h+z), \quad w = A_{33}\sigma_{zz}^+(h+z)$$

$$A_{13} = (a_{12}a_{23} - a_{22}a_{13})/\Delta_1, \quad A_{23} = (a_{12}a_{13} - a_{11}a_{23})/\Delta_1$$

$$A_{33} = a_{13}A_{13} + a_{23}A_{23} + a_{33}, \quad \Delta_1 = a_{11}a_{22} - a_{12}^2$$

Boundary conditions (39), (41) at $u^- = v^- = w^- \equiv 0$, u^+, v^+, $w^+ = const$ for orthotropic plates the precise solution corresponds

$$\sigma_{xx} = \frac{A_{13}}{A_{33}} \frac{w^+}{2h}, \ \sigma_{yy} = \frac{A_{23}}{A_{33}} \frac{w^+}{2h}, \ \sigma_{xy} = 0$$

$$\sigma_{xz} = G_{13} \frac{u^+}{2h}, \ \sigma_{yz} = G_{23} \frac{v^+}{2h}, \ \sigma_{zz} = \frac{1}{A_{33}} \frac{w^+}{2h} \tag{46}$$

$$u = \frac{u^+}{2h}(h+z), \ v = \frac{v^+}{2h}(h+z), \ w = \frac{w^+}{2h}(h+z)$$

Asymptotics (4), (42) is applicable for the solution of the second and mixed boundary-value problems of layered anisotropic plates, as well as for shells [5].

5 Solutions of Plane and Space Dynamic Problems

The asymptotic method is especially effective for the solution of the problems on forced vibrations of thin bodies.

Consider forced vibrations of orthotropic beams-strips $D = \{(x, y) : 0 \le x \le \ell, | y | \le h, h \ll \ell\}$ with the series of the boundary conditions on the facial surfaces $y = \pm h$:

$$\text{a)} \ \sigma_{xy}(x, \pm h) = \pm X^{\pm}(x) \exp i\Omega t$$

$$\sigma_{yy}(x, \pm h) = \pm Y^{\pm}(x) \exp i\Omega t \tag{47}$$

$$\text{b)} \ \sigma_{xy}(x, h), \ \sigma_{yy}(x, h) = (X^+(x), Y^+(x)) \exp i\Omega t$$

$$u(x, -h) = 0, \ v(x, -h) = 0 \tag{48}$$

$$\text{c)} \ u(x, h), \ v(x, h) = (u^+(x), v^+(x)) \exp i\Omega t$$

$$u(x, -h) = 0, \ v(x, -h) = 0 \tag{49}$$

where $X^{\pm}, Y^{\pm}, u^+, v^+$ are known functions, Ω is the frequency of the forcing action. It is considered that the beam is in the conditions of the plane deformation.

The solution of dynamic equations of the plane problem of elasticity theory will be sought in the form of [6,7]

$$\sigma_{\alpha\beta}(x, y, t) = \sigma_{jk}(x, y) \exp(i\Omega t), \ \alpha, \beta = x, y; \ j, k = 1,2$$

$$u(x, y, t), v(x, y, t) = (u_x(x, y), u_y(x, y) \exp(i\Omega t)) \tag{50}$$

Substituting (50) into the equations of dynamic problem, then passing to dimensionless variables $\xi = x/\ell$, $\zeta = y/h$ and displacements $U = u_x/\ell$, $V = u_y/\ell$, we obtain a singularly perturbed by small parametre $\varepsilon = h/\ell$ system

$$\frac{\partial \sigma_{11}}{\partial \xi} + \varepsilon^{-1}\frac{\partial \sigma_{12}}{\partial \zeta} + \varepsilon^{-2}\Omega_*^2 U = 0$$

$$\frac{\partial \sigma_{12}}{\partial \xi} + \varepsilon^{-1}\frac{\partial \sigma_{22}}{\partial \zeta} + \varepsilon^{-2}\Omega_*^2 V = 0$$

$$\frac{\partial U}{\partial \xi} = \beta_{11}\sigma_{11} + \beta_{12}\sigma_{22}$$

$$\varepsilon^{-1}\frac{\partial V}{\partial \zeta} = \beta_{12}\sigma_{11} + \beta_{22}\sigma_{22} \tag{51}$$

$$\varepsilon^{-1}\frac{\partial U}{\partial \zeta} + \frac{\partial V}{\partial \xi} = a_{66}\sigma_{12}, \quad \Omega_*^2 = \rho h^2 \Omega^2,$$

$$\beta_{jk} = \frac{1}{a_{33}}(a_{jk}a_{33} - a_{j3}a_{k3}), \quad j,k,= 1,2, \quad a_{66} = \frac{1}{G_{12}}$$

The solution of system (51) has the form (1), where

$$\sigma_{jk}^{\text{int}} = \varepsilon^{-1+s}\sigma_{jk}^{(s)}(\xi,\zeta), \quad (U,V) = \varepsilon^s(U^{(s)},V^{(s)}), \quad s = \overline{0,N} \tag{52}$$

Note a very important fact – asymptotics (52) of the dynamic problem solution principally differs from asymptotics (4), (5) of the corresponding static problem. Asymptotics (52) is universal, as it remains unchangeable in all dynamic plane and space boundary-value problems for thin bodies – beams, plates and shells.

Substituting (52) into (51) from the obtained system it is possible to express $\sigma_{jk}^{(s)}$ by $U^{(s)}, V^{(s)}$:

$$\sigma_{11}^{(s)} = \frac{1}{\Delta}\left(-\beta_{12}\frac{\partial V^{(s)}}{\partial \zeta} + \beta_{22}\frac{\partial U^{(s-1)}}{\partial \xi}\right), \quad \sigma_{22}^{(s)} = \frac{1}{\Delta}\left(\beta_{11}\frac{\partial V^{(s)}}{\partial \zeta} - \beta_{12}\frac{\partial U^{(s-1)}}{\partial \xi}\right)$$

$$\sigma_{12}^{(s)} = \frac{1}{a_{66}}\left(\frac{\partial U^{(s)}}{\partial \zeta} + \frac{\partial V^{(s-1)}}{\partial \xi}\right), \quad \Delta = \beta_{11}\beta_{22} - \beta_{12}^2, \quad Q^{(m)} \equiv 0 \text{ at } m < 0 \tag{53}$$

Values $U^{(s)}, V^{(s)}$ are determined from the equations

$$\frac{\partial^2 U^{(s)}}{\partial \zeta^2} + a_{66}\Omega_*^2 U^{(s)} = f_u^{(s)}, \qquad \frac{\partial^2 V^{(s)}}{\partial \zeta^2} + \frac{\Delta}{\beta_{11}}\Omega_*^2 V^{(s)} = f_v^{(s)}$$

$$f_u^{(s)} = -\left(a_{66}\frac{\partial \sigma_{11}^{(s-1)}}{\partial \xi} + \frac{\partial^2 V^{(s-1)}}{\partial \xi \partial \zeta}\right), \quad f_v^{(s)} = \frac{\beta_{12}}{\beta_{11}}\frac{\partial^2 U^{(s-1)}}{\partial \xi \partial \zeta} - \frac{\Delta}{\beta_{11}}\frac{\partial \sigma_{12}^{(s-1)}}{\partial \xi}$$

(54)

The solutions of equations (54) are

$$U^{(s)} = C_1^{(s)}(\xi)\sin\sqrt{a_{66}}\Omega_*\zeta + C_2^{(s)}(\zeta)\cos\sqrt{a_{66}}\Omega_*\zeta + \overline{u}^{(s)}$$

$$V^{(s)} = C_3^{(s)}(\xi)\sin\sqrt{\frac{\Delta}{\beta_{11}}}\Omega_*\zeta + C_4^{(s)}(\zeta)\cos\sqrt{\frac{\Delta}{\beta_{11}}}\Omega_*\zeta + \overline{v}^{(s)}$$

(55)

where $\overline{u}^{(s)}, \overline{v}^{(s)}$ are the particular solutions of equations (54).

Four functions $C_j^{(s)}(\xi)$ are determined from the conditions for each group of equations (47)-(49). For example, applying (53), (55) satisfying conditions (47), we find $C_j^{(s)}(\xi)$, substituting them into (55), we determine the following solution of the inner problem

$$U^{(s)} = -\frac{\sqrt{a_{66}}}{\Omega_* \sin 2\sqrt{a_{66}}\Omega_*}[(X^{+(s)} - f_{\sigma_{12}}^{(s)}(\xi,1))\cos\sqrt{a_{66}}\Omega_*(1+\zeta) +$$

$$+ (X^{-(s)} + f_{\sigma_{12}}^{(s)}(\xi,-1))\cos\sqrt{a_{66}}\Omega_*(1-\zeta)] + \overline{u}^{(s)}(\xi,\zeta)$$

$$V^{(s)} = -\frac{1}{\Omega_* \sin 2\sqrt{\frac{\Delta}{\beta_{11}}}\Omega_*}\frac{\Delta}{\beta_{11}}[(Y^{+(s)} - f_{\sigma_{22}}^{(s)}(\xi,1))\cos\sqrt{\frac{\Delta}{\beta_{11}}}\Omega_*(1+\zeta) + \text{(56)}$$

$$+ (Y^{-(s)} + f_{\sigma_{22}}^{(s)}(\xi,-1))\cos\sqrt{\frac{\Delta}{\beta_{11}}}\Omega_*(1-\zeta)] + \overline{v}^{(s)}(\xi,\zeta)$$

$$f_{\sigma_{12}}^{(s)} = \frac{1}{a_{66}}\left(\frac{\partial \overline{u}^{(s)}}{\partial \zeta} + \frac{\partial V^{(s-1)}}{\partial \xi}\right), \quad f_{\sigma_{22}}^{(s)} = \frac{1}{\Delta}\left(\beta_{11}\frac{\partial \overline{v}^{(s-1)}}{\partial \zeta} - \beta_{12}\frac{\partial U^{(s-1)}}{\partial \xi}\right)$$

$$X^{\pm(0)} = \varepsilon X^{\pm}, \quad Y^{\pm(0)} = \varepsilon Y^{\pm}, \quad X^{\pm(s)} = Y^{\pm(s)} = 0, \; s \neq 0$$

In the analogous way the solutions corresponding conditions (48), (49) are written out. From the solution (56) it follows, that the solution of the dynamic inner problem is fully determined from the conditions on the longitudinal boundaries $y = \pm h$, unlike the first static boundary-value problem (2). Therefore, the dynamic boundary

layer will not influence on the solution of the inner problem and will remove the residual on the transversal edges $x = 0, \ell$ i.e. on the lateral surface. Solution (56) will be final, if

$$\sin 2\sqrt{a_{66}}\,\Omega_* \neq 0, \ \ \sin 2\sqrt{\Delta/\beta_{11}}\,\Omega_* \neq 0$$

These conditions are broken, when the value Ω coincides with the frequency value of the free vibrations, then a resonance will arise.

Again, if the functions $X^{\pm}, Y^{\pm}$ are polynomials, iteration process cuts off and mathematically exact solution of dynamic problem for layer is obtained.

In space dynamic problems for plates and shells, including layered, asymptotics (50), (52) is preserved for all stresses $\sigma_{jk}, (j,k = 1,2,3)$ and displacements u, v, w. By the above described procedure the solutions of the three-dimensional problem equations satisfying space boundary conditions on the facial surfaces, like conditions (47)-(49) are determined. We bring this solution for an orthotropic plate $D = \{x, y, z : 0 \leq x \leq a, \ 0 \leq y \leq b, -h \leq z \leq h; \ell = \min(a,b), h \ll \ell\}$ corresponding to the conditions

$$z = h: \ \sigma_{xz} = \sigma_{yz} = \sigma_{zz} = 0$$
$$z = -h: \ (u, v, w) = (u^-, v^-, w^-)\exp(i\Omega t), \ u^-, v^-, w^- = const \tag{57}$$

particularly, simulating behaviour of the constructions foundations and airfields flying strips on the seismic actions

$$u = \tilde{u}\exp(i\Omega t), \ (u, v, w), \quad \sigma_{jk} = \tilde{\sigma}_{jk}\exp(i\Omega t), \ j,k = 1,2,3$$

$$\tilde{u} = \frac{u^-}{\cos 2\Omega_*\sqrt{a_{55}}}\cos\Omega_*\sqrt{a_{55}}\,(1 - \zeta), \quad (u, v; a_{55}, a_{44})$$

$$\tilde{w} = \frac{w^-}{\cos\dfrac{2\Omega_*}{\sqrt{A_{11}}}}\cos\frac{\Omega_*}{\sqrt{A_{11}}}(1 - \zeta) \tag{58}$$

$$\tilde{\sigma}_{11} = -\frac{A_{23}}{h}\frac{\partial\tilde{w}}{\partial\zeta}, \ \ \tilde{\sigma}_{22} = -\frac{A_{13}}{h}\frac{\partial\tilde{w}}{\partial\zeta}, \ \ \tilde{\sigma}_{33} = -\frac{A_{11}}{h}\frac{\partial\tilde{w}}{\partial\zeta}$$

$$\tilde{\sigma}_{13} = \frac{1}{ha_{55}}\frac{\partial\tilde{u}}{\partial\zeta}, \ \ \tilde{\sigma}_{23} = \frac{1}{ha_{44}}\frac{\partial\tilde{v}}{\partial\zeta}, \ \ \tilde{\sigma}_{12} = 0$$

$$A_{11} = (a_{11}a_{22} - a_{12}^2)/\Delta, \ A_{13} = (a_{11}a_{23} - a_{12}a_{13})/\Delta, \ A_{23} = (a_{22}a_{13} - a_{12}a_{23})/\Delta$$
$$\Delta = a_{11}a_{22}a_{33} + 2a_{12}a_{23}a_{13} - a_{11}a_{23}^2 - a_{22}a_{13}^2 - a_{33}a_{12}^2$$

By the asymptotic method the solutions of the space dynamic problems for layered plates [8] and shells [9] can be written out, as well.

6 Conclusions

An asymptotic method for the solution of two-dimensional and three-dimensional static and dynamic problems of elasticity theory for isotropic and anisotropic thin bodies is expounded. The effectiveness of the method for the solution of new classes of thin-body problems – in particular, for those problems that cannot be solved by the classic and refined theories, is illustrated.

References

1. Aghalovyan, L.A.: Asymptotic theory of anisotropic plates and shells, p. 414. Nauka, Fizmathlit, Moscow (1997)
2. Vazov, V.: Asymptotic decompositions of solutions of ordinary differential equations, p. 464. Mir, Moscow (1968)
3. Nayfeh, A.H.: Perturbation methods, p. 455. John Wiley and Sons, Chichester (1973)
4. Vasiljeva, A.W., Boutuzov, V.F.: Asypmtotic decompositions of solutions of singularly perturbed equations, p. 272. Nauka, Moscow (1973)
5. Aghalovyan, L.A., Gevorgyan, R.S.: Nonclassical boundary-value problems of anisotropic layered beams, plates and shell, p. 468. Yerevan, Publish. House, Gitutjun, NAS of Armenia (2005)
6. Aghalovyan, L.A.: An asymptotic method for solving three-dimensional boundary value problems of statics and dynamics of thin bodies. In: Proceed. of the IUTAM symposium on the relations of shell, plate, beam, and 3D models, pp. 1–20. Springer, Heidelberg (2008)
7. Aghalovyan, L.A.: On one method of solution of three-dimensional dynamic problems for layered elastic plates and applications in seismology and seismosteady construction. In: Proceeding European Conference on Structural Control, vol. 1, pp. 25–33. Saint-Petersburg, Russia (2008)
8. Aghalovyan, L.A., Hovhannisyan, R.Z.: Theoretical proof of seismoisolators application necessity. In: Proceedings of International Workshop on Base Isolated High-Rise Buildings, Yerevan, Armenia, June 15-17, pp. 185–199. "Gasprint" LTD, Yerevan (2008)
9. Aghalovyan, L.A., Ghulghazaryan, L.G.: Asymptotics solutions of non-classical boundary-value problems of the natural vibrations of orthotropic shells. Journal of Applied Mathematics and Mechanics 70(2006), 102–115 (2006)

Reliable Optimal Design in Contact Mechanics

Nickolay V. Banichuk, Svetlana Yu. Ivanova, and Evgeniy V. Makeev

A. Yu. Ishlinsky Institute for Problems in Mechanics,
Russian Academy of Sciences, Moscow, Russia

Abstract. The problem of contact pressure optimization is formulated for the case of rigid punch interacted with elastic medium. Coupling of the punch penetration and action of external loads at the outside regions is taken into account. The shape of the punch is considered as an unknown design variable. The minimized integral functional characterizes the discrepancy between the actual contact pressure and the required pressure distribution. The problem is studied under condition that the total forces and moments applied to the punch and the loads acted at the outside regions are given. It is shown that the considered optimization problem can be splitted and transformed to two successively solved problems. Optimal shapes are found analytically for the punches having rectangular contact domains.

1 Introduction

In the engineering and mathematical literature there are many results concerning the shape optimization in contact problems of the theory of elasticity (see, for example, Contry and Sereig (1971), Haug and Kwak (1978), Paczelt (1980), Benedict and Taylor (1981), Haslinger and Neittaanmaki (1984, 1986, 1987, 1988), Haslinger et al. (1986), Paczelt and Szabo (1994)). In many papers devoted to contact interaction of rigid bodies (punchs) and elastic (deformable) medium the analysis and optimization problems were considered in the frame of static, quasistatic and dynamic approaches. It was also supposed that the loading configuration fully describes the distribution, magnitude and domains of application of all the mechanical loads; no variability of the load configuration was allowed.

The problems of contact stress minimization have been rigorously formulated and investigated by Haug and Kwak (1978). In this paper the unknown contour was taken as a design variable and numerical optimization method was proposed. It was shown by Benedict and Taylor (1981) that a Lagrange multiplier technique can be used to transform the inequality equilibrium relations found for contact problems to equality relations. Besides, an efficient numerical contact problem solution based on a direct minimization of the potential energy function by a constrained quadratic programming algorithm was developed and demonstrated on several examples.

A new optimization problem of controlling the contact pressure p was presented by Paczelt and Szabo (1994). The minimum of the maximal contact pressure $p_{\max}$ was investigated under the constraints that the contact pressure should satisfy the inequality $p \geq 0$ as well as the controlling condition $vp_{\max} \geq p$, where $v(x)$ is the controller function. It was also taken into account that the gap between two bodies should be positive or zero after deformation. Some numerical examples demonstrated of the controlling technique for the shape optimization problem of a roller bearing were presented.

Some mathematical aspects of the shape optimization theory have been studied by Haslinger, Neittaanmaki and Tiihonen. The existence of the optimal shapes in contact problem was proved by Haslinger and Neittaanmaki (1984). The questions of approximation and numerical realization were investigated by Haslinger and Neittaanmaki (1986, 1987, 1988), Haslinger et al. (1986). Note that a nonlinear programming approach to the contact optimization problems for elastic plates with pointed supports has been described by Kartvelishvily (1974) and Banichuk (1983).

After the pioneering theoretical works by Galin (1976, 1980), Galin and Goryacheva (1977), the wear process was taken into account in analysis and optimization of contact interaction. Some important results in this direction were obtained by Goryacheva and her coworkers (Goryacheva and Chekina 1989, Goryacheva and Dobychin 1984, Goryacheva and Torskaya 1992) and Paczelt and Mroz (2005. 2007, 2009).

Note also some new optimization problems in contact mechanics with incomplete data concerning external loadings studied by Banichuk and Ivanova (2009).

The purpose of this investigation is to develop an effective approach for a class of optimal design problems for system consisting of rigid and elastic bodies interacted without friction. Problems involving two loading systems are considered. The first one consists of a given forces and moments applied to a punch and the second one is represented by a fixed distributed loads acted at the regions outside the contact domain. The pressure positiveness constraint is important to the nature of these problems imposes a unilateral constraint on the contact pressure distribution.

A contact problem formulation that is well suited to optimal design techniques is developed. This formulation is used to derive an effective decomposition method and optimality conditions for contact pressure distribution. As a result of performed decomposition of the original shape optimization problem we effectively find the optimal contact pressure (at the first stage) and the corresponding shape of the rigid punch penetrated into elastic half-space (at the second stage). The last sub-problem is solved taking into account the application of found pressure distribution in the contact domain and given normal loads in the outside regions. Some analytical solutions are obtained for a rectangular (in-plane) punch and various pointed loads.

2 Formulation of the Problem

Consider in rectangular coordinate system $0xyz$ the equilibrium of a rigid punch interacted without friction with an elastic half-space. The plane $x0y$ bounding elastic half-space $z \geq 0$ and denoting by Ω contains the domain of contact Ω_f (base of the punch), the regions of external forces $q_i(x, y)$ application Ω_q^i ($i = 1, 2, ..., m$) and the domain Ω_0 that is free of loads, i.e. $\Omega = \Omega_f + \Omega_q + \Omega_0$, where $\Omega_q = \bigcup \Omega_q^i$. Here we suppose that $\Omega_f \cap \Omega_q^i = 0$ for $i = 1, 2, ..., m$. The punch is in equilibrium under applied external forces and moments and reaction of the elastic medium. Surface of the punch is described by the equation $z = f(x, y)$, $(x, y) \in \Omega_f$. Boundary conditions for considered problem of the theory of elasticity are written in the case of frictionless contact interaction as

$$w = f(x, y), \quad \sigma_{xz} = 0, \quad \sigma_{yz} = 0, \quad (x, y) \in \Omega_f \tag{1}$$

$$\sigma_{zz} = 0, \quad \sigma_{xz} = 0, \quad \sigma_{yz} = 0, \quad (x, y) \in \Omega_0 \tag{2}$$

$$\sigma_{zz} = q_i(x, y), \quad \sigma_{xz} = 0, \quad \sigma_{yz} = 0, \quad (x, y) \in \Omega_q^i \tag{3}$$

where $i = 1, 2, ..., m$ and m - given number. The normal component w of the displacement vector is oriented in z - direction and σ_{kj} ($k, j = x, y, z$) – components of the stress tensor. Contact pressure is described by the function $p(x, y)$, i.e. $\sigma_{zz} = p(x, y)$, $(x, y) \in \Omega_f$. If the pressure distribution $p(x, y)$ defined on the bottom of the punch is known, then the resulting force P and moments M_x, M_y can be evaluated. In what follows we suppose that the values P, M_x, M_y are given and play the role of the problem constraints. We have

$$P(p) = \int_{\Omega_f} p(x, y) d\Omega_f = P^* \tag{4}$$

$$M_y(p) = \int_{\Omega_f} xp(x, y) d\Omega_f = M_y^* \tag{5}$$

$$M_x(p) = \int_{\Omega_f} yp(x, y) d\Omega_f = M_x^* \tag{6}$$

where $P^* \geq 0$, $M_y^* \geq 0$, $M_x^* \geq 0$ - given positive values.

It is required also that

$$p = p(x, y) \geq 0, \quad (x, y) \in \Omega_f \tag{7}$$

As an optimized functional we consider the following integral

$$J = J(p[f]) = \int_{\Omega_f} (p - p_g)^2 d\Omega_f \tag{8}$$

where $p_g(x, y)$ - given function characterized the required pressure distribution. Functional (8) determines the discrepancy between the actual pressure $p(x, y)$ corresponding some punch shape $f(x, y)$ and required pressure distribution $p_g(x.y)$. In particular, the function p_g can be given as the constant pressure distribution.

Let us consider the following shape optimization problem. It is required to determine the function $f(x, y)$ describing the shape of the punch and minimizing the discrepancy functional

$$J_* = \min_f J(p[f]) = J(p[f_*]) \tag{9}$$

under conditions (1)-(7).

Formulated optimization problem (1)-(9) can be reduced to two successively solved problems. The first problem consists in finding such contact pressure distribution p_* that minimizes the discrepancy functional (8) under constraints (4)-(7). The second problem consists in determining the shape of the punch $f_*(x, y)$ for which the obtained optimal pressure distribution $p_*(x, y)$ is realized.

3   Finding of the Optimal Pressure Distribution

To find the optimal pressure distribution $p_*(x, y)$ minimizing the functional (8), let us consider the constraints (4)-(7) imposed on the integral characteristics (4)-(6) and local constraint (7). To take into account the local constraint we represent the condition (7) in the form

$$p - \psi^2(x, y) = 0, \quad (x, y) \in \Omega_f \tag{10}$$

where $\psi(x, y)$ - unknown variable determined in the process of solution. Construct the augmented Lagrange functional J^L for the formulated problem of pressure optimization. We have

$$J^L = \int_{\Omega_f} \left\{ \left(p - p_g \right)^2 - \lambda p - \alpha x p - \beta y p - \chi \left(p - \psi^2 \right) \right\} d\Omega_f \qquad (11)$$

where λ, α, β - Lagrange multipliers and $\chi(x, y)$ - Lagrange function. Extremum conditions for the functional (11) with respect to variables p and ψ are written in the form

$$p = p_g + \frac{1}{2}\left(\lambda + \alpha x + \beta y + \chi \right), \quad (x, y) \in \Omega_f \qquad (12)$$

$$\psi \chi = 0, \quad (x, y) \in \Omega_f \qquad (13)$$

The pressure distribution (12) contains the unknown values λ, α, β, χ. To determine the constraints λ, α, β we can use the equalities (4)-(6). The function χ is found with the help of (13). Using the condition (13) and representation $p(x, y) = \psi^2(x, y)$ we can find that $\chi(x, y) = 0$ for $(x, y) \in \Omega_f^+ \subset \Omega_f$, if $\psi(x, y) \neq 0$. If $\psi(x, y) = 0$, then $p(x, y) = 0$ for $(x, y) \in \Omega_f^- \subset \Omega_f$. In general case we can divide the original domain Ω_f into two sub-domains Ω_f^+, Ω_f^- ($\Omega_f^+ + \Omega_f^- = \Omega_f$), where $p(x, y) > 0$ (($x, y) \in \Omega_f^+$) and $p(x, y) = 0$ (($x, y) \in \Omega_f^-$).

Taking into account (10), (12), (13) we will have the following expression for the optimal pressure distribution in the domain Ω_f

$$p_*(x, y) = \max\left\{ 0, p^+(x, y) \right\} \qquad (14)$$

$$p^+(x, y) = p_g(x, y) + \frac{1}{2}\left(\lambda + \alpha x + \beta y \right) \qquad (15)$$

The operation $\max$ in (14) means that we choose the maximum of two values written in parentheses. The unknown Lagrange multipliers are found with the help of the linear system of algebraic equations

$$\lambda S^+ + \alpha S_y^+ + \beta S_x^+ = 2\tilde{P} = 2\left(P^* - P^{+g} \right)$$

$$\lambda S_y^+ + \alpha I_y^+ + \beta I_{xy}^+ = 2\tilde{M}_y = 2\left(M_y^* - M_y^{+g} \right) \qquad (16)$$

$$\lambda S_x^+ + \alpha I_{xy}^+ + \beta I_x^+ = 2\tilde{M}_x = 2\left(M_x^* - M_x^{+g} \right)$$

where the contact area S^+, the statical moments S_y^+, S_x^+, the moments of inertia I_x^+, I_y^+, I_{xy}^+ and the values P^+, M_y^+, M_x^+ are determined as

$$S^+ = \int_{\Omega_f^+} dxdy, \quad S_y^+ = \int_{\Omega_f^+} xdxdy, \quad S_x^+ = \int_{\Omega_f^+} ydxdy$$

$$I_y^+ = \int_{\Omega_f^+} x^2 dxdy, \quad I_x^+ = \int_{\Omega_f^+} y^2 dxdy, \quad I_{xy}^+ = \int_{\Omega_f^+} xydxdy \qquad (17)$$

$$P^{+g} = \int_{\Omega_f^+} p_g dxdy, \quad M_y^{+g} = \int_{\Omega_f^+} xp_g dxdy, \quad M_x^{+g} = \int_{\Omega_f^+} yp_g dxdy$$

Let the contact pressure is positive ($p > 0$) in the domain $\Omega_f \left(\Omega_f^+ = \Omega_f \right)$ and this domain is symmetrical with respect to the axes x and y. Then $S_x = S_y = I_{xy} = 0$ and we have

$$\lambda = 2\tilde{P}, \quad \alpha = \frac{2\tilde{M}_y}{I_y}, \quad \beta = \frac{2\tilde{M}_x}{I_x} \qquad (18)$$

If in addition the function $p_g(x, y)$ is also symmetrical with respect to x and y then the following equalities will be satisfied

$$M_y^g = \int_{\Omega_f} xp_g dxdy = 0, \quad M_x^g = \int_{\Omega_f} yp_g dxdy = 0$$

$$\alpha = \frac{2M_y^*}{I_y}, \quad \beta = \frac{2M_x^*}{I_x} \qquad (19)$$

Consider the case when the middle pressure

$$p_m = \frac{1}{S} \int_{\Omega_f} p(x, y) dxdy$$

is taken as a required pressure distribution $p_g(x, y)$, i.e.

$$p_g = p_m = \frac{P^*}{S}, \quad P^* = \int_{\Omega_f} p_g(x, y) dxdy = P^*, \quad \tilde{P} = 0 \qquad (20)$$

In this case we obtain

$$\lambda = 0, \quad p_*(x, y) = \frac{P^*}{S} + \frac{1}{2}\alpha x + \frac{1}{2}\beta y \tag{21}$$

4 Determination of the Optimal Punch Shape

The direct determination of the optimal punch shape is reduced to the following boundary value problem. It is required to find normal displacements $w(x, y, 0)$ defined in the contact domain Ω_f and corresponding boundary conditions (2), (3) and

$$\sigma_{zz} = p_*(x, y), \quad \sigma_{xz} = 0, \quad \sigma_{yz} = 0 \quad (x, y) \in \Omega_f \tag{22}$$

The solution of the boundary value problem of the theory of elasticity is found with the help of potential of "simple layer" $\omega(x, y, z)$ and is written as

$$w(x, y, z) = \kappa\omega(x, y, z) = \kappa \int_{\Omega_f} \frac{p_*(x', y')\,dx'dy'}{\sqrt{(x-x')^2 + (y-y')^2 + z^2}} +$$

$$+ \kappa \sum_{i=1}^{m} \int_{\Omega_q^i} \frac{q_i(x', y')\,dx'dy'}{\sqrt{(x-x')^2 + (y-y')^2 + z^2}} \tag{23}$$

where $\kappa = (1 - v^2)/\pi E$. Consequently, the optimal punch shape corresponding to the optimal contact pressure $p_*(x', y')$ and given normal loads $q_z(x', y')$ applied to the region Ω_q can be represented in the form

$$f_*(x, y) = \kappa\omega(x, y, 0) = \kappa\left[\omega_{p_*}(x, y, 0) + \sum_{i=1}^{m} \omega_{q_i}(x, y, 0)\right]$$

$$\omega_{p_*} = \int_{\Omega_f} \frac{p_*(x', y')\,dx'dy'}{\rho(x, y, x', y')}, \quad \omega_{q_i} = \int_{\Omega_q^i} \frac{q_i(x', y')\,dx'dy'}{\rho(x, y, x', y')} \tag{24}$$

Here $\rho(x, y, x', y') = \sqrt{(x-x')^2 + (y-y')^2}$. The influence of the external loads $q_i(x, y)$ on the optimal shape is described by the terms

$$f_{q_i}(x, y) = \kappa \omega_{q_i}(x, y, 0), \quad i = 1, \dots, m \tag{25}$$

and the term

$$f_{p_*}(x, y) = \kappa \omega_{p_*}(x, y, 0) \tag{26}$$

determines the optimal shape in the case $q_i = 0, \quad i = 1, \dots, m$, i.e.

$$f_*(x, y) = f_{p_*}(x, y) + f_q(x, y) = f_{p_*}(x, y) + \sum_{i=1}^{m} f_{q_i}(x, y) \tag{27}$$

If the external loads are represented by the pointed forces

$$q_i(x, y) = Q_i \delta(x - x_i, y - y_i), \quad (x_i, y_i) \in \Omega_q^i \tag{28}$$

then, as it follows from (25), (28) and (24), we have

$$f_q(x, y) = \kappa \sum_{i=1}^{m} \frac{Q_i}{\rho(x, y, x_i, y_i)}$$
$$\rho(x, y, x_i, y_i) = \sqrt{(x - x_i)^2 + (y - y_i)^2} \tag{29}$$

Consider the case of rectangular (in plane) punch $\Omega_f \ (-a \le x \le a, -b \le y \le b)$ where a, b - given values. Suppose that

$$p_g(x, y) = \text{const} > 0 \tag{30}$$

and introduce the notation

$$C = p_g + \frac{1}{2}\lambda, \quad A = \frac{1}{2}\alpha, \quad B = \frac{1}{2}\beta$$

In this case the optimal pressure distribution is given by a linear function of the independent coordinates x', y', i.e.

$$p_*(x, y) = C + Ax' + By' \tag{31}$$

Corresponding solution for $f_{p_*}(x, y)$ has been found by Banichuk (2009) and has the explicit form

$$f_{p_*} = \kappa \left\{ (C + Ax + By) D_0(x, y) + \frac{1}{2} A D_C(x, y) + \frac{1}{2} B D_s(x, y) \right\}$$

$$D_0 = \frac{1}{2} \left[t_1 \varphi_1(x, y) + t_2 \varphi_2(x, y) + t_3 \varphi_3(x, y) + t_4 \varphi_4(x, y) \right]$$

(32)

$$D_C = t_1^2 \varphi_1(x, y) + t_2^2 \varphi_2(x, y) + t_3^2 \varphi_3(x, y) + t_4^2 \varphi_4(x, y)$$

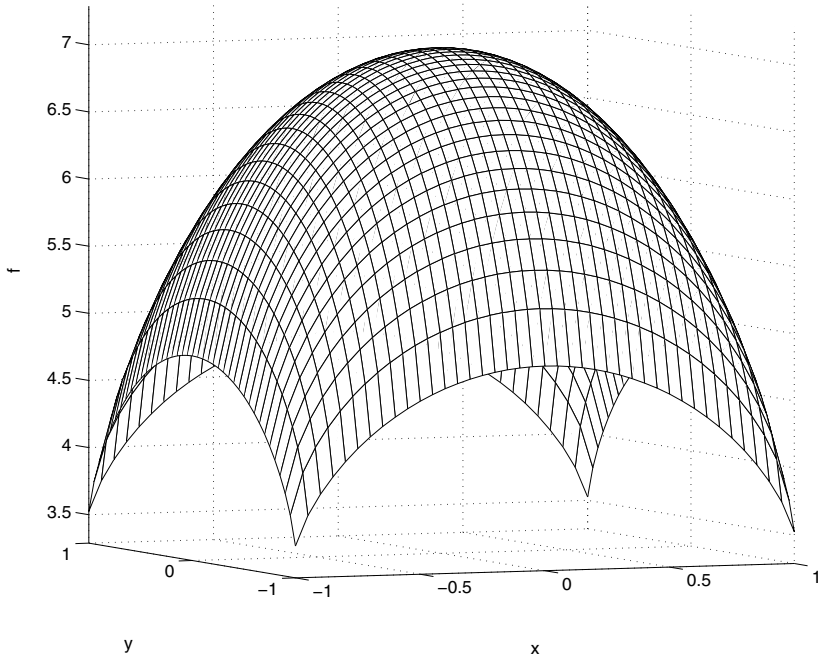$$D_s = t_1 g_1(x, y) + t_2 g_2(x, y) + t_3 g_3(x, y) + t_4 g_4(x, y)$$

Fig. 1. Optimal shape f without outside contact domain loading $(\gamma = 0)$.

Here we use the following notations

$$t_1 = a - x, \quad t_2 = b - y, \quad t_3 = a + x, \quad t_4 = b + y,$$
$$\rho_1 = \sqrt{t_3^2 + t_4^2}, \quad \rho_2 = \sqrt{t_2^2 + t_3^2}, \quad \rho_3 = \sqrt{t_1^2 + t_4^2}, \quad \rho_4 = \sqrt{t_1^2 + t_2^2},$$

$$g_1 = \rho_3 + \rho_4 - 2t_1, \quad g_2 = \rho_2 + \rho_4 - 2t_2,$$

$$g_3 = \rho_1 + \rho_2 - 2t_3, \quad g_1 = \rho_1 + \rho_3 - 2t_4, \tag{33}$$

$$\varphi_1 = \ln\left(\frac{\rho_3 + t_4}{\rho_3 - t_4} \frac{\rho_4 + t_2}{\rho_4 - t_2}\right), \quad \varphi_2 = \ln\left(\frac{\rho_4 + t_1}{\rho_4 - t_1} \frac{\rho_2 + t_3}{\rho_2 - t_3}\right),$$
$$\varphi_3 = \ln\left(\frac{\rho_2 + t_2}{\rho_2 - t_2} \frac{\rho_1 + t_4}{\rho_1 - t_4}\right), \quad \varphi_4 = \ln\left(\frac{\rho_4 + t_3}{\rho_4 - t_3} \frac{\rho_3 + t_1}{\rho_3 - t_1}\right)$$
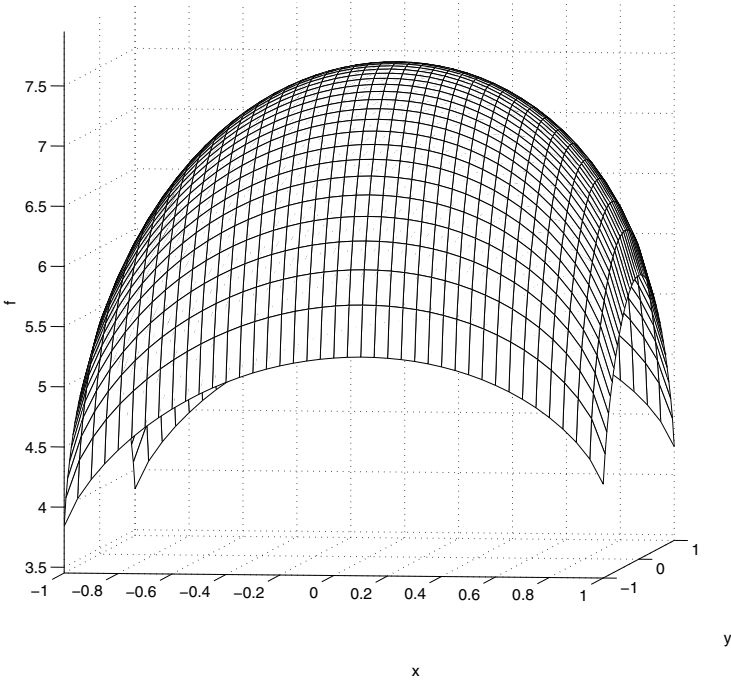

Fig. 2. Optimal shape f for the only force applied outside contact domain at the point $(x = 2a, y = 0)$, when $\gamma = 1$.

Let us present some particular examples for rectangular punch $(-a \le x \le a, -b \le y \le b)$, when

$$M_x^* = 0, \quad M_y^* = 0, \quad P = P^*, \quad p_g = \frac{P^*}{S} \tag{34}$$

and consequently, as it is seen from (16)-(21), we have ($\tilde{P} = \tilde{M}_x = \tilde{M}_y = 0$)

$$\lambda = \alpha = \beta = 0, \quad p_*(x, y) = \frac{P^*}{S} \tag{35}$$

Consider at first the case of action of one pointed load $q_1 = Q\delta(x - c, y)$ applied at the point $x_1 = c, \ y_1 = 0 \ \ (c > a)$. With the help of (27), (29), (32), (33) we obtain

$$f = f_{p_*} + f_q = \kappa p_g \left[D_0(x, y) + \frac{Q}{p_g \sqrt{(x - c)^2 + y^2}} \right] \tag{36}$$
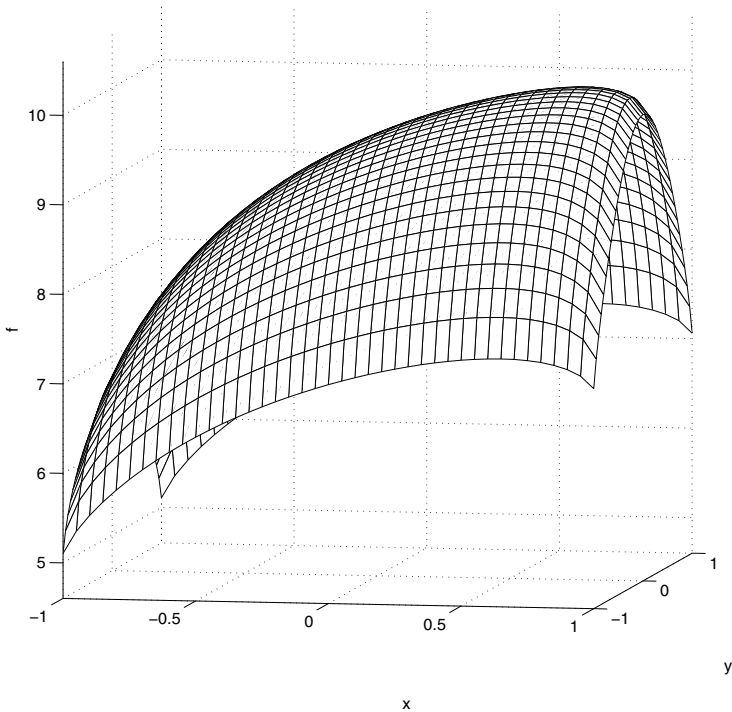

Fig. 3. Optimal shape f for the only force applied at the point $(x = 2a, y = 0)$, when $\gamma = 5$.

Using the dimensionless values

$$\tilde{x} = \frac{x}{a}, \quad \tilde{y} = \frac{y}{a}, \quad \tilde{f} = \frac{f}{a\kappa p_g}, \quad \gamma = \frac{Q}{a^2 p_g} \tag{37}$$

we present at fig. 1, fig. 2 and fig. 3 the optimal shape

$$\tilde{f} = D_0(\tilde{x}, \tilde{y}) + \frac{\gamma}{\sqrt{\left(\tilde{x} - \dfrac{c}{a}\right)^2 + \tilde{y}^2}} \tag{38}$$

Presented optimal shapes correspond to the following parameters: $\gamma = 0, \ 1.0, \ 5.0$; $b/a = 1$; $c/a = 2$; $-1 \le \tilde{x} \le 1$; $-1 \le \tilde{y} \le 1$. (The tilde at all figures is omitted). Note that the optimal shape shown in fig. 1 when $\gamma = 0$ (the punch is free of outside contact domain loadings) is symmetrical with respect to the coordinates x and y.

Fig. 4. Optimal shape f under loading of four pointed forces $(x = 2a, y = 0)$, $(x = -2a, y = 0)$, $(x = 0, y = 2b)$, $(x = 0, y = -2b)$ applied outside contact domain, when $\gamma = 5$.

Consider another case when a system of four pointed forces $q_i = Q\delta(x - x_i, y - y_i)$, $i = 1, 2, 3, 4$ is applied outside contact domain at the points $(x_1 = 2a, y_1 = 0)$, $(x_2 = 0, y_2 = 2b)$, $(x_3 = -2a, y_3 = 0)$, $(x_4 = 0, y_4 = -2b)$. Using (27), (29), (32), (33) we will obtain

$$f = \kappa p_g \left[D_0(x, y) + \frac{Q}{p_g} \sum_{i=1}^{4} \frac{1}{\sqrt{(x - x_i)^2 + (y - y_i)^2}} \right] \tag{39}$$

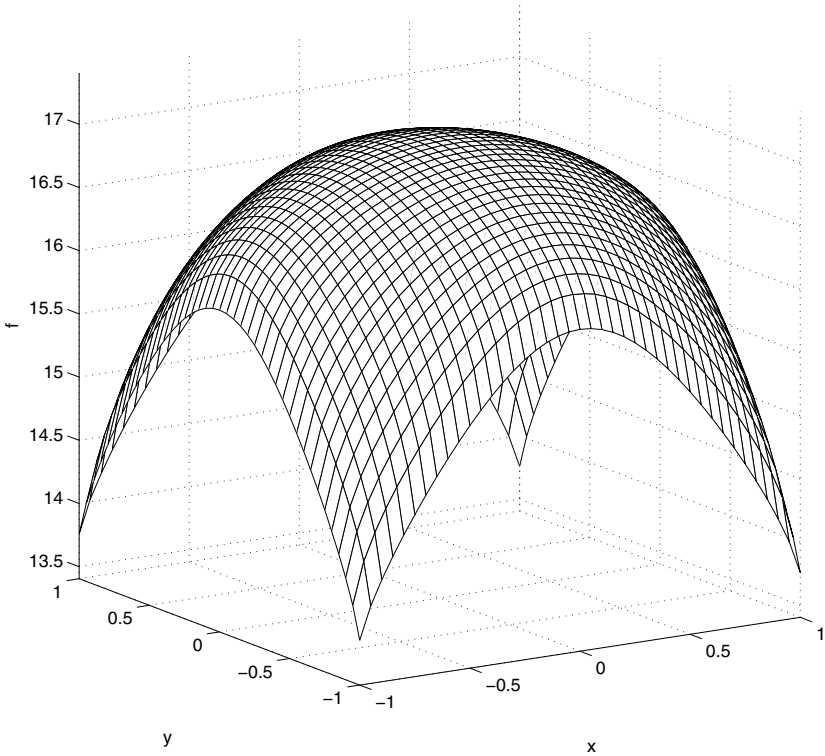In dimensionless variables (37) we have the following expression
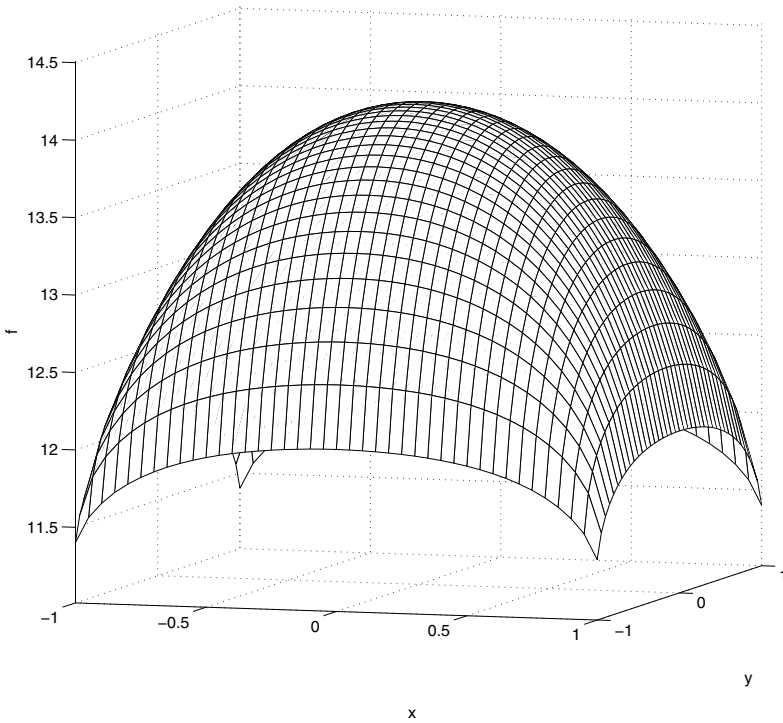
Fig. 5. Optimal shape f under loading of four pointed forces $(x = 2a, y = 2b)$, $(x = -2a, y = 2b)$, $(x = 2a, y = -2b)$, $(x = -2a, y = -2b)$ applied outside contact domain, when $\gamma = 5$.

$$\tilde{f} = D_0\left(\tilde{x}, \tilde{y}\right) + \gamma \sum_{i=1}^{4} \frac{1}{\sqrt{\left(\tilde{x} - \dfrac{x_i}{a}\right)^2 + \left(\tilde{y} - \dfrac{y_i}{a}\right)^2}} \tag{40}$$

depending on parameters γ, b/a.

The optimal shape (40) is shown in fig. 4 for $\gamma = 5.0$, $b/a = 1$. This optimal shape is also symmetrical with respect to coordinates x and y but in comparison with the shape shown in fig. 1 it is more truncated.
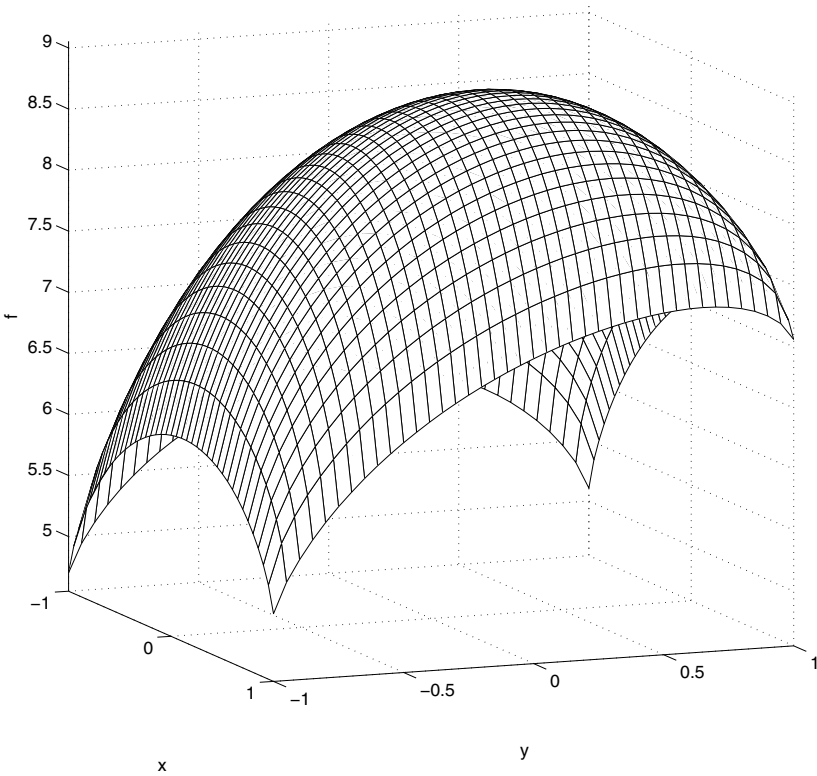
Fig. 6. Optimal shape f for the only force applied outside contact domain at the point $\left(x = 2a,\, y = 2b\right)$, when $\gamma = 5$.

The optimal shape presented in fig. 5 corresponds to the case of four pointed forces $q_i = Q\delta\left(x - x_i,\, y - y_i\right)$, $i = 1, 2, 3, 4$ applied outside contact domain at the points $\left(x_1 = 2a,\, y_1 = 2b\right)$, $\left(x_2 = -2a,\, y_2 = 2b\right)$, $\left(x_3 = 2a,\, y_3 = -2b\right)$,

$\left(x_4 = -2a,\, y_4 = -2b\right)$ for $\gamma = 5.0$, $b/a = 1$. The shape shown in fig. 6 corresponds to the case of the only pointed force applied outside contact domain at the point $\left(x = 2a,\, y = 2b\right)$ for $\gamma = 5.0$, $b/a = 1$. As it is seen from the presented figures, the depth of punch penetration is increased, if the outside contact domain force is increased.

5 Conclusions

In this paper we formulated and investigated the problem of contact pressure optimization for the rigid punch interacted without friction with an elastic medium. The forces and moments applied to the punch and the external loads acted at the outside regions were taken into account. All considerations have been performed in the frame of quasistatical loading of the system: rigid punch – elastic foundation. It was shown that the application of the proposed approach gives us the possibility to decompose the formulated optimization problem to two successively solved problems. The first problem is concerned with the finding of the pressure distribution realized the minimal value of considered discrepancy functional under constraints on the equilibrium equations and positive pressure condition. The second problem is concerned with the finding of the optimal punch shape and is reduced to determination of the normal displacements arising as a result of solution of the first problem. The shape of optimal punch has been found in the form of "simple layer potential" corresponding to the case of linear distributed contact pressure.

It was obtained analytical solution of the shape optimization problem for the punch having rectangular form in plan. Note, that the proposed approach can be applied to the case of a system of contacted punches. The main results obtained in this study are illustrated using examples of normal loads application in the some given domain. Of course, there are many other cases with tangential loads action, which can be effectively represented.

Acknowledgement

References

Banichuk, N.V.: Problems and Methods of Optimal Structural Design. Plenum Press, New York (1983)

Banichuk, N.V.: On optimal shapes in mechanics of contact interaction. Doklady AN 427(2), 1–5 (2009) (in Russian)

Banichuk, N.V., Ivanova, S.Y.: Optimization Problems in Contact Mechanics with Uncertaities. Mechanics Based Design of Structures and Machines 37(2), 143–156 (2009)

Benedict, R.L., Taylor, J.E.: Optimal design for elastic bodies in contact. In: Haug, E.J., Cea, J. (eds.) Optimization of Distributed Parameter Structures, Alphen aan den Rijn, Netherlands, Sijthoff, Nordhoff, vol. II, pp. 1553–1599 (1981)

Contry, T.F., Sereig, A.: A mathematical programming method for design of elastic bodies in contact. J. Appl. Mech. 38, 387–392 (1971)

Galin, L.A.: Contact problem of the theory of elasticity in the presence of wear. Journal of applied mathematics and mechanics 40(6), 981–986 (1976)

Galin, L.A.: Contact problems of elasticity and viscoelasticity theories. Nauka, Moscow (1980) (in Russian)

Galin, L.A., Goryacheva, I.G.: Axisymmetric contact problem of the theory of elasticity in the presence of wear. Journal of applied mathematics and mechanics 41(5), 826–831 (1977)

Goryacheva, I.G.: Wear contact problem for the ring inserted into cylinder. Journal of applied mathematics and mechanics 44(2), 363–367 (1980)

Goryacheva, I.G.: Wear contact problem for system of punches. Izv. AN SSSR, Mechanics of solids 6, 62–68 (1987)

Goryacheva, I.G.: Changes in the contact characteristics of junctions during the wear. In: Proceedings of the 5th International congress of tribology, Helsinki, vol. 3, pp. 360–366 (1989)

Goryacheva, I.G., Chekina, O.G.: Control of surface deformation during wear. Soviet journal of friction and wear 10(1), 1–7 (1989)

Goryacheva, I.G., Dobychin, M.N.: Wear kinetics of pain journal bearing with solid lubricant. Soviet journal of friction and wear 5(4), 581–588 (1984)

Goryacheva, I.G., Torskaya, E.V.: Contact problems for bodies with wear resistance variable on the surface. Soviet journal of friction and wear 13(1), 151–158 (1992)

Haug, E.J., Kwak, B.M.: Contact stress minimization by contour design. Numerical Methods in Engineering 12, 917–930 (1978)

Haslinger, J., Neittaanmaki, P.: On the existence of optimal shapes in contact problems. Numer. Func. Anal. and Optimiz. 7, 107–124 (1984)

Haslinger, J., Neittaanmaki, P.: On optimal shape design of systems governed by mixed Dirichlet-Signorini boundary value problems. Math. Meth. Appl. Sci. 8, 157–181 (1986)

Haslinger, J., Neittaanmaki, P., Tiihonen, T.: Shape optimization in contact problems based on penalization of the state inequality. Appl. Math. 31, 54–57 (1986)

Haslinger, J., Neittaanmaki, P.: Shape optimization in contact problems. Approximation and numerical realization. RAIRO. Math. Model. Numer. Anal. 21, 269–291 (1987)

Haslinger, J., Neittaanmaki, P.: Finite Element Approximation for Optimal Shape Design. John Wiley & Sons, London (1988)

Kartvelishvily, V.M.: Numerical solution of two contact problems for elastic plates. Mech. of Solids 6, 68–72 (1974) (MTT, in Russian)

Paczelt, I.: Optimization of the distribution of contact pressure. Müszaki Tudomany 60, 111–146 (1980) (in Hungarian)

Paczelt, I., Szabo, T.: Optimal shape design for contact problems. Structural Optimization 7(1/2), 66–75 (1994)

Paczelt, I., Mroz, Z.: On optimal contact shapes generated by wear. International journal of numerical methods in engineering 63, 1250–1287 (2005)

Paczelt, I., Mroz, Z.: Optimal shapes of contact interfaces due to sliding wear in the steady relative motion. International journal of solids and structures 44, 895–925 (2007)

Paczelt, I., Mroz, Z.: On the analysis of steady-state sliding wear processes. Tribology international 42, 275–283 (2009)

Scaling of Strength and Lifetime Distributions of Quasibrittle Structures[*]

Zdeněk P. Bažant and Jia-Liang Le

Northwestern University
{z-bazant,jialiang-le}@northwestern.edu

Abstract. Engineering structures such as aircraft, bridges, dams, nuclear containments and ships, as well as computer circuits, chips and MEMS, should be designed for failure probability $< 10^{-6}$–10^{-7} per lifetime. The safety factors required to ensure it are still determined empirically, even though they represent much larger and much more uncertain corrections to deterministic calculations than do the typical errors of modern computer analysis of structures. The empirical approach is sufficient for perfectly brittle and perfectly ductile structures since the cumulative distribution function (cdf) of random strength is known, making it possible to extrapolate to the tail from the mean and variance. However, the empirical approach does not apply to structures consisting of quasibrittle materials, which are brittle materials with inhomogeneities that are not negligible compared to structure size. This paper presents a refined theory on the strength distribution of quasibrittle structures, which is based on the fracture mechanics of nanocracks propagating by activation energy controlled small jumps through a nano-structure and an analytical model for the multi-scale transition of strength statistics. Based on the power law for creep crack growth rate and the cdf of material strength, the lifetime distribution of quasibrittle structures under constant load is derived. Both the strength and lifetime cdf's are shown to be size- and geometry- dependent. The theory predicts intricate size effects on both the mean structural strength and lifetime, the latter being much stronger. The theory is shown to match the experimentally observed systematic deviations of strength and lifetime histograms of industrial ceramics from the Weibull distribution.

1 Introduction

In the design of various engineering structures, it is of paramount importance to understand and ascertain the types of probability distributions of structural strength since an experimental verification of design strength for the tolerable failure probability $P_f < 10^{-6}$ [21, 38, 36] is virtually impossible. For perfectly brittle structures

---

[*] This paper is an authorized republication, with minor modification, of a previous paper in CD proceedings [6].

failing at initiation of a macro-crack from one representative volume element (RVE) with a negligible size, the strength distribution is known to be Weibullian, based on the infinite weakest link model. For perfectly ductile structures, the failure load is a weighted sum of the strengths of the RVEs along the failure surface. According to the Central Limit Theorem, the strength distribution must follow the Gaussian (or normal) distribution, except the remote tail.

It has been shown that the failure behavior of quasibrittle structures varies from quasi-plastic to perfectly brittle as the structure size increases [14, 2, 3]. Consequently, it must be expected that the type of probabilistic distribution of strength of quasibrittle structures will vary with the structure size and geometry.

This study deals with quasibrittle structures of positive geometry, which is a broad class of sturctures that fail at the macro-crack initiation from one RVE. Extensive experimental data showed that the strength histograms of various quasibrittle materials, such as concrete [56], industrial and dental ceramics[37, 34, 46, 47, 52], and fiber composites [55, 54], consistently deviate from the two-parameter Weibull distribution. Recently, the three-parameter Weibull distribution with a non-zero threshold has been adopted as a remedy [27, 49, 22].

It is observed, however, that the three-parameter Weibull distribution still shows a systematic deviation from sufficiently broad experimental histograms in the high probability regime (Fig. 10 in [13]). Furthermore, the three-parameter Weibull distribution implies a vanishing size effect on the mean strength for large size structures, which does not agree with the experimental observations [32, 39]. In fact, the experimental size effect curve on concrete and fiber composites [16, 18] at large size limit implies that the threshold must be zero [39].

Recent studies [12, 13] showed that the problem actually lies in the assumption of infinite weakest-link model which underlies the Weibull statistics of strength. One must consider a finite weakest-link model because of the fact that the size of one RVE is not negligible compared to the structure size, which is the salient feature of all quasibrittle structures. A probabilistic theory was recently developed to model the strength distribution of quasibrittle structures [12, 13, 8].

The theory is derived from the strength statistics of a nano-structure considered as a nano-scale block of either a regular lattice or a disordered nano-structure, which is based on the probabilistic fracture mechanics of random jumps of the crack tip propagating through the nano-structure [7, 8]. The transition of strength statistics from the nano-scale to the RVE scale can be statistically represented by a hierarchical model consisting of bundles and chains [12, 13]. Based on the asymptotic properties of strength cdf's of bundles and chains, it has been shown that the strength cdf of one RVE can be approximately modeled as a Gaussian distribution onto which a power-law tail is grafted at the failure probability of about $P_f \approx 10^{-4}$–10^{-3}.

With the crack growth rate law, the theory is further extended to model the lifetime cdf of quasibrittle structures under constant loads [8, 33, 5]. The model agrees well with the strength and lifetime histograms of various quasibrittle materials such as concrete, industrial and dental ceramics, and fiber composites [13, 39, 32].

This paper, representing both a digest and an extension of [8], reviews the recently developed theory, and derives some key asymptotic properties of strength

distribution of bundles with softening stress-strain behavior, which further validates the grafted distribution of RVE strength underlying the weakest-link model of structural failure. The theory is then verified by optimum fits of some recent tests of the strength and lifetime histograms of industrial ceramics.

2 Failure Statistics of Nano-structure

The failure of a structure originates from the failure of its nano-structures, either atomic lattice blocks or disordered nano-structures. Naturally, the statistics of structural failure at macro-scale must be related to the statistics of breakage of nano-structures. In the present theory, a nano-crack is considered to propagate by random jumps through either an atomic lattice block or through a disordered nano-structure. These jumps are governed by the activation energy barriers separating a series of metastable states on the surface of the free energy potential of the nano-structure.

When the nano-crack advances by one atomic spacing or one nano-inhomogeneity, the energy release due to fracture must correspond to the change of activation energy barrier. Based on the equivalent linear elastic fracture mechanics, the energy release can be explicitly related to the remote stress applied on the nano-structure [7, 8].

Since the interatomic separation across the crack line increases by only a small fraction of the atomic spacing during each jump, the activation energy barrier for the forward jump differs very little from the backward jump. Therefore, the jumps of the state of nano-structure must be happening in both directions, though with slightly different frequencies.

By virtue of the transition rate theory [30, 40], the first-passage time for each transition can be calculated by Kramer's formula [45], which gives the net frequency of the propagation of nano-crack. After a number of jumps of the nano-crack tip, the crack loses its stability and propagates dynamically, which leads to the break of nano-structure.

It may reasonably be assumed that each jump of the nano-crack tip is history independent [31]. Therefore, the failure probability of the nano-structure is proportional to the sum of frequencies of all the jumps needed to reach a certain critical crack length. The failure probability has thus been found to follow a power-law function of the remote stress with a zero threshold (e.g. [7] and [8]).

3 Multi-scale Transition of Strength Statistics

To relate the strength cdf of an RVE at the macro-scale to the strength cdf of a nano-structure, a certain statistical multiscale transition framework is needed. Though various stochastic multi-scale numerical approaches have been proposed [53, 26, 57], the capability of these approaches is always limited due to incomplete knowledge of the uncertainties in the information across all the scales. Instead, for the sole purpose of statistics, the multi-scale transition of strength statistics has been characterized by a hierarchical model, which consists of bundles and chains shown in Fig. 1 [12, 13].
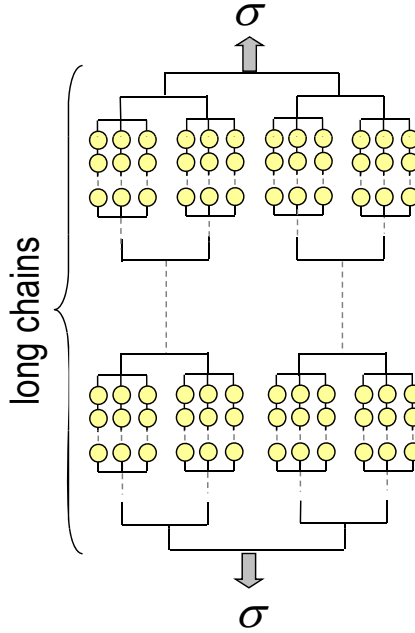
Fig. 1. Hierarchical model for multiscale transition of strength statistics.

For a chain of n_c elements where all of the elements have a strength cdf with a power-law tail of exponent p, the strength cdf of the entire chain has also a power-law tail and its exponent is also p. If the tail exponents for different elements in the chain are different, then the smallest one is the tail exponent of the cdf of strength.

For a bundle of n_b elements (or fibers) of random strength, the strength cdf of a bundle depends on the load-sharing mechanism of the fiber. Various load sharing rules have been discussed in the literatures [20, 41, 42, 43, 35]. A more realistic model is to derive the load redistribution rule based on a mechanical model. Consider that all the elements (fibers) have the same elastic stiffness and are subjected to the same displacement.

Two limiting cases are now well understood: 1) the brittle failure, in which the stress in the fiber suddenly drops to zero once it reaches the peak stress, and 2) the plastic failure, in which, after the fiber reaches the peak stress, the stress remains constant as the displacement increases. Two asymptotic properties are of interests here: the tail behavior of strength cdf of a bundle and the type of strength cdf for a large bundle.

For a bundle of n_b fibers, if the strength cdf of each fiber has a power-law tail of exponent $p_i (i = 1,...,n_b)$, then the strength cdf of the bundle has also a power-law tail, with its exponent being $p = \sum_{i=1}^{n} p_i$. For the plastic bundle, this property can simply be proven by asymptotic expansion of cdf [13] or through Laplace transform of cdf. For the brittle bundle, this property was proven by induction based on the set

theory [28, 44]. A simpler proof was presented in [13] based on asymptotic expansion of the recursive equation for the strength cdf of brittle bundle by Daniels [20], who also showed that the cdf of a brittle bundle approaches Gaussian distribution as $n_b \to \infty$. For a plastic bundle, such a convergence is obvious by virtue of the Central Limit Theorem.

However, the actual behavior of a fiber may exhibit gradual post-peak softening. For this intermediate case, the proof of additivity of tail exponents and the convergence to Gaussian distribution for a large bundle is still lacking. Here we present a simple proof.

Consider a bundle with two fibers having the same cross section area, although a generalization to any number of fibers is easy. Assume that each element has a bi-linear stress-strain curve (Fig. 2a), which has an elastic modulus E and softening modulus E_t ($E_t \le 0$). Let the only random variable be the peak strength σ_i ($i = 1, 2$). Then the peak of average stress in the bundle can be written as:

$$\sigma_b = \max_{\varepsilon} [s_1(\varepsilon) + s_2(\varepsilon)] / 2 \tag{1}$$

where ε = strain in the fiber, and s_1, s_2 = stresses in fibers 1 and 2. We seek the critical strain ε^* at which the load on the bundle reaches its maximum. The critical strain depends on the ratio $\alpha = -E_t/E$ ($\alpha \ge 0$). Two cases must be distinguished, depending on whether the weaker element fails completely (1) before or (2) after the stronger element reaches its peak.

Let the two fibers be numbered such that $\sigma_1 \le \sigma_2$. Then the peak stress of the bundle, σ_b, can be written as follows:

Case 1: $0 \le \alpha \le 1$

$$\text{if } (1+\alpha)\sigma_1/\alpha > \sigma_2: \quad \sigma_b = [(1+\alpha)\sigma_1 + (1-\alpha)\sigma_2]/2 \tag{2}$$
$$\text{if } (1+\alpha)\sigma_1/\alpha \le \sigma_2: \quad \sigma_b = \sigma_2/2 \tag{3}$$

Case 2: $\alpha > 1$

$$\text{if } (1+\alpha)\sigma_1/\alpha > \sigma_2: \quad \sigma_b = \sigma_1 \tag{4}$$
$$\text{if } (1+\alpha)\sigma_1/\alpha \le \sigma_2: \quad \sigma_b = \max(\sigma_1, \sigma_2/2) \tag{5}$$

Note that these results cover not only the softening bundles but also the limit cases of both the plastic and brittle bundles. When $\alpha = 0$, the element is plastic and the peak average stress in the bundle is $(\sigma_1 + \sigma_2)/2$ (which was statistically analyzed in [13]). When $\alpha \to \infty$, the element is brittle and the peak stress of the bundle is $\max(\sigma_1, \sigma_2/2)$ [20].

If the average bundle strength is less than a prescribed value S, i.e. $\sigma_b \le S$, then, based on Eqs. 2-5, the strength of each fiber must lie in the domain $\Omega_2(S)$, shown in Figs. 2 b and c. Since the strengths of these two fibers are independent random variables, we may use the joint probability theorem to express the cdf of the average bundle strength;

$$G_2(S) = 2 \int_{\Omega_2(S)} f_1(\sigma_1) f_2(\sigma_2) d\sigma_1 d\sigma_2 \tag{6}$$
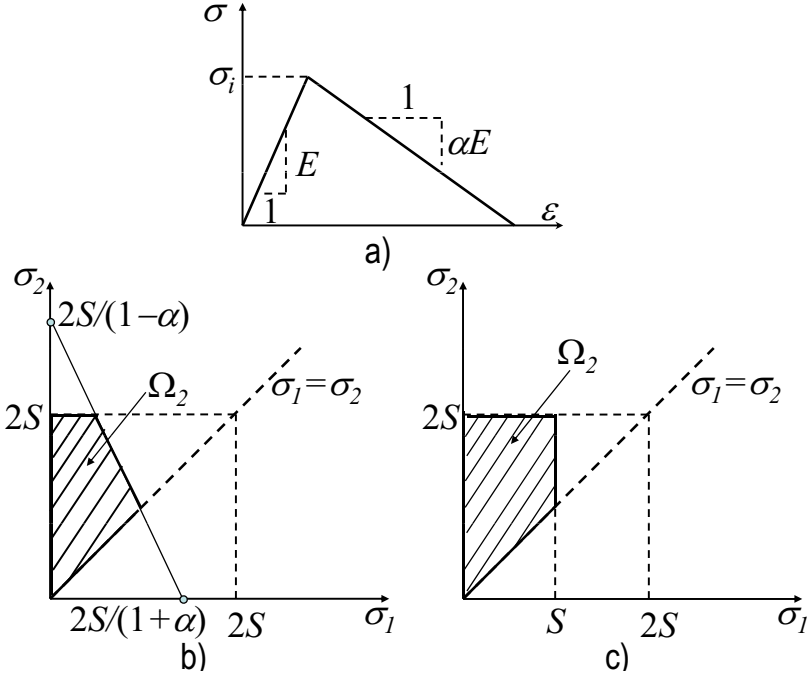
Fig. 2. a) Mechanical behavior of softening fiber, b) Feasible region of strength of fibers for $\alpha < 1$, c) Feasible region of strength of fibers for $\alpha \geq 1$.

where f_i = probability density function (pdf) of the strength of the ith element ($i = 1, 2$). For the limiting cases of brittle and plastic bundles, Eq. 6 becomes equivalent to Daniels' formulation for the brittle bundle [20] and the convolution integral for the plastic bundle becomes equivalent to the formulation in [13].

Now we assume that the strength of each fiber has a cdf with a power-law tail, i.e. $P_i(\sigma) = (\sigma/s_0)^{p_i}$. Considering the transformation: $y_i = \sigma_i/S$, we can write the cdf of bundle strength as:

$$G_2(S) = 2S^{(p_1+p_2)} \int_{\Omega_2(1)} \frac{p_1 p_2}{s_0^{p_1+p_2}} y_1^{p_1-1} y_2^{p_2-1} \mathrm{d}y_1 \mathrm{d}y_2 \tag{7}$$

where $\Omega_2(1)$ denotes the feasible region $\Omega_2(S)$ normalized by S. Since the integral in Eq. 7 results in a constant, the cdf of bundle strength has a power-law tail whose exponent is $p_1 + p_2$. Q.E.D.

By induction, the foregoing analysis is then easily extended to a bundle with n_b fibers, for which the cdf of average bundle strength can be written as:

$$G_{n_b}(S) = n_b! \int_{\Omega_{n_b}(S)} \prod_{i=1}^{n_b} f_i(\sigma_i) \mathrm{d}\sigma_1 \mathrm{d}\sigma_2 ... \mathrm{d}\sigma_{n_b} \tag{8}$$

$$= n_b! S^{p_1+p_2+...+p_{n_b}} \int_{\Omega_{n_b}(1)} \left(\prod_{i=1}^{n_b} \frac{p_i y_i^{p_i-1}}{s_0^{p_i}} \right) \mathrm{d}y_1 \mathrm{d}y_2...\mathrm{d}y_{n_b} \qquad (9)$$

where $\Omega_{n_b}(S)$ is the feasible region of stresses in all the fibers, which defines an n_b-dimensional space, and $\Omega_{n_b}(1)$ is the corresponding feasible region of normalized stresses, $y_i = \sigma_i/S$.

Thus, regardless of the post-peak slope E_t of each fiber, it is proven that, if each fiber strength has a cdf with a power-law tail, then the cdf of bundle strength will also have a power-law tail, and the power-law exponent will be the sum of the exponents of the power-law tails of the cdf's of all the fibers in the bundle.

The reach of power-law tail of the strength cdf of softening bundle was shown to be another important consideration [13]. It can be calculated from Eq. 9. However, for large bundles, it is difficult to handle the integral in Eq. 9 numerically. Previous studies [12, 13] showed that the reach of power-law tail decreases with the number n_b of elements rapidly as $P_{tn_b} \sim (P_{t1}/n_b)^{n_b} - (P_{t1}/3n_b)^{n_b}$ for brittle bundles, or $(P_{t1}/n_b)^{n_b}$ for plastic bundles, where $P_{t1} = $ failure probability at the terminal point of the power-law tail of one fiber. Since the behavior of softening bundles is bounded between these two extreme cases, the rate of shortening of power-law tail of strength cdf of the softening bundles must lie between them; i.e.

$$P_{tn_b} \sim (P_{t1}/n_b)^{n_b} - (P_{t1}/3n_b)^{n_b} \qquad (10)$$

The series coupling, by contrast, was shown to extend the power-law tail [13]—roughly by one order of magnitude for each ten-fold increase in the number links.

Another important asymptotic property is the type of cdf of strength of large bundles. For brittle bundles, Daniels derived a recursive equation for the strength cdf of a bundle with n_b fibers and showed that the strength cdf of large bundles approaches the Gaussian (or normal) distribution [20]. This property is obviously also true for plastic bundles; it is a natural consequence of the Central Limit Theorem since the strength of a plastic bundle is the sum of strengths of all the fibers.

To prove that this asymptotic property applies to all the bundles regardless of their post-peak softening stiffness E_t, consider a bundle of $3n_b$ fibers (or elements). The load carried by the bundle is given by $F(\varepsilon) = \max \left[\sum_{j=2}^{3n_b+1} \sigma_j(\varepsilon)A \right]$, where $A = $ cross section area of each fiber, $\sigma_j = $ stress in jth element, and $\varepsilon = $ strain in each element. The mechanical behavior of each fiber can be random. This causes the randomness of the critical value ε^* of strain ε, at which F reaches its maximum value. We label the $3n_b$ elements by $j = 2,3,4,...3n_b+1$, arrange them according to their breaking order, and divide them into two groups with different load resultants:

$$F_A(\varepsilon) = \sum_{i=3k} \sigma_i(\varepsilon)A, \quad F_B(\varepsilon) = \sum_{i=3k\pm1} \sigma_i(\varepsilon)A \quad (k = 1,2,3,...n_b). \qquad (11)$$

The maximum load carried by the bundle is:

$$F_{max} = F_A(\varepsilon^*) + F_B(\varepsilon^*) \qquad (12)$$

23          $\cdots$ $3n_b+1$
Stress distribution in the bundle

3 6 9 12 $\cdots$ 2 4 5 $\cdots$
Stress distribution in   Stress distribution in
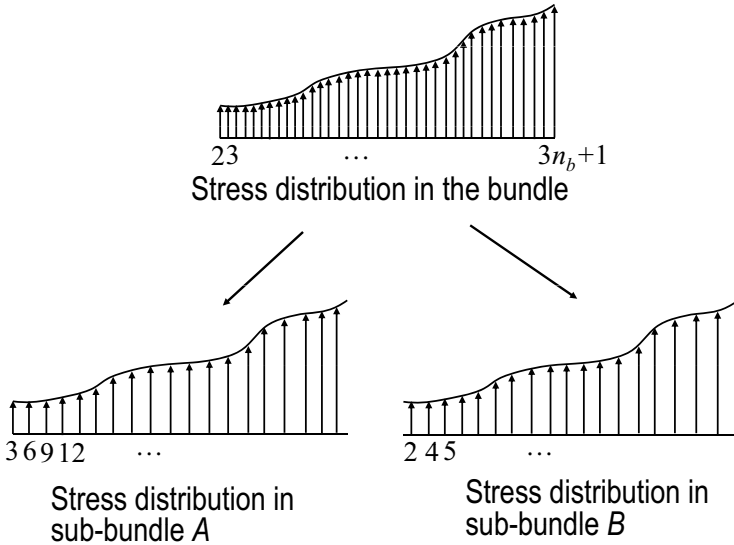sub-bundle *A*   sub-bundle *B*

Fig. 3. Stress distribution of fibers within a large bundle.

If n is large, then the stress distribution over the elements in these two groups will be similar to that in the bundle (Fig. 3). It follows that the cdf of F_{max} (i.e. the strength of bundle) and the cdf's of $F_A(\varepsilon^*)$ and $F_B(\varepsilon^*)$ are of the same type. Then, to satisfy Eq. 12, the only possible distribution of F_{max} is the Gaussian distribution (note that this argument would not apply if the we divided the bundle into 2 groups with the same number of elements and the same resultant for large n_b).

However, the rate of convergence depends on the post-peak softening stiffness E_t of the elements. The slowest convergence, of the order of $O(n_b^{-1/3}(\log n_b)^2)$ [48], occurs for brittle bundles. The fastest convergence, of the order of $O(n_b^{-1/2})$, occurs for plastic bundles [13].

To figure out the type of cdf of strength of one RVE, one must specify the mechanical behavior of the bundles in the hierarchical model. Although different assumptions yield about the same results, here the following assumption is made: For the bundles at the lowest scale, the elements are connected between two rigid plates, and thus they are subjected to the same deformation. For the bundles at higher scales, they follow the equal-load sharing mechanism.

Note that one should calculate the strength cdf in a hierarchical manner, at the lowest scale, each element represents a nano-structure whose strength cdf is a power-law function. One can then calculate the strength cdf of the sub-chain that connects these elements. At the next scale, the strength cdf of the sub-bundle, which consists of these sub-chains, can be calculated based on the strength cdf of these sub-chains. Following in this manner, one could move up through the scales, and finally obtain the strength cdf of one RVE.

The strength cdf of all the sub-chains follows from the joint probability theorem. For the bundles at the lowest scale, where all the elements are subjected to a roughly uniform deformation, the strength cdf will depend on the mechanical behavior of each element, which is given by Eq. 8, and for the bundles at higher scales, equal-load sharing is assumed. Regardless of the mechanical behavior of each element, the strength of a bundle with the equal-load sharing mechanism is given by:

$$\sigma_b = \max \left[\sigma_1, \frac{n_b - 1}{n_b} \sigma_2, ..., \frac{1}{n_b} \sigma_{n_b} \right] \tag{13}$$

where $\sigma_1, \sigma_2, ... \sigma_{n_b}$ are the strength values ordered by the sequence of their breaking. In fact, the strength distribution of such a bundle is exactly the same as the strength distribution of the brittle bundle. Therefore, the strength distribution of the equal-load sharing bundle can be calculated by Daniels' recursive equation [20, 28, 13].

As an example, we calculate the strength cdf of the hierarchical model shown in Fig. 1. Every element in the hierarchical model represents one nanoscale element, which has a power-law cdf of strength. Three cases are considered:

1) Each element has an elastic-brittle behavior.
2) Each element exhibits a linear post-peak softening, where the softening modulus magnitude is 40% of the elastic modulus of the element.
3) Each element has an elastic-plastic behavior.

Fig. 4a shows the calculated strength cdf's of the hierarchical model for these three cases on the Weibull scale. For all these cases, the lower portion of the calculated strength cdf is a straight line on the Weibull plot, which indicates that it follows the Weibull distribution (a power-law tail). Such a property is expected since the power-law tail of the cdf of strength is indestructible in the chain and bundle models.

For the upper portion, the strength cdf deviates from the straight line in Fig. 4a. Among the three cases considered, case 1 (i.e., elements with brittle behavior) gives the shortest Weibull tail, which terminates at the probability of about 0.7×10^{-4}, while case 3 (elements with plastic behavior) gives the longest Weibull tail, which terminates at the probability of about 0.7×10^{-3}.

To identify the type of distribution for the upper portion of the cdf, the cdf's of strengths are plotted on the normal probability paper; see Figs. 4b-d where the upper portion of the cdf's is seen to be fitted quite closely by a straight line. The straight line not is not too close for case 1 and for $P_f \geq 0.8$. For the cases 2 and 3, the straight line fits quite closely, with a slight deviation occurring only for $P_f \geq 0.99$. This means that, the upper portion of the strength cdf can be approximated as the Gaussian distribution. Since, for real quasibrittle structures, the nano-element is expected to have a softening behavior, the strength cdf of one RVE should be close to case 2.

In general, the strength distribution of one RVE can be approximately described by a Gaussian distribution with a Weibull tail grafted on the left at the probability of
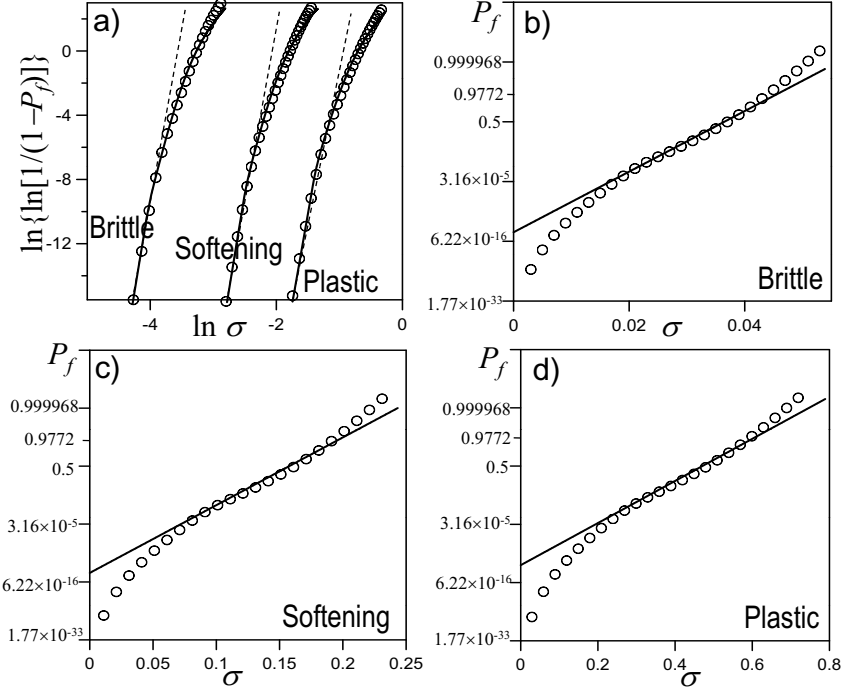
Fig. 4. a) Calculated cdf of strength of one RVE on the Weibull scale, b)–d) Calculated cdf of strength of one RVE on the normal distribution paper.

about $10^{-4} - 10^{-3}$. The grafted cdf of strength of one RVE may be mathematically described as [12, 13]:

$$P_1(\sigma_N) = 1 - e^{-(\sigma_N/s_0)^m} \qquad (\sigma_N \leq \sigma_{gr}) \tag{14}$$

$$P_1(\sigma_N) = P_{gr} + \frac{r_f}{\delta_G \sqrt{2\pi}} \int_{\sigma_{gr}}^{\sigma_N} e^{-(\sigma'-\mu_G)^2/2\delta_G^2} d\sigma' \qquad (\sigma_N > \sigma_{gr}) \tag{15}$$

where σ_N = nominal strength, which is a maximum load parameter of the dimension of stress. In general, $\sigma_N = c_n P_{max}/bD$ or $c_n P_{max}/D^2$ for two- or three-dimensional scaling (P_{max} = maximum load of the structure or parameter of load system, c_n = parameter chosen such that σ_N represents the maximum principal stress in the structure, b = structure thickness in the third dimension, D = characteristic structure dimension or size). Furthermore, m (Weibull modulus) and s_0 are the shape and scale parameters of the Weibull tail, and μ_G and δ_G are the mean and standard deviation of the Gaussian core if considered extended to $-\infty$; r_f is a scaling parameter required to normalize the grafted cdf such that $P_1(\infty) = 1$, and P_{gr} = grafting probability = $1 - \exp[-(\sigma_{gr}/s_0)^m]$. Finally, continuity of the probability density function at the grafting point requires that $(dP_1/d\sigma_N)|_{\sigma_{gr}^+} = (dP_1/d\sigma_N)|_{\sigma_{gr}^-}$.

4 Lifetime Distribution of One RVE

It has recently been shown [8, 33, 5] that one can derive the lifetime cdf of one RVE by using the power law for creep crack growth, which has been empirically described as [23, 51, 24, 15, 14, 4, 37]:

$$\dot{a} = Ce^{-Q_0/kT}K^n \tag{16}$$

where C, n = empirical constant, Q_0 = activation energy, k = Boltzmann's constant, T = absolute temperature, K = stress intensity factor. Recent studies [8, 33] showed that, under certain plausible assumptions, the power law for creep crack growth can be physically justified on the basis of atomistic fracture mechanics and a multi-scale transition framework of fracture kinetics.

Now consider one RVE undergoing strength and lifetime tests, where a linearly ramped load is applied in the strength test and a constant load is applied in the lifetime test. By applying Eq. 16 to these two cases, one finds the relation between the strength and lifetime of one RVE as:

$$\sigma_N = \beta \sigma_0^{n/(n+1)} \lambda^{1/(n+1)} \tag{17}$$

where σ_N = nominal strength of RVE, $\sigma_0 = P/l_0^2$ = applied nominal stress in the lifetime test (P = applied load), l_0 = RVE size, λ = lifetime of RVE, $\beta = [r(n+1)]^{1/(n+1)}$, and r = rate of loading in the strength test. Since the distribution of RVE strength is given by Eqs. 14 and 15, the lifetime distribution of one RVE can be easily obtained by substituting Eq. 17 for σ_N of Eqs. 14 and 15:

$$\text{for } \lambda < \lambda_{gr}: \quad P_1(\lambda) = 1 - \exp[-(\lambda/s_\lambda)^{\bar{m}}]; \tag{18}$$

$$\text{for } \lambda \geq \lambda_{gr}: \quad P_1(\lambda) = P_{gr} + \frac{r_f}{\delta_G\sqrt{2\pi}} \int_{\gamma\lambda_{gr}^{1/(n+1)}}^{\gamma\lambda^{1/(n+1)}} e^{-(\lambda'-\mu_G)^2/2\delta_G^2} d\lambda' \tag{19}$$

where $\gamma = \beta \sigma_0^{n/(n+1)}$ $\lambda_{gr} = \beta^{-(n+1)}\sigma_0^{-n}\sigma_{N,gr}^{n+1}$, $s_\lambda = s_0^{n+1}\beta^{-(n+1)}\sigma_0^{-n}$, and $\bar{m} = m/(n+1)$. Similar to the strength distribution of one RVE, the lifetime cdf of one RVE also has a Weibull tail (power-law tail). However, the rest of the lifetime cdf of one RVE does not follow the Gaussian distribution. Note that the grafting probability P_{gr} for the lifetime distribution of one RVE is the same as that for the strength cdf of one RVE.

5 Finite Weakest Link Model and Optimum Fits of Histograms

To analyze softening damage and failure, the RVE must be defined as the smallest material volume whose failure triggers the failure of entire structure [12, 13]. Therefore, the structure can be statistically represented by a chain of RVEs. By virtue of the joint probability theorem, and under the assumption of independence of random strengths or lifetimes of the links in a finite weakest-link model, one can calculate the strength or lifetime cdf of a structure as:

$$P_f(x) = 1 - \prod_{i=1}^{N}[1 - P_1(x)] \tag{20}$$

where $x = \sigma_N$ for strength distribution and $x = \lambda$ for lifetime distribution, $P_1 =$ strength or lifetime cdf of one RVE given by Eqs. 14 and 15 or Eqs. 18 and 19. Here we assume that the principal stresses in one RVE are fully statistically correlated to the maximum one, which seems realistic. If they were uncorrelated, each principal stress would require one element in the chain.

For large size structures, what matters for P_f is only the tail of the strength or life-time cdf of one RVE, i.e $P_1 = (\sigma_N/s_0)^m$ or $P_1 = (\lambda/s_\lambda)^{\bar{m}}$. By taking the logarithm of Eq. 20 and setting $\ln(1 - P_1) \approx -P_1$ for small P_1, one can easily show that the strength and lifetime distributions for large size structure converge to the Weibull distribution:

$$P_f(\sigma_N) = 1 - \exp[-N_{eq,\sigma}(\sigma/s_0)^m] \tag{21}$$
$$P_f(\lambda) = 1 - \exp[-N_{eq,\lambda}(\lambda/s_\lambda)^{\bar{m}}] \tag{22}$$

where $N_{eq,\sigma}, N_{eq,\lambda}$ are the equivalent numbers of RVEs for the strength and lifetime distributions, which can be calculated based on the elastic stress distribution in the structure [13, 5]. The equivalent number of RVE physically means that a chain that has $N_{eq,\sigma}$ or $N_{eq,\lambda}$ RVEs subjected to a uniform stress gives the same strength or lifetime cdf as Eq. 20. The Weibull modulus of lifetime distribution is much smaller than the Weibull modulus of strength distribution. They are related by:

$$\bar{m} = m/(n+1) \tag{23}$$

Fig. 5 presents the optimum fits of the strength and lifetime histograms of 99.9 % Al_2O_3 beam under four point bend test [25]. For each histogram, a total of 30 specimens were tested. Obviously, on the Weibull scale, both histograms do not appear to be straight lines. Instead, there is a kink separating the histogram into two parts where the lower part is a straight line and the upper part is curved. Such a pattern cannot be explained by the two-parameter Weibull distribution.

Fig. 5 shows that the present theory gives excellent fits of both the strength and lifetime histograms. The location of kink actually corresponds to the grafting probability, which measures the degree of quasibrittleness of the structure.

From the data fits, it is further observed that the grafting probabilities of the strength and lifetime cdf's are about the same. This agrees well with the present theory, in which the grafting probability can be calculated as: $P_{gr} = 1 - [1 - P_{gr,1}]^{N_{eq}}$. Since the grafting probabilities $P_{gr,1}$ of strength and lifetime cdf's for one RVE is the same and the equivalent number of RVE for strength cdf is almost identical to the equivalent number of RVE for lifetime cdf, then the grafting probabilities for strength and lifetime cdf's must be approximately the same.

By optimum fitting, the Weibull moduli for strength and lifetime distributions are estimated to be about 30 and 1.1, respectively. From Eq. 23 one can get exponent n of the power law for creep crack growth for 99.9 % Al_2O_3, which is about 26.
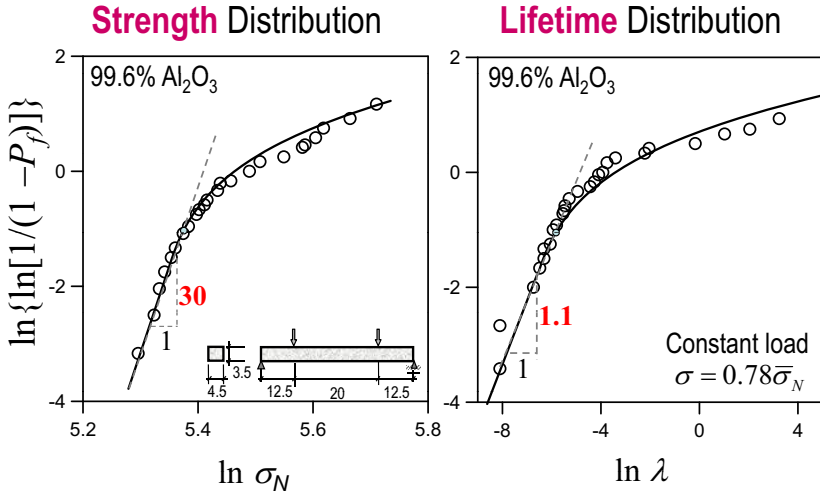
Fig. 5. Optimum fits of strength and lifetime histograms of 99.9 % Al_2O_3 [25].

6   Size Effect on Mean Structural Strength and Lifetime

With the grafting probability distributions of strength and lifetime of one RVE, Eq. 20 directly implies the size effects on the strength and lifetime cdf's. One can further compute the size effects on the mean strength and lifetime. Based on the calibrated strength and lifetime distributions of 99.9 % Al_2O_3 (Fig. 5), one can calculate the corresponding size effects on the mean structural strength and lifetime as shown in Fig. 6.

Although a close-form expression for such size effects is impossible, one can obtain the approximate form for the mean strength and lifetime by asymptotic matching. It has been proposed that the size effect on mean strength can be approximated by [2, 3, 11]:

$$\bar{\sigma}_N = \left[\frac{N_a}{D} + \left(\frac{N_b}{D} \right)^{\psi/m} \right]^{1/\psi} \tag{24}$$

where parameters N_a, N_b, ψ and m are to be determined by asymptotic properties of the size effect curve.

It has been shown that such a size effect curve agrees well with the predictions by other mechanical models such as the nonlocal Weibull theory [9, 10], as well as with the experimental observations on concrete [16] and fiber composites [18]; m = Weibull modulus of the strength distribution, which can be determined by the slope of the left tail of the strength histogram plotted on the Weibull scale, or more accurately by size effect tests. The other three parameters, N_a, N_b, and r, can be determined by solving three simultaneous equations based on three asymptotic conditions, $[\bar{\sigma}_N]_{D \to l_0}$, $[d\bar{\sigma}_N/dD]_{D \to l_0}$, and $[\bar{\sigma}_N D^{1/m}]_{D \to \infty}$.
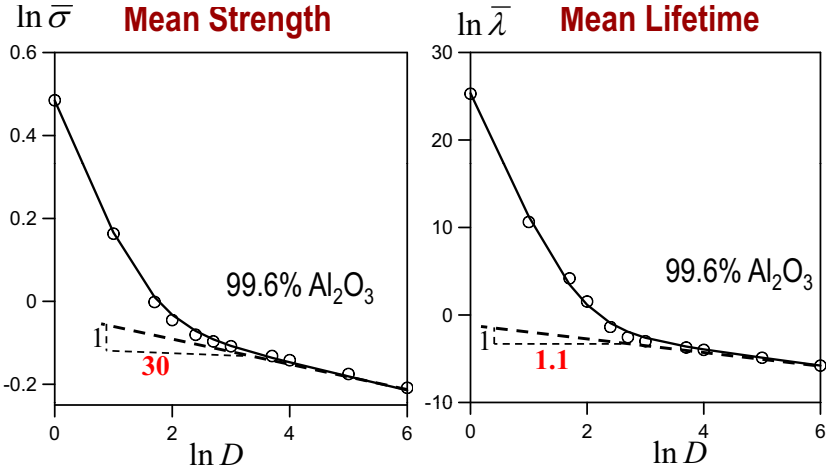
Fig. 6. Calculated size effects on mean structural strength and lifetime.

One can approximate the size effect on the mean structural lifetime by an equation with the same form as Eq. 24:

$$\bar{\lambda} = \left[\frac{C_a}{D} + \left(\frac{C_b}{D} \right)^{\varphi/m} \right]^{(n+1)/\varphi} \tag{25}$$

where m is the Weibull modulus of the cdf of strength, and $n =$ exponent of the power law for subcritical creep crack growth rate. Similar to the size effect on mean strength, C_a, C_b, and φ can be obtained from three asymptotic conditions: $[\bar{\lambda}]_{D \to l_0}$, $[d\bar{\lambda}/dD]_{D \to l_0}$, and $[\bar{\lambda} D^{(n+1)/m}]_{D \to \infty}$.

It is obvious that the size effect on the mean structural lifetime is much stronger than that on the mean strength. This is physically plausible. Consider two geometrically similar beams, with size ratio 1:8. Let the nominal strength of the small beam be ς. Due to the size effect on the mean strength, the nominal strength of the large beam is about $\varsigma/2$. If one applied a nominal load $\varsigma/2$ to both beams, the large beam will fail within standard laboratory testing period (i.e. about 5 minutes) while the small beam is expected to survive at that load for decades if not forever.

7 Conclusion

The present theory shows that the types of strength and lifetime distributions depend on the structure size and geometry. This has important implications for the safety factors to be used in reliability assessment for the design of many engineering structures, such as large prestressed concrete bridges, large aircraft or ships made of fiber composites, and various micro- and nano-electronic devices.

The present theory indicates that the safety factors guarding against the uncertainties in strength and lifetime cannot be empirical, and cannot be constant. They must be calculated as a function of the size, geometry of structures and environment.

References

1. Basquin, O.H.: The Exponential Law of Endurance Tests. In: Proc. Amer. Soc.Testing and Mater., ASTEA, vol. 10, pp. 625–630 (1910)
2. Bažant, Z.P.: Scaling theory of quaisbrittle structural failure. Proc. Nat'l. Acad. Sci., USA 101(37), 13397–13399 (2004)
3. Bažant, Z.P.: Scaling of Structural Strength, 2nd edn. Elsevier, London (2005)
4. Bažant, Z.P., Jirásek, M.: R-curve modeling of rate and size effects in quasibrittle fracture. Int. J. of Frac. 62, 355–373 (1993)
5. Bažant, Z.P., Le, J.-L.: Nano-mechanics based modeling of lifetime distribution of quasibrittle structures. J. Engrg. Failure Ana. 16, 2521–2529 (2009)
6. Bažant, Z.P., Le, J.-L.: Size effect on strength and lifetime distributions of quasibrittle structures. In: Proc. (CD), ASME 2009 Int. Mech. Engrg. Congress (IMECE 2009), Lake Buena Vista, Florida, pp. 1–9 (2009)
7. Bažant, Z.P., Le, J.-L., Bazant, M.Z.: Size effect on strength and lifetime distribution of quasibrittle structures implied by interatomic bond break activation. In: Proc. of 17th European Conference on Fracture, Brno, Czech Rep., pp. 78–92 (2008)
8. Bažant, Z.P., Le, J.-L., Bazant, M.Z.: Scaling of strength and lifetime distributions of quasibrittle structures based on atomistic fracture mechanics. Proceeding of National Academy of Sciences 106(28), 1484–11489 (2009)
9. Bažant, Z.P., Novák, D.: Probabilistic nonlocal theory for quasibrittle fracture initiation and size effect. I. Theory. J. of Engrg. Mech. 126(2), 166–174 (2000)
10. Bažant, Z.P., Novák, D.: Probabilistic nonlocal theory for quasibrittle fracture initiation and size effect. II. Application. J. of Engrg. Mech. ASCE 126(2), 175–185 (2000)
11. Bažant, Z.P., Novák, D.: Energetic-statistical size effect in quasibrittle failure at crack initiation. ACI Mater. J. 97(3), 381–392 (2000)
12. Bažant, Z.P., Pang, S.-D.: Mechanics based statistics of failure risk of quasibrittle structures and size effect on safety factors. Proceeding of National Academy of Sciences 103(25), 9434–9439 (2006)
13. Bažant, Z.P., Pang, S.-D.: Activation energy based extreme value statistics and size effect in brittle and quasibrittle fracture. J. Mech. Phys. Solids 55, 91–134 (2007)
14. Bažant, Z.P., Planas, J.: Fracture and Size Effect in Concrete and Other Quasibrittle Materials. CRC Press, Boca Raton (1998)
15. Bažant, Z.P., Prat, P.C.: Effect of temperature and humidity on fracture energy of concrete. ACI Mater. J. 85-M32, 262–271 (1988)
16. Bažant, Z.P., Vořechovský, M., Novák, D.: Asymptotic prediction of energetic-statistical size effect from deterministic finite element solutions. J. Engrg. Mech., ASCE 128, 153–162 (2007)

17. Bažant, Z.P., Xi, Y.: Statistical size effect in quasi-brittle structures: II. Nonlocal theory. J. Engrg. Mech., ASCE 117(7), 2623–2640 (1991)

18. Bažant, Z.P., Zhou, Y., Daniel, I.M., Caner, F.C., Yu, Q.: Size effect on strength of laminate-foam sandwich plates. J. of Engrg. Materials and Technology ASME 128(3), 366–374 (2006)

19. Chiao, C.C., Sherry, R.J., Hetherington, N.W.: Experimental verification of an accelerated test for predicting the lifetime of oragnic fiber composites. J. Comp. Mater. 11, 79–91 (1977)

20. Daniels, H.E.: The statistical theory of the strength of bundles and threads. Proc. R. Soc. London A. 183, 405–435 (1945)

21. Duckett, K.: Risk analysis and the acceptable probability of failure. The Structural Engineering 83(15), 25–26 (2005)

22. Duffy, S.F., Powers, L.M., Starlinger, A.: Reliability analysis of structural ceramic components using a three-parameter Weibull distribution. Tran. ASME J. Eng. Gas Turbines Power 115, 109–116 (1993)

23. Evans, A.G.: A method for evaluating the time-dependent failure characteristics of brittle materials and its application to polycrystalline alumina. J. Mater. Sci. 7, 1146–1173 (1972)

24. Evans, A.G., Fu, Y.: The mechanical behavior of alumina. In: Fracture in Ceramic Materials, pp. 56–88. Noyes Publications, Park Ridge (1984)

25. Fett, T., Munz, D.: Static and cyclic fatigue of ceramic materials. In: Vincenzini, P. (ed.) Ceramics Today – Tomorrow's Ceramics, pp. 1827–1835. Elsevier Science Publisher B. V., Amsterdam (1991)

26. Graham-Brady, L.L., Arwadea, S.R., Corrb, D.J., Gutiérrezc, M.A., Breyssed, D., Grigoriue, M., Zabaras, N.: Probability and Materials: from Nano- to Macro-Scale: A summary. Prob. Engrg. Mech. 21(3), 193–199 (2006)

27. Gross, B.: Least squares best fit method for the three parameter Weibull distribution: analysis of tensile and bend specimens with volume or surface flaw failure. NASA TM-4721, 1–21 (1996)

28. Harlow, D.G., Smith, R.L., Taylor, H.M.: Lower tail analysis of the distribution of the strength of load-sharing systems. J. Appl. Prob. 20, 358–367 (1983)

29. Kawakubo, T.: Fatigue crack growth mechanics in ceramics. In: Kishimoto, H., Hoshide, T., Okabe, N. (eds.) Cyclic Fatigue in Ceramics, pp. 123–137. Elsevier Science B. V. and The Society of Materials Science, Japan (1995)

30. Kaxiras, E.: Atomic and Electronic Structure of Solids. Cambridge University Press, Cambridge (2003)

31. Krausz, A.S., Krausz, K.: Fracture Kinetics of Crack Growth. Kluwer Academic Publisher, Netherlands (1988)

32. Le, J.-L., Bažant, Z.P.: Finite weakest link model with zero threshold for strength distribution of dental restorative ceramics. Dent. Mater. 25(5), 641–648 (2009)

33. Le, J.-L., Bažant, Z.P., Bazant, M.Z.: Crack growth law and its consequences on lifetime distributions of quasibrittle structures. Journal of Physics D: Applied Physics 42, 214008, 8 (2009)

34. Lohbauer, U., Petchelt, A., Greil, P.: Lifetime prediction of CAD/CAM dental ceramics. Journal of Biomedical Materials Research 63(6), 780–785 (2002)

35. Mahesh, S., Phoenix, S.L.: Lifetime distributions for unidirectional fibrous composites under creep-rupture loading. Int. J. Fract. 127, 303–360 (2004)

36. Melchers, R.E.: Structural Reliability, Analysis & Prediction. Wiley, New York (1987)

37. Munz, D., Fett, T.: Ceramics: Mechanical Properties, Failure Behavior, Materials Selection. Springer, Berlin (1999)

38. NKB (Nordic Committee for Building Structures). Recommendation for loading and safety regulations for structural design. NKB Report, No. 36 (1978)
39. Pang, S.-D., Bažant, Z.P., Le, J.-L.: Statistics of Strength of ceramics: Finite weakest link model and necessity of zero threshold. Int. J. Frac., Special Issue on Physical Aspects of Scaling 154, 131–145 (2008)
40. Philips, R.: Crystals, Defects and Microstructures: Modeling Across Scales. Cambridge University Press, Cambridge (2001)
41. Phoenix, S.L.: Stochastic strength and fatigue of fiber bundles. Int. J. Frac. 14(3), 327–344 (1978a)
42. Phoenix, S.L.: The asymptotic time to failure of a mechanical system of parallel members. SIAM J. Appl. Maths. 34(2), 227–246 (1978b)
43. Phoenix, S.L., Tierney, L.-J.: A statistical model for the time dependent failure of unidirectional composite materials under local elastic load-sharing among fibers. Engrg. Fract. Mech. 18(1), 193–215 (1983)
44. Phoenix, S.L., Ibnabdeljalil, M., Hui, C.-Y.: Size effects in the distribution for strength of brittle matrix fibrous composites. Int. J. Solids Struct. 34(5), 545–568 (1997)
45. Risken, H.: The Fokker-Plank Equation, 2nd edn. Springer, Heidelberg (1989)
46. Salem, J.A., Nemeth, N.N., Powers, L.P., Choi, S.R.: Reliability Analysis of Uniaxially Ground Brittle Materials. Journal of Engineering for Gas Turbines and Power 118, 863–871 (1996)
47. Santos, C.D., Strecker, K., Piorino Neto, F., de Macedo Silva, O.M., Baldacum, S.A., da Silva, C.R.M.: Evaluation of the reliability of Si_3N_4-Al_2O_3 -CTR_2O_3 ceramics through Weibull analysis. Materials Research 6(4), 463–467 (2003)
48. Smith, R.L.: The asymptotic distribution of the strength of a series-parallel system with equal load sharing. Ann. Probab. 10(1), 137–171 (1982)
49. Stanley, P., Inanc, E.Y.: Assessment of surface strength and bulk strength of a typical brittle material. In: Eggwertz, S., Lind, N.C. (eds.) Probabilistic methods. I. The mechanics of solids and structures, pp. 231–251. Springer, Heidelberg (1985)
50. Suresh, S.: Fatigue of Materials. Cambridge University Press, Cambridge (1998)
51. Thouless, M.D., Hsueh, C.H., Evans, A.G.: A damage model of creep crack growth in polycrystals. Acta. Metall. 31(10), 1675–1687 (1983)
52. Tinschert, J., Zwez, D., Marx, R., Ausavice, K.J.: Structural reliability of alumina-, feldspar-, leucite-, mica- and zirconia-based ceramics. J. Dent. 28, 529–535 (2000)
53. Xu, X.F.: A multiscale stochastic finite element method on elliptic problems involving uncertainties. Comput. Meth. Appl. Mech. Engrg. 196, 2723–2736 (2007)
54. Wagner, H.D.: Stochastic concepts in the study of size effects in the mechanical strength of highly oriented polymeric materials. J. Polym. Sci. 27, 115–149 (1989)
55. Wagner, H.D., Schwartz, P., Phoenix, S.L.: Lifetime statistics for single Kevlar 49 filaments in creep-rupture. J. Polym. Sci. 21, 1868–1878 (1986)
56. Weibull, W.: The phenomenon of rupture in solids. In: Proc. Royal Swedish Inst. Eng. Res., Stockholm, vol. 153, pp. 1–55 (1939)
57. Williams, T., Baxer, S.C.: A framework for stochastic mechanics. Prob. Engrg. Mech. 21(3), 247–255 (2006)

Directional Distortional Hardening in Plasticity within Thermodynamics

Yannis F. Dafalias[1] and Heidi P. Feigenbaum[2]

[1] Department of Mechanics, Faculty of Applied Mathematical and Physical Science, National Technical University of Athens, Zographou, Hellas, and Department of Civil and Environmental Engineering, University of California, Davis CA, USA
   yfdafalias@central.ntua.gr
[2] Department of Mechanical Engineering, Northern Arizona University, Flagstaff AZ, USA
   Heidi.Feigenbaum@nau.edu

Abstract. This paper presents a complete theory for metal plasticity that includes directional distortional hardening, supplemented by the classical kinematic and isotropic hardenings. Starting from an isotropic yield surface, the distortional hardening will be modeled either by fourth-order tensor-valued internal variable multiplied by a scalar, a scalar-valued internal variable in conjunction with the back stress, or a second-order tensor-valued internal variable. These models are unique because the rate equations for all internal variables, including the fourth order tensor, are derived strictly on the basis of sufficient conditions for the satisfaction of the second law of thermodynamics for positive dissipation, in conjunction with a few simple and plausible assumptions about free energy storage and release in the material. The models are shown to fit experimentally found yield surfaces rather well, in particular the model with the fourth-order tensor. Furthermore, this model is shown to simulate stress controlled biaxial ratchetting better than the same model without distortion of the yield surface.

1 Introduction

In the field of continuum mechanics it has long been recognized that plastic deformations may induce anisotropy in materials that are initially isotropic. For metals such anisotropy is due to the development of internal stresses and texture formation because of preferred orientations of grains in a polycrystal, among other reasons. The macroscopic manifestation of metal anisotropy takes the form of translation and shape distortion of the yield surface in stress space, modeled by kinematic and distortional hardening, respectively. Isotropic hardening or softening is an additional feature that is modeled by a uniform increase or decrease of the size of the yield surface and does not reflect anisotropic development but rather it is related to change of the density of dislocations.

In particular, "directional distortion" is a distortion of the shape of the yield surface such that a region of high curvature (sharpening) develops roughly in the

direction of loading while a region of lower curvature (flattening) develops in the opposite direction. This observation has been seen in numerous experiments on various types of metals including, but not limited to, those by Phillips et al. [14], Naghdi et al. [12], McComb [11], Wu and Yeh [18], and Boucher et al. [3]. In general, directional distortion of the yield surface is observed when a relatively sensitive definition of yield is used. For example, Phillips et al. [14], Wu and Yeh [18], and Boucher et al. [3] define yield by offset strains of 3×10^{-6}, 5×10^{-6}, and 4×10^{-5}, correspondingly.

Fig. 1 illustrates the directional distortion by showing a sample yield surface in a two-dimensional stress space of a normal and a shear stress component, often used in plotting experimental data. The factor $\sqrt{3}$ multiplying the shear stress component aims at representing the Mises-type yield surface as a circle, had it not been distortion, and such circular yield surface is also shown by dashed line for comparison with the distorted one. Also, anticipating the associative flow rule, the unit deviatoric tensor $\mathbf{n}$, normal to the yield surface, is drawn at a current stress point symbolized by $\mathbf{s}$. Notice that $\mathbf{s}$ is not the tension stress that induced the yield surface configurations of Fig. 1, but it was chosen for illustration purposes at an arbitrary location on the distorted yield surface. In general the "directions" of the back-stress $\boldsymbol{\alpha}$, unit radial expressed by the $\mathbf{n}_r$, and outward unit normal $\mathbf{n}$, are different tensors, as shown in the figure, where the direction of $\boldsymbol{\alpha}$ is along the tension axis for this figure. In particular, the unit tensors $\mathbf{n}_r$ and $\mathbf{n}$ are different because of the distortion, since without it the yield surface remains a circle and the direction of the radius along $\mathbf{n}_r$ coincides with that of the normal along $\mathbf{n}$.

The modeling of directional distortion has been addressed at various degrees of success by Ortiz and Popov [13], Voyiadjis and Foroozesh [16], Kurtyka and Zyczkowski [10], Yeh et al. [17], and François [7], among others. Most recently Feigenbaum an Dafalias [5, 6] developed models for directional distortional hardening. The Feigenbaum and Dafalias 2007 uses a fourth order tensor multiplied by a scalar to capture directional distortional hardening. In Feigenbaum and Dafalias 2008 two simpler models are proposed which capture directional distortional hardening. The first uses a scalar-valued internal variable in conjunction with the back-stress to model the directional distortion, and the second model uses a new second order tensor to capture directional distortion, and thus distortion and kinematic hardening are completely decoupled. In all the Feigenbaum and Dafalias models [5, 6] the rate equations for all internal variables, including the fourth order tensor, are derived strictly on the basis of sufficient conditions for the satisfaction of the second law of thermodynamics for positive dissipation, in conjunction with a few simple plausible assumptions of free energy storage and release in the material. One aspect of any distortional hardening model, including directional distortion, is the preservation of convexity of the yield surface during its change of shape process, an issue of great importance in plasticity theory for reasons of uniqueness and stability. In Plesek et al. [15] conditions to ensure convexity of the Feigenbaum and Dafalias models [5, 6] were derived.

The current paper examines the models by Feigenbaum and Dafalias [5, 6] including the mathematical formulation of the models and model performance. The
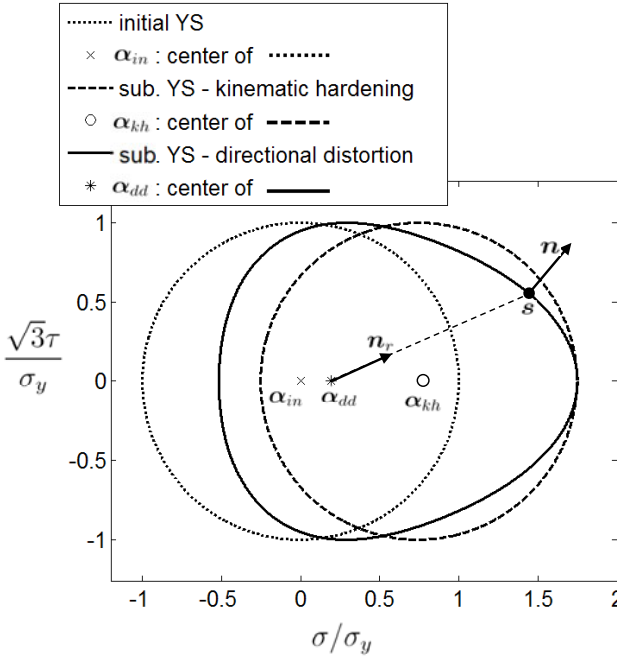
Fig. 1. An example of directional distortion of the yield surface for loading in pure tension. Note the two subsequent yield surfaces have the same final stress point in tension, but the center of the directionally distorted yield surface is moved less than that with kinematic hardening.

performance of the models will be evaluated against experimentally found yield surfaces as well as experimental results from cyclic loading in the plastic range, a.k.a. ratchetting. Modeling ratchetting behavior is extremely difficult because any small error in plastic strain during a single cycle will add to become a large error after many cycles. As is typical with metals, most constitutive models used to fit ratcheting use the associative flow rule which states that the plastic strain increment is in the direction normal to the yield surface. When the associative flow rule is used, it is important to have the shape of the yield surface modeled accurately because small deviations in shape may result in large deviations in the normal to the yield surface and thus the plastic strain increment. During cyclic plastic loading these deviations will accumulate and may result in large errors for the predicted strains.

In terms of notation, all second order tensors will be denoted, henceforth, by bold face in direct notation, e.g. $\mathbf{m}$, and all fourth order tensors will be capitalized in bold calligraphy, e.g. $\mathcal{M}$. No bold face symbols will be used when indexed components of tensors are used. The proposed constitutive model is confined to small deformations. The stress tensor is denoted by $\boldsymbol{\sigma}$ and the linearized strain tensor is denoted by $\boldsymbol{\varepsilon}$. As usual, the strain tensor is decomposed into elastic and plastic parts ($\boldsymbol{\varepsilon} = \boldsymbol{\varepsilon}^e + \boldsymbol{\varepsilon}^p$) and the elastic constitutive law will be assumed linear and isotropic.

2   Mathematical Formulation of Models

The Feigenbaum and Dafalias 2007 model uses the following yield function:

$$f = (\mathbf{s} - \boldsymbol{\alpha}) : [\mathfrak{I} + (\mathbf{n}_r : \boldsymbol{\alpha})\mathcal{A}](\mathbf{s} - \boldsymbol{\alpha}) - k^2 = 0. \tag{1}$$

where $\mathbf{s}$ is the deviatoric component of the stress tensor, $\boldsymbol{\alpha}$ is the deviatoric back-stress tensor that represents the "center" of the yield surface, k represents the size of the yield surface, $\mathcal{A}$ is the fourth-order evolving anisotropic tensor, $\mathfrak{I}$ is the fourth order isotropic unit tensor given by the expression $\mathfrak{I}_{ijkl} = \frac{3}{2} \left[\frac{1}{2} \left(\delta_{ik}\delta_{jl} + \delta_{il}\delta_{jk} \right) - \frac{1}{3}\delta_{ij}\delta_{kl} \right]$, with δ_{ij} the Kronecker delta, and $\mathbf{n}_r$ is the radial, in regards to the center of the yield surface, deviatoric unit tensor illustrated in Fig. 1 and defined by

$$\mathbf{n}_r = \frac{\mathbf{s} - \boldsymbol{\alpha}}{|\mathbf{s} - \boldsymbol{\alpha}|} \tag{2}$$

with the symbol $|\cdot|$ representing the norm of a tensor defined as $|\mathbf{m}| = \sqrt{\mathbf{m} : \mathbf{m}}$, and where : denote the trace operation of the product of two adjacent tensors. The fourth order anisotropic tensor, $\mathcal{A}$, is responsible for distortional hardening in general, and the trace-type scalar multiplier, $\mathbf{n}_r : \boldsymbol{\alpha}$, is responsible for the directionality of distortion. This can be intuitively understood if one observes that the trace $\mathbf{n}_r : \boldsymbol{\alpha}$ is an inner product between the tensors $\mathbf{n}_r$ and $\boldsymbol{\alpha}$, thus, it actually takes the "projection" of $\boldsymbol{\alpha}$ along the different "unit" directions $\mathbf{n}_r$. This product can vary from $|\boldsymbol{\alpha}|$ to $-|\boldsymbol{\alpha}|$ passing through zero, and such variation effects the role of the distortional tensor $\mathcal{A}$ which is multiplied by it. Since the fourth-order tensor $\mathcal{A}$ is the corner stone of this model, it will henceforth be referred to as the "$\mathcal{A}$-model."

In Feigenbaum and Dafalias 2008 two yield functions are proposed, the first of which can been understood as a special case of (1) where $\mathcal{A}$ is constantly aligned with the fourth order unit isotropic tensor $\mathfrak{I}$ by means of a possibly varying proportionality factor, which gives rise to the following simpler expression for the yield function:

$$f = \frac{3}{2} \left[1 - c(\mathbf{n}_r : \boldsymbol{\alpha}) \right] (\mathbf{s} - \boldsymbol{\alpha}) : (\mathbf{s} - \boldsymbol{\alpha}) - k^2 = 0 \tag{3}$$

where c is a scalar-valued internal variable (c can be also a constant) whose magnitude is directly associated with the amount of distortion of the yield surface. Since the back stress $\boldsymbol{\alpha}$ is the entity which dictates the directional distortion, this model will be referred to as the "$\boldsymbol{\alpha}$-model." One criticism one might raise for the models in Eqs. (1) and (3) is that distortional hardening is coupled with kinematic hardening due to the role the back stress plays in the distortion scheme, while the underlying physics would imply an uncoupled consideration. To alleviate this problem a second yield function was proposed in Feigenbaum and Dafalias 2008,

$$f = \frac{3}{2} \left[1 - (\mathbf{n}_r : \mathbf{r}) \right] (\mathbf{s} - \boldsymbol{\alpha}) : (\mathbf{s} - \boldsymbol{\alpha}) - k^2 = 0 \tag{4}$$

where $\mathbf{r}$ is a second order deviatoric tensor-valued directional distortional hardening internal variable. By introducing $\mathbf{r}$ in Eq. (4) the scalar quantity $\mathbf{n}_r : \mathbf{r}$ is completely

responsible for directional distortion, therefore, kinematic hardening has been decoupled from distortional hardening. Since $\mathbf{r}$ is the entity which dictates the directional distortion, this model will be referred to as the "$\mathbf{r}$-model."

All models in consideration use the associative flow rule, as is typical with metal plasticity:

$$\dot{\boldsymbol{\varepsilon}}^{\mathbf{p}} = \lambda \frac{\partial f}{\partial \boldsymbol{\sigma}} = \lambda \left| \frac{\partial f}{\partial \boldsymbol{\sigma}} \right| \mathbf{n} \tag{5}$$

where $\dot{\boldsymbol{\varepsilon}}^{\mathbf{p}}$ is the rate of plastic strain, λ is the loading index (alias plastic multiplier), which can be determined from the consistency condition and the hardening rules for the internal variables, and $\mathbf{n}$ is the unit tensor ($\mathbf{n} : \mathbf{n} = 1$) normal to the yield surface as shown in Fig. 1.

The hardening rules for these models are obtained from conditions sufficient for satisfaction of the second law of thermodynamics, in conjunction with a few simple and plausible assumptions about energy storage and release in the material. Details of these thermodynamic assumptions and how the hardening rules are derived in a way which is sufficient to satisfy the second law of thermodynamics can be found in Feigenbaum and Dafalias [5, 6]. For now only the hardening rules themselves along with some thermodynamically necessary restrictions will be presented.

All three models give rise to the same form of isotropic and kinematic hardening, namely:

$$\dot{k} = \lambda \kappa_1 k (1 - \kappa_2 k) \tag{6}$$

$$\dot{\boldsymbol{\alpha}} = \lambda \left| \frac{\partial f}{\partial \boldsymbol{\sigma}} \right| a_1 (\mathbf{n} - a_2 \boldsymbol{\alpha}) \tag{7}$$

where κ_1, κ_2, a_1 and a_2 are non-negative material constants whose exact values depend on which model is used, i.e. the values for these constants will not be the same in the $\mathcal{A}$-model as in the $\boldsymbol{\alpha}$-model or in the $\mathbf{r}$-model, since the form for the plastic modulus depends on which model is used.

The hardening rules that arise for the distortional parameters for the three models are as follows:

$$\dot{\mathcal{A}} = -\lambda A_1 |\mathbf{s} - \boldsymbol{\alpha}|^2 \left[(\mathbf{n}_r : \boldsymbol{\alpha}) \mathbf{n}_r \otimes \mathbf{n}_r + \frac{3}{2} A_2 \mathcal{A} \right] \tag{8}$$

$$\dot{c} = \frac{3}{2} \lambda c_1 |\mathbf{s} - \boldsymbol{\alpha}|^2 [(\mathbf{n}_r : \boldsymbol{\alpha}) - c_2 c] \tag{9}$$

$$\dot{\mathbf{r}} = \frac{3}{2} \lambda \rho_1 |\mathbf{s} - \boldsymbol{\alpha}|^2 (\mathbf{n}_r - \rho_2 \mathbf{r}) \tag{10}$$

where A_1, A_2, c_1, c_2, ρ_1 and ρ_2 are non-negative material constants. These hardening rules are sufficient for the satisfaction of the second law of thermodynamics provided that

$$A_2 |\mathcal{A}|^2 \leqslant 1 \quad , \quad c_2 c^2 \leqslant 1 \quad , \quad \rho_2 |\mathbf{r}|^2 \leqslant 1 \tag{11}$$

for all time, where $|\mathcal{A}|^2 = \mathcal{A} :: \mathcal{A}$ and $|\mathbf{r}|^2 = \mathbf{r} : \mathbf{r}$ are Euclidean norms.

Notice that all hardening rules for all models are of the evanescent memory type, therefore the internal variables all reach finite limits. These limits can be found by setting the rate equations in (6)-(10) equal to zero, which yields:

$$k^l = \frac{1}{\kappa_2} \tag{12}$$

$$\boldsymbol{\alpha}^l = \frac{1}{a_2}\mathbf{n}^l \tag{13}$$

$$\boldsymbol{\mathcal{A}}^l = -\frac{2}{3A_2 a_2}\mathbf{n}_r^l \otimes \mathbf{n}_r^l \tag{14}$$

$$c^l = \frac{1}{a_2 c_2} \tag{15}$$

$$\mathbf{r}^l = \frac{1}{\rho_2}\mathbf{n}_r^l \tag{16}$$

where the superscript l denotes the limit values of the quantities involved, and the fact that $\mathbf{n}_r^l = \mathbf{n}^l$ at the limit, as shown in Feigenbaum and Dafalias [5, 6], has been evoked. Assuming that the maximum of the inequalities in (11) occurs at the limit, the thermodynamic requirements in (11) give the following restrictions on material constants for the $\boldsymbol{\mathcal{A}}$-model, $\boldsymbol{\alpha}$-model and $\mathbf{r}$-model, correspondingly:

$$a_2^2 A_2 \geqslant \frac{4}{9} \quad , \quad a_2^2 c_2 \geqslant 1 \quad , \quad \rho_2 \geqslant 1 \tag{17}$$

The assumption of associative flow in conjunction with Drucker's or Il'iushin's postulates makes it necessary to explore the issue of convexity for these models. In Plesek et al. [15] conditions for convexity were proven. For the $\boldsymbol{\mathcal{A}}$-, $\boldsymbol{\alpha}$-, and $\mathbf{r}$ models, respectively,

$$a_2^2 A_2 > 0.55 \quad , \quad a_2^2 c_2 > 1 \quad , \quad \rho_2 > 1 \tag{18}$$

is required for the yield surface to remain convex. Note that as explained in Plesek et al. [15], for the $\boldsymbol{\mathcal{A}}$-model it is assumed that the most distorted yield surface occurs at the limit state. Also notice for the $\boldsymbol{\alpha}$- and $\mathbf{r}$-models the requirement for convexity is the same as the requirement for the satisfaction of thermodynamic requirements.

3 Model Performance

In order to show the effectiveness of the model, its simulations will be compared to experimentally found yield points. Figs. 2 - 7 show experimental data from Wu and Yeh [18]. These experiments were performed on thin-walled tubes of annealed 304 stainless steel. The data in Figs. 2 - 4 were obtained using a strain controlled procedure and loading in torsion (shear). For Figs. 5 - 7 the data was obtained using stress controlled procedure with loading in combination of tension and torsion.

Table 1. Material constants used to fit Wu and Yeh [18] experimental data on stainless steel 304 found in Figs. 2 - 7.

	$\mathcal{A}$-model	α-model	$\mathbf{r}$-model
E	196687 MPa	196687 MPa	196687 MPa
ν	0.28	0.28	0.28
k_0	128 MPa	128 MPa	128 MPa
κ_1	6000 MPa^2	6000 MPa^2	6000 MPa^2
κ_2	0.008 MPa^{-1}	0.012 MPa^{-1}	0.012 MPa^{-1}
a_1	40000 MPa	17000 MPa	18000 MPa
a_2	0.0065 MPa^{-1}	0.012 MPa^{-1}	0.01 MPa^{-1}
A_1	0.5 MPa^{-4}	-	-
A_2	20000 MPa^2	-	
c_1	-	0.01 MPa^{-3}	-
c_2	-	10001 MPa^2	-
ρ_1	-	-	1.9 MPa^{-1}
ρ_2	-	-	1.3

Fig. 5 shows both loading, unloading and negative loading in this path. Wu and Yeh [18] defined yield as an offset equal to 5×10^{-6}.

Figs. 8 - 9 show experimental data from Boucher et al. [3]. These experiments were performed on thin-walled tubes of aluminum alloy AU4G T4 (2024). The tubes were loaded using stress control in combination of tension and torsion (shear) and yield was defined by an offset equal to 4×10^{-5}. Figs. 8 - 9 shows loading and unloading in non-proportional path (path is given by O-A-B-C as shown in the figures). Notice that there is a scale difference in the plotings of Figs. 8 and 9, hence, the same data appear to be different at first impression.

To fit these experiments, the three versions of the model were implemented numerically using the procedure outlined by Bardet and Choucair [1]. This procedure essentially takes loading increments of stress, strain, or combinations of the two and converts them into increments of stress only. Using this procedure, the numerical loading conditions exactly matched those from the experiment, and each increment of load is converted into stress increments. Once the stress increment is obtained, incremental changes of strain and internal variables are calculated using the associative flow rule and the hardening rules, along with the standard calculations for loading index and plastic modulus. The numerical procedure solves the rate equations by an explicit method, and thus small steps were used to ensure convergence and good accuracy.

Table 1 shows the material parameters used to obtain the model fitting in Figs. 2 - 7. For Fig. 8 the kinematic and distortional hardening constants are given by: $a_1 = 2 \times 10^6$ MPa, $a_2 = 0.015$ MPa^{-1}, $A_1 = 20$ MPa^{-4}, and $A_2 = 2.5 \times 10^3$ MPa^2. To determine the plastic material parameters, first experimental data were fit using only Armstrong-Frederick kinematic hardening along with isotropic hardening, then the amount of kinematic hardening was reduced (the limit value was
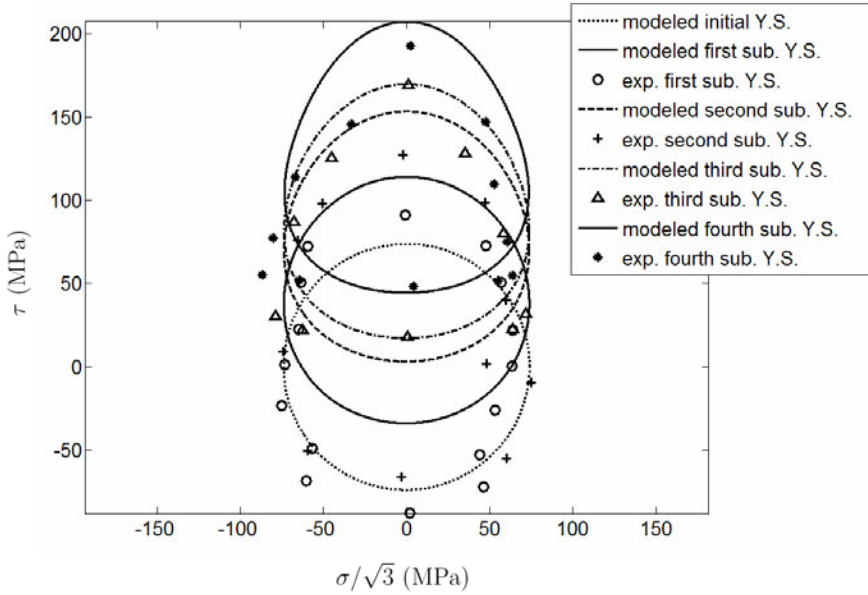
Fig. 2. $\mathcal{A}$-model compared to torsion experiments by Wu and Yeh [18]. The first, second, third, and fourth subsequent yield surfaces resulted from strain controlled loading with final values $\gamma = 0.19\%, 0.38\%, 0.49\%$ and 1.03%, respectively. Lines represent the proposed constitutive model and discrete points represent experimental data.

increased and the rate of saturation slowed) to allow for distortion to be added. Lastly, both the parameters associated with kinematic hardening (a_1 and a_2) as well as those associated with distortion (A_1 and A_2, or c_1 and c_2, or ρ_1 and ρ_2) were adjusted, using the constraint in Eqs. (17) and (18) as a guide. Thus the material parameters are not necessarily optimal for the material, but rather a relatively good fit for the data shown. It was also observed that with the $\boldsymbol{\alpha}$-model the use of a constant value of c gave very good results compared to the choice of a variable c (this can also be detected from the large difference of the numerical values of c_1 and c_2 in Table 1). The constant value of c still allows for the directional distortional feature of the α-model and can be viewed as a special case that is even simpler than those presented in this paper. Fig. 9 shows the fitting of the Boucher et al. [3] data using the α-model and a constant c=0.019MPa^{-1}.

Clearly, there are some flaws in the way the models fit the data. Since the Wu and Yeh [18] data in Figs. 2 - 4 were fit using strain control, it was much more difficult to match the stress points, which can be seen in these figures. With both the $\boldsymbol{\alpha}$ and $\mathbf{r}$-models, the simulations fit the region of high curvature relatively well, but they do not show sufficient flattening in the direction opposite, whereas the experiments do. The same could be said for the $\mathcal{A}$-model, however, overall that model fits the data better than either of the other two. Figs. 8 - 9 show that the
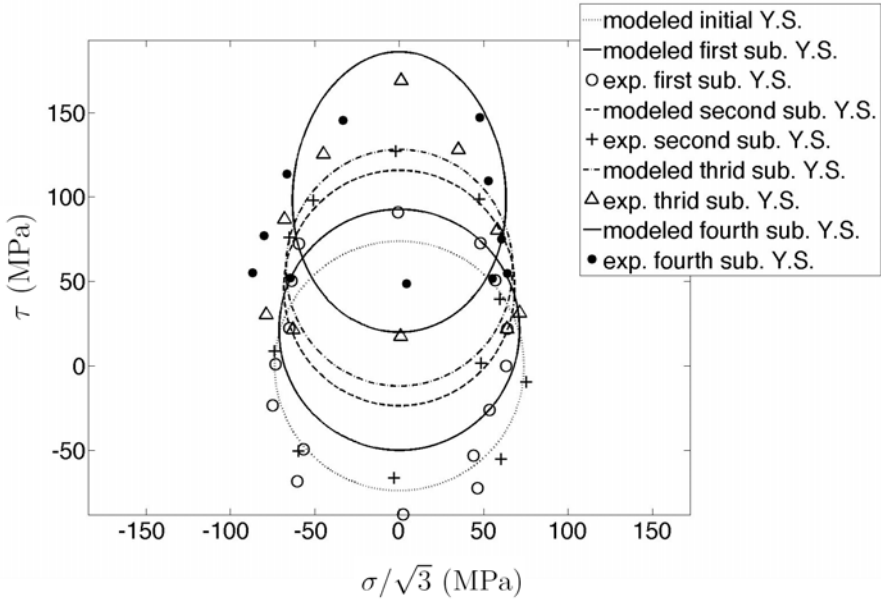
Fig. 3. α-model with evolving c compared to torsion experiments by Wu and Yeh (1991). The first, second, third, and fourth subsequent yield surfaces resulted from strain controlled loading with final values $\gamma = 0.19\%, 0.38\%, 0.49\%$ and 1.03%, respectively. Lines represent the proposed constitutive model and discrete points represent experimental data.

models can simulate complex loading paths. The fitting of the data in Fig. 9 may be considered satisfactory given the simplicity of the model used, however, as Fig. 8 shows the $\mathcal{A}$-model simulates the data better.

3.1 Ratchetting

Since the $\mathcal{A}$-model is the most complete and fits experimentally found yield surfaces best, it will be used to simulate experimental cyclic plastic loading data. During cyclic plastic loading, plastic strain accumulates and this is called ratchetting. When the load is applied in two directions biaxial ratchetting occurs. Both stress and stress controlled cyclic biaxial tests from Hassan et al. [9] will be simulated, and uniaxial cyclic tests from Hassan and Kyriakides [8] will be used for calibration. In biaxial stress controlled tests the material ratchets in two directions, and thus these test have been especially difficult to simulate.

Experiments in the study by Hassan and Kyriakides [8] and Hassan et al. [9] were performed on thin walled tubes of carbon steel 1026. For the uniaxial experiments, axial stress was applied cyclically. Various levels of mean stress σ_{xm} were used and the stress amplitude was $\sigma_{xa} = 0.79\sigma_0$, where $\sigma_0 = 40$ ksi. For the strain controlled biaxial data, the tubes were first loaded with internal pressure σ_θ and then cycled axially using various levels of strain amplitude ε_{xc}. While the cyclic loading was
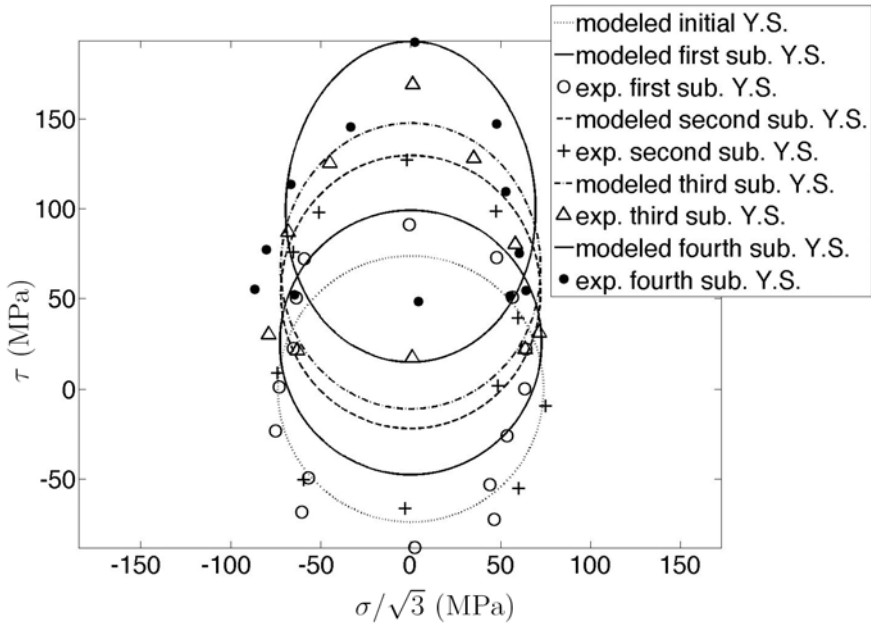
Fig. 4. r-model compared to torsion experiments by Wu and Yeh (1991). The first, second, third, and fourth subsequent yield surfaces resulted from strain controlled loading with final values $\gamma = 0.19\%, 0.38\%, 0.49\%$ and 1.03%, respectively. Lines represent the proposed constitutive model and discrete points represent experimental data.

occurring the internal pressure was kept constant. This results in strain accumulation, i.e., ratchetting, in the circumferential direction ε_θ. For the stress controlled biaxial data, tubes were first stabilized by strain symmetric axial cycles in the range of $\pm 1\%$ and in approximately twelve cycles the hysteresis loops were stable. Following the strain symmetric cycling the specimens were unloaded to approximately zero axial stress and strain, although typically some small residual circumferential strain remained non-zero, then preloaded using stress control with various internal pressures. Following the internal pressure, the tubes were stress controlled cyclically loaded in the axial direction about a nonzero mean stress σ_{xm} with amplitude σ_{xa}. The stress controlled biaxial loading in conjunction with the cycling about nonzero mean axial stress results in plastic strains accumulating in both the circumferential and the axial directions.

With kinematic hardening alone, the Armstrong-Frederick kinematic hardening rule generally does not fit experimental results from cyclic plastic loading paths very well, therefore researchers have developed numerous other kinematic hardening rules which show improvement in fitting cyclic loading. This paper will use the
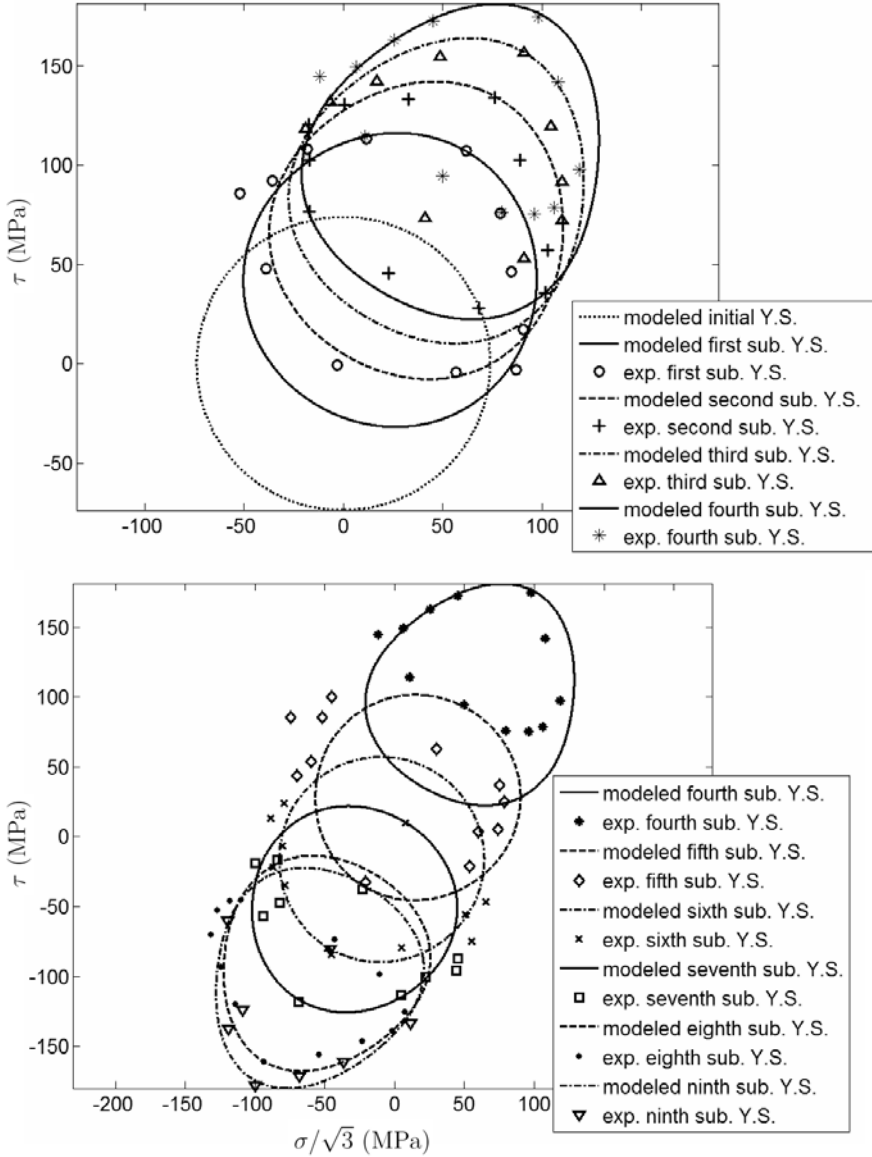
Fig. 5. $\mathcal{A}$-model compared to stress controlled combined tension-torsion experiments by Wu and Yeh [18]. Top figure shows the loading and bottom figure shows unloading and negative loading. For both figures the loading path was proportional with normal stress equal to shear stress, i.e., $\sigma = \tau$. Lines represent the proposed constitutive model and discrete points represent experimental data.
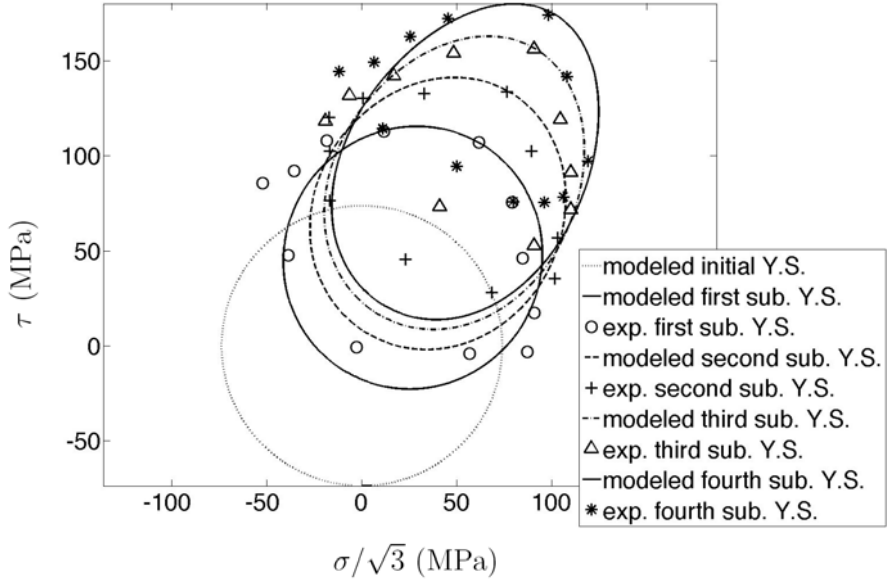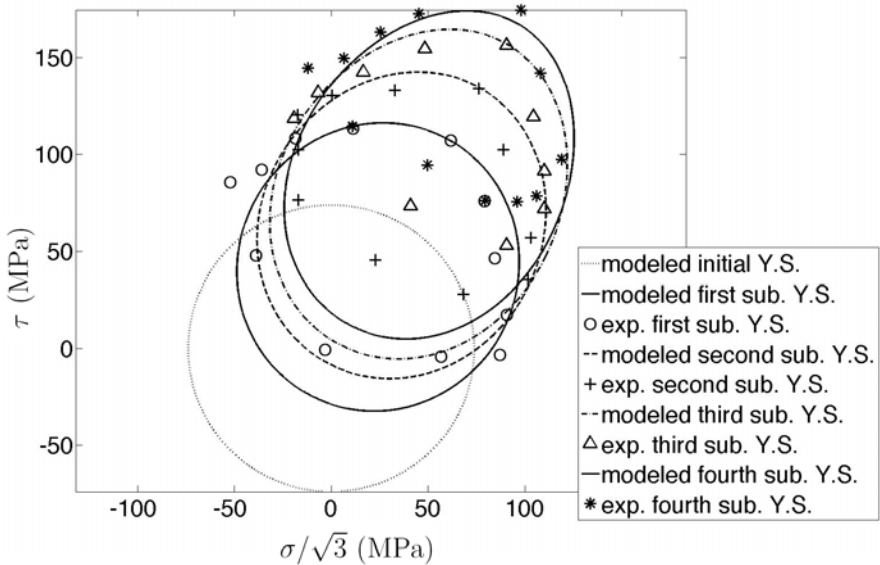
Fig. 6. α-model with evolving c compared to stress controlled combined tension-torsion experiments by Wu and Yeh (1991). The loading path was proportional with normal stress equal to shear stress, i.e., $\sigma = \tau$. Lines represent the proposed constitutive model and discrete points represent experimental data.

Fig. 7. r-model compared to stress controlled combined tension-torsion experiments by Wu and Yeh (1991). The loading path was proportional with normal stress equal to shear stress, i.e., $\sigma = \tau$. Lines represent the proposed constitutive model and discrete points represent experimental data.
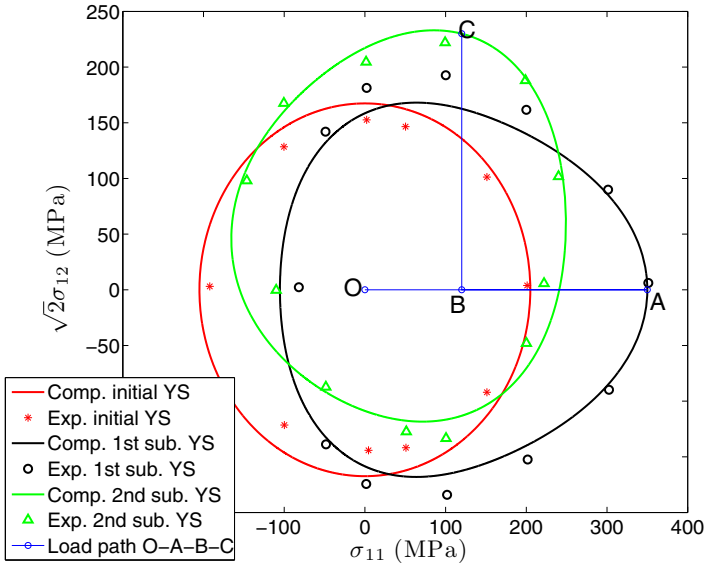
Fig. 8. $\mathcal{A}$-model compared to stress controlled combined tension and shear experiments by Boucher et al. [3]. Specimens were loaded in pure tension, unloaded some, then loaded in pure torsion. The load path is shown on the figure as O-A-B-C.
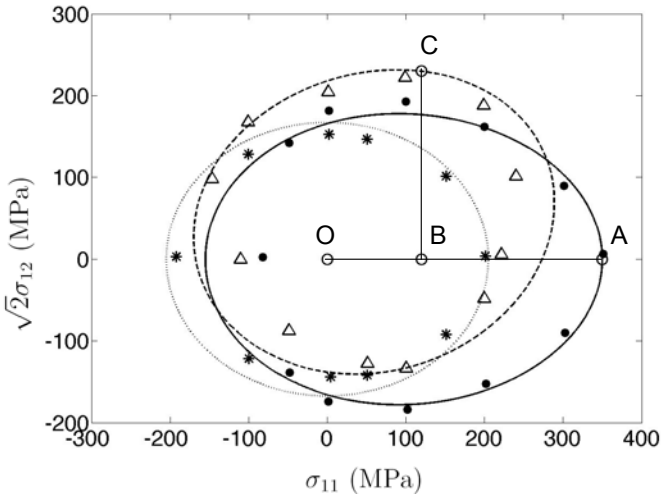

Fig. 9. α-model with fixed c compared to stress controlled combined tension and shear experiments by Boucher et al. [3]. Specimens were loaded in pure tension, unloaded some, then loaded in pure torsion. The load path is shown on the figure as O-A-B-C. Computed initial yield surface: $\cdots$, experiential initial yield points: $*$, computed first subsequent yield surface: —, experiential first subsequent yield points: $\bullet$, computed second subsequent yield surface: - - -, experiential second subsequent yield points: $\triangle$.

Table 2. Material constants used to fit ratchetting data from Hassan et al. [9].

	without distortion	with distortion
k_0	18.8	18.8
c_1	20000	19000
a_1^s	3	2.85
c_2	400	380
a_2^s	8.07	7.67
c_3	10.45	11
a_3^s	39.3	41.36
c_4	5000	5000
a_4^s	3	3
$\bar{a}$	5	5
A_1	-	2
A_2	-	1125

kinematic hardening rule proposed by Chaboche [4] for cyclic loading. This kinematic hardening rule can be expressed as:

$$\boldsymbol{\alpha} = \sum_{i=1}^{4} \boldsymbol{\alpha}_i$$

$$\dot{\boldsymbol{\alpha}}_i = \lambda \left| \frac{\partial f}{\partial \boldsymbol{\sigma}} \right| \sqrt{\frac{2}{3}} (\sqrt{\frac{2}{3}} a_i^s \mathbf{n} - \boldsymbol{\alpha}_i) \qquad (i = 1, 2, 3)$$

$$\dot{\boldsymbol{\alpha}}_4 = \lambda \left| \frac{\partial f}{\partial \boldsymbol{\sigma}} \right| \sqrt{\frac{2}{3}} \left(\sqrt{\frac{2}{3}} a_i^s \mathbf{n} - \boldsymbol{\alpha}_i \left\langle 1 - \frac{\bar{a}}{f(\boldsymbol{\alpha}_4)} \right\rangle \right) \qquad (19)$$

where $f(\boldsymbol{\alpha}) = \sqrt{\frac{3}{2} \boldsymbol{\alpha} : \boldsymbol{\alpha}}$.

To calibrate the model for ratchetting data, the model with kinematic hardening alone was calibrated by Bari and Hassan [2] and then both material parameters associated rate and saturation values for kinematic hardening are decreased and direction distortional hardening parameters are added using Eqns. (17) and (18) as a guide. This procedure exactly mimics what was done to fit experimentally found yield surfaces, except in this case the strain symmetrically stabilized data as well as the uniaxial cyclic data were used for calibration. For simplicity no isotropic hardening was included and no adjustments were made to the parameters associated with $\boldsymbol{\alpha}_4$, where the threshold is contained, and approximately equal adjustments were made to the parameters associated with $\boldsymbol{\alpha}_i$ where $i = 1$, 2, or 3. The results of the calibration can be seen in Fig. 10 and the parameters are given in Table 2 where all units are consistent with ksi.

Figs. 11 and 12 show the model simulating ratchetting data from Hassan et al. [9]. For the strain controlled ratchetting in Fig. 11 the model with directional distortional hardening performs about as well as the model with kinematic hardening alone. For the stress controlled ratchatting in Fig. 12, the model with directional disortional
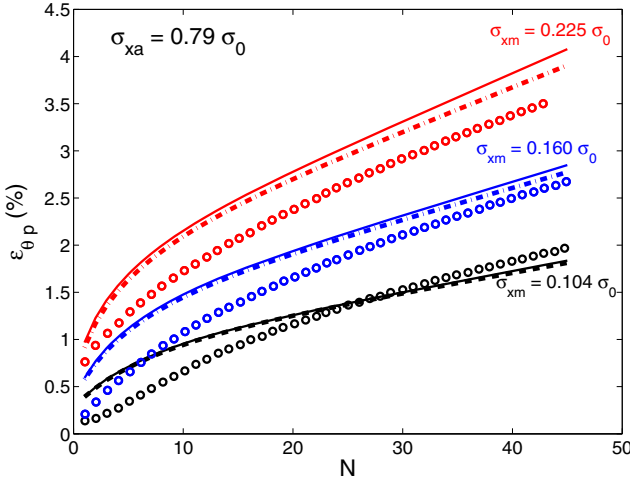
Fig. 10. $\mathcal{A}$-model as calibrated to the uniaxial ratchetting experimental data. The simulations with kinematic hardening alone are shown as solid lines, the simulation with kinematic hardening and directional distortional hardening are shown as dashed lines, and the experimental data are shown as discrete points. In all cases the stress amplitude is $\sigma_{xa} = 0.79\sigma_0$ and three different mean stress σ_{xm} values are shown.
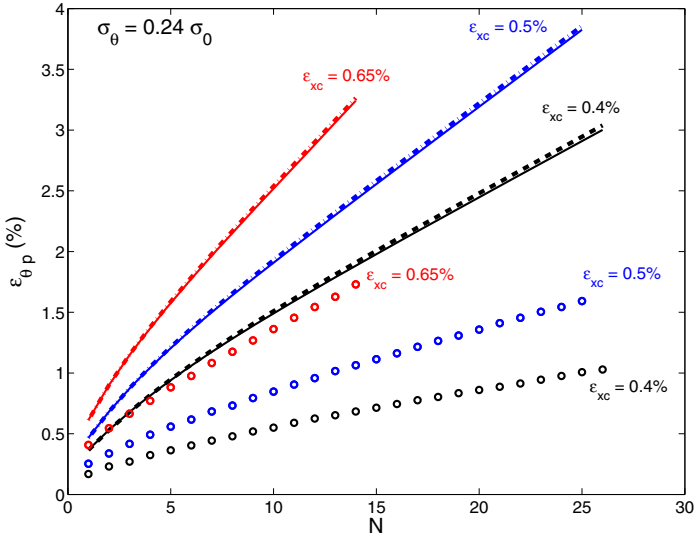

Fig. 11. Strain controlled biaxial ratchetting simulations and experimental data. The simulations with kinematic hardening alone are shown as solid lines, the simulation with kinematic hardening and directional distortional hardening are shown as dashed lines, and the experimental data are shown as discrete points. In all cases the internal pressure is kept constant ($\sigma_\theta = 0.24\sigma_0$) while the strain is cycled symmetrically at different amplitude, ε_{xc}.
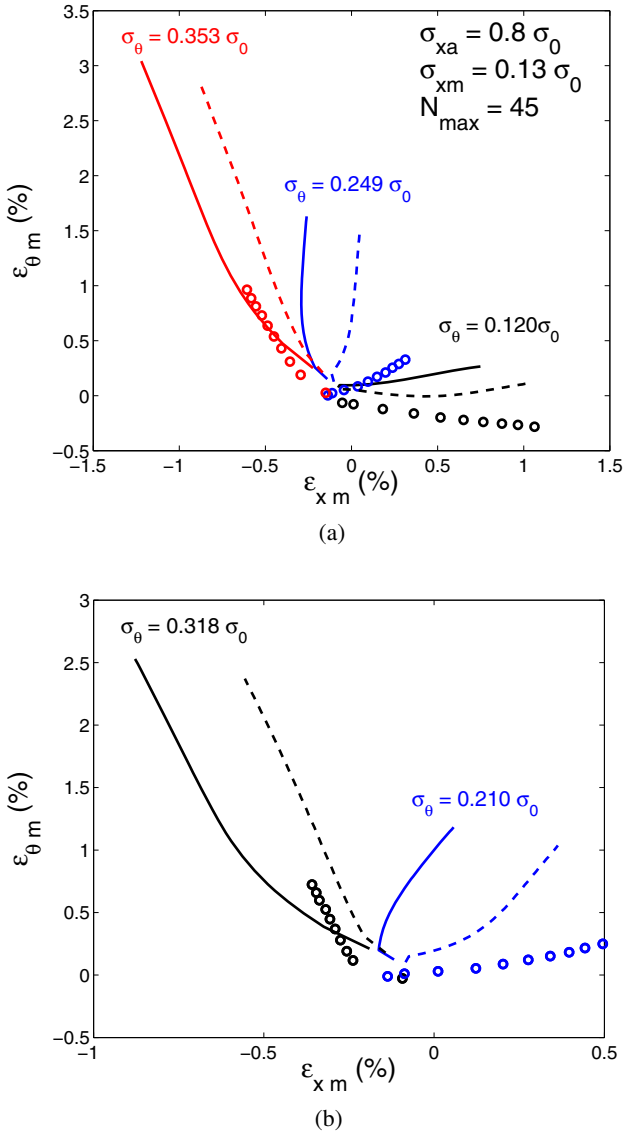
Fig. 12. Stress controlled biaxial ratchetting simulations and experimental data. The simulations with kinematic hardening alone are shown as solid lines, the simulation with kinematic hardening and directional distortional hardening are shown as dashed lines, and the experimental data are shown as discrete points. The mean axial strain ε_{xm} and the mean circumferential strain $\varepsilon_{\theta m}$ per cycle are both predicted values. In both 12(a) and 12(b) the axial stress amplitude is $\sigma_{xa} = 0.8\sigma_0$, the mean axial stress is $\sigma_{xm} = 0.13\sigma_0$ and 45 cycles were performed. Each data set has a different the value for the internal pressure (which leads to σ_θ).

hardening performs consistently better. For some data sets the addition of directional distortion hardening results in more dramatic improvement (e.g., Fig. 12(b) with $\sigma_\theta = 0.210\sigma_0$), while in others the improvement is minor (e.g., Fig. 12(a) with $\sigma_\theta = 0.353\sigma_0$). Nonetheless, from Fig. 12 it is clear that directional distortional hardening improves the simulation of stress controlled biaxial ratchetting.

4 Conclusion

It is very importance to accurately model the shape of the yield surface when using the associative flow rule not only for capturing accurately the yield point, but mainly because any deviation in shape may result in significant deviation of the direction of the normal to the yield surface and, thus, of the coaxial plastic strain increment, which during cyclic loading and resulting ratcheting accumulates the error to unacceptable levels. Three different models were developed within thermodynamics by Feigenbaum and Dafalias [5, 6] capturing this phenomenon of directional distortion of the yield surface, and for the first time are presented in unison in this paper. The Feigenbaum and Dafalias model [5] (i.e., the $\mathcal{A}$-model) uses a fourth order tensor and a scalar multiplier to capture directional distortion, and is the most successful in data fitting, albeit the most complex as well, of the three models. In particular this model is used to simulate experimental data from biaxial cyclic loading test showing the improvement of simulations for ratchetting obtained by the introduced directional distortional hardening scheme as compared with simulations which do not involve directional distortion of the yield surface.

References

[1] Bardet, J.P., Choucair, W.: A linearized integration technique for incremental constitutive equations. International Journal for Numerical and Analytical Methods in Geomechanics 15, 1–19 (1991)
[2] Bari, S., Hassan, T.: Anatomy of coupled consititutive models for ratcheting simulation. International Journal of Plasticity 16, 381–409 (2000)
[3] Boucher, M., Cayla, P., Cordebois, J.P.: Experimental studies of yield surfaces of aluminum alloy and low carbon steel under complex biaxial loadings. European Journal of Mechanics, A/Solids 14(1), 1–17 (1995)
[4] Chaboche, J.L.: On some modifications of kinematic hardening to improve the description of ratcheting effects. International Journal of Plasticity 7, 661–678 (1991)
[5] Feigenbaum, H.P., Dafalias, Y.F.: Directional distortional hardening in metal plasticity within thermodynamics. International Journal of Solids and Structures 44, 7526–7542 (2007)
[6] Feigenbaum, H.P., Dafalias, Y.F.: Simple model for directional distortional hardening in metal plasticity within thermodynamics. ASCE Journal of Engineering Mechanics 134(9), 730–738 (2008)
[7] François, M.: A plasticity model with yield surface distortion for non proportional loading. International Journal of Plasticity 17, 703–717 (2001)
[8] Hassan, T., Kyriakides, S.: Ratcheting in cyclic plasicity, part i: Uniaxial behavior. International Journal of Plasticity 8, 91–116 (1992)

[9] Hassan, T., Corona, E., Kyriakides, S.: Ratcheting in cyclic plasicity, part ii: Multiaxial behavior. International Journal of Plasticity 8, 117–146 (1992)

[10] Kurtyka, T., Zyczkowski, M.: Evolution equations for distortional plastic hardening. International Journal of Plasticity 12(2), 191–203 (1996)

[11] McComb, H.G.: Some experiments concerning subsequent yield surfaces in plasticity. Tech. Rep. D-396, National Aeronautics and Space Adminstration (1960)

[12] Naghdi, P.M., Essenburg, F., Koff, W.: An experimental study of initial and subsequent yield surfaces in plasticity. Journal of Applied Mechanics 25(2), 201–209 (1958)

[13] Ortiz, M., Popov, E.P.: Distortional hardening rules for metal plasticity. Journal of Engineering Mechanics 109(4), 1042–1057 (1983)

[14] Phillips, A., Tang, J.L., Ricciuti, M.: Some new observations on yield surfaces. Acta Mechanica 20, 23–39 (1975)

[15] Plesek, J., Feigenbaum, H.P., Dafalias, Y.F.: Convexity of yield surfaces with directional distortional hardening. ASCE Journal of Engineering Mechanics 136(4), 477–484 (2010)

[16] Voyiadjis, G.Z., Foroozesh, M.: Anisotropic distortional yield model. Journal of Applied Mechanics 57, 537–547 (1990)

[17] Wei-Ching Yeh, C.D.H., Pan, W.F.: An endochronic theory accounting for deformation induced anisotropy of metals under biaxial load. International Journal of Plasticity 12(8), 987–1004 (1996)

[18] Wu, H.C., Yeh, W.C.: On the experimental determination of yield surfaces and some results of annealed 304 stainless steel. International Journal of Plasticity 7, 803–826 (1991)

Forced Vibrations of the System: Structure – Viscoelastic Layer

Boris V. Gusev and Alexander S. Faivusovich

Moscow State University of Railway Engineering (MIIT) 125009, Moscow, Russia
Lugansk national agrarian university 91008, Lugansk, Ukraina
`info-rae@mail.ru`

Abstract. Analytical solutions of the problems about interrelated vibrations of an elastic (deformable) structure with viscoelastic layer are obtained. The investigations were made to workout the method of the dynamical computations and optimization of technological processes for forming of reinforced concrete articles on the shock-and-vibration machines and shock machines. The analysis of numerical results and experimental data are presented.

1 Introduction

The authors developed the method for dynamical computations of the system "concrete mix – form – forming machine" (FFM) based on the solutions of 2-D problems. This method differs from known approach, in which the vibrations of a viscoelactic rod with point mass and elastic support is considered. It was determined by experimental and theoretical investigations that such model is suitable for qualitative analysis of FFM dynamical behavior only. It is inadmissible to neglect the bending stiffness of the tray form and its envelope in common case [1]. It is necessary to take additionally into account the friction force on vertical walls investigating the vibrations of high concrete articles.

2 Investigation and Analysis of the FFM Vibrations

The statement and solution of the problem for vibrations of the FFM system has been performed taking into account a set of prepositions and assumptions concerning the properties of the concrete mix and the mechanical system. These prepositions are confirmed in experiments. The prepositions for the concrete mix [1, 2] are:

- the compaction process is long enough;
- the density of the mix is constant during the compaction process;
- the concrete mix is a transversely isotropic viscoelastic media;

- the case of the plane deformation is investigated in the absence of lateral (in plane) mix deviations and friction in the form envelope;
- the vibrations without separations are considered.
  The prepositions for the mechanical system:
- the tray of the form is rigidly connected to the forming machine;
- the structure of the tray is a periodical and consists of a homogeneous cells.

Further, the tray and envelope cells of the beam type are considered for simplification purposes.

The vibrations of the FFM system can be considered as a superposition of vibrations for two particular systems:

- the tray of the form like a beam with point masses (vibroexciters, and so on) interacted with a viscoelastic layer (concrete mix);
- sepateted cells of the tray envelope interacted with a viscoelastic layer.

On a first step, using the first scheme, the natural frequencies for the form with concrete mix and the amplitudes of forced oscillations are found. Then, using the second scheme, the optimization of the forming regimes are performed taking into account the possibility of the admissible closeness for the natural and forced frequencies of the system to enhance the dynamical influence on the concrete mix [1, 2].

The scheme of the tray is shown in fig.1, where m_d is a linear mass density of the beam; m_p is mass of devices (for example, vibroexciters); l is length of the beam; P_0 is amplitude of the force of the vibroexciter; C is a rigidity of the supports (springs); ω is a frequency of forced vibrations.
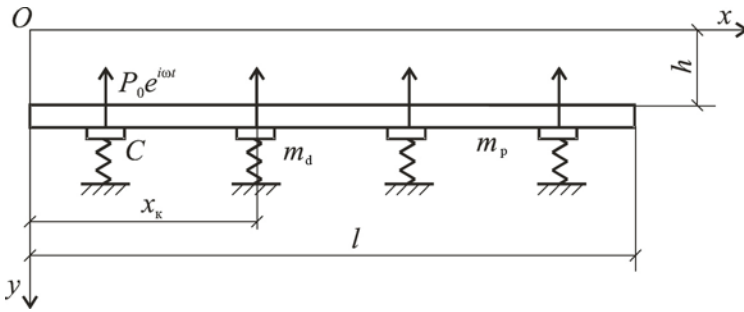

Fig. 1. The system "concrete mix – vibrostand"

The beam with point pass can be reduced to the equivalent one with uniform distributed mass. In this case

$$m_0 = m_\mathrm{d} + \sum_{k=1}^{N} \frac{m_\mathrm{p} x_k^2}{bl} + \sum_{k=1}^{N} \frac{I_\mathrm{p}\left(x_k^J\right)^2}{bl}, \tag{1}$$
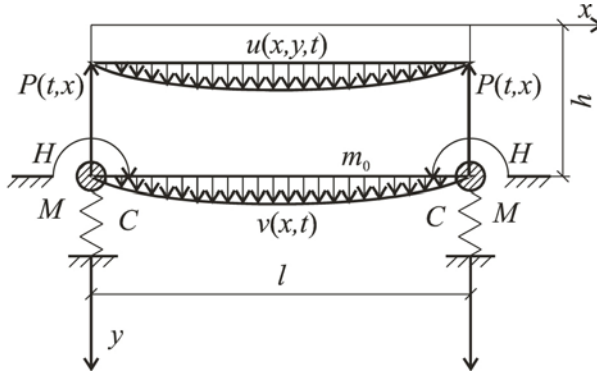
Fig. 2. The system "concrete mix – envelope cell – forming machine"

where x_k^1 is the first derivative of the beam function in the considered point; b is a width of the beam; I_p - is a moment of inertia of the point mass m_p, $I_p = m_p a^2$ (a is a distance from the center of gravity of the vibroexciter to the beam axe).

The problem about steady-state vibrations of a beam interacted with viscoelastic layer can be presented in the form:

$$E_* \frac{\partial^2 u}{\partial y^2} + G_* \frac{\partial^2 u}{\partial x^2} = \rho \frac{\partial^2 u}{\partial t^2}, \tag{2}$$

$$y = 0, \quad \frac{\partial u}{\partial y} = 0, \tag{3}$$

$$y = h, \quad v = u, \tag{4}$$

$$x = 0, \quad x = l, \quad \frac{\partial u}{\partial x} = \frac{u \eta i \omega}{d G_*}, \tag{5}$$

$$y = h m_0 \frac{\partial^2 v}{\partial t^2} + D_* \frac{\partial^4 v}{\partial x^4} = b E_* \frac{\partial u}{\partial y} + \sum_{k=1}^{N} P_0 \delta(x - x_k) e^{i\omega t} - \sum_{k=1}^{N} cv \delta(x - x_k) \tag{6}$$

$$x = 0, \quad x = l, \quad \frac{\partial^2 v}{\partial x^2} = \frac{\partial^3 v}{\partial x^3} = 0, \tag{7}$$

$$E_* = E(E + v_0 i\omega), \tag{8}$$

$$G_* = G(1 + v_1 i\omega), \tag{9}$$

$$D_* = D(1 + i\gamma), \tag{10}$$

$$P = P_0 e^{i\omega t} (\cos \omega t), \tag{11}$$

where u, ρ are a strain and a density of the concrete mix, respectively; E, G are a dynamical elasticity and shear moduli of the concrete mix, respectively; v_0, v_1 are inelastic resistance vibration coefficients of the concrete mix; v is a beam strain; D is a beam stiffness; γ is an inelastic resistance vibration coefficient of the beam; η, d are a viscosity coefficient and thickness of the wall viscous layer, respectively; δ is impulse delta function; N is amount of the vibrators and point masses.

The empirical data stated relations between structural and mechanics character-istics of concrete mixes and initial composition which used for engineering computations [1, 2] have been obtained based on experimental investigations of two-phase media.

For long-term vibrations we have

$$u = U(x, y)^{i\omega t} \tag{12}$$

$$v = V(x)e^{i\omega t} \tag{13}$$

According the method of separation of variables the solution (2) taking into ac-count (12) and boundary conditions (3), (5) has the form:

$$U(x, y) = \sum_{n=1}^{\infty} A_n \operatorname{ch}\varphi_n y \cdot \cos(n\pi x/l) e^{i\omega t} \tag{14}$$

where $\varphi_n = \pm\sqrt{\left[G_*\left(\pi n/l\right)^2 - \rho\omega^2 \right]/E_*} = \pm(\alpha + \beta i)$.

Analogously for beam:

$$v = \sum_{m=1}^{\infty} C_m X_m(x) e^{i\omega t} \tag{15}$$

The eigenfunctions $X_m(x)$ are the fundamental beam ones for beam with free ends:

$$
\begin{aligned}
X_m(x) = \left(\operatorname{ch} r_m - \cos r_m\right)&\left[\operatorname{ch}\left(\frac{r_m x}{l}\right) + \sin\left(\frac{r_m x}{l}\right) \right] \\
- \left(\operatorname{sh} r_m - \sin r_m\right)&\left[\operatorname{ch}\left(\frac{r_m x}{l}\right) + \cos\left(\frac{r_m x}{l}\right) \right]
\end{aligned}
\tag{16}
$$

The coefficients r_m are found from the following frequency equation

$$\operatorname{ch} r_m \cos r_m = 1 \tag{17}$$

The solution of the Eq. (6) is found as an expansion in the series over eigenfunc-tions of the corresponded homogeneous problem.

Substituting (14) and (15) into (4) and (6) we have the system of equations with respect to unknown A_n and C_m, applying the numerical algorithm described in

[1, 2] we obtain the following expression for the contact dynamical stresses $\sigma(x,h,t)$ as follows:

$$\sigma(x,h,t) = \sum_{m=n}^{M} \left(\frac{E}{2lm_0}\right) \pi n (-1)^{(n+1/2)} \sum_{k=1}^{N} x_m (a_k) L_m P_0 \cos\left(\frac{n\pi x}{l}\right) T_n \cos(\omega t + \xi),$$ (18)

$$m = 1,2,3,\ldots, \quad n = 1,3,5,\ldots,$$

where

$$T_n = \lambda_3 / \lambda_2 \lambda_4 \sqrt{M_1^2 + M_2^2} \,,$$

$$M_1 = \omega_m^2 - \omega^2 - \left(\frac{b\lambda_1\lambda_2\lambda_3\lambda_5}{m_0\lambda_4}\right)\cos(\Phi_1 + \Phi_2 + \Phi_3 + \Phi_4),$$

$$M_2 = -\left(\frac{b\lambda_1\lambda_2\lambda_3}{m_0\lambda_4}\right)\cos(\Phi_1 + \Phi_2 + \Phi_3 + \Phi_4),$$

$$\operatorname{tg}\Phi_1 = v_0\omega, \quad \operatorname{tg}\Phi_2 = \beta/\alpha, \quad \operatorname{tg}\Phi_3 = \frac{\operatorname{tg}\beta h}{\operatorname{th}\alpha h},$$

$$\operatorname{tg}\Phi_4 = \operatorname{tg}\alpha h \cdot \operatorname{th}\beta h, \quad \operatorname{tg}\Phi_5 = -M_2/M_1, \quad \xi = \Phi_3 - \Phi_4 - \Phi_2 - \Phi_5,$$

$$L_m = \frac{l}{r_m}\left[(\operatorname{ch} r_m - \cos r_m)^2 - \operatorname{sh}^2 r_m + \sin^2 r_m\right],$$

$$\omega_m^2 = \frac{Dr_m^4}{l^4 m_0} + \frac{C}{m_0}\sum_{k=1}^{N}\frac{x_m(a_k)}{L_m}.$$

In Eq (18) ω_m is the eigenfrequency of the beam without loads. The amplitudes of vibrations have finite values at resonance since $M_2 \neq 0$.

Supposing $P_0 = 0$, the eigenfrequensies f_m are found from the original system. For the tray as a rectangular plate the values f_m are given the formula

$$f_{ms} = \frac{\theta_{ms} E}{\rho h^2} + Gh^2\left[\left(\frac{\pi m}{l}\right)^2 + \left(\frac{\pi s}{b}\right)^2\right]$$ (19)

The frequency coefficient θ_{ms} is found from the characteristic equation:

$$\omega_{np}^2 = \frac{\theta_{ms}^2 E}{\rho h^2}\left\{1 + \frac{Gh^2}{E\theta_{ms}^2}\left[\left(\frac{\pi m}{l}\right)^2 + \left(\frac{\pi s}{b}\right)^2 + \frac{m_6 \operatorname{tg}\theta_{ms}}{m_0 \theta_{ms}}\right]\right\},$$ (20)

$$m = p = 1,3,5,\ldots, \quad p = s = 1,3,5,\ldots,$$

where m_6 is mass of the concrete mix.

The mathematical model of the cell of the envelope, connected to one mass vibrostand can be reduce to the plate model with the boundary conditions including the equivalent mass M_0 and the stiffness C and H with respect to the lateral and angular deviations (fig. 2).

For shock and vibration process analogous scheme is obtained after linearization of the boundary conditions with respect to lateral displacements. The original equation of motion (2) is also valid for this case. The boundary conditions have the form [1, 2]:

$$y = h, \quad m_0 \frac{\partial^2 v}{\partial t^2} + D \frac{\partial^4 v}{\partial x^4} = b\left[E \frac{\partial^2 u}{\partial y^2} + \mu_0 \frac{\partial^2 u}{\partial y \partial t} \right] + P(x,t),$$

$$x = 0, \quad D_1 \frac{\partial^3 v}{\partial x^3} - Cv - M_0 \frac{\partial^2 v}{\partial t^2} = 0, \quad D_1 \frac{\partial^2 v}{\partial x^2} - H \frac{\partial v}{\partial x} = 0,$$

$$x = l, \quad D_1 \frac{\partial^3 v}{\partial x^3} + Cv + M_0 \frac{\partial^2 v}{\partial t^2} = 0, \quad D_1 \frac{\partial^2 v}{\partial x^2} + H \frac{\partial v}{\partial x} = 0.$$

Here D_1 is a bending stiffness of the cell.

For the cases of vibration, shock and vibration, and shock effects the value $P(t,x)$ is equal, respectively

$$P(t,x) = \operatorname{Re} P_0 e^{i\omega t} \left[\delta(x) + \delta(l-x) \right], \tag{21}$$

$$P(t,x) = \sum_{j,m=1}^{\infty} B_{jm} X_m(x) \cos(\omega_j t / T), \tag{22}$$

$$P(t,x) = R \sum_{r=0}^{\infty} \delta(t - rT), \tag{23}$$

where $\delta(x)$ is the impulse delta function, R is impulse of force.

Eq (22) is obtained by expanding the periodical function in Fourier expansion. For the case of shock effects the initial conditions have the form:

$$t = 0, \quad 0 \le y \le h, \tag{24}$$

$$\partial u / \partial y = v_0, \quad 0 \le y \le h. \tag{25}$$

When $H = \infty$ the eigenfunctions for the cell are

$$X_m(x) = S(kx) - \frac{C_0}{k^3} V(kx) + \frac{A}{k} U(kx) \tag{26}$$

where $S(kx)$, $U(kx)$, $T(kx)$, $V(kx)$ are the Krylov beam functions.

$$A = -\frac{k^6 T(k)}{k^5 V(k)} - \frac{k^3 C_0^2 S(k) + C_0 V(k)}{k^3 C_0 T(k) - k^2 C_0 U(k)},$$

$$\mu = M/m_0 l, \quad C_0 = C_{np} l^3/D_1, \tag{27}$$

where m_0 is the linear mass density of the envelope.

The eigenvalues k_m are found from the following equation

$$\frac{2\,\mathrm{sh}\,k \cdot \sin k}{Q} + Q(\mathrm{ch}\,k \cdot \cos k - 1) + (\cos k \cdot \mathrm{sh}\,k + \mathrm{ch}\,k \cdot \sin k) = 0, \quad Q = C_0/k^3. \tag{28}$$

For the case of shock and vibration effects the contact dynamical pressures are equal to:

$$\sigma(x,h,t) = \sum_{m=n=1,3,5}^{M} \sum_{j=1}^{\infty} \frac{E_* B_{mj} \pi n \cos\dfrac{\pi n x}{l} R_m \varphi_n \,\mathrm{th}\,\varphi_n h \cdot e^{i\omega_j t}}{2l(-1)^{\frac{n-1}{2}} m_0 \left[\omega_m^2 - \omega_j^2 - bE_* \dfrac{\mathrm{th}\,\varphi_{nj} h}{m_0}\right]} \tag{29}$$

where, $R_m = \dfrac{1}{k_m}\left\{T(k_m) - \dfrac{C_0}{k_m^2}[S(k_m) - 1] + \dfrac{A}{k_m}V(k_m)\right\}$, $\omega_m^2 = k_m^4 \dfrac{D_1}{m_0 l}$, B_{mj} are the

coefficients of the expansion of the periodical function (22).

Compaction of concrete mixes under shock actions can be considered as a deforming process of a concrete layer loading by a set of shock impulses sequentially imposed with time interval T. The stresses arisen after such action can be arithmetically summed since the maximum of dynamical pressures achieves in a time interval just after the impulse action.

The solution of the corresponded problem written in displacement form for the case of hinge-supported cell under instantaneous impulse can be presented as

$$u(x,y,t) = \sum_{n=m=1,3,5}^{N} \sum_{r=1}^{\infty} A_{mn} \cos\frac{m\pi x}{l} \cos\lambda_n y\, e^{\frac{-\alpha_{nm}}{2}(1-rT)} \sin\frac{\varphi_{mn}}{2}(t-rT),$$

$$\alpha_{mn} = \frac{\lambda_n^2 \mu_0}{\rho} + \mu_1 \frac{m^2 \pi^2}{l^2}, \quad A_{mn} = \frac{16 v_0 \sin\lambda_n h}{\pi m \varphi_{mn}\left(\lambda_n h + \dfrac{\sin^2 \lambda_n h}{2}\right)}, \tag{30}$$

$$\varphi_{mn} = \sqrt{4\left(\frac{E\lambda^2}{\rho} + \frac{m^2 \pi G}{\rho}\right) - \left(\frac{\mu_0 \lambda_n^2}{\rho} + \frac{\mu_1}{\rho}\frac{\pi^2 m^2}{h}\right)^2}.$$

The corresponded frequency equation at $\mu_0 = \mu_1 = 0$ is reduced to the form

$$\omega_{mn}^2 = P_6^2 \left(1 + \frac{G h^2 \pi m^2}{E \theta^2 l^2} + \frac{m_6}{m_0} \cdot \frac{\operatorname{tg} \theta_n}{\theta_n} \right),$$

$$P_6^2 = \frac{\theta_n^2 E}{h^2 \rho}, \quad \theta_n = \lambda_n h, \quad P_6^2 = \frac{\theta_n^2}{h^2} \cdot \frac{E}{\rho},$$

(31)

where m_6 is the linear mass density of the viscoelastic layer.

The analysis of the solutions (18), (29), (30) shows that the distribution of dynamical pressures along the height of a layer is different for these three cases. The envelope curve of the dynamical pressures diagram has a sinusoidal character at the vibration action, but the envelope curve is the sum of sinusoids at the shock action (instantaneous impulse). Note, that the vibrations are in-phase along the height of layer independently from its vertical size. But the periodical regime of motion changes on an aperiodic one if the height of layer grows and static component of compression arises. It leads to considerable diminish of the process efficiency. So, it is necessary to diminish the vibration frequency at growth of the height of layer.

The availability of the zones with zero points depends on the relation of the duration of shock impulse on the period natural vibrations of the system.

The frequency equations characterized the eigenfrequensies for systems (20) and (30) define the dependence between the eigenfrequencies ω_n for free of loading and interacted with concrete mix layer P_6 of the elastic system. The difference is that the frequency coefficients for the tray are taken as ones for the beam with free ends, but for cell of the envelope these coefficients are found from eq. (28). The character of changing the parameter k_1 versus on dimensionless parameters C_0 and μ is shown in fig. 3. The areas I, II, and III correspond approximately to the values of parameters for vibration, sock and vibration, and shock machines, respectively.
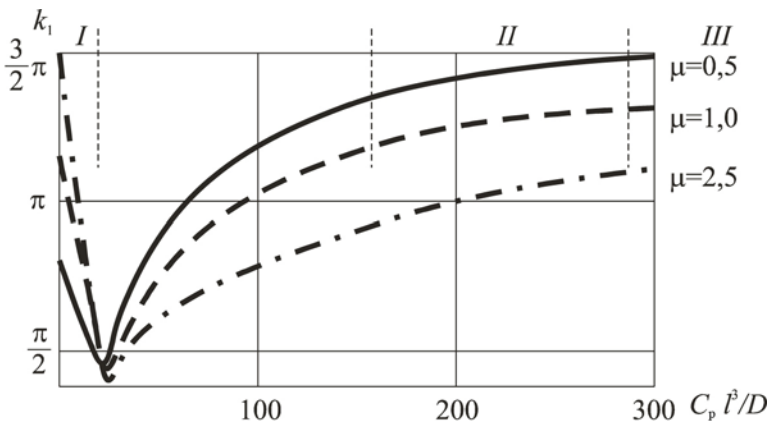

Fig. 3. Dependence the frequency coefficient k_1 vs. on parameters μ and C_0

Thereby, the obtained solutions give us possibility to show the influence the bending stiffness, point masses, and elastic bracing on the eigenfrequencies. The comparison the eigenfrequencies for loaded and free of loading structures allows to compute the coefficient of added mass $\alpha_{\text{пр}}$, which uses in engineering computations:

$$\alpha_{\text{пр}} = \left(\frac{\omega_n^2}{P_6^2} - 1 \right) \frac{m_0}{m_6} \tag{32}$$

The parameter $\alpha_{\text{пр}}$ depends on the mechanical properties of the mix and ratio of linear mass densities and is unique for any concrete mix. So, implementation this parameter as a constant ($\alpha_{\text{пр}} = \text{const}$) can not ensure the satisfactory accuracy for practical calculations.

It is followed from obtained solutions, that viscoelastic layer reduces the eigenvalues of the system. It is also determined, that the inertial resistance dominates at $h \geq 0,1\,m$, but the influence of the mechanical properties of the mix is more essential when layer thickness less than $0,1\,m$.

The experimental investigations and numerical computations show, that the value of dynamical stresses depends essentially on lowest eigenfrequency and in a less degree on a correlation of frequencies in the spectrum at shock actions [1, 2].

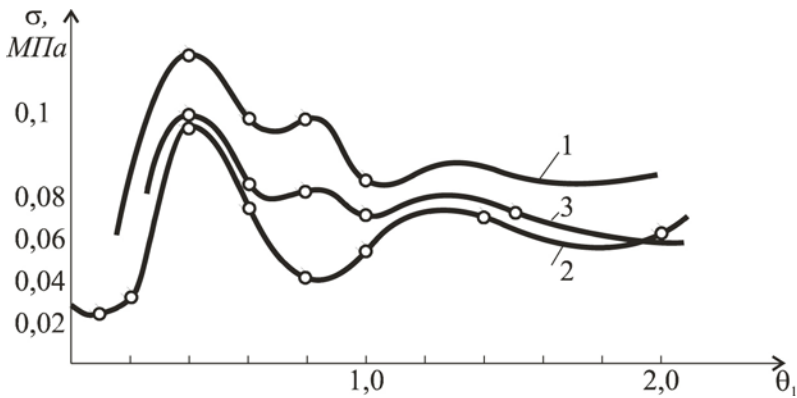The dependence of dynamical pressure versus the dimensionless frequency θ_1 is presented in fig. 4.

Fig. 4. Dependence of the dynamical pressure vs. the frequency coefficient θ_1. *E = 7 MПа*, 1– *h = 0,05 м* ; 2– *h = 0,3 м* ; 3– *h = 1,0 м*.

If the frequency of shock impulses is multiple to the eigenfrequency of the system then the phenomenon of the impulse resonance can be realized. However, taking into account the natural scatter of mechanical characteristics influencing on the dynamical properties of the system, this phenomenon is practically unrealizable. If

the eigenfrequency of the layer is less than the frequency of shock impulses, then the accumulation of the stresses of unit sign (compression) realizes, i.e., the static component of the pressure appears when the dynamical one is not great enough. So, the efficiency of the compaction process diminishes considerably. Limiting frequencies presents in [1, 2] for which the unloading of the layer is reached in each cycle of vibrations. Thereby, the possibility for optimization of the compaction regimes is connected to choice of optimal values of the dimensionless eigenfrequencies θ_1 and maximal frequency of forced impacts taking into account constraints above mentioned.

The frequency spectrum of driving force has an essential sense for shock and vibration regimes of vibrations. The increase of dynamical impacts on the concrete mix can be reached via approaching the eigenfrequencies to one of the driving force harmonic. Note, that the tuning out resonance is not necessary in view of not great grows of the vibration amplitudes.

The recommendations on the dynamical computations with optimization are given in [1, 2]. As for the dynamical computations in whole, the basic problem is to find the dynamical system characteristics in such way, that to exclude the tray service at the resonance regimes taking into account the longevity constraints. It is also important to achieve even distribution of the vibration amplitudes along the surface of the tray at the expense of rational placement of the vibroexciters.

Note the one important speciality of obtained solutions. Since, the value $P_{\bar{6}}$ is normalized, the value ω_m (eigenvalue of free loading structure) is found using the frequency equations. It is seen from fig. 4 that this value can be defined by changing the values D, l, C_0, μ.

The steel intensity of the cell (form) will be different for each case. The analysis of the equations (28) and (29) shows that the minimal value of the steel intensity is reached at the maximal values for k_1. So, it is necessary to tend to the following values for parameter C_0: for shock and vibration machines – $C_0 \geq 300$; for shock machines – $C_0 \to \infty$; for vibration machines – $C_0 \leq 5$. Up to now all elements of FFM are designed separately. It can lead to unexpected phenomena:

- exploitation of the tray forms in resonance regimes due to a compact spectrum of the eigenfrequencies;
- irregularity in the distribution of the vibration amplitudes along the surface;
- necessity to grow shock actions on the forms and to increase its steel intensity.

The engineering methodic for dynamical computations with optimization of the process, the laboratory and full-scale experience of application of the form with improved dynamics parameters are given in [1, 2].

3 Conclusion

The realized complex of theoretic and experimental researches, including the identification of the structural and mechanical characteristics of the viscoelastic media

(concrete mix) as well as investigation of the system vibrations gave us the possibility to develop the method of the dynamical computations taking into account process optimization. It can be supposed that application of the method will allow one decreasing of the tray steel intensity in the range about 10-15% under given longevity.

References

1. Gusev, B.V., Faivusovich, A.S.: Technological mechanics of vibrated concrete mixes. Litera, Moscow (2002)
2. Gusev, B.V., Kondrashchenko, V.I., Maslov, V.P., et al.: Forming of the composite materials structure and their properties. Nauchny mir, Moscow (2006)

Extreme Instability Phenomena in Autonomous Weakly Damped Systems: Hopf Bifurcations, Double Pure Imaginary Eigenvalues, Load Discontinuity

Anthony N. Kounadis

Academy of Athens,
Soranou Efessiou 4, Athens 115 27, Greece
`kounadis@bioacademy.gr`

Abstract. The dynamic asymptotic instability of autonomous multi-parameter discrete systems under step compressive loading either of constant direction (conservative load) or of varying direction (follower or nonconservative loading) is thoroughly reconsidered using the efficient - and rather forgotten - Liénard-Chipart stability criterion. Attention is focused on the interaction of nonuniform mass and stiffness distribution with infinitesimal damping. Such parameters alone or combined with others may have a tremendous effect on the Jacobian eigenvalues and thereafter on the local asymptotic dynamic instability which – strangely enough –may occur before static (divergence) instability, even in the case of a positive definite damping matrix. It was also found that such systems when unloaded, although being statically stable, under certain conditions may become dynamically locally unstable to any small disturbance. Hopf bifurcations, double zero eigenvalues, double pure imaginary eigenvalues, loading discontinuity and other phenomena are properly established.

1 Introduction

The importance of *damping* on the local dynamic stability of flexurally vibrating systems under follower (step) load (nonconservative autonomous systems) was recognized long time ago as a decisive factor [1, 2, 3]. Particular attention was given on nonconservative *discrete* systems which lose their stability either by *flutter* (dynamic) or by *divergence* (static) instability depending on the region of variation of the nonconservativeness loading parameter. However, this effect was, in general, ignored when the above autonomous systems are subjected to a *constant in magnitude and direction loading* with infinite duration (conservative systems [4]). The dynamic *stability* of **both** types of such autonomous discrete systems when damping is included can be described using a *local* (linear) analysis by the matrix-vector differential equation [4, 5, 6]

$$\mathbf{M}\ddot{q} + \mathbf{C}\dot{q} + \mathbf{V}q = 0 \tag{1}$$

where the dot denotes derivative with respect to time t; q(t) is an n-dimensional *state* vector with coordinates $q_i(t)$ (i = 1,…n); $\mathbf{M}$ and $\mathbf{C}$ are nxn real *symmetric* matrices. More specifically, matrix $\mathbf{M}$ associated with the *total kinetic energy* of the system is a function of the concentrated masses m_i (i = 1,…n) being always *positive definite*; matrix $\mathbf{C}$ with elements the damping coefficients c_{ij} (i,j = 1,…n) may be *positive definite*, *positive semi-definite* as in the case of pervasive damping [7, 8] or *indefinite* [9, 10]; $\mathbf{V}$ is a generalized *stiffness* matrix whose elements V_{ij} are linear functions of a *suddenly* applied external load λ of constant magnitude with *varying* (in general) direction and *infinite* duration, of stiffness coefficients k_{ij} (i, j = 1,…,n) and of the nonconservativeness loading parameter η, i.e. $V_{ij} = V_{ij}(\lambda; k_{ij}, \eta)$. $\mathbf{V}$ is an *asymmetric* matrix for η≠1 (since η=1 corresponds to a conservative load[11]). Apparently, due to this type of loading the system under discussion is *autonomous*. The static (divergence) *instability* or *buckling* loads λ_i^c (i = 1,…n) are obtained by vanishing the determinant of the *stiffness* asymmetric (η≠1) matrix $\mathbf{V}(\lambda; k_{ij}, \eta)$, i.e.

$$|\mathbf{V}(\lambda; k_{ij}, \eta)| = 0 \tag{2}$$

Clearly, eq.(2) yields an nth degree algebraic equation in λ for given values of k_{ij} and η. Assuming *distinct* critical states the determinant of the matrix $\mathbf{V}(\lambda; k_{ij}, \eta)$ is *positive* for $\lambda < \lambda_1^c$, *zero* for $\lambda = \lambda_1^c$ and *negative* for $\lambda > \lambda_1^c$.

The *boundary* between *flutter* and *divergence* instability is obtained by solving with respect to λ and η the system of algebraic equations [12]

$$\mathbf{V} = \partial\mathbf{V}/\partial\lambda = 0 \tag{3}$$

for given stiffness parameters k_{ij} (i,j = 1,…,n).

Kounadis [4, 13] in two very recent publications has established the *conditions* under which the above autonomous *dissipative* discrete systems under step loading of constant magnitude and direction with infinite duration (conservative load) may exhibit dynamic bifurcational modes of instability *before divergence* (static instability), i.e. for $\lambda < \lambda_1^c$, when *infinitesimal* damping is included. These dynamic bifurcational modes may occur through either a *degenerate Hopf bifurcation* (leading to periodic motion around centers) or a *generic* Hopf bifurcation (leading to periodic attractors or to flutter). These unexpected findings (implying failure of Ziegler's kinetic criterion and other singularity phenomena) may occur for a certain *combination* of values of the *mass* (primarily) and *stiffness* distribution of the system in connection with a *positive semi-definite or an indefinite damping matrix* [4, 13].

Very recently Kounadis [14] established that there are combinations of values of the above mentioned parameters – i.e. mass and stiffness distribution - which in connection with *positive definite* damping matrices may lead to *dynamic* bifurcational modes of instability when the system is *nonconservative* due to a partial follower compressive load associated with the *nonconservativeness* parameter η. These systems of *divergence* (static) instability, occurring for suitable values of η,

are called *pseudo–conservative* systems when subjected to *nonconservative circulatory* forces, being therefore essentially *nonconservative* systems [6]. Systems exhibiting *flutter* are called by Ziegler *circulatory,* although in this terminology pseudo - conservative systems are not distinguished [1].

In this work the *local* dynamic stability of autonomous discrete *conservative* or *nonconservative* systems is discussed by studying the coupling effect of the damping matrix with other parameters (i.e. mass and stiffness distribution, nonconservativeness parameter η) on the Jacobian eigenvalues. Attention is focused mainly on *infinitesimal damping* which may have a considerable effect on these systems *asymptotic instability*. Such *local* dynamic instability will be sought through the set of *asymptotic stability* criteria of Liénard–Chipart [15, 16] which are very elegant and more readily employed than the well known Routh-Hurwitz stability criteria. Moreover, the conditions for the existence of Hopf (generic or degenerate) bifurcations, of double zero eigenvalue bifurcations and of a double purely imaginary eigenvalue bifurcation will be assessed. The **local** dynamic asymptotic stability of these systems using the above criteria is also discussed if there is **no** loading (i.e. λ=0). In addition to the above main objectives of this work, some new cases of dynamic bifurcations will be also discussed by analyzing 2-DOF (two degrees of freedom) systems for which a lot of numerical results are available [17].

Hence, this work is rather a recapitulation, assessment and expansion of previous studies [4, 13, 14, 18] whose impetus was that such *local* dynamic bifurcations, which could be explored via classical (linear) analysis, escaped the attention of eminent researchers in the past.

2 Basic Equations

Solutions of eq(1) are sought in the form

$$\mathbf{q} = \mathbf{r}e^{\rho t} \tag{4}$$

where ρ is in general a **complex** number and **r** a **complex** vector, independent of time (t).

Introducing **q**(t) into eq.(1) we obtain [13]

$$\mathbf{L}(\rho)\,\mathbf{r} = (\mathbf{M}\,\rho^2 + \mathbf{C}\,\rho + \mathbf{V})\,\mathbf{r} = 0 \tag{5}$$

where $\mathbf{L}(\rho) = \mathbf{M}\,\rho^2 + \mathbf{C}\,\rho + \mathbf{V}$ is a matrix-valued function.

The *characteristic* (secular) equation based on eq.(5), det$\mathbf{L}(\rho)$=0, is

$$\rho^{2n} + \alpha_1 \rho^{2n-1} + \dots + \alpha_{2n-1}\rho + \alpha_{2n} = 0 \tag{6}$$

where the real coefficients α_i = (i=1,...,2n) are determined by means of Bôcher formula [19]. The eigenvalues (roots) of eq.(6) ρ_j = (j = 1,...,2n) are, in general, *complex conjugate* pairs $\rho_j = \nu_j \pm \mu_j i$ (where $i = \sqrt{-1}$, ν_j and μ_j real numbers) with corresponding *complex conjugate* eigenvectors r_j and $\bar{r}_j$ (j = 1,…,n). Since

$\rho_j = \rho_j(\lambda)$, clearly $v_j = v_j(\lambda)$, $\mu_j = \mu_j(\lambda)$, $r_j = r_j(\lambda)$ and $\bar{r}_j = \bar{r}_j(\lambda)$. Thus, the solutions of eq.(1) are of the form

$$Ae^{vt}\cos\mu_j t, \quad Be^{vt}\sin\mu_j t \tag{7}$$

where A and B *constants* which are determined from the *initial* conditions. Solutions (7) are *bounded* tending to zero as t→∞, if all eigenvalues of eq.(6) have *negative* real parts, i.e. when $v_j < 0$ for all j.

The seeking *of a pair* of *imaginary roots* of the secular eq (6) which represents a *border* line between dynamic *stability* and *instability* is a first but important *step* in our discussion. Clearly, an imaginary root gives rise to an *oscillatory* motion of the form $e^{i\mu t}$, ($i = \sqrt{-1}$, μ = real number) around the trivial state. However, the existence of at least one *multiple imaginary root* of κth order of multiplicity leads to a solution containing functions of the form $e^{i\mu t}$, $te^{i\mu t}$, ..., $t^{k-1}e^{i\mu t}$, which increase with time. Hence, the *multiple* imaginary roots on the imaginary axis denote local dynamic asymptotic instability.

All findings presented bellow which are based on **linearized** solutions have been confirmed via **non-linear dynamic analyses** using an improved Runge-Kutta numerical scheme.

Subsequently, we will discuss firstly the more simple case of *conservative* and then the case of *nonconservative* systems under *partial follower* load.

3   Conservative Systems

Kounadis [4,13,18] has established recently the *conditions* under which the above autonomous systems under *step* loading of constant magnitude and direction (conservative load) with infinite duration may exhibit dynamic bifurcational modes of instability *before divergence* (static instability), i.e. for $\lambda < \lambda_1^c$, when *infinitesimal* damping is included These unexpected findings (implying failure of Ziegler's kinetic criterion and other singularity phenomena) may occur for a certain *combination* of values of the *mass* (primarily) and *stiffness* distribution of the system in conjunction with a *positive semi-definite or indefinite damping matrix* [4,13,18] .

From the above matrix-valued function L(ρ) one can obtain

$$\bar{\mathbf{r}}^{T}(\rho^2\mathbf{M}+\rho\mathbf{C}+\mathbf{V})\mathbf{r} = 0 \tag{8}$$

where $\bar{\mathbf{r}}^{T}$ is the conjugate transpose of **r**.

Since all *quadratic* forms are real (scalar) quantities, eq. (8) is a 2nd degree algebraic polynomial with respect to ρ from which we obtain

$$\rho = \frac{1}{2\bar{\mathbf{r}}^{T}\mathbf{M}\mathbf{r}}\left[-\bar{\mathbf{r}}^{T}\mathbf{C}\mathbf{r} \pm \sqrt{(\bar{\mathbf{r}}^{T}\mathbf{C}\mathbf{r})^2 - 4(\bar{\mathbf{r}}^{T}\mathbf{M}\mathbf{r})(\bar{\mathbf{r}}^{T}\mathbf{V}\mathbf{r})}\right]$$

or $\rho = v + i\mu$, $(i = \sqrt{-1})$, $v = -\dfrac{\bar{\mathbf{r}}^{T}\mathbf{C}\mathbf{r}}{2\bar{\mathbf{r}}^{T}\mathbf{M}\mathbf{r}}$, $\mu^2 = \dfrac{\bar{\mathbf{r}}^{T}\mathbf{V}\mathbf{r}}{\bar{\mathbf{r}}^{T}\mathbf{M}\mathbf{r}} - v^2$. $\tag{9}$

For $\lambda < \lambda_1^c$ matrix **V**, for given values of the stiffness parameters k_{ij} (i,j=1,...,n), is positive definite. If in addition matrix **C** is positive definite and given that matrix M

is always positive definite, according to the Parodi theorem [20] all eigenvalues (roots) of eq.(6) have *negative* real parts. Hence, the system is *asymptotically stable*. Indeed, if $\mathbf{C}$ is *positive definite*, as λ increases gradually from zero, at least a pair of complex conjugate eigenvalues follows in the ρ-complex plane the path shown in Fig.1a becoming a *double* negative eigenvalue at a certain $\lambda = \lambda_0$ slightly smaller than λ_1^c due to the vanishing of the discriminant of eq.(9). For $\lambda > \lambda_0$ but less than λ_1^c the discriminant becomes positive related to *two unequal negative* eigenvalues moving in *opposite* directions in the real axis. At $\lambda = \lambda_1^c$ one of these eigenvalues vanishes, becoming positive and increasing for $\lambda > \lambda_1^c$, yielding *static* (divergence) *instability*, while the other (negative) eigenvalue decreases algebraically.

3.1 Conditions for Dynamic Bifurcation

Attention is mainly focused on dynamic bifurcations associated either with *degenerate* or *generic Hopf bifurcations* (Fig.1b,c) which may occur before divergence (i.e. for $\lambda < \lambda_1^c$). This will be discussed in connection with the *sign* of the *quadratic* form $\bar{\mathbf{r}}^T\mathbf{C}\mathbf{r}$ which may be *positive, semi-definite* or *indefinite*. Fig. 1d shows a double zero eigenvalue bifurcation at $\lambda_H = \lambda_1^c$ [13].
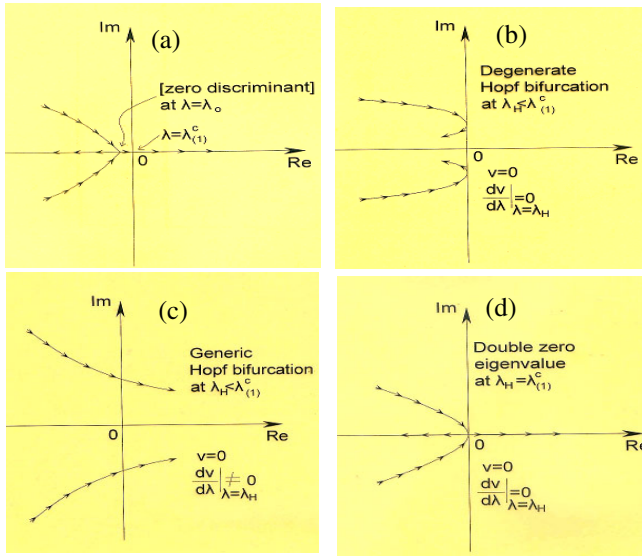

Fig. 1. Types of dynamic bifurcations.

The *necessary condition* for a degenerate or a generic Hopf bifurcation is the existence of **one** at least pair of *conjugate pure imaginary* eigenvalues $\pm i\mu$ (i.e. $v=0$), while the remaining eigenvalues are complex conjugate with negative real parts. Since $v=0$ from eq.(9) it follows that

$$\bar{\mathbf{r}}^T \mathbf{C} \mathbf{r} = 0 \qquad \text{(for } \mathbf{r} \neq 0\text{)} \tag{10}$$

Eq.(10) is satisfied when the damping matrix $\mathbf{C}$ is either *positive semi-definite* (since $|\mathbf{C}|=0$) or *indefinite*. When $\mathbf{C}$ is a given matrix, the *indefinite* quadratic form $\bar{\mathbf{r}}^T \mathbf{C} \mathbf{r}$ may become zero for a suitable value of $\mathbf{r}$ depending on the loading λ and the stiffness coefficients k_{ij} (i,j=1,…,n), since $\mathbf{r}=\mathbf{r}(\lambda; k_{ij})$.

The *sufficient* condition for a *generic* Hopf bifurcation is the fulfillment of the *transversality condition* [5]

$$\left.\frac{dv}{d\lambda}\right|_{\lambda=\lambda_H} \neq 0 \tag{11}$$

where $\lambda = \lambda_H (< \lambda_1^c)$ is the critical load for which the real part of ρ becomes zero, i.e. $v(\lambda_H; k_{ij})=0$. Clearly, if condition (11) is violated, namely if

$$\left.\frac{dv}{d\lambda}\right|_{\lambda=\lambda_H} = 0 \tag{12}$$

a *degenerate* Hopf bifurcation occurs.

The conditions for establishing the dynamic instability load λ_H related to Hopf bifurcations (generic or degenerate) are analytically obtained by Kounadis [4, 13, 18].

Assuming that the *necessary* condition for a Hopf (degenerate or generic) bifurcation is satisfied, we can introduce into eq.(5) the pair of conjugate pure imaginary eigenvalues $\pm i\mu$. This leads to

$$(\mathbf{A} \pm i\mu\mathbf{C})\mathbf{r} = 0 \tag{13}$$

where $\mathbf{A}=\mathbf{V}-\mu^2\mathbf{M}$. Clearly, for a non-trivial solution (i.e. for $\mathbf{r}\neq 0$), the corresponding determinant must be zero, namely

$$|\mathbf{A} \pm i\mu\mathbf{C}| = 0. \tag{14}$$

According to the proof by Peremans–Duparc–Lekkerkerrer [20] if $\mathbf{A}$ and $\mathbf{C}$ are *real symmetric* matrices such that $\mathbf{A}$ is non-negative definite, then eq.(14) implies that there exists a non-trivial *real* vector $\mathbf{r}$ satisfying eq.(13) which yields

$$\mathbf{A}\mathbf{r} = 0, \quad \mathbf{C}\mathbf{r} = 0 \quad (\mathbf{r} \neq 0). \tag{15}$$

Eqs.(15) are simultaneously satisfied if the *determinants* of both matrices $\mathbf{A}$ and $\mathbf{C}$ are zero, i.e.

$$|\mathbf{A}| = 0, \qquad |\mathbf{C}| = 0. \tag{16}$$

The second of eqs.(16) is fulfilled if matrix $\mathbf{C}$ is positive semi-definite.

(a) *C is positive semi-definite*
It can readily be shown that if *C* is a *positive semi-definite* matrix the *dynamic* bifurcation is a *degenerate* Hopf bifurcation since the *transversality condition* is violated (Fig. 1b). Indeed, using the expression of v given in eqs.(9), one can show that condition (12) is satisfied. Clearly, since $\bar{\mathbf{r}}^T \mathbf{C}\mathbf{r} =0$ while $\bar{\mathbf{r}}^T \mathbf{M}\mathbf{r} \neq 0$, condition (12) is fulfilled provided that

$$\frac{d}{d\lambda}\left(\bar{\mathbf{r}}^{T}\mathbf{Cr}\right) = 2\frac{d\bar{\mathbf{r}}^{T}}{d\lambda}\mathbf{Cr} = 0 \tag{17}$$

which is true since due to eq.(15) $\mathbf{Cr} = 0$. Such a result was anticipated since $\mathbf{r}$ evaluated through the 2nd of homogeneous eqs.(15) is independent of λ. Note also that a *real* eigenvector $\mathbf{r}$ corresponds to both pure imaginary eigenvalues $+i\mu$ and $-i\mu$ [4]. It is worth noticing that the above finding is also valid if $\mathbf{C}$ is a symmetric *singular* matrix (i.e. $\mathbf{C}$ is not necessarily positive semi-definite).

One can now obtain a *new* finding of paramount importance for a *multi-parameter* system. By means of the 2nd of eqs.(15) we can determine $\mathbf{r}_j = \mathbf{r}_j(r_n)$, where $j = 1,\ldots, n-1$. Inserting these values into the 1st of eqs.(15), after setting $\mathbf{A} = \mathbf{V} - \mu^2\mathbf{M}$, we obtain

$$(\mathbf{V} - \mu^2\mathbf{M})\mathbf{r} = 0. \tag{18}$$

Writing eq.(18) *analytically* and solving each of the resulting equations with respect to μ^2 we find

$$\mu^2 = \frac{V_{11}r_1 + \ldots V_{1n}r_n}{M_{11}r_1 + \ldots M_{1n}r_n} = \frac{V_{21}r_1 + \ldots V_{2n}r_n}{M_{21}r_1 + \ldots M_{2n}r_n} = \ldots = \frac{V_{n1}r_1 + \ldots V_{nn}r_n}{M_{n1}r_1 + \ldots M_{nn}r_n} \tag{19}$$

Relations (19) and (9) yielding μ^2, furnish n equations from which we can determine λ and $(n-1)$ from the mass and stiffness parameters. In this solution we are looking for the *minimum positive* value of λ which must be less than λ_1^c. For instance, if n = 2 we can determine in addition to $\lambda = \lambda_H$ one parameter.

(b) *C is indefinite*
If the matrix $\mathbf{C}$ is *indefinite* (since $|\mathbf{C}|<0$) the eigenvectors satisfying eq.(13) must be complex. Multiplication of eq.(13) by $\bar{\mathbf{r}}^{T}$ (complex conjugate transpose of $\mathbf{r}$) leads to

$$\bar{\mathbf{r}}^{T}(\mathbf{A} \pm i\mu\mathbf{C})\mathbf{r} = 0. \tag{20}$$

Since $\bar{\mathbf{r}}^{T}\mathbf{Ar}$ and $\bar{\mathbf{r}}^{T}\mathbf{Cr}$ are *real* (scalar) quantities, eq.(20) yields

$$\bar{\mathbf{r}}^{T}\mathbf{Ar} = 0, \qquad \bar{\mathbf{r}}^{T}\mathbf{Cr} = 0. \tag{21}$$

Eqs.(21) are also obtained from relation (9), after setting $\nu=0$ and $\mathbf{V}=\mathbf{A}+\mu^2\mathbf{M}$, since matrix $\mathbf{M}$ is always positive definite.

If $\mathbf{C}$ is an *indefinite* matrix the quadratic form $\bar{\mathbf{r}}^{T}\mathbf{Cr}$ depending on the values of $\nu \neq 0$ may be negative or positive. Hence, it may also vanish for a certain $\nu \neq 0$ depending on the value of λ for given values of the parameters (masses and stiffnesses).

Given that conditions (15) are *not* valid (since $|\mathbf{C}|\neq 0$, $|\mathbf{A}|\neq 0$), the procedure established previously based on $\bar{\mathbf{r}}^{T}\mathbf{Cr}=0$ cannot be adopted in connection with conditions (21). Instead of this, one can apply eq.(14), the expansion of which, after setting *real* and *imaginary* parts equal to zero, furnishes two equations in λ and μ^2 that can be determined provided that all (mass and stiffness) parameters

and matrix **C** are known. Clearly, the determinant in eq.(14) can be established for n>2 by using *symbolic* algebra. For n=2, eq.(14), after setting $\mathbf{A}=\mathbf{V}-\mu^2\mathbf{M}$, yields

$$\left(V_{11}-\mu^2 M_{11}\right)\left(V_{22}-\mu^2 M_{22}\right)-\left(V_{12}-\mu^2 M_{12}\right)^2-\mu^2\left(c_{11}c_{22}-c_{12}{}^2\right)=0$$
$$c_{11}\left(V_{22}-\mu^2 M_{22}\right)+c_{22}\left(V_{11}-\mu^2 M_{11}\right)-2c_{12}\left(V_{12}-\mu^2 M_{12}\right)=0 \tag{22}$$

Eqs.(22) can also be written as follows [13]

$$\left|\,\mathbf{V}\text{-}\mu^2\mathbf{M}\,\right|=\left|\,\mathbf{A}\,\right|=\mu^2\left|\,\mathbf{C}\,\right|$$

$$\mu^2=\frac{c_{11}V_{22}+c_{22}V_{11}-2c_{12}V_{12}}{c_{11}M_{22}+c_{22}V_{11}-2c_{12}M_{12}} \tag{23}$$

Eliminating μ^2 from eqs.(23) we can find λ for given matrix **C** and known values of the parameters. The *lowest* positive value of $\lambda(<\lambda_1^c)$ is the dynamic *instability critical* (flutter) load $\lambda=\lambda_H$ which implies a dynamic bifurcation occurring *before* divergence. This dynamic bifurcation is a *generic* Hopf bifurcation since the *sufficient* condition related to the *transversality condition* is satisfied, namely $d\nu/d\lambda\neq0$ (Fig. 1c). Indeed, due to eqs.(9), it follows that $\nu=0$ which yields $\bar{\mathbf{r}}^T\mathbf{Cr}=0$.

Thus, one has to show

$$\frac{d}{d\lambda}\left(\bar{\mathbf{r}}^T\mathbf{Cr}\right)\bigg|_{\lambda=\lambda_H}\neq 0 \tag{24}$$

where **r** is a function of λ and the mass and stiffness parameters. For a given matrix **C** the quadratic form $\bar{\mathbf{r}}^T\mathbf{Cr}$, corresponding to a critical condition (since $\rho=\pm i\mu$), is a real polynomial of 2nd degree with respect to the loading λ for known values of the parameters. If the derivative of this polynomial with respect to λ is zero, then at $\lambda=\lambda_H$, eq.(6) yields a two-fold root; a case which is excluded since herein only *distinct* critical points are considered.

Clearly, the proof for the transversality condition presented here for both, the degenerate and generic Hopf bifurcation, is simpler than that recently reported [4].

The above, rather cumbersome, analysis for establishing the load $\lambda=\lambda_H$ associated with a generic Hopf bifurcation can be drastically simplified in the case of an *indefinite* matrix **C** when $|\mathbf{C}|<-\varepsilon^2$ for $\varepsilon\rightarrow0$. In the following an approximate technique for a simple, rapid and reliable evaluation of $\lambda=\lambda_H$ and μ^2 will be presented. The accuracy of the results obtained by using this technique increases substantially as ε approaches zero.

3.2 Approximate Technique: $|\mathbf{C}|<-\varepsilon^2$ for $\varepsilon\rightarrow0$

If this case in which the determinant of the damping matrix **C** is *negative* but *negligibly small* and $\mathbf{Cr}\neq0$, we may consider that $\bar{\mathbf{r}}^T\mathbf{Cr}=0$ in eq.(21) can be approximately satisfied by a real vector, $\mathbf{r}\neq0$, as in the previous case of a positive semi-definite matrix **C**, where $|\mathbf{C}|=0$. Namely, we may assume that at a certain $\lambda=\lambda_H$ there exists a vector $\mathbf{r}\neq0$ for given values of the parameters for which

$$\bar{\mathbf{r}}^T \mathbf{Cr} = 0 \tag{25}$$

and due to eqs.(21)

$$\bar{\mathbf{r}}^T \mathbf{Ar} = 0. \tag{26}$$

We may also assume that the latter case is satisfied if $|\mathbf{A}|=0$ which implies

$$\mathbf{Ar} = 0 \quad (\mathbf{r} \neq 0). \tag{27}$$

Analytically eq.(27) is written as follows:

$$
\begin{bmatrix}
\alpha_{11} & \alpha_{12} & \cdots & \alpha_{1,n-1} & \alpha_{1n} \\
\alpha_{21} & \alpha_{22} & \cdots & \alpha_{2,n-1} & \alpha_{2n} \\
\cdots & \cdots & \cdots & \cdots & \cdots \\
\alpha_{n1} & \alpha_{n2} & \cdots & \alpha_{nn} & \alpha_{nn}
\end{bmatrix}
\begin{bmatrix}
r_1 \\
r_2 \\
\cdot \\
\cdot \\
\cdot \\
r_{n-1} \\
r_n
\end{bmatrix}
= 0 \tag{28}
$$

or in a partitioned form

$$
\begin{bmatrix}
A_{11} & A_{12} \\
A_{21} & \alpha_{nn}
\end{bmatrix}
\begin{bmatrix}
\widetilde{r} \\
r_n
\end{bmatrix}
= 0 \tag{29}
$$

where A_{11} is an $(n-1)\times(n-1)$ non-singular symmetric matrix, A_{12} an $n\times1$ (column) matrix such that $A_{21}^T = A_{21}$; α_{nn} is a real (scalar) quantity, $\widetilde{r} = (r_1,..., r_{n-1})^T$ is a vector and r_n the nth component of the vector r. From eq.(29) one can find

$$\widetilde{r} = -r_n A_{11}^{-1} A_{12} \quad (r_n \neq 0). \tag{30}$$

Introducing this expression of $\widetilde{r}$ into eq. (25) we obtain

$$
\left(\widetilde{r}^T \, r_n \right)
\begin{bmatrix}
\mathbf{C}_{11} & \mathbf{C}_{12} \\
\mathbf{C}_{21} & \mathbf{C}_{nn}
\end{bmatrix}
\begin{bmatrix}
\widetilde{r} \\
r_n
\end{bmatrix}
= 0 \tag{31}
$$

where

$$
C_{11} =
\begin{bmatrix}
c_{11} & \cdots & c_{1,n-1} \\
\cdots & \cdots & \cdots \\
c_{n-1,1} & & c_{n-1,n-1}
\end{bmatrix},
\qquad
C_{12} = C_{21}^T =
\begin{bmatrix}
c_{1n} \\
\cdot \\
\cdot \\
\cdot \\
c_{n-1,n}
\end{bmatrix}
\tag{32}
$$

From eq. (31) it follows that

$$\tilde{r}^T \mathbf{C_{11}} \tilde{r} + 2r_n \mathbf{C_{21}} \tilde{r} + r_n^2 c_{nn} = 0 \tag{33}$$

or due to eq.(30)

$$\mathbf{A}_{12}^T \mathbf{A}_{11}^{-1} \mathbf{C}_{11} \mathbf{A}_{11}^{-1} \mathbf{A}_{12} - 2\mathbf{C}_{21} \mathbf{A}_{11}^{-1} \mathbf{A}_{12} + c_{nn} = 0 \,. \tag{34}$$

Eq. (34) along with the determinantal equation

$$|\mathbf{A}| = 0 \tag{35}$$

furnish a non-linear system of two equations with unknowns λ and μ^2 which can be solved numerically provided that the matrix $\mathbf{C}$ and all parameters are known. The lowest positive $\lambda(<\lambda_1^c)$ is the dynamic instability load $\lambda=\lambda_H$ which corresponds to a *generic* Hopf bifurcation. This is so because the transversality condition is also satisfied according to the proof given above.

4   Non-conservative Systems

We consider the above autonomous, weakly damped, system subjective now to a partial *follower* (step) load with $\eta\neq1$ (nonconservative system). Then, the generalized stiffness matrix $\mathbf{V}=\mathbf{V}(\lambda; k_{ij}, \eta)$ is *asymmetric* and hence the previous outlined procedure with $\eta=1$ is **not** applicable. However, one can overcome such a difficulty by employing either the very efficient *asymptotic* stability criterion of Liénard- Chipart [16] or to render the system *symmetric* through suitable matrix transformations. Subsequently, both procedures will be presented.

4.1 Liénard-Chipart Stability Criterion

Consider the general case of a polynomial in z with real coefficients α_i (i=0,1,…,n)

$$f(z) = \alpha_0 z^n + \alpha_1 z^{n-1} + ... + \alpha_{n-1} z + \alpha_n = 0 \,, \quad (\alpha_0 > 0). \tag{36}$$

We will seek the *necessary and sufficient* conditions so that all its roots have *negative* real parts. Denoting by z_κ ($\kappa = 1,…,$ m) the real and by $r_j \pm is_j$ (j = 1,…, (n-m)/2; $i=\sqrt{-1}$) the complex roots of eq.(36) we may assure that all these roots in the complex plane lie to the *left* of the imaginary axis, i.e.

$$z_\kappa < 0, \ r_j < 0 \ (\kappa=1,…,m; \ j=1,…,(n-m)/2) \tag{37}$$

Then one can write

$$f(z) = \alpha_0 \prod_{\kappa=1}^{m} (z - z_\kappa) \prod_{j=1}^{n-m} \left(z^2 - 2r_j z + r_j^2 + s_j^2\right) \tag{38}$$

Since due to inequality (37) each term in the last part of eq.(38) has *positive* coefficients, it is deduced that *all* coefficients of eq.(36) are also *positive*. However, this (i.e. $\alpha_i > 0$ for all i with $\alpha_0 > 0$) is a *necessary* but by no means *sufficient* condition for all roots of eq.(36) to lie in the left half-plane (i.e. $\mathrm{Re}(z) < 0$).

According to Routh–Hurwitz criterion [15, 16] for *asymptotic* stability, i.e. for all roots of eq.(36) to have negative real parts the *necessary* and *sufficient* conditions are

$$\Delta_1 > 0,\ \Delta_2 > 0,\ \ldots\ldots,\ \Delta_n > 0 \tag{39}$$

where

$$\Delta_1 = \alpha_1,\ \Delta_2 = \begin{vmatrix} \alpha_1 & \alpha_3 \\ \alpha_0 & \alpha_2 \end{vmatrix},\ \Delta_3 = \begin{vmatrix} \alpha_1 & \alpha_3 & 0 \\ \alpha_0 & \alpha_2 & \alpha_4 \\ 0 & \alpha_1 & \alpha_3 \end{vmatrix},\ \ldots,\ \Delta_i = \begin{vmatrix} \alpha_1 & \alpha_3 & \alpha_5 & \ldots & \ldots & \ldots & \ldots \\ \alpha_0 & \alpha_2 & \alpha_4 & \ldots & \ldots & \ldots & \ldots \\ 0 & \alpha_1 & \alpha_3 & \ldots & \ldots & \ldots & \ldots \\ 0 & \alpha_0 & \alpha_2 & \alpha_4 & \ldots & \ldots & \ldots \\ \ldots & \ldots & \ldots & \ldots & \ldots & \ldots & \ldots \\ \ldots & \ldots & \ldots & \ldots & \ldots & \ldots & \ldots \\ \ldots & \ldots & \ldots & \ldots & \ldots & \ldots & \alpha_i \end{vmatrix} \tag{40}$$

where Δ_i (with $\alpha_\kappa = 0$ for $\kappa > n$) is the Hurwitz determinant of order i (i = 1,2,…,n).

It should be also noted that when the above necessary conditions $\alpha_i > 0$ (for all i) hold, inequalities (39) are **not** independent according to Liénard and Chipart who established the following elegant criterion for asymptotic stability [16].

The Liénard – Chipart asymptotic stability criterion

Necessary and *sufficient* conditions for all roots of the real polynomial $f(z) = \alpha_0 z^n + \alpha_1 z^{n-1} + \ldots + \alpha_{n-1} z + \alpha_n = 0,\ (\alpha_0 > 0)$ to have *negative real parts* can be given in any one of the following forms:

1. $\quad \alpha_n > 0,\ \alpha_{n-2} > 0,\ldots;\qquad$ with $\begin{cases} \text{either}\ \Delta_1 > 0,\ \ \Delta_3 > 0,\ \ \ldots, \\ \text{or}\ \Delta_2 > 0,\ \ \Delta_4 > 0,\ \ \ldots, \end{cases}$ (41a)

2. $\quad \alpha_n > 0;\ \alpha_{n-1} > 0,\ \alpha_{n-3} > 0,\ldots;$ with $\begin{cases} \text{either}\ \Delta_1 > 0,\ \ \Delta_3 > 0,\ \ \ldots, \\ \text{or}\ \Delta_2 > 0,\ \ \Delta_4 > 0,\ \ \ldots, \end{cases}$ (41b)

This asymptotic stability criterion was rediscovered by Fuller [21].

4.2 Symmetrization of Asymmetric Matrices

If the generalized stiffness matrix **V** *is asymmetric* one should adopt the procedure that follows after recalling some theorems from *the theory of matrices*. A real asymmetric matrix **A** $(\neq \mathbf{A}^T)$ is *symmetrizable* if it can be expressed as the product of *two symmetric* matrices one of which is *positive definite* [6], i.e.

$$\mathbf{A} = \mathbf{S}_1 \mathbf{S}_2 \tag{42}$$

where $\mathbf{S}_1$ is *positive definite* and $\mathbf{S}_2 = \mathbf{S}_2^T$ (symmetric matrix). Clearly, from relation (42) it is deduced $\mathbf{S}_1^{-1}\mathbf{A} = \mathbf{S}_2$ which indicates that a s*ymmetrizable* matrix becomes *symmetric a*fter multiplication by an appropriate *positive definite matrix.* Moreover, since a symmetrizable matrix is *similar* to a symmetric matrix, its eigenvalues are necessarily *real*.

From $(\rho^2\mathbf{M}+ \rho\ \mathbf{C}+\mathbf{V})\mathbf{r} = 0$ it follows that

$$\mathbf{M}(\rho^2\mathbf{I}+\rho^2\tilde{\mathbf{C}}+\tilde{\mathbf{V}})\mathbf{r} = 0 \ \text{ or } \ (\rho^2\mathbf{I}+\rho^2\tilde{\mathbf{C}}+\tilde{\mathbf{V}})\mathbf{r} = 0 \tag{43}$$

where $\tilde{\mathbf{C}} = \mathbf{M}^{-1}\mathbf{C}$ and $\tilde{\mathbf{V}} = \mathbf{M}^{-1}\mathbf{V}$.

One can find transformations of the form

$$\tilde{\mathbf{V}} = \mathbf{S}_1\mathbf{S}_2, \qquad \tilde{\mathbf{C}} = \beta\,\mathbf{S}_1\mathbf{T} \tag{44}$$

where $\mathbf{S}_1$ is a positive definite matrix, $\mathbf{S}_2$ and $\mathbf{T}$ are symmetric matrices, while β is a small positive number.

Using relations (44) ,eq.(43) is written as follows

$$(\rho^2\mathbf{I}+\rho\beta\mathbf{S}_1\mathbf{T}+\mathbf{S}_1\mathbf{S}_2)\mathbf{r} = 0 \ \text{ or } \ (\rho^2\mathbf{S}_1^{-1/2}+\rho\beta\mathbf{S}_1^{1/2}\mathbf{T}+\mathbf{S}_1^{1/2}\mathbf{S}_2)\mathbf{r} = 0 \tag{45}$$

$$\text{or} \qquad (\rho^2\mathbf{I}+\rho\beta\mathbf{S}_1^{1/2}\mathbf{T}\mathbf{S}_1^{1/2}+\mathbf{S}_1^{1/2}\mathbf{S}_2\mathbf{S}_1^{1/2})\,\mathbf{S}_1^{-1/2}\,\mathbf{r} = 0 \tag{46}$$

where $\mathbf{S}_1^{1/2}$ and $\mathbf{S}_1^{-1/2}$ are also symmetric matrices, since $\mathbf{S}_1$ is a symmetric matrix.

Similarly from $(\rho^2\mathbf{M}+ \rho\ \mathbf{C}+\mathbf{V})\mathbf{r} = 0$ one can write

$$\begin{aligned} &\mathbf{q}^T\mathbf{M}(\rho^2\mathbf{I}+\rho\beta\mathbf{S}_1\mathbf{T}+\mathbf{S}_1\mathbf{S}_2) = 0 \ \text{ or } \\ &\mathbf{q}^T\mathbf{M}\,\mathbf{S}_1^{1/2}(\rho^2\mathbf{I}+\rho\beta\mathbf{S}_1^{1/2}\mathbf{T}\mathbf{S}_1^{1/2}+\mathbf{S}_1^{1/2}\mathbf{S}_2\mathbf{S}_1^{1/2})\,\mathbf{S}_1^{-1/2} = 0 \end{aligned} \tag{47}$$

or

$$\mathbf{q}^T\mathbf{M}\,\mathbf{S}_1^{1/2}(\rho^2\mathbf{I}+\rho\beta\mathbf{S}_1^{1/2}\mathbf{T}\mathbf{S}_1^{1/2}+\mathbf{S}_1^{1/2}\mathbf{S}_2\mathbf{S}_1^{1/2}) = 0 \tag{48}$$

The transpose of eq.(48) is

$$(\rho^2\mathbf{I}+\rho\beta\mathbf{S}_1^{1/2}\mathbf{T}\mathbf{S}_1^{1/2}+\mathbf{S}_1^{1/2}\mathbf{S}_2\mathbf{S}_1^{1/2})\mathbf{S}_1^{1/2}\mathbf{M}\mathbf{q}^T = 0 \tag{49}$$

Comparing eqs(46) and (49) we obtain

$$\mathbf{S}_1^{-1/2}\,\mathbf{r} = \mathbf{S}_1^{1/2}\mathbf{M}\mathbf{q}, \ \mathbf{r} = \mathbf{S}_1\,\mathbf{M}\mathbf{q} \tag{50}$$

Using eqs(44) one can write

$$\mathbf{S}_1^{-1}\,\tilde{\mathbf{V}} = \mathbf{S}_2, \ \ \mathbf{S}_1^{-1}\tilde{\mathbf{C}} = \beta\mathbf{T} \tag{51}$$

where $\mathbf{S}_2$ and $\mathbf{T}$ are (as stated above) symmetric matrices, while $\mathbf{S}_1$ is a positive definite matrix. Note that transformations of the form (44) are **not** always possible for systems with more than three degrees of freedom.

Subsequently the procedure for a conservative symmetric system outlined above can be established.

5 Numerical Results

Since numerical results are available from previous studies [4, 12, 13, 14, 18] which are based on 2 or 3-DOF models for the sake of comparison we will use the spring cantilevered dynamic model of 2-DOF shown in Fig.2 under a partial follower load with noncocervativeness parameter $\eta \neq 1$ (nonconservative system) as well as for $\eta = 1$ (conservative system). Numerical results will be presented in graphical (mainly) but also in tabular form. Moreover, attention will be focused on the effect of the *violation* of one or more of the conditions of the Liénard-Chipart asymptotic stability criterion.
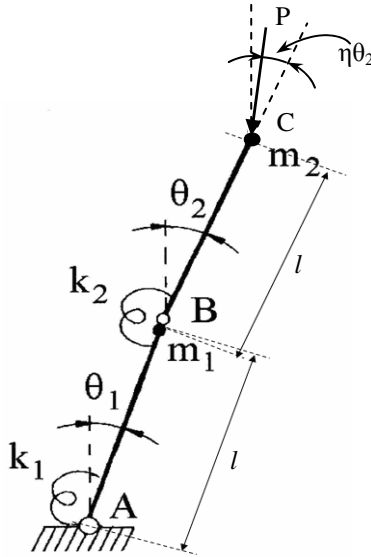
Fig. 2. 2-DOF autonomous cantilever model under a partial follower load P.

The response of this dynamic model, carrying two concentrated masses, is studied when it is either *unloaded* or *loaded* by a suddenly applied load of constant magnitude and varying ($\eta \neq 1$) or constant ($\eta = 1$) direction with infinite duration. Such an autonomous dissipative system with *infinitesimal* damping (including the case of zero loading) is properly discussed. If at least one root of the secular eq.(6) has a *positive* real part, the corresponding solution (7) will contain an exponentially increasing function and the system will become *unstable*. The nonlinear equations of motion for the 2-DOF nonconservative model of Fig.2 with rigid links of equal length l are given by Kounadis [12].

$$(1+m)\ddot{\theta}_1 + \ddot{\theta}_2 \cos(\theta_1 + \theta_2) + \dot{\theta}_2^2 \sin(\theta_1 - \theta_2) + c_{11}\dot{\theta}_1 + c_{12}\dot{\theta}_2 + V_1 = 0$$
$$\ddot{\theta}_2 + \ddot{\theta}_1 \cos(\theta_1 - \theta_2) - \dot{\theta}_1^2 \sin(\theta_1 - \theta_2) + c_{22}\dot{\theta}_2 + c_{12}\dot{\theta}_1 + V_2 = 0$$

(52)

where $V_1 = (1+k)\theta_1 - \theta_2 - \lambda\sin[\theta_1 + (\eta-1)\theta_2]$, $V_2 = \theta_2 - \theta_1 - \lambda\sin\eta\theta_2$, and η is the nonconservativeness loading parameter, $m=m_1/m_2$, $k=k_1/k_2$ and $\lambda=Pl/k_2$.

Linearization of eqs.(52) after setting

$$\Theta = \begin{bmatrix} \theta_1 \\ \theta_2 \end{bmatrix} = e^{\rho t}\begin{bmatrix} \varphi_1 \\ \varphi_2 \end{bmatrix} = e^{\rho t}\boldsymbol{\varphi}$$

gives

$$\left(\rho^2\mathbf{M} + \rho\mathbf{C} + \mathbf{V}\right)\boldsymbol{\varphi} = 0 \tag{53}$$

where

$$\mathbf{M} = \begin{bmatrix} m_{11} & m_{12} \\ m_{12} & m_{22} \end{bmatrix} = \begin{bmatrix} 1+m & 1 \\ 1 & 1 \end{bmatrix}, \mathbf{C} = \begin{bmatrix} c_{11} & c_{12} \\ c_{12} & c_{22} \end{bmatrix},$$

$$\mathbf{V} = \begin{bmatrix} V_{11} & V_{12} \\ V_{21} & V_{22} \end{bmatrix} = \begin{bmatrix} k+1-\lambda & -1-\lambda(\eta-1) \\ -1 & 1-\lambda\eta \end{bmatrix}. \tag{54}$$

The *static* buckling (divergence) equation is given by

$$\eta\lambda^2 - \eta(2+k)\lambda + k = 0 \tag{55}$$

whose lowest root is the *first* buckling load λ_1^c equal to

$$\lambda_1^c = 0.5[k + 2 - \sqrt{(k+2)^2 - 4k/\eta}\,] \tag{56}$$

which for real roots yields $\eta=4k/(k+2)^2$ that defines the *boundary* between the region of *existence* and *non-existence* of adjacent equilibria.

In case of a Rayleigh's dissipative function the damping coefficients are, $c_{11} = c_1+c_2$, $c_{12} = -c_2$, $c_{21} = -c_2$ and $c_{22} = c_2$, where c_i (i=1,2) is dimensionless coefficient for the ith rigid link. This case (for which $\det\mathbf{C}=c_1c_2$) is a specific situation of the damping matrix $\mathbf{C}$ which is not discussed herein.

5.1 Conservative System ($\eta=1$)

The corresponding equations of motion are obtained for the 2-DOF conservative model from eqs(52) after setting $\eta=1$. Thus eqs(53&54) are also valid after inserting $\eta=1$ into matrix $\mathbf{V}$ and λ_1^c.

For a *degenerate* Hopf bifurcation (Fig.1b), associated with a positive semi-definite matrix C, using eqs(15) and (16) for n=2, we get

$$r = r_1/r_2 = -c_{22}/c_{11} \tag{57}$$

Application of eq.(19) due to eqs(54) gives

$$\frac{(k+1-\lambda)r - 1}{(1+m)r + 1} = \frac{-r+1-\lambda}{r+1} \tag{58}$$

from which we obtain the degenerate Hopf bifurcation load $\lambda = \lambda_H$, i.e.

$$(r^2 - mr - 1)\lambda_H = r^2(m + k + 2) + r(k - m) - 2, \qquad (59)$$

where m and k are positive quantities, while r may be positive or negative. Note that if $r^2 - mr - 1 = 0$, the critical load λ_H exhibits *a discontinuity* (varying from $+\infty$ to $-\infty$). For $r^2(m+k+2)+r(k-m)-2=0$ it follows that $\lambda=0$. Clearly, for given r the above extreme values of λ_H may occur for various combinations of values of the parameters m and k.

It is worth noticing that the *discontinuity* in the flutter load λ_H (being independent of the stiffness ratio k) occurs at $m=(r^2-1)/r$. Namely, for a given damping ratio r, one can find a critical value of m, i.e. $m=m_{cr}$, which corresponds to a *discontinuity* in the load λ_H. As stated above, since $r(=-c_{22}/c_{11})$ does not depend on λ, eq.(9) yields $dv/d\lambda=0$ (violation of the transversality sufficient condition for a degenerate Hopf bifurcation).

From eq.(19) we obtain

$$\mu^2 = -\rho^2 = \frac{-r + 1 - \lambda}{1 + r} \quad (r \neq 0) \qquad (60)$$

For the above 2-DOF model with $k = 1$, $m = 10$ and a positive semi-definite matrix **C** with $c_{11} = 0.01$, $c_{12} = c_{21} = 0.002$ and $c_{22} = 0.0004$ (i.e. $|\mathbf{C}|=0$) we find $\lambda_1^c = 0.381966011$ $r = -0.20$, $\lambda_H = 0.32/1.04 = 0.307692307$, and $\rho^2 = -\mu^2 = -1.115384615$ [4]. The *critical* mass ratio for which a discontinuity in the flutter load λ_H for this degenerate Hopf bifurcation occurs for $m_{cr} = 4.80$.

For a *generic* Hopf bifurcation (Fig.1c), associated with a given *indefinite* matrix C, according to the exact analysis, one can obtain λ_H and μ^2 by solving the system of eqs.(23). The discontinuity in the flutter load λ_H in the above degenerate Hopf bifurcation appears also in generic Hopf bifurcations a shown below.

In case of an indefinite matrix **C** for which $|\mathbf{C}|< -\varepsilon^2$ with $\varepsilon\to 0$, the determination of the flutter load λ_H (and then μ^2) is appreciably simplified without diminishing its accuracy.

Thus, application of eq.(19) gives

$$\mu^2 = \frac{V_{11}r + V_{12}}{M_{11}r + M_{12}} = \frac{V_{12}r + V_{22}}{M_{12}r + M_{22}} \qquad (61)$$

which leads to eq.(58) and then to eq.(59). The ratio r is obtained from eq.(25), i.e.

$$c_{11}r^2 + 2c_{12}r + c_{22} = 0,$$

$$\text{or} \qquad r = \frac{1}{c_{11}}\left(-c_{12} \pm \sqrt{c_{12}^2 - c_{11}c_{22}}\right) \qquad (62)$$

Clearly, the equation yielding a *discontinuity* in the flutter load λ_H, i.e. $r^2 - mr - 1 = 0$, is still valid. For the above 2-DOF model with $k=1$ and $m=10$ related to an indefinite matrix **C** with $c_{11}=0.01$, $c_{12}=c_{21}=0.0325$ and $c_{22}=0.012$ (i.e. $|\mathbf{C}|=-9.3625\times10^{-4}<0$) we

find, according to the exact analysis, $\lambda_H = 0.193698381 < \lambda_1^c$, and $\mu = 1.109221303$ [4]. On the basis of the *approximate* analysis we obtain using eq.(62) $r = -0.190179743$ and thereafter through eq.(61), $\lambda_H = 0.193830151$ and $\mu = 1.109204333$, respectively, which practically coincide with the previously found values of λ_H and μ. The plot λ_H versus $m > 0$ with the corresponding asymptotes $m = 5.068$ and $\lambda = 1.19018$ is shown in Fig.3.
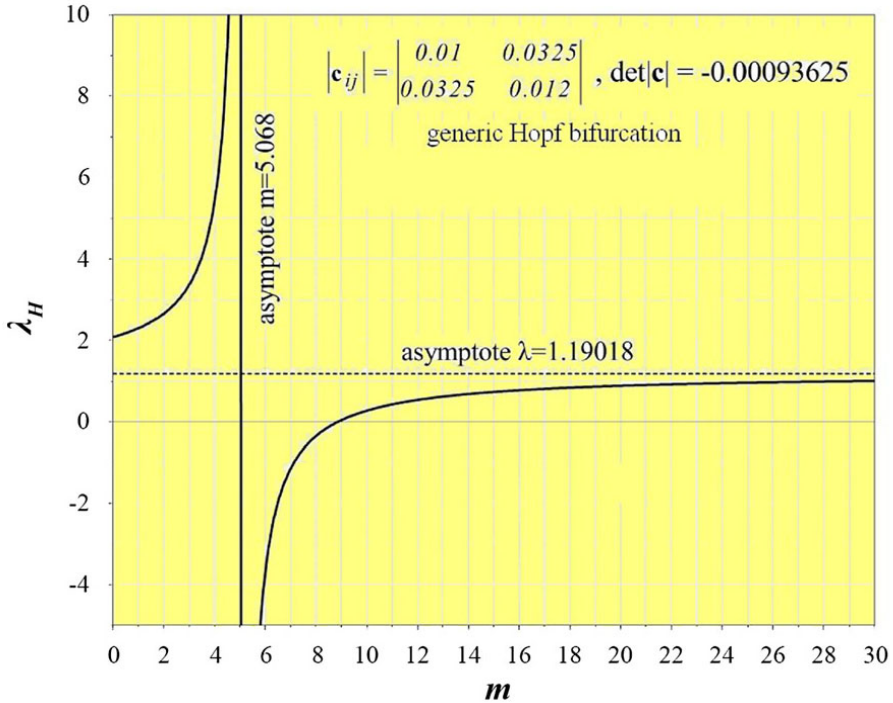
Fig. 3. Variation of λ_H versus mass ratio m for stiffness ratio k=1 with a discontinuity of the flutter load λ_H for m=5.068.

Fig.4a shows the generic Hopf bifurcation load λ_H versus mass ratio $m(= m_1/m_2) > 5.068$ for various values of stiffness ratio $k(= k_1/k_2)$. The small circle in each k-curve corresponds to the critical divergence or static (buckling) load $\lambda_1^c (\equiv \lambda_H)$. This corresponds to a dynamic bifurcation associated with a coupled *divergence–flutter* instability (Fig.1d). This *double zero* eigenvalue dynamic bifurcation is called an Arnold–Bogdanof dynamic bifurcation [4]. Below the small circle we have $\lambda_H < \lambda_1^c$ for each value of k. Clearly, both λ_1^c and λ_H increase with the increase of k. Fig.4b shows a generic Hopf bifurcations load λ_H versus mass ratio $m(= m_1/m_2) < 5.068$ for various stiffness ratios $k(= k_1/k_2)$. The values of λ_H are higher than $\lambda = 1.19018$ (asymptote). It is worth noticing that a discontinuity in the flutter load versus mass was first observed in a continuous damped cantilever model carrying concentrated (attached) masses [22, 23].
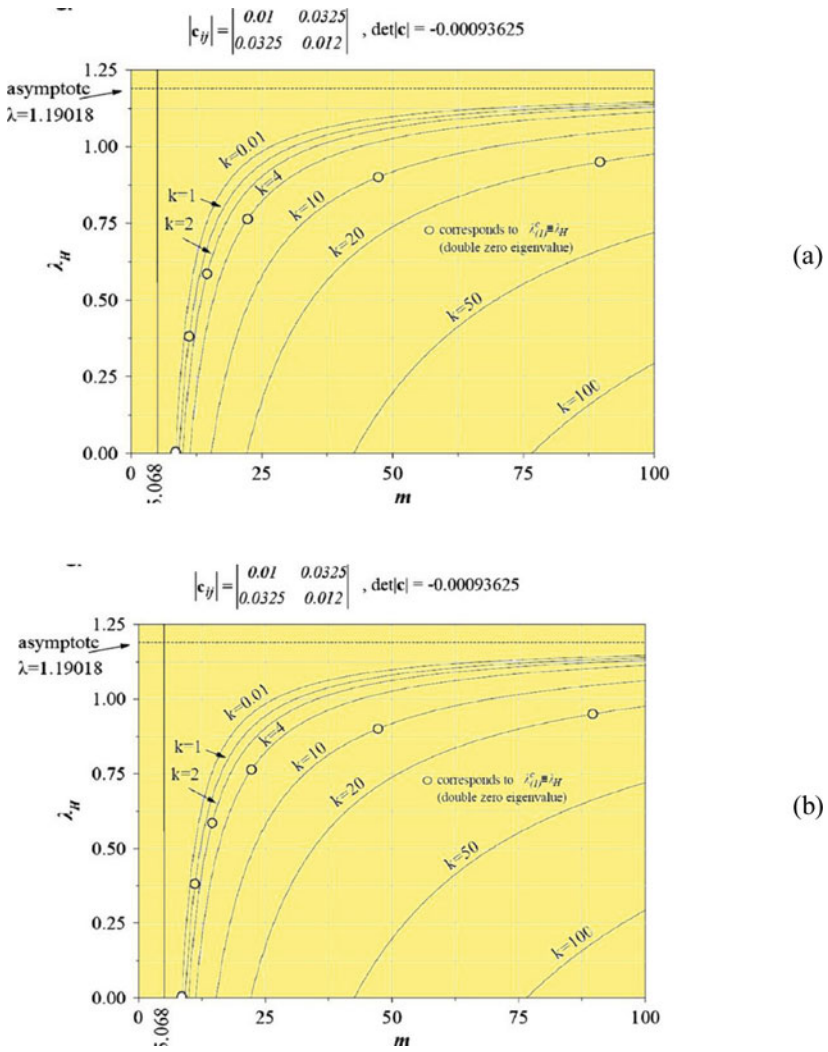
$$|c_{ij}| = \begin{vmatrix} 0.01 & 0.0325 \\ 0.0325 & 0.012 \end{vmatrix} , \det|c| = -0.00093625$$

(a)

$$|c_{ij}| = \begin{vmatrix} 0.01 & 0.0325 \\ 0.0325 & 0.012 \end{vmatrix} , \det|c| = -0.00093625$$

(b)

Fig. 4. Hopf bifurcation load λ_H versus mass ratio $m(=m_1/m_2)$ for various values of stiffness ratios $k(=k_1/k_2)$: (a) for $m>5.068$; (b) for $m<5.068$.

Table 1. Buckling and flutter loads λ_1^c and λ_H as well as $|\max\theta(\tau)|$ for various stiffness and mass ratios k and m

k	$\lambda_{(1)}^c$	$m\ (\lambda_H \equiv \lambda_{(1)}^c)$	m / λ_H	Max absolute amplitude of limit cycle response $|\max\theta_1(\tau)|$	m / λ_H	Max absolute amplitude of limit cycle response $|\max\theta_1(\tau)|$
0.01	0.0049875000078124096	8.5381671820524	8.530898922049763 / 0.0025	1.266×10^{-4}	8.537910996697269 / 0.0049	1.443×10^{-4}
0.05	0.024687548812872162	8.624620682147096	8.58721493692014 / 1.0123	1.345×10^{-4}	8.624048427854003 / 0.0245	1.512×10^{-4}
0.10	0.048750780274960714	8.735080373142841	8.66032855429743 / 0.025	1.361×10^{-4}	8.732669827235092 / 0.048	1.405×10^{-4}
0.20	0.09501243788791092	8.96341923121673	8.800309959352578 / 0.047	1.423×10^{-4}	8.96034346927522 / 0.094	1.511×10^{-4}
0.50	0.21922359359558485	9.712596429979081	9.242934965700924 / 0.11	1.607×10^{-4}	9.706750465869224 / 0.218	1.812×10^{-4}
1.00	0.3819660112501051	11.148927626097844	10 / 0.1936983908834291	1.852×10^{-4}	11.145423271996046 / 0.3815	2.353×10^{-4}
2.00	0.5857864376269049	14.53770234116409	11.498810153696272 / 0.30	2.372×10^{-4}	14.51185531175303 / 0.584	3.624×10^{-4}
4.00	0.7639320225002102	22.29891798820193	14.133179512599185 / 0.38	2.983×10^{-4}	22.221165740849916 / 0.762	6.161×10^{-4}
10.0	0.9009804864072155	47.268958942233375	21.55582361428882 / 0.45	4.645×10^{-4}	46.83845564604463 / 0.898	0.001075
20.0	0.95012437887911	89.649282067276	33.4568798886462 / 0.475	6.221×10^{-4}	88.90731487411975 / 0.948	0.00145
50	0.9800079936063923	217.29095024741068	68.76698107585851 / 0.49	7.963×10^{-4}	215.28247546849224 / 0.978	0.00177
100	0.9900009998000527	430.1966503540317	128.36449052490056 / 0.50	9.365×10^{-4}	425.98894651830915 / 0.988	0.00196

$k = 10, \quad m = 46.838455646$

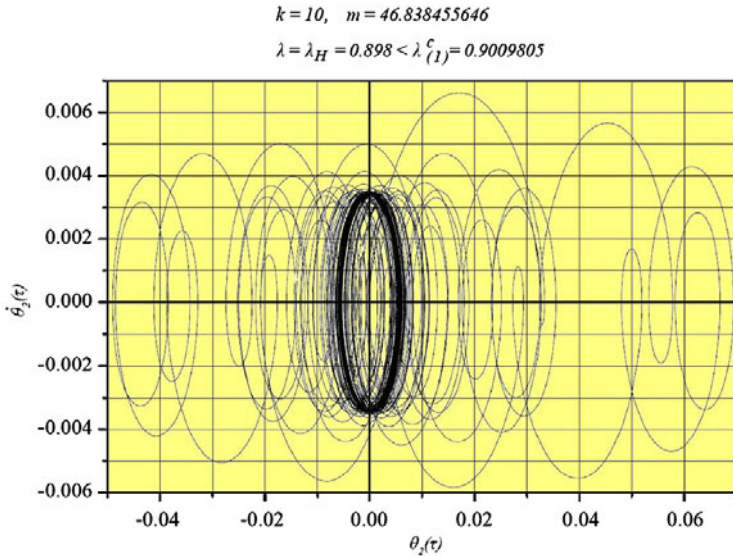$\lambda = \lambda_H = 0.898 < \lambda_{(1)}^c = 0.9009805$

Fig. 5. Phase-plane portrait of the Hopf bifurcation of a 2-DOF model with k=10 and m=46.838455646.

Table 1 gives values of $\lambda_1^c \equiv \lambda_H$, of $\lambda_H < \lambda_1^c$ and of λ_H slightly smaller than λ_1^c for various values of the stiffness and mass ratio k and m, respectively, together with the corresponding final amplitudes $\theta_1(\tau)$ of the stable *limit cycles*. Note that $\theta_1(\tau)$ increases with the increase of k and m. Fig.5 shows the phase-plane portrait θ_2 vs $\dot{\theta}_2$ corresponding to the above generic Hopf bifurcation with k=10, m=46.838455646 and $\lambda_H=0.898 < \lambda_c=0.9009805$. Note that the (absolutely) *maximum* amplitude of $\theta_1(\tau)$ corresponding to this generic Hopf bifurcation, is nearly 0.008 rad. The *maximum* (absolutely) amplitudes of $\theta_1(\tau)$ are, as expected, lower than the corresponding $|\max\theta_2(\tau)|$.

Liénard-Chipard Stability Criterion

Subsequently we will discuss the effect of *violation* of the above stability criterion for $\lambda \neq 0$ and $\lambda = 0$.

The characteristic (secular) equation is

$$\rho^4 + \alpha_1\rho^3 + \alpha_2\rho^2 + \alpha_3\rho + \alpha_4 = 0 \tag{63}$$

where

$$\left.\begin{aligned}
\alpha_1 &= \frac{1}{m}\left(m_{11}c_{22} + m_{22}c_{11} - 2m_{12}c_{12}\right), \\
\alpha_2 &= \frac{1}{m}\left(m_{11}V_{22} + m_{22}V_{11} - 2V_{12}m_{12} + |c|\right), \\
\alpha_3 &= \frac{1}{m}\left(c_{11}V_{22} + c_{22}V_{11} - 2V_{12}c_{12}\right), \\
\alpha_4 &= \frac{1}{m}\left(V_{11}V_{22} - V_{12}^2\right).
\end{aligned}\right\} \tag{64}$$

where $|c| = \det \mathbf{C}$.

Let us first examine the effect of *violation* of the Liénard-Chipart criterion on the system stability in the case of *zero loading* (i.e., $\lambda = 0$). Then eqs(64) due to relations (54) are written as follows:

$$\left.\begin{aligned}
\alpha_1 &= \frac{1}{m}\left[(1+m)c_{22} + c_{11} - 2c_{12}\right], \\
\alpha_2 &= \frac{1}{m}\left[k + m + 4 + c_{11}c_{22} + c_{12}^2\right], \\
\alpha_3 &= \frac{1}{m}\left[c_{11} + c_{22}(k+1) - 2c_{12}\right], \\
\alpha_4 &= \frac{k}{m}.
\end{aligned}\right\} \tag{65}$$

According to Liénard-Chipart criterion inequalities (41a) imply

$$\alpha_4 > 0, \; \alpha_2 > 0, \; \Delta_1 > 0, \; \Delta_3 > 0, \tag{66}$$

where $\Delta_1 = \alpha_1 > 0$ and $\Delta_3 = \alpha_3(\alpha_1\alpha_2 - \alpha_3) - \alpha_1^2\alpha_4 > 0$. Clearly, from the last inequality, it follows that $\alpha_3 > 0$.

For $c_{ii} > 0$ ($i=1, 2$), $k > 0$ and $m > 0$ (implying $\alpha_4 > 0$), it is deduced that this criterion is violated if either one of α_1 or α_2 is zero or Δ_3 is zero. These three cases will be discussed separately in connection with the algebraic structure of the damping matrix $C = [c_{ij}]$.

Case 1 ($\alpha_1 = 0$ with $\alpha_2 > 0$)

If $\alpha_1 = 0$ (yielding $\Delta_3 = -\alpha_3^2 < 0$), then

$$(1+m)c_{22} + c_{11} - 2c_{12} = 0 \tag{67}$$

Eq.(67), being independent of λ and k, is satisfied only when the damping matrix C is indefinite, that is,

$$c_{11}c_{22} - c_{12}^2 < 0 \qquad (c_{ii} > 0 \text{ for } i,j=1,2) . \tag{68}$$

Indeed, the last inequality due to relation (67) implies

$$(1+m)^2 c_{22}^2 + 2(m-1)c_{11}c_{22} + c_{11}^2 > 0 \tag{69}$$

which is always satisfied, regardless of the value of c_{22}/c_{11}, since for $m > 0$, the discriminant of eq.(69) (equal to $-16m$) is always negative.

Thus, we have explored the *unexpected* finding that an *unloaded* (stable) structural system ($\lambda=0$) becomes dynamically *unstable* at any small disturbance in case of an *indefinite* damping matrix even when infinitesimal damping is included.

If all coefficients of eq.(63) are *positive* from the *theory of algebraic equations* it follows that this equation **cannot** have positive root. Also the case of existence of a pair of pure imaginary roots associated with $\Delta_3 = 0$ is ruled out, since $\Delta_3 < 0$ (due to $\alpha_1 = 0$). Hence, eq.(63) has either two *negative* roots combined with a pair of complex conjugate roots with *positive* real part or *two pairs* of *complex conjugate* roots with *opposite* real parts. Both cases imply local dynamic instability.

Case 2 ($\alpha_2 = 0$ with $\alpha_1 > 0$)

If $\alpha_2 = 0$ (implying also $\Delta_3 < 0$), then

$$|c| = -k - m - 4 < 0 \qquad (k, m > 0). \tag{70}$$

Namely, the damping matrix $[c_{ij}]$ is *indefinite* but with a large negative determinant (rather unrealistic case). Since the Liénard-Chipart criterion is violated, the model is again locally dynamically unstable.

The observation mentioned above at the end of **Case 1** is also valid for **Case 2**. Namely, we have again *local* dynamic asymptotic instability.

Case 3 ($\Delta_3 = 0$)

In this case, stability conditions in eq.(66) are satisfied except for the last one, since $\Delta_3 = 0$ which yields

$$\Delta_3 = \alpha_3 (\alpha_1 \alpha_2 - \alpha_3) - \alpha_1^2 \alpha_4 = 0 \tag{71}$$

Note that $\lambda < \lambda_1^c$ implies $\alpha_4 > 0$ (i.e., $\det \mathbf{V} > 0$).

This is a *necessary condition* for the secular eq.(63) to have one pair of *pure imaginary* roots $\rho = \pm\mu i$. Indeed, this can be readily established by inserting $\rho = \pm\mu i$ into eq.(63) and then equating to zero *real* and *imaginary* parts.

Consider now the more general case of *nonzero* loading (i.e. $\lambda \neq 0$). Using relations (64), eq.(71) can be written as follows

$$A \lambda^2 + B \lambda + \Gamma = 0 \tag{72}$$

where

$$A = (c_{11} + c_{22})(m+2)\overline{\alpha}_1 - m(c_{11} + c_{22})^2 - \left[(1+m)c_{22} + c_{11} - 2c_{12}\right]^2 \tag{73a}$$

$$B = -\overline{\alpha}_1\left\{(m+2)\left[c_{11} + (k+1)c_{22} + 2c_{12}\right] + (c_{11} + c_{22})\left[k + m + 4 + |c|\right]\right\}$$
$$+ 2m\left[c_{11} + (k+1)c_{22} + 2c_{12}\right](c_{11} + c_{22}) + (k+2)\left[(1+m)c_{22} + c_{11} - 2c_{12}\right]^2 \tag{73b}$$

$$\Gamma = \left[k + m + 4 + |c|\right]\left[c_{11} + (k+1)c_{22} + 2c_{12}\right]\overline{\alpha}_1 - m\left[c_{11} + (k+1)c_{22} + 2c_{12}\right]^2$$
$$- k\left[(1+m)c_{22} + c_{11} - 2c_{12}\right]^2 \tag{73c}$$

where

$$c_{11} = (c_{12}^2 + |c|)/c_{22}, \qquad \overline{\alpha}_1 = m\alpha_1 \tag{73d}$$

For real λ, the discriminant $\mathbf{D}$ of eq.(72) must be greater than or equal to zero, that is,

$$\mathbf{D} = B^2 - 4A\Gamma \geq 0. \tag{74}$$

Subsequently, attention is focused on the following: (a) matrix $\mathbf{C}$ is positive semi-definite (i.e., $|c| = 0$ with $c_{ii} > 0$, $i=1, 2$) and (b) matrix $\mathbf{C}$ is indefinite ($|c| < 0$ with $c_{ii} > 0$, $i = 1, 2$).

Using the *symbolic* manipulation of Mathematica [24], one can find that

$$\mathbf{D} = |c|f(|c|) \tag{75}$$

where $f(|c|)$ is an algebraic polynomial of 5th degree in $|c|$.

Case 4 ($|c|=0$, $f \neq 0$)

For $|c|=0$, eq.(72) implying $\mathbf{D}=0$ admits a double root, which due to (73a), (73b), (73c), (73d) is given by

$$\lambda_1^H = \frac{2c_{12}^2 + c_{12}c_{22}(k-m) - c_{22}^2(k+m+2)}{c_{12}^2 - c_{22}^2 - c_{12}c_{22}m} \tag{76}$$

Using the *Reduce Command* embedded in Mathematica, one can find the conditions under which, $0 < \lambda_1^H < \lambda_1^c$, given in the appendix of ref [18].

Case 5 $(f = 0, |c|{\neq}0)$

Moreover, it was found *symbolically* that the 5th degree polynomial f(|c|) possesses *three* real roots (one double and one single) and *two pure imaginary* ones. Discussing their nature, one can find that the double root of f(|c|), being equal to $|c| = -(c_{12}-c_{22})^2 - c_{22}^2\, m{<}0$, yields

$$c_{12} = \frac{1}{2}\left[c_{11} + (m+1)c_{22}\right]$$ (77)

Then, the double root of eq.(72) becomes

$$\lambda_1^H = \frac{2c_{11} + c_{22}(k+m+2)}{c_{11} + c_{22}}$$ (78)

which is always *greater* than λ_1^c and hence of minor importance for the present analysis.

The *third* real root of f(|c|), if substituted in eq.(72), yields again a *double* root in λ, always less than zero, which is rejected. Thus, only the case of a positive semi-definite damping matrix may lead to an *acceptable* value of the corresponding load (i.e., $0{<}\lambda_H{<}\lambda_1^c$) associated with a *degenerate* Hopf bifurcation as theoretically was shown by Kounadis [4, 13].

Case 6 $(\lambda = 0)$

If λ=0, eq.(72) implies Γ=0, which after symbolic manipulation of eq.(73c) can be written in the following form

$$\Gamma = \frac{1}{c_{22}^2}\left(|c|^3 + A_2|c|^2 + A_1|c| + A_0\right) = 0,$$ (79)

where A_i (i = 0, 1, 2) are given in the appendix of ref.[18] . It is evident that $A_2{>}0$ and $A_0{\geq}0$, a fact implying that eq.(79) can be satisfied only for $|c| \leq 0$ if also $A_1{\geq}0$; otherwise (i.e., if $A_1{<}0$) the system may be dynamically *locally* stable or unstable. For |c|=0, one can find the corresponding values of $c_{ii}(i = 1, 2)$, given in the appendix of ref. [18] which are always positive. This *special* case, for which the *trivial* (unloaded) state is associated with a pair of *pure imaginary* eigenvalues (necessary condition for a Hopf bifurcation) implies local dynamic asymptotic instability.

Conditions for a double imaginary root

For a *double imaginary root* the first derivative of the secular eq.(63) must be also zero which yields

$$4\rho^3 + 3\alpha_1\rho^2 + 2\alpha_2\rho^2 + \alpha_3 = 0.$$ (80)

Inserting into eq.(80) $\rho = \mu i$, we obtain $\mu^2 = 0.5\alpha_2 = \alpha_3/3\alpha_1$ and thus $\alpha_3 = 3\alpha_1\alpha_2/2$. Introducing this expression of α_3 into eq.(71), it follows that $\alpha_1{=}0$, which also implies that $\alpha_3{=}0$ and hence eq.(80) becomes $\rho^2 = -0.5\alpha_2$. If $\rho^2 = -0.5\alpha_2$ is inserted into the secular equation $\rho^4 + \alpha_2\rho^2 + \alpha_4 = 0$, for a double imaginary root, it follows that $\alpha_{22} - 4\alpha_4 = 0$ which due to relations (64) yields

$$\left(m^2 + 4\right)\lambda^2 - 2\lambda\left(m^2 + (2-k)m + 2k + 8 + (m+2)|c|\right) + |c|^2$$
$$+ 2(k+m+4)|c| + (k+m+4)^2 - 4mk = 0. \tag{81}$$

For *real* λ, the discriminant **D** of eq.(81) must satisfy the inequality

$$\mathbf{D} = |c|^2 + (4 - mk)|c| - (m+k)^2 \geq 0 \tag{82}$$

which yields

$$\text{either } |c| < 0.5\left(mk - 4 - \sqrt{m^2(k^2+4) + 4k^2 + 16}\right),$$
$$\text{or } \quad |c| > 0.5\left(mk - 4 + \sqrt{m^2(k^2+4) + 4k^2 + 16}\right). \tag{83}$$

Using the conditions found above

$$\alpha_1 = \alpha_3 = 0, \tag{84}$$

relations (65) yield

$$(1+m)c_{22} + c_{11} - 2c_{12} = 0,$$
$$c_{11}(1-\lambda) + c_{22}(k+1-\lambda) + 2c_{12} = 0. \tag{85}$$

Adding the last two equations, we obtain

$$(2 - \lambda)\, c_{11} + (k + m + 2 - \lambda)\, c_{22} = 0. \tag{86}$$

Since k, m>0, and $\lambda < \lambda_1^c < 1$, it follows that both coefficients of c_{11} and c_{22} in eq.(86) are *positive*. Hence, c_{11} and c_{22} are of *opposite* sign (i.e., $c_{11}/c_{22}<0$) and consequently $|c|=c_{11}c_{22} - c_{12}^2 <0$; thus the 2nd of inequalities (83) is excluded.

Solving simultaneously the system of equations $\alpha_{22}-4\alpha_4=0$, $\alpha_1=\alpha_3=0$ in k, m, λ, two ternaries of values for k, m, and λ are obtained, given in the appendix of ref. [18].

For all these values to be greater than zero, the *Reduce Command* embedded in Mathematica [24] yields two sets of conditions, given also in the appendix of ref. [18]. Further symbolic computations are needed for establishing the conditions for a *double pure imaginary* root for loading values *less* than λ_1^c. Nevertheless, suitable combinations of values of c_{ij}, k, and m may be found. The corresponding dynamic response, since the system is associated with a codimension-2 local bifurcation, is anticipated to be related to isolated *periodic* orbits which will be established via a straightforward complete *nonlinear* dynamic analysis.

Subsequently, numerical results corresponding to all the above cases of *violation* of the Liénard-Chipart stability criterion are given below in graphical and tabular forms.

Case 1 ($\alpha_1 = 0$)
(a) $\lambda=0$. For an unloaded system with k = m = 1, choosing $c_{11} = 0.015$ and $c_{22} = 0.002$, eq.(67) yields $c_{12} = 0.0095$ and as expected the damping matrix is *indefinite* with determinant $|c| = -0.0006025$. The two pairs of corresponding

eigenvalues are $\rho_{1,2} = -0.00332577\pm0.41421i$ and $\rho_{3,4} = 0.00335877\pm0.41421i$ ($i=\sqrt{-1}$), implying local dynamic instability. Solving numerically the system of nonlinear equations of motion (52), we find that the dynamic response of the system is associated with a *divergent* (unbounded) motion, as depicted in Fig.6 with the aid of the plot angular velocities $\dot{\theta}_1(\tau)$ versus time τ.
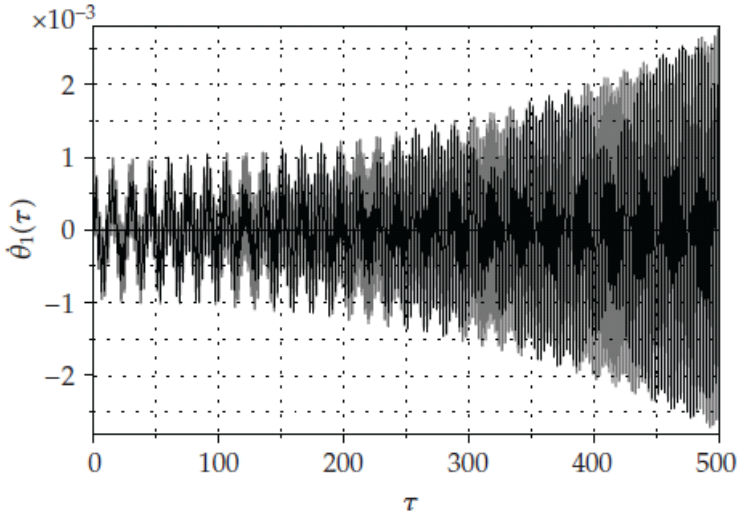
Fig. 6. Angular velocities $\dot{\theta}_1(\tau)$ versus time τ.

(b) $\lambda \neq 0$. For a system with k=5, m=4, and $\lambda=0.5 < \lambda_1^c = 0.807418$ and for $c_{11}=0.01$, $c_{22}=0.005$, eq.(67) yields $c_{12}=-0.0175$ implying $|c|=-2.5625\times10^{-4}$. The trivial state is locally dynamically unstable, since $\rho_{1,2}=-0.00397748\pm0.4351i$ and $\rho_{3,4}=0.00397748\pm0.4351i$. The corresponding dynamic response is again related to a *divergent* (unbounded) motion.

Case 2 ($\alpha_2 = 0$)

(a) $\lambda = 0$: If k=m=1 relation (70) is satisfied, for example, for the damping coefficients $c_{11} = 0.50$, $c_{22} = 2.00$, yielding $c_{12} = \sqrt{7}$ and $|c| = -6$. For this, rather unrealistic subcase, the corresponding eigenvalues are equal to $\rho_1 = -1.86617$, $\rho_2 = -0.102227$, and $\rho_{3,4} = 1.37995 \pm 1.8269i$ (local instability). Hence, the response of the system is also related to a divergent (unbounded) motion, presented graphically in the phase-plane portrait of Fig. 7(a,b).

(b) $\lambda \neq 0$. Similarly, for a system with k=0.10, m=0.20 (for which $\lambda_1^c = 0.0487508$) in order that $\alpha_2 = 0$, we must choose an indefinite damping matrix with $|c| = -4.25$. Setting, for example, $c_{11} = 2.375$, $c_{12} = 3.00$, $c_{22} = 2.00$, and $\lambda = 0.227273 < \lambda_1^c$, the trivial state is locally dynamically unstable with $\rho_1 = -2.46657$, $\rho_2 = -0.00503929$, and $\rho_{3,4} = 4.2983 \pm 1.6612i$. The system exhibits again a divergent (unbounded) motion [18].

Divergent motion

$a_2 = 0, \lambda = 0$
$k = 1, m = 1$

$p_1 = -1.86617, p_2 = -0.102227$
$p_{3,4} = 1.37995 \pm 1.8269j$

$C = \begin{pmatrix} 0.5 & \sqrt{7} \\ \sqrt{7} & 2 \end{pmatrix}$

$\text{Det} C = -k - m - 4 = -6$

Axis labels: $\dot{\theta}_1(\tau)$ (vertical), $\theta_1(\tau)$ (horizontal), $\times 10^{-2}$

(a)

The figure (b) contains annotations:

$C = \begin{pmatrix} 0.5 & \sqrt{7} \\ \sqrt{7} & 2 \end{pmatrix}$

$\text{Det} C = -k - m - 4 = -6$

$a_2 = 0, \lambda = 0$
$k = 1, m = 1$

$p_1 = -1.86617, p_2 = -0.102227$
$p_{3,4} = 1.37995 \pm 1.8269j$

Divergent motion

Axis labels: $\dot{\theta}_2(\tau)$ (vertical), $\theta_2(\tau)$ (horizontal), $\times 10^{-2}$

(b)
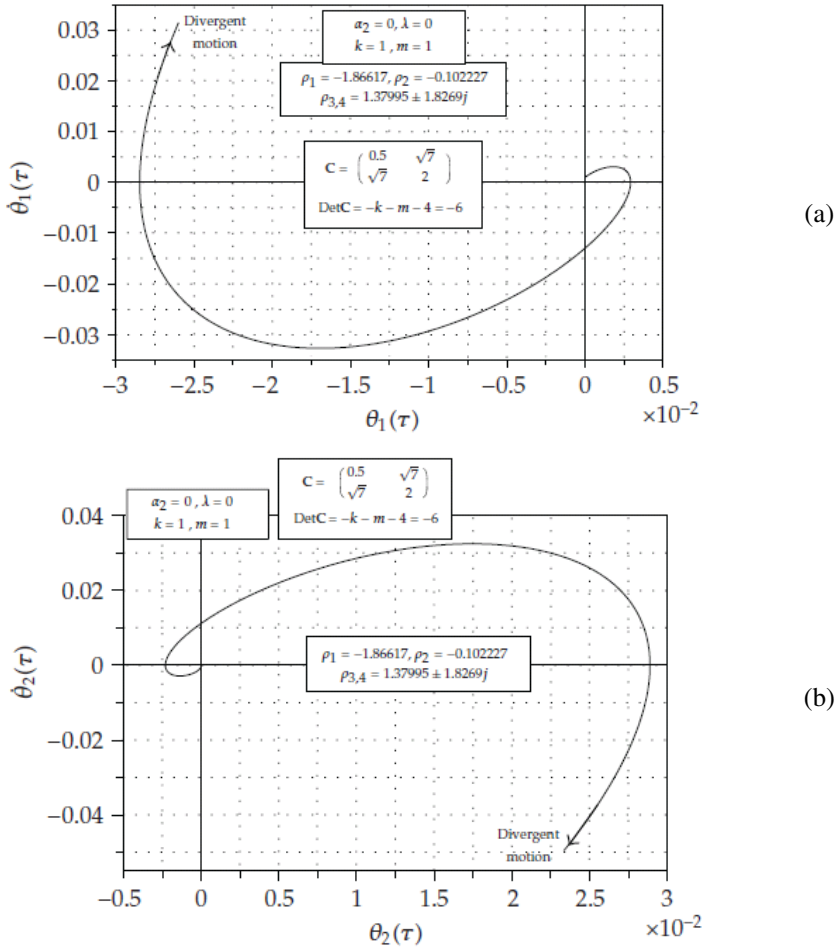
Fig. 7a, b. Phase-plane portraits $[\theta_i(\tau), \dot{\theta}(\tau)]$ (i=1,2) for the system of Case 2(a), associated with a divergant motion.

Case 3 ($\Delta_3=0$ with $\alpha_1\alpha_2 \neq 0$)

(a) Positive semi-definite damping matrix $\mathbf{C}$ ($|c| = 0$).

Choosing $c_{11} = 0.01$, $c_{22} = 0.0004$ (and thus $c_{12} = 0.002$), the 1st requirement of the 2nd set of conditions given in the appendix of ref. [18] is satisfied (i.e., $c_{12} > c_{22}$). The 2nd requirement, that is $m > 2(c_{12}-c_{22})/c_{22}$, yields $m > 8$, and hence one can choose m=10. The 3rd requirement given in the appendix of ref. [18] implies that $0.8333<k<3$ and thus one can take k=1. Solving numerically eq.(71) with respect to λ, we obtain the value of $\lambda_H = 0.307692256 < \lambda_i^c = 0.381966$ associated with a pair of *pure imaginary* eigenvalues, while the other pair has negative real parts.

The evolution of both pairs of eigenvalues in the complex plane as λ varies is presented in Fig.8(a,b) for $\lambda < \lambda_1^c$. For $\lambda = \lambda_H$, a *degenerate* Hopf bifurcation occurs and the system exhibits a *periodic* motion, whose final amplitude depends on the *initial conditions*. Relevant results in graphical form can also be found in recent publications [4, 13].

(b) Indefinite damping matrix **C** ($|c| < 0$).

It has been proven by Kounadis [4, 13] that in this subcase (for $\lambda < \lambda_1^c$) all the *necessary* and *sufficient* conditions for a *generic* Hopf bifurcation are fulfilled and hence the system experiences a periodic *attractor* response (stable limit cycles) with constant final amplitudes, regardless of the initial conditions.
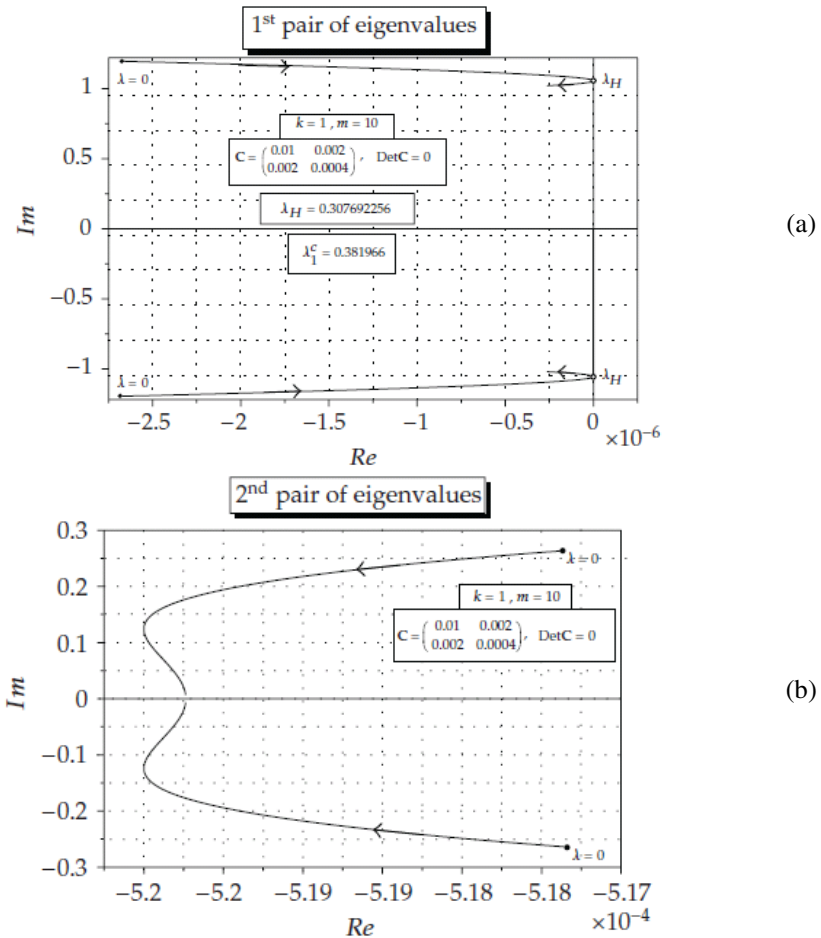
Fig. 8 a, b. Evolution of both eigenvalues in the p-complex plane for the system of Case3(a) associated with a degenerate Hopf bifurcation.

(c) $\Delta_3 = 0$ and $\lambda = 0$.

If at the same time $|c|=0$, one can find the values of $c_{ii} = (i = 1, 2)$ given in the appendix of ref.[18] which are always positive. A further investigation of this case as well as of the case $|c|<0$ for the **global** stability of the system can be performed through a *nonlinear* dynamic analysis.

(d) Double pure imaginary eigenvalues

For this special case, three combinations of damping matrix coefficients c_{ij} are examined. These, along with the corresponding critical values of k, λ and m, satisfying the appropriate relations given in the appendix of ref.[18], are presented in Table 2.

Table 2. Values of the damping coefficients (c_{ij}) and critical system parameters (k, λ_{cr}, m) for three subcases with double pure imaginary eigenvalues.

Case no.	c_{11}	c_{12} $|c|$	c_{22}	k	λ_{cr}	m	λ_1^c
3(d)1	3.45	1.00 −5.83	−1.40	2.65201108	0.164480292	0.035714286	0.665195
3(d)2	3.60	1.00 −5.32	−1.20	3.178585026	0.244040821	0.333333333	0.711568
3(d)3	3.40	1.00 −5.08	−1.20	2.346316274	0.629282032	0.166666666	0.631633

In the three above subcases, the evolution of both pairs of λ-dependent eigenvalues in the ρ-complex plane is depicted in Figs 9, 10, 11(a) and 11(b), from
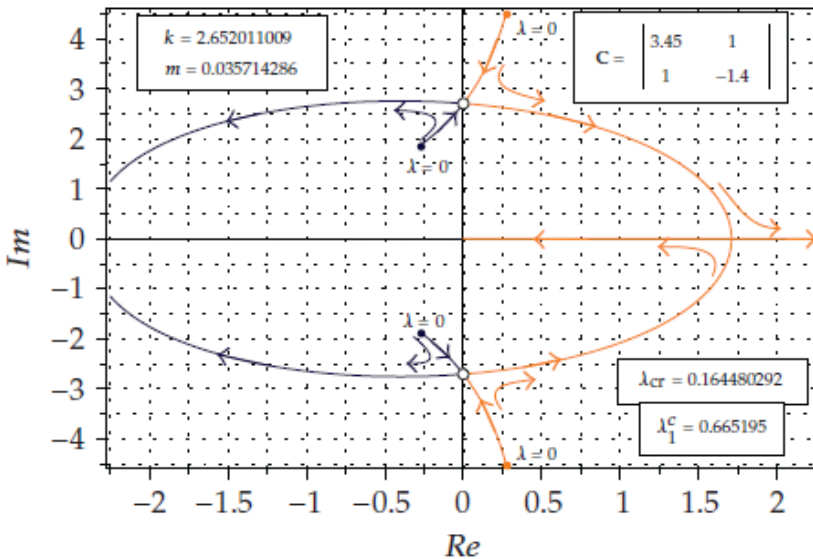
Fig. 9. Evolution of both pairs of eigenvalues in the ρ-complex plane for the system of Case 3(d)1.
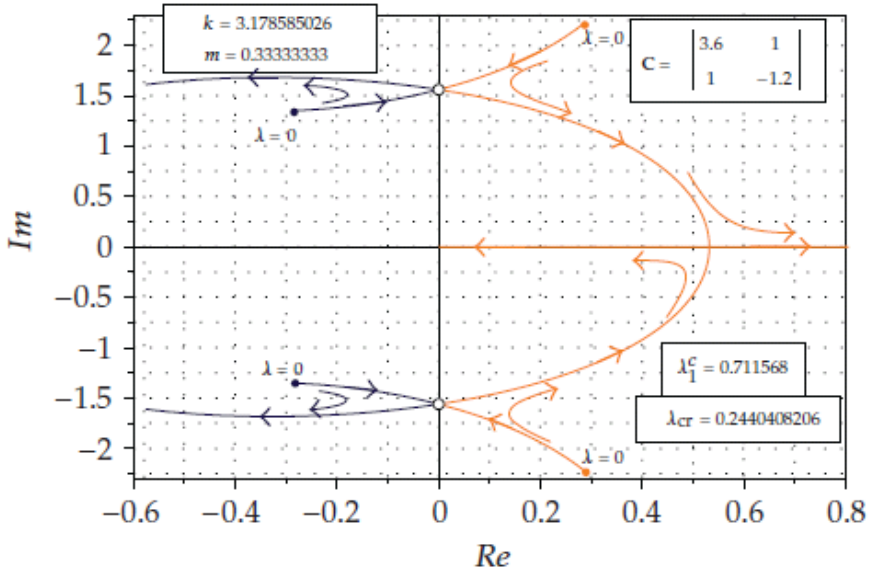
Fig. 10. Evolution of both pairs of eigenvalues in the ρ-complex plane for the system of Case 3(d)2.

which it is evident that for all $\lambda<\lambda_1^c$, except for $\lambda<\lambda_{cr}$ (where a codimension-2 bifurcation occurs), the pairs of eigenvalues remain always in *opposite* planes of the Im axis, but symmetric with respect to the Re axis. This symmetry is always present for the pair with negative real parts, while for the other pair (with positive real parts), this feature remains until their imaginary part vanishes simultaneously at a certain value of the loading λ less than λ_1^c.

The dynamic response of the system for all these subcases is associated with isolated *periodic* orbits (whose final amplitude is constant and independent of the initial conditions). A relative phase-plane portrait is shown in Fig.12a,b The corresponding dynamic bifurcations related to the above *double pure imaginary* eigenvalues behave like a *generic* Hopf bifurcation, whose basic feature is the intersection of the λ-dependent path of one eigenvalue with the imaginary axis. On the other hand, in all the above subcases, the branches of two consecutive λ-dependent eigenvalues meet the imaginary axis at the same point with $\lambda=\lambda_{cr}$. Namely, the *transversality condition* is satisfied through two intersected lines at the same point of the imaginary axis, but whose branches in the left (negative) and right (positive) half planes belong to the 1st and 2nd pairs of eigenvalues, respectively.
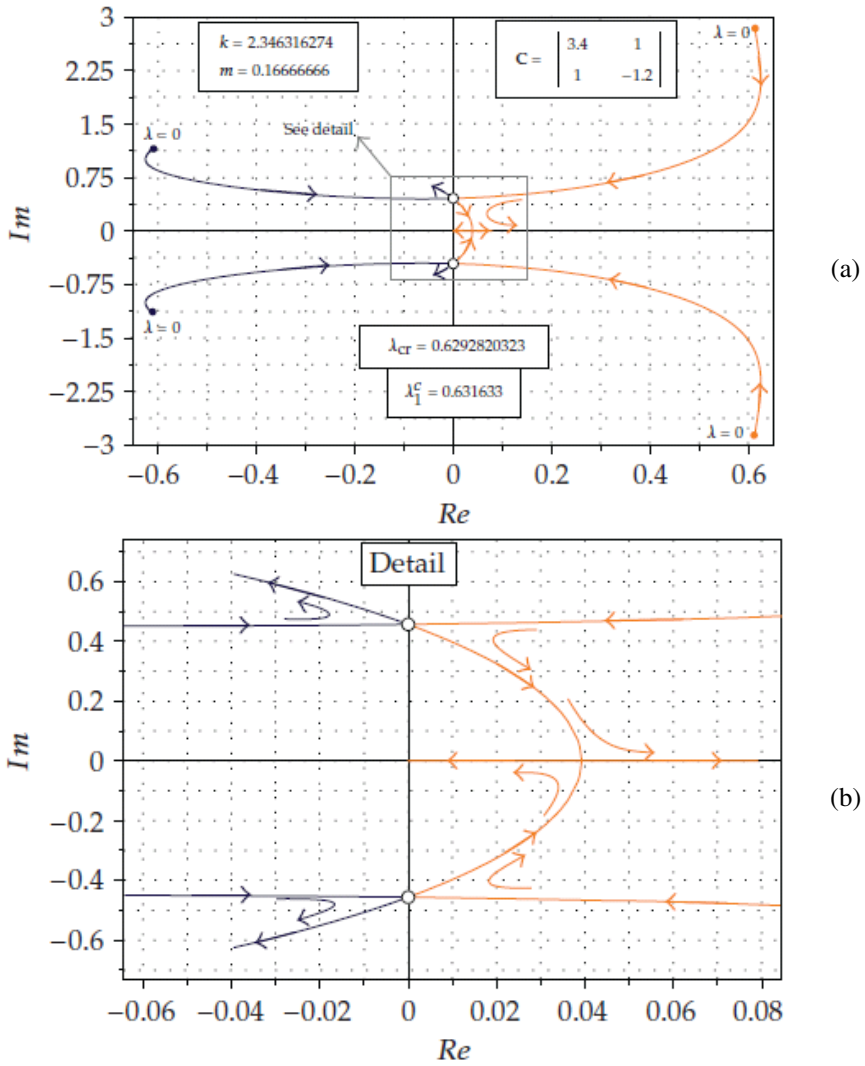
Fig. 11. (a) Evolution of both pairs of eigenvalues in the ρ-complex plane and (b) corresponding detail for the system of Case 3(d)3.
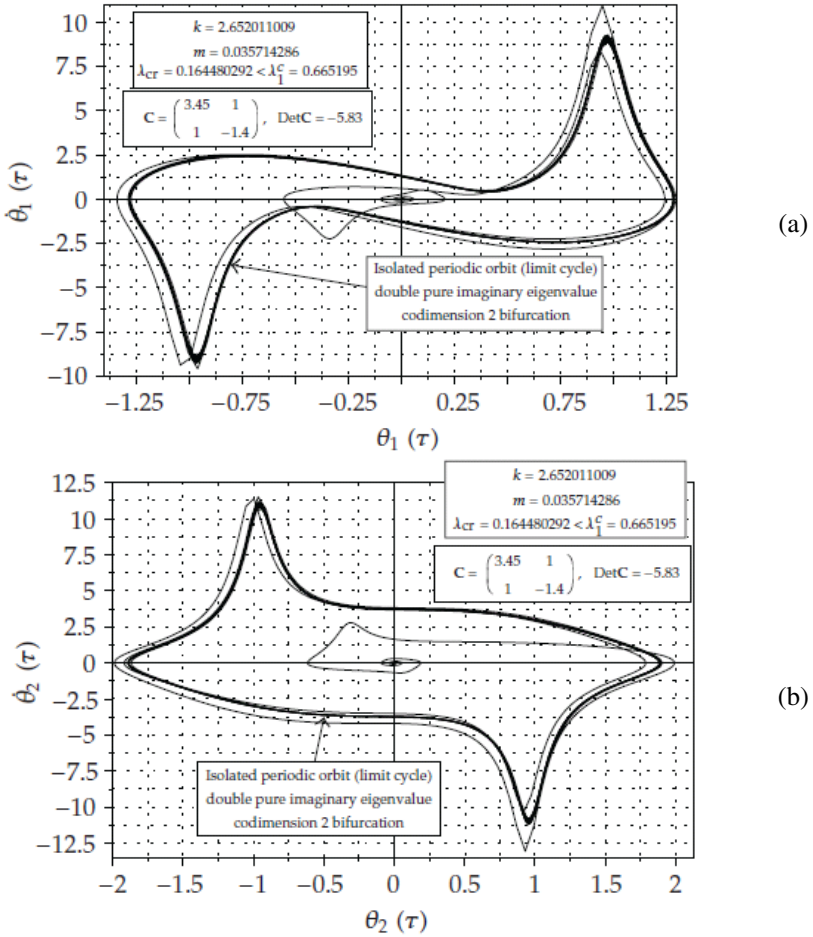
Fig. 12. Phase-plane portraits $[\theta_i(\tau),\ \dot\theta(\tau)]$ (i=1,2) for the system of Case 3(d)1, associated with an isolated periodic orbit.

5.2 Non Conservative Systems (η≠1)

In this case the coefficients of the secular equation(63) α_i=(1,2,3,4) are

$$\alpha_1 = \frac{1}{m}\left[(1+m)c_{22}+c_{11}-2c_{12}\right]$$

$$\alpha_2 = \frac{1}{m}\left[(1+m)(1-\lambda\eta)+3+k-\lambda+\lambda(\eta-1)+|c|\right]$$

$$\alpha_3 = \frac{1}{m}\left\{c_{11}(1-\lambda\eta)+c_{22}(1+k-\lambda)+[2+\lambda(\eta-1)]c_{12}\right\}$$

$$\alpha_4 = \frac{1}{m}\left[\eta\lambda^2-\eta(k+2)\lambda+k\right]=\frac{1}{m}\det V$$

$$(87)$$

where $|c| = \det C$.

   The region of existence of adjacent equilibria (region of divergence instability) is related to static bifurcations with two *distinct* critical loads obtained via $\alpha_4=0$ or eq.(55). The *boundary* between the region of *existence* and *non-existence* of adjacent equilibria is defined by (see also eq.(3))

$$\alpha_4 = \frac{d\alpha_4}{d\lambda} = 0 \tag{88}$$

which due to relations (87) gives (see eq.(56))

$$\eta_0 = \frac{4k}{(k+2)^2}, \quad \lambda_0 = \frac{k+2}{2}. \tag{89}$$

This is a *double* (compound) branching point related to a double root of eq.(55) with respect to λ. Considering the function $\eta=\eta(\lambda, k)$ the necessary condition for an extremum, $\partial\eta/\partial\lambda = \partial\eta/\partial k = 0$, yields $\lambda_0=2$ and $k_0=2$ implying $\eta_0=0.5$ Note that η_0 is the maximum distance of the double branching point from the λ^c-axis (curve η vs λ^c).Two characteristic cases are considered for k<2 and k>2. It is clear that $\lambda_0^c \rightarrow 1$ and $\eta_0\rightarrow0$ as k$\rightarrow$0, whereas k>2 yields $\lambda_0^c \rightarrow \infty$, $\eta_0\rightarrow0$ as k$\rightarrow\infty$.It is easy now to establish the *locus* of the *double* branching points in the plane of η versus λ^c (Fig.13), being independent of m . Note that for k$\rightarrow$0 or k$\rightarrow\infty$ the region of *flutter* instability *disappears*.
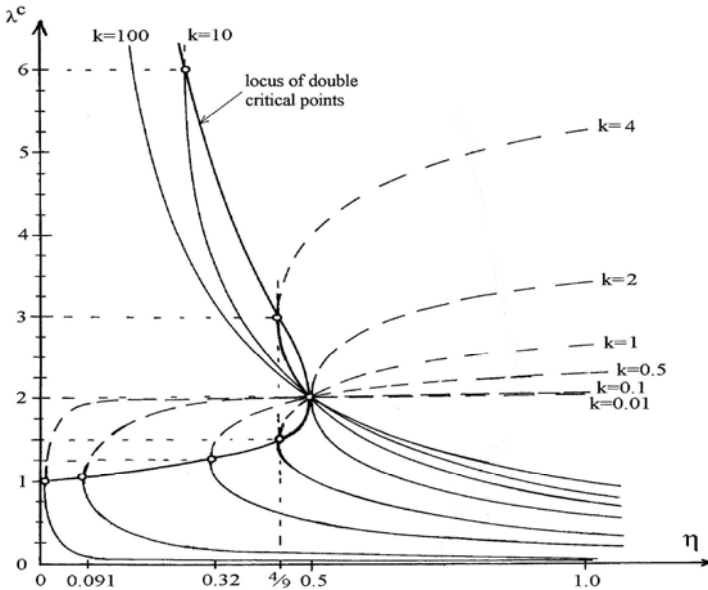
Fig. 13. Locus of double branching points (λ_0^c, η_0).

Subsequently, the Linéard-Chipart criterion for *asymptotic stability* is used which is more simple and efficient than that of Routh-Hurwitz. Clearly, if one of the conditions (41α,b) is violated there is **no** asymptotic stability. We will apply this criterion for the above 2-DOF cantilevered model (n = 4, $\alpha_0 = 1$) in case of a *positive definite* damping matrix for which one can show that m>0 always implies α_1>o. Let us now consider the case of the Rayleigh *positive definite* viscous damping matrix in the region of *divergence* (static) stability, i.e. for $\eta \geq \eta_0 = 4k/(k+2)^2$. Then since $c_{11} = c_1 + c_2$, $c_{12} = c_{21} = -c_2$ and $c_{22} = c_2$ ($c_i > 0$, i=1,2) relations (87) become

$$\alpha_1 = \frac{1}{m}\left[c_1 + (4+m)c_2\right], \ \alpha_2 = \frac{1}{m}\left[m + k + 4 + c_1c_2 - \lambda(\eta m + 2)\right]$$

$$\alpha_3 = \frac{1}{m}\left[c_1(1 - \lambda\eta) + c_2(k - 2\lambda\eta)\right], \ \alpha_4 = \frac{1}{m}\left[\eta\lambda^2 - \eta(k+2)\lambda + k\right] \tag{90}$$

According to the 1st set of conditions (41a) we have

$$\alpha_4 > 0, \ \alpha_2 > 0, \ \Delta_1 = \alpha_1 > 0, \ \Delta_3 > 0 \tag{91}$$

where

$$\Delta_3 = \begin{vmatrix} \alpha_1 & \alpha_3 & 0 \\ 1 & \alpha_2 & \alpha_4 \\ 0 & \alpha_1 & \alpha_3 \end{vmatrix} = \alpha_3(\alpha_1\alpha_2 - \alpha_3) - \alpha_1^2\alpha_4. \tag{92}$$

From eqs(90) it follows that $\alpha_1 > 0$. Since $\alpha_4 = \det(V/m)$ (m>0) one may consider the following cases regarding the interval of variation of λ:

$$\left. \begin{array}{l} \text{For } \lambda < \lambda_1^c \Rightarrow \det V > 0 \text{ and hence } \alpha_4 > 0 \\ \text{For } \lambda_1^c < \lambda < \lambda_2^c \Rightarrow \det V < 0 \text{ and hence } \alpha_4 < 0 \\ \text{For } \lambda \geq \lambda_2^c \Rightarrow \det V > 0 \text{ and hence } \alpha_4 > 0. \end{array} \right\} \tag{93}$$

Considering always the region of *divergence* (static) *instability* [i.e. $\eta \geq 4k/(k+2)^2$] and in connection with above interval of values of λ the following cases of violation of conditions (91) are discussed below:

1st case: $\alpha_4 > 0$ (for $\lambda < \lambda_1^c$), $\alpha_2 < 0$, $\Delta_3 > 0$.

Due to eq.(92), clearly $\Delta_3 > 0$ implies $\alpha_3 < 0$ (since always $\alpha_1 > 0$) or due to relation (90)

$$c_1(1-\lambda\eta) + c_2(k-2\lambda\eta) < 0. \tag{94}$$

Since c_1, $c_2 > 0$ the quantities $1 - \lambda\eta$ and $k - 2\lambda\eta$ must be of *opposite* sign. Inequality (94) can always be satisfied for suitable values of $c_i > 0$ (i=1, 2). Subsequently one can find suitable values for k,η and m for which $\lambda < \lambda_1^c = 0.5\left[k + 2 - \sqrt{(k+2)^2 - 4k/\eta}\right]$ is also consistent with $\alpha_2 < 0$ The important *conclusion* which then can be drawn is that *a local dynamic asymptotic instability* in

regions of *divergence* (for λ less than the 1st buckling load) may occur in case of a *positive definite* damping matrix. This is excluded in case of a *conservative* loading (η=1) as was shown recently by Kounadis [4, 13].

More specifically one can establish to the following proof:

Condition $\alpha_2 < 0$ due two relations (90) implies

$$\lambda > \frac{m + k + 4 + c_1 c_2}{\eta m + 2} \tag{95}$$

which must be consistent with eq.(56), i.e.

$$\lambda < 0.5\left[k + 2 - \sqrt{(k+2)^2 - 4k/\eta} \right]. \tag{96}$$

One can show that there are values of λ for which both inequalities (95) and (96) are satisfied for $\eta \geq 4k/(k+2)^2$, m>0, k>0 and c_i>0 (i=1,2). For example for k=5, m=8, $c_1 = 0.001$ and $c_2 = 0.00013$ we get $\eta \geq 4k/(k+2)^2 = 20/49 = 0.408163265$. Choosing η=0.41 we obtain $\lambda_1^c = 3.26574$, as well as

$$\lambda > \frac{m + k + 4 + c_1 c_2}{\eta m + 2} = 3.219697 \cdot$$

For $\lambda = 3.26 < \lambda_1^c = 3.26574$, we find: $\alpha_1 = 0.00032$, α_2 = -0.0266, α_3 = -4.26x10^{-6}, $\alpha_4 = 0.0001395$ and $m^3\Delta_3 = 1.96x10^{-9} \approx 0$. Fig. 14 using these values of parameters α_i
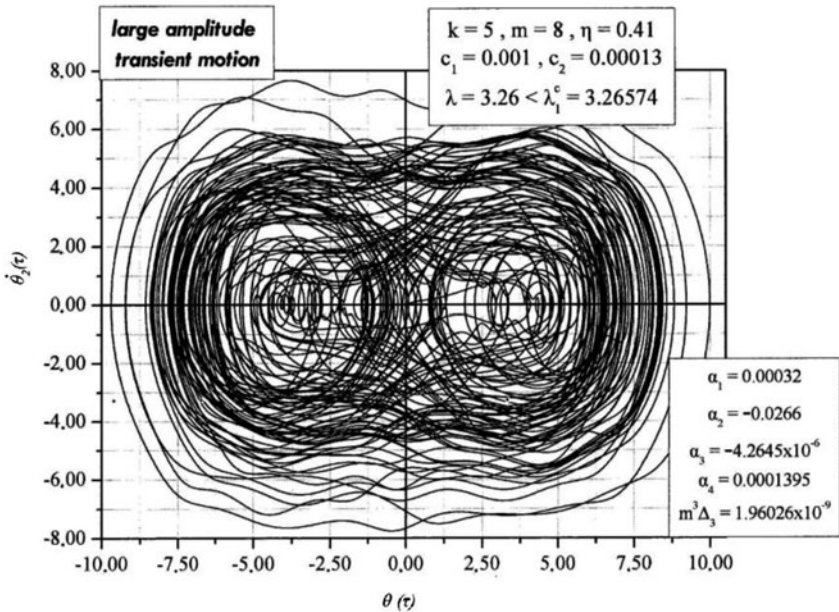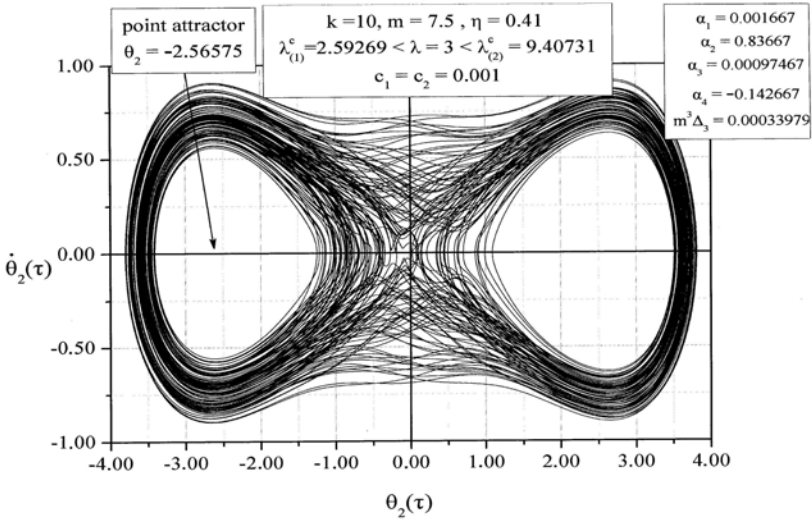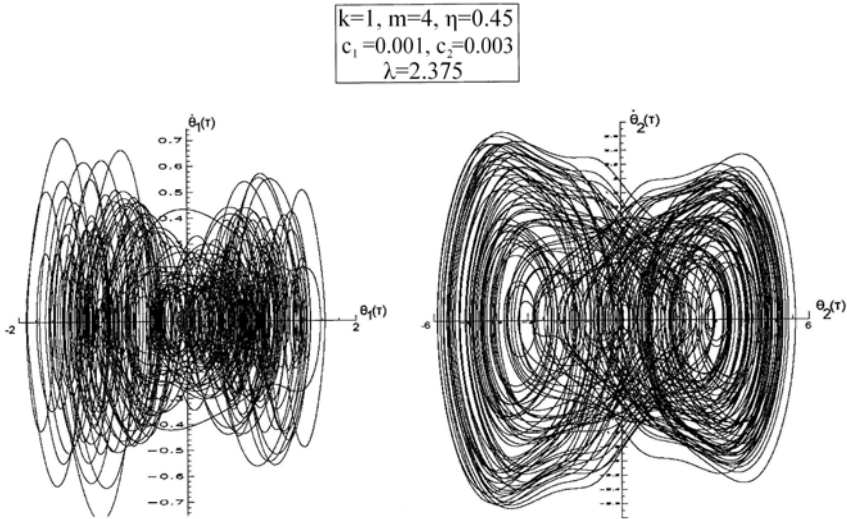

Fig. 14. Phase-plane response $[\theta_2(\tau), \dot{\theta}_2(\tau)]$ for a cantilever with k=5, η=0.41, m=8, c_1=0.001, c_2=0.00013 and λ=3.26<$\lambda_1^c = 3.26574$. The model is locally dynamically unstable exhibiting a large amplitude chaoticlike motion.

(i = 1,...,4) shows a large amplitude *chaoticlike response* in the phase-plane portrait $[\theta_2(\tau)$ vs $\dot{\theta}_2(\tau)]$. Hence, for $3.26 \le \lambda \le 3.26574$ the *damped* autonomous system exhibits *local asymptotic instability before divergence* for a *positive* definite damping matrix (with coefficients practically zero) of the Rayleigh viscous type. This is an *unexpected* finding which does not occur for the same system under *conservative* (η=1) load [4, 13].

2nd case: $\alpha_4 < 0$ (for $\lambda_1^c < \lambda < \lambda_2^c$), $\alpha_2 > 0$, $\Delta_3 > 0$.

By virtue of relations (90) the condition $\alpha_2 > 0$ implies

$$\lambda < \frac{m + k + 4 + c_1 c_2}{\eta m + 2} \tag{97}$$

and hence

$$\lambda_1^c < \frac{m + k + 4 + c_1 c_2}{\eta m + 2} < \lambda_2^c \tag{98}$$

or due to eq.(55)

$$0.5\left[k + 2 - \sqrt{(k+2)^2 - \frac{4k}{\eta}}\right] < \frac{m + k + 4 + c_1 c_2}{\eta m + 2} < 0.5\left[k + 2 + \sqrt{(k+2)^2 - \frac{4k}{\eta}}\right] \tag{99}$$

For instance, if k = 10, then $\eta \ge 4k/(k+2)^2 = 0.2777777$. Choosing η=0.41, $c_1 = c_2 = 0.001$ and m = 7.5 inequality (99) yields 2.59269<4.23645 <9.40731. For λ=3 we get: α_1=0.001667, α_2=0.83667, α_3=0.00097467, α_4=-0.142667 and $m^3\Delta_3$=3.39795x10^{-4}.

As was anticipated the system is *locally* dynamically asymptotically *unstable*. However, a *nonlinear dynamic analysis* will show that the system is *globally* stable. This is so, because the cantilever under *statically* applied load exhibits *postbuckling strength* and hence the postbuckling stable equilibria act as *point attractors*. Fig.15 shows the corresponding to the above parameters α_i(i=1,…,4) motion in the phase-plane portrait $[\theta_2(\tau)$ vs $\dot{\theta}_2(\tau)]$ which after large amplitude chaoticlike vibrations is finally *captured* by the left stable equilibrium point (of the cantilever) acting as *point attractor*.

3rd case: $\alpha_4 > 0$ (for $\lambda > \lambda_2^c$), $\alpha_2 < 0$, $\Delta_3 > 0$.

Apparently $\alpha_2 < 0$ and $\Delta_3 > 0$ imply $\alpha_3 < 0$. Inequality $\alpha_2 < 0$ due to relations (90) yields

$$\lambda > \frac{k + m + 4 + c_1 c_2}{\eta m + 2}. \tag{100}$$

On the other hand we must also have

$$\lambda > \lambda_2^c = 0.5\left[k + 2 + \sqrt{(k+2)^2 - 4k/\eta}\right]. \tag{101}$$

One can readily show that both inequalities (100) and (101) can be satisfied for various values of λ and of the parameters m>0, k>0, c_i>0 (i=1,2) and $\eta \ge 4k/(k+2)^2$.
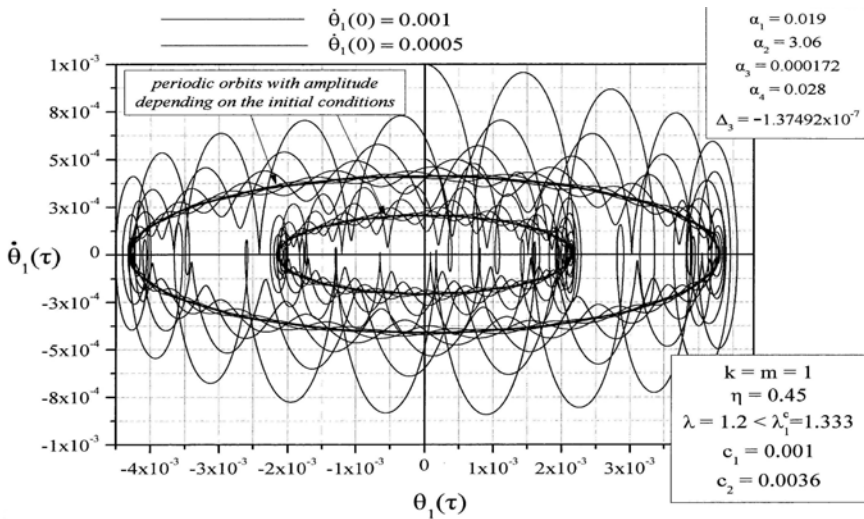
Fig. 15. Phase-plane response $[\theta_2(\tau), \dot{\theta}_2(\tau)]$ for a cantilever with k=10, η=0.41, m=7.5, c_1=c_2=0.001 and $\lambda_1^c = 2.59269 < \lambda = 3 < \lambda_2^c = 9.40731$. The model exhibits a large amplitude chaoticlike motion which finally is captured by the left stable equilibrium point acting as *point attractor*.

For instance, for m = 4, c_1 = 0.001, c_2 = 0.003 and k=1 implying η= 4/9, after choosing η = 0.45 we obtain $\lambda \geq$(k+m+4+$c_1 c_2$)/(ηm+2) = 2.36842 and $\lambda_2^c = 1.66666$. Hence, for λ = 2.375 we have *local asymptotic instability*. Fig.16 shows the

Fig. 16. Phase-plane responses $[\theta_i(\tau), \dot{\theta}_i(\tau), i=1,2]$ for a cantilever with k=1, η=0.45, m=4, c_1=0.001, c_2=0.003 and λ=2.37>(k+m+4+$c_1 c_2$)/(ηm+2)= 2.36842.

corresponding to these values of the parameters phase-plane responses $[\theta_i(\tau)$ vs $\dot{\theta}(\tau)$, i= 1,2].

4th case: $\alpha_4 > 0$ for $\lambda < \lambda_1^c$, $\alpha_2 > 0$, $\Delta_3 \leq 0$

The condition $\Delta_3 = 0$ (being necessary for a Hopf bifurcation) yields

$$\alpha_3(\alpha_1\alpha_2 - \alpha_3) - \alpha_1^2\alpha_4 = 0 \tag{102}$$

which due to $\alpha_1 > 0$ implies also $\alpha_3 > 0$. $\tag{103}$

For instance, if k=1 then $\eta = 4k/(k+2)^2 = 4/9$. Subsequently choosing η=0.45 we

obtain $\lambda_1^c = 0.5\left[k+2-\sqrt{(k+2)^2 - 4k/\eta}\right] = 1.3333$. Let us take λ=1.2, m=1,

c_1 = 0.001 and c_2 = 0.0036 which yield: α_1 = 0.019, α_2 = 3.06, α_3 = 0.000172, α_4 = 0.028 and Δ_3=-1.3749x10^{-7}. On the basis of these values of parameters α_i(i=1,...,4) Fig.17 shows *periodic motion* around centers in the phase-plane portrait $[\theta_1(\tau), \dot{\theta}_1(\tau)]$, whose *final* amplitude depends on the *initial* conditions.

Fig. 17. Phase-plane response $[\theta_1(\tau), \dot{\theta}_1(\tau)]$ for a cantilever with k=1, η=0.45, m=1, c_1=0.001, c_2=0.0036 and $\lambda = 1.2 < \lambda_1^c = 1.33333$. The model is locally dynamically unstable exhibiting periodic motion around centers, whose final amplitude depends on the initial conditions.

Eq.(102) is the *necessary condition* for the existence of a pair of *purely imaginary* roots of the characteristic eq.(63). This case is associated either with a *degenerate* Hopf *bifurcation* or with a *generic* Hopf bifurcation [4, 13].

Using relations (87), eq.(102) reduces to the following 2nd degree algebraic equation with respect to λ

$$A\lambda^2 + B\lambda + \Gamma = 0 \qquad (104)$$

where

$A = m[\eta c_{11} + c_{22} - c_{12}(\eta-1)]^2 + \eta[(1+m)c_{22} + c_{11} - 2c_{12}]^2$
$\quad -(\eta m + 2)[(1+m)c_{22} + c_{11} - 2c_{12}][\eta c_{11} + c_{22} - c_{12}(\eta-1)]$

$B = [(1+m)c_{22} + c_{11} - 2c_{12}]\{(\eta m + 2)[c_{11} + c_{22}(1+k) + 2c_{12}] + (4m + k + |c|)[\eta c_{11} + c_{22} - c_{12}(\eta-1)]\}$
$\quad -2m[c_{11} + c_{22}(1+k) + 2c_{12}][\eta c_{11} + c_{22} - c_{12}(\eta-1)] - \eta(k+2)[(1+m)c_{22} + c_{11} - 2c_{12}]^2$

$\Gamma = m[c_{11} + c_{22}(1+k) + 2c_{12}]^2 + k[(1+m)c_{22} + c_{11} - 2c_{12}]^2$
$\quad -[(1+m)c_{22} + c_{11} - 2c_{12}](4m + k + |c|)[c_{11} + c_{22}(1+k) + 2c_{12}] \qquad (105)$

Note that contrary to A and B, the coefficient Γ is independent of η.

For *real* λ the discriminant **D** of eq.(104) must satisfy the inequality

$$\mathbf{D} = B^2 - 4A\Gamma \geq 0. \qquad (106)$$

Three characteristic cases are related to eq.(104): (a) **D**>0 [two unequal roots of eq.(104)], (b) **D**=0 [two equal roots: $\lambda_H = -B/2A$] and (c) $\lambda=0$ implying $\Gamma=0$. Note also that the intersection between the curve of eq.(102) and the curve of the 1st static load λ_1^c, corresponds to a dynamic coupled *flutter-divergence* bifurcation.

Conditions for a double imaginary root

For a *double imaginary* root the first derivative of the secular eq.(63) must also be zero, which yields

$$4\rho^3 + 3\alpha_1\rho^2 + 2\alpha_2\rho + \alpha_3 = 0. \qquad (107)$$

Inserting into eq.(106) $\rho = \mu i$ ($i = \sqrt{-1}$) we obtain $\mu^2 = 0.5\alpha_2 = \alpha_3/3\alpha_1$ and thus $\alpha_3 = 1.5\alpha_1\alpha_2$. Since $\rho = \mu i$ must also be a root of eq.(63) we obtain $\mu^2 = \alpha_3/\alpha_1$ which implies $\alpha_3 = 0.5\alpha_1\alpha_2$. This is consistent with the previous expression of $\alpha_3 = 1.5\alpha_1\alpha_2$ only when $\alpha_3 = 0$ due to either $\alpha_1 = 0$ (which is *excluded* for a positive definite damping matrix) or $\alpha_2 = 0$ (which is also excluded since it implies $\mu=0$). Hence, if the damping matrix **C** is positive definite of Rayleigh viscous type (i.e. $c_{11} = c_1 + c_2$, $c_{12} = c_{21} = -c_2$ and $c_{22} = c_2$ with c_1, c_2 both positive) then the case of a *double imaginary* root is excluded.

6 Conclusions

The most important conclusions are:

- A thorough, comprehensive and readily employed technique was developed for discussing the effect of the algebraic structure of the damping matrix in connection with other parameters on the **asymptotic stability** of autonomous weakly damped symmetric or asymmetric systems using mainly the more simple and efficient **Liénard and Chipart** stability criterion.
- The above systems under certain conditions may exhibit a **dynamic mode** of instability due to: (a) an isolated **degenerate** Hopf bifurcation, (b) an isolated

generic Hopf bifurcation, (c) a **double zero** eigenvalue bifurcation and (d) a **purely double imaginary** bifurcation.

- Unlike case (b) related to **limit cycles**, the **global** stability in cases (a), (c) and (d) is due to **periodic motion** (around centers) **not** leading to limit cycles.

Conservative (symmetric) systems

- **Degenerate** Hopf bifurcations may occur for a **positive semi-definite damping** matrix and **positive definite stiffness** matrix; then the final amplitude of resulting periodic motions depends on the initial conditions.
- **Generic** Hopf bifurcations (related to flutter mode of instability or periodic attractors) may occur for an **indefinite damping matrix**. Generic and degenerate Hopf bifurcations may occur **before** divergence even in cases of infinitesimal damping; a fact that may be important in applied engineering problems. In this case, **Zieglers's** kinetic (dynamic) criterion fails to predict the correct critical load.
- A *double zero eigenvalue* bifurcation associated with a coupled **flutter-divergence** mode of instability may occur when both the **damping and stiffness** matrix are **positive semi-definite** with a common **real** eigenvector.
- The *eigenvector* corresponding to an isolated **degenerate** Hopf bifurcation is *real*, while that of a **generic** Hopf bifurcation is *complex*.
- In case of a *positive* eigenvalue the *linearized* analysis of the cantilevered model leads to the *erroneous* result of an **unbounded** motion, while a *nonlinear* analysis shows that the long term response is associated with a **point attractor**. Moreover, the existence of closed trajectories involving *saddle* separatrices passing through the origin may lead to a misleading conclusion. To avoid this, one should also confirm the stability of postbuckling equlilibria via a **nonlinear** *static* stability analysis.
- Infinitesimal **damping** combined with **mass** (mainly) and **stiffness** distribution may lead to the **unexpected result** of **discontinuity** in the flutter load.
- The coupling effect **on** the dynamic critical (**flutter)** load of weak **damping** with **mass** and **stiffness** distributions, as well as **on** the final (maximum) **amplitude** of the stable limit cycles, is also established.
- The cantilevered model when *unloaded (*being statically stable), strangely enough, under certain conditions becomes dynamically *unstable* to any small disturbance leading to a *divergent (*unbounded) motion.
- The above model when *loaded* under analogous of the previous conditions exhibits also a *divergent* motion at a certain value of the external load. It is worth noting that the above cases of divergent motion may occur for *negligibly small* negative determinant of the damping (indefinite) matrix when $\alpha_1=0$, while for $\alpha_2=0$ (regardless of whether $\lambda = 0$ or $\lambda \neq 0$), the determinant of the damping matrix is negative but *finite*.
- The case of a *double pure imaginary eigenvalue* may occur for an *indefinite* damping matrix with *finite* determinant and *negative ratio* of the corresponding diagonal elements. In this special case, there are *two pairs* of eigenvalues in the ρ-complex plane which touch the imaginary axis at the same point for a certain value $\lambda=\lambda_{cr}$. This situation yields *local* instability leading to a motion with final

constant amplitude, regardless of the initial conditions. Namely, such a dynamic bifurcation behaves in a way similar to that of a *generic* Hopf bifurcation. **This new type** of dynamic bifurcation was also verified via a nonlinear dynamic analysis.

Nonconservative (asymmetric) systems

- The **asymptotic stability** can be conveniently established by using the rather forgotten but very simple and efficient criterion of **Liénard and Chipart**.

- The geometric *locus* of the double branching point (η_0, λ_0^c) corresponding to various values of k is established via the relation η versus λ^c. The locus is independent of the mass m whose effect on the dynamic stability is considerable.

  The intersection between the curve (102) or (104) and the curve λ_1^c corresponds to a *coupled flutter-divergence* instability bifurcation.

- The **region of flutter** (dynamic) instability may disappear for suitable values of **stiffness** parameters.

- **Contrary to existing**, widely accepted results, for a **positive definite damping matrix** (of Rayleigh viscous type) the system (under certain combinations of mass and stiffness distributions) may exhibit **local asymptotic instability** even for a load **smaller** than the 1ˢᵗ buckling (critical) load.

- **Double purely imaginary eigenvalues** (leading to a divergent motion) may occur in case of an **indefinite** (infinitesimal) damping matrix, while in case of a *positive semi-definite* damping matrix is excluded.

References

1. Ziegler, H.: Die Stabilitätskriterien der Elastomechanik. Ing. Arch. 20, 49–56 (1952)
2. Nemat-Nasser, S., Herrmann, G.: Some general considerations concerning the destabilizing effect in nonconservative systems. ZAMP 17, 305–313 (1966)
3. Crandall, S.H.: The role of damping in vibration theory. J. Sound Vib. 11, 3–18 (1970)
4. Kounadis, A.N.: Hamiltonian weakly damped autonomous systems exhibiting periodic attractors. ZAMP 57, 324–350 (2006)
5. Huseyin, K.: Multiple Parameter Stability Theory and its Applications. Oxford Eng. Sciences, vol. 18. Clarendon Press, Oxford (1986)
6. Huseyin, K.: Vibrations and stability of Damped Mechanical Systems. Sijthoff & Noordhoff Intern. Publishing, Alphein (1978)
7. Zajac, E.E.: The Kelvin-Tait-Chetaev theorem and extensions. J. Aeronaut. Sci. 11, 46–49 (1964)
8. Zajac, E.E.: Comments on stability of damped mechanical systems, and a further extension. AIAA J. 3, 1749–1750 (1965)
9. Sygulski, R.: Dynamic stability of pneumatic structures in wind: theory and experiment. J. Fluids Struct. 10, 945–963 (1996)
10. Laneville, A., Mazouzi, A.: Wind-induced ovalling oscillations of cylindrical shells: critical onset velocity and mode prediction. J. Fluids Struct. 10, 691–704 (1996)
11. Kounadis, A.N.: A geometric approach for establishing dynamic buckling loads of autonomous potential two-DOF systems. J. Appl. Mech., ASME 66, 55–61 (1999)

12. Kounadis, A.N.: Non-potential dissipative systems exhibiting periodic attractors in region of divergence. Chaos, Solitons Fractals 8(4), 583–612 (1997)
13. Kounadis, A.N.: Flutter instability and other singularity phenomena in symmetric systems via combination of mass distribution and weak damping. Int. J. of Non-Linear Mechanics 42(1), 24–35 (2007)
14. Kounadis, A.N.: The effect of infinitesimal damping on non conservative divergence instability systems. J. of Mechanics and Materials and Structures 4, 1415–1428 (2009)
15. Gantmacher, F.R.: The Theory of Matrices. Chelsea, New York (1959)
16. Gantmacher, F.R.: Lectures in Analytical Mechanics, Mir, Moscow, Russia (1970)
17. Kounadis, A.N.: On The Failure Of Static Stability Analysis Of Nonconservative Systems In Regions Of Divergence Instability. Int. J. Solids & Structures 31(15), 2099–2120 (1994)
18. Sophianopoulos, D.S., Michaltsos, G.T., Kounadis, A.N.: The Effect of Infinitesimal Damping on the Dynamic Instability Mechanism of Conservative Systems. Mathematical Problems in Engineering, Special Issue on Uncertainties in Nonlinear Structural Dynamics, vol. 2008, Artic. ID 471080, 25 Pages (2008)
19. Pipes, L.A., Harvill, L.R.: Applied Mathematics for Engineers and Physicists. International Student Edition, 3rd edn. McGraw-Hill, Kogakusha (1970)
20. Bellman, R.: Introduction to Matrix Analysis, 2nd edn. McGraw-Hill, New York (1970)
21. Fuller, A.T.: Conditions for a matrix to have only characteristic roots with negative real parts. Journal of Mathematical Analysis and Applications 23, 71–98 (1968)
22. Kounadis, A.N.: Stability of elastically restrained Timoshenko cantilevers with attached masses subjected to follower loads. J. of Applied Mechanics, ASME 44, 731–736 (1977)
23. Kounadis, A.N., Katsikadelis, G.T.: On the discontinuity of the flutter load for various types of cantilevers. Int. J. of Solid and Structures 16, 375–383 (1980)
24. Bahder, T.B.: Mathematica for Scientists and Engineers. Addison-Wesley, Reading (1995)

Variational Approach to Static and Dynamic Elasticity Problems

Georgy V. Kostin and Vasily V. Saurin

Institute for Problems in Mechanics of the Russian Academy of Sciences,
pr. Vernadskogo 101-1, 119526 Moscow, Russia
kostin@ipmnet.ru, saurin@ipmnet.ru

Abstract. The integrodifferential approach incorporated in variational technique for static and dynamic problems of the linear theory of elasticity is considered. A families of statical and dynamical variational principles, in which displacement, stress, and momentum fields are varied, is proposed. It is shown that the Hamilton principle and its complementary principle for the dynamical problems of linear elasticity follow out the variational formulation proposed. A regular numerical algorithm of constrained minimization for the initial-boundary value problem is worked out. The algorithm allows us to estimate explicitly the local and integral quality of numerical solutions obtained. As an example, a problem of lateral controlled motions of a 3D rectilinear elastic prism with a rectangular cross section is investigated.

1 Introduction

Variational principles in mechanics involving the theory of elasticity have been very thoroughly developed and intensively studied by scientists. Among these formulations the minimum principles for potential and complementary energy, the Hamilton principle can be mentioned (see [22], for example). Many different approaches to deduce variational principles for mechanical problems are presented in the literature. It can be noted the recent publication concerning the semi-inverse method suggested by He [7]. The variational formulation of the finite element method is broadly used in scientific and engineering applications. The mathematical origin of the method can be traced to a paper by Courant [5]. Other numerical approaches, e.g., Petrov-Galerkin method [3, 4] or the least squares method [20], are being actively developed for solid mechanics. In all these methods it is supposed that some of the elasticity relations (equilibrium equations, boundary conditions in terms of stresses and etc.) are generalized and the exact solution is approximated by a finite set of trial functions.

Elastic properties of structure elements can essentially affect the dynamical behavior of the whole system. Some parts of mechanical structures with distributed

parameters are modeled as elastic bodies with given stiffness and inertia characteristics. A significant number of numerical methods has been developed for modeling the behavior of dynamical systems described by initial-boundary value problems. One of the most widespread approaches to solving problems of such kind is the method of separation of variables [6]. In [1] a regular perturbation method (a small parameter method) for investigating the dynamics of weakly non-uniform thin rods with arbitrary distributed loads and different boundary conditions was proposed. Based on the classical Rayleigh-Ritz approach, a numerical analytical method of fast convergence was developed in [2] to find precise values of unknown functions for arbitrary distributed stiffness and inertia characteristics of elastic systems. In modeling the elastic systems the methods of finite-dimensional approximations, for example the decomposition method and the regularization method, were developed to reduce an initial-boundary value problem for partial differential equations to a system of ordinary differential equations [8, 9]. The direct discretization methods in optimal control problems are also well known (see, e.g. [10]).

The aim of this contribution is to develop the method of integrodifferential relations (MIDR) for static and dynamic linear elasticity problems based on the integral formulation of the constitutive equations and to apply this approach to analysis of 3D elastic body behavior. The basic ideas of MIDR were proposed and discussed by Kostin and Saurin [11-19, 21].

In the next section, the statements of static and dynamic linear elasticity problems and its conventional variational formulations are discussed. In the third section a parametric family of quadratic functionals is considered and their stationary conditions equivalent to the constitutive relation are obtained. The relations of proposed and conventional variational principles are shown in Section 4. In Section 5 a new variational formulation in displacements and stresses for the initial boundary value problem of linear elasticity is given. In Section 6 a numerical algorithm used the piecewise polynomial approximations of unknown functions (displacements, stresses, and momentums) is developed [19] and the effective integral and local bilateral estimates of solution quality are obtained relying on the extremal properties of the finite dimensional variational problem. Sections 7 and 8 are devoted to numerical modeling, optimization, and analysis of controlled motions of a 3D elastic beam. Concluding remarks are given in the last section.

2 Statement of the Problems

2.1 Dynamical Formulation

Consider an elastic body occupying a bounded domain Ω with an external piecewise smooth boundary γ. Taking into account the assumption of the linear theory of elasticity about smallness of elastic deformations and relative velocities the motion of the body can be described by the following system of partial differential equations [16]:

$$\boldsymbol{\sigma} = \mathbf{C} : \boldsymbol{\varepsilon}, \tag{1}$$

$$\mathbf{p} = \rho \mathbf{u}^{\bullet} \, , \tag{2}$$

$$\nabla \cdot \boldsymbol{\sigma} - \dot{\mathbf{p}} + \mathbf{f} = 0 \, , \tag{3}$$

$$\boldsymbol{\varepsilon} = \frac{1}{2}\left(\nabla \mathbf{u} + \nabla \mathbf{u}^{\mathrm{T}}\right). \tag{4}$$

Here $\boldsymbol{\sigma}$ and $\boldsymbol{\varepsilon}$ are the stress and strain tensors, $\mathbf{p}$ and $\mathbf{u}$ are the momentum density and displacement vectors, $\mathbf{f}$ is the vector of volume forces, $\mathbf{C}$ is the elastic modulus tensor, and ρ is the volume density of the body. The dots above the symbols denote partial time derivatives, and $\nabla = (\partial/\partial x_1, \partial/\partial x_2, \partial/\partial x_3)^{\mathrm{T}}$ is the gradient operator in the Cratesian coordinate space $x = \{x_1, x_2, x_3\}$. The dots and colons between vectors and tensors point out to their scalar and double scalar products, respectively. The components C_{ijkl} of the tensor $\mathbf{C}$ are characterized by the following symmetry property: $C_{ijkl} = C_{ijlk} = C_{klij}$. The superscript T denotes the transposition operator.

Let us constrain ourselves to the case of the linear boundary conditions expressed componentwise in the form:

$$\alpha_k(x)u_k + \beta_k(x)q_k = v_k, \quad x \in \gamma; \quad \mathbf{q} = \boldsymbol{\sigma} \cdot \mathbf{n}, \quad k = 1, 2, 3, \tag{5}$$

where $\mathbf{q}$ is the loading vector, $\mathbf{n}$ is the unit vector pointing in the direction of the outward normal to the boundary γ, u_k and q_k are the components of the vector functions $\mathbf{u}$ and $\mathbf{q}$, α_k and β_k are given coordinate functions defining the type of boundary conditions. In particular, if $\alpha_k = 1$ and $\beta_k = 0$ on some part of the boundary γ then, according to Eq.(5), the displacement u_k is set by the boundary vector function $\mathbf{v}$ via its component v_k. To the contrary, if $\alpha_k = 0$ and $\beta_k = 1$ then the external load component q_k are defined through v_k on γ. Conditions (5) include also various combinations of linear elastic supports if the pair α_k, β_k is simultaneously nonzero on a certain part of the boundary.

It is supposed that at the initial instant $t = 0$ the distribution of momentum density $\mathbf{p}$ and displacements $\mathbf{u}$ are given as sufficiently smooth functions of the coordinates x

$$\mathbf{u}(0, x) = \mathbf{u}^0(x), \quad \mathbf{p}(0, x) = \mathbf{p}^0(x), \quad x \in \Omega \, . \tag{6}$$

Note that initial conditions (6) and boundary conditions (5) should be consistent [14]. The components of boundary vector $\mathbf{v}$ are either given functions of the time t and coordinates x or unknown control inputs defined in some functional space

$$\mathbf{v} = \mathbf{v}(t, x), \quad x \in \gamma \setminus \gamma_v; \quad \mathbf{v} \in V, \quad x \in \gamma_v \, . \tag{7}$$

Let us formulate two classical variational principles for dynamical boundary value problems of linear elasticity (see [22]). If the functions of strain energy density $A(\mathbf{u})$ and kinetic energy density $K(\mathbf{u})$ exist, the displacements $\mathbf{u}$ as a coordinate vector function are given at the initial ($t=0$) and final ($t=t_f$) instants, and boundary conditions (5) do not change under displacement variations then Hamilton's principle follows the principal of virtual work:

$$\delta \mathrm{H} = \delta \int_0^{t_f} \left[\mathrm{T} - \Pi \right] dt = 0, \quad \mathrm{T} = \int_\Omega K d\Omega, \quad \Pi = \int_\Omega \left[A - \mathbf{f} \cdot \mathbf{u} \right] d\Omega - \sum_{i=1}^3 \int_{\gamma_\sigma^{(i)}} u_i v_i \, d\gamma;$$

$$K = \frac{\rho}{2} \mathbf{u} \cdot \mathbf{u}, \quad A = \frac{1}{2} \boldsymbol{\varepsilon} : \mathbf{C} : \boldsymbol{\varepsilon}; \tag{8}$$

$$u_k = v_k, \quad x \in \gamma_u^{(k)}, \quad k = 1,2,3; \quad \mathbf{u}(0,x) = \mathbf{u}^0, \quad \mathbf{u}(t_f, x) = \mathbf{u}^f.$$

In this problem the displacement field $\mathbf{u}$ must rigorously satisfy the kinematic relation (4) and, according to Eq. (5), the displacement conditions on $\gamma_u^{(k)} \subset \gamma$, where $\alpha_k = 1$, $\beta_k = 0$. The equilibrium relation (3) and stress boundary conditions on $\gamma_\sigma^{(k)} = \gamma \setminus \gamma_u^{(k)}$, where $\alpha_k = 0$, $\beta_k = 1$, appear in the stationary conditions of the Hamiltonian H in Eq. (8).

If the functions of stress energy density $A_c(\boldsymbol{\sigma})$ and kinetic energy density $K_c(\mathbf{p})$ exist for the same type of boundary conditions on $\gamma = \gamma_\sigma^{(k)} \cup \gamma_u^{(k)}$, the momentum vector $\mathbf{p}$ is given in the initial ($t=0$) and final ($t=t_f$) instants, and boundary conditions (5) do not change under stress and momentum variations then the stationary principle for the complementary energy follows the principal of virtual complementary work:

$$\delta \mathrm{H}_c = \delta \int_0^{t_f} \left[\mathrm{T}_c - \Pi_c \right] dt = 0, \quad \mathrm{T}_c = \int_\Omega K_c d\Omega, \quad \Pi_c = \int_\Omega A_c d\Omega - \sum_{i=1}^3 \int_{\gamma_u^{(i)}} q_i v_i \, d\gamma;$$

$$K_c = \frac{1}{2\rho} \mathbf{p} \cdot \mathbf{p}, \quad A_c = \frac{1}{2} \boldsymbol{\sigma} : \mathbf{C}^{-1} : \boldsymbol{\sigma}; \tag{9}$$

$$q_k = v_k, \quad x \in \gamma_\sigma^{(k)}, \quad k = 1,2,3; \quad \mathbf{p}(0,x) = \mathbf{p}^0, \quad \mathbf{p}(t_f, x) = \mathbf{p}^f.$$

According to this principle the fields of stress $\boldsymbol{\sigma}$ and momentum $\mathbf{p}$ must rigorously satisfy the equilibrium equation in Eq. (3) and boundary conditions on $\gamma_\sigma^{(k)}$. The kinematic equation in (4) together with boundary conditions on $\gamma_u^{(k)}$ are implicitly equivalent to the stationary conditions of the functional H_c in Eq. (9).

2.2 Formulation for the Static Problem

The static stress-strain state of the body is governed by the differential equations of linear elasticity (1) - (4), supposing that the momentum dencity vector $\mathbf{p}$ is

equal to zero. Let us restrict ourselves to the case when the boundary conditions can be presented in the form

$$q_i \equiv \sigma_{ij} n_j = \overline{q}_i , \quad x \in \gamma_1^j \tag{10}$$

$$u_i = \overline{u}_i , \quad x \in \gamma_2^j \tag{11}$$

$$q_i + \kappa_i u_i = 0 , \quad \kappa_i > 0, \quad x \in \gamma_3^j \tag{12}$$

Here $\overline{q}_i$ and $\overline{u}_i$ are given components of the vector functions of external loads $\overline{\mathbf{q}}$ and boundary displacements $\overline{\mathbf{u}}$; κ_i are given moduli of elastic foundations. The boundary parts γ_j^j satisfy the following conditions: $\gamma_1^j \cup \gamma_2^j \cup \gamma_3^j = \gamma$; $\gamma_j^j \cap \gamma_k^j = \varnothing$, $j \neq k$ ($i, j, k = 1, 2, 3$).

Different variational approaches are broadly used for solving the linear elasticity problems. In the case when the function of strain energy density A, introduced in (8), exists and boundary conditions (10) do not change under displacement variations, the minimum principle for potential energy follows the principal of virtual work [22]:

$$\Pi = \int_\Omega A(\mathbf{u}) d\Omega - \int_\Omega \mathbf{f} \cdot \mathbf{u} d\Omega - \sum_{i=1}^{3} \int_{\gamma_1^j} \overline{q}_i u_i d\gamma_1^j \rightarrow \min_{\mathbf{u}} \tag{13}$$

Note that the displacement fields $\mathbf{u}$ must rigorously satisfy kinematic relations (4), Hooke's law relation (1), and boundary conditions (11). Equilibrium equation (3) and boundary conditions (10) are implicitly contained in the functional Π in Eq. (13) as its stationary conditions.

When the function of stress energy density A_c (see (9)) exists and boundary conditions (11) do not change under stress variations, then the minimum principle for complementary energy follows the principal of virtual complementary work

$$\Pi_c = \int_\Omega A_c(\boldsymbol{\sigma}) d\Omega - \sum_{i=1}^{3} \int_{\gamma_2^j} q_i \overline{u}_i d\gamma_2^j \rightarrow \min_{\boldsymbol{\sigma}} \tag{14}$$

According to this principle the stress fields $\boldsymbol{\sigma}$ must rigorously satisfy equilibrium equation in (3), Hooke's law relation (1), and boundary conditions (10). The kinematic relations (4) and boundary conditions (11) are Euler's equations for the functional Π_c in Eq. (14).

It is considered [22] that both variational principles are equivalent each other under the hypotheses of the linear theory of elasticity.

Note that the approximate displacement fields $\mathbf{u}$ obtained from the minimum principle for potential energy let one find corresponding stress fields $\boldsymbol{\sigma}^0(\mathbf{u})$ taking into account the linear kinematic relations in (4) and stress-strain relation in (1):

$$\boldsymbol{\sigma}^0 \equiv \mathbf{C} : \boldsymbol{\varepsilon}^0(\mathbf{u}) \tag{15}$$

On the other hand by using Eq. (1) the stress fields $\boldsymbol{\sigma}$ obtained from the minimum principle for complementary energy can be related to the following strain fields $\boldsymbol{\varepsilon}(\boldsymbol{\sigma})$:

$$\boldsymbol{\varepsilon} \equiv \mathbf{C}^{-1} : \boldsymbol{\sigma} \tag{16}$$

It is difficult enough to identify corresponding displacements $\mathbf{u}$ since one has to solve the overdetermined system of differential equations $\boldsymbol{\varepsilon}^0 = (\nabla \mathbf{u} + \nabla \mathbf{u}^{\mathrm{T}})/2$. In the general case the stresses $\boldsymbol{\sigma}^0$ and $\boldsymbol{\sigma}$ found by these approaches may not be equal to each other ($\boldsymbol{\sigma} \neq \boldsymbol{\sigma}^0$).

3 The Method of Integrodifferential Relations

Relations (1)–(6) describe the deformed state of an elastic body at any internal point x and any instant t. In addition, it is assumed that the stresses and displacements at the internal points of the body should tend to boundary stresses and displacements, i.e. conditions (5) are satisfied. It is implied that the components of the elastic modulus tensor $\mathbf{C}$ and mass density ρ, defined in the interior of the domain Ω, continuously pass through the boundary γ. Analogously, the displacement and momentum density vectors tend continuously to their initial values given by relations (6). On the other hand, it is necessary to take into account that boundary and initial conditions (5), (6) are generated by specific physical and geometrical factors. For example, some part of the boundary could be an interface between two or more media (elastic or inelastic). In this case, any boundary point belongs simultaneously to the body under consideration and the bodies which generate these boundary conditions. So such points on the boundary belong simultaneously to material parts with different mechanical properties. In other words, the elastic modulus tensor $\mathbf{C}$ and mass density function ρ on such surfaces, strictly speaking, are not defined.

3.1 MIDR for Static Problems

To introduce this uncertainty into the static linear elasticity problem we propose the integral formulation of the stress-strain relation [11, 15]:

$$\Phi_1 = \int_{\Omega} \varphi_1 d\Omega = 0, \quad \varphi_1 = \boldsymbol{\eta} : \boldsymbol{\eta}, \quad \boldsymbol{\eta} \equiv \boldsymbol{\sigma} - \boldsymbol{\sigma}^0 \tag{17}$$

where $\boldsymbol{\sigma}^0 = \boldsymbol{\sigma}^0(\mathbf{u})$ is the tensor function defined in Eq. (15). Taking into account Eq. (17) the boundary value problems of the linear theory of elasticity can be reformulated: to find the kinematically admissible displacements $\mathbf{u}$ and equilibrium stresses $\boldsymbol{\sigma}$ that satisfy relations (3), (4), (17) and boundary conditions (10)–(12).

The integrand φ_1 in Eq. (17) is nonnegative for arbitrary functions $\mathbf{u}$ and $\boldsymbol{\sigma}$ ($\varphi_1 \geq 0$). Hence, the corresponding integral Φ_1 is also nonnegative. Under the circumstances, the integrodifferential problem (3), (4),(10)–(12), (17) can be reduced to a variational problem: to find unknown functions $\mathbf{u}$ and $\boldsymbol{\sigma}$ minimizing the functional Φ_1

$$\Phi_1(\mathbf{u},\boldsymbol{\sigma}) \to \min_{\mathbf{u},\boldsymbol{\sigma}} \tag{18}$$

under constraints (3), (4),(10)–(12) on the stress-strain state of the elastic body.

Let us denote the actual and arbitrary admissible displacements and stresses by $\mathbf{u}^*$, $\boldsymbol{\sigma}^*$ and $\mathbf{u}$, $\boldsymbol{\sigma}$, respectively, and specify that $\mathbf{u} = \mathbf{u}^* + \delta\mathbf{u}$, $\boldsymbol{\sigma} = \boldsymbol{\sigma}^* + \delta\boldsymbol{\sigma}$. Then $\Phi_1(\mathbf{u},\boldsymbol{\sigma}) = \delta_{\mathbf{u}}\Phi_1 + \delta_{\boldsymbol{\sigma}}\Phi_1 + \delta^2\Phi_1$, where $\delta_{\mathbf{u}}\Phi_1$, $\delta_{\boldsymbol{\sigma}}\Phi_1$ are the first variations of the functional Φ_1 with respect to $\mathbf{u}$, $\boldsymbol{\sigma}$ and $\delta^2\Phi_1$ is its second variation.

Integrating the first variations by parts and taking into account Eqs. (3), (4),(10)–(12), (17) result in the following relations

$$\delta_{\mathbf{u}}\Phi_1 = -2\int_{\Omega} \nabla\cdot\mathbf{C}:\boldsymbol{\eta}\cdot\delta\mathbf{u}\,d\Omega + 2\int_{\gamma} \mathbf{n}\cdot\mathbf{C}:\boldsymbol{\eta}\cdot\delta\mathbf{u}\,d\gamma$$
$$\delta_{\boldsymbol{\sigma}}\Phi_1 = 2\int_{\Omega} \boldsymbol{\eta}:\delta\boldsymbol{\sigma}\,d\Omega \tag{19}$$

It is seen from Eqs. (19) that the fist variations $\delta_{\mathbf{u}}\Phi_1$ and $\delta_{\boldsymbol{\sigma}}\Phi_1$ are equal to zero for any $\delta\mathbf{u}$ and $\delta\boldsymbol{\sigma}$ if the following equations are valid

$$\boldsymbol{\eta} = 0, \quad \nabla\cdot\mathbf{C}:\boldsymbol{\eta} = 0, \quad [\mathbf{n}\cdot\mathbf{C}:\boldsymbol{\eta}]\big|_{\gamma} = 0 \tag{20}$$

Hence, Hooke's local relation (1) is the stationary condition of the functional Φ_1 and together with constraints (3), (4),(10)–(12) constitutes the complete system of equations for the linear theory of elasticity.

The second variation

$$\delta^2\Phi_1 = \int_{\Omega} \varphi_1(\delta\mathbf{u},\delta\boldsymbol{\sigma})d\Omega \geq 0$$

which is quadratic with respect to the displacement and stress variations $\delta\mathbf{u}$ and $\delta\boldsymbol{\sigma}$, is nonnegative because the integrand $\varphi_1(\delta\mathbf{u},\delta\boldsymbol{\sigma}) \geq 0$.

It is possible to derive other variational formulations for the linear elasticity problems using properties of the functional Φ_1. If $\Phi_1 = 0$ then the corresponding integral equalities for the components of the stress tensors $\boldsymbol{\sigma}$ and $\boldsymbol{\sigma}^0$ hold

$$\int_{\Omega} \eta_{kl}^2\,d\Omega = 0, \quad k,l = 1, 2, 3 \tag{21}$$

where η_{kl} are the components of the stress tensor $\boldsymbol{\eta}$.

Using Eqs. (15), (16), (21) one can shown that the integral equalities for the components of the strain tensors $\boldsymbol{\varepsilon}$ and $\boldsymbol{\varepsilon}^0$ is also valid

$$\int_{\Omega} \left(\varepsilon_{kl} - \varepsilon_{kl}^0 \right)^2 d\Omega = 0, \quad k,l = 1, 2, 3 \tag{22}$$

Thus, let us introduce into consideration the following nonnegative quadratic functional

$$\Phi_2 = \int_{\Omega} \varphi_2 d\Omega \ge 0, \quad \varphi_2 = \boldsymbol{\xi} : \boldsymbol{\xi}, \quad \boldsymbol{\xi} \equiv \boldsymbol{\varepsilon} - \boldsymbol{\varepsilon}^0 \tag{23}$$

which reaches its absolute minimum (zero value) on the actual displacements $\mathbf{u}^*$ and stresses $\boldsymbol{\sigma}^*$. The first variations the functional in Eq. (23) have the form

$$\delta_{\mathbf{u}} \Phi_2 = -2 \int_{\Omega} \nabla \cdot \boldsymbol{\xi} \cdot \delta \mathbf{u} \, d\Omega + 2 \int_{\gamma} \mathbf{n} \cdot \boldsymbol{\xi} \cdot \delta \mathbf{u} \, d\gamma$$

$$\delta_{\boldsymbol{\sigma}} \Phi_2 = 2 \int_{\Omega} \boldsymbol{\xi} : \mathbf{C}^{-1} : \delta \boldsymbol{\sigma} \, d\Omega \tag{24}$$

The stationary condition for the functional Φ_2 (the same as for Φ_1) is Hooke's law rewritten in the form $\boldsymbol{\xi} = 0$, and its second variation is also nonnegative.

Taking into account Eqs. (15) and (16), the functional Φ_2 expressed in Eq. (23) in terms of the strain tensor $\boldsymbol{\xi}$ can be rewritten in terms of the components of the stress tensor $\boldsymbol{\eta}$. In particular, for the 2D case (plane stressed state) of homogeneous isotropic material the integral Φ_2 has the form

$$\Phi_2 = \frac{(1+\mu^2)}{E^2} \int_{\Omega} \left[\eta_{11}^2 - \frac{4\mu}{(1+\mu^2)} \eta_{11}\eta_{22} + \eta_{22}^2 + \frac{2(1+\mu)^2}{(1+\mu^2)} \eta_{12}^2 \right] d\Omega \tag{25}$$

Here E is Young's modulus, μ is Poisson's ratio. The nonnegativity of the functional in Eq. (25) follows the fact that the factor of the mixed term $4\mu/(1+\mu^2) < 2$ because $-1 < \mu < 1/2$.

Generalizing the approach, one can introduce into consideration a parametric family of nonnegative quadratic functionals

$$\Phi = c^2 \int_{\Omega} \left(\eta_{11}^2 - 2a\eta_{11}\eta_{22} + \eta_{22}^2 + b^2\eta_{12}^2 \right) d\Omega \ge 0, \quad |a| < 1 \tag{26}$$

for which the stationary conditions are equivalent to Hook's relation (1). Here a, b и c are some real constants. Analogous functional families can be constructed for an arbitrary anisotropic 3D case.

Let us consider a functional from such families which has the dimension of energy

$$\Phi_3 = \int_\Omega \varphi_3 d\Omega \geq 0, \quad \varphi_3 = \frac{1}{2}\boldsymbol{\eta} : \boldsymbol{\xi} \tag{27}$$

and formulate the following variational problem: to find unknown functions $\mathbf{u}$ and $\boldsymbol{\sigma}$ minimizing the functional

$$\Phi_3(\mathbf{u},\boldsymbol{\sigma}) \rightarrow \min_{\mathbf{u},\boldsymbol{\sigma}} \tag{28}$$

under constraints (3), (4),(10)–(12).

It is possible to transform the integral in Eq. (27) to the form

$$\Phi_3 = W_u + W_\sigma - 2W$$
$$W_u = \frac{1}{2}\int_\Omega \boldsymbol{\sigma}^0 : \boldsymbol{\varepsilon}^0 d\Omega, \quad W_\sigma = \frac{1}{2}\int_\Omega \boldsymbol{\sigma} : \boldsymbol{\varepsilon} d\Omega, \quad W = \frac{1}{2}\int_\Omega \boldsymbol{\sigma} : \boldsymbol{\varepsilon}^0 d\Omega \tag{29}$$

where W_u and W_σ are the strain and stress energies, respectively, and W is the work of external forces. Note that W_u and W_σ are positively defined functionals, and W is a bilinear functional independent explicitly of elastic material properties.

Integrating by parts the work of external forces W and using equilibrium equation (3) give

$$2W = \int_\gamma (\boldsymbol{\sigma} \cdot \mathbf{n}) \cdot \mathbf{u} d\gamma + \int_\Omega \mathbf{f} \cdot \mathbf{u} d\Omega \tag{30}$$

Firstly, let us consider the case when the stress (Eq. (10)) and displacement (Eq. (11)) boundary conditions are only given. The mixed boundary conditions (12) (elastic foundation) are absent. Then, after substituting Eq. (30) into Eq. (29), the functional Φ_3 will have the form

$$\Phi_3 = W_u - \int_\Omega \mathbf{f} \cdot \mathbf{u} d\Omega - \sum_{i=1}^{3} \int_{\gamma_1^j} \bar{q}_i u_i d\gamma_1^j + W_\sigma - \sum_{i=1}^{3} \int_{\gamma_2^j} q_i \bar{u}_i d\gamma_2^j \geq 0 \tag{31}$$

Taking into account the expressions for the potential energy in Eq. (13) and complementary energy in Eq. (14) one can present inequality (31) as follows

$$\Phi_3(\mathbf{u},\boldsymbol{\sigma}) = \Pi(\mathbf{u}) + \Pi_c(\boldsymbol{\sigma}) \geq 0 \tag{32}$$

Thus, the following theorem formulated in [18, 21] is valid for this case: for any equilibrium stress fields $\boldsymbol{\sigma}$ under boundary conditions (10) and any kinematically admissible displacement fields $\mathbf{u}$ under boundary conditions (11) the sum of the potential and complementary energies is nonnegative.

Consequently, this constrained minimization problem is equivalent to the independent minimization of the potential energy over displacements $\mathbf{u}$ under boundary condition (11) and the complementary energy over equilibrium stresses $\boldsymbol{\sigma}$ under boundary condition (10)

$$\min_{\mathbf{u},\boldsymbol{\sigma}} \Phi_3(\mathbf{u},\boldsymbol{\sigma}) = \min_{\mathbf{u}} \Pi(\mathbf{u}) + \min_{\boldsymbol{\sigma}} \Pi_c(\boldsymbol{\sigma}) = 0 \tag{33}$$

It is worth to emphasize that for such boundary value problems the approximate displacement fields are found using the minimum principle for potential energy (13) while based on the minimum principle for complementary energy (14) the stress fields are obtained. Moreover, the method of integrodifferential relations enables one to construct effective bilateral estimates for the total elastic energy stored $W(\mathbf{u}^*,\boldsymbol{\sigma}^*) = W_u(\mathbf{u}^*) = W_\sigma(\boldsymbol{\sigma}^*)$ as a function of the actual displacements $\mathbf{u}^*$ and stresses $\boldsymbol{\sigma}^*$. In particular, if $\bar{u}_i = 0$ ($x \in \gamma_2^j$) or $\gamma_2^j = \varnothing$ ($i=1,2,3$) then for arbitrary admissible displacements $\mathbf{u}$ and stresses $\boldsymbol{\sigma}$ the following estimates hold

$$-\Pi(\mathbf{u}) \leq W(\mathbf{u}^*,\boldsymbol{\sigma}^*) \leq \Pi_c(\boldsymbol{\sigma}) \tag{34}$$

On the other hand, if $\bar{q}_i = 0$ ($x \in \gamma_1^j$) or $\gamma_1^j = \varnothing$ ($i=1,2,3$) then the inequalities are valid

$$-\Pi_c(\boldsymbol{\sigma}) \leq W(\mathbf{u}^*,\boldsymbol{\sigma}^*) \leq \Pi(\mathbf{u}) \tag{35}$$

The positivity of the second variation $\delta^2\Phi_3$ with respect to $\mathbf{u}$ and $\boldsymbol{\sigma}$ follows from the corresponding properties of the second variations $\delta^2\Pi \geq 0$ and $\delta^2\Pi_c \geq 0$. The equality $\delta^2\Phi_3 = 0$ is valid if and only if all the components of the strain tensor $\boldsymbol{\varepsilon}^0(\delta\mathbf{u})$ and stress tensor $\delta\boldsymbol{\sigma}$ are equal to zero [22].

Let us consider the case when the mixed conditions (12) (elastic foundation) are given on some part of the boundary γ ($\gamma_3^j \neq \varnothing$). One can show that the decomposition of the variational problem (28) on two independent problems in displacement and stresses, respectively, is not possible. Indeed, after integrating by parts the work of external forces W has the form

$$2W = \int_\Omega \mathbf{f} \cdot \mathbf{u}\, d\Omega + \sum_{i=1}^3 \int_{\gamma_1^j} \bar{q}_i u_i d\gamma_1^j + \sum_{i=1}^3 \int_{\gamma_2^j} q_i \bar{u}_i d\gamma_2^j + \sum_{i=1}^3 \int_{\gamma_2^j} q_i u_i d\gamma_2^j \tag{36}$$

The last term in relations (36) depends explicitly on both the displacements $\mathbf{u}$ and stresses $\boldsymbol{\sigma}$.

Taking into account that the variations $\delta\mathbf{u}$ and $\delta\boldsymbol{\sigma}$ on γ_3^j ($i=1,2,3$) are related by the equality $\delta\sigma_{ij}n_j + \kappa_i \delta u_i = 0$ the second variation $\delta^2\Phi_3$ can be presented as follows

$$\delta^2\Phi_3 = W_u(\delta\mathbf{u}) + W_\sigma(\delta\boldsymbol{\sigma}) + \sum_{i=1}^3 \int_{\gamma_3^j} \kappa_i (\delta u_i)^2 d\gamma_3^j \geq 0, \quad \kappa_i > 0 \tag{37}$$

The equality $\delta^2\Phi_3 = 0$ is valid if and only if all components of the strain tensor $\boldsymbol{\varepsilon}^0(\delta\mathbf{u})$, stress tensor $\delta\boldsymbol{\sigma}$ as well as the components δu_i of the displacement vector on γ_3^i ($i = 1, 2, 3$) are equal to zero.

3.2 MIDR for Dynamical Problems

To introduce uncertainties into the dynamical linear elasticity problem a combined integral relation instead of stress-strain and velocity-momentum relations (1)–(2) was proposed in [12] and the following integrodifferential formulation of initial-boundary value problem (1)–(6) was given: to find such functions $\mathbf{u}^*$, $\boldsymbol{\sigma}^*$, and $\mathbf{p}^*$ that satisfy integral relation

$$\Phi_+ = \int_0^{t_f}\int_\Omega \varphi_+(\mathbf{u},\boldsymbol{\sigma},\mathbf{p})\,d\Omega\,dt = 0, \quad \varphi_+ = \frac{1}{2}[\rho\boldsymbol{\eta}\cdot\boldsymbol{\eta} + \boldsymbol{\xi}:\mathbf{C}:\boldsymbol{\xi}]; \tag{38}$$

$$\boldsymbol{\eta} = \mathbf{u} - \rho^{-1}\mathbf{p}, \qquad \boldsymbol{\xi} = \boldsymbol{\varepsilon} - \mathbf{C}^{-1}:\boldsymbol{\sigma} \tag{39}$$

under equilibrium, kinematical, boundary, and initial conditions (3)–(6). Here the auxiliary velocity vector $\boldsymbol{\eta}$ and strain tensor $\boldsymbol{\xi}$ are introduced.

Note that the integrand φ_+ in Eq. (38) has the dimension of energy density and is nonnegative. Hence, the corresponding integral Φ_+ is nonnegative for arbitrary functions $\mathbf{u}$, $\boldsymbol{\sigma}$, and $\mathbf{p}$ ($\Phi_+ \geq 0$). The proposed integrodifferential problem (3)–(6) and (38) can be reduced to a variational one: to find unknown functions $\mathbf{u}^*$, $\boldsymbol{\sigma}^*$, and $\mathbf{p}^*$ minimizing the functional Φ_+

$$\Phi_+(\mathbf{u}^*, \boldsymbol{\sigma}^*, \mathbf{p}^*) = \min_{\mathbf{u},\boldsymbol{\sigma},\mathbf{p}} \Phi_+(\mathbf{u}, \boldsymbol{\sigma}, \mathbf{p}) = 0 \tag{40}$$

subject to constraints (3)–(6).

It was shown in previous Subsection for static linear elasticity that the method of integrodifferential relations give one the possibility to formulate various variational problems. Analogously to the static case, let us introduce into consideration a parametric family of quadratic functionals

$$\Phi = \int_0^{t_f}\int_\Omega \varphi\,d\Omega\,dt = 0, \quad \varphi = \alpha\rho\boldsymbol{\eta}\cdot\boldsymbol{\eta} + \beta\boldsymbol{\xi}:\mathbf{C}:\boldsymbol{\xi}, \quad \alpha^2 + \beta^2 = \frac{1}{2}, \quad \alpha \geq 0, \tag{41}$$

which stationary conditions are equivalent to relations (1) and (2). Here α and β are real constants. At $\alpha = \beta = 1/2$ integral (41) is equivalent to the nonnegative functional Φ_+ defined in Eq. (38). If $\beta > 0$, $\alpha \neq 0$ the minimization problems appropriate to corresponding functional $\Phi[\alpha]$ is formulated in much the same way as it was made for the functional Φ_+. The general variational formulation can be proposed for all nonzero values of α and β ($\alpha \neq 0$, $\beta \neq 0$): to find unknown functions $\mathbf{u}^*$, $\boldsymbol{\sigma}^*$, $\mathbf{p}^*$ providing the stationary value for the functional Φ

$$\delta_u \Phi + \delta_\sigma \Phi + \delta_p \Phi = 0 \tag{42}$$

and satisfying constraints (3)–(6).

After integrating the first variations by parts and taking into account Eqs. (3)–(6) the first variations of Φ have the following form

$$\frac{1}{2}\delta_u \Phi = -\int_0^{t_f}\int_\Omega \left[\alpha\boldsymbol{\eta}^\bullet + \beta\nabla\cdot(\mathbf{C}:\boldsymbol{\xi}) \right]\cdot\delta\mathbf{u}\,d\Omega\,dt + \alpha\int_\Omega \left[\boldsymbol{\eta}\cdot\delta\mathbf{u}\right]_{t=0}^{t=t_f}\,d\Omega$$

$$+\beta\int_0^{t_f}\int_\gamma \mathbf{n}\cdot\mathbf{C}:\boldsymbol{\xi}\cdot\delta\mathbf{u}\,d\gamma\,dt, \tag{43}$$

$$\delta_\sigma \Phi = -2\beta\int_0^{t_f}\int_\Omega \boldsymbol{\xi}:\delta\boldsymbol{\sigma}\,d\Omega\,dt, \quad \delta_p \Phi = -2\alpha\int_0^{t_f}\int_\Omega \boldsymbol{\eta}\cdot\delta\mathbf{p}\,d\Omega\,dt.$$

It is seen from Eq. (43) that the fist variation of the functional Φ is equal to zero for any admissible variations $\delta\mathbf{u}$, $\delta\boldsymbol{\sigma}$, $\delta\mathbf{p}$ if the following equations equivalent to Eqs. (1) are valid

$$\boldsymbol{\eta} = 0, \quad \boldsymbol{\xi} = 0. \tag{44}$$

The stress tensor $\boldsymbol{\sigma}$ and momentum density vector $\mathbf{p}$ as well as their variation $\delta\mathbf{p}$ and $\delta\boldsymbol{\sigma}$ are related each other through the equilibrium equation (3)

$$\delta\mathbf{p}^\bullet = \nabla\cdot\delta\boldsymbol{\sigma}. \tag{45}$$

Introduce the auxiliary tensor $\boldsymbol{\chi}$ so that

$$\mathbf{p} = \nabla\cdot\boldsymbol{\chi} + \int\mathbf{f}\,dt, \quad \boldsymbol{\sigma} = \boldsymbol{\chi}. \tag{46}$$

Then equation (45) is fulfilled automatically and the stationary conditions for the functional Φ can be rewritten in the forms

$$\delta_u \Phi + \delta_\chi \Phi = 0;$$

$$\frac{\delta_u \Phi}{2} = -\int_0^{t_f}\int_\Omega \left(\alpha\rho\boldsymbol{\eta}^\bullet + \beta\nabla\cdot\mathbf{C}:\boldsymbol{\xi}\right)\cdot\delta\mathbf{u}\,d\Omega\,dt + \int_0^{t_f}\int_\gamma \beta\mathbf{n}\cdot\mathbf{C}:\boldsymbol{\xi}\cdot\delta\mathbf{u}\,d\gamma\,dt$$

$$+\int_\Omega \left[\alpha\boldsymbol{\eta}\cdot\delta\mathbf{u}\right]_{t=0}^{t=t_f}\,d\Omega, \tag{47}$$

$$\frac{\delta_\chi \Phi}{2} = \int_0^{t_f}\int_\Omega \left(\alpha\boldsymbol{\varepsilon}_\eta + \beta\boldsymbol{\xi}^\bullet\right):\delta\boldsymbol{\chi}\,d\Omega\,dt - \alpha\int_0^{t_f}\int_\gamma \boldsymbol{\eta}\cdot\delta\boldsymbol{\chi}\cdot\mathbf{n}\,d\gamma\,dt - \beta\int_\Omega \left[\boldsymbol{\xi}:\delta\boldsymbol{\chi}\right]_{t=0}^{t=t_f}\,d\Omega$$

$$\boldsymbol{\varepsilon}_\eta = \frac{1}{2}(\nabla\boldsymbol{\eta} + \nabla\boldsymbol{\eta}^T).$$

From Eqs (47) it is following the system of Euler's equations with the conditions on the boundary γ and at the initial and terminal instants $t = 0, t_f$

$$\alpha\rho\boldsymbol{\eta}^{\bullet} + \beta\nabla\cdot\mathbf{C}:\boldsymbol{\xi} = 0, \quad \alpha\boldsymbol{\varepsilon}_{\eta} + \beta\boldsymbol{\xi}^{\bullet} = 0 \quad \Rightarrow \quad \rho\boldsymbol{\eta}^{\bullet\bullet} = \nabla\cdot\mathbf{C}:\boldsymbol{\varepsilon}_{\eta};$$
$$\boldsymbol{\eta}|_{t=0,t_f} = \boldsymbol{\xi}|_{t=0,t_f} = \boldsymbol{\eta}|_{x\in\gamma} = \mathbf{n}\cdot\mathbf{C}:\boldsymbol{\xi}|_{x\in\gamma} = 0. \tag{48}$$

Taking into account the type of boundary and initial conditions(5), (6) and system (48) it can be proven that if the unique solution $\mathbf{u}^*$, $\boldsymbol{\sigma}^*$, $\mathbf{p}^*$ exists then the stationary conditions (47) for the functional Φ are equivalent to relations (1), (2) and together with constraints (3)–(6) constitute the full system of dynamical equations for the linear theory of elasticity. Moreover the nonnegative functional Φ for $\beta > 0$ reaches its absolute minimum on this solution and can serve as integral quality criteria for any admissible approximations of the displacements, stresses, and momentum densities $\mathbf{u}$, $\boldsymbol{\sigma}$, $\mathbf{p}$. At the same time the integrand φ can be used to estimate the local quality of approximations.

4   Relations of the Dynamical Variational Principles

Consider a functional of the family defined in Eq. (41) at $\beta = -\alpha = 1/2$ ($\Phi_- = \Phi|_{\alpha=1/2}$) in more detail. It is possible to transform the integral Φ_- to the form

$$\Phi_- = \int_0^{t_f}\int_\Omega \varphi_-(\mathbf{u},\boldsymbol{\sigma},\mathbf{p})d\Omega\,dt = 0, \quad \varphi_- = \frac{1}{2}[\rho\boldsymbol{\eta}\cdot\boldsymbol{\eta} - \boldsymbol{\xi}:\mathbf{C}:\boldsymbol{\xi}];$$

$$\Phi_- = \Theta_u + \Theta_{\sigma p} - 2\Theta, \quad \Theta = \frac{1}{2}\int_0^{t_f}\int_\Omega\left[\mathbf{p}\cdot\mathbf{u}^\bullet - \boldsymbol{\sigma}:\boldsymbol{\varepsilon}\right]d\Omega\,dt \tag{49}$$

$$\Theta_u = \frac{1}{2}\int_0^{t_f}\int_\Omega\left[\rho\mathbf{u}^\bullet\cdot\mathbf{u}^\bullet - \boldsymbol{\varepsilon}:\mathbf{C}:\boldsymbol{\varepsilon}\right]d\Omega\,dt, \quad \Theta_{\sigma p} = \frac{1}{2}\int_0^{t_f}\int_\Omega\left[\rho^{-1}\mathbf{p}\cdot\mathbf{p} - \boldsymbol{\sigma}:\mathbf{C}^{-1}:\boldsymbol{\sigma}\right]d\Omega\,dt$$

where Θ_u, $\Theta_{\sigma p}$, Θ are space-time integrals. Note that the functional Θ_u depends only on the vector function $\mathbf{u}$, whereas $\Theta_{\sigma p}$ is independent of the displacements. The bilinear functional Θ does not include explicitly elastic and inertial material properties of the body, and after integrating by parts and using relations (3) it can be presented as

$$2\Theta = \int_\Omega\left[\mathbf{p}\cdot\mathbf{u}\right]_{t=0}^{t=t_f}d\Omega - \int_0^{t_f}\int_\Omega\mathbf{f}\cdot\mathbf{u}\,d\Omega\,dt - \int_0^{t_f}\int_\gamma\mathbf{q}\cdot\mathbf{u}\,d\gamma\,dt \tag{50}$$

Let us analyze the case of the boundary conditions when the components q_k of the loading vector $\mathbf{q}$ are given on the parts $\gamma_\sigma^{(k)}$ of the boundary γ ($\alpha_k = 0$,

$\beta_k = 1$ in Eq. (5)) whereas on the parts $\gamma_u^{(k)} \subset \gamma$ the displacement components are defined ($\alpha_k = 1$, $\beta_k = 0$). These patches $\gamma_\sigma^{(k)}$, $\gamma_u^{(k)}$ of the boundary γ satisfy the following conditions: $\gamma_u^{(k)} \cup \gamma_\sigma^{(k)} = \gamma$, $\gamma_u^{(k)} \cap \gamma_\sigma^{(k)} = \varnothing$ ($k = 1, 2, 3$). In this case mixed boundary conditions like an elastic foundation are absent. Then, after substituting Eq. (50) into Eq. (49), the functional Φ_- can be rewritten as follows

$$
\begin{aligned}
\Phi_- = \Theta_u &+ \int_0^{t_f}\int_\Omega \mathbf{f}\cdot\mathbf{u}\, d\Omega\, dt + \sum_{i=1}^{3}\int_0^{t_f}\int_{\gamma_\sigma^{(i)}} v_i u_i\, d\gamma_\sigma^{(i)}\, dt + \Theta_{\sigma p} \\
&+ \sum_{i=1}^{3}\int_0^{t_f}\int_{\gamma_u^{(i)}} q_i v_i\, d\gamma_u^{(i)}\, dt - \int_\Omega \left[\mathbf{p}\cdot\mathbf{u}\right]_{t=0}^{t=t_f}\, d\Omega
\end{aligned}
\tag{51}
$$

If at both initial time $t = 0$ and finale time $t = t_f$ either the displacement or momentum density vector is given, the functional Φ_- decomposes into two independent parts

$$
\begin{aligned}
\Phi_- &= \mathrm{H}_u + \mathrm{H}_{\sigma p}, \\
\mathrm{H}_u &= \Theta_u + \int_0^{t_f}\int_\Omega \mathbf{f}\cdot\mathbf{u}\, d\Omega\, dt + \sum_{i=1}^{3}\int_0^{t_f}\int_{\gamma_\sigma^{(i)}} v_i u_i\, d\gamma_\sigma^{(i)}\, dt + \Xi_u, \\
\mathrm{H}_{\sigma p} &= \Theta_{\sigma p} + \sum_{i=1}^{3}\int_0^{t_f}\int_{\gamma_u^{(i)}} q_i v_i\, d\gamma_u^{(i)}\, dt + \Xi_p.
\end{aligned}
\tag{52}
$$

Here the functional H_u depends only on the displacement vector $\mathbf{u}$, $\mathrm{H}_{\sigma p}$ is a function of the stress tensor $\boldsymbol{\sigma}$ and momentum density vector $\mathbf{p}$, Ξ_u and Ξ_p are volume integrals dependent only on $\mathbf{u}$ and $\mathbf{p}$, respectively. In Table 1 the integrals Ξ_u and Ξ_p are presented for several kinds of initial and terminal conditions. The first four cases correspond to space-time boundary value problems, and the last row describes periodic body motions.

The stationary conditions for the functional Φ_- under equilibrium relation and space-time boundary conditions discussed above can be written according to relation (46) as

$$
\delta\Phi_- = \delta_{\mathbf{u}}\mathrm{H}_u + \delta_{\boldsymbol{\chi}}\mathrm{H}_{\sigma p} = 0.
\tag{53}
$$

Consequently, this constrained variational problem is equivalent to two independent problems:

Problem 1. To find a displacement vector $\mathbf{u}^*$ providing the stationary value for the functional H_u

$$\delta_{\mathbf{u}} \mathbf{H}_u = 0 \tag{54}$$

and strictly satisfying boundary conditions on $\gamma_u^{(k)}$ ($k = 1, 2, 3$) as well as initial and/or terminal conditions on the displacement fields shown in Table 1.

Problem 2. To find a stress tensor $\boldsymbol{\sigma}^*$ and momentum density vector $\mathbf{p}^*$ guarantying the stationarity for the functional $H_{\sigma p}$

$$\delta_{\boldsymbol{\chi}} \mathbf{H}_{\sigma p} = 0 \tag{55}$$

and obeying relations (46), stress conditions on $\gamma_\sigma^{(k)}$ ($k = 1, 2, 3$), and the initial and/or terminal momentum conditions from Table 1.

Table 1. Volume integrals Ξ_u and Ξ_p for different initial and terminal conditions

	Condition I	Condition II	Ξ_u	Ξ_p
1	$\mathbf{u}(0,x) = \mathbf{u}^0(x)$	$\mathbf{u}(t_f,x) = \mathbf{u}^f(x)$	0	$\int_\Omega \left[\mathbf{u}^f \cdot \mathbf{p}\big|_{t=t_f} - \mathbf{u}^0 \cdot \mathbf{p}\big|_{t=0} \right] d\Omega$
2	$\mathbf{p}(0,x) = \mathbf{p}^0(x)$	$\mathbf{p}(t_f,x) = \mathbf{p}^f(x)$	$\int_\Omega \left[\mathbf{p}^f \cdot \mathbf{u}\big|_{t=t_f} - \mathbf{p}^0 \cdot \mathbf{u}\big|_{t=0} \right] d\Omega$	0
3	$\mathbf{u}(0,x) = \mathbf{u}^0(x)$	$\mathbf{p}(t_f,x) = \mathbf{p}^f(x)$	$\int_\Omega \left[\mathbf{p}^f \cdot \mathbf{u}\big|_{t=t_f} \right] d\Omega$	$-\int_\Omega \left[\mathbf{u}^0 \cdot \mathbf{p}\big|_{t=0} \right] d\Omega$
4	$\mathbf{p}(0,x) = \mathbf{p}^0(x)$	$\mathbf{u}(t_f,x) = \mathbf{u}^f(x)$	$-\int_\Omega \left[\mathbf{p}^0 \cdot \mathbf{u}\big|_{t=0} \right] d\Omega$	$\int_\Omega \left[\mathbf{u}^f \cdot \mathbf{p}\big|_{t=t_f} \right] d\Omega$
5	$\mathbf{u}(0,x) = \mathbf{u}(t_f,x)$	$\mathbf{p}(0,x) = \mathbf{p}(t_f,x)$	0	0

The displacement fields $\mathbf{u}^*$ obtained from Problem 1 let one find corresponding stress tensor $\mathbf{C} : \boldsymbol{\varepsilon}(\mathbf{u}^*)$ and momentum density vector $(\rho \mathbf{u}^*)^\bullet$. On the other hand the stress fields $\boldsymbol{\sigma}^*$ obtained from Problem 2 can be related to the following strain fields $\mathbf{C}^{-1} : \boldsymbol{\sigma}^*$. In this case it is difficult enough to identify corresponding displacements $\mathbf{u}$ since one has to solve the overdetermined system of differential equations ($\mathbf{u}^\bullet = \mathbf{p}/\rho$, $\nabla\mathbf{u} + \nabla\mathbf{u}^T = 2\boldsymbol{\varepsilon}$).

It is important to emphasize that if displacements are given at the initial and terminal instants (the first row in Table 1) then Problem 1 is equivalent to Hamilton's principle (8) ($\mathbf{H}_u = \mathbf{H}$). If the initial and terminal momentum fields are fixed (the second row in Table 1) then Problem 2 coincides with complementary principle (9)

($H_{\sigma p} = H_c$). Both classical principles are also valid in the case of periodic conditions (the last row in Table 1).

In contrast to variational principles (8) and (9) which are only formulated for space-time boundary value problems, the functional Φ_- can be applied to the initial-boundary value problem (1)–(6) as well. The initial conditions (6) do not allow us to separate this functional, because the last term in relation (51) depends explicitly on both displacements $\mathbf{u}$ and momentum density $\mathbf{p}$. In this case the variational problem must be solved simultaneously with respect to unknown displacement, stress, and momentum functions.

As it will be seen in Section 6, the value of the nonnegative functional Φ_+ can serve to estimate the integral quality of approximate solutions of problem (3)–(6), (42) for $\alpha = 1/2$, $\beta = -1/2$. But even if the decomposition of the variational formulation for Φ_- onto Problems 1 and 2 is possible, nevertheless, both problems have to be solved to estimate explicitly the quality of the numerical results.

5 Dynamical Variational Principle in Displacements and Stresses

As it was shown in the previous sections the variational formulations for the initial-boundary value problem of controlled motions of an elastic body can be proposed with the displacement vector $\mathbf{u}$, stress tensor $\boldsymbol{\sigma}$, and momentum density vector $\mathbf{p}$ to be unknown functions. After introducing into consideration the auxiliary tensor $\boldsymbol{\chi}$ nine independent functions (components of tensor $\boldsymbol{\chi}$ and vector $\mathbf{u}$) remain in the system. In numerical approaches to 3D dynamical problems this fact leads to sufficiently large dimension of system parameters. To decrease the number of unknown functions in the variational formulation and raise the effectiveness of numerical computation a special member of functional family (41), namely, the nonnegative functional Φ at $\alpha = 0$, $\beta = 1/\sqrt{2}$ can be proposed

$$\Phi_0 \equiv \frac{1}{\sqrt{2}}\Phi\big|_{\alpha=0} = \int\limits_0^{t_f}\int\limits_\Omega \varphi_0(\mathbf{u},\boldsymbol{\sigma})d\Omega\,dt, \quad \varphi_0 = \frac{1}{2}\boldsymbol{\xi}:\mathbf{C}:\boldsymbol{\xi}. \tag{56}$$

To formulate a constrained minimization problem fitting for Φ_0 the velocity-momentum vector relation $\boldsymbol{\eta} = 0$ in Eq. (1) must be considered as an additional differential constraint. After that the variational problem is to find unknown functions $\mathbf{u}^*$ and $\boldsymbol{\sigma}^*$ minimizing the following functional Φ_0 under constraints

$$\Phi_0(\mathbf{u}^*, \boldsymbol{\sigma}^*) = \min_{\mathbf{u},\boldsymbol{\sigma}} \Phi_0(\mathbf{u},\boldsymbol{\sigma}) = 0,$$

$$\rho\mathbf{u}^{\bullet\bullet} = \nabla\cdot\boldsymbol{\sigma} + \mathbf{f},$$

$$\alpha_k(x)u_k + \beta_k(x)q_k = v_k, \quad x\in\gamma; \quad \mathbf{q} = \boldsymbol{\sigma}\cdot\mathbf{n}, \quad k=1,2,3\,, \tag{57}$$

$$\mathbf{u}(0,x) = \mathbf{u}^0(x), \quad \mathbf{u}^\bullet(0,x) = \rho^{-1}\mathbf{p}^0(x).$$

In the same way as in Section 3 denote the actual and arbitrary admissible displacements and stresses by $\mathbf{u}^*$, $\boldsymbol{\sigma}^*$ and $\mathbf{u}$, $\boldsymbol{\sigma}$, respectively, and specify that $\mathbf{u} = \mathbf{u}^* + \delta\mathbf{u}$, $\boldsymbol{\sigma} = \boldsymbol{\sigma}^* + \delta\boldsymbol{\sigma}$ then $\Phi_0(\mathbf{u},\boldsymbol{\sigma}) = \delta_\mathbf{u}\Phi_0 + \delta_\boldsymbol{\sigma}\Phi_0 + \delta^2\Phi_0$. The second variation quadratic with respect to $\delta\mathbf{u}$, $\delta\boldsymbol{\sigma}$ is nonnegative ($\delta^2\Phi_0 \geq 0$). The fist variation of the functional Φ_0 is equal to zero for any admissible variations $\delta\mathbf{u}$, $\delta\boldsymbol{\sigma}$ if $\boldsymbol{\xi} = 0$. The displacement vector $\mathbf{u}$ and stress tensor $\boldsymbol{\sigma}$ as well as their variations $\delta\mathbf{u}$ and $\delta\boldsymbol{\sigma}$ are related through the equilibrium equation shown in Eq. (57) and

$$\delta\mathbf{u}^{\cdot\cdot} = \nabla \cdot \delta\boldsymbol{\sigma}. \tag{58}$$

Introduce the auxiliary tensor $\boldsymbol{\chi}$ so that

$$\mathbf{u} = \nabla \cdot \boldsymbol{\chi} + \iint \mathbf{f}\,dt\,dt, \quad \boldsymbol{\sigma} = \rho\boldsymbol{\chi}^{\cdot\cdot} \tag{59}$$

and write down the stationary conditions for Φ_0

$$\delta_\boldsymbol{\chi}\Phi_0 = 0;$$

$$\delta_\boldsymbol{\chi}\Phi_0 = \int_0^{t_f}\int_\Omega \left[\Delta_\boldsymbol{\xi} - \rho\boldsymbol{\xi}^{\cdot\cdot}\right] : \delta\boldsymbol{\chi}\,d\Omega\,dt$$

$$+ \int_0^{t_f}\int_{\gamma_\sigma} \left[(\mathbf{n}\cdot\mathbf{C}:\boldsymbol{\xi})\cdot(\nabla\cdot\delta\boldsymbol{\chi}) - (\nabla\cdot\mathbf{C}:\boldsymbol{\xi})\cdot(\delta\boldsymbol{\chi}\cdot\mathbf{n})\right]d\gamma\,dt + \tag{60}$$

$$\int_\Omega \left[\boldsymbol{\xi}^{\cdot} : \delta\boldsymbol{\chi} - \boldsymbol{\xi} : \delta\boldsymbol{\chi}^{\cdot}\right]_{t=0}^{t=t_f} d\Omega,$$

$$\Delta_\boldsymbol{\xi} = \frac{1}{2}\left[\nabla(\nabla\cdot\mathbf{C}:\boldsymbol{\xi}) + \nabla(\nabla\cdot\mathbf{C}:\boldsymbol{\xi})^{\mathrm{T}}\right].$$

The system of Euler's equations with the corresponding conditions on the boundary γ and at initial and terminal instants $t = 0, t_f$ can be obtained from Eq. (60). It is possible to show (as in Section 3) that the stationary conditions for the functional Φ_0 are equivalent to relations $\boldsymbol{\xi} = 0$ and together with constraint $\boldsymbol{\eta} = 0$ and Eqs. (3)–(6) constitute the full system of dynamical equations for linear elasticity.

6 Numerical Algorithm and Error Analysis

Let us describe one of the possible algorithms approximating the solution $\mathbf{u}^*$, $\boldsymbol{\sigma}^*$, $\mathbf{p}^*$ of the variational problem defined by Eq. (42). Constrain ourselves to the case of zero volume force $\mathbf{f} = 0$. At the beginning the positive integers N_u, N_σ, and N_p are chosen and the approximations $\tilde{\mathbf{u}}$, $\tilde{\boldsymbol{\sigma}}$, and $\tilde{\mathbf{p}}$ of the solution are defined in the finite dimensional form

$$\tilde{\mathbf{u}} = \sum_{k=1}^{N_u} \mathbf{u}^{(k)} \psi_k(t,x), \quad \tilde{\boldsymbol{\sigma}} = \sum_{k=1}^{N_\sigma} \boldsymbol{\sigma}^{(k)} \psi_k(t,x), \quad \tilde{\mathbf{p}} = \sum_{k=1}^{N_p} \mathbf{p}^{(k)} \psi_k(t,x). \tag{61}$$

Here $\{\psi_k(t,x), k=1,2,\ldots\}$ is some complete countable system of linearly independent functions and $\mathbf{u}^{(k)}$, $\boldsymbol{\sigma}^{(k)}$, $\mathbf{p}^{(k)}$ are unknown real coefficients presented in the vector and tensor forms. The basis functions ψ_k should be chosen so that the approximations $\tilde{\mathbf{u}}$, $\tilde{\boldsymbol{\sigma}}$, and $\tilde{\mathbf{p}}$ were able to satisfy exactly the equilibrium equation in Eq. (3) as well as boundary and initial conditions (5), (6). The admissible set of the boundary vector $\mathbf{v}$ and initial functions $\mathbf{u}^0$ and $\mathbf{p}^0$ is defined. It is follows from Eq. (61) that the vectors $\mathbf{v}$, $\mathbf{u}^0$, $\mathbf{p}^0$ must have the structure

$$\mathbf{v} = \sum_{k=1}^{N_v} \mathbf{v}^{(k)} \psi_k \big|_{x\in\gamma}, \quad \mathbf{u}^0 = \sum_{k=1}^{N_u} \mathbf{u}^{(0k)} \psi_k(0,x), \quad \mathbf{p}^0 = \sum_{k=1}^{N_p} \mathbf{p}^{(0k)} \psi_k(0,x),$$

where $\mathbf{u}^{(0k)}$, and $\mathbf{p}^{(0k)}$ are fixed coefficients; $\mathbf{v}^{(k)}$ are either given constants on $\gamma \setminus \gamma_v$ defined on the boundary patch γ_v.

In the next step the conditions (3)–(6) are fulfilled with respect to unknown coefficients $\mathbf{u}^{(k)}$, $\boldsymbol{\sigma}^{(k)}$, and $\mathbf{p}^{(k)}$ and the admissible approximations $\tilde{\mathbf{u}}$, $\tilde{\boldsymbol{\sigma}}$, and $\tilde{\mathbf{p}}$ obtained are substituted into the functional Φ. Since the functional Φ is quadratic with respect to the parameters $\mathbf{u}^{(k)}$, $\boldsymbol{\sigma}^{(k)}$, $\mathbf{p}^{(k)}$, and $\mathbf{v}^{(k)}$, the stationary problem (42) is reduced to the linear system of the algebraic equations versus unknown coefficients $\mathbf{u}^{(k)}$, $\boldsymbol{\sigma}^{(k)}$, and $\mathbf{p}^{(k)}$. To estimate the quality of the numerical solution $\tilde{\mathbf{u}}(t,x)$, $\tilde{\boldsymbol{\sigma}}(t,x)$, and $\tilde{\mathbf{p}}(t,x)$ the following criterion is proposed [19]

$$\begin{aligned}
&\Delta = \tilde{\Phi}_+ / \tilde{\Psi} < \delta, \quad \tilde{\Phi}_+ = \Phi_+(\tilde{\mathbf{u}}, \tilde{\boldsymbol{\sigma}}, \tilde{\mathbf{p}}); \\
&\tilde{\Psi} = \int_0^{t_f} \tilde{W}\, dt, \quad \tilde{W}(t) = \int_\Omega \psi(\tilde{\mathbf{u}})d\Omega, \quad \psi = \frac{1}{2}\left[\rho\mathbf{u}^\bullet \cdot \mathbf{u}^\bullet + \boldsymbol{\varepsilon} : \mathbf{C} : \boldsymbol{\varepsilon}\right] \\
&\tilde{\varphi}_+(t,x) = \frac{1}{2}\left[\rho\tilde{\boldsymbol{\eta}} \cdot \tilde{\boldsymbol{\eta}} + \tilde{\boldsymbol{\xi}} : \mathbf{C} : \tilde{\boldsymbol{\xi}}\right], \quad \tilde{\boldsymbol{\eta}} = \tilde{\mathbf{u}}^\bullet - \rho^{-1}\tilde{\mathbf{p}}, \quad \tilde{\boldsymbol{\xi}} = \tilde{\boldsymbol{\varepsilon}} - \mathbf{C}^{-1} : \tilde{\boldsymbol{\sigma}} \\
&\dot{\tilde{W}} = \int_\gamma \tilde{\mathbf{q}} \cdot \tilde{\mathbf{u}}^\bullet d\gamma + \dot{W}_{err}, \quad \dot{W}_{err} = \int_\Omega \left[\rho\tilde{\boldsymbol{\eta}} \cdot \tilde{\mathbf{u}}^{\bullet\bullet} + \tilde{\boldsymbol{\xi}} : \mathbf{C} : \tilde{\boldsymbol{\varepsilon}}^\bullet\right]d\Omega, \quad \tilde{\mathbf{q}} = \mathbf{C} : \tilde{\boldsymbol{\sigma}}.
\end{aligned} \tag{62}$$

Here δ is a small positive constant, $\tilde{\Phi}_+ \geq 0$ is the value of functional Φ_+ on the numerical solution, $\Psi > 0$ is the time integral of the total mechanical energy W, and ψ is the volume density of this energy. The ratio Δ of these two values can serve as a relative integral error of the approximate solution $\tilde{\mathbf{u}}$, $\tilde{\boldsymbol{\sigma}}$, and $\tilde{\mathbf{p}}$, whereas function $\tilde{\varphi}_+$ shows the distribution of local error. The time derivative

(the power) $\dot{W}$ of energy (the power) includes a term $\dot{W}_{err}$ which shows the energy change rate caused by system discretization. It is follows from Eq. (62) that the value of parasitic energy $\int_0^{t_f} |\dot{W}_{err}| dt$ is related to the value of the error Δ.

7   3D Beam Lateral Motions

As an example of algorithm implementation, let us consider the 3D problem of lateral controlled motions for the rectilinear beam with a quadratic cross section (see Fig. 1). The sizes of the cross section do not change along the beam length. It is supposed that the volume forces are absent ($\mathbf{f} = 0$) and the beam is made of homogeneous and isotropic material with given Young's modulus E, Poisson's ratio μ, and volume density ρ. The geometrical beam parameters such as the beam length L and structural height $2a$ as well as terminal time are fixed, and hence the problem is defined in the following 4D time-space domain

$$\Sigma = \{t, x : t \in (0, T), x \in \Omega\}, \quad \Omega = \{x_1, x_2, x_3 : 0 < x_1 < L, |x_2| < a, |x_3| < a\}.$$
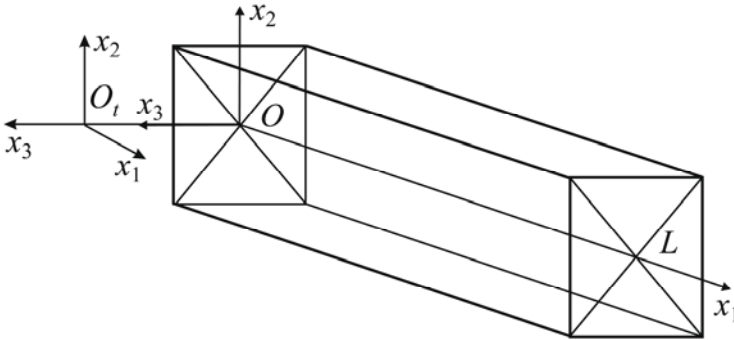
Fig. 1. Rectilinear elastic beam

Let us introduce the fixed reference frame $Ox_1x_2x_3$. Its origin O coincides with the central point of the left beam cross section in the initial time. The x_1-axis is directed along the beam and the coordinate axes Ox_2 and Ox_3 are parallel to the cross section sides. The boundary conditions under consideration are

$$\sigma_{12}|_{x_2=\pm a} = \sigma_{22}|_{x_2=\pm a} = \sigma_{23}|_{x_2=\pm a} = \sigma_{13}|_{x_3=\pm a} = \sigma_{23}|_{x_3=\pm a} = \sigma_{33}|_{x_3=\pm a} = 0$$
$$\sigma_{11}|_{x_1=L} = \sigma_{12}|_{x_1=L} = \sigma_{13}|_{x_1=L} = 0, \quad u_1|_{x_1=0} = u_2|_{x_1=0} = 0$$

(63)

The time-dependent polynomial displacement u_3 of the left beam cross section is chosen as a control boundary function v:

$$u_3\big|_{x_1=0} = v = \sum_{k=2}^{N_v} v_k t^k, \tag{64}$$

where N_v is a given integer defined the number of independent control parameters.

To find an approximate solution and optimize control in the problem of 3D lateral beam dynamics a polynomial representation of the unknown functions was used by Kostin and Saurin [17]. In [19] bivariate piece-wise polynomial splines defined on rectangular meshes were applied to modeling and optimization of lateral Bernoulli beam motions. In this example a finite element approach and spline techniques are used to model 3D beam dynamics.

Let us consider the variational problem (57), fix an approximation order M_p, and choose the following approximations $\tilde{u}_k^{(M_p)}$, $\tilde{\sigma}_{kl}^{(M_p)}$, $k,l = 1,2,3$, for unknown components of displacement vector $\mathbf{u}$ and the stress tensor $\boldsymbol{\sigma}$

$$\tilde{\sigma}_{11}^{(M_p)} = \sum_{i+j=0}^{M_p} \sigma_{11}^{(i,j)}(t,x_1) x_2^{2i} x_3^{2j+1}, \quad \tilde{\sigma}_{23}^{(M_p)} = \sum_{i+j=0}^{M_p-2} \sigma_{23}^{(i,j)}(t,x_1)(a^2-x_2^2)(a^2-x_3^2) x_2^{2i-1} x_3^{2j-2},$$

$$\tilde{\sigma}_{22}^{(M_p)} = \sum_{i+j=0}^{M_p} \sigma_{22}^{(i,j)}(t,x_1)(a^2-x_2^2) x_2^{2i} x_3^{2j+1}, \quad \tilde{\sigma}_{33}^{(M_p)} = \sum_{i+j=0}^{M_p} \sigma_{33}^{(i,j)}(t,x_1)(a^2-x_3^2) x_2^{2i} x_3^{2j+1},$$

$$\tilde{\sigma}_{12}^{(M_p)} = \sum_{i+j=0}^{M_p-1} \sigma_{12}^{(i,j)}(t,x_1)(a^2-x_2^2) x_2^{2i+1} x_3^{2j+1}, \quad \tilde{\sigma}_{13}^{(M_p)} = \sum_{i+j=0}^{M_p} \sigma_{13}^{(i,j)}(t,x_1)(a^2-x_3^2) x_2^{2i} x_3^{2j}; \tag{65}$$

$$\tilde{u}_1^{(M_p)} = \sum_{i+j=0}^{M_p} u_1^{(i,j)}(t,x_1) x_2^{2i} x_3^{2j+1}, \quad \tilde{u}_2^{(M_p)} = \sum_{i+j=0}^{M_p-1} u_2^{(i,j)}(t,x_1) x_2^{2i+1} x_3^{2j+1},$$

$$\tilde{u}_3^{(M_p)} = \sum_{i+j=0}^{M_p} u_3^{(i,j)}(t,x_1) x_2^{2i} x_3^{2j}.$$

Here $u_k^{(i,j)}$ and $\sigma_{kl}^{(i,j)}$ are functions of the time t and coordinate x_1 which will be defined below. These approximations obey the boundary conditions on the beam sides parallel to the x_1-axis.

The symmetry with respect to coordinate planes Ox_1x_2 and Ox_1x_3 allows one to decompose the original problems to four independent subproblems including 3D beam compression-stretching, bending around Ox_2 axis, bending around Ox_3 axis, and torsion. In this example the control displacement in (64) excites only bending motions around Ox_2 axis. The polynomials with respect to the variables x_2 and x_3 proposed in Eq. (65) do not violate the symmetry properties of problem (57) under the boundary and initial conditions (63)–(65) as it has been shown in [17].
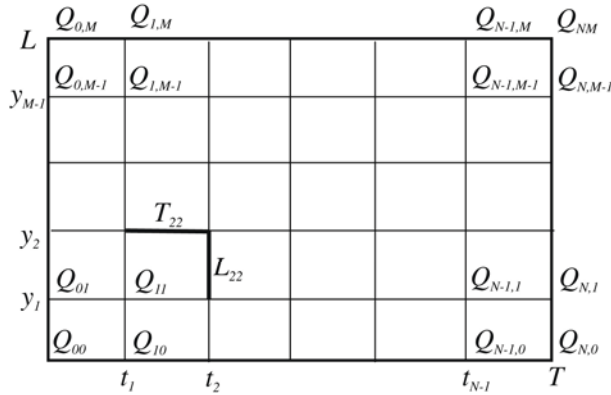
Fig. 2. Space-time mesh.

Divide the two-dimensional time-space domain $\{t, x_1\} \in \Upsilon = (0, T) \times (0, L)$ on $N \times M$ rectangles Υ_{kl} which vertices have coordinates $Q_{k-1, l-1}$, $Q_{k-1, l}$, $Q_{k, l-1}$, $Q_{k, l}$, where $Q_{k, l} = \{t_k, y_l\}$; $t_k > t_{k-1}$, $k = 1, \ldots, N$; $y_l > y_{l-1}$, $l = 1, \ldots, M$; $t_0 = 0$, $t_N = T$, $y_0 = 0$, $y_M = L$ (see Fig. 2). Let also the boundary edges of these time-space rectangles be named $L_{kl} = (Q_{k,l-1}, Q_{kl})$, $k = 0, \ldots, N$, $l = 1, \ldots, M$, and $T_{kl} = (Q_{k-1,l}, Q_{kl})$, $k = 1, \ldots, N$, $l = 0, \ldots, M$. In each 4D time-space subdomain

$$\Sigma_{kl} = \{t, x_1, x_2, x_3 : (t, x_1) \in \Upsilon_{kl}, |x_2| < a, |x_3| < a\}.$$

approximating polynomials $u_\alpha^{(i,j)}$ and $\sigma_{\alpha\beta}^{(i,j)}$ are given

$$u_\alpha^{(j_2, j_3)}(t, x_1) = \sum_{j_0 + j_1 = 0}^{N_p} u_\alpha^{(J)} t^{j_0} x_1^{j_1}, \quad \sigma_{\alpha\beta}^{(j_2, j_3)}(t, x_1) = \sum_{j_0 + j_1 = 0}^{N_p} \sigma_{\alpha\beta}^{(J)} t^{j_0} x_1^{j_1}, \quad \alpha, \beta = 1, 2, 3;$$

$$J = \{j_i\}, \quad i = 0, \ldots, 5; \quad j_0, j_1 \le N_p, \quad j_2, j_3 \le M_p, \quad j_4 = 0, \ldots, N, \quad j_5 = 0, \ldots, M. \tag{66}$$

Here $u_\alpha^{(J)}$ and $\sigma_{\alpha\beta}^{(j_2, j_3)}$ are unknown real coefficients. The integer N_p is chosen so that the equilibrium equation and zero initial conditions in Eq. (57), boundary conditions (63), (64) can be exactly satisfied. In addition, to apply the variational formulation given above the following conformed interelement relations must obey

$$\{t, x_1\} \in L_{kl}, \quad k = 1, \ldots, N-1, \quad l = 1, \ldots, M:$$
$$\tilde{\mathbf{u}}^{(kl)}(t_k, x_1, x_2, x_3) = \tilde{\mathbf{u}}^{(k+1, l)}(t_k, x_1, x_2, x_3),$$
$$\tilde{\mathbf{u}}^{\cdot(kl)}(t_k, x_1, x_2, x_3) = \tilde{\mathbf{u}}^{\cdot(k+1, l)}(t_k, x_1, x_2, x_3);$$
$$\{t, x_1\} \in T_{kl}, \quad k = 1, \ldots, N, \quad l = 1, \ldots, M-1:$$
$$\tilde{\mathbf{u}}^{(kl)}(t, y_l, x_2, x_3) = \tilde{\mathbf{u}}^{(k, l+1)}(t, y_l, x_2, x_3),$$
$$\mathbf{n} \cdot \tilde{\boldsymbol{\sigma}}^{(kl)}(t, y_l, x_2, x_3) = \mathbf{n} \cdot \tilde{\boldsymbol{\sigma}}^{(k, l+1)}(t, y_l, x_2, x_3), \quad \mathbf{n} = (1, 0, 0).$$
$$\tag{67}$$

After satisfying local constraints in Eq. (57) and interelement conditions (67) the resulted finite-dimensional unconstrained minimization problem yields an approximate solution $\tilde{\mathbf{u}}^*(t,x,v)$, $\tilde{\boldsymbol{\sigma}}^*(t,x,v)$ for arbitrary control parameters v_k in (64).

8 Numerical Results

In this section the numerical results of 3D modeling for the lateral beam motions described in the previous section are presented. For geometrical and mechanical parameters the following dimensionless values have been chosen:

$$L=1, \quad a=0.05, \quad T=2, \quad \rho S=1, \quad EI=1, \quad v=0.3, \quad S=4a^2, \quad I=4a^4/3,$$

and the mesh and approximation numbers are assigned: $N=5$, $M=1$, $M_p=2$, $N_p=10$. For numerical solution of this dynamical problem a time uniform mesh with node instants $t_i=iT/N$, $i=1,\ldots,N$, is used. After satisfying equilibrium equation, initial, boundary, and interelement conditions, the total number of degrees of freedom is equal to $N_{DOF}=1985$. The following function of lateral displacement for the left beam cross section is fixed as a sample control law

$$v=(3t^2-t^3)/4, \quad v(0)=\dot{v}(0)=\dot{v}(T)=0, \quad v(T)=1. \tag{68}$$

For the given system data the estimated value of the energy time integral is $\Psi=0.1822$. The absolute and relative integral error defined in Eq. (62) are $\Phi_0=0.0020$, $\Delta_0=1.1\%$.

In the Fig. 3 the relative displacement of the central point $u_3(t,L,0,0)-v(t)$ of the right free beam cross section versus time t is shown.
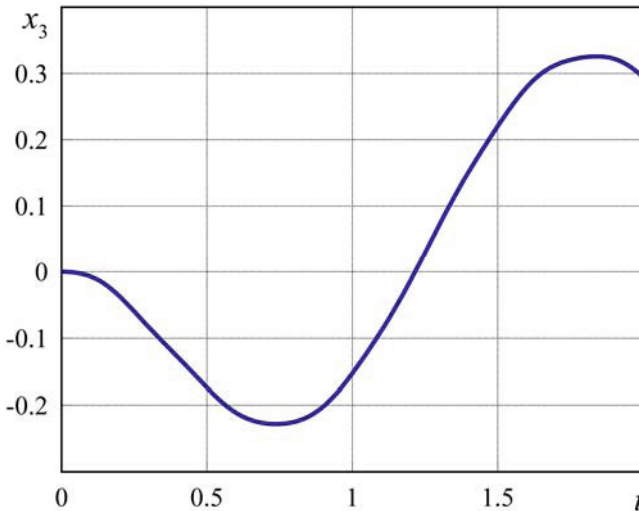
Fig. 3. Relative displacement at the central point of the right free beam cross section vs. time.

In Fig. 4 the function of energy linear density $\psi_1(t, x_1) = \int_{-a}^{a} \int_{-a}^{a} \psi dx_2 dx_3$ is depictured. The distribution of solution local error $\varphi_1(t, x_1) = \int_{-a}^{a} \int_{-a}^{a} \varphi_0 dx_2 dx_3$ along axis Ox_1 is presented in Fig. 5. As it is seen from the figure the maximal errors is concentrated in the area near the left cross section of the beam.
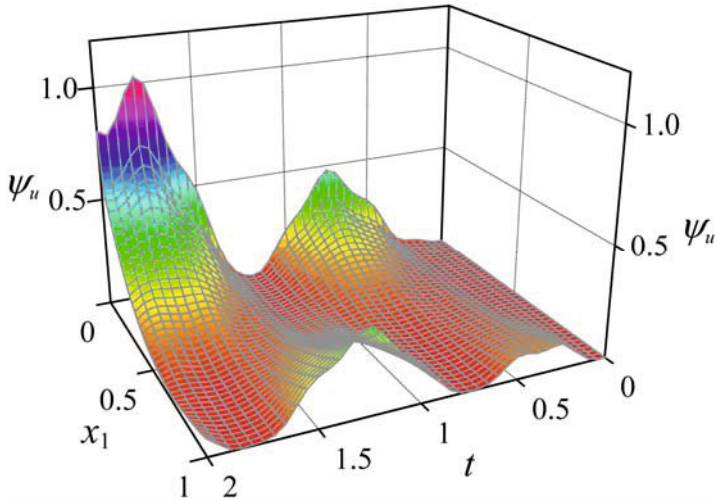
Fig. 4. Linear density of the total mechanical energy along beam axis.
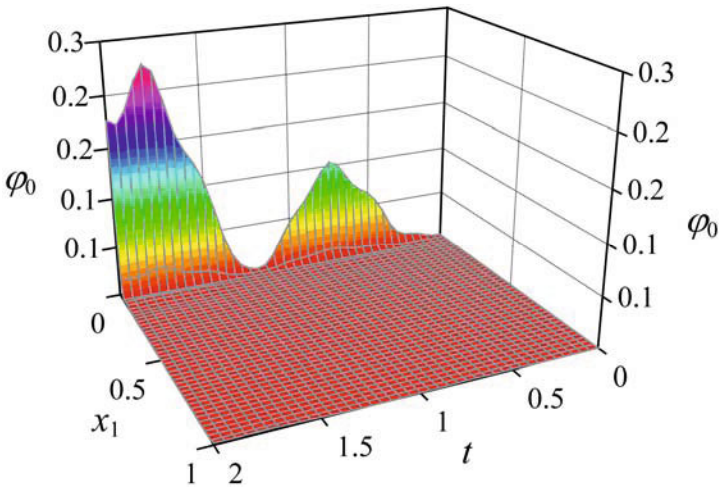
Fig. 5. Distribution of solution local error along beam axis.

The 3D beam model takes into account space deflections in any beam cross section at an arbitrary control instant. As an example, the deformed cross-section shape of the beam at $t = 0.8$ and $x_1 = 0.05$ is displayed in Fig. 6. The local error distribution φ_0 in this cross section at the same time is shown in Fig. 7. The error function on this rectangle reaches its maximal values at the beam edges.
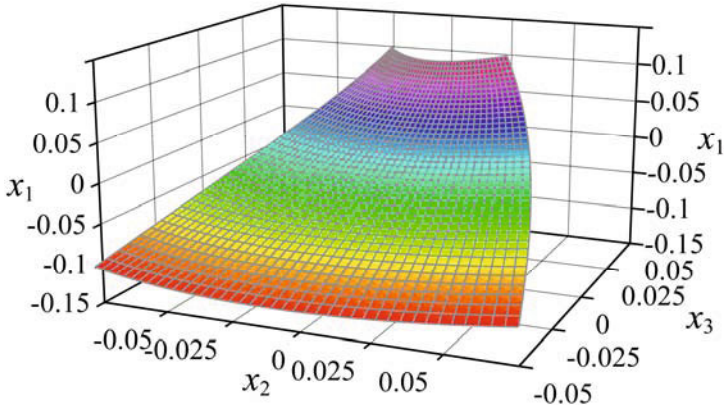
Fig. 6. Deformed cross-section shape.
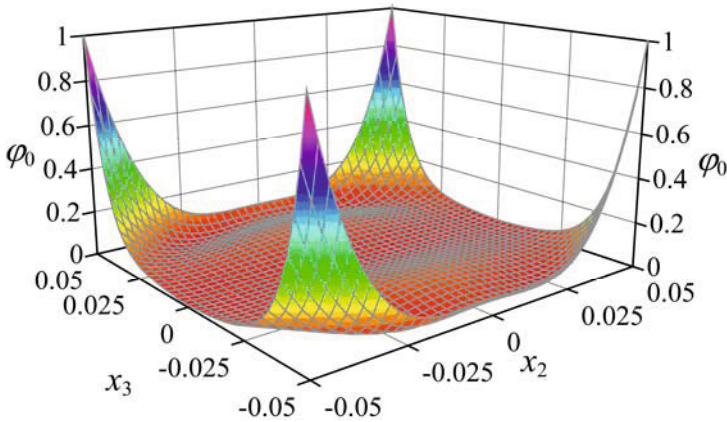
Fig. 7. Distribution of local error in a beam cross section at a fixed time instant.

In this controlled process the total mechanical energy W starting with zero value reaches its maximum during this motion as depictured in Fig. 8. The energy change rate $\dot{W}_{err}$ caused by system discretization is reflected in Fig. 9. The numerical parasitic power defined in Eq. (62) result in noticeable energy underestimate. The linear density distribution along beam axis Ox_1 $\omega(t, x_1) = \int_{-a}^{a} \int_{-a}^{a} \tilde{\xi} : \mathbf{C} : \tilde{\varepsilon} \, dx_2 dx_3$ for this

numerical disbalance is shown in Fig. 10. As it is seen from the figure the maximal energy parasitic source is, analogously to the error distribution φ_1 , the area near the left cross section of the beam.
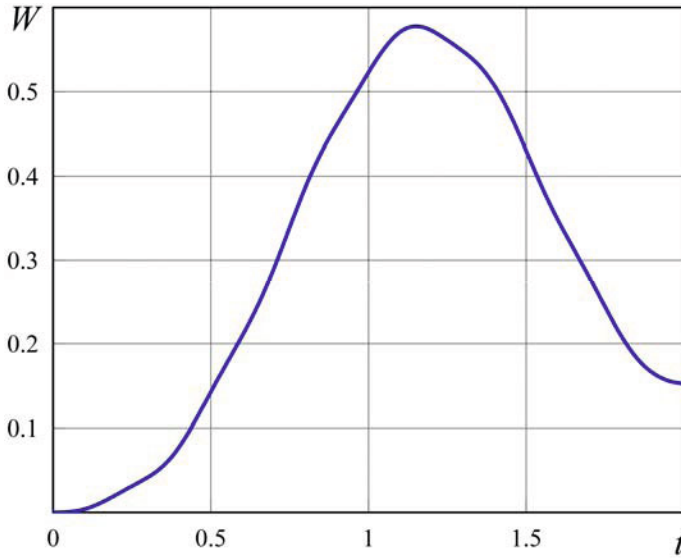
Fig. 8. Mechanical energy versus time.
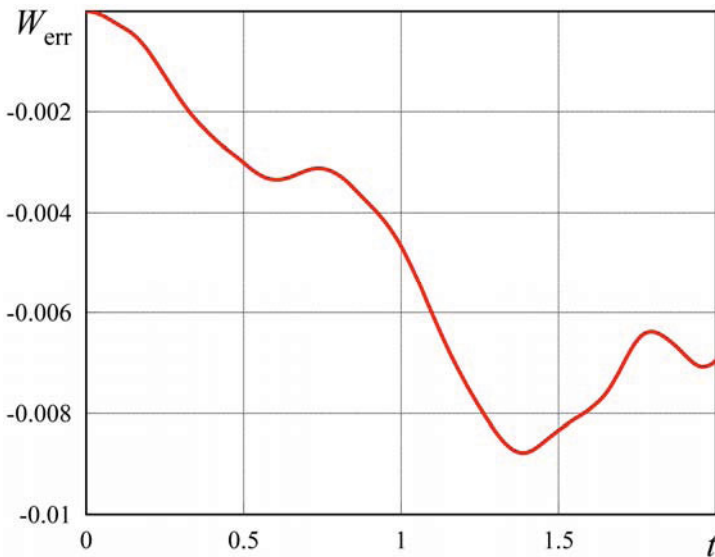
Fig. 9. Energy changes over numerical parasitic disbalance.
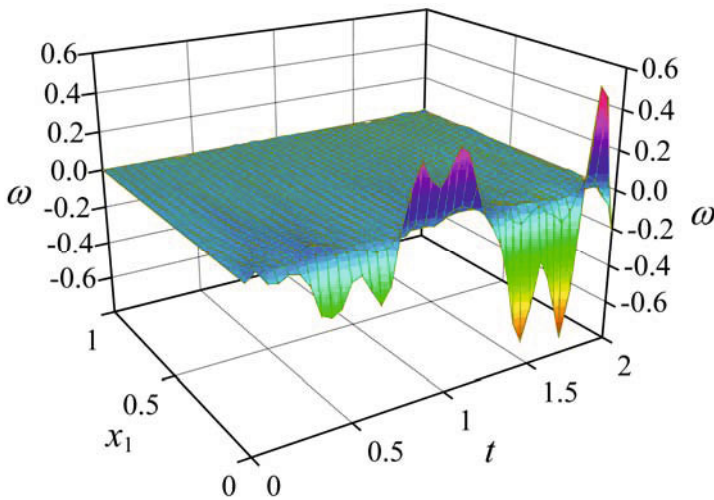
Fig. 10. Linear density distribution along beam axis for the numerical energy disbalance.

9 Conclusions

Based on the method of integrodifferential relations a family of variational principles which stationary conditions are equivalent to the constitutive relation was deduced for the initial boundary value problems of linear elasticity. For these principles the nonnegative functionals under minimization can serve as integral criteria of the solution quality, whereas their integrands characterize the local error distribution. In the case of dynamical boundary value problems under separated boundary constraints on displacement and stress components one of the variational formulations with the action-type functional is decomposed to the Hamilton principle over displacements and its complementary principle on stress and momentum fields.

The numerical algorithm used the time-space piecewise polynomial approximations enables one to construct effective estimates for various integral characteristics (elastic energy, displacements, etc.). This algorithm can be directly applied to nonhomogeneous anisotropic structures. The case of more complex boundary conditions such as aero- and hydrodynamic forces, nonconservative loading, etc. does not encounter principal difficulties. The polynomial spline technique (FEM) incorporated in the algorithm allows one to consider bodies with irregular shapes. The FEM realization will give one the possibility to work out various strategies of p-h adaptive mesh refinement by using a local error estimate. The method can appear to be useful also in advanced beam, plate, and shell theories. The approach worked out can be also applied to other inverse mechanical problems such as shape optimization, identification, and so on as well as to optimal control problems with inequality constraints.

Acknowledgments

References

1. Akulenko, L.D., Kostin, G.V.: The perturbation method in problems of the dynamics of inhomogeneous elastic rods. J. Appl. Math. and Mech. 56, 372–382 (1992)
2. Akulenko, L.D., Nesterov, S.V.: High-Precision Methods in Eigenvalue Problems and their Applications. Charman & Hall/CRC, Boca Raton (2005)
3. Atluri, S.N., Zhu, T.: A new meshless local Petrov-Galerkin (MLPG) approach in computational mechanics. Comput. Mech. 22, 117–127 (1998)
4. Belytschko, T., Lu, Y.Y., Gu, L.: Element-free Galerkin method. Int. J. Num. Methods Eng. 37, 229–256 (1994)
5. Courant, R.: Variational methods for the solution of problem of equilibrium and vibration. Bulletin of American Math Society 49, 1–23 (1943)
6. Courant, R., Hilbert, D.: Methods of mathematical physics, vol. 1. Wiley, Chichester (1937)
7. He, J.H.: Generalized variational principles for thermopiezoelectricity. Arch. Appl. Mech. 72, 248–256 (2002)
8. Chernousko, F.L.: Control of elastic systems by bounded distributed forces. Appl. Math. and Comp. 78, 103–110 (1996)
9. Chernousko, F.L., Ananievski, I.M., Reshmin, S.A.: Control of Nonlinear Dynamical Systems: Methods and Applications. Springer, Heidelberg (1996)
10. Leineweber, D., Bauer, E.I., Bock, H., et al.: An efficient multiple shooting based reduced SQP strategy for large dynamic process optimization. Part 11: Theoretical aspects. Comp. and Chem. Eng. 27, 157–166 (2003)
11. Kostin, G.V., Saurin, V.V.: Integro-differencial approach to solving problems of linear elasticity theory. Doklady Physics 50, 535–538 (2005)
12. Kostin, G.V., Saurin, V.V.: Modeling of controlled motions of an elastic rod by the method of integro-differential relations. J. Comp. and Sys. Sci. Int. 45, 56–63 (2006)
13. Kostin, G.V., Saurin, V.V.: The optimization of the motion of an elastic rod by the method of integro-differential relations. J. Comp. and Sys. Sci. Int. 45, 217–225 (2006)
14. Kostin, G.V., Saurin, V.V.: Modeling and optimization of elastic system motions by the method of integro-differential relations. Doklady Math. 73, 469–472 (2006)
15. Kostin, G.V., Saurin, V.V.: The method of integrodifferential relations for linear elasticity problems. Arch. Appl. Mech. 76, 391–402 (2006)
16. Kostin, G.V., Saurin, V.V.: Variational statement of optimization problems for elastic body motions. Doklady Mathematics 76(1), 629–633 (2007)
17. Kostin, G.V., Saurin, V.V.: An asymptotic approach to the problem of the free oscillations of a beam. J. Appl. Math. and Mech. 71, 611–621 (2007)

18. Kostin, G.V., Saurin, V.V.: A variational formulation in fracture mechanics. Int. J. Fructure 150, 195–211 (2008)
19. Kostin, G.V., Saurin, V.V.: Motion analysis and optimization for beam structures. In: Awrejcewicz, J. (ed.) Modeling, Simulation and Control of Nonlinear Engineering Dynamical Systems: State-of-the-Art, Perspectives and Applications. Springer, Netherlands (2008)
20. Kwon, K.C., Park, S.H., Jiang, B.N., et al.: The least-squares meshfree method for solving linear elastic problems. Comp. Mech. 30, 196–211 (2003)
21. Saurin, V.V.: Variational approaches in the linear theory of elasticity. Doklady Phys. 52(8), 426–430 (2007)
22. Washizu, K.: Variational methods in elasticity and plasticity. Pergamon Press, Oxford (1982)

An Accelerated Newmark Scheme
for Integrating the Equation of Motion
of Nonlinear Systems Comprising Restoring
Elements Governed by Fractional Derivatives

Georgios I. Evangelatos[1] and Pol D. Spanos[2]

[1] Rice University, Department of Civil and Environmental Engineering,
  Houston, Texas USA
  `gie1@rice.edu`
[2] Rice University, L.B. Ryon Endowed Chair in Engineering,
  Houston, Texas USA
  `spanos@rice.edu`

Abstract. In this paper a new efficient algorithm for numerical integration of the equation of motion of a non linear system with restoring forces governed by fractional derivatives in the time domain is devised. This approach is based on the Grunwald-Letnikov representation of a fractional derivative and on the well known Newmark numerical integration scheme for structural dynamic problems. A Taylor expansion is used at every time step to represent the near past terms of the solution; thus, a dual mesh of the time domain is introduced: the coarse mesh is used for the time integration and the fine mesh is used for the fractional derivative approximation. It is shown that with this formulation the problem yields an equivalent non linear system without fractional terms which involves effective values of mass, damping, and stiffness coefficients as a predictive approach and a correction on the excitation. The major advantage of this approach is that a rather small number of past terms are required for the numerical propagation of the solution; and that the calculation of the effective values of mass, damping, and stiffness is performed only once. Several examples of applications are included.

Keywords: Non linear fractional differential equations, Newmark integration scheme, Taylor expansion, Duffing oscillator.

1 Introduction

Fractional calculus has been successfully applied in many engineering fields. Several papers have been published describing the advantages of using fractional derivatives in order to approximate hysteretic behavior [1,2,3], and base isolation with frequency dependent materials [21,24,25]. The advantage of using fractional

derivatives of time lies in their fading memory property [4,5,6]. That is, the fractional derivative of a function in a certain time instant depends on the history of the function and not on a small neighborhood as it is the case of the integer order derivatives. This dependence is computationally inefficient when it comes to numerical evaluation. Specifically, for a small increment forward one must re-evaluate the value of the fractional derivative from the entire history. Using the Grunwald-Letnikov representation, the complexity increases in a quadratic wayyer with the time steps taken. However, due to the fading effect of the Grunwald-Letnikov coefficients which are monotonically decreasing, one can truncate the series after a certain order and achieve a linearly increasing complexity. Padovan [7], suggested another way to lower the computational cost by evaluating the fractional derivative every b number of predetermined steps since the time integration mesh can be fine and the value of fractional derivative would be slowly changing between every time step. Yuan and Agrawal [8], Adolfsson [9] and Ford et all [10], suggested algorithms based on the so-called logarithmic memory principal. When it comes to multi-degree-of -freedom systems the complexity of the integration increases significantly. Schmidt and Gaul [13] implemented an algorithm using finite differences that updates the current fractional derivative value using a so-called transfer function with very good results for multi degree of freedom systems.

The equation of motion of a non linear system with terms governed by fractional derivatives is essentially a multi-term non linear fractional differential equation which accommodates a series of solutions in the time domain. In [17] the general form of linear multi term fractional differential equations is solved and the method can be expanded for the non linear case; in [18] the general non linear multi term fractional differential equation is solved by an algorithm based on the A domain decomposition. In [19] a series of explicit Adams-Bashforth and Adams-Moulton methods were presented for efficient solutions of fractional differential equations. An interesting paper on the pitfalls of fast solvers of fractional differential equations is referenced [22], where points in implementing multi step methods for numerical efficiency are presented. In [23] a selection of algorithms for the estimation of the fractional derivative was given. In [20] the case of the linear spring and non linear fractional derivative terms is considered; efficiency in solving this system was achieved by using the nested mesh variant technique in the convolution integral.

In many respects, the way all these improved algorithms are programmed and implemented is quite complex. For engineering applications where typically the highest derivative appearing is of order two, an algorithm based on commonly used tools is desirable. In this paper, the Newmark time integration scheme is used, the non linearity of the system is readily handled by Newton-Raphson iterations, and the fractional derivative is approximated by the truncated Grunwald-Letnikov representation. The additional efficiency of the algorithm is based on the dual mesh of the time domain and on the continuous Taylor's expansion of the near past terms with respect to the current step. The coarse mesh is used as in the Newmark scheme for time integration, and the fine mesh is used to approximate accurately the fractional derivative at the specific time step. The Taylor expansion up to the second order yields a system with new effective values for the mass and stiffness. Further, a

correction must be made to the excitation. In this formulation one must calculate the effective values of the mass, damping and stiffness coefficients that depend on the order of the fractional derivative and on the time step of the coarse time mesh. Then an equivalent second order non linear differential equation with a correction on the excitation that depends on few past terms must be solved.

2 Fractional Derivative Estimation

Prior to the derivation of the new algorithm, a basic mathematical background is presented on the Grunwald-Letnikov representation of fractional derivatives. The GL representation of a fractional derivative of a function x(t) at a point of time t is given by

$$_{GL}D_{0,t}^{a}x(t) = \lim_{h \to 0} h^{-a} \sum_{k=0}^{\infty} (-1)^{k} \binom{a}{k} x(t - kh),\qquad (1)$$

where alpha is the order of the fractional derivative and 0,t are the terminals as defined in [16] representing the entire history of the function that is taken into account. Equation (1) can now be cast in the form

$$_{GL}D_{0,t}^{a}x(t) = \lim_{h \to 0} h^{-a} \sum_{k=0}^{n} GL_{k}x(t - kh),\qquad (2)$$

where GL_k are the coefficients and n represents the number of past terms used such as

$$GL_{k} = (-1)^{k} \binom{a}{k}\qquad (3)$$

and

$$GL_{n} = (-1)^{n} \binom{a}{n} < threshold .\qquad (4)$$

It is easily proven in [12,14] that

$$GL_{k=0} = 1,\qquad (5)$$

and

$$GL_{k} = \frac{\Gamma(k - a)}{\Gamma(-a)\Gamma(k + 1)} = \frac{k - a - 1}{k} GL_{k-1}.\qquad (6)$$

Thus, equation (6) justifies the fading memory effect of the fractional derivatives since the scalar that multiplies the GL coefficient of step k, yields

$$\frac{k-a-1}{k} < 1. \tag{7}$$

The above described method to approximate the fractional derivative of a function is known as the G1 algorithm and is extensively discussed in [14]. Next, using equation (5) and (7) it is easily deduced that the second coefficient is always the order of the fractional differentiation with a negative sign. A quite accurate estimate can be obtained by using small h [11,14,15,16]. The smaller the h becomes, the larger is the number of past terms that are involved in the estimation of the fractional derivative. It will be shown later that, in the process of solving the non linear fractional differential equation in the time domain, the time step for the time integration is much larger than the time step h for the derivative approximation. Due to this kind of dual meshing of the time domain, useful computational advantages can be obtained.

3   Dual Mesh of the Time Domain

The time domain is discretized in two separate meshes; one coarse mesh for the Newmark time integration scheme, and one fine mesh for the fractional derivative estimation. The integration step is of length Δt and is shown in Figure 1 as the interval between the tall vertical lines. The step of length h is the fine mesh and is the interval between the short vertical lines, each time step of length Δt includes p steps of length h, thus Δt/h=p, Figure 1 helps show the dual meshing technique.
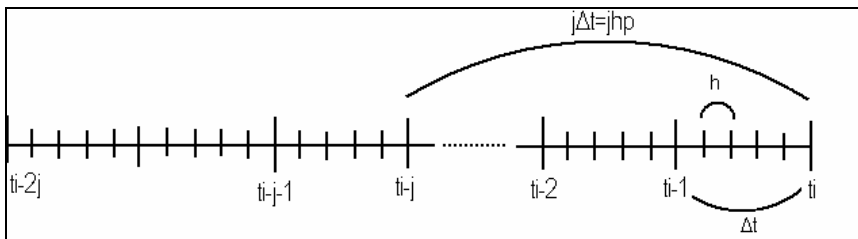
Fig. 1. Time axis discritization, with both the integration time step and the fractional derivative estimation mesh

The accelerated algorithm is based on representing the past terms needed for the Grunwald-Letnikov approximation of the fractional derivative at one point by the Taylor expansion of the same point in time. Since, the Newmark scheme

determines the displacement velocity and acceleration at each time step, a Taylor expansion can be performed for at least up to second order terms. However, the range of an accurate approximation is limited and is shown in Figure 1 as jΔt. Therefore, it is assumed that a small number j of previous terms can be accurately captured by a Taylor expansion, and since several past terms are needed for an accurate approximation, more than one Taylor expansions are needed. The overall number of past terms needed for the fractional derivative estimation is denoted by kj and, thus, k Taylor expansions are needed.

4 Accelerated Algorithm

A non linear fractional differential equation representing the equation of motion of a single degree of freedom system under an arbitrary excitation is given below. Specifically,

$$
m\ddot{x} + cD_{0,t}^{a}x + q(x) = f(t),
\tag{8}
$$

with time integration step of length,

$$
\Delta t = \frac{T}{N},
\tag{9}
$$

where T is the overall time interval of integration and N is the total number of steps to be considered. Clearly considering the equation of motion at two consecutive time instants one derives

$$
m\Delta\ddot{x}_i + c(_{GL}D_{0,t_i}^{a}x_i - {}_{GL}D_{0,t_{i-1}}^{a}x_{i-1}) + \Delta q(x)_i = \Delta f_i,
\tag{10}
$$

where,

$$
\Delta x_i = x_{i+1} - x_i.
\tag{11}
$$

Assuming a constant stiffness coefficient during this small time step equation (10) yields,

$$
m\Delta\ddot{x}_i + c(_{GL}D_{0,t_i}^{a}x_i - {}_{GL}D_{0,t_{i-1}}^{a}x_{i-1}) + k_i\Delta x_i = \Delta f_i.
\tag{12}
$$

Note that the time step Δt is much larger than the step h of the fine mesh and therefore, $\dfrac{\Delta t}{h} = p$ is of the order 5~20. Next, adopting the Grunwald-Letnikov

representation of the fractional derivative and using equation (2) in the fine mesh one derives the form,

$$x_i^{(a)} = h^{-\alpha} \begin{bmatrix} GL_0 & \cdots & GL_{k \bullet j \bullet p} \end{bmatrix} \begin{bmatrix} x_i \\ \cdots \\ x_{i-p} \\ \cdots \\ x_{i-2p} \\ \cdots \\ x_{i-k \bullet j \bullet p} \end{bmatrix} \tag{13}$$

where, p is the number of past terms of length h in a time integration step of length Δt. The number j represents the previous time steps of length Δt that can be approximated accurately by a backwards Taylor expansion using the displacement, velocity and acceleration at a certain time step i. Note that, the number k represents the overall chunks of j time steps that must be taken into consideration to accurately approximate the fractional derivative at a given point. Proceeding to approximating the jph past terms which are of time length $j\Delta t$, using a Taylor expansion one can obtain those terms utilizing the displacement, velocity and acceleration at a given time step i. The Taylor backwards expansion yields the first $j\Delta t$ past terms with respect to the current step x_i. Specifically,

$$x_{i-1} = x_i - h \cdot x_i^{(1)} + h^2/2 \cdot x_i^{(2)} + O(h^3) \tag{14.a}$$

$$x_{i-2} = x_i - 2h \cdot x_i^{(1)} + 4h^2/2 \cdot x_i^{(2)} + O(h^3) \tag{14.b}$$

$$x_{i-3} = x_i - 3h \cdot x_i^{(1)} + 9h^2/2 \cdot x_i^{(2)} + O(h^3) \tag{14.c}$$

$$x_{i-jp} = x_i - jph \cdot x_i^{(1)} + j^2 p^2 h^2/2 \cdot x_i^{(2)} + O(h^3) \tag{14.d}$$

where the number inside the brackets represents the order of the derivative and the power of the time step h respectively. The set of Equations (14) can be cast in a matrix form, and assuming that the $O(h^3)$ can be truncated since the mesh of the time axis for the estimation of the fractional derivative is fine and the past terms $jph << 1$ is quite small, yields

$$
\begin{bmatrix}
x_i \\
x_{i-1} \\
x_{i-2} \\
x_{i-3} \\
\cdots \\
x_{i-jp+1}
\end{bmatrix}
=
\begin{bmatrix}
1 & 0 & 0 \\
1 & -h & h^2/2 \\
1 & -2h & 4h^2/2 \\
1 & -3h & 9h^2/2 \\
1 & \cdots & \cdots \\
1 & -(jp-1)h & (jp-1)^2 h^2/2
\end{bmatrix}
\begin{bmatrix}
x_i \\
x_i^{(1)} \\
x_i^{(2)}
\end{bmatrix}.
\tag{15}
$$

In the same manner the displacements from the step i-jp to the i-2jp+1 can be cast in a matrix form in terms of the displacement, velocity and acceleration of the i-jp step. Equation (16) yields the relationship of these past terms with the Taylor expansion matrix, herein called connectivity matrix, and the displacement, velocity and acceleration of the given step. The same approach can be followed for all the past terms until the i-kjp term. However, it is possible to include higher order derivatives than the acceleration. This can be proven quite helpful in approximating more past terms. Thus, the connectivity matrix of the remaining past terms will have one more column if one selects to include the jerk in the computation.

$$
\begin{bmatrix}
x_{i-jp} \\
x_{i-jp-1} \\
x_{i-jp-2} \\
x_{i-jp-3} \\
\cdots \\
x_{i-2jp+1}
\end{bmatrix}
=
\begin{bmatrix}
1 & 0 & 0 & 0 \\
1 & -h & h^2/2 & -h^3/6 \\
1 & -2h & 4h^2/2 & -8h^3/6 \\
1 & -3h & 9h^2/2 & -27h^3/6 \\
1 & \cdots & \cdots & \cdots \\
1 & -(jph-1) & (jp-1)^2 h^2/2 & -(jp-1)^3 h^3/6
\end{bmatrix}
\begin{bmatrix}
x_{i-j} \\
x_{i-j}^{(1)} \\
x_{i-j}^{(2)} \\
x_{i-j}^{(3)}
\end{bmatrix}
$$

$$\tag{16}$$

Note, that the connectivity matrix is of dimensions jp x 3 for the first p terms, and the connectivity matrix is of dimensions jp x 4 for the rest of the past terms if someone includes the jerk. Note also that the connectivity matrix is constant through out the time integration and it is once built in the beginning. These constant connectivity matrices are called H_0 and H. It can be readily seen that every set of j past steps of length Δt can be obtained in terms of the matrices H_0, H and the displacement, velocity and acceleration of the corresponding time steps. Substituting equation (15), (16) etc into equation (13) one obtains

$$x_i^{(a)} = h^{-\alpha}\begin{bmatrix} 1 & .. & GL_{jp-1} \end{bmatrix}[H_0]\begin{bmatrix} x_i \\ x_i^{(1)} \\ x_i^{(2)} \end{bmatrix} + h^{-\alpha}\begin{bmatrix} GL_{jp} & .. & GL_{2jp-1} \end{bmatrix}[H]\begin{bmatrix} x_{i-j} \\ x_{i-j}^{(1)} \\ x_{i-j}^{(2)} \\ x_{i-j}^{(3)} \end{bmatrix} +$$

$$.. + h^{-\alpha}\begin{bmatrix} GL_{(k-1)jp} & .. & GL_{kjp-1} \end{bmatrix}[H]\begin{bmatrix} x_{i-(k-1)j} \\ x_{i-(k-1)j}^{(1)} \\ x_{i-(k-1)j}^{(2)} \\ x_{i-(k-1)j}^{(3)} \end{bmatrix}. \tag{17}$$

Note that the GL coefficients are fixed after the order of the fractional derivative alpha is fixed and the connectivity matrices H_0 and H are fixed after the time axis is divided by choosing h, Δt, j and k. The vector matrix multiplication will produce a vector 1x3 and a vector 1x4 therefore equation (17) yields

$$x_i^{(a)} = \begin{bmatrix} D_{01} & D_{02} & D_{03} \end{bmatrix}\begin{bmatrix} x_i \\ x_i^{(1)} \\ x_i^{(2)} \end{bmatrix} + \begin{bmatrix} D_{11} & D_{12} & D_{13} & D_{14} \end{bmatrix}\begin{bmatrix} x_{i-j} \\ x_{i-j}^{(1)} \\ x_{i-j}^{(2)} \\ x_{i-j}^{(3)} \end{bmatrix} + ...$$

$$... + \begin{bmatrix} D_{(k-1)1} & D_{(k-1)2} & D_{(k-1)3} & D_{(k-1)4} \end{bmatrix}\begin{bmatrix} x_{i-(k-1)j} \\ x_{i-(k-1)j}^{(1)} \\ x_{i-(k-1)j}^{(2)} \\ x_{i-(k-1)j}^{(3)} \end{bmatrix}. \tag{18}$$

Next, forming the difference of the fractional derivatives from two consecutive time steps yields

$$\Delta x_i^{(a)} = \begin{bmatrix} D_{01} & D_{02} & D_{03} \end{bmatrix}\begin{bmatrix} \Delta x_i \\ \Delta x_i^{(1)} \\ \Delta x_i^{(2)} \end{bmatrix} + \begin{bmatrix} D_{11} & D_{12} & D_{13} & D_{14} \end{bmatrix}\begin{bmatrix} \Delta x_{i-j} \\ \Delta x_{i-j}^{(1)} \\ \Delta x_{i-j}^{(2)} \\ \Delta x_{i-j}^{(3)} \end{bmatrix} + ..$$

$$... + \begin{bmatrix} D_{(k-1)1} & D_{(k-1)2} & D_{(k-1)3} & D_{(k-1)4} \end{bmatrix}\begin{bmatrix} \Delta x_{i-(k-1)j} \\ \Delta x_{i-(k-1)j}^{(1)} \\ \Delta x_{i-(k-1)j}^{(2)} \\ \Delta x_{i-(k-1)j}^{(3)} \end{bmatrix}. \tag{19}$$

Further, combining equation (19) with equation (12) yields

$$(m + cD_{03})\Delta \ddot{x}_i + cD_{02}\Delta \dot{x}_i + (cD_{01} + k)\Delta x_i = \Delta f_i - \Delta f_{correction}. \tag{20}$$

where

$$\Delta f_{correction} = c\begin{bmatrix} D_{11} & D_{12} & D_{13} & D_{14} \end{bmatrix} \begin{bmatrix} \Delta x_{i-j} \\ \Delta x_{i-j}^{(1)} \\ \Delta x_{i-j}^{(2)} \\ \Delta x_{i-j}^{(3)} \end{bmatrix} + ... \tag{21}$$

$$... + c\begin{bmatrix} D_{(k-1)1} & D_{(k-1)2} & D_{(k-1)3} & D_{(k-1)4} \end{bmatrix} \begin{bmatrix} \Delta x_{i-(k-1)j} \\ \Delta x_{i-(k-1)j}^{(1)} \\ \Delta x_{i-(k-1)j}^{(2)} \\ \Delta x_{i-(k-1)j}^{(3)} \end{bmatrix}.$$

The equation of motion is integrated in time using the Newmark time integration scheme where, mass, damping and stiffness are substituted by the effective values shown in equation (20). The solution of this equivalent second order differential equation can be considered as a prediction, and a correction in the same time step of the excitation is due to the additional past terms. Note that the number k is of the order of 3~5. The above algorithm needs a small number of past terms for every integration step in time, and the complete information at these steps such as displacement, velocity and acceleration. However, the steps needed are separated by a number of j steps. There is a convenient way to avoid the saving of the velocity and acceleration at each time step by approximating these quantities using the displacements at neighboring points. However, since the velocity and the acceleration are readily given by the Newmark algorithm it is deemed appropriate to describe the method avoiding the jerk and the approximation through the displacements of the steps. Therefore, for simplification purposes the correction is considered to be given by the equation

$$\Delta f_{correction} = c\begin{bmatrix} D_{11} & D_{12} & D_{13} \end{bmatrix} \begin{bmatrix} \Delta x_{i-j} \\ \Delta x_{i-j}^{(1)} \\ \Delta x_{i-j}^{(2)} \end{bmatrix} + ...$$

(22)

$$... + c\begin{bmatrix} D_{(k-1)1} & D_{(k-1)2} & D_{(k-1)3} \end{bmatrix} \begin{bmatrix} \Delta x_{i-(k-1)j} \\ \Delta x_{i-(k-1)j}^{(1)} \\ \Delta x_{i-(k-1)j}^{(2)} \end{bmatrix}.$$

Next, note that the saving of the velocity and acceleration every j steps is needed along with the displacements to advance the algorithm. This can be proven to be quite powerful for the implementation of the algorithm in multi-degree-of-freedom systems. As Figure 1 shows, the jp steps of the fractional derivative estimation are approximated by the Taylor backwards expansion with respect to the displacement, velocity and acceleration of the ith step. The multiplication of the first jp GL coefficients with the connectivity matrix H produces an equivalent mass, damping and stiffness coefficient matrix which can be added to the original equation of motion turning the fractional non linear differential equation into a non linear equation without fractional terms. The solution of this equation can be called the predictor step. Clearly, this equation takes into account only a limited number of past terms, specifically jp terms of time duration jph=jΔt. The correction step comes from the adjustment of the excitation by a term representing the rest of the past terms associated with the displacement, velocity and acceleration of previous time steps. Once again this is accomplished by a set of equivalent mass, damping and stiffness coefficients that are calculated once in the beginning as a product of the H connectivity matrix and the GL coefficients vector.

5 Numerical Example

As an example, consider a simple linear system of unit mass under a sinusoidal excitation with the equation of motion

$$\ddot{x} + 0.5 D_{0,t}^{0.5} x + 4x = \sin(2t).$$

(23)

Dividing the time domain in Δt of length 0.02 sec, h of 0.001 sec and therefore Δt/h=p=20, and estimating that the max Δt for Newmark is T/10=0.2962 where T is the natural period of the system, one can obtain the number j= Δt max/Δt=15 steps. In 15 coarse steps that are approximated by a Taylor expansion there are 15x20=300 fine past terms, where $h^{-\alpha} GL_{300} \approx 10^{-3}$. The connectivity matrix

H_0 is constructed from equation (15) and the vector of dimensions 1x3 representing the correction on the mass, damping and stiffness is calculated by the multiplication GLxH$_0$ and yields $D_0 = [1.0314 \quad 0.3084 \quad -0.0155]$. Therefore, by utilizing equation (20), the equation to be solved now becomes

$$(0.5\bullet(-0.0155) + 1)\Delta\ddot{x} + 0.5\bullet0.3084\Delta\dot{x} + (4 + 0.5\bullet1.0314)\Delta x = \Delta\sin(2t) - \Delta f$$

(24)

where Δf is the rest of the past terms given by equation (22).

Solving this equation without any correction and comparing it to the readily derivable frequency domain solution one can assess the accumulating error from Figure 2.
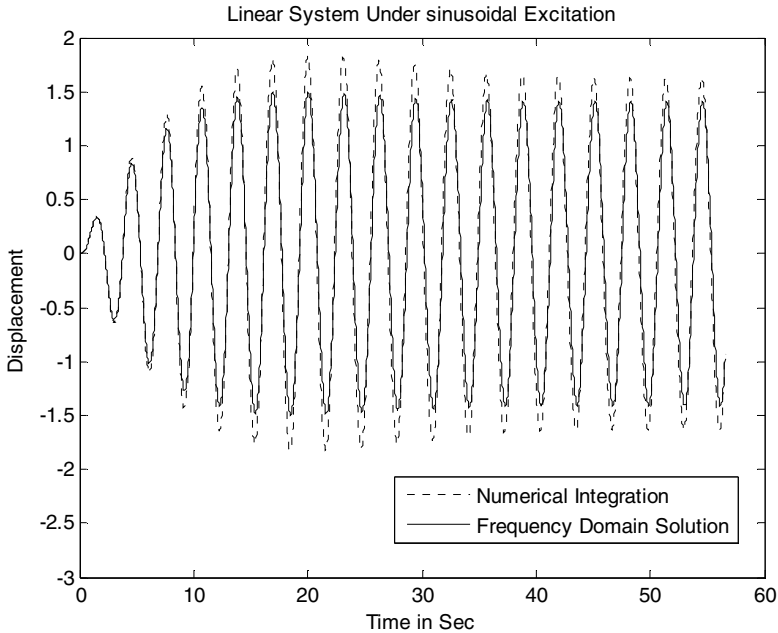
Fig. 2. Frequency domain solution vis a vis numerical integration without correction step, p=20, j=15, k=1.

It is easily seen the 300 past terms are not enough to capture the steady state response as well as the transient response. Calculating next the D_1 and D_2 vectors that are derived as the product of the next 600 GL coefficients with the H_0 avoiding the use of the jerk, one obtains

$$D_1 = [-0.3025 \quad 0.0374 \quad -0.0034]$$

(25)

and

$$D_2 = \begin{bmatrix} -0.1339 & 0.0180 & -0.0017 \end{bmatrix}. \tag{26}$$

These vectors multiplied by $\begin{bmatrix} \Delta x_{i-15} \\ \Delta x_{i-15}^{(1)} \\ \Delta x_{i-15}^{(2)} \end{bmatrix}$ and $\begin{bmatrix} \Delta x_{i-30} \\ \Delta x_{i-30}^{(1)} \\ \Delta x_{i-30}^{(2)} \end{bmatrix}$ respectively will correct

the solution by taking into account another 600 past terms. Figure 3 shows the solution with correction of 2 past terms and specifically of the past terms x_{i-15} and x_{i-30}.
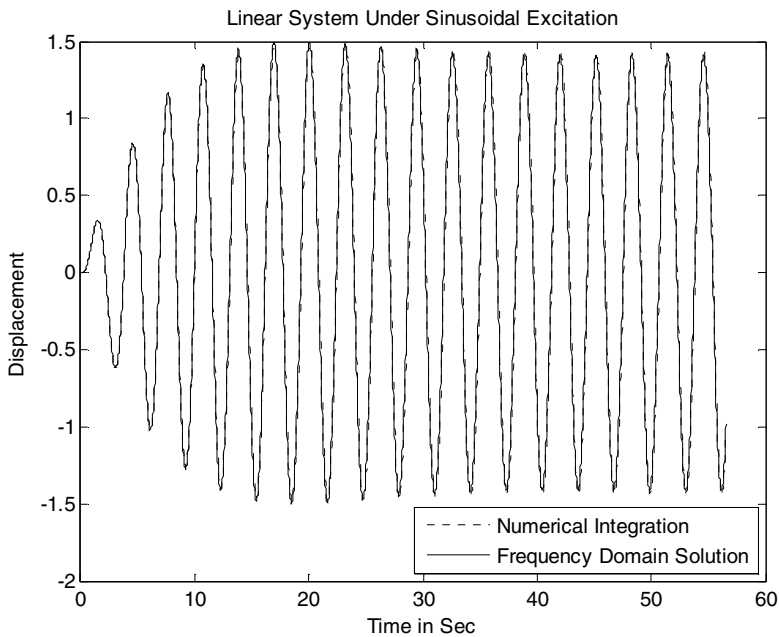
Fig. 3. Frequency domain solution vis a vis numerical integration with correction step of two past terms, p=20, j=15, k=3.

Figure 4 shows the solution with correction step of three past terms and specifically of the past terms x_{i-15}, x_{i-30} and x_{i-45}. Calculating the vector D_3 one obtains

$$D_3 = \begin{bmatrix} -0.0691 & 0.0128 & -0.0016 \end{bmatrix}. \tag{27}$$
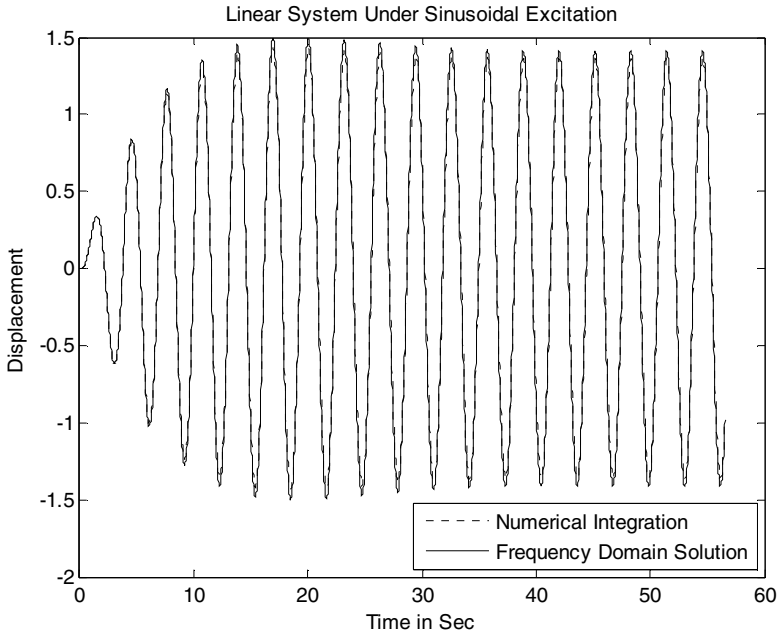
Fig. 4. Frequency domain solution vis a vis numerical integration with correction step of three past terms, p=20, j=15, k=4.

6 Numerical Results for Earthquake Excitation

Consider next the earthquake excitation of ElCentro California 1940 USA, and a single degree of freedom oscillator with restoring forces governed by fractional derivatives. Proceed in implementing the described algorithm to obtain the system response. In this regard, Figure 5 shows the El Centro accelerogram.

The coarse time mesh for the integration in time is of length $\Delta t=0.02$ seconds and the fine mesh is h=0.001 and h=0.004 seconds, thus p=20 and p=5. The range of the Taylor expansion is equal to $3\Delta t$, $4\Delta t$, $5\Delta t$ and $6\Delta t$ thus j=3,4,5 and 6. Since four past steps have been used in every simulation k=5. The range of the Taylor expansion can be obtained as in the previous numerical example, thus assuming that the max Δt for Newmark is T/10 where T is the natural period of the system, one can obtain the number j as j=Δt max/Δt. It can be argued that the choice of the number j representing the range of an acceptable approximation by the Taylor expansion can be rigorously addressed. However such an attempt would be a quite laborious process and is currently out of the scope of this article. Empirically, however it is seen that the first jΔt seconds including the jp past terms must have a significantly high threshold. That is equation (4) for n=jp must have a much larger value than n=kjp which is the threshold for the entire representation range. This is
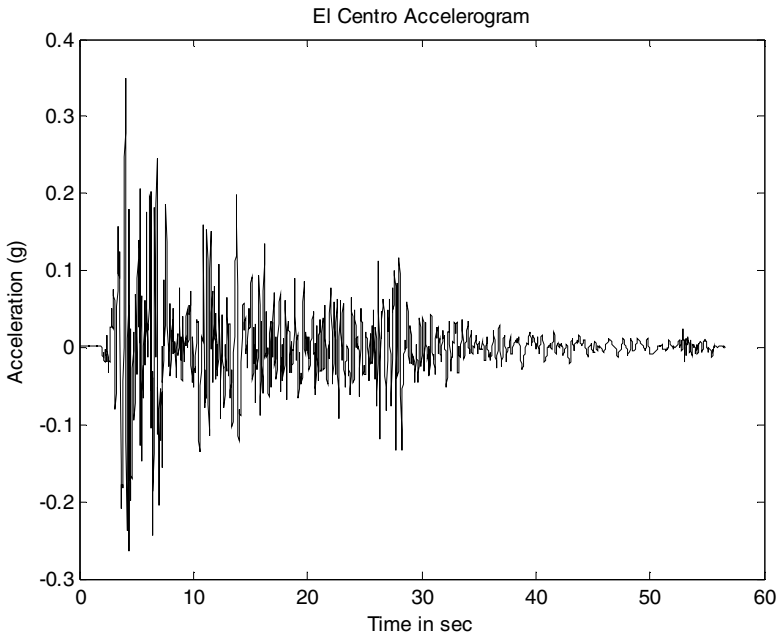
Fig. 5. The El-Centro Accelerogram; g is the gravitational acceleration.

readily explained, by the fact that the correcting terms must account for larger correction than the correction achieved by the first Taylor expansion and the changing of the mass damping and stiffness values. Results are presented for linear systems, and non linear systems of the Duffing type. The same values of fractional derivatives have been used for both the linear and non linear cases and quite large values of the non linearity strength ε have been considered. The system considered herein has an equation of motion given by equation (8) with a Duffing kind nonlinearity

$$m\,\ddot{x} + cD_{0,t}^{\alpha}x + kx(1 + \varepsilon x^2) = f(t). \qquad (28)$$

The results of solving equation (25) with the proposed algorithm are compared to the benchmark algorithm results which uses the truncated Grunwald-Letnikov representation. Pertinent results for various values of fractional derivatives are shown in Figures 7, 9 and 11, in addition for linear systems this approach is verified through comparison with the frequency domain solution and the results are shown in Figures 6, 8 and 10.
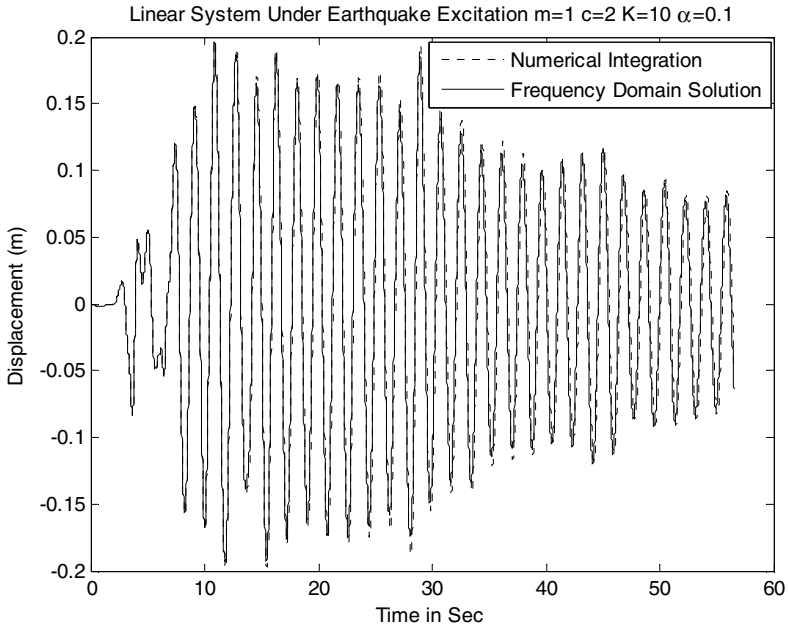
Fig. 6. Frequency domain solution vis a vis numerical integration with correction step of four past terms p=20, j=5, k=5.
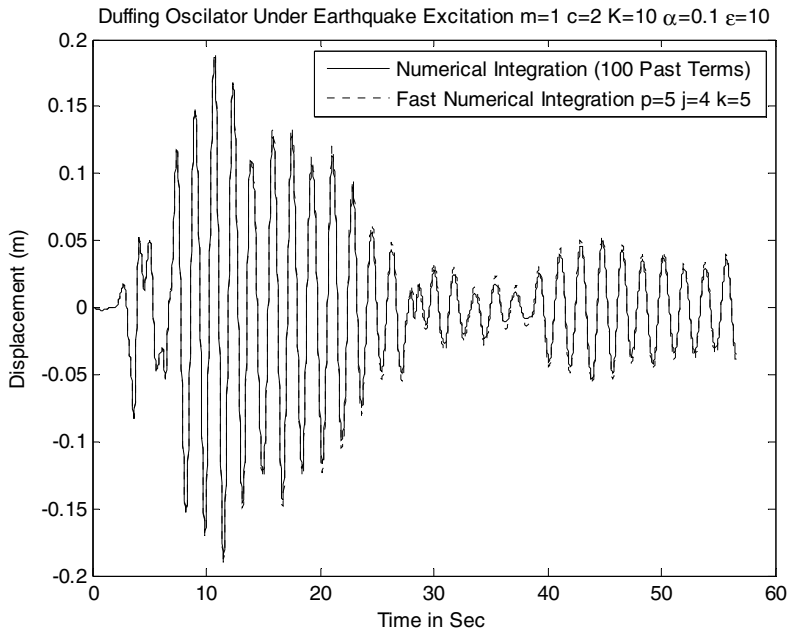
Fig. 7. Numerical solution with past terms corresponding to GL coefficients of the order 10^{-3} vis a vis the enhanced numerical integration algorithm
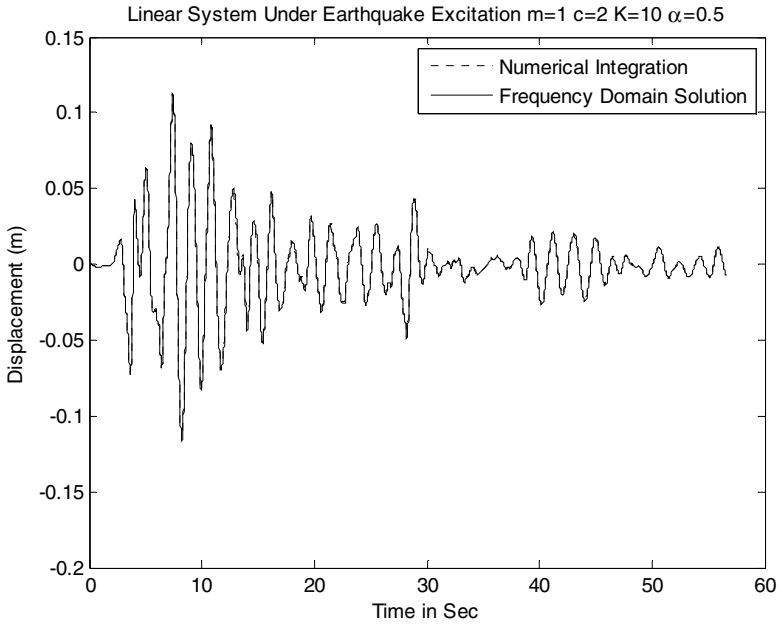
Fig. 8. Frequency domain solution vis a vis numerical integration with correction step of four past terms p=20, j=9, k=5.
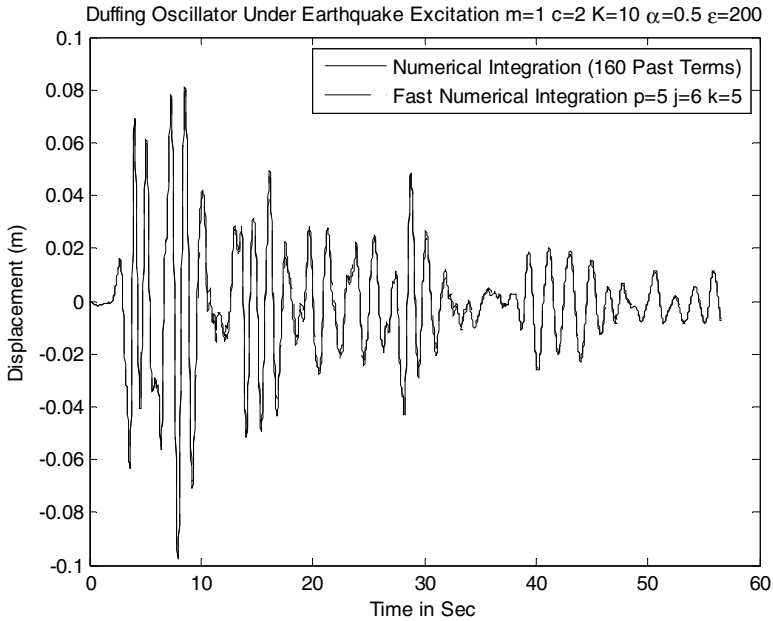
Fig. 9. Numerical solution with past terms corresponding to GL coefficients of the order 10^{-3} vis a vis the enhanced numerical integration algorithm
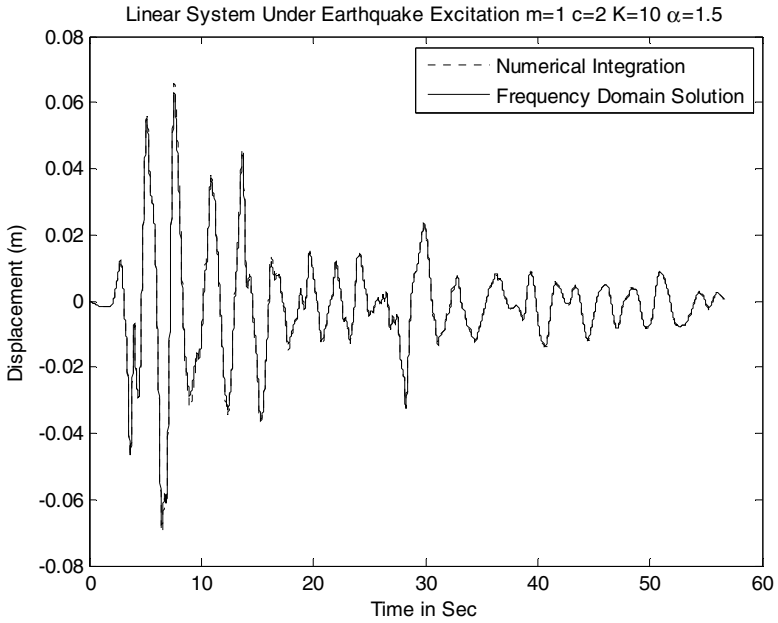
Fig. 10. Exact solution vis a vis numerical integration with correction step of four past terms p=20, j=9, k=5.
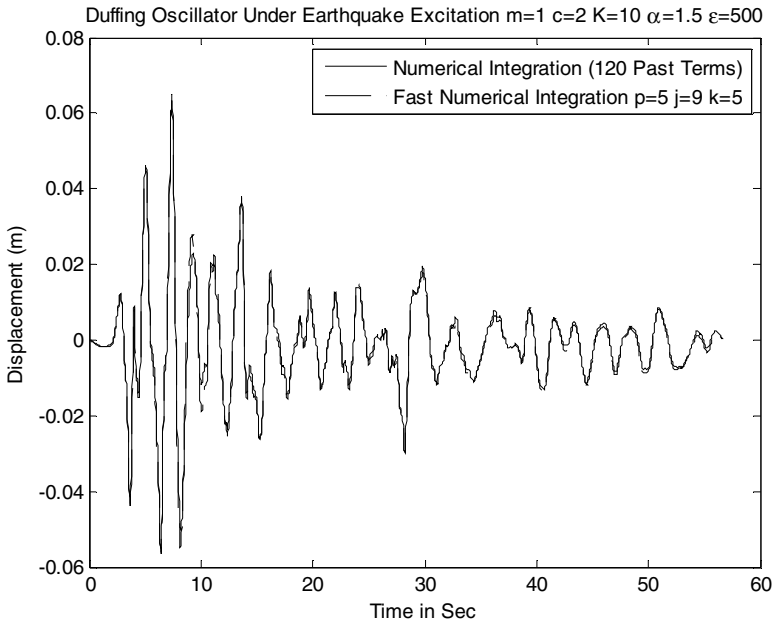
Fig. 11. Numerical solution with past terms corresponding to GL coefficients of the order 10^{-3} vis a vis the enhanced numerical integration algorithm

7 Concluding Remarks

Efficient determination of the response of systems of single or multi –degree-of-freedom endowed with restoring terms governed by fractional derivatives has been pursued in this paper. For this purpose the Grunwald-Letnikov representation of the fractional derivative has been adopted; this representation involves several past terms of the process itself. Thus, the numerical evaluation of fractional derivatices requires a high number of computations due to their memory effect.

A modified Newmark algorithm that includes a correction on the excitation has been used to numerically solve the equation. It has been shown that a dual meshing technique in the time domain in conjunction with the Taylor expansion and the Grunwald-Letnikov fractional derivative representation yields an efficient Newmark time integration scheme for the determination of the response of non linear oscillators comprising fractional derivative terms. In this context, the governing equation of motion can be transformed into a second order differential equation using new effective values of mass, damping, and stiffness without any fractional terms involved. The effective values are calculated once by a vector representing the GL coefficients and the connectivity matrix representing the Taylor expansion. Next, this equation is solved for an excitation corrected by the contribution of few past terms. The new scheme has been used to obtain simulation results for linear systems under seismic excitation which have been validated by the solution derived by frequency domain techniques. For similar excitations, it has been shown that the new scheme can be effectively implemented for determining the dynamic response of nonlinear systems endowed with fractional derivative terms.

Acknowledgements

References

1. Nutting, P.G.: A new general law deformation. Journal of the Franklin Institute 191, 678–685 (1921)
2. Gemant, A.: A method of analyzing experimental results obtained by elasto-viscous bodies. Physics 7, 311–317 (1936)
3. Caputo, M.: Vibrations on an infinite viscoelastic layer with a dissipative memory. Journal of the Acoustical Society of America 56(3), 897–904 (1974)
4. Galucio, A.C., Deu, J.F., Ohayon, R.: Finite element formulation of viscoelastic sandwich beams using fractional derivative operators. Comput. Mech. 33, 282–291 (2004)
5. Bossemayer, H.: Evaluation technique for dynamic moduli. Mech Time-depend Mat 5, 273–291 (2001)
6. Adolfsson, K., Enelund, M., Olson, P.: On the fractional order model of viscoelaticity Mech. Time-depend Mat 9, 15–24 (2005)

7. Padovan, J.: Computational Algorithms for FE formulations involving fractional operators. Computational Mechanics 2, 271–287 (1987)
8. Yuan, L., Agrawal, O.P.: A numerical scheme for dynamic systems containing fractional derivatives. Vibration Acoustics 124, 321–324 (2002)
9. Adolfsson, K., Enelund, M., Larsson, S.: Adaptive discretization of fractional order viscoelasticity using sparse time history. Computational Methods of Applied Mechanical Engineering 193, 4567–4590 (2004)
10. Ford, N.J., Simpson, A.C.: The numerical solution of fractional differential equations speed vs accuracy. Numerical Algorithms 26, 333–346 (2001)
11. Fractional differential equations: an introduction to fractional derivatives, fractional differential equations, to methods of their solution and some of their applications by P.A. Podlubny Mathematics in Science and Engineering, vol. 198. Academic Press, London (1999)
12. Schmidt, A., Gaul, L.: Finite Element Formulation of Viscoelastic Constitutive Equations Using Fractional Time Derivatives. Non linear Dynamics 29, 37–55 (2002)
13. Schmidt, G.L.: On the numerical evaluation of fractional derivatives in multi degree of freedom systems. Signal Processing 86, 2592–2601 (2006)
14. Oldham, K.B., Spanier, J.: The fractional calculus. Mathematics in Science and Engineering, vol. III. Academic Press, New York
15. Samko, S.G., Kilbas, A.A., Marichev, O.I.: Fractional Integrals and Derivatives Theory and Applications. Gordon and Breach Science Publishers (1993)
16. Miller, K.S., Ross, B.: An Introduction to Fractional Calculus and Fractional Differential Equations. John Wiley & Sons, Chichester (1993)
17. Katsikadelis, J.T.: Numerical solutions of multi-term fractional differential equations. ZAMM 89(7), 593–608 (2009)
18. Momani, S.: A numerical scheme for the solution of multi-order fractional differential equations. Aplied mathematics and computation 182, 761–770 (2006)
19. Garappa, R.: On some explicit Adams multistep methods for fractional differential equations. Journal of computational and applied mathematics 229, 392–399 (2009)
20. Hiroshi, N., Nouyuki, S.: Power time numerical integration algorithm for non linear fractional differential equations. Journal of Vibration and control 14(9-10), 1313–1322 (2008)
21. Makris, N.: Complex parameter Kelvin model for elastic foundations. Earthquake Engineering and Structural Dynamics 23, 251–264 (1994)
22. Diethelm, K., Ford, J.M., Ford, N.J., Weilbeer, M.: Pitfalls in fast numerical solvers for fractional differential equations. Journal of computational and applied mathematics 186, 482–503 (2006)
23. Diethelm, K., Ford, N.J., Freed, A.D., Luchko, Y.: Algorithms for the fractional calculus: A selection of numerical methods. Computational methods in applied mechanical engineering 194, 743–773 (2005)
24. Makris, N., Constantinou, M.C.: Fractional derivative Maxwell model for viscous dampers. Journal of Structural Engineering ASCE 117(9), 2708–2724 (1991)
25. Koh, C.G., Kelly, L.M.: Application of fractional derivatives to seismic analysis of base isolated models. Earthquake Engineering and Structural Dynamics 19(2), 229–241 (1990)

Part II
Experimental Mechanics

Photoelastic Tomography as Hybrid Mechanics

H. Aben, L. Ainola, and A. Errapart

Institute of Cybernetics, Tallinn University of Technology,
21 Akadeemia tee, 12618 Tallinn, Estonia
aben@cs.ioc.ee, aben@glasstress.com

Abstract. Photoelastic tomography is a non-destructive method of 3D stress analysis. It permits determination of normal stress distribution in an arbitrary section of a 3D test object. In case of axial symmetry also the shear stress distribution can be determined directly from the measurement data. To determine also the other stress components one can use equations of the theory of elasticity. Such a combined application of experimental measurements and numerical handling of the equations of the theory of elasticity is named hybrid mechanics. It is shown that if stresses are due to external loads, the hybrid mechanics algorithm is based on the equations of equilibrium and compatibility. In the case of the measurement of the residual stress in glass the compatibility equation can not be applied. In this case a new relationship of axisymmetric thermoelasticity, the generalized sum rule can be applied.

1 Classical Tomography

Tomography is a powerfull method for the analysis of the internal structure of different objects, from human bodies to parts of atomic reactors [1]. In tomography, some radiation (X-rays, protons, acoustic waves, light, etc.) is passed through a section of the object in many directions, and properties of the radiation after it has passed the object (intensity, phase, deflection, etc.) are measured on many rays (Fig. 1). Experimental data $g(l, \theta^*)$ for different values of the angle θ^* are called *projections*.

If $f(r, \varphi)$ is the function that determines the distribution of a certain parameter of the field, the experimental data for a real pair l, θ^* can be expressed by the Radon transform of the field,

$$g(l, \theta^*) = \int_{-\infty}^{\infty} f[r(l, \theta^*, z), \varphi(l, \theta^*, z)] \mathrm{d}z . \qquad (1.1)$$
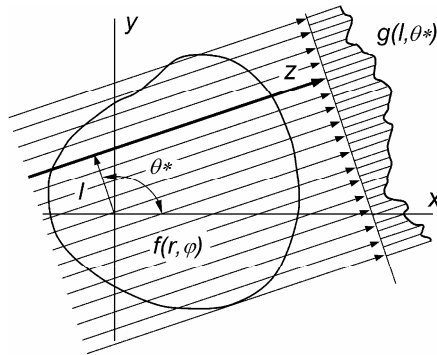
Fig. 1. Scheme of tomographic measurements.

When projections for many values of $\theta*$ have been recorded, the function $f(r, \varphi)$ is determined from the Radon inversion

$$f(r, \varphi) = \frac{1}{2\pi^2} \int_0^\pi d\theta' \int_{-\infty}^\infty \frac{\partial g(l, \theta*)}{\partial l} \frac{dl}{r\cos(\theta*-\varphi) - l}. \tag{1.2}$$

Many numerical algorithms for solving Eq. (1.2) have been elaborated [1].

The question arises whether it is possible to determine tomographically also the stress fields in 3D objects. This problem is not trivial, for the following reason. Classical tomography considers only determination of scalar fields, i.e., every point of the field is characterized by a single number (the coefficient of attenuation of the X-rays, the acoustical or optical index of refraction, etc.). Since stress is a tensor, in stress field tomography every point of the field is characterized by six numbers. Thus the problem is much more complicated in principle. Let us mention that while many books are devoted to scalar field tomography, there is only a single book, written by Sharafutdinov [2], devoted to mathematical problems of the tensor field tomography.

2 Photoelastic Tomography

2.1 Linear Approximation in Integrated Photoelasticity

Let us assume that in two parallel sections $z = z_0$ and $z = z_0 + \Delta z$ of an arbitrary 3D specimen tomographic photoelastic measurements have been carried out and the integrals V_1 and V_2 have been measured for many azimuths β (Fig. 2):
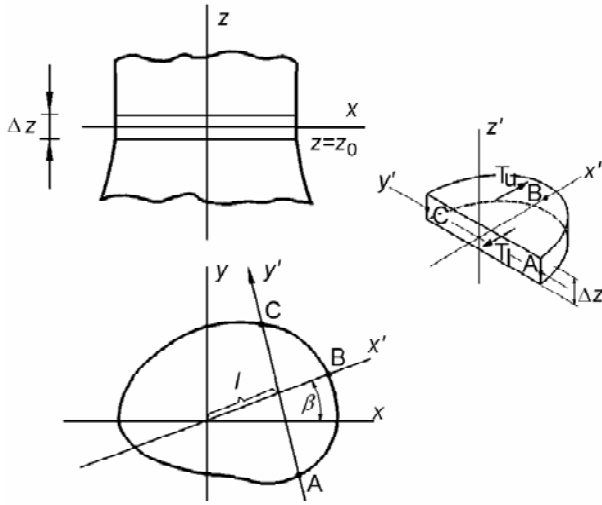
Fig. 2. Illustration explaining tomographic measurement scheme.

$$V_1 = \Delta \cos 2\varphi = C\int (\sigma_{x'} - \sigma_{z'})dy', \tag{2.1}$$

$$V_2 = \Delta \sin 2\varphi = 2C\int \tau_{x'z'}dy'. \tag{2.2}$$

It is assumed that for tomographic measurements the specimen is rotated around the z axis. Equations (2.1) and (2.2) are valid if birefringence is weak or rotation of the principal stress axes is small [3, 4].

Sharafutdinov suggested the following method for the measurement of the distribution of the axial stress σ_z [2]. Besides the measurement of the functions V_1 and V_2, the value of the axial stress σ_z is to be measured on the boundary of the cross-section. Applying to the functions V_1 and V_2 the transverse ray transformation [2], the σ_z field is determined from the boundary value problem for the Poisson equation. Sharafutdinov has shown that the solution of this tomographic problem is unique and that only distribution of σ_z can be determined in this way.

The drawback of this method is that in addition to tomographic photoelastic measurements the boundary values of σ_z must be measured. That is possible only in the case when boundary of the cross-section is described by a convex curve. Besides, the transverse ray transformation is rather complicated. The tomographic algorithm of Sharafutdinov has not been applied in practice, although it is important from the point of view of the theory of photoelastic tomography.

Let us mention that Schupp [5] has developed a method for 3D stress field tomography based on interferometric measurement of the absolute optical retardation. Such measurements are carried out by rotating the test object around three mutually perpendicular axes x, y, and z. The author also limits himself to linear approximation. The method proposed is mathematically correct and has been proved also with numerical and physical experiments. Unfortunately, the author had to confess that he

was able to obtain only qualitative results concerning the stress field. We have to conclude that to base photoelastic tomography on the interferometric measurement of the absolute optical retardations is very complicated.

2.2 The Method of Decomposition

Since Radon inversion for the tensor field does not exist, the problem of stress field tomography can be solved if we can reduce it to a problem of scalar field to-mography for a single component of the stress tensor. That can be done in the fol-lowing way [4, 6]. Let us assume that photoelastic tomographic measurements have been carried out on two parallel sections, a distance Δz apart from each other, rotating the specimen around the z axis (Fig. 2). The values of the functions V_1 and V_2 in the auxiliary section we denote V'_1 and V'_2. Considering the equilibrium of the three-dimensional segment ABC in the direction of the x' axis (Fig. 2), we may write

$$\Delta z \int_{A}^{C} \sigma_{x'} \mathrm{d}y' = T_{\mathrm{u}} - T_{\mathrm{l}} \,, \tag{2.3}$$

where T_{u} and T_{l} are the shear forces on the upper and lower surfaces of the seg-ment, respectively:

$$T_u = \frac{1}{2C} \int_{l}^{B} V'_2 \mathrm{d}x' , \quad T_l = \frac{1}{2C} \int_{l}^{B} V_2 \mathrm{d}x' . \tag{2.4}$$

Taking into consideration the relationships (2.3) and (2.4), Eq. (2.1) reveals

$$\int_{A}^{C} \sigma_z \mathrm{d}y' = \frac{1}{2C\Delta z} (\int_{l}^{B} V'_2 \mathrm{d}x' - \int_{l}^{B} V_2 \mathrm{d}x') - \frac{V_1}{C} . \tag{2.5}$$

Since tomographic photoelastic measurement data can be obtained for all the light rays y', Eq. (2.5) expresses the Radon transform of the field of the stress σ_z. Thus we have reduced a problem of tensor field tomography to a problem of scalar field tomography for a single stress component σ_z. The field of σ_z can be determined using any of the well-known Radon inversion techniques [1]. Rotating the speci-men by tomographic measurements around the axes x and y, fields of σ_x and σ_y can also been determined.

  In case of an axisymmetric stress field, the problem is reduced to a problem of one-dimensional tomography [7]. In this case the distribution of σ_z is determined from Eq. (2.5) with Abel inversion [8]. The shear stress $\tau_{x'z'}$ can be expressed as

$$\tau_{x'z'} = \tau_{rz} \cos \beta \,, \tag{2.6}$$

where τ_{rz} is shear stress in cylindrical coordinates. Inserting (2.6) into (2.2), a modi-fied algorithm of Abel inversion can be elaborated for the calculation of τ_{rz} [8].

3 Algorithms of Hybrid Mechanics

3.1 Stresses due to External Loads

The first hybrid mechanics algorithm for complete determination of the axisymmetric stress field with photoelastic tomography was elaborated by Doyle and Danyluk [9, 10]. We consider the same problem in a somewhat different way.

Let us express the stress components as power series:

$$\sigma_r = \sum_{k=0}^{m} a_{2k}\rho^{2k}, \quad \sigma_\theta = \sum_{k=0}^{m} b_{2k}\rho^{2k}, \quad \sigma_z = \sum_{k=0}^{m} c_{2k}\rho^{2k}, \quad \tau_{rz} = \sum_{k=1}^{m} d_{2k-1}\rho^{2k-1}, \quad (3.1)$$

where a_{2k}, b_{2k}, c_{2k} and d_{2k-1} are the coefficients to be determined and ρ is dimensionless radius.

Introducing expression for σ_z into Eq. (2.5) we have

$$\sum_{k=0}^{m} c_{2k} G_{2k} = F(x), \qquad (3.2)$$

where

$$G_0 = \sqrt{1 - \xi^2}, \qquad G_{2k} = \frac{1}{2k+1}(G_0 + 2k\xi^2 G_{2k-2}), \qquad (3.3)$$

and $\xi = x/R$.

Since according to Eq. (2.5) $F(x)$ has been determined experimentally, formula (3.2) reveals a system of algebraic equations from which the coefficients c_{2k} can be determined. Thus, distribution of the axial stress σ_z has been determined.

Inserting expressions for $\tau_{x'z'}$ (2.6) into Eq. (2.2) reveals after integration

$$\frac{\Delta \sin 2\varphi}{4CR} = \sum_{k=1}^{m} d_{2k-1} T_{2k-1}, \qquad T_{2k-1} = \xi G_{2k-2}. \qquad (3.4)$$

From the system of equations (3.4) the shear stress coefficients d_{2k-1} can be calculated.

The axial stress σ_z and the shear stress τ_{rz} are the only stress components which can be determined directly from measurement data. However, in hybrid mechanics one can use equations of the theory of elasticity. If expansions (3.1) are introduced into the compatibility equation

$$\frac{\partial}{\partial \rho}[\sigma_\theta - \mu(\sigma_r + \sigma_z)] - (1+\mu)\frac{\sigma_r - \sigma_\theta}{\rho} = 0, \qquad (3.5)$$

and into the equilibrium equation

$$\frac{\partial \sigma_r}{\partial \rho} + \frac{\sigma_r - \sigma_\theta}{\rho} + \frac{\partial \tau_{rz}}{\partial \zeta} = 0, \qquad \zeta = \frac{z}{2(R+R')}, \qquad (3.6)$$

we obtain after some transformations

$$a_{2k} = \frac{2k\mu}{(2k+1)^2 - 1} c_{2k} - \frac{2k+1+\mu}{(2k+1)^2 - 1} d''_{2k-1}, \tag{3.7}$$

$$b_{2k} = \frac{2k\mu}{(2k+1)^2 - 1} c_{2k} - \frac{1 + (2k+1)\mu}{(2k+1)^2 - 1} d''_{2k-1}, \tag{3.8}$$

where

$$d''_{2k-1} = \frac{1}{\delta\zeta} \left[d'_{2k-1} \left(\frac{R}{R'} \right)^{2k-1} - d_{2k-1} \right]. \tag{3.9}$$

Thus, stresses due to external loads are completely determined.

Above R denotes the radius of the main section at $z = z_0$, and R' is radius of the auxiliary section at $z = z_0 + \Delta z$.

3.2 The Case of Residual Stresses in Glass

In the case of axial symmetry the compatibility equation written through deformations is

$$\frac{\partial \varepsilon_\theta}{\partial \rho} - \frac{\varepsilon_r - \varepsilon_\theta}{\rho} = 0. \tag{3.10}$$

The compatibility equation (3.5) was obtained introducing into Eq. (3.10) the Hooke's law

$$\varepsilon_r = \frac{1}{E} \left[\sigma_r - \mu(\sigma_\theta + \sigma_z) \right] + \alpha T, \tag{3.11}$$

$$\varepsilon_\theta = \frac{1}{E} \left[\sigma_\theta - \mu(\sigma_z + \sigma_r) \right] + \alpha T, \tag{3.12}$$

$$\varepsilon_z = \frac{1}{E} \left[\sigma_z - \mu(\sigma_r + \sigma_\theta) \right] + \alpha T, \tag{3.13}$$

where α is the thermal expansion coefficient and T is temperature.

In the case of external loads T is either absent or known. In Eq. (3.5) we have omitted T.

In the case of residual stresses in glass, in Eqs. (3.11) to (3.13) the term αT must be included. Since residual stresses in glass have thermal origin, the residual stresses can be considered as being caused by a fictitious temperature field T [11, 12]. Unfortunately, this temperature field is not known. Therefore, the compatibility equation cannot be used when investigating residual stresses in glass and one has to look for other analytical relationships between the stress components.

Thermal stresses in an axisymmetric body can be expressed as [13]

$$\sigma_r = 2G\left(\frac{\partial^2 F}{\partial r^2} - \Delta F\right) + \frac{2G}{1-2\mu}\frac{\partial}{\partial z}\left(\mu\Delta L - \frac{\partial^2 L}{\partial r^2}\right), \tag{3.14}$$

$$\sigma_\theta = 2G\left(\frac{1}{r}\frac{\partial F}{\partial r} - \Delta F\right) + \frac{2G}{1-2\mu}\frac{\partial}{\partial z}\left(\mu\Delta L - \frac{1}{r}\frac{\partial L}{\partial r}\right), \tag{3.15}$$

$$\sigma_z = 2G\left(\frac{\partial^2 F}{\partial z^2} - \Delta F\right) + \frac{2G}{1-2\mu}\frac{\partial}{\partial z}\left[(2-\mu)\Delta L - \frac{\partial^2 L}{\partial z^2}\right], \tag{3.16}$$

$$\tau_{rz} = 2G\frac{\partial^2 F}{\partial r\partial z} + \frac{2G}{1-2\mu}\frac{\partial}{\partial r}\left[(1-\mu)\Delta L - \frac{\partial^2 L}{\partial z^2}\right], \tag{3.17}$$

where F is stress function and L Love's displacement function,

$$\Delta F = \frac{1+\mu}{1-\mu}\alpha T, \ \Delta\Delta L = 0, \ G = \frac{E}{2(1+\mu)}, \ \Delta\frac{\partial^2}{\partial r^2} + \frac{1}{r}\frac{\partial}{\partial r} + \frac{\partial^2}{\partial z^2}. \tag{3.18}$$

Let us assume that a long cylinder or tube is manufactured by solidifying it in an axisymmetric temperature field without gradient in the axial direction. In this case the thermal (and residual) stresses are the same in all cross-sections of the cylinder, except the parts near the ends of the latter. Now from Eqs. (3.14) to (3.16) follows the classical sum rule

$$\sigma_r + \sigma_\theta = \sigma_z. \tag{3.19}$$

The classical sum rule (3.19) was in a somewhat different way first derived by O'Rourke [14].

Inserting expansions (3.1) into the equilibrium equation (3.6) and into the sum rule (3.19), we obtain

$$a_{2k} = \frac{1}{2(k+1)}c_{2k}, \qquad b_{2k} = \frac{2k+1}{2(k+1)}c_{2k}. \tag{3.20}$$

Thus, in the absence of the stress gradient in axial direction, all the residual stress components can be determined since c_{2k} have been determined experimentally.

This method has been widely used for residual stress measurement in glass cylinders, axisymmetric fibers and fiber preforms [4].

In the general case, in axisymmetric glass articles stress gradient in axial direction cannot be ignored. Let us try to derive from Eqs. (3.14) to (3.17) a relationship between stress components for that case.

If stress gradient in axial direction is present but smooth, we may write

$$\frac{\partial^2 F}{\partial z^2} = \frac{\partial^2 L}{\partial z^2} = 0. \tag{3.21}$$

Now from Eqs. (3.14) to (3.17) follows

$$\sigma_r + \sigma_\theta = \sigma_z + \frac{2G}{1-2\mu}\frac{\partial}{\partial z}\left[3(\mu-1)\Delta L\right]. \tag{3.22}$$

Differentiating (3.17) relative to z and integrating along r reveals

$$\int_0^r \frac{\partial \tau_{rz}}{\partial z}\,dr = \frac{2G}{1-2\mu}\frac{\partial}{\partial z}\left[(1-\mu)\Delta L\right] + C(z), \tag{3.23}$$

where $C(z)$ is the integration constant.

From (3.22) and (3.23) follows

$$\sigma_r + \sigma_\theta = \sigma_z - 3\int_0^r \frac{\partial \tau_{rz}}{\partial z}\,dr + C(z). \tag{3.24}$$

The last relationship is named the generalized sum rule in first approximation. By handling Eqs. (3.14) to (3.17) asymptotically, the second approximations of the generalized sum rule can be obtained:

$$\sigma_r + \sigma_\theta = \sigma_z - 2\int_0^r \frac{\partial \tau_{rz}}{\partial z}\,dr + C_1(z). \tag{3.25}$$

By using the photoelastic measurement data, equilibrium equation (3.5) and the generalized sum rule (3.25), all components of the residual stress in an axisymmetric glass article can be determined.

As an example, Fig. 3 shows geometry of a wine glass and fringe pattern in the area of the lower part of the stem. Using the hybrid algorithm described above, all the stress components were determined in the section B – B (Fig. 4).
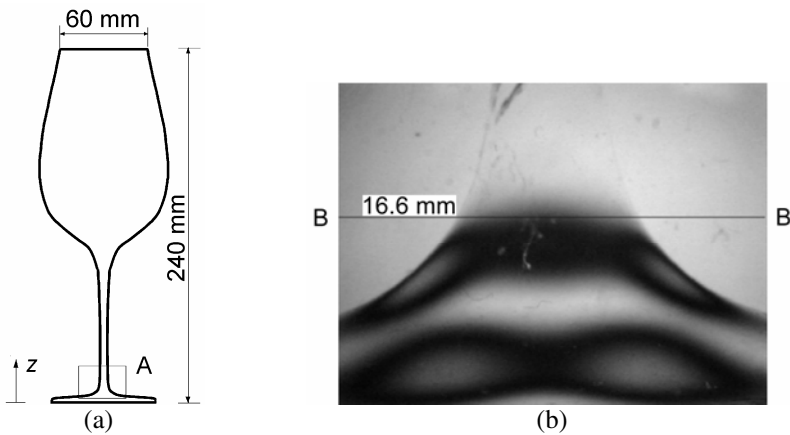
Fig. 3. Geometry of the wine glass (a) and fringe pattern in the area A (b).
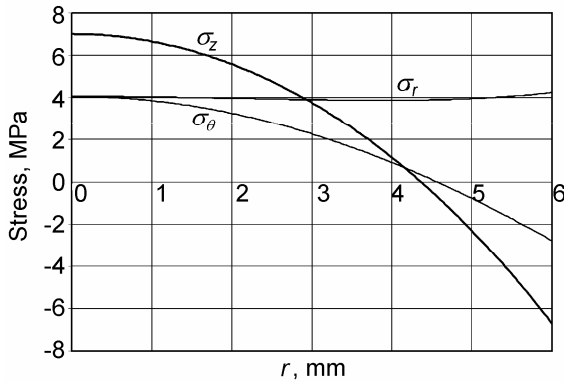
Fig. 4. Normal stress components in section B – B.

4 Conclusions

It has been shown that using equations of the theory of elasticity, hybrid algorithms can be constructed for complete determination of axisymmetric stress fields in photoelastic tomography. Determination of the residual stress in glass needs application of a different algorithm as compared with the case of external loads.

Acknowledgments

References

1. Herman, C.T.: Image Reconstruction from Projections. Academic Press, New York (1980)
2. Sharafutdinov, V.A.: Integral Geometry of Tensor Fields. VSP, Utrecht (1994)
3. Aben, H.K., Josepson, J.I., Kell, K.-J.: The case of weak birefringence in integrated photoelasticity. Opt. Lasers Eng. 11, 145–157 (1989)
4. Aben, H., Guillemet, C.: Photoelasticity of Glass. Springer, Berlin (1993)
5. Schupp, D.: Optische Tensortomographie zur Bestimmung räumlicher Spannungsverteilungen. Tech. Mess. 66, 54–60 (1999)
6. Aben, H., Errapart, A., Ainola, L., et al.: Photoelastic tomography for residual stress measurement in glass. Opt. Eng. 44, 093601-1–8 (2005)
7. Dash, C.J.: One-dimensional tomography: a comparison of Abel, onion-peeling, and filtered backprojection methods. Appl. Opt. 31, 1146–1152 (1992)
8. Aben, H., Ainola, L., Errapart, A.: Application of the Abel inversion in case of a tensor field. Inverse Problems in Sci. Eng. 18, 241–249 (2010)
9. Doyle, J.F., Danyluk, H.T.: Integrated photoelasticity for axisymmetric problems. Exp. Mech. 18, 215–220 (1978)

10. Doyle, J.F.: Closed-form inversion of the axisymmetric integrated photoelasticity equations. Appl. Mech. 47, 431–433 (1980)
11. Bartenev, G.M.: The Structure and Mechanical Properties of Inorganic Glasses. Wolters-Nordhoff, Groningen (1970)
12. Gardon, R.: Thermal tempering of glass. In: Uhlman, D.R., Kreidl, N.J. (eds.) Elasticity and strength of glass, vol. 5, pp. 146–170. Academic Press, New York (1980)
13. Melan, E., Parkus, H.: Wärmespannungen infolge stationärer Temperaturfelder. Springer, Wien (1953)
14. O'Rourke, R.C.: Three-dimensional photoelasticity. J. Appl. Phys. 22, 872–878 (1951)

Using an Electronic Speckle Interferometry for Measurement of a Stress-Deformation State of Elastic Bodies and Structures

Robert V. Goldstein, Viktor M. Kozintsev, and Aleksandr L. Popov

A.Yu.Ishlinsky Institute for Problems in Mechanics, the Russian
Academy of Sciences, 119526, Vernadskogo 101, Moscow, Russia
`goldst@ipmnet.ru`

Abstract. The method and equipment of the electronic speckle pattern interferometry (ESPI) for studying a stress-deformation state (SDS) of elastic bodies and structures are presented. Examples of use ESPI for measurements of residual stresses in welded structures, microdisplacements related to delamination of thin coatings, diagnostics of shrinkage stresses in coatings, determination of their elastic characteristics, generalization of the ESPI method for measurements of displacements of the nanometer scale fulfilled in IPMech RAS are given.

1 Introduction

Starting from pioneer studies by Burch and Tokarski [1] a practical speckle interferometry of small surface displacements of a body being analyzed has gained wide recognition of scientists and engineers as one of effective tools for studying SDS of elastic bodies and structures, in particular, - after replacement of photographic plates by analogue television systems [2, 3] and introduction of numerical handling of images on computer [4]. The key advantages of the method are related with quickness of information receiving, contact-free measurements, almost full absence of special requirements for preparing an analyzed surface, presentation of direct measurements as a map of level lines of microdisplacements of a surface under consideration.

Two methods of microdisplacements recording are used. The first two-exposition method implies registration of specklograms of a part of an investigated surface before and after creation of the perturbation providing small displacements. The level lines of the displacements are reflected in the form of interference bands with a step equals a half-length of the wave induced by laser used in the interferometer. The second method consists in observation of time changes of a specklogram of a surface transmitted through a specklogram of some reference state (analogue of a holographic interferogram of real time). As a result of such superposition a continuously changing speckle interferogram occurs. The interferogram represents a system of mobile interference bands. The used algorithm of the image treatment provides

translation of the mobile interferogram of DVD-quality (768x576 points) on the screen of a computer monitor with the rate being non less than the translation rate of specklograms without superposition (30 frames per second).

Generally the scheme of using the ESPI method consists of following stages:

- development of a theoretical model of an expected stress-deformed state of a body;
- making a speckle image of a body initial state;
- action on a body;
- making a speckle image of the body deformed state;
- interferogram making;
- determination of number, shifts and orientation of fringes;
- comparison of the real and calculated interferograms;
- evaluation of stresses and displacements levels of a body, elastic properties, etc.

The technique for SDS measuring by means of the ESPI method was implemented in the portable speckle interferometer "LIMON-TV" designed and fabricated in IPMech RAS. The equipment provides visual and numerical registration of fields of small elastic surfaces displacements, observation of a deformation process in time, recalculation of levels of the registered displacements to stresses.

2   Combined Methods of the ESPI and Blind-Hole Drilling

Among the applications of the electronic speckle interferometry for SDS measurements, in particular, - in welded joints, first of all one can mention a direction of studying residual stresses by measuring the displacements near a part through probing hole. This direction has scored recently 75th anniversary. Accuracy of the method is essentially higher as compared to other methods (ultrasonic, X-ray, magnetic, etc.) which have the errors comparable to the measured value in view of heterogeneity of a welded joint, ambiguity of interrelation of registered physical properties with mechanical stresses. A range of stresses measured by the ESPI method, e.g. in steels, is rather wide - from 15 MPa to yield strength. The error of measurements is varied from ~ 10% for small stresses to ~ 2-3% for the stresses of order the yield strength.

2.1   Calculating Models in the Blind-Hole Method

Calculating models in the blind-hole method are based on several assumptions:

   a)   within the diameter of a blind hole residual stresses are remained constant in any section parallel to the surface of a body;
   b)   changes of stresses through the depth of a hole are approximated by linear functions;
   c)   a mutual influence of adjacent holes and body edges is absent.

The initial hypotheses are illustrated in Fig. 1 where interrelations between a hole diameter *2R* and a characteristic curvature radius of a surface of investigated body R_1 (*a*) as well as linear approximation for changes of the principal residual stresses

at depth h of a small blind hole (b) are shown. These changes are described by the formula

$$\sigma_{ii} = \sigma_{ii}^0 + \sigma_{ii}^1(1-2z/h), \quad i = x, y$$

where the first term - constant component of residual stresses, and second - the component self-counterbalanced on depth of a hole.
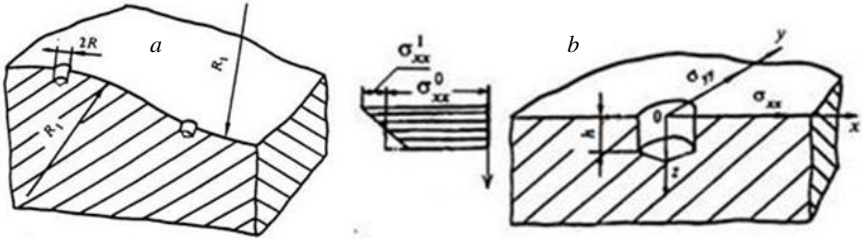
Fig. 1. Calculating models in the blind-hole method: a - interrelations between a hole diameter $2R$ and a characteristic curvature radius of a surface of investigated body R_1, R_2; b - linear approximation for changes of the principal residual stresses at depth h of a blind hole

Despite simplified nature of a model of stress changes through depth of a hole, the numerical solution of the appropriate 3D elasticity problem is needed for searching for interrelations between the interior SDS and surface microdisplacements. As a result of making of a hole of radius R and depth h in an stressed body the lateral area and a bottom of a hole became to be stress free. Under the influence of the stresses acting in a remaining part of a body, the lateral area and a bottom of a hole are deformed; together with them the body surface in a hole neighbourhood is also deformed. Microdisplacements of this surface are a diagnostic indication for evaluation of the interior stresses existing in a body before drilling of a hole.

At the numerical solving of the problem on searching for a SDS perturbed by a hole it was accounted for that at hole drilling by an usual drill, the hole has a cylindroconical form. This circumstance leads to additional difficulties at generation of a finite-element mesh, but as it became clear, has a small influence on the final dependences between the stresses in a body and displacements at its external surface.

The longitudinal section of the hole and the scheme of finite elements near to a hole is given in Fig. 2. One of the stress components is also shown by arrows. Calculations were performed at the given unit value of one of the stress σ_{xx}^0, or σ_{xx}^1 for different ratios of the hole depth and radius. Plots of displacements w of a surface of an aluminum body in the direction of the action of the stress $\sigma_{xx}^0 = 10$ MPa are given in Fig. 3 (curves $1 \div 5$) for various hole depths: from $0.4R$ to $2R$ with a step $0.4R$ at $R=1mm$. The surface displacements in the transverse direction are also given in Fig. 3 (curves $6 \div 10$). The coordinate r on the abscissa axis can have a sense of a distance from the hole edge on axis Ox, or - on axis Oy depending on the plots considered: above the value $w=0$ or below this value.
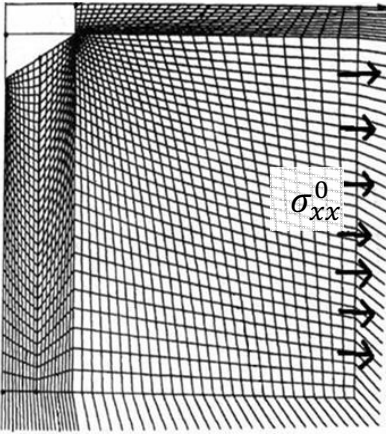
Fig. 2. The form of hole and the finite element mesh
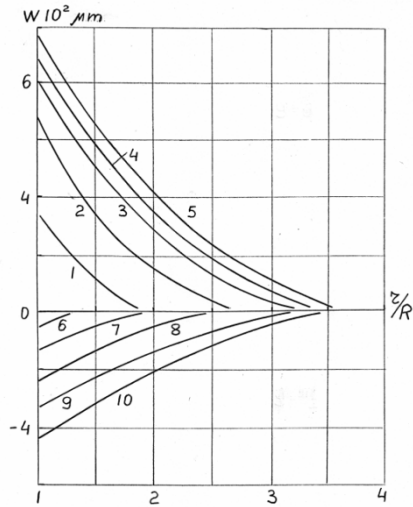
Fig. 3. Plots of normal displacements *w*: 1 - 5 - on an axis *Ox*, 6 - 10 - on axis *Oy*; numbering corresponds to increase of a reference blind-hole (*R = 1 mm*) depth from

0,4R to 2R with step *0,4R* at $\sigma_{xx}^0 = 10\ MPa$

    On the basis of the results given in Fig. 3 one can determine an interference fringe value at the experimental diagnostics of stresses in a body, i.e. the quantity of a stress providing displacement of an edge of a hole on a step of fringes. The step of fringes is a difference of heights between the adjacent fringes of the same type (dark or bright) equals the length of a half-wave of the laser used in a measuring system. One of the characteristic interferograms of microdisplacements of a surface of a body in a neighbourhood of the blind- hole (dark circle) is given in Fig. 4.
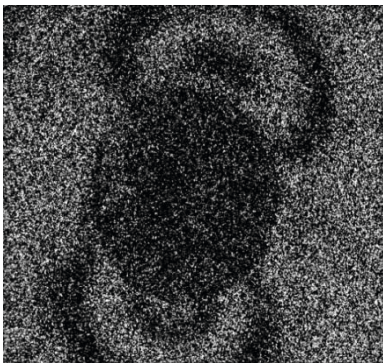
Fig. 4. The interferogram of uniaxial stress state
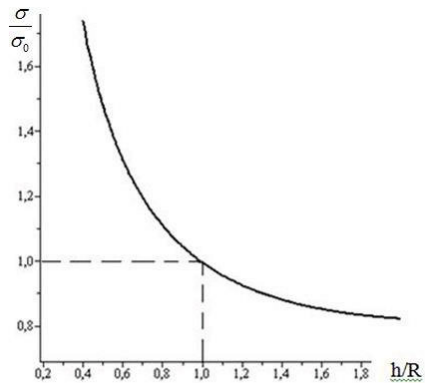
Fig. 5. The fringe value in stresses depending on a reference blind-hole depth ($\sigma_0 = 40$ *MPa, R=1 mm*)

Level lines of normal surfaces displacements near to a hole are mapped on an interferogram by the system of dark and bright fringes. Multiplying the number of fringes by the fringe value, it is possible to calculate the quantity of an acting stress. Directions of the displacement gradient related to a difference of the states before and after the blind-hole drilling are also seen in Fig. 4. Owing to the adopted linear model of a deforming of a body, the gradient directions coincides with the directions of principal stresses in a body in the same place before hole drilling. Note that a dominating stress of one direction is better established namely by not deep holes ($h/R < 1$) whereas in case of a through hole the stress of one direction leads to displacements of the same moduli both in the direction of the stress action and in the perpendicular direction [5]. At the same time the general threshold of the method sensitivity to stresses decreases with growth of the relative depth of a hole (see Fig. 5). At this figure the unit stress is related to the displacement of one fringe value at the hole edge.

On the basis of the dependence, given in Fig. 5 and similar ones for different materials the express method for stresses evaluation in a direction of the symmetry axis of the interferogram has been formulated. The stress value is calculated by the following formula

$$\sigma = (\frac{A}{h} + B) \frac{D_{ref}}{D} \frac{E}{E_{ref}} N$$

where h and $D=2R$ are depth and diameter of a hole, E is the Young modulus of a tested material, N is number of the fringes registered on an interferogram in the chosen direction, A and B are the calculated constants, $D_{ref} = 2\ mm$ is the diameter of a hole in an etalon material aluminium ($E_{ref} = 70\ GPa$).

Deficiency of a two-exposition speckle interferometry is lack of a possibility for the determining of the stress sign (compressive or tensile) by the form interferograms; in both cases interferograms are identical if the values of stresses moduli coincide. To overcome this difficulty one can observe a neighbourhood of a hole after its drilling in the conditions of an interferogram of real time and making a small shift of fringes (without change of their number) in the course of this observation. The shift for instance, can be caused by an action on the optical block of the interferometer. As a result of this action the course of the beams is changed leading to a shift of interferogram fringes. In the direction of this shift the relief of the surface displacements in a hole neighbourhood becomes visible. Then by incorporating relations between stresses and displacements given in [5] the sign of the stress can be determined. The given process of definition of a stress sign searching for is illustrated in Fig. 6. A three-dimensional element of the body model (*a*) in a neighbourhood of a blind- hole with the given tensile, σ_x, and compressive, σ_y, stresses is shown in Fig. 6a. The central sections of the element xOz and yOz with a hole contour and a profile of a deflection of a surface of a body after deformation from stresses σ_x and σ_y are shown in Fig. 6b and Fig. 6c, respectively. Under each section it is shown the top view on the level lines of a deflection of a surface. The level lines contain a point, marked on a deflection lateral view by the black stain, similar to the form of the interference fringes observed in experiment. The horizontal lines located on the
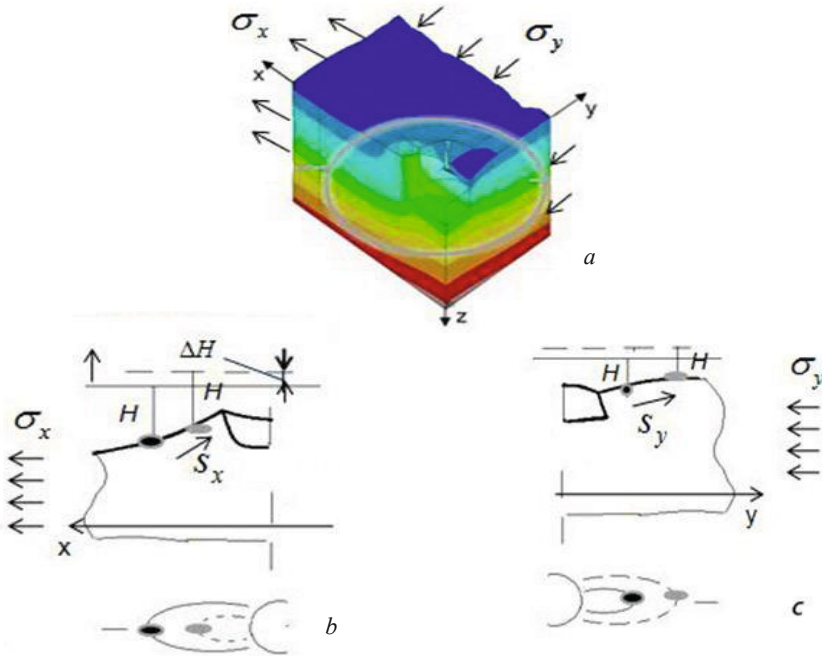
Fig. 6. Directions of shift of «live fringes» at small change of an optical difference of a beam path length in the interferometer are determined by the stress sign (*a* - a three-dimensional element of the body model in a neighbourhood of a blind hole, *b* - central cross section of a body along the direction of tensile stress Ϭ$_x$, *c* - cross section along the direction of compressive stress Ϭ$_y$

distance H from these points show the initial position of an optical axis of an interferometer. It can be seen that at small change, ΔH, of the value H it is required a shift of the appropriate fringe in the direction S_x to the hole or in the direction S_y from the hole in cases of tensile or compressive stresses, respectively, to restore the optical trajectory for the given fringe (final positions of the fringes are shown in Fig. 6*b,c* with grey stains and dashed lines).

2.2 Experimental Studies of the Residual Stresses

The method for studying SDS by means of an electronic speckle-pattern interferometry was realized in portable speckle interferometer "LIMON-TV" designed and fabricated in IPMech RAS. The device provides visual and numerical registration of fields of small elastic surfaces displacements of a body, as well as observation of a deformation process in time. The general view of interferometer "LIMON-TV" in portable variant is given in Fig. 7. The device consists of computer (1) and optical blocks of an interferometer (2). The sample with a weld is also presented (3). Overall dimensions of the optical block - 30x10x10 cm, weight - 2 kg; the observation area varies in limits from 0,5 to 100 cm^2; measurement limits: on normal displacements $10^{-7} \div 10^{-3}$ cm, on angular velocities of the relative motion of separate parts of an observable surface of object $-10^{-2} \div 10^2$ degrees per hour.
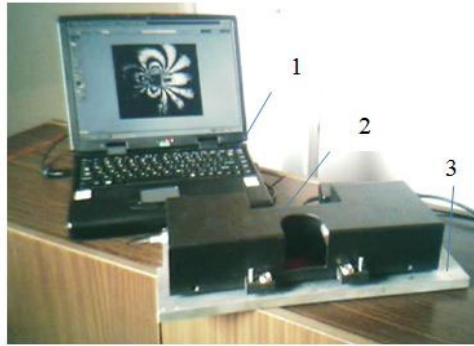
Fig. 7. The electronic speckle-pattern interferometer "LIMON-TV": 1 - the computer block, 2 - the optical block, 3 - the sample with a weld

Experimental studies of the residual stresses were performed on various objects in laboratory, industrial and field conditions. Drilling of a blind hole in a weld in a gas pipe of large diameter is shown in Fig. 8*a*. Numerous blind holes in a neighbourhood of a spiral weld on an external surface of this pipe are shown in Fig. 8*b*. On the basis of the measurement the data of principal stresses were evaluated. To increase the data accuracy a surface region of hole drilling was coated with a diffusely reflecting paint.
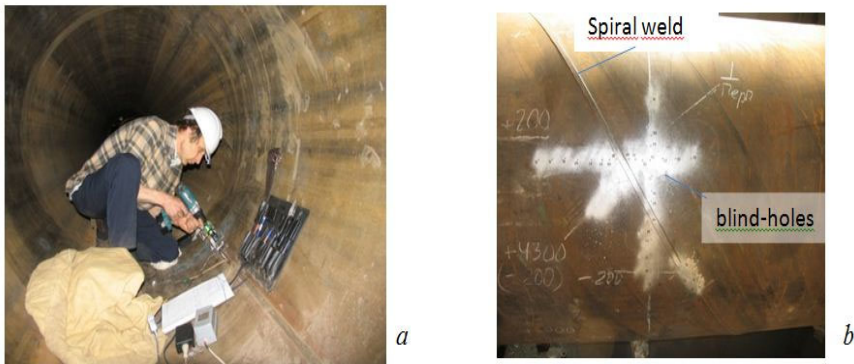
Fig. 8. The studies of the residual stresses in industrial conditions: *a* - drilling of a blind-hole in a weld in a gas pipe of large diameter, *b* - disposition of blind holes in a neighbourhood of a spiral weld on an external surface of a pipe

Directions of compressive and tensile stresses in welds and in heat affected zones, as a rule, corresponded to theoretical predictions (see Fig. 9). The drilled hole on an axis of a weld and a ruler marked a direction of a weld is shown in Fig. 9a. The interferogram of normal surfaces displacements of a pipe in a neighbourhood of this hole is given in Fig. 9b. The fringes characterize tensile (along a weld) and compressive (in the transverse direction) stresses with similar moduli in a weld before drilling of a hole.
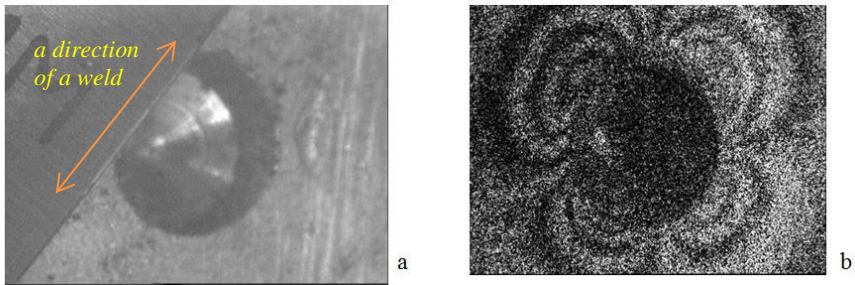
Fig. 9. Appearance of a biaxial stress state on a weld axis: a - the drilled hole on an axis of a weld and a ruler marked a direction of a weld, b - the interferogram of normal surfaces displacements in a neighbourhood of this hole

Epures of principal stresses on an external surface of a pipe with a spiral weld far from its end sections are given in Fig. 10. Stress distributions along pipe circles and its generators are given in Fig. 10a and Fig.10b respectively. Maximal moduli of tensile and compressive stresses are denoted by σ_x and σ_y.
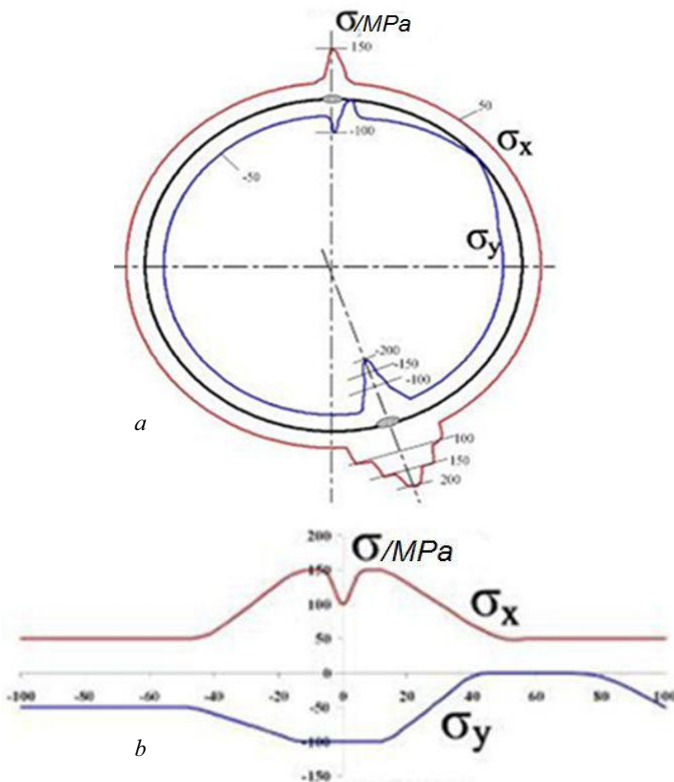
Fig. 10. The diagrams of the measured residual stresses in the gas pipe along pipe circles (*a*) and its generators (*b*)

The weld section is shown in Fig. 10a by grey ovals. In weld neighbourhoods one can see the peaks of stresses.

The next drawing (Fig. 11) illustrates an influence of technology of repair welded joints on levels of the residual stresses. Two such repair "patches" on a gas pipe with the optical block of an electronic speckle interferometer installed on them are shown in Fig.11a. A part of a thick-wall (thickness of 100 mm) chemical reactor with a repair weld and the optical block of a speckle interferometer installed on it is shown in Fig. 11b. The repair niches cutting out on the place of flaws, were filled according to different technologies by longitudinal or transverse welds. The characteristic cases of filling up of repair niches are shown in Fig. 11c,d (thirteen narrow longitudinal welds superimposed in the conditions of the continuous heat-conducting path (Fig. 11c) and two wide longitudinal welds (Fig. 11d)). The measured residual stresses differed almost on 50% at identical volumes of filling up of niches levels. Smaller stress values were observed at filling up of a niche with a considerable amount of thin welds (*max σ_x = 120 MPa*). This result testifies partial neutralization of stresses in welding layers (the direction of the peak tensile stresses is shown in Fig. 11b by an arrow.
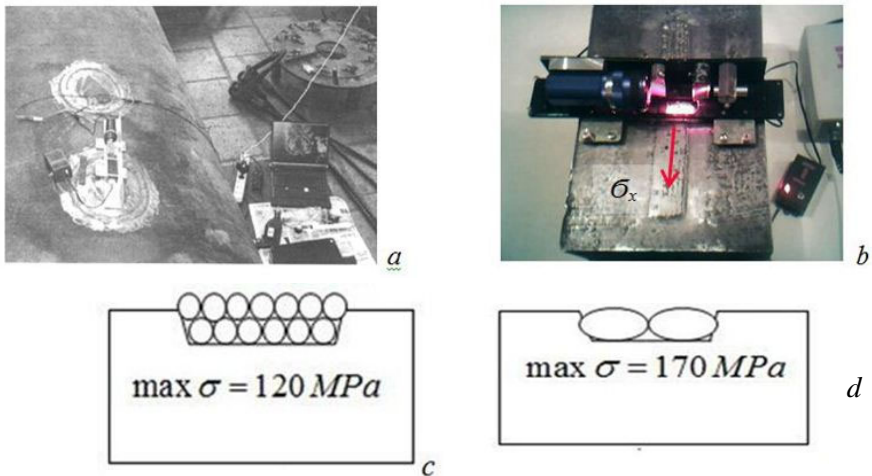
Fig. 11. The influence of technology of repair welded joints on levels of the residual stresses: *a* - repair "patches" on a gas pipe, *b* - a part of a chemical reactor wall with a repair weld, *c, d* - the maximal stresses at thirteen and two repair welds

The given and other examples show that the possibility of express-diagnostics of the residual stresses allows to solve the problems on an influence of various technological operations on SDS. Hence, the method and device can serve as a basis for development of optimal technological conditions of fabrication and treatment of products, to reveal places of a structure dangerous from the strength point of view, to develop recommendations for reducing the levels of these stresses and to verify the efficiency of the recommendations.

3   Other Applications of Use ESPI

Along with determination of the residual stresses, the method and electronic speckle interferometry equipment are successfully used for solving other problems. We will point out some of them:

- monitoring of evolution of residual stresses;
- determination of elastic characteristics of homogeneous and composite materials;
- diagnostics of delamination in multilayered thin coatings; evaluation of elastic parameters of layers and shrinkage stresses;
- diagnostics of nanoscale displacements;
- using the electronic speckle interferometry in the sensor system for registration of physical fields of low intensity.

One of the representative problem of the list is the problem on searching for the value of a force and a point of its application to the invisible side of a plate using the observed data on number of interference fringes of microdisplacements and their pattern at the visible side of a plate. In this case the loaded plate serves as a sensitive element [6, 7].

The calculated scheme of the problem on the noncentral application of normal concentrated force P to the round rigidly clamped plate of radius a is given in Fig. 12*a*.
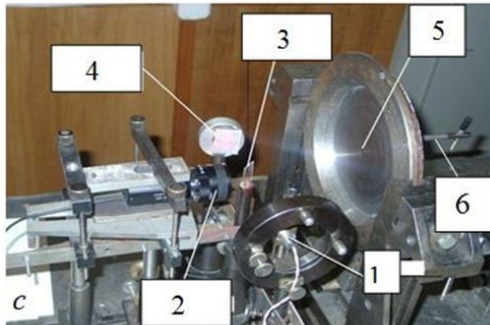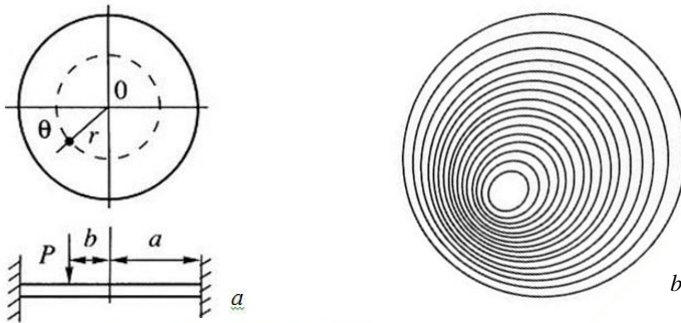
Fig. 12. Solution of a problem of searching for value of the force and point of its application: *a* - the calculated scheme, *b* - level lines of the plate deflection, c - experimental setup (1 - the laser, 2 - the video camera, 3 - the split mirror, 4 - a diffusely reflecting surface, 5 - a round plate, 6 - the loading device)

Calculated level lines of the plate deflection (w), received by means of the unique closed formula by J.H. Michell [8] are shown in Fig. 12b.

$$w(r,\theta) = \frac{Pa^2}{16\pi D}\left[(1-\xi^2)(1-\eta^2)+(\xi^2+\eta^2-2\xi\eta\cos\theta)\ln\left(\frac{\xi^2+\eta^2-2\xi\eta\cos\theta}{1+\xi^2\eta^2-2\xi\eta\cos\theta}\right)\right],$$

where r, θ are the polar coordinates referenced from the center of a plate $\xi=r/a$, $\eta=b/a$, b is the distance from a plate center to the point of force action (in this case $b=0{,}4a$), D is the cylindrical stiffness of a plate. Similar level lines of a deflection of a plate in the form of a system of closed interference fringes are also obtained by means of a pilot experimental system given in a Fig. 12c. Its optical part represents a modified scheme by Michelson (1 - the laser, 2 - the video camera, 3 - the split mirror, 4 - a diffusely reflecting surface, 5 - a round plate, 6 - the loading device). The pattern of fringes and their number univalently determine the parameters of a concentrated force.

On the same plate used as a substrate, the possibility of registration of small delaminations of a thin coating is shown. The method implies comparison of a reference state of a substrate with a coating (shown by the straight lines and a semicircle delamination) with the state after a substrate bending (shown by dashed lines and oval delamination), see Fig. 13a. The displacements in the delamination zone at bending differ from displacements of a coating part without delamination [6]. On an interferogram it is shown by local distortion of the fringes form. Level lines
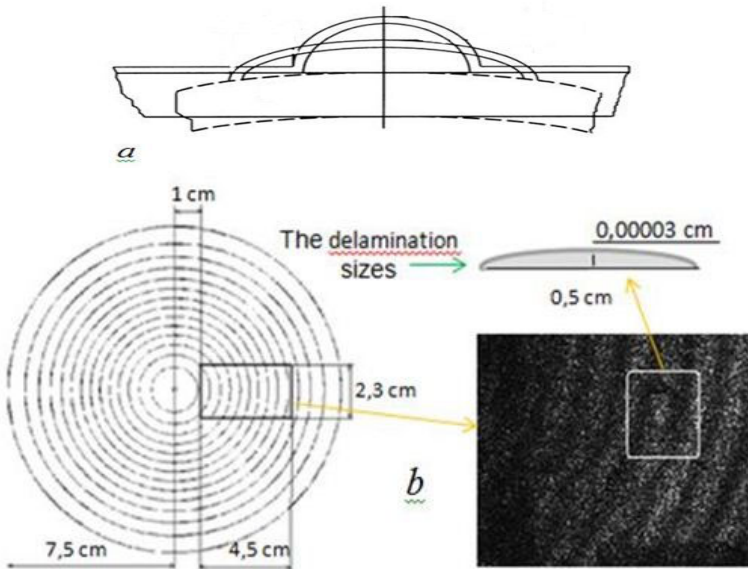
Fig. 13. Registration of small delaminations of a thin coating: *a* - displacements in the delamination zone at bending differ from displacements of a coating part without delamination; *b* - delamination on an interferogram

of an axially symmetric deflection of a plate are shown in Fig. 13b at application of a force at its center. In a certain place of the selected rectangular interval of a plate with the sides 4,5 on 2,3 cm, a delamination invisible by an eye has been created. After a substrate bending this delamination was detected in the form of an oval between the adjacent interference fringes (it is marked by a white rectangle). Thereby, its location and the linear dimensions were determined. The displacements are in limits of a step of fringes, which is known if the value of the applied force is known.

The shrinkage stresses arising after deposition of a thin coating on a substrate can be estimated [6, 9] by the similar method implying the substrate bending. The model of a rodlike substrate of length l and thickness h, hinge-supported at the edges $x=0,l$ with the coating of thickness $\delta \ll h$ is superimposed is shown in Fig. 14a. After the coating deposition its shrinkage occurs leading to generation of stresses in a substrate and a coating film. A substrate bending is caused by the influence of these stresses. Assuming that contraction of a coating without a substrate would have the value Δl, it is possible to estimate the appropriate longitudinal force N constraining these contraction: $N=EF\Delta l/l$, where F is the section area, E is the coating modulus of elasticity. The force N leads to the equivalent bending moment in a substrate: $M=Nh/2$ and a deflection which in case of a hinge-supported rod has the maximum value $w_{max}=Ml^2/(8E_0J)$ where E_0 is the modulus of elasticity of a substrate, J is the inertia moment of inertia of its cross-section.

Hence, having measured a substrate deflection by means of an electronic speckle interferometer, we can evaluate the shrinkage stresses in a coating

$$\sigma = \frac{N}{F} = \frac{16E_0J}{hl^2F}\,w_{max}$$

Note, that this formula does not include a coating modulus of elasticity, i.e., the stress in a coating are determined by the given algorithm even if the basic elastic characteristic of the coating is not known.

Clear representation of coating action on a substrate is given in Fig. 14b. There are shown steel (1) and cardboard (made of a punched card) (2) beams after a bending caused by contraction of an aerosol paint, superimposed on one of front sides of beams.

Elastic characteristics of a coating are not determined by the given algorithm directly. For their determination one needs to compare the flexural stiffnesses of the coated and uncoated beams. Interferograms of a bending of identical cantilever beams from a board are shown in Fig. 14c: 1 - with a coating of thickness of 0,01mm, 2 - without a coating. In both cases the loads at the free edges were caused by mass of 4 mg.

As an example of determined moduli of elasticity and shrinkage stresses in coatings, the table of their values taken from [6] is given in Fig. 14d.

One of the most interesting directions of development of the ESPI method is related to its extension for measurement of nanometer displacements and rates of these displacements. The idea of registration of such displacements consists in insertion in a set of informative parameters small changes in positions of level lines of preliminary induced microdisplacements which lead to shifts of fringes without

Material	Sizes / mm	w_{max}/μm	E_0 / GPa	E / GPa	Shrinkage stresses / MPa
Steel	30 × 6 × 0,15	0,55	200	24	2,8
Cardboard	17,5 × 8 ×0,1	3	2,5	24	1,3
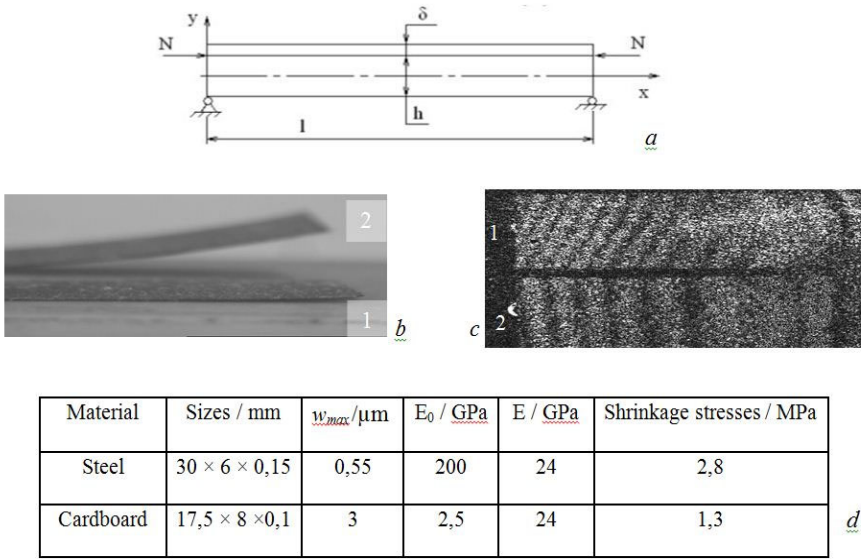
Fig. 14. Determination of shrinkage stresses in a thin coating: *a* - the calculated scheme, b - steel (1) and cardboard (2) beams after a bending caused by contraction of an aerosol paint, c - interferograms of a bending of beams (1 - with a coating, 2 - without a coating), d - moduli of elasticity and shrinkage stresses in coatings

changing the total number of observable fringes [10]. It is possible to evaluate the order of normal displacements registered by the method, for instance, follow a bending of a cantilever beam such that the length of the observation area along the beam axis is more than 10 millimeters while a difference of heights on this basis is mapped by several (three-four) interference fringes, equals ~ 1 micron. As, the digitized image of the observation area, pitched to the monitor screen from the standard video camera of a DVD-format, represents a matrix of bright points (pixels) with the sizes about 800 pixels across on 600 on a vertical. Hence, the screen distance between fringes at a small number of fringes equals hundreds pixels, in particular, about 300 pixels for two fringes. Thus, difference of height in the form of a deflection between the adjacent fringes of the same type, being equal 266 nanometers, is related to 300 pixels on the screen. Hence, registration of a fringe shift of the minimal distinguishable value, 1 pixel of the screen resolution of an interferogram, corresponds to additional small normal displacement of a beam of order of 1 nanometers in a place of a fringe shift.

Metrological testing of measurements of the nanodisplacements using the described method, was performed on the equipment presented in Fig. 15 (*a* is the general view, *b* is the kinematic scheme).

The optical block of the equipment (1) related to the Leith-Upatnieks scheme was almost the same, as was used for measurements of the residual stresses. For

the high-precision assignment of supersmall displacements and velocities in the field of the observation, limited in Fig. 15b by vertical dashed lines, we used the two-cascade girder reduction gear transmitting a rotation from a cam (2), fayed on an axis of an hour hand of a quartz clock, through two unequal-arm beams (3, 4) with a proportion of shoulders of order 1/30 for everyone. As a result, the angular velocity of a cam equals 30 grade/hour, is decreased to a zone of observation of an interferometer approximately in 1000 times. This provides displacements of edges of this zone during 5s within 10 nanometers if the image processing of speckle interferograms can be done with an interval equals 0,5s.
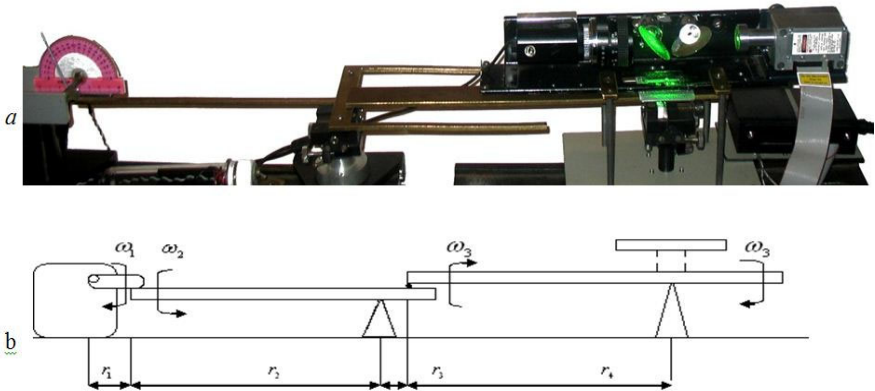
Fig. 15. Metrological testing of measurements of the nanodisplacements *(a* is the general view, *b* is the kinematic scheme of the equipment)

The typical speckle interferogram of displacements is given in Fig. 16 ((a) - beam displacements in the field of observation; (b, c) - stages of fringe centers separation). First, averaging of values of brightnesses through the columns of a matrix of the interferogram image is performed (b), then a band-pass filtration of this averaged brightness profile (c) is made (on the abscissa axis in Fig. 16 b,c coordinates of columns of a numerical matrix of an electronic speckle interferogram in screen pixels are put aside, while on the ordinate axis the values of brightness according to eight-bit scale are given). Note, that the stage of averaging of brightness along interferogram fringes provides an essential decrease of the speckle-noise attaining hundreds of percents in line cross sections of an interferogram, to the level of order 10%. This level is enough low for confident using known filtration methods.

Extremums of filtered brightness of an interferogram profile are identified as centers of interference bands. Determination of nanodisplacements in places of shifts of these centers is performed by the formula:

$$w = \lambda \frac{(m-1)(n_1 + n_2)}{4N}$$

where w is the value of the displacement of the body surface, λ is the laser wavelength, m is the amount of stocked fringes ($m \geq 2$), N is the number of pixels between centers of maximally remote fringes from taking into account, n_1 is the number of pixels corresponding to equal shift of centers of fringes which characterizes the displacement of rigid body, n_2 is the number of pixels corresponding to differential shift between fringe centers which characterizes variation of angle of inclination.
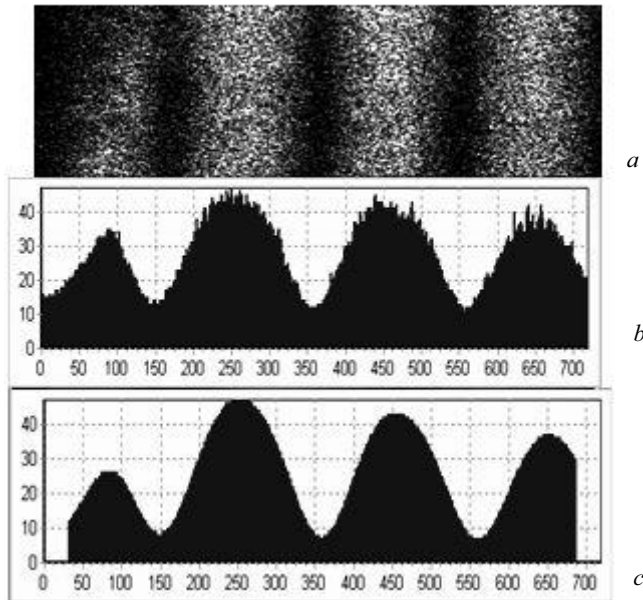
Fig. 16. Determination of fringe center: a - speckle interferogram of beam displacements, b, c - stages of fringe centers separation.

Comparing the set of given and gauged measured displacements showed a high degree of their correlation: the maximal differences did not exceed 0,5 nanometers. Thereby, the possibility of using the suggested method of speckle-interferometric measurement of displacements from the level of 1 nanometer and angular velocities - from 0,03 grade/hour has been confirmed.

Acknowledgement

Compactness and mobility of the developed equipment, operationability of realization of SDS measurements and the given examples of measurements results show ample opportunities and perspectives of the ESPI method for the solving a set of problems of a statics and dynamics of solids.

References

1. Burch, J.M., Tokarski, M.J.: Production of Multiple Beam Fringes from Photographic Scatteres. Optica Acta. 15(2), 101–111 (1968)
2. Butters, J.N., Leendertz, J.A.: Holographic and video techniques applied to engineering measurements. Meas Control (4), 349–354 (1971)
3. Macovski, A., Ramsey, S.D., Schaefer, L.F.: Time-lapse interferometry and contouring using television systems. Appl. Opt. (10), 2722–2727 (1971)
4. Peters, W.H., Ranson, W.F.: Digital Imaging Techniques in Experimental Stress Analysis. Opt. Eng. 21(3), 427–432 (1982)
5. Kirsch, G.: Die Theorie d. Elastizität u. d. Bedurfnisse d. Festigkeitslehre. Zeitchrift Vevein Deutscher Ingenieure. B 42(29), 797–807 (1898)
6. Goldstein, R.V., Kozintsev, V.M., Podlesnyh, A.V., Popov, A.L., Chelyubeev, D.A.: A method of an electronic speckle interferometry for the solution of some inverse problems of mechanics of elastic bodies. Mechanics of Solids (2), 5–13 (2006)
7. Tian-hua, X., Chao, J., Wen-cai, J., Hong-xia, Z., Da-gong, J., Yi-mo, Z.: Design and experiment of electronic speckle shearing phase-shifting pattern interferometer. Optoelectronics Letters 4(1), 59–61 (2008)
8. Timoshenko, S., Woinowsky-Krieger, S.: Theory of Plates and Shells. Mcgraw-Hill Comp., N.Y. (1959)
9. Stoney, G.G.: The tension of metallic films, deposited by electrolysis. Proc. Roy Soc. London Ser. A. 82(553), 172–175 (1909)
10. Goldstein, R.V., Kozintsev, V.M., Podlesnyh, A.V., Popov, A.L., Chelyubeev, D.A.: Use of an electronic speckle interferometry for registration of nanodisplacements. Mechanics of Solids (4), 662–670 (2008)

Structural Integrity and Residual Strength of Composites Exposed to Fire

George A. Kardomateas

School of Aerospace Engineering,
Georgia Institute of Technology,
Atlanta, Georgia 30332-0150, USA
george.kardomateas@aerospace.gatech.edu

Abstract. The compressive response of an axially restrained composite column, which is exposed to a heat flux due to fire is studied by both analytical and experimental means. The column is exposed to fire from one-side and an analytical approach is outlined for the resulting heat damage, the charred layer formation and non-uniform transient temperature distribution. Due to the nonuniform stiffness and the effect of the ensuing thermal moment, the structure behaves like an imperfect column, and responds by bending rather than buckling in the classical Euler (bifurcation) sense. In order to verify the mechanical response, the compressive buckling behavior of the same material subjected to simultaneous high intensity surface heating and axial compressive loading were investigated experimentally in a specially designed cone calorimeter. Experiments on the residual compressive strength following exposure to fire are also conducted for a range of heat fluxes and exposure times.

1 Introduction

Fiber reinforced polymeric composites are used extensively in aerospace, marine, infrastructure and chemical processing applications. In these applications, fire events and their resulting effects on the structural integrity, are of considerable concern. In addition to the implications for design, quantitative information regarding the nature of the strength loss is required to make decisions regarding, for example, the seaworthiness of a ship that has sustained fire damage.

Many of the thermal properties of composites related to fire have been thoroughly studied and are well understood, including ignition times, heat release rates, smoke production rates and gas emissions [1-5]. However, little attention has been given to the structural integrity issues. For example, one important gap in the understanding of composites is their response and structural integrity due to the combined effect of mechanical loading and thermal loading due to fire. Another important issue is their residual strength following exposure to fire of a given intensity and for a given period of time. This paper addresses these issues,

both from analysis and experiments, as far as compressive loading, which in an otherwise purely mechanical loading (no fire) would lead to bifurcational (Euler) buckling.

2 Temperature, Char Distribution and Thermal Buckling Analysis

The problem of predicting the behavior of polymer composite materials exposed to a fire environment may be divided into two different parts: internal and external processes. The internal processes include all the physical and chemical processes, which occur in any laminate. The external processes deal first with the determination of the shape, size and intensity of the flame in the boundary layer and, second, with the heat transfer to the laminate and the surroundings. The finite element model used in the paper to predict the behavior of composites in a fire environment is based on the mathematical model proposed by Henderson *et al* [6] and developed by Gibson *et al* [7] and Looyeh *et al* [8]. The non-linear partial differential equations that govern the behavior of the laminate in the fire have been solved numerically using a mixed explicit-implicit finite element technique. Accordingly, the remaining resin material *vs.* exposure time can be obtained. Based on the experiments and calculations performed by Gibson *et al* [10], we assume that when the residual resin context is less than 80%, the material can be treated as charred.

The predicted temperature and charred layer thickness distribution with time along the thickness direction are obtained by the thermal finite element model just discussed. Now the quasi-static assumption is made to analyze the thermal buckling response of the column consisting of an undamaged layer and a charred layer, as shown in Figure 1. The quasi-static assumption means at each different time, the column is in an equilibrium state and the temperature distribution and the charred layer thickness at that time obtained by the finite element model can be used in the static buckling analysis. The length and total thickness of the column are denoted by L and H respectively. The thickness of the undamaged layer is represented by l, which is dependent on the time, t. It is reasonable to assume that the mechanical properties of the charred (fire-damaged) layer are negligible because of the thermal decomposition of resin material; this assumption was also made by Mouritz and Mathys [11]. Therefore, we only considered the undamaged layer in the thermal buckling analysis; nevertheless, the temperature distribution in the undamaged region is influenced by the existence of the char layer. Based on the approach discussed, Figure 2 shows the resulting temperature distribution and Figure 3 the normalized charred layer thickness for a fire intensity of $Q = 25$ kW/m^2.

Regarding the Young's modulus, E, of the undamaged composite, it is well known that the modulus of polymers depends strongly on the temperature and especially on how close the temperature is to the glass transition temperature, T_g, of the matrix. A recent paper by Kulcarni and Gibson [12] studied the effects of temperature on the elastic modulus of E-glass/Vinyl-Ester composites. They provided measurements of temperature dependence of the elastic modulus of the composite in the range of 20°C to 140°C. The glass transition temperature of the matrix was
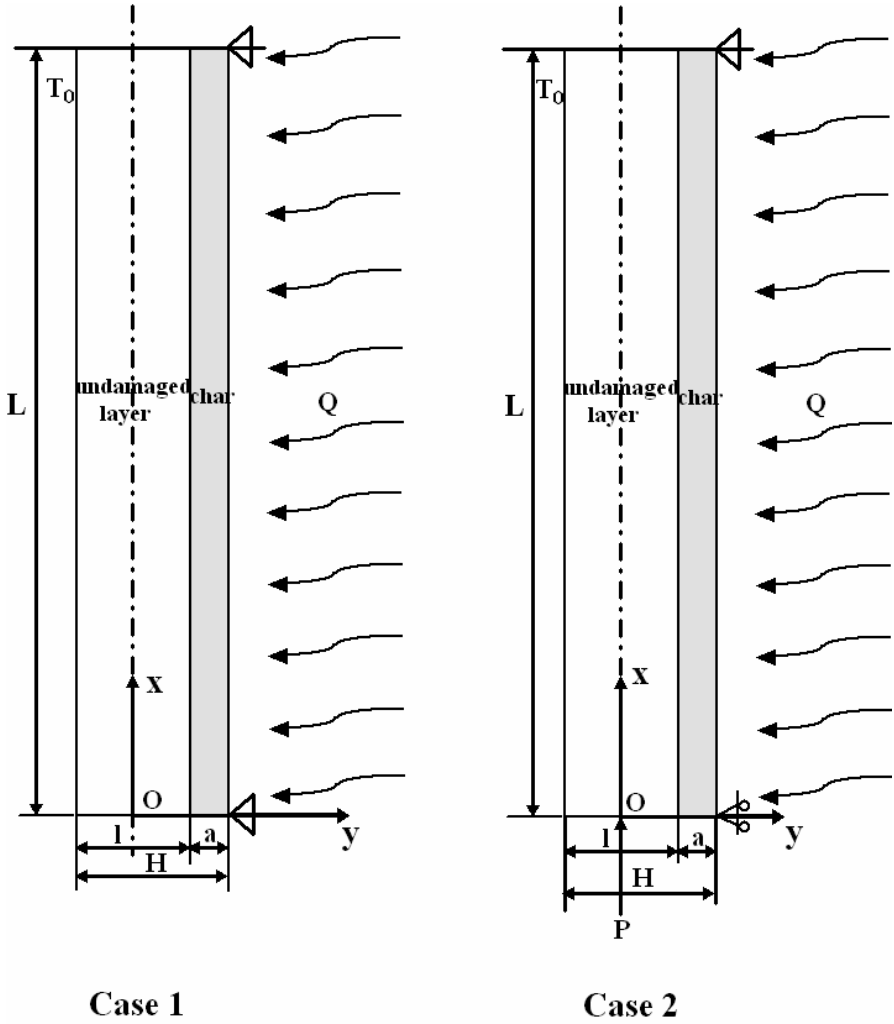
Fig. 1. Definition of the geometry for the laminated column, which is composed of an undamaged layer and a charred layer, and is subjected to a heat flux due to fire, Q, and a compressive load, P.

$T_g = 130$ °C. Near this temperature, the elastic modulus shows a significant variation, but below T_g the variation is small. The variation of the modulus [12] fits a 3rd order polynomial equation very well, as we show in Figure 4. If we denote by E_0
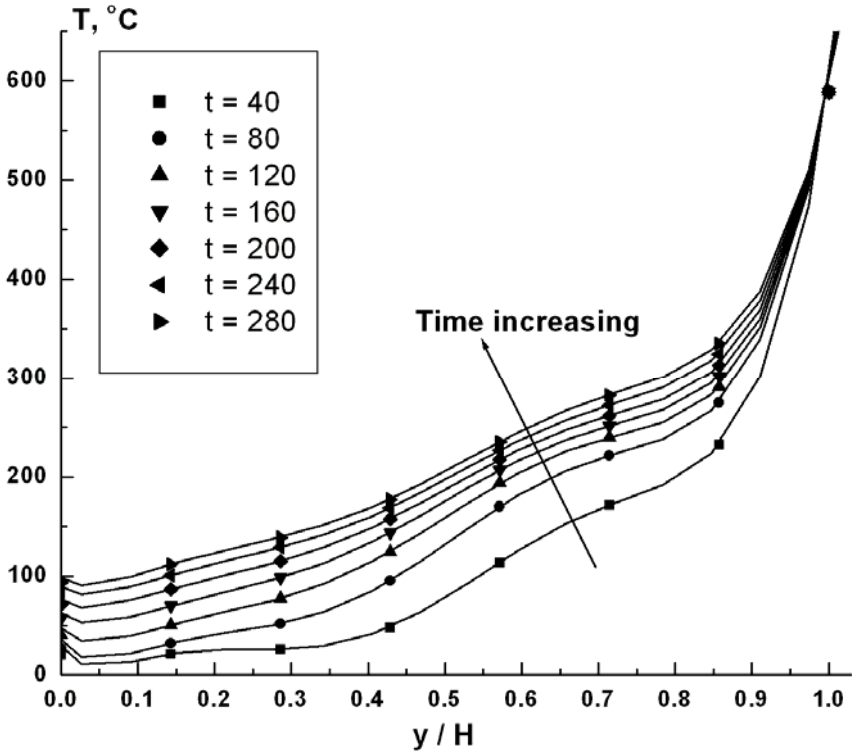
Fig. 2. Temperature distribution of the column subjected to heat flux $Q = 25$ kW/m^2, the y-axis is normalized by the total thickness of the column. The 7th order polynomial fit curves are obtained by interpolation.

the modulus at room temperature, $T_0 = 20°C$, then the modulus E at the temperature T is a function of temperature T and

$$\frac{E}{E_0} = 1 - a_1\left(\frac{T-T_0}{T_g-T_0}\right) + a_2\left(\frac{T-T_0}{T_g-T_0}\right)^2 - a_3\left(\frac{T-T_0}{T_g-T_0}\right)^3$$

$$= 1 - a_1\left(\frac{\Delta T}{\Delta T_g}\right) + a_2\left(\frac{\Delta T}{\Delta T_g}\right)^2 - a_3\left(\frac{\Delta T}{\Delta T_g}\right)^3 . \tag{1}$$
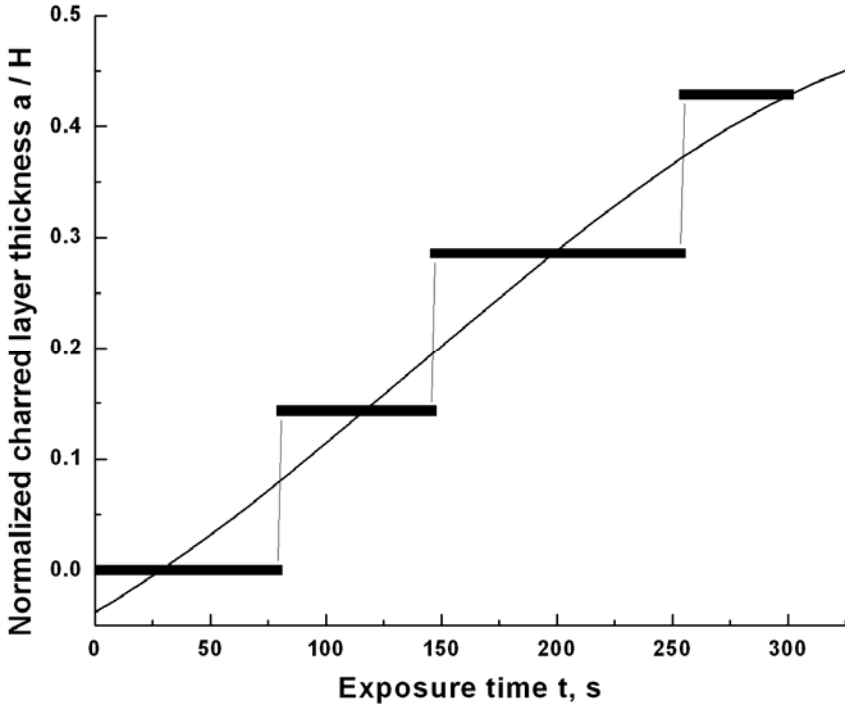
Fig. 3. Normalized charred layer thickness variation with exposure time, which is not a continuous function, due to the assumption that residual resin material less than 80% determines the charred layer thickness. The fire heat flux is $Q = 25 \text{ kW/m}^2$.

For the present E-glass/Vinyl-Ester, $E_0 = 20.6$ GPa and $a_1 = 0.348$, $a_2 = 0.715$ and $a_3 = 0.843$. The composite studied has a fiber volume fraction of 0.516 and consists of four sub-layers with the orientation of each sub-layer [0/90/+45/-45/Random]. Equation (1) captures the physics of the non-linear dependence of the composite modulus on the glass transition temperature of the matrix, T_g. Temperature distribution in the undamaged layer, ΔT, can be determined from the finite element analysis, as described in the previous section. In order to simplify the formulations in the thermal buckling analysis, the axis x is located at the mid-surface of the undamaged layer, as shown in Figure 1.

We define an "average" modulus E_{av} and "a first and second moment" of the modulus with respect to the mid-surface y-axis, E_{m1} and E_{m2}, respectively, by:

$$E_{av} A = \int_A E \, dA \, ; \quad E_{m1} l A = \int_A E y \, dA \, ; \quad E_{m2} I = \int_A E y^2 \, dA, \qquad (2)$$
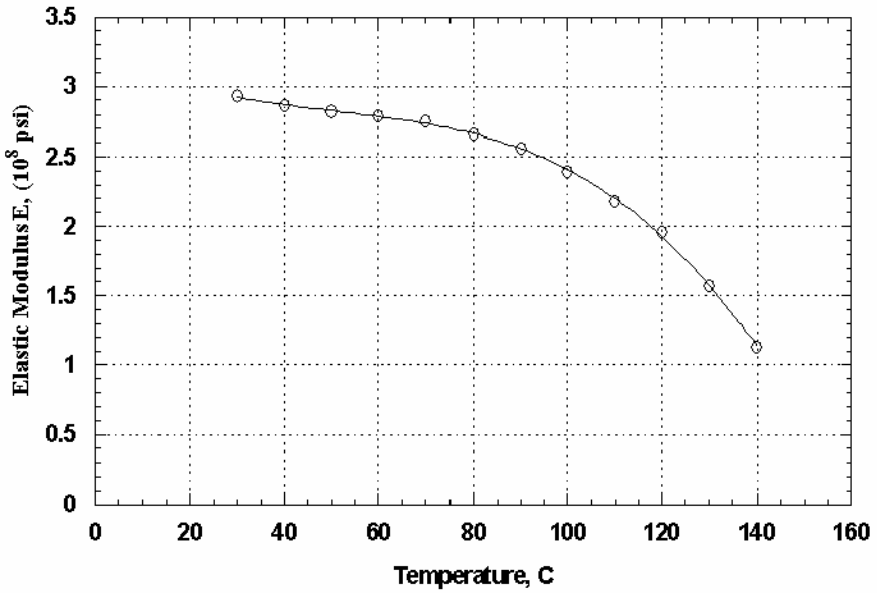
Fig. 4. The effects of temperature on the elastic modulus of E-glass/Vinyl-Ester composites.

where A is the cross sectional area of the undamaged layer, l is the thickness of the undamaged layer; and I is the moment of inertia ($I = \int_A y^2 \, dA$). The integral is evaluated numerically as the modulus E is dependent on the temperature distribution, which has been solved numerically.

Due to the nonuniform modulus E, the neutral axis of the column is not at the mid-surface. The distance, e, of the neutral axis from the mid-surface axis x, is determined from:

$$e \int_A E(y) \, dA = \int_A E(y) \, y \, dA \, , \tag{3}$$

which, by use of Equation (2) leads to:

$$e = E_{m1} \, l \, / \, E_{av} \quad . \tag{4}$$

Assuming the longitudinal thermal expansion coefficient, α_l, independent of temperature, and the thermal force along the longitudinal axis x, is:

$$N_x^T = \int_A E(y) \alpha_l \Delta T(y) \, dA, \tag{5}$$

which, by use of Equation (2) and the temperature distribution results, can be evaluated numerically.

The thermal force develops due to the constraints at both ends of the column, which causes buckling. However, the problem is not a bifurcation buckling because a thermal moment also develops. The thermal moment (with respect to the neutral axis of the column) is:

$$M_Z^T = \int_A E(y)\alpha_l \Delta T(y)(y-e)dA,$$ (6)

and this would cause bending of the column.

The problem now is to determine the response of the column under the influence of both N_x^T and M_Z^T, which changes the character of the problem from bifurcation buckling to a bending problem. That is, the column will bend as M_Z^T is applied.

We consider two cases: one is the column constrained at the two ends, which cannot move axially; the other is the column under a certain constant applied load P, but ends free to move axially. First of all, we assume the external support force P that develops due to the boundaries is large enough to constrain the column, which means both ends of the column are immovable. The axial force N_x does not vary with the axial position x. Thus, it can be seen that N_x^T is equal to -P, due to the axial equilibrium. However, unlike the case of a uniformly heated column, the force P is less than N_x^T because of the thermal moment M_x^T. That is, the column bends away from its original straight configuration due to the thermal moment M_x^T, which relieves some of the external support force at the immovable ends.

Notice that P is a derived quantity, not a controlled quantity at the first case of immovable ends. The controlled quantity is the thermal loading due to the fire, and the response quantity is the mid-span transverse deflection of the column.

Let us denote by u_0 and w_0 the displacements along the x and y directions at the neutral axis and by θ the rotation of the cross section due to bending. The nonlinear strain at the neutral axis $y=e$, is:

$$\varepsilon_0 = u_{0,x} + \frac{1}{2}\theta^2 \quad .$$ (7)

In the following we account for the transverse shear following the procedure in Huang and Kardomateas [13]. In particular, we can set:

$$\frac{dw}{dx} = \sin(\theta + \gamma_{eq}),$$ (8)

where γ_{eq} is the equivalent shear angle, i.e. the difference between the slope of the deflected column axis and the rotation θ of the cross section due to bending.

It is reasonable to assume the shear modulus, G, changes with temperature in the same manner as the elastic young's modulus, E. We can write:

$$\frac{G}{G_0}=1-a_1\left(\frac{T-T_0}{T_g-T_0}\right)+a_2\left(\frac{T-T_0}{T_g-T_0}\right)^2-a_3\left(\frac{T-T_0}{T_g-T_0}\right)^3$$

$$=1-a_1\left(\frac{\Delta T}{\Delta T_g}\right)+a_2\left(\frac{\Delta T}{\Delta T_g}\right)^2-a_3\left(\frac{\Delta T}{\Delta T_g}\right)^3 \ . \tag{9}$$

An effective shear modulus, $\overline{G}$ is now defined based on the shear compliance as [13]:

$$\frac{l}{\overline{G}}=\int_{-l/2}^{l/2}\frac{dy}{G(y)} \ . \tag{10}$$

The equivalent shear angle, γ_{eq}, is defined as:

$$\gamma_{eq}=\frac{\beta P \sin\theta}{\overline{G} A} \ , \tag{11}$$

where β is the shear correction factor which accounts for the no-nuniform distribution of shear stresses throughout the cross section.

Then, the strain at an arbitrary point, $\overline{\varepsilon}(x, y)$, can be represented by:

$$\overline{\varepsilon}=\varepsilon_0(x)-(y-e)\frac{d(\theta+\gamma_{eq})}{dx} \ . \tag{12}$$

When the resulting force from Equation (12) is integrated throughout the section, the resultant should equal $-P+N_x^T$, i.e.:

$$\int_A E(y)\overline{\varepsilon}(x,y)dA=-P+N_x^T \ . \tag{13}$$

Then, by use of Equations (7) and (11), Equation (13) becomes:

$$E_{av}A\left(u_{0,x}+\frac{1}{2}\theta^2\right)+(E_{av}e-E_{m1}h)A\left(1+\frac{\beta P\cos\theta}{\overline{G}A}\right)\theta_{,x}=N_x^T-P \ , \tag{14}$$

and by use of Equation (4) results in:

$$u_{0,x}=\frac{N_x^T-P}{E_{av}A}-\frac{1}{2}\theta^2 \ , \tag{15}$$

which we can integrate over the length of the column subject to the boundary conditions that the ends are restrained in the axial direction, i.e. $u_0(0)=0$ and $u_0(L)=0$.

Therefore, we obtain the following:

$$\left(N_x^T - P\right)\frac{L}{E_{av} A} - \frac{1}{2}\int_0^L \theta^2 \, dx = 0 \ , \tag{16}$$

which is applicable for the entire loading range of the column and is a "constraint equation" expressing the condition that the overall change in displacement between the end supports must be zero because the two ends of the beam are immovable and there is a support load P.

Now, the bending rigidity, $(EI)_{eq}$ of the column, is likewise influenced by the no-nuniform stiffness and is defined by:

$$\left(EI\right)_{eq} = \int_A E(y)(y - e)^2 \, dA \ . \tag{17}$$

By use of Equation (2), this results in:

$$\left(EI\right)_{eq} = E_{m2} I - \frac{E_{m1}^2 l^2 A}{E_{av}} \ . \tag{18}$$

Next, we modify the column equation to consider the thermal loading including thermal force and moment, and moderately large deflections. Transverse shear will also be included. In doing so, we shall properly modify the equations developed in [13]. The moment including the thermal effect is given by:

$$M = -\left(EI\right)_{eq}\frac{d\theta}{dx} - M_z^T \ . \tag{19}$$

From equilibrium, taking into account the (compressive) applied force, P, at both ends, the moment at any position is given by:

$$M = Pw + M_0 \ , \tag{20}$$

where M_0 is the moment at x = 0.

Differentiating Equations (19) and (20) with respect to x and using Equations (8) and (11) with the additional assumption that the shear angle is small, so that $\sin\gamma_{eq} \approx \gamma_{eq}$ and $\cos\gamma_{eq} = 1$, results in:

$$\left(EI\right)_{eq}\frac{d^2\theta}{dx^2} + P\left(\frac{\beta P}{2A\overline{G}}\sin 2\theta + \sin\theta\right) + \frac{dM_z^T}{dx} = 0 \ . \tag{21}$$

As far as the ends (simple supports), we have the moment boundary conditions of:

$$-\left(EI\right)_{eq}\frac{d\theta}{dx}(0)-M_z^T=0\,; \quad -\left(EI\right)_{eq}\frac{d\theta}{dx}(L)-M_z^T=0\,. \tag{22}$$

3 Numerical Results

To illustrate the foregoing analysis, numerical results are presented for a composite column, which is exposed to a high heat flux $Q = 25$ kW/m^2. Let us consider two cases, one is the column is constrained and the ends are immovable; the other is that a constant axial compressive load P is applied to the column. The column is shown in Figure 1. Let us assume the entire column of length, $L = 0.15$ m, thickness, $H = 0.012$ m and width $b = 0.025$ m. Case 1 represents the constrained column (immovable ends); case 2 represents the column exposed to the heat flux Q is under the constant axial compressive load P. The x-axis is located at the center of the cross section of the undamaged material in order to simplify the calculation of the thermal buckling analysis by symmetry.

Based on the thermal model/finite element analysis, the temperature and charred layer thickness can be obtained with time. In Figure 2, we show the temperature distribution of the column exposed to a heat flux $Q = 25$ kW/m^2 at exposure times from 0 to 280 s. Since only the temperatures at the eight nodes are given, the 7th order polynomial fit curves are obtained by the interpolation, which we can use in the thermal buckling analysis in the future. It is obvious that the temperature increases along with the time t. In Figure 3, we show the charred layer thickness variation with time, in which we assume the residual resin context is less than 80%. The variation of residual resin content with time is continuous, however the variation of charred layer thickness is not continuous since if the residual resin content (RRC) is more than 80%, we treated it as the undamaged material; if not, we treated it as the charred material. Thus, the normalized charred layer thickness jumps at the time when the ratio of RRC becomes less than 80%. The variation of the thickness of the charred layer or the undamaged layer is used in the quasi-static thermal buckling analysis as follows: The two-layer approximation used treats the undamaged layer as the original material. The temperature distribution in the undamaged region obtained by the thermal/finite element model is used to analyze the thermal resultant force and moment, and the variation of the material properties with temperature is accounted for as well in the calculation. The effect of temperature on the elastic modulus of E-glass/Vinyl-Ester composites is shown in Figure. 4.   Moreover, since the experimental data are available only up to about the glass transition temperature of the matrix, T_g, we assume that beyond T_g, if the material is not charred yet, the properties of the material such as Young's modulus and shear modulus do not decrease any more.

With the quasi-static assumption, we analyze the thermal buckling response of the column at exposure times from $t = 0$ s until $t = 300$ s. Obviously, the column is

made of two different materials, undamaged (original) layer and charred layer respectively, which have different material properties as shown in Table 1. The mechanical properties are given at room temperature, which is $T_0 = 20°C$ and the original material is E-glass/Vinyl-Ester.

First of all, the thermal moment developed in the column with the exposure time is shown in Figure 5, which is not continuous since the RRC is not continuous. The thermal moment variation is very important, since it shows the influences of the temperature and material properties distributions on the column. At the beginning of the heat exposure, the resin material decomposed due to high temperature and RRC varied with time continuously, but as $t < 80$ s, the RRC is more than 80% for the entire column, therefore we considered no material charred.

Table 1. Material- properties

Properties	Original material	Charred material
α_l, 1/°C	$18.0 * 10^{-6}$	-
E_l ,MPa	$20.6 * 10^3$	-
G_l ,MPa	$2.1 * 10^3$	-

The temperature can be determined by the thermal model/finite element analysis; the thermal moment can be obtained from Equation (6) with the known material properties and temperature distributions. It can be seen from the beginning of the heat exposure $t = 0$ s until $t = 60$ s, it increased with the exposure time obviously, which is due to the temperature variation development in the column. With the time increasing and from the exposure time $t = 80$ s until $t = 140$ s, part of material (1/7 of the entire thickness of the column) is charred based on the Figure 3, the properties of the charred material are neglected; the thermal buckling response of the remaining material is determined. The absolute value of the thermal moment decreased a lot in

this time zone; the decreasing of thickness of the column and the variation of the temperature resulted in the decreasing of the thermal moment, and the moment did not change too much compared with the beginning of the heat exposure from t = 0 s until t = 60 s.   Similarly, with the exposure time increasing further, more material is charred and the thermal moment decreased further.
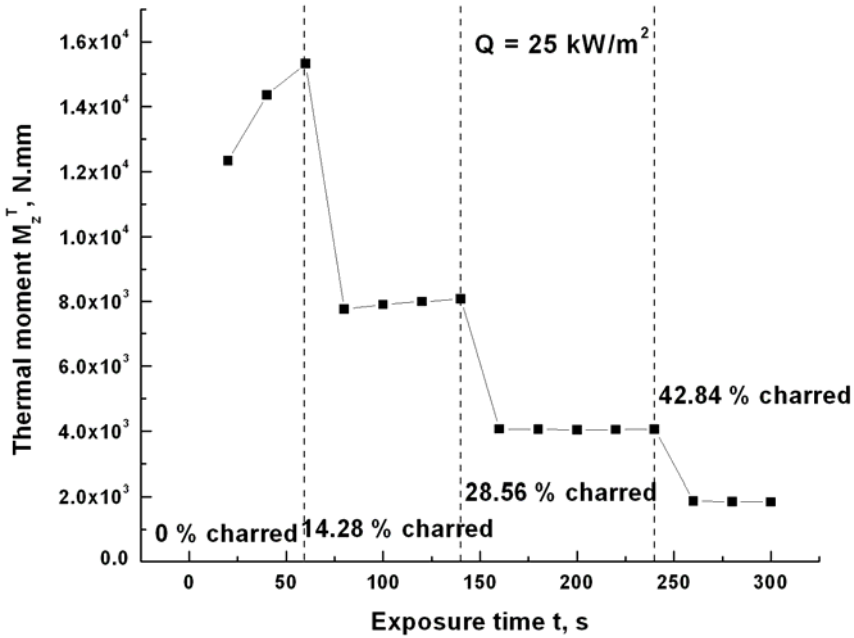
Fig. 5. The thermal moment developed in the column *vs.* exposure time, which is not a continuous function, since the residual resin content does not have a continuous variation with exposure time.

We show the axial constraint stress σ_{xx} in Figure 6; the column is pinned at both ends, which are immovable, and is subjected to an heat flux $Q = 25$ kW/m^2. The axial constraint stress is determined at different exposure time from $t = 20$ s until $t = 300$ s with the quasi-static assumption. It is obvious that the axial constraint stress increases with time t as $t < 140$ s, but σ_{xx} decreases with exposure time as t > 140 s; the 2nd order polynomial curve was obtained to fit the variation trend approximately. We can analyze the variation of the axial constraint by dividing the exposure time into four zones, the thickness of charred material being constant in each zone (the definition of each zone can refer to Figure 3). We can see that the variation of the constraint stress is nonlinear in each zone, which is due to the material properties, which decrease with the exposure time nonlinearly.   For the entire exposure time, there exists a peak value of the axial constraint stress at exposure time t = 140 s; After that, σ_{xx} decreases, which is coming from the fact

that the ends are restrained; therefore, beyond a certain level of deformation, the structure starts to "pull" from the ends rather than "push" against the ends.

Based on the axial support force obtained, the deformation of the column can be determined from Equation (28). It is found that the deformation increases with the exposure time from $t = 60$ s until $t = 300$ s. Actually, the increasing of the deformation before $t = 120$ s is smaller than that of the deformation after $t = 120$ s. The reason for that is coming from the decreasing of the bending rigidity EI_{eq}, which is strongly associated with the thickness of the column.
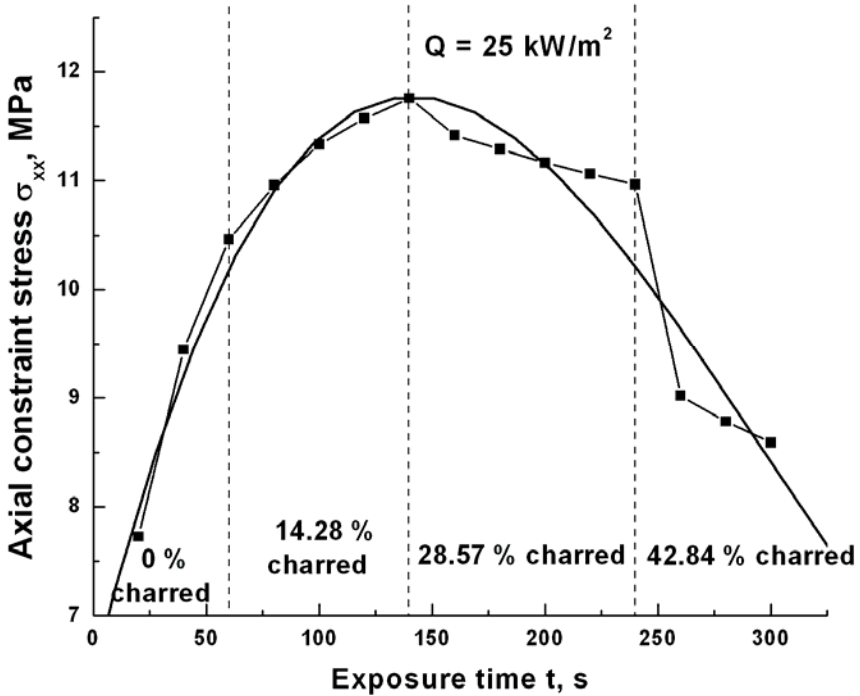
Fig. 6. The axial constraint stress σ_{xx} vs. exposure time t.   A 2nd order polynomial curve was obtained to fit the variation trend.

With increasing the heat exposure time, the thickness of the column decreases due to the resin material decomposition, which results in the decreasing of the bending rigidity EI_{eq}, therefore the column bends more with even lower thermal bending moment. The mid-point deflection w_m normalized by the original thickness of the column is shown in Figure 7. The variation of the mid-point deflection is not smooth, however the linear curve can be obtained to fit it approximately. It can be seen that the mid-point deflection of the column increases in general with the exposure time. Since the direction of the mid-point deflection is always positive, this means that the column bends toward the heat source under the

constrained boundary conditions. In the experimental study reported in the subsequent section, a positive deflection can be observed in the tests for the column exposed to the heat flux $Q = 25$ kW/m^2 under the constant compressive axial load P, corresponding to a stress of 10.5 MPa (based on the original section).
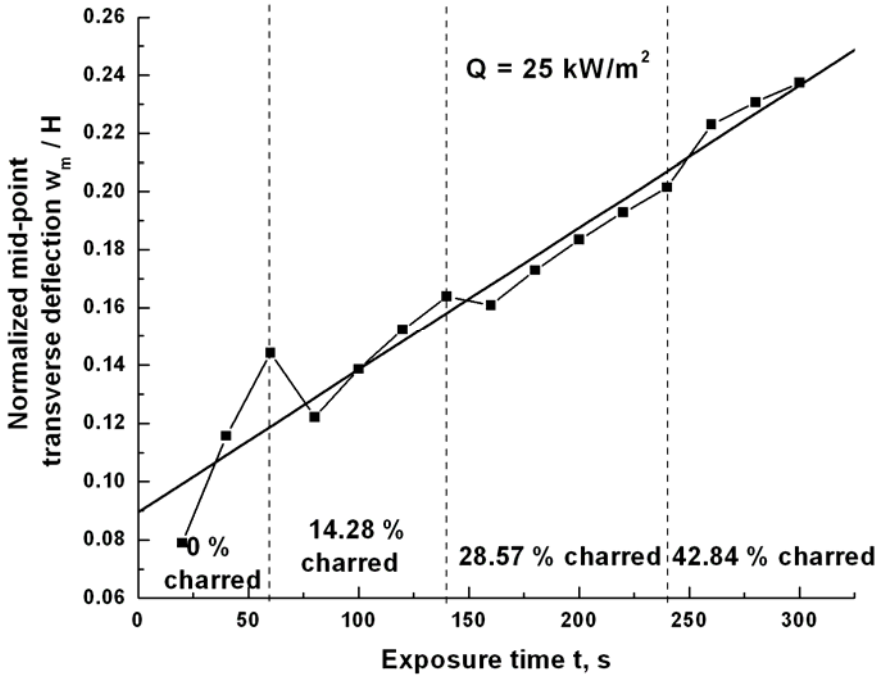
Fig. 7. The normalized mid-point transverse deflection vs. exposure time for the constrained column under the heat flux due to fire, $Q = 25$ kW/m^2.

Figure 8 presents a plot of the axial support force P vs the mid-point deflection w_m for different exposure times. In each case, the mid-point deflection w_m was calculated from the linear analysis for the pinned column under the external heat flux and the end of the column is free to move, so the constraint condition shown in Equation (26) is not applicable. The solution of the problem is in Equation (28) and the variation between the axial force P and the mid-point deflection w_m can be obtained from Equation (29). The Figure shows that, at the beginning of the heat exposure, the axial force P increases initially with only a small bending deflection; But as P approaches the classical buckling load, P_{Euler}, the transverse deflection then increases rapidly. The column behaves much like an "imperfect" column. Eventually, in all cases, the axial support force approaches P_{Euler} as the mid-span deflection becomes large. The temperature change through the thickness has effectively an analogous role for an axially restrained column, as that of an imperfection on a mechanically loaded column.
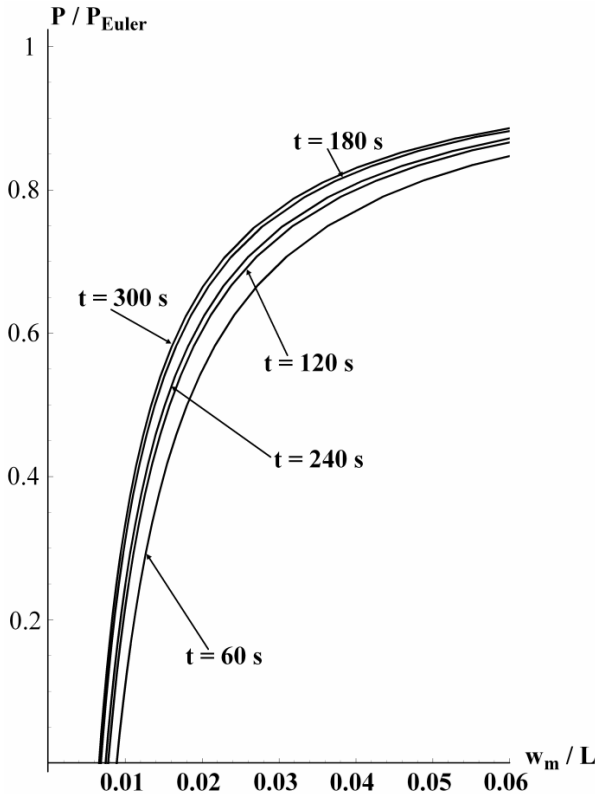
Fig. 8. Axial force *vs* mid-point deflection for a pinned beam with external fire heat flux Q = 25 kW/m^2 at different exposure times; the axial force and the mid-point deflection are normalized by the Euler buckling load, P_{euler}, and the length of the column L, repetitively. The ends of the columns are free to move axially (unconstrained case).

4 Experiments

The goal of the present experimental investigation was to characterize the compressive mechanical response, failure mode and time-to-failure for a fiberglass-reinforced polymeric composite simultaneously exposed to high heat flux and compressive axial loading. The experiments utilized a specially modified cone calorimeter that permitted direct mechanical loading of samples during simultaneous exposure to heat fluxes of 25 kW/m^2, 25 kW/m^2 and 75 kW/m^2. In order to analyze the response of the test samples and compare the experimental data with theoretical results, the axial displacement and mid-point transverse deflection were measured. Many of the test data presented herein are from Liu *et al* [14].

A fiberglass-reinforced vinyl-ester (Derakane 510A) composite laminate was used in the experiments. The laminate panels were manufactured with twenty plies (Seemann Composites Inc., Gulfport, MS) in the form of flat 24-inch × 24-inch panels. The 12.5 mm thick panels had a [(0/90/45/-45/)$_S$] ply lay-up. Test coupons were machined dry from the panels using carbide tooling. Two different specimen

lengths, 150 mm and 100 mm, were utilized in the experiments. In both cases, the nominal thickness was 12.5 mm and the width was 25.4 mm. The broad (25.4 mm wide) faces of the specimens, one of which was exposed to the heat source, were left in the as processed condition.

The ends of the composite specimens fit into flat-bottom cavities that were machined by EDM into Inconel 718 alloy grips. Each grip had a fixed cavity depth of 25 mm. For the shorter 100 mm long specimens, inserts were placed in the grip cavities to fix the heated length of the specimens to 74 mm. For the 150 mm long specimens, the distance between grip faces was 100 mm (this corresponds to the heated length of the specimen); for the 100 mm long specimens the distance between grip faces was 74 mm.[1] In order to minimize heat loss from the specimen to the grips, the surfaces of the specimens located within the grips were insulated with a thin ceramic layer (Zircar Inc., Alumina Cement) approximately 0.4 mm thick. IN-718 shims between the sides of the specimen and grip cavity were used to firmly fix specimen within the grips and minimize any transverse specimen movement in the grips. The grips approximated clamped end-conditions for axial loading.

A cone-calorimeter equipped with a 5000 W electric cone-heater was used as the heat source for the simulated fire tests (Fire Testing Technology Limited, West Sussex, U.K.). In a cone-calorimeter, the heat flux is applied to only one surface of a test specimen. The exit diameter of the cone heater was 158 mm. For this exit diameter and cone design, uniform heat fluxes as high as 100 kW/m^2 were possible over a 100 mm x 100 mm surface area. In the present investigation, the region of uniform heating limited the maximum length of test specimens to 100 mm. Although larger specimen widths were possible, a 25.4 mm specimen width was chosen to reduce the size of the test fixtures and actuator used to apply axial compressive loads. To minimize heating of the specimen sides, a thin (0.3 – 0.4 mm thick) alumina ceramic layer was applied to both sides of the specimens (along the 12.5 mm faces). In an initial study, performed to determine the effect of surface insulation on failure time, several experiments were conducted with 150 mm long specimens with and without surface coatings on the unheated specimen face. These trial experiments showed that coating the backside of the specimens did not significantly affect failure time or failure mode. Therefore, all remaining experiments discussed in this paper were performed with the specimens coated only on their sides and along the surfaces located within the loading grips.

For all tests, the distance between the exit of the cone heater and the specimen surface was maintained at 25 mm. The applied heat flux was varied from 25 kW/m^2 to 75 kW/m^2 to simulate the surface heating expected for fires ranging from small to large intensity. Prior to testing, a heat flux meter was used to measure the heat flux at the surface of the specimens.

To investigate the effect of simultaneous mechanical loading on the compressive behavior of the composite laminate, a load frame with pneumatic actuator was designed to fit directly beneath the cone heater . A load cell mounted at one end of the load frame was used to monitor specimen load level. To minimize transverse and axial deflections that can occur with low stiffness load cells, a load

---

[1] 100 mm was the maximum length over which uniform heating could be obtained in the cone-calorimeter.

cell with very high axial and lateral stiffness was utilized (110 kN capacity, Interface Inc., Model # 120AF-25K). The grip at one end of the specimen was rigidly attached to a load cell. The grip at the opposite end of the specimen was attached to an aluminum H-block that was mounted to a linear bearing system; this arrangement permits axial motion only. An LVDT was used to measure the axial displacement of the specimen.

The time-to failure data for all specimens are summarized in Table 2. Failure times were readily determined since all specimens exhibited catastrophic collapse. Analysis of the video recordings from the experiments showed that, for all specimens, the final failure event was exceedingly rapid (the transition from an intact, load bearing specimen, to catastrophic collapse was less than 50 ms). For a heat flux of 25 kW/m^2, failure times ranged from approximately 2549 s at 3.5 MPa to 251 s at 10.5 MPa. At 50 kW/m^2, failure times were considerably shorter, 404 s at 3.5 MPa and 131 s at 10.5 MPa. For the highest heat flux used, 75 kW/m^2, failure times were much shorter, 191 s at 3.5 MPa and 123 s at 7.0 MPa.

As shown in Figure 9, the relationship between time-to-failure and axial applied load is nonlinear, and the slope of the curve decreases with increasing compressive load. The non-linear variation is most likely caused by char formation and degradation of the material properties. The rate of char formation decreases with increasing exposure time since the char layer influences the transport rate of oxygen to the combustion front and, because of its lower thermal conductivity, reduces heat conduction to the un-charred material. Notice that two specimen lengths were used: 150 mm (100 mm heated length) and 125 mm (74 mm heated length).

Table 2. Time-to-failure (t_f) of fiberglass-reinforced vinyl-ester composites under simultaneous surface heating and axial compressive loading. At 50 kW/m^2, heated specimen lengths of 100 mm and 74 mm were studied.

Heat flux (kW/m^2)		Axial Compressive Stress, MPa			
		3.5	5.25	7.0	10.5
25		t_f = 2549 s	t_f = 660 s	t_f = 366 s	t_f = 251 s
50	100 mm	404	242	178	131
50	74 mm	385	207	133	117
75		191	171	123	---
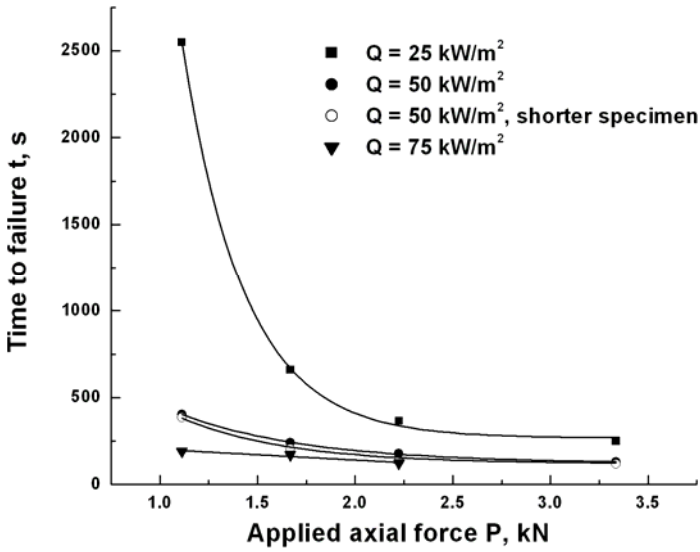
Fig. 9. Relationship between the time-to-failure and compressive axial force for specimens subjected to single-sided heat flux levels of 25 kW/m², 50 kW/m² and 75 kW/m².
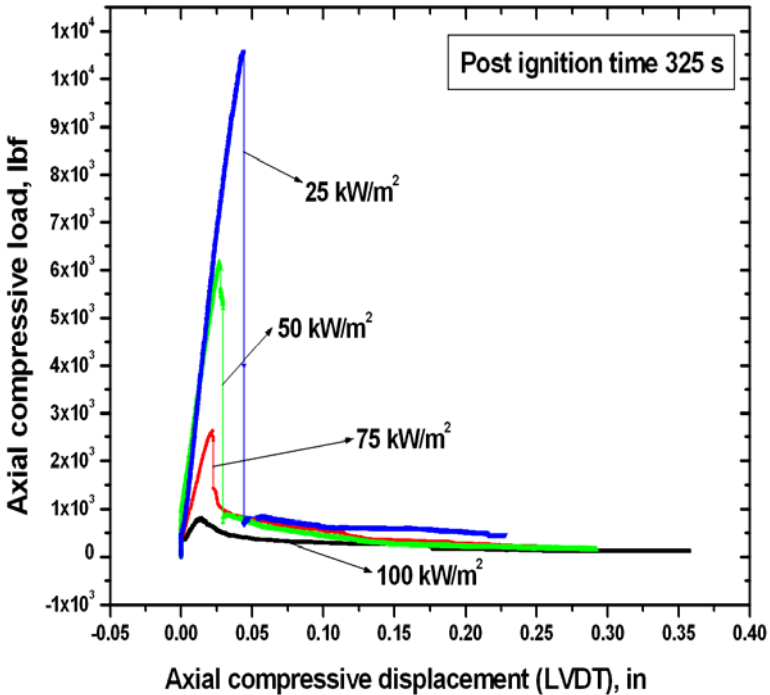
Fig. 10. Effect of heat flux on the post-fire compressive response (experiments).

Post Fire Compression Tests

Compressive tests were conducted following exposure to fire of specific intensity and for a specific exposure time.

Figure 10 shows the effect of heat flux on the compressive response for an exposure time of 325 s. The peak load is reduced as the heat flux increases.

Figure 11 shows the effect of exposure time for a heat flux of 50 kW/m^2. We can see how the peak load is decreased with an increase in exposure time.
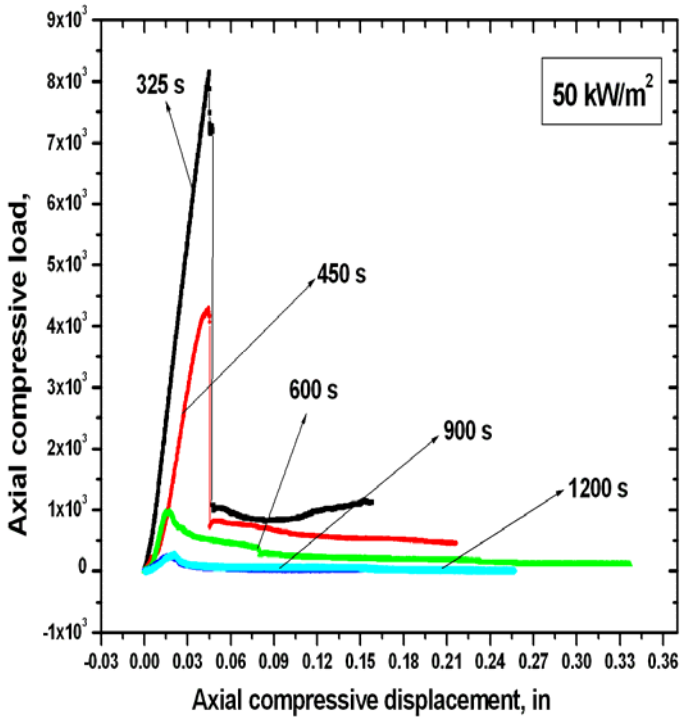
Fig. 11. Effect of exposure time on the post-fire compressive response (experiments).

Acknowledgments

References

[1] Sorathia, U., Rollhauser, C.M., Hughes, W.A.: Improved fire safety of composites for naval applications. Fire Mater 16, 119–125 (1992)
[2] Egglestone, G.T., Turley, D.M.: Flammability of GRP for use in ship superstructures. Fire Mater 18, 255–260 (1994)

[3] Scudamor, M.J.: Fire performance studies on glass-reinforced plastic laminates. Fire Mater 18, 313–325 (1994)

[4] Gibson, A.G., Hume, J.: Fire performance of composite panels for large marine structures. Plast. Rubber Compos. Process Appl. 23, 175–183 (1995)

[5] Mouritz, A.P., Gardiner, C.P.: Compression properties of fire-damaged polymer sandwich composites. Composites Part A 33, 609–620 (2002)

[6] Henderson, J.B., Wiebelt, J.A., Tant, M.R.: A model for the thermal response of polymer composites materials with experimental verification. Journal of Composite Materials 19, 579–595 (1985)

[7] Gibson, A.G., Wu, Y.S., Chandler, H.W., Wilcox, J.A.D., Bettess, P.: A model for the thermal performance of thick composite laminates in hydrocarbon fires. In: Composite Materials in the Petroleum Industry, Revue de l'Institute Francais du Petrole, vol. 50, pp. 69–74 (1995)

[8] Looyeh, M.R.E., Bettess, P., Gibson, A.G.: A one-dimensional finite element simulation for the fire-performance of GRP panels for offshore structures. International Journal of Numerical Methods for Heat and Fluid Flow 7(6), 609–625 (1997)

[9] Liu, L., Kardomateas, G.A.: Thermal Buckling of a Fire-Damaged Composite Column Exposed to Heat Flux. AIAA J. 44(9), 2024–2033 (2006)

[10] Gibson, A.G., Wright, P.N.H., Wu, S.Y., Mouritz, A.P., et al.: Modeling residual mechanical properties of polymer composites after fire. Plastic, Rubber and Composites 32(2), 81–90 (2003)

[11] Mouritz, A.P., Mathys, Z.: Post-fire mechanical properties of glass-reinforced polyester composites. Composites science and Technology 61, 475–490 (2001)

[12] Kulkarni, A.P., Gibson, R.F.: Nondestructive Characterization of Effects of Temperature and Moisture on Elastic Moduli of Vinyl ester Resin and E-glass/vinylester Composite. In: Proceedings of the American Society of Composites 18th Annual Technical Conference, Florida (2003)

[13] Huang, H., Kardomateas, G.A.: Buckling and Initial Postbuckling Behavior of Sandwich Beams Including Transverse Shear. AIAA Journal 40(11), 2331–2335 (2002)

[14] Liu, L., Holmes, J.W., Kardomateas, G.A., Birman, V.: Compressive Response of Composites Under Combined Fire and Compression Loading. In: Couchman, L., Mouritz, A.P. (eds.) Modeling of Naval Composite Structures in Fire, pp. 109–142. Cooperative Research Centre for Advanced Composite Structures, RMIT University, Melbourne, Victoria, Australia (2006)

Theory and Application of Sampling Moiré Method

Yoshiharu Morimoto[1] and Motoharu Fujigaki[2]

[1] Moire Institute Inc.,
 2-1-4-804, Hagurazaki, Izumisano, Osaka 598-0046, Japan
 `morimoto@moire.or.jp`
[2] Departement of Opto-Mechatronics, Faculty of Systems Engineering,
 Wakayama University,
 930 Sakaedani, Wakayama 640-8510, Japan
 `fujigaki@sys.wakayama-u.ac.jp`

Abstract. Sampling moiré method is a newly developed moiré method using an image processor for a grating pattern to measure shape or displacement or strain distributions. A grating pattern on an object is recorded by a digital camera. Though the digitized image shows the grating, a moiré fringe pattern appears by thinning-out the pixels, i.e., sampling the image with a larger pitch than the pixel pitch. If the sampling pitch is changed, the moiré pattern is changed very much. If the phase of the sampling is changed, the phase of the moiré pattern is changed. The phase analysis of moiré pattern provides accurate result of displacement of the grating. If the number of the phase-shifted moiré patterns i.e. the number of pixels for a pitch of grating is larger, the resolution of phase analysis becomes more accurate but the spatial resolution becomes worse. Since the sampling moiré method is useful to analyze the phases of a moiré fringe and a grating from one image of a grating pattern, it is possible to analyze dynamic deformation accurately.

In this paper, the theory of the sampling moiré method is introduced and some applications of the sampling moiré method to displacement measurement of a beam, and shape and strain measurement of a rubber structure are shown.

1 Introduction

It is important for integrity and safety of structures to measure shape, deformation and strain distributions of the structures. Optical methods such as grating projection method, moire method, moire interferometry, speckle interferomrty digital image correlation method are used for the measurement [1-4]. Since these optical methods use the characterictics of light, it is basically possible to measure them

accurately with non-contact and high resolution using phase analysis. Especially moire method has long history as visualized measurement method to obtain the distributions of height, displacement and strain [5-38].

In order to analyze fringe patterns, it is possible to perform quantitative analysis using image processing with a computer. Furthermore, by the phase analysis of grating or fringe patterns, the analysis becomes accurate and high speed[12-21].

Moiré method has been investigated by many researchers such as Theocaris [5], Durelli [6], Suzuki [7], and Post [8]. A moiré fringe pattern appears as the interference between a specimen grating and a reference grating. However, a moiré fringe pattern also appears when the specimen grating lines are sampled by the scanning lines of a TV camera or by the pixels of an image processor [22-33]. This method is called 'scanning moiré method'.

The authors also developed scanning moiré method which does not use a reference grating on the specimen [23,24,28,31-33]. A specimen grating pattern on an object was recorded by a TV camera or a digital camera. Though the digitized image shows only the grating, a moiré fringe pattern appears by thinning-out the pixels, i.e., sampling the image with a larger pitch than the pixel pitch. If the sampling pitch is changed, the moiré pattern is changed very much. If the phase of the sampling is changed, the phase of the moiré pattern is changed. The phase analysis of a moiré pattern provides accurate result of displacement of the grating. The phase analysis of the sampling moiré method using interpolation is proposed by Arai et. al. [25,27,29] If the number of the phase-shifted moiré patterns is larger, the resolution of phase analysis becomes more accurate, but the spatial resolution becomes worse. This method can analyze phase values from one image of a grating pattern. The analyzed phase is very accurate because several phase-shifted moiré fringe patterns are obtained by changing the sampling phase. This method is called 'sampling moiré method'.

Phase-shifting method is the most popular method in the phase analysis methods. However, this method cannot be usually applied to dynamic phenomenon measurement because it requires movement of the master grating for phase-shifting and capturing the specimen grating more than three or four images. Furthermore, if the grating is drawn on the specimen surface, the phase shifting of the grating cannot be performed. However, the sampling moiré method uses only one image and then it can be applied to dynamic phenomena.

In this paper, the theory of sampling moire method and the applications for deflection distribution measurement of a beam and shape and strain distribution measurement of a rotating object at high speed are introduced[32-38].

2 Theory of Moiré Method

The relationship between the moiré fringe pattern and the deformation of a grating has been described by many researchers already [5-11]. Here, the basic essence is introduced in order to explain sampling moiré method.

Let us consider the case that a grating consisting of equally spaced lines shown in Fig. 1(a) is deformed as shown in Fig. 1(b). The grating before deformation is called 'reference grating' and the grating after deformation is called 'specimen grating'.
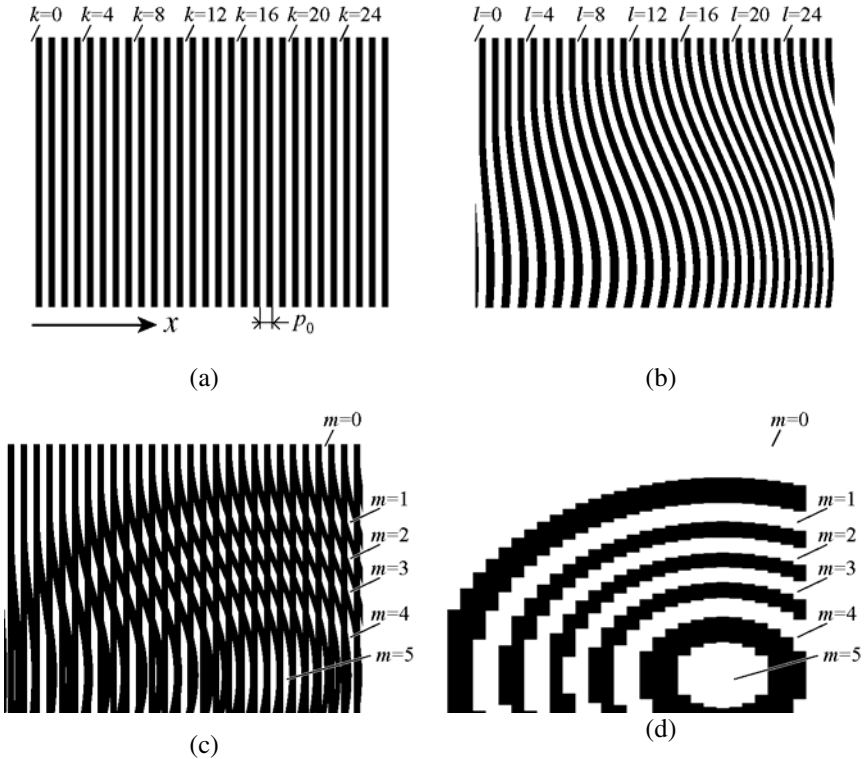
Fig. 1. Theoretical explanation of moiré appearance showing equal-displacement contours: (a) Reference grating; (b) Specimen grating; (c) Moiré fringe pattern obtained by superposing Figs. (a) and (b); (d) Moiré fringe pattern obtained by sampling of TV scanning lines or digital camera

When the reference grating shown in Fig. 1(a) is superposed on the specimen grating shown in Fig. 1(b), a new fringe pattern shown in Fig. 1(c) appers. The fringe pattern is called 'moire fringe'. A white moiré fringe line appears on the parts where a black line of the reference grating and a black line of the specimen grating are superposed or where a white line of the reference grating and a white line of the specimen grating are superposed. A black moiré fringe line appears on the parts where a black line of the reference grating and a white line of the specimen grating are superposed or where a white line of the reference grating and a black line of the specimen grating are superposed.

When the specimen grating shown in Fig. 1(a) is recorded by a TV camera or a digital camera, a moiré fringe pattern is also observed as shown in Fig. 1(d). Scanning moiré method [22-33] or sampling moiré method [34-38] is used this phenomenon.

Let us show the principle for obtaining displacement and strain distributions from this moiré fringe pattern. Each white line from the left edges of the reference grating is numbered as k=0, 1, 2, … as shown in Fig. 1(a). These numbers are called 'line number.' By considering that the deformation is one-dimensional for simplicity, each point moves along the x-direction, that is, normal to the original grating line. Fig. 1(b) shows a deformed grating with x-directional deformation. The lines of the deformed specimen grating are numbered as l=0, 1, 2, … respectively, as shown in Fig. 1(b).

On a continuous moiré fringe line in Fig. 1(c), the difference between the line number of the reference grating and the line number of the specimen grating is a constant. The number m is the difference of the two line numbers.

$$m=k\text{-}l \tag{1}$$

It is called 'fringe order' of the moiré fringe line. When the pitch of the grating lines of the reference grating is p, the specimen grating is deformed as mp along the line normal to the grating lines of the reference grating. That is, on the fringe lines with moiré fringe order m, the displacement is mp. By looking at the moiré fringe pattern, displacement distribution is determined. This is the principle of moiré method to measure deformation.

That is, the x-directional displacement u at the place with a fringe order m is expressed as follows:

$$u=mp \tag{2}$$

The x-directional strain is defined as differentiation of the x-directional displacement with respect to x. Then the strain is obtained as follows.

$$\varepsilon = \frac{du}{dx} = p\frac{dm}{dx} \tag{3}$$

On the other hand, the fringe distance δ between the neighboring fringes shows that the displacement difference between the both ends of the distance is 1 pitch of the reference grating. Therefore the strain at the distance is expressed as follows.

$$\varepsilon = \frac{\text{elongation}}{\text{length before deformation}} = \frac{p}{\delta - p}$$
$$\cong \frac{p}{\delta}(\text{When } \delta \text{ is sufficiently larger than } p) \tag{4}$$

From this equation, strain is obtained from the fringe space δ.

When a grating is projected on an object, the grating is deformed according to the shape of the object. When the reference grating is superposed on this deformed grating, a moiré fringe pattern is observed. By analyzing this moiré fringe pattern, the shape of the object is measured. This method is called 'moiré topography'.

3 Phase Analysis of Grating or Fringe Pattern

In order to analyze a grating pattern or an optical interference pattern such as a moiré fringe, image processing techniques such as thinning of lines to obtain frin-ge center lines were used. It was time–consuming and the accuracy was not good. Recently phase analysis is popular. It provides high-speed, automatic and accurate analysis at each point of the object image. That is, the brightness distributions of a grating pattern or a fringe pattern are regarded as cosinusoidal waves, and the pha-ses at each pixel point of the object image is obtained from the brightness data of the images [12-21]. The theory is as follows.
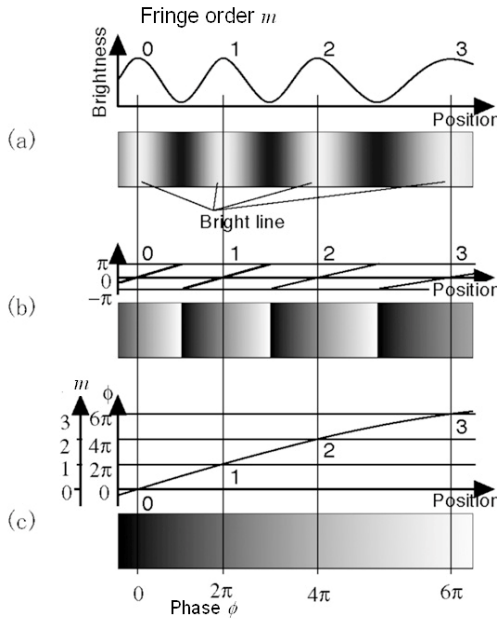
Fig. 2. Brightness and phase distribution of fringe pattern: (a) Brightness distribution; (b) Wrapped phase distribution; (c) Unwrapped phase distribution

As shown in Fig. 2, the brightness distribution $I(x, y)$ of a grating or a fringe pattern is cosinusoidal, expressed as the following equation.

$$I(x, y) = I_a(x, y)\cos[\phi(x, y)] + I_b(x, y) \tag{5}$$

where $I_a(x, y)$ and $I_b(x, y)$ are the brightness amplitude and the brightness of background at a point (x, y) in the image, respectively. When the phase of the grating or fringe pattern is shifted, the brightness of the grating or the fringe pattern is expressed as follows:

$$I(x, y, \alpha) = I_a(x, y)\cos[\phi(x, y) + \alpha] + I_b(x, y) \tag{6}$$

where α is the phase-shift value obtained by moving the grating or the fringe pattern. The wave has a phase at each pixel point, which is the 2π ($= 360°$) for one cycle. The phase ϕ is obtained from the fringe order m.

$$\phi = 2\pi m \tag{7}$$

(a)

(b)
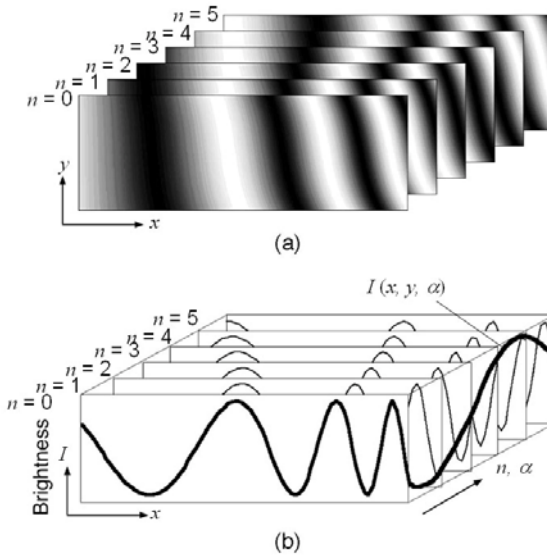
Fig. 3. Fringe patterns obtained by phase shifting method: (a) Brightness distributions obtained by phase shifting; (b) Brightness distributions along centerline and brightness change at edge point

If the phase shift α is given as $2\pi n/N$, $(n=0\sim N-1)$ i. e., N times for one cycle and N images are obtained as shown in Fig. 3(a). That is, the brightness values $I(x, y, \alpha)$ are expressed in Fig. 3(a).

The brightness change at a pixel point expressed in Fig. 3 is cosinusoidal for one cycle. The phase of the first image is the initial phase to obtain.

In order to analyze the initial phase $\phi(x, y)$, several methods such as Fourier transform method, phase-shifting method, extraction of characteristic, integral phase-shifting method [19-21] were proposed. These methods using phase analysis are basically accurate.

The intensity of the n-th phase-shifted images $I_n(x, y)$ can be expressed as follows:

$$I_n(x, y) = I_a(x, y)\cos[\phi(x, y) + n\frac{2\pi}{N}] + I_b(x, y) \tag{8}$$

$$(n = 0, 1, ..., N-1)$$

The phase change at a pixel point of the fringe pattern can be obtained from the frequency 1 of the discrete Fourier transform (DFT) or the phase-shifting method using Fourier transform (PSM/FT) of Eq. (8). As the results, the wrapped phase ϕ of the frequency 1 is expressed as follows [14,38].

$$\tan\phi(x, y) = -\frac{\sum_{n=0}^{N-1} I_n(x, y)\sin(n\frac{2\pi}{N})}{\sum_{n=0}^{N-1} I_n(x, y)\cos(n\frac{2\pi}{N})} \tag{9}$$

In Eq. (8), the three unknown values $I_a(x, y)$, $\phi(x, y)$, $I_b(x, y)$ are obtained from measuring more than three brightness values $I_n(x, y)$ and the initial phase $\phi(x, y)$ can be obtained using Eq. (9). By recording the grating in defocus of the camera if the grating is not cosinusoidal, the recorded grating image is changed into a cosinusoidal pattern approximately. Conventionally, $N=3$ or $N=4$ are used. However, if larger N is used, the accuracy becomes better in the cases of noisy, non-cosinusoidal and/or non-equal division of phase-shift.

The phase obtained by Eq. (9) is wrapped into $-\pi \frown \pi$. The wrapped phase is unwrapped by adding or subtracting 2π as shown in Fig. 2(c). In the case of moiré fringe, the unwrapped phase $\phi(x, y) = 2\pi m$ is proportional to the displacement u as sown in Eq. (2).

4 Measurement Method of Displacement and Strain by Phase Analysis of Moiré Fringe

The moiré fringe order m is the difference of the specimen grating number l and the reference grating number k as shown in Eq. (1). The phases of the moiré fringe, the specimen grating and the reference grating are obtained by multiplying 2π to the moiré fringe order and the grating numbers. Then Eq. (1) becomes as follows.

$$\phi_m = 2\pi m = 2\pi(k - l) = \phi_r - \phi_s \tag{10}$$

where ϕ_m is the phase of the moiré fringe, ϕ_s is the phase of the specimen grating, and ϕ_r is the phase of the reference grating. From Eq. (10),

$$\phi_s = \phi_r - \phi_m \tag{11}$$

If the phase ϕ_m is analyzed when the phase ϕ_r is given, the phase ϕ_s of the specimen grating is calculated.

When the phase ϕ_r of the sampling is shifted by 2π, i.e., one pitch of the reference grating, the phase ϕ_m of the moiré fringe is shifted by 2π. When the phase of the moiré fringe is also changed by the deformation, the phase difference $\Delta\phi_s$ of the grating lines is the same as the minus of the phase-difference $\Delta\phi_m$ of the moiré fringe before and after deformation at a pixel point.

Even if the grating is already deformed in the initial state, the displacement u after the initial state is obtained from the phase difference of moiré fringes $\Delta\phi_m$ between before and after deformation. Then the displacement u is obtained as the following equation from Eqs. (1)～(3), (10).

$$u = (m_2 - m_1)p = \frac{p}{2\pi}(\phi_{m2} - \phi_{m1}) = -\frac{p}{2\pi}(\phi_{s2} - \phi_{s1}) \tag{12}$$

$$u = p\frac{\Delta\phi_m}{2\pi} = -p\frac{\Delta\phi_s}{2\pi} \tag{13}$$

$$\varepsilon = \frac{du}{dx} = \frac{p}{2\pi}\frac{d(\Delta\phi_m)}{dx} = -\frac{p}{2\pi}\frac{d(\Delta\phi_s)}{dx} \tag{14}$$

where, the suffix, 1 and 2 are express before and after deformation, respectively.

In the case of fringe order analysis, the fringe orders and the distances of neighboring fringes are given as integer numbers. And the number of data is few, because the data are given one between the fringe distance. While, phase analysis is very accurate because the data are given at every pixel point and the phase is given as decimal. Practically the accuracy of phase analysis is 100 to 1000 times better than the one by fringe distance analysis. The analysis algorithm is very simple and the process is same at all the pixel points.

5 Sampling Moire Method (Scanning Moire Method)

5.1 Background of Sampling Moiré Method

Moiré fringe appears by sampling with a digital camera as shown in Fig. 1(d). The phenomenon is called 'scanning moiré method' because the moiré pattern appears by sampling of scanning lines of a TV camera [22-33]. The authors applied this method to two-dimensional analysis of a 2-D grating with x- and y-directional gratings using a digital camera or an image processor which samples an image at each pixel point. A moiré fringe pattern is obtained by changing the sampling pitch of the recorded image. Therefore this method is called 'sampling moiré method' [34-38].

Let us explain the history of scanning moiré method and sampling moiré method.

Idesawa et. al. [22] proposed scanning moire method by changing the scanning pitch ellectorically. Morimoto et. al. [23,24] proposed sanning moire method by thinning-out the scanning line of a TV camera using an image processor. Arai et. al. [25,27,29] proposed phase-shifting scanning moire method using thinning-out and interpolation and discussed the accuracy according to the interpolation method. Yoshizawa et. al. [26] proposed a phase analysis method measuring the phase difference at two points electoronically using rotating reference grating. Morimoto et. al. [28,31-33] also proposed a method to obtain smooth moire fringe pattern by shifting the thinning-out of scanning lines. Kato et. et. al. [30] proposed a real-time shape measurement system by low-pass filtering and superposing a phase-shited virtual reference grating on a recorded specimen grating. The authors [34-38] analyzed shape, displacement and strain distributions using the interpolation method developed by Arai et. al.

Conventional phase-shifting method requires multiple phase-shifted images. However, sampling moire method requires only one image. From the one image, phase-shifted moire patterns are obtained by changing the start pixel of sampling, and then it is possible to analyze a moving object.

If a two-dimensional grating with x- and y-directional gratings is used, two dimensional deformation analysis can be performed. In this case, by eliminating one directional grating with averaging in the other directional grating for one pitch, one directional analysis is performed by the one-dimensional sampling moire method mentioned above. By changing the direction, two-dimensional analysis is performed. The processes are as follows.

5.2 Process of Sampling Moiré Method Using 1-D Grating

A grating pattern is recorded by a digital camera. The recorded image is analyzed by sampling moiré method. The process is as follows.

Figure 4 illustrates the appearance of a moiré fringe pattern by sampling moiré method. Figure 4(a) shows the center position of the sampling points (pixel points) of a digital camera. Figure 4(b) shows a specimen grating. The image of Fig. 4(b) recorded by the camera is shown in Fig. 4(c). The image shows only the original grating, not a moiré fringe pattern. If every N-pixel (in this case, thinning-out index $N = 4$) from the first sampling point is picked up from Fig. 4(c), a moiré fringe pattern is obtained as shown in Fig. 4(d). Figure 4(d) is obtained by selecting the first pixel and sampling every Nth -pixel (in this figure, $N = 4$). If instead the second, third or fourth sampling point is selected, the images of a moiré fringe pattern with $\pi/2$, π and $3\pi/2$ phase-shift shown in Fig. 4(e), (f) and (g), respectively, are obtained. This process corresponds to the phase shifting of the fringe pattern. If all the sampled images that are thinned-out in Figs. 4(d)-(g) are interpolated using the neighboring data, the image becomes clearer and easy to observe as shown in Figs. 4(h)-(k) from Figs. 4(d)-(g), respectively. From these phase-shifted fringe patterns, the phases of the moiré fringes are analyzed.
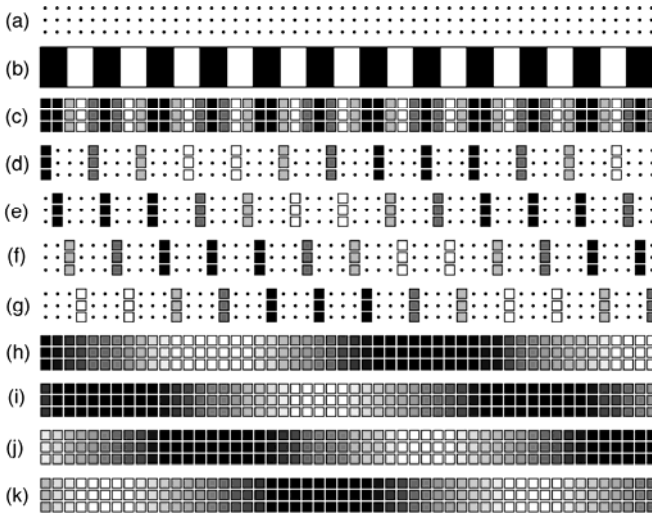
Fig. 4. Phase analysis by sampling moiré method: (a) Sampling points of camera; (b) Specimen grating; (c) Sampled image of Fig. (b); (d) Thinned-out image from Fig. (c) (N=4, α=0); (e) Thinned-out image from Fig. (c) (N =4, α=π/2); (f) Thinned-out image from Fig. (c) (N =4, α=π); (g) Thinned-out image from Fig. (c) (N =4, α=3π/2); (h) Interpolated image of Fig. (d); (i) Interpolated image of Fig. (e); (j) Interpolated image of Fig. (f); (k) Interpolated image of Fig. (g)

When the number of phase-shifting for one cycle is N, and the intensity of the n-th phase-shifted images $I_n(x, y)$, the wrapped phase ϕ is obtained from Eq. (9).

If the phase ϕ_m of the moiré fringe is analyzed when the phase ϕ_r of the reference grating i.e. sampling phase is given, the phase ϕ_s of the specimen grating is determined from Eq. (11).

From the phase ϕ_s of the specimen grating, shape, displacement and strain is accurately obtained according to the optical systems, respectively.

In this case, the gage length is one or two pitches of the grating. It is smaller than Fourier transform method which uses whole data of the image. In the sampling moiré method, the phase analysis of moiré pattern provides accurate result of displacement of the grating. If the number of the phase-shifted moiré patterns i.e., the number of pixels for a pitch of the grating is larger, the resolution of phase analysis becomes more accurate but the spatial resolution becomes worse.

5.3 Process of 2-D Displacement Analysis by Sampling Moiré Method Using 2-D Cross Grating

In order to analyze two-dimensional (2-D) displacement, a 2-D cross grating is used. Figure 5 shows images in the 2-D analysis process by sampling moiré method. Figure 5(a) shows the image of a 2-D grating captured by a CCD camera. Figure 5(b)

shows the extracted *x*-directional grating pattern obtained by averaging (smoothing) of Fig. 5(a) in the *y*-directional one pitch. Figure 5(c) shows several phase-shifted moiré patterns which are produced by sampling moiré method from Fig. 5(b).

Figure 5(d) shows the phase distribution of the moiré pattern produced from Fig. 5(c) by phase-shifting method using Eq. (9). Figure 5(e) shows the phase distribution of the reference grating which is smoothed in the *y*-direction from the 2-D cross grating pattern. From the phase distribution ϕ_m of the moiré, and the phase distribution ϕ_r of the reference grating, the phase distribution ϕ_s of the deformed specimen grating can be calculated using Eq. (11). Figure 5(f) shows the wrapped phase distribution of the deformed specimen grating.

(a) 2-D grating pattern image (b) Grating image obtained after the *y*-dimensional smoothing process (c) Phase-shifted moire patterns (d) *x*-directional phase distribution of moire (e) *x*-directional reference image (f) Phase distribution (g) Unwrapped phase
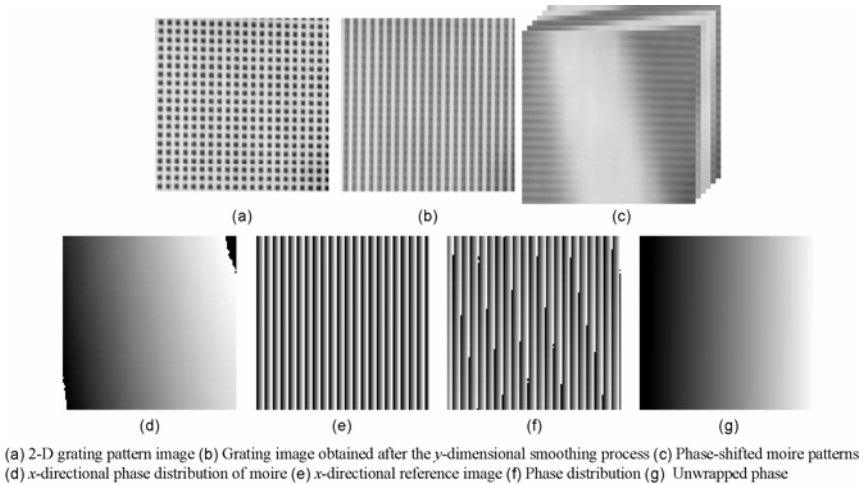
Fig. 5. Process of x-directional phase analysis using 2-D grating

The period of the reference phase distribution is usually taken as same as the pitch of sampling pixels in sampling moiré method. Figure 2(g) shows the *x*-directional unwrapped phase distribution. In the same manner, the y-dimensional phase distribution of the specimen grating can be obtained.

6 Deflection Measurement by Sampling Moiré Method

The sampling moiré method proposed above was applied to the measurements of shape, displacement and so on. The deflection distribution of a three-point-bending beam was measured by one camera system [36,38]. The sampling moiré method using phase shifting was applied to the deflection measurement of a beam under symmetric three-point bending. Conventional deflection measurement of bridges is usually performed by using many deflection sensors for point-by-point

measurement. It is time-consuming, hard-working and expensive for distribution measurement. The sampling moiré method is very useful for the measurement because of high-accuracy, high-speed, low-cost and easy implementation.

6.1 Experimental Setup and Grating Tape

A special tape of a two-dimensional cross grating with 2.0 mm pitch shown in Fig. 5 was pasted over the steel beam (SS400) as shown in Fig. 7. The size of the beam is 30 mm in width, 20 mm in height and 1000 mm in length. The experimental setup is shown in Figs. 8 and 9. A normal digital camera (Nikon, E8800), with 3264 pixels by 2448 pixels resolution, was used to record the image. The distance from the specimen to the camera was 990 mm as shown in Fig. 8(b). The camera was aligned so that its seven pixels were corresponding to the grating pitch.

The specimen was loaded by increasing the number of 1.0 kg weight blocks. The steel beam was loaded at the center position from 9.8 N to 127.4 N. To check the actual displacement of the specimen, a laser displacement sensor with 0.02 μm resolution accuracy was located at the position of the loading point.

In recorded images, one pixel of the digital camera was adjusted to correspond to about 0.3 mm on the beam.
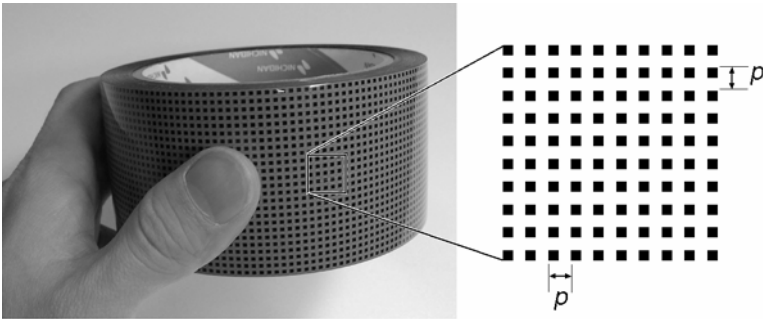
Fig. 6. Tape with grating for deformation measurement. (Pitch p = 2.032 mm)
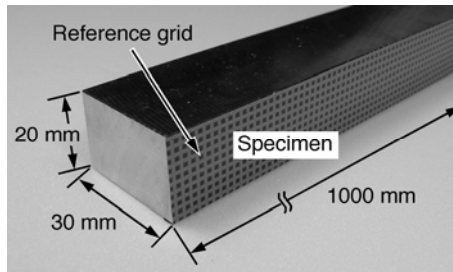
Fig. 7. Steel beam specimen, Size: 30 mm (W), 20 mm (H) and 1000 mm (L)
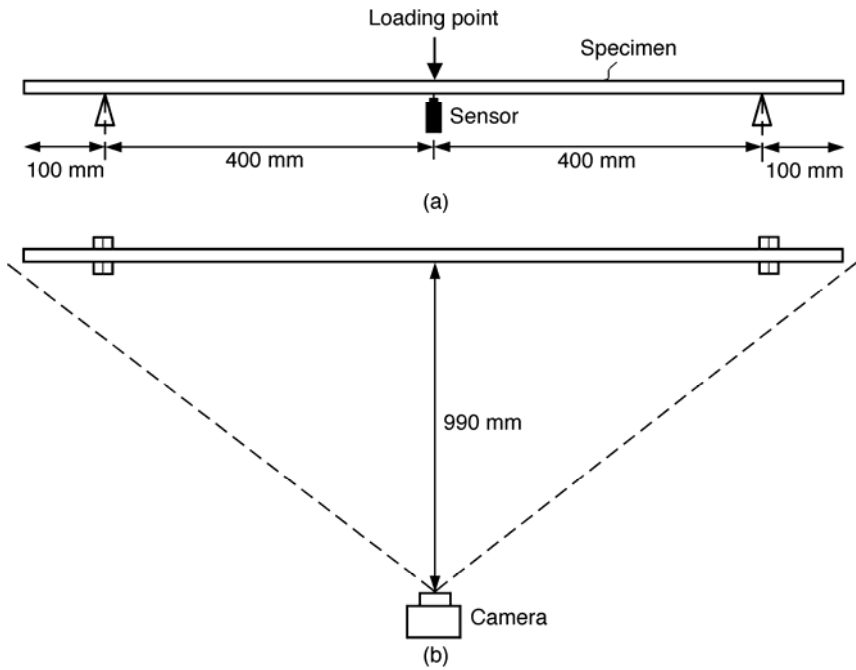
Fig. 8. Experimental setup: (a) Side view; (b) Top view
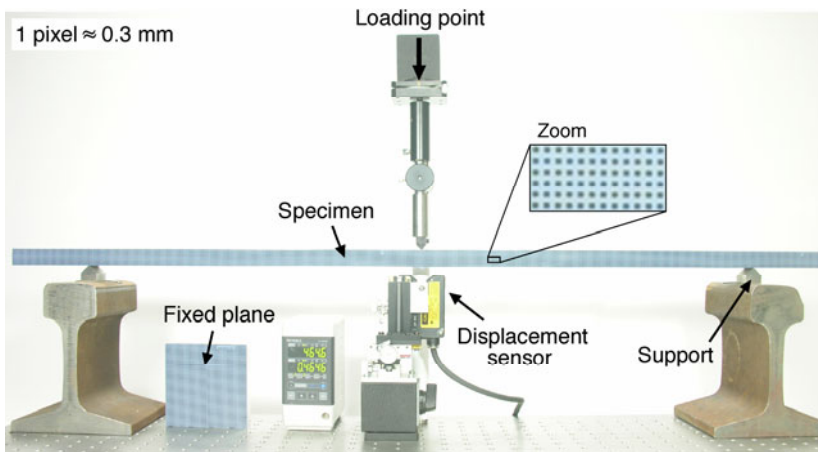
Fig. 9. Photograph of experimental setup
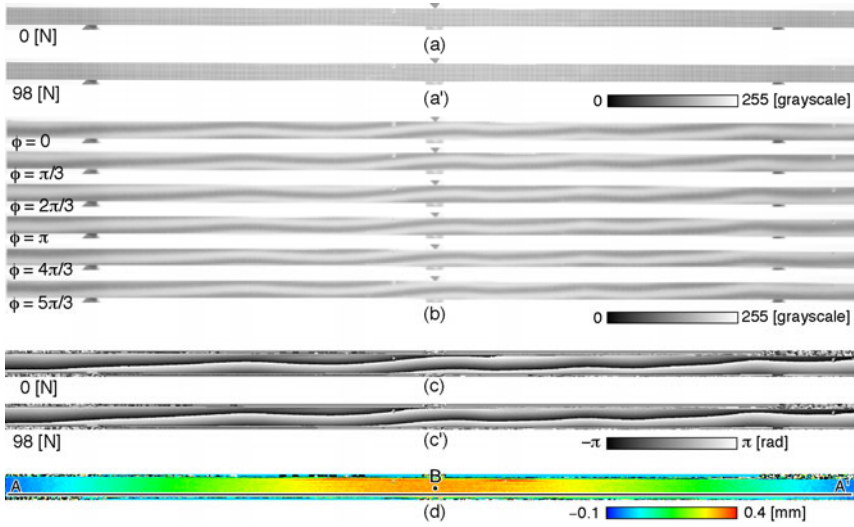
Fig. 10. Experimental results: images of the specimen before (a) and after (a') loading; (b) phase-shifted images obtained by sampling moiré method; wrapped phase distribution before (c) and after (c') loading at 98N; (d) deflection distribution

6.2 Experimental Results of Deflection Measurement

Figure 10 shows the captured and analyzed images. Figure 10(a) shows the captured image of the specimen before loading. Figure 10(b) shows the phase-shifted images obtained when the thinning-out index N is equal to 6. Then the $\pi/3$ phase-shifted moiré patterns were obtained. Figures 10(c) and (c') show the wrapped phase distributions before loading and after 98 N loading, respectively. Figure 10(d) shows the displacement distribution obtained from Eq. (13). Figure 11 shows the deflection distributions under loading at 9.8 to 127.4 N.
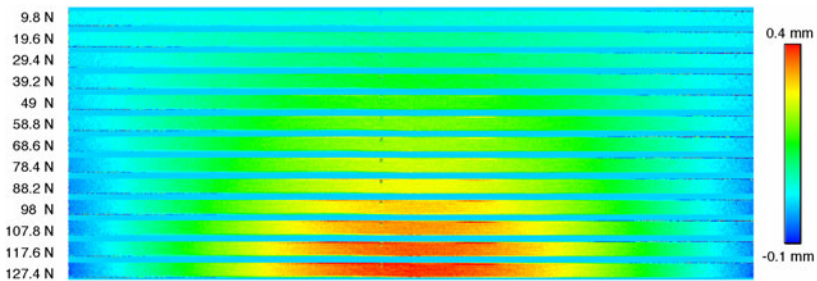
Fig. 11. Deflection distributions under loading at 9.8 to 127.4 N

Figure 12 shows the results of displacement along the line AA' in Figure 10(d). Figure 13 shows the comparison of the measured displacement values by the sampling moiré method and with the values measured by the laser displacement sensor at the position B in Fig. 10(d) in different loading condition. The results show that the displacement values of the steel beam agree well with the data obtained by the sensor. The average error was 3.8 μm and the standard deviation was 3.15 μm. This means that the average error of the detected displacement was less than 1/500 of the grating pitch 2.0 mm.
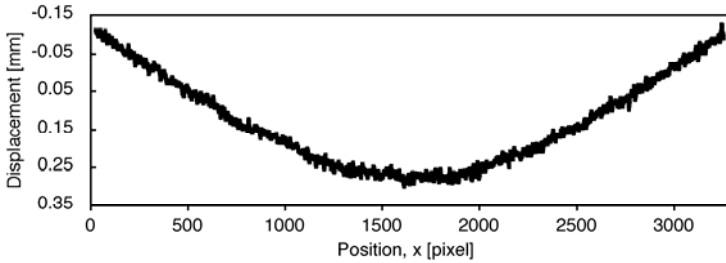
Fig. 12. Displacement distribution along line AA' in Figure 10(d)
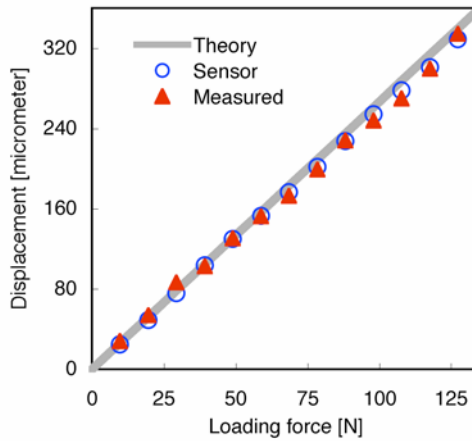
Fig. 13. Accuracy check by comparing measured displacements by sampling moiré method with those by laser sensor and those obtained from beam theory

7 Shape and Displacement Measurement by Sampling Moiré Method

Sampling moire method was applied to measurement of shape, displacement distributions and strain distributions on the surface of a rotating rubber object running at 80 km/h speed using a two-camera stereoscopic system [37].
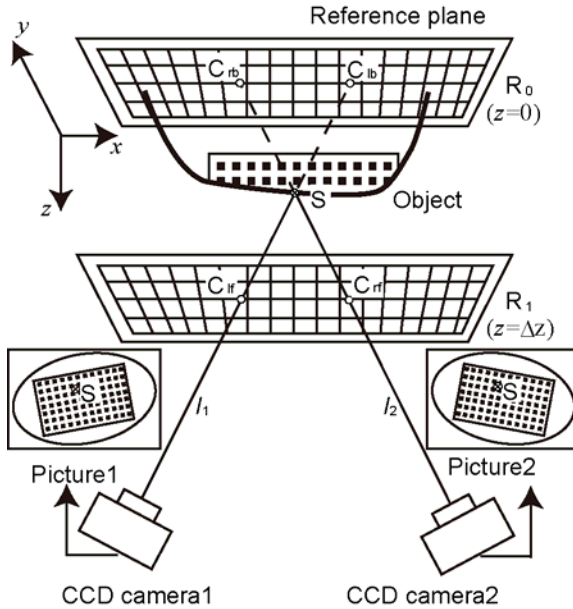
Fig. 14. Arrangement of cameras, reference plane and object

7.1 Process of Measurement

Let us explain the process of the measurement using Fig. 14. Figure 14 shows a schema of the arrangement of two cameras, two reference planes and an object. At first, in order to calibrate, two reference planes R_0 and R_1 with gratings are recorded and the phase distributions of the gratings are obtained. Secondary, each corresponding point of the gratings on the reference planes of the images recorded by the two cameras is determined each other on the whole area of the planes. Then the view lines of each pixel point of the cameras are obtained. Thirdly, an object with a grating on the surface is recorded by the two cameras. Corresponding points at the same point on the object are obtained from the two images. The coordinates of each point of the object is determined from the intersection of the view lines from the two cameras. From the coordinates, the shape is determined. From the position of each point before and after deformation, strain distributions are obtained. The concrete measurement is as follows.
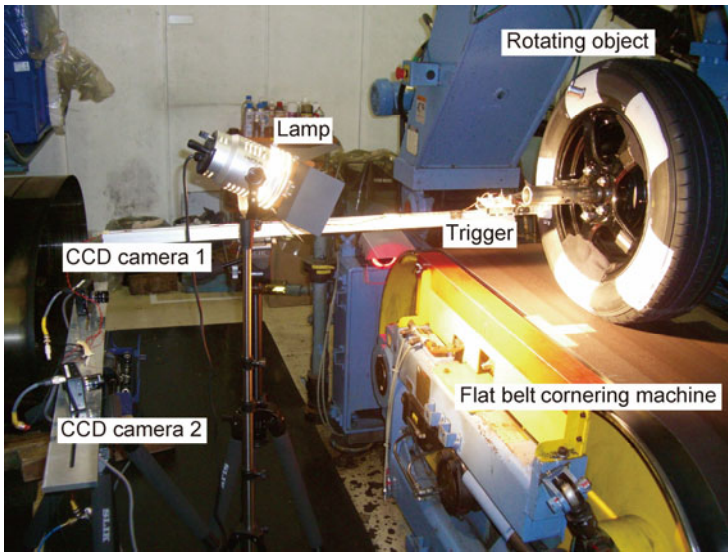
(a) Photograph
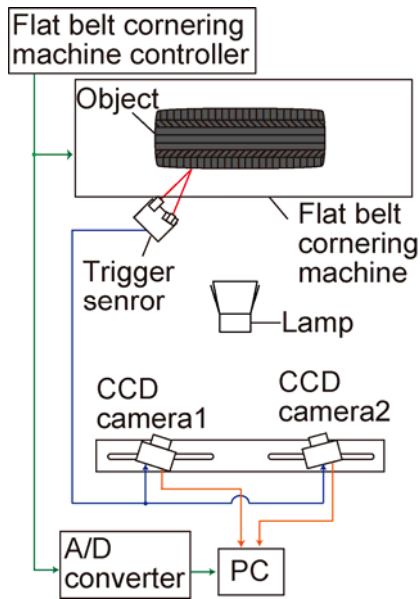
(b) Diagram

Fig. 15. Experimental setup to measure moving object

7.2 Calibration with Two Reference Planes

Both left and right CCD cameras capture a reference planes. A liquid crystal display (LCD) is used as the reference plane. The reference plane is moved at two positions, R_0 and R_1. The reference plane can display grating patterns for the x- and y- directions with phase-shifting. Initial phase distributions of the grating patterns can be obtained accurately using phase-shifting method. The initial phase distribution is obtained as unwrapped phases for the x- and y- directions (ψ_{nx}, ψ_{ny}) on the two reference planes R_n ($n = 0, 1$).

The 3-D coordinates (x, y, z) at a point on the reference plane is calculated from the x-directional grating pitch p_x, the y-directional grating pitch p_y and the z position of the reference plane z_n ($n = 0, 1$) as shown in Eq. (15).

$$x = \frac{p_x \psi_{nx}}{2\pi} + x_0, \quad y = \frac{p_y \psi_{ny}}{2\pi} + y_0, \quad z = z_n, \tag{15}$$

where p_x and p_y are the grating pitches for the x- and y-directions, respectively, and (x_0, y_0) is the coordinates at the point where (ψ_{nx}, ψ_{ny}) = (0, 0).

7.3 Shape and Strain Distribution Measurement

An object is placed between the two reference planes. A 2-D grating attached on the object is captured by two sets of CCD cameras as shown in Fig. 14.

The view line l_1 from a pixel of CCD camera 1 passes through the point S on the object and the view line l_2 from a pixel of CCD camera 2 also passes through the point S on the object. The points C_{lb} and C_{lf} are intersections of the view line l_1 with the reference planes R_0 and R_1, respectively. The points C_{rb} and C_{rf} are intersections of the view line l_2 with the reference planes R_0 and R_1, respectively. The position of the reference plane R_0 and R_1 are $z = 0$ and $z = \Delta z$, respectively. An expression of the view lines l_1 and l_2 can be obtained from the four points C_{lb}, C_{lf}, C_{rb} and C_{rf}. The 3-D coordinates of the point S are obtained as the intersection of the two view lines l_1 and l_2.

Strain can be calculated from the 3-D coordinates of the two points at each corresponding point on the object before and after deformation.

7.4 Experimental Results of Shape and Strain Distributions of Rotating Object

Figure 15 shows the photograph of the experimental setup. A rotating object was set on a flat belt cornering machine. This test machine can control the rotating of the object. The rotating object had a 2-D grating with 2.0 mm pitch on the surface. The 2-D grating was made of a thin rubber sheet. The 2-D grating was printed on the rubber sheet.

(a) 2-D -grating (b) Phase distribution of moiré

(c) Phase distribution of grating (d) Unwrapped phase of grating
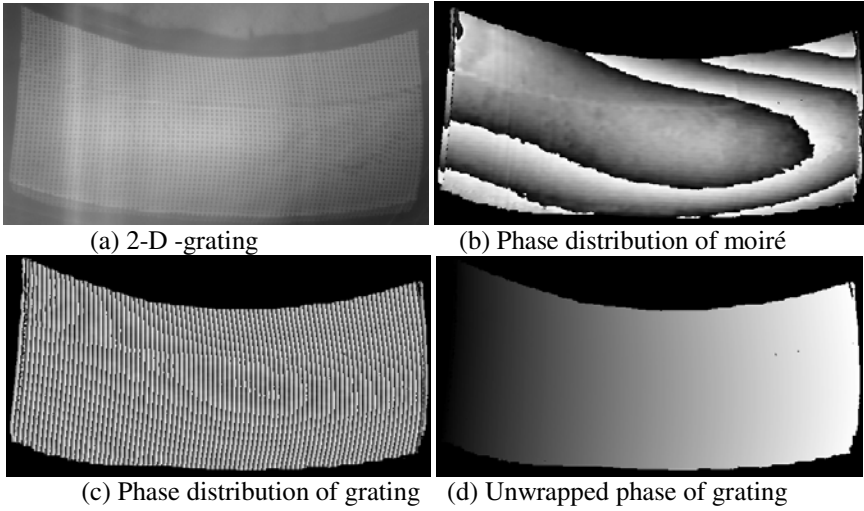
Fig. 16. Phase analysis (in x-direction)

Fig. 17. Analyzed shape

(a) x-directional strain (b) y-directional strain (c) Shear strain
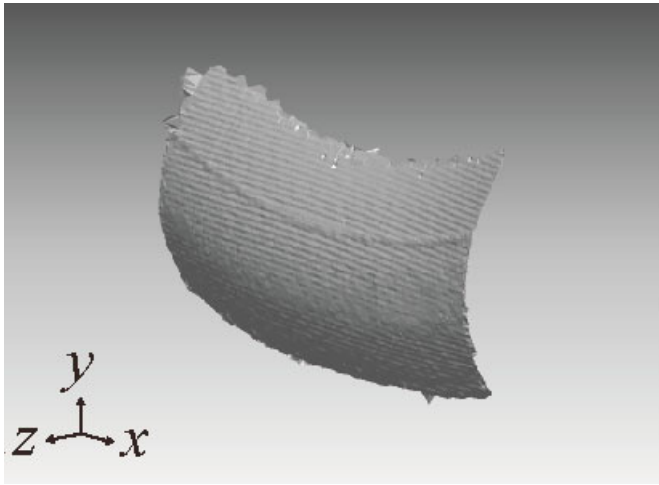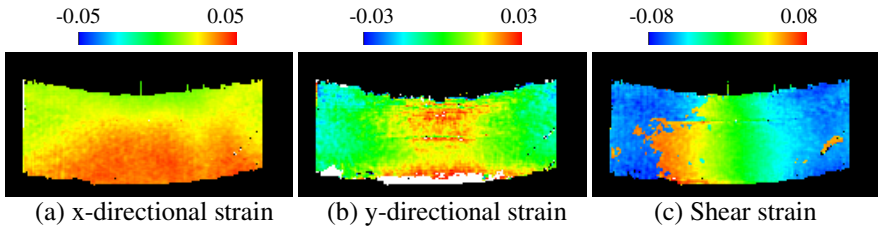
Fig. 18. Analyzed strain distributions

In this experiment, the object was rotating at 80km/h in circumferential velocity. The images of the grating are captured by two CCD cameras. The trigger signal is produced by a trigger sensor placed behind the object. The sensor seeks a white mark attached on the object. The CCD cameras 1 and 2 can capture images simultaneously with the trigger signal when the rotating object comes at the same position.

The grating image recorded by the left camera is shown in Fig. 16(a). The phase distribution of the moiré fringe pattern analyzed by sampling moiré method is shown in Fig. 16(b). The phase distribution of the grating shown in Fig. 16(c) was obtained by using Eq. (9). By unwrapping the phase distribution, the unwrapped phase distribution was obtained as shown in Fig. 16(d). The image recorded by the right camera was also analyzed in the same process.

Figure 17 shows the measurement result of the 3-D shape. The measured shape was the initial shape when the axis load was 0. Figures 18(a), (b) and (c) show the distributions for the *x*- and *y*-directional and shear strains, respectively.

8   Conclusions

Sampling moiré method using accurate phase analysis of a specimen grating was proposed. Deflection of a beam and shape and strain distribution of a moving object were measured by sampling moiré method. The main advantage of the sampling moiré method is non-contact displacement distribution measurement with simple, easy, high accuracy, high speed, and low cost. By comparing the conventional phase shifting methods using multiple phase-shifted images, the sampling moiré method requires only one image for phase-analysis. Therefore, this method can be easily applied to dynamic phenomenon using a high-speed camera. Moreover, this method also can analyze from small to large deformation by changing the grating pitch. It will be a new tool for experimental mechanics and health monitoring of structures.

Acknowledgements

References

1. Takahashi, S. (ed.): Photomechanics. Sankaido Publishing, Tokyo (1997) (in Japanese)
2. Rastogi, P.K. (ed.): Photomechanics (Topics in Applied Physics). Springer, New York (2000)
3. Japanese Society for Experimental Mechanics (ed.), Handbook on Experimental Mechanics, Asakura Publishing, Tokyo (2008) (in Japanese)

4. Sharpe, W.N.J. (ed.): Handbook of Experimental Solid Mechanics, Soc. for Exp. Mech. Springer, New York (2008)

5. Theocaris, P.S.: Moiré Fringes in Strain Analysis. Pergamon Press, Oxford (1969)

6. Durelli, A., Parks, V.: Moiré Analysis of Strain. Prentice-Hall, Englewood Cliffs (1970)

7. Japanese Society for Moiré Contourography (ed.), Moiré Contourography and Its Application (1984) (in Japanese)

8. Post, D., Han, B., Ifju, P.: High Sensitivity Moiré. Experimental Analysis for Mechanics and Materials. Springer, New York (1994)

9. Amidror, I.: The Theory of the Moiré Phenomenon. Kluwer Academic Publishers, Dordrecht (2000)

10. Walker, C.A. (ed.): Handbook of Moiré Measurement. Series in Optics and Optoelectronics. Inst. of Physics Publishing (2004)

11. Yoshizawa, T.: Handbook of Optical Metrology, Principles and Applications. CRC Press, Boca Raton (2009)

12. Sciammarella, C.A., Sturgeon, D.L.: Digital-filtering Techniques Applied to the Interpolation of Moiré-Fringes Data. Experimental Mechanics 7(11), 468–475 (1967)

13. Brunning, J.H., Herriott, D.R., Gallagher, J.E., Rosenfeld, D.P., White, A.D., Brangaccio, D.J.: Digital Wave Front Measuring Interferometer for Testing Optical Surface and Lenses. Appl. Opt. 13, 2693–2703 (1974)

14. Creath, K.: Phase Measurement Interferometry Techniques. Prog. Opt. 26, 349–393 (1988)

15. Takeda, M., Ina, H., Kobayashi, S.: Fourier Transform Method of Fringe Pattern Analysis for Computer-Based Topography and Interferometry. J. Opt. Soc. Am. 72(1), 156–160 (1982)

16. Morimoto, Y., Seguchi, Y., Higashi, T.: Moiré Analysis of Strain by Fourier Transform. Trans. of the Japan Society of Mechanical Engineers 54(504 A), 1546–1552 (1988) (in Japanese)

17. Morimoto, Y., Seguchi, Y., Higashi, T.: Two-dimensional Moiré Method and Grid Method Using Fourier Transform. Exp. Mech. 29, 399–404 (1989)

18. Morimoto, Y.: Digital Image Processing. In: Kobayashi, A.S. (ed.) Handbook on Experimental Mechanics, ch. 21, pp. 969–1029. Prentice-Hall, Inc., Englewood Cliffs (1993)

19. Morimoto, Y., Fujigaki, M.: Techniques for Stress and Strain Measurements using Various Transformations. Journal of JSNDI 46(7), 473–480 (1997) (in Japanese)

20. Morimoto, Y., Fujigaki, M., Yoneyama, S.: Recent Studies on Shape and Deformation Measurements by Moiré Method and Grid Method. Journal of JSNDI 52(3), 116–121 (2003) (in Japanese)

21. Morimoto, Y., Matui, T., Fujigaki, M., Yamamoto, Y., Ri, S.: Applications of Accurate Phase Analysis to Optical Measurement. Journal of JSNDI 54(3), 120–126 (2005) (in Japanese)

22. Idesawa, M., Yatagai, T., Soma, T.: Scanning Moiré Method and Automatic Measurement of 3-D Shapes. Applied Optics 16(8), 2152–2162 (1977)

23. Morimoto, Y., Hayashi, T.: Deformation Measurement During Powder Compaction by a Scanning-Moiré Method. Exp. Mech. 24(2), 112–116 (1984)

24. Morimoto, Y., Hayashi, T., Yamaguchi, N.: Strain Measurement by Scanning Moiré Method. Transaction of JSME 50(451A), 489–494 (1984) (in Japanese)

25. Arai, Y., Kurata, T.: On the Representative of Scanning Moiré Fringe. Journal of the Japan Society of Precision Engineering 51(3), 6–100 (1985) (in Japanese)

26. Yoshizawa, T., Tashiro, H., Nakagawa, S.: High-sensitive Moiré Method by Phase Detection. Journal of the Japan Society of Precision Engineering 51(4), 154–159 (1985) (in Japanese)
27. Arai, Y., Kurata, T.: High Speed- and High Resolutive-Moiré Topography by the Method of Fringe Scanning Interferometry. Japanese Journal of Optics 15(5), 402–406 (1986) (in Japanese)
28. Morimoto, Y., Yang, I.H., Gu, C.G.: Scanning Moiré Method for Obtaining Smooth Fringe Patterns. Optics and Lasers in Engineering 24, 3–17 (1996)
29. Arai, Y., Yokozeki, S., Shiraki, K., Yamada, T.: High Precision Two-dimensional Spatial Fringe Analysis Method. Journal of Modern Optics 44(4), 739–751 (1997)
30. Kato, J., Yamaguchi, I., Nakamura, T., Kuwashima, S.: Video-rate Fringe Analyzer Based on Phase-shifting Electronic Moiré. Patterns. Appl. Opt. 36(32), 8403–8412 (1997)
31. Fujigaki, M., Kim, W.G., Morimoto, Y.: Shape Measurement by Phase Shifting Scanning Moiré Method. In: Proc. of Int. Conf. on Advanced Technology in Exp. Mech. (ATEM 1997), pp. 161–164 (1997)
32. Ri, S., Fujigaki, M., Morimoto, Y., Matui, T.: Pixel-to-pixel Correspondence Adjustment Method Using Moiré Pattern for DMD Reflection-type CCD Camera. Journal of JSEM 5(4), 361–366 (2005) (in Japanese)
33. Ri, S., Fujigaki, M., Matui, T., Morimoto, Y.: Accurate Pixel-to-pixel Correspondence Adjustment in a Digital Micromirror Device Camera by Using the Phase-shifting Moiré Method. Appl. Opt. 45(27), 6940–6946 (2006)
34. Fujigaki, M., Iwai, K., Morimoto, Y.: Shape Measurement with Grating Projection Using Sampling Moiré Method. In: 3rd International Symposium on Advanced Fluid/Solid Science and Technology in Experimental Mechanics (ISEM2008), #145(CD-ROM) (2008)
35. Morimoto, Y., Fujigaki, M.: Accuracy of Sampling Moiré Method. Mechanics of Materials 35, 511–522 (2008)
36. Ri, S., Morimoto, M., Fujigaki, M.: Non-contact Displacement Distribution Measurement by Sampling Moiré Method. Inspection Engineering 14(5), 1–6 (2009) (in Japanese)
37. Shimo, K., Fujigaki, M., Masaya, A., Morimoto, Y.: Development of Dynamic Shape and Strain Measurement System by Sampling Moiré Method. In: Proc. SPIE 7522, 75224M (2009), doi:10.1117/12.854780 online Publication (2010)
38. Ri, S., Fujigaki, M., Morimoto, Y.: Sampling Moiré Method for Accurate Small Deformation Distribution Measurement. Exp. Mech. 50(4), 501–508 (2010)

Recent Advances in Microelectromechanical Systems and Their Applications for Future Challenges

Ryszard J. Pryputniewicz

NEST – NanoEngineering, Science, and Technology
CHSLT – Center for Holographic Studies and Laser micro-mechaTronics
Mechanical Engineering Department
Professor of Electrical and Computer Engineering
Worcester Polytechnic Institute
Worcester, MA 01609 USA
Tel.: (508) 831-5536; Fax: (508) 831-5713
rjp@wpi.edu

Abstract. Recent advances in optoelectronic methodology for microscale measurements are described and their use is illustrated with representative examples of microelectromechanical systems (MEMS) operating at high frequencies and used in demanding environments. Today, the word MEMS is employed to describe a process used as well as the resulting products. Therefore, a MEMS-process is also known as a "microsystem technology" (MST).

Advances in emerging technologies (ETs) of MEMS and nanotechnology, especially relating to the applications, constitute one of the most challenging tasks in today's micromechanics and nanomechanics. In addition to design, analysis, and fabrication capabilities, these tasks also require advanced test methodologies for determination of functional characteristics of devices produced to enable verification of their operation as well as refinement and optimization of specific designs. In particular, development of miniscule devices requires sophisticated design, analysis, fabrication, testing, and characterization tools.   These tools can be categorized as analytical, computational, and experimental. Solutions using the tools from any one category alone do not usually provide necessary information on MEMS and extensive merging, or hybridization, of the tools from different categories is used. One of the approaches employed in this development of structures of contemporary interest, is based on a combined use of the analytical, computational, and experimental solutions (ACES) methodology. Development of this methodology was made possible by recent advances in optoelectronic methodology, which was coupled with the state-of-the-art computational methods, to offer a considerable promise for effective development of various designs. This approach facilitates characterization of dynamic and thermomechanical behavior of the individual components, their packages, and other complex material

structures. In this paper, recent advances in optoelectronic methodology for micro- and nano-scale measurements are described and their use is illustrated with representative examples.

Keywords: MST, emerging technologies, optoelectronic methodology, operating conditions, quantitative measurements, performance characteristics, reliability.

1 Introduction

Continued advances of contemporary microcomponents have made them ubiquitous. Today, these components are used in multitude of applications ranging from everyday (automotive and household appliances) through national security to space exploration. For example, Fig.1 illustrates some of the devices used in automobiles for fuel injecton, tire pressure sensors, inertial measurement units (IMUs), and airbag deployment.
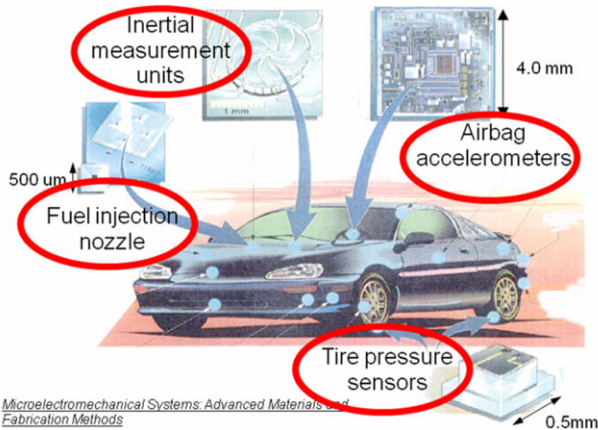
Fig. 1. Some of the microsensors used in automotive applications.

These automotive as well as a number of other present-day applications of the microcomponents, and structures they enable, are summarized in Fig. 2 illustrating numerous and much diversified functions, which require sophisticated design, analysis, fabrication, testing, and characterization tools [1-3]. These tools can be categorized as analytical, computational, and experimental [4]. Solutions using the tools from any one category alone do not usually provide necessary information on the components being developed and, as a result, extensive merging, or hybridization, of the tools from different categories is used [5-7]. One of the approaches employed in the development of microcomponents, as well as other complex structures of current interest, is based on a combined use of analytical, computational, and experimental solutions (ACES) methodology [4, 8-10].

Fig. 2. Representative applications of present-day MEMS.

In general, *analytical tools* are based on exact, closed form solutions. These solutions, however, are usually applicable to simple geometries for which, boundary, initial, and loading (BIL) conditions can be readily specified. However, analytical solutions are indispensable to gain insight for overall representation of the ranges of anticipated results. They also facilitate determination of "goodness" of the results based on uncertainty analysis [11]. *Computational tools*, i.e., finite element methods (FEMs), boundary element methods (BEMs), and finite difference methods (FDMs), provide approximate solutions as they discretize the domain of interest and the governing partial differential equations (PDEs). The characteristics of discretization, in conjunction with the BIL conditions, influence degree of approximation and careful convergence studies should be performed to establish correct computational solutions and modelling [12]. It should be noted that both analytical and computational solutions depend on material properties. If material properties are well known, then solutions typically give correct results, providing convergence was achieved subject to properly specified BIL conditions; if material properties are not sufficiently known, in spite of having a good knowledge of other modelling parameters, erroneous results may be obtained [10]. *Experimental tools*, however, in contrast to analytical and computational tools, evaluate actual objects, subjected to actual/realistic operating conditions (including BIL conditions), and provide ultimate results characterizing objects being investigated.

Until recently, this characterization was hindered by lack of a readily available methodology suitable for use in the development of emerging technologies (ETs).

However, building on recent advances in photonics, electronics, and computer technology, a novel optoelectronic methodology particularly suitable for quantitative studies of microsystems was developed [13]. This methodology remotely and noninvasively evaluates the systems of interest and produces full-field-of-view results with very high spatial resolution and nanometer accuracy in near real-time; it also facilitates generation of animations of experimental results which display time-dependent 3D deformation fields due to thermal and/or mechanical/dynamic loads to which the components are subjected during a given characterization/measurement.

Implementation of the optoelectronic methodology for development of ETs, as presented in this paper, is based on the use of samples described in Section 2.

2   Representative MEMS Samples

The following representative MEMS samples are used in this paper: 1) high rotational speed (HRS) microengine, 2) microgyroscope, 3) pressure sensor, and 4) cantilever-type Ohmic-contact for a microswitch.

The electrostatically driven HRS microengine, developed at Sandia National Laboratories (SNL) to operate at 1,000,000 revolutions per minute (rpm), was used, in one of its applications, to actuate micromirror devices [14], Fig. 3.
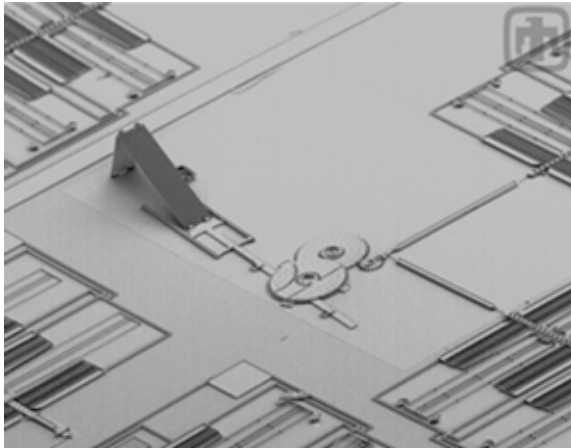
Fig. 3. Sandia micromirror device actuated by electrostatically driven HRS microengine.

The microgyroscope (aka MEMS gyroscope, or microgyro) sensor is a Coriolis-force electrostatic comb driven, tuning fork (i.e., differential pair) design [15] and is a fundamental microcomponent for development of inertial measurement units (IMUs). In the configuration shown in Fig. 4, used in this study, a microgyro is actuated by electrostatic comb drives. The comb drives, in

turn, are excited in such a way that the electrostatic forces they generate depend on lateral position(s) of the proof masses (i.e., shuttles). The resulting (large) amplitude vibrations/oscillations, parallel to teeth of the comb drives, increase sensitivity of a microgyro and reduce errors from external forces. Angular rate, with respect to the axis located in the plane of the shuttles, lifts one mass up and lowers the other mass down due to the Coriolis forces. Capacitors, usually located below the shuttles, accurately sense these up and/or down motions. The shuttles are mounted/attached to the substrate through suspension springs, Fig. 5. The mode of operation where the shuttles move in opposite directions lowers sensitivity of a microgyro to linear acceleration. The two vibrating shuttles, suspended by folded springs, are driven by electrostatic comb drives to maintain lateral in-plane oscillation.
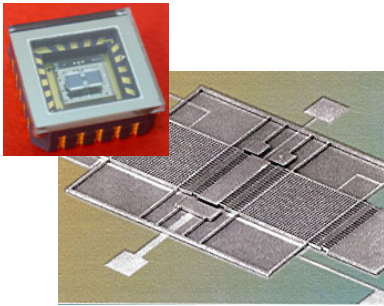
Fig. 4. Typical microgyro package (top left) and a representative inertial MEMS sensor (in the background).
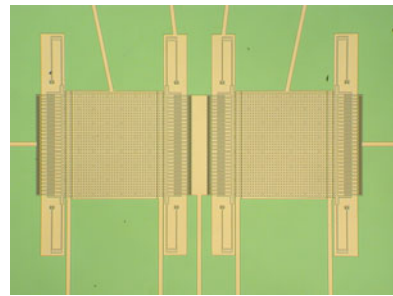
Fig. 5. Close-up of the shuttles and folded suspension springs, one spring is used in each of 4 corners of every proof mass/ shuttle.

A MEMS pressure sensor, Fig. 6, utilizing polysilicon sensing technology, can provide high performance, long-term stability, and low overall cost of installation and operation [16]. In addition, safety and environmental concerns can increase the benefits of this sensor by reducing the potential of fugitive emissions through fewer process penetrations. This unique polysilicon piezoresistive sensor (PPS) measures differential pressure (DP), absolute pressure (AP), and temperature (T) on a single chip.

The PPS technology differs significantly from conventional single crystal technology in that it employs dielectric isolation, which allows consistent deposition of the polysilicon sensing diaphragms to a specific controllable thickness, and facilitates placement of multiple sensing diaphragms on a single chip, Fig. 7. The diaphragm, which senses the applied DP, is shown in the center of the chip; it is some 160 µm wide, 650 µm long, its multilayer/multimaterial thickness is about 2 µm, and the cavity (providing overpressure protection) under the diaphragm is 0.9 µm deep.
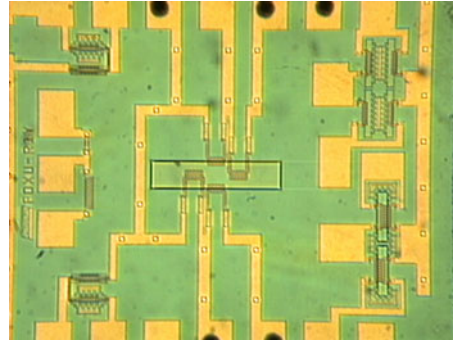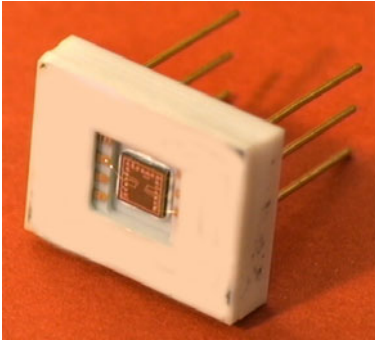
Fig. 6. MEMS multivariable PPS package.   **Fig. 7.** MEMS multivariable PPS that measures DP, AP and T on a single sensing chip.

Deformations of a diaphragm are sensed by four piezoresistive bridge elements that are 0.4 µm thick and are electrically connected into the Wheatstone bridge configuration. Determination of pressure from strains of the piezoresistors is based on computations relying on a number of material specific and process dependent coefficients that certainly can vary, which may lead to uncertainties in displayed results. To establish an independent means for measurements by the PPS diaphragms and to validate the coefficients used, we have developed a hybrid methodology [17] for measurements and characterization of MEMS pressure sensors.

The microswitch considered in this paper is a cantilever-type radio frequency (RF) MEMS switch [18], Fig. 8. The figure shows a microcantilever-type contact of active length L fabricated parallel to a substrate in such a way that separation between the electrodes (one electrode is on a microcantilever and the other is directly below on top of a substrate) is d_e; for stable operation of a microswitch d_e should be at least 3 times greater than the contact gap distance d_g. During functional operation, voltage applied to the electrodes induces an electrostatic force that activates/actuates a microswitch [19]. The electrostatic force bends a microcantilever causing the contacts to touch (i.e., by reducing the gap distance, d_g, to zero), which closes an electrical path (by making a cross bar to bridge/close an "opening", defined by L_{to} in Fig. 8, in a trace usually located below the free end of a microcantilever) and facilitates propagation of an electrical signal. As the activation/actuation voltage is released, elasticity of the microcantilever is used to return it to its original, or open, position (i.e., making $d_g > 0$). Mechanically, the microcantilever of a switch behaves like a conventional cantilever [20]. In fact, traditional equations can be used to find microcantilever stiffness, natural frequency, pull-in voltage, and magnitude of the activation/actuation force. The switch fabrication methods are particularly important because they dictate the material type, surface finish, texture, and overall size of the microswitch components (especially electrical interfaces of a microswitch). Consequently, material properties have a direct influence on thermal management characteristics of a microswitch and its behavior under actual operating conditions [18]. In fact,

fabrication tolerances and accuracy of material properties have profound influence on dynamics as well as the thermomechanical performance of microswitches [18,21].

Fig. 8. Geometry and dimensions of a cantilever-type microswitch.

To develop a better understanding of dynamic behavior of microcantilevers, an extensive study of their vibration characteristics was conducted using bare base-material as well as the material coated with metal layers of up to 30 nm thick on one side as well as on both sides [22].

3   ACES Methodology

Effective development of structures, regardless whether they are macro- micro-, or nano-size, requires knowledge of design, analysis/simulation, materials, fabrication with special emphasis on packaging, and testing/characterization of the finished products [1-3,23,24].   These issues are best addressed via an integrated use of analytical, computational, and experimental solution (ACES) methodology [4].

ACES methodology [9,10] unifies the analytical, computational, and experimental solutions to obtain answers to problems where they would not be otherwise possible, to improve existing-results, or to validate data obtained using other methodologies.

In the ACES methodology [4], the *analytical results* are obtained using a closed form solution, the *computational results* use either the finite element method (FEM), the finite boundary method (FBM), or the finite difference method (FDM) solutions, and the *experimental results* (typically) rely on the full-field-of-view (FFV) optoelectronic laser interferometric microscope (OELIM) system-based solutions, as discussed in Section 3.3.1.

With the development of more and more complex, but smaller, structures we find that there are a great number of design variables that affect their manufacture and performance. In the analysis of such structures, we find that experimental and theoretical models are equally important and equally indispensable for a successful development of viable, reliable, and low cost (i.e., affordable) products.

Although computational models can provide accurate simulations of specific designs of RF MEMS switches [25-27], simple analytical models are sometimes preferred to develop an intuitive understanding of the behavior of these microswitches. Also, the analytical models facilitate uncertainty analysis, which

are invaluable in determination of the influence that variations in different process parameters (specified by tolerances, aka uncertainties) defining a microswitch have on the nominal results produced by the particular analytical model [21].

3.1   Analytical Solution

An initial goal of the analysis of a microgyroscope (a microswitch, or other moving/dynamic structure) is to determine accelerations of all of its moving parts. Then, using Newton's Second Law, forces acting on the microgyro (or a microswitch/structure) are calculated. Once the dynamic forces are known, we can determine whether the microgyro (or a microswitch/structure) will perform as anticipated under expected operating conditions, or not.

   Dynamic forces are based on accelerations, both linear and angular. In order to calculate accelerations we must first determine positions of all moving-components in a microsystem for each increment of the input motion in a given cycle of operation. Once equations defining positions are known, we differentiate them with respect to time to calculate velocities, and then differentiate again to obtain accelerations [8].

3.2   Computational Solution

Computational modeling of MEMS can be performed using commercial simulation tools [28,29]. Parametric templates, utilizing, e.g., Python scripting, for modeling MEMS can be developed and utilized for in-depth understanding of the designed/ expected operation of microsystems. MEMS geometry, material properties, stress, contact forces, dynamic response, and other parameters can be investigated using the parametric templates to optimize performance. Atmospheric conditions (including vacuum), geometry of MEMS, as well as optimized pull-down voltage profiles can be modeled to understand and optimize the dynamic damping conditions of a packaged or unpackaged MEMS [19].

   The coupled electrostatics-structures-flow simulations can also be performed using CFD-ACE+ software because it has the necessary multiphysics capabilities including flow, heat-transfer, mechanics, and electrostatics [27], as summarized in Fig. 9. All CFD-ACE+ capabilities are fully coupled to facilitate fast solution and determination of accurate results, Fig. 10.

3.3   Optoelectronic Methodology

The optoelectronic methodology, as presented in this paper, is based on the principles of *optoelectronic holography* (OEH) [7,13,30]. Basic configuration of the OEH system is shown in Fig. 11. In this configuration, laser light is launched into a single mode optical fiber by means of a microscope objective (MO). Then, the single mode fiber is coupled into two fibers by means of a fiber optic directional coupler (DC). One of the optical fibers comprising the DC is used to illuminate an object, while the output from the other fiber provides reference against which the signals from the object are recorded. Both, the object and the reference beams are combined by the interferometer (IT) and recorded by a system camera (CCD).
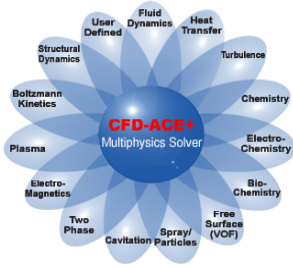
Fig. 9. Coupled multiphysics structure of CFD-ACE+ software for MEMS.
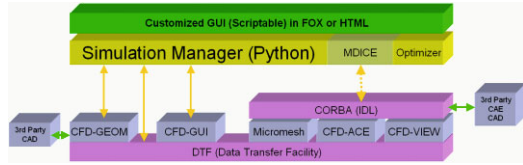
Fig. 10. CFD-ACE+ coupling capabilities.
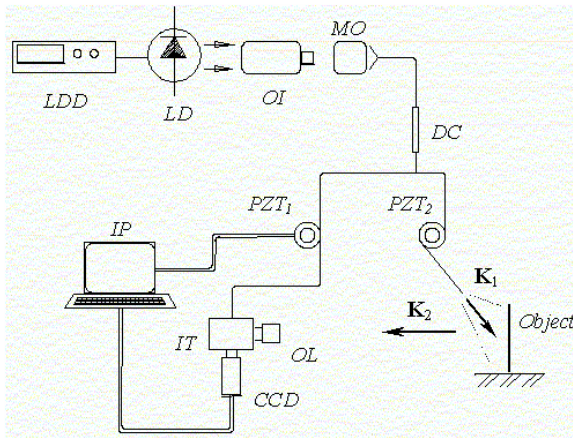
Fig. 11. Single-illumination and single-observation geometry of a fiber-optic-based OEH system: *LDD* is the laser diode driver, *LD* is the laser diode, *OI* is the optical isolator, *MO* is the microscope objective, *DC* is the fiber optic directional coupler, *PZT₁* and *PZT₂* are the piezoelectric fiber optic modulators, *IP* is the image-processing computer, *IT* is the interferometer, *OL* is the objective lens, *CCD* is the camera, while $\mathbf{K}_1$ and $\mathbf{K}_2$ are the directions of illumination and observation, respectively.

Images recorded using the CCD are processed by the system computer to determine the fringe-locus function, $\Omega(x,y)$, constant values of which define fringe loci on the surface of an object under investigation. The values of Ω relate to the system geometry and the unknown vector **L,** defining displacements and deformations, via the relationship [31]

$$\Omega(x, y) = \left[\mathbf{K}_2(x, y) - \mathbf{K}_1(x, y)\right] \bullet \mathbf{L}(x,y) = \mathbf{K} \bullet \mathbf{L} \quad , \tag{1}$$

where $\mathbf{K}$ is the sensitivity vector defined in terms of vectors $\mathbf{K}_1$ and $\mathbf{K}_2$ identifying directions of illumination and observation, respectively, (i.e., geometry) of the OELIM system as illustrated in Fig. 11.

Quantitative determination of structural displacements/deformations due to the applied loads can be obtained, by solving a system of equations similar to Eq. 1, to yield [31]

$$\mathbf{L} = \left[\tilde{\mathbf{K}}^{\mathrm{T}}\tilde{\mathbf{K}}\right]^{-1}\left(\tilde{\mathbf{K}}^{\mathrm{T}}\Omega\right) \quad, \tag{2}$$

where $\tilde{\mathbf{K}}^{\mathrm{T}}$ represents a transpose of the matrix of the sensitivity vectors $\mathbf{K}$.

Equation 2 indicates that displacements/deformations determined from interferograms are functions of $\mathbf{K}$ and Ω, which have spatial, i.e., (x,y), distributions over the field of interest on an object being investigated. Thus Eq. 2 can be represented by a phenomenological relation [11] as

$$\mathbf{L} = \mathbf{L}(\mathbf{K},\Omega) \quad, \tag{3}$$

based on which the RSS-type (i.e., the square *Root of the Sum of the Squares*) uncertainty in $\mathbf{L}$, i.e., $\delta\mathbf{L}$, can be determined to yield

$$\delta\mathbf{L} = \left[\left(\frac{\partial\mathbf{L}}{\partial\mathbf{K}}\delta\mathbf{K}\right)^2 + \left(\frac{\partial\mathbf{L}}{\partial\Omega}\delta\Omega\right)^2\right]^{1/2} \quad, \tag{4}$$

where $\partial\mathbf{L}/\partial\mathbf{K}$ and $\partial\mathbf{L}/\partial\Omega$ represent partial derivatives of $\mathbf{L}$ with respect to $\mathbf{K}$ and Ω, respectively, while $\delta\mathbf{K}$ and $\delta\Omega$ represent the corresponding uncertainties in $\mathbf{K}$ and Ω, respectively. It should be remembered that $\mathbf{K}$, $\mathbf{L}$, and Ω are all functions of spatial coordinates (x,y,z), i.e., $\mathbf{K} = \mathbf{K}(x,y,z)$, $\mathbf{L} = \mathbf{L}(x,y,z)$, and $\Omega = \Omega(x,y,z)$, respectively, when performing partial differentiations required to solve Eq. 4. After solution of Eq. 4, the result indicates that $\delta\mathbf{L}$ is proportional to a product of the local value of $\mathbf{L}$ with the RSS value of the ratios of the uncertainties in $\mathbf{K}$ and Ω to their corresponding local values, i.e.,

$$\delta\mathbf{L} \propto \mathbf{L}\left[\left(\frac{\delta\mathbf{K}}{\mathbf{K}}\right)^2 + \left(\frac{\delta\Omega}{\Omega}\right)^2\right]^{1/2} \quad. \tag{5}$$

For typical geometries of the OEH systems used in recording of interferograms, the values of $\delta\mathbf{K}/\mathbf{K}$ are less than 0.01. However, for small deformations, the typical values of $\delta\Omega/\Omega$ are (usually) more than one order of magnitude greater than the values for $\delta\mathbf{K}/\mathbf{K}$. Therefore, the accuracy with which the *fringe orders* (based on which Ω values are calculated [31]) are determined influences the accuracy in the overall determination of displacements/deformations [32] and, as

such, is critical to implementation of this methodology for development of MEMS as discussed herein.

Therefore, to minimize this influence, a number of algorithms for determination of Ω were developed. Some of these algorithms require multiple recordings of each of the two states, in the case of *double-exposure method*, of the object being investigated with introduction of a discrete phase step between the recordings [3,33]. For example, the intensity patterns of the first and the second exposures, $I_n(x,y)$ and $I'_n(x,y)$, respectively, in the *double-exposure sequence*, can be represented by the following equations [7]:

$$
\begin{aligned}
I_n(x,y) = I_o(x,y) + I_r(x,y) + \\
+ 2\{[I_o(x,y)][I_r(x,y)]\}^{1/2}\cos\{[\Delta\varphi(x,y)] + \theta_n\}
\end{aligned}
\tag{6}
$$

and

$$
\begin{aligned}
I'_n(x,y) = I_o(x,y) + I_r(x,y) + 2\{[I_o(x,y)][I_r(x,y)]\}^{1/2} \times \\
\times \cos\{[\Delta\varphi(x,y)] + \theta_n + \Omega(x,y)\} \quad ,
\end{aligned}
\tag{7}
$$

where $I_o(x,y)$ and $I_r(x,y)$ denote the object and the reference beam intensities, respectively, with (x,y) representing spatial coordinates, $\Delta\varphi(x,y) = \varphi_o(x,y) - \varphi_r(x,y)$ is the optical phase difference based on $\varphi_o(x,y)$, denoting random phase of the light reflected from an object, and $\varphi_r(x,y)$, denoting the phase of the reference beam, θ_n represents the discrete applied n^{th} phase step, and $\Omega(x,y)$ is the fringe-locus function relating to the displacements/deformations that an object incurred between the first and the second exposures; Ω *is what we need to determine*. When Ω is known, it is used in Eq. 2 to find **L**.

In the case of the 5-phase-steps algorithm with θ_n=0, $\pi/2$, π, $3\pi/2$, and 2π, the distribution of the values of $\Omega(x,y)$ can be determined using [7]

$$
\Omega(x,y) = \tan^{-1}\left\{\frac{2[I_2(x,y) - I_4(x,y)]}{2I_3(x,y) - I_1(x,y) - I_5(x,y)}\right\} \quad .
\tag{8}
$$

Results produced by Eq. 8 depend on capabilities of the illuminating, the imaging, and the processing subsystems of the OEH system used in a specific application. Developments in laser, fiber optic, CCD camera, and computer technologies have led to advances in the OEH methodology; in the past, these advances have almost paralleled the advances in the image recording media [34]. These developments resulted in educational procedures [2] and led to MEMS education alliance [35].

In response to the needs of the emerging MEMS technology, an *optoelectronic laser interferometric microscope* (OELIM) system for studies of objects with micron size features was developed [36,37], Fig. 12.
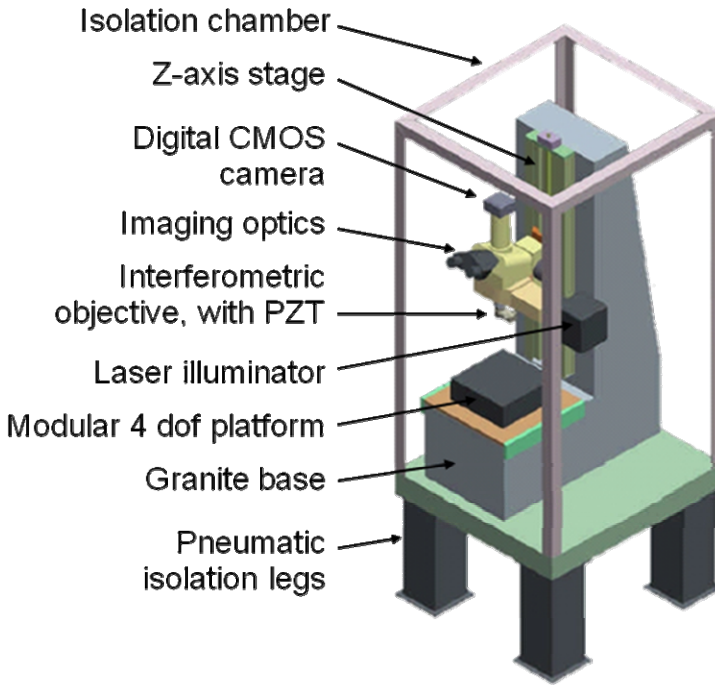
Fig. 12. OELIM configuration used herein.

3.3.1 OELIM System

In the OELIM system, Fig. 12, light beam produced by a laser illuminator is directed into a directional beam splitter cube, which produces an *object beam* that is sent into an interferometric objective with PZT phase stepper controlled microscope lens. The lens, in turn, illuminates MEMS being investigated. The particular characteristic of the configuration shown is that its specially designed interferometric objective has a *long working distance* providing ample space for installation of an *environmental chamber* and/or other *loading device(s)*, as needed to characterize various MEMS.

It should be noted that in the implementation of the OELIM system used in this study, the environmental chamber permitted simultaneous control of pressure/ vacuum, temperature (heating and cooling), as well as dynamic excitation (needed for vibrations) of the test samples being characterized/developed.

In the configuration of Fig. 12 the object beam reflected by the MEMS passes back through the objective to the beam splitter cube where it is combined with a *reference beam*. The two beams, recombined at the beam splitter, are imaged onto the sensing element of a CCD camera, which digitally records intensity distributions of the resulting *interference patterns*. These patterns are transferred to the system computer for subsequent quantitative processing to determine $\Omega(x,y)$ according to Eq. 8, which is needed to determine **L** based on the use of Eq. 2.

4 Representative Results

The *optoelectronic methodology* described in the preceding Section was used to determine displacements and deformations of the MEMS samples described in the Section 2. Results of these determinations are summarized in Sections 4.1 to 4.4, respectively.

4.1 Motions of HRS Microengine

Using the analytical model [8,13,32], forces acting on the microengine during its operation were calculated to be a nonlinear function of rpm indicating that the force increases at an increasing rate as the rotational speed of a microengine increases; for example this function indicates that at 6,000 rpm magnitude of the force acting on a connecting pin is 4 nN while at 500,000 rpm it is 27 μN.

Forces generated during operation of a microengine, load the drive gear and make it wobble as it rotates around its shaft. A unique capability to measure this wobble is provided by the OELIM methodology. Typical results obtained for two different positions in a rotation cycle of the drive gear are shown in Fig. 13, where fringe patterns vividly display changes in magnitude and direction of the displacements of the microgears. These displacements, based on the fringe patterns of Fig. 13 vary in magnitude from 0.8 μm to 1.7 μm, respectively; it should be noted that, in comparison with these displacements, thickness of gears is about 2 μm. These variations in displacements are due to kinematics and kinetics caused by impulsive loading forces generated by the input signals during rotational/operational cycle. In addition, the experimental results show that the wobble depends on the angular position in the rotation cycle, which can be related to the forces exerted on the drive gear by the pin during a typical operational cycle.
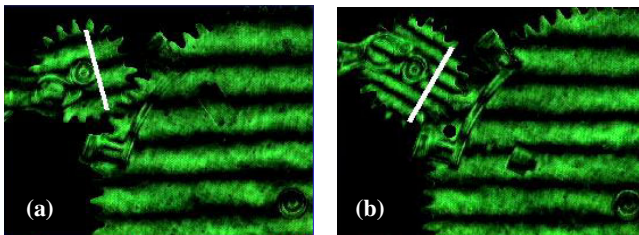
Fig. 13. Representative OELIM fringe patterns recorded during the study of dynamic characteristics of microengines, at two different positions in a rotation cycle. White lines indicate locations (a) and (b) where measurements of displacements, quoted in the text, were made.

Operational functionality of a micromirror system depends also on the quality of motions of section AB of the hinged micromirror, Fig. 14. OELIM was used to measure these motions by recording fringe patterns, Fig. 15, which were, in turn, interpreted to determine deformations/motions of the section AB of the micromirror, Fig. 16.
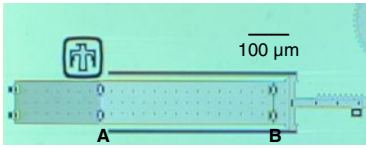
Fig. 14. Measurements were made on the AB section, 100 µm wide and about 400 µm long, of a hinged micromirror.
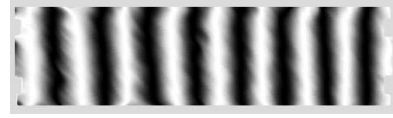
Fig. 15. Representative OELIM fringe pattern of the AB section of a hinged micromirror, shown in Fig. 14.
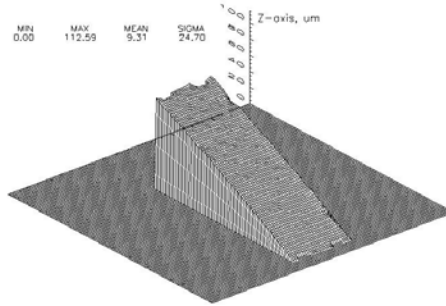
Fig. 16. Wireframe representation of absolute shape and deformations/motions of the section AB of a hinged micromirror, corresponding to the upright position displayed in Fig. 3. Measurements show that the micromirror displacements range from 0 µm at hinge B to 113 µm at hinge A at which there is also a tilt of 18 mrad, based on results of Fig. 17.

Using Fig. 16, detailed information about deformations/motions of a micromirror can be obtained, Fig. 17. This figure displays traces that were made parallel to the long edges of section AB of the micromirror. Noticeable differences between the two traces were measured and led to estimate of a tilt of 18 mrad at the hinge A.
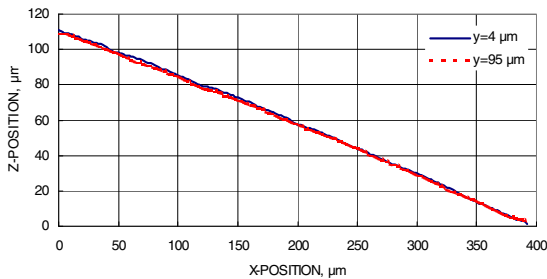
Fig. 17. Vertical displacements (Z-POSITION) of section AB as a function of position along the length (X-POSITION) of a micromirror as determined from traces parallel to the long edges of the wireframe display of Fig. 16, resulting tilt of 18 mrad was determined at hinge A (on the left side) of section AB shown in Fig. 14.

4.2   Deformations of a Microgyroscope

Deformations of proof masses/shuttles were measured during operation of a microgyroscope. In this application, interferograms were recorded stroboscopically while microgyros were driven at their operating frequencies. To facilitate these recordings, the optoelectronic system was set up to be sensitive to the out-of-plane motions. Representative interferograms, corresponding to deformations of the left shuttle, while a microgyro was operating at 10.1 kHz are shown in Fig. 18. Observation of the fringe patterns of this figure clearly indicates asymmetry in deformations of the proof mass(es) of a microgyroscope. This can be related to structural design and suspension of the shuttles as well as to the way that electrostatic forces affect their motions and deformations. A representative display of deformations of the left shuttle of a microgyro operating at 10.1 kHz, during a specific instant in a vibration cycle, is given in Fig. 19, indicating deformations ranging up to 212 nm, which ideally should not exist. However, the deformations/motions were measured, in this case, to be orders of magnitude greater than typical (magnitudes of) motions of the proof masses due to the Coriolis forces.
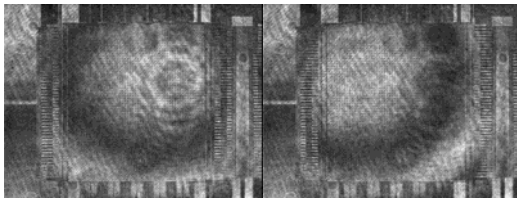
Fig. 18. Representative OELIM fringe patterns of the left shuttle, at different times in a vibration cycle, while a microgyro is operating at 10.1 kHz.
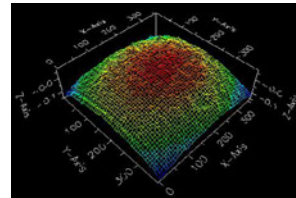
Fig. 19. The out-of-plane 212 nm deformation component of the left shuttle, based on Fig. 18.

Accuracy and precision of a microgyro depends on the quality of its suspension. This suspension is provided by folded springs attached, at one end, to proof masse/shuttle and, at the other end, to a post forming a part of a substrate, Fig. 20a. Any deformations of the springs that are not in response to functional operation of a sensor will cause an incorrect (i.e., erroneous) output. For example, thermomechanical distortions of a package affect shape of posts and these, in turn, lead to undesired deformations of the springs and erroneous results produced by a sensor supported by these springs [3]. Because of the nanoscale of these deformations and microsize objects over which they take place, it was not until the advancement of optoelectronic metrology that such deformations were quantified in the FFV, Fig. 20. This figure shows that the thermomechanical deformations of a post are on the order of 40 nm [37].

Functional operation of MEMS microgyros (usually) depends on motion of a proof mass in response to an applied load. The proof masses of a microgyro are (typically) suspended by folded springs: one spring in each corner of a proof
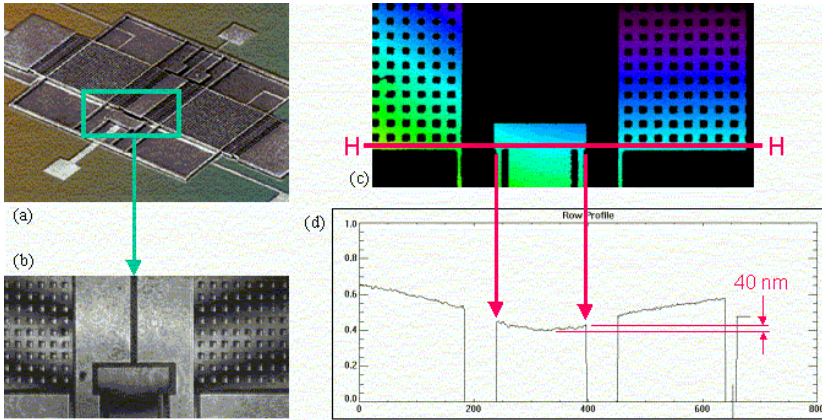
Fig. 20. OELIM measurements of thermomechanical deformations of a post in a microgyro: (a) dual shuttle configuration with the rectangle indicating one of the posts, (b) interference fringe pattern over the post section selected in part (a), (c) contour representation of deformations corresponding to the fringe pattern shown in part (b) - horizontal line HH indicates the trace along which deformations of the post were determined, (d) deformations determined along the line HH of part (c).

mass/shuttle, Fig. 5. Because of advances in design, suspension springs that have several folds (or turns) were implemented. These multi-fold spring configurations allow compact design of MEMS, which facilitates a fast response. Figure 21 displays representative deformations of the upper-right folded spring supporting the left proof mass of a microgyro, as measured using the OELIM methodology [38]. These deformations are about 300 nm, over the section of the microgyro displayed in the figure. More specifically, the folded spring, shown in Fig. 21, deforms approximately 126 nm between the point where it is attached to the post and the point of its attachment to the proof mass. The proof mass itself has the deformation of about 174 nm. To mitigate adverse effects of packaging, new design/fabrication approaches are being developed [39].
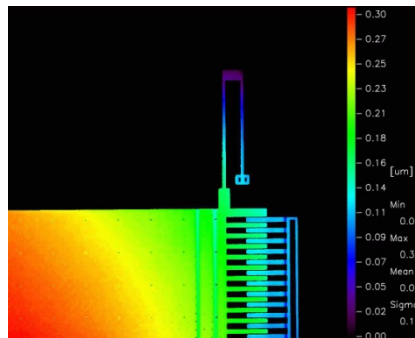
Fig. 21. OELIM measured thermomechanical deformations of the upper-right section of the left proof mass of a MEMS gyroscope, Fig. 5, maximum deformation is 300 nm: 2D contour representation.

4.3 Deformations of a Pressure Sensor

Using the specially designed test fixture, the MEMS PPSs were subjected to high pressure side (HPS) and low pressure side (LPS) loads [17,40]. These loads ranged from the rest (i.e., reference) pressure, set at atmospheric, up to 100 psig [41]. Representative OELIM fringe patterns, corresponding to deformations of the diaphragms subjected to these loads, are shown in Figs 22 and 23.

It should be noted that the absolute shapes of the diaphragms at rest, Figs 22a and 23a, influence their response to the applied pressures. That is, deformed shapes of a specific diaphragm are different under HPS and LPS loads of the same magnitude as, e.g., can be seen comparing Figs 22b and 23b. Both of these figures show OELIM fringe patterns of the diaphragms subjected to the loads having the magnitude of 10 psig. Based on previous studies [17], deformations of the diaphragms due to HPS and LPS loads of this magnitude are unobstructed. Yet, the fringe patterns vividly indicate different deformation patterns because of influence that the initial shape, due to the residual stresses that developed while fabricating these MEMS, has on their operational performance.

Clearly, as the load magnitudes increase so do the deformations of the diaphragms.
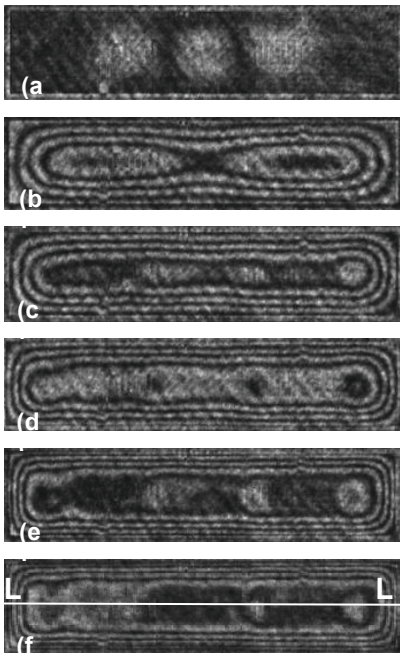
Fig. 22. Representative OELIM fringe patterns corresponding to the HPS loadings of: (a) 0 psig (rest state), (b) 10 psig, (c) 20 psig, (d) 40 psig, (e) 80 psig, and (f) 100 psig.
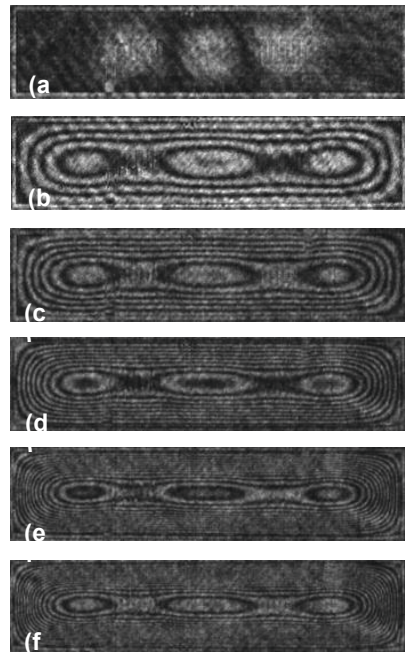
Fig. 23. Representative OELIM fringe patterns corresponding to the LPS loadings of: (a) 0 psig (rest state), (b) 10 psig, (c) 20 psig, (d) 40 psig, (e) 80 psig, and (f) 100 psig.

Figure 22c shows that at the HPS load of 20 psig the diaphragm has already reached the bottom of the cavity and rests on it. Increasing pressure beyond 20 psig flattens the diaphragm and makes its sides steeper as displayed by corresponding fringe patterns. Also, the diaphragm begins to fill the etch holes located at the bottom of the cavity, as can be seen from the fringe patterns. This is also illustrated in Fig. 24 showing deformations measured along the longitudinal line LL through the center of the diaphragm subjected to the HPS load of 100 psig, for which the OELIM fringe pattern is displayed in Fig. 22f.

Examination of Fig. 23 shows that, because there is no mechanical stop on the LPS, the diaphragm deforms without any obstructions reaching maximum deformation/displacement of 3.458 μm at the LPS load of 100 psig (Fig. 23f). This result is in good correlation with the maximum deformation/displacement of 3.724 μm determined computationally using the FEM model, Fig. 25; representative von Mises stress field, based on the FEM half-model, is displayed in Fig. 26.
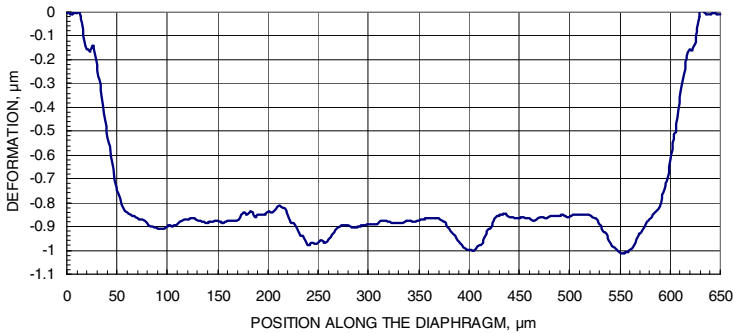
Fig. 24. Deformations of a DP diaphragm along the longitudinal line LL through the center of a diaphragm, corresponding to the HPS load of 100 psig (see Fig. 22f).
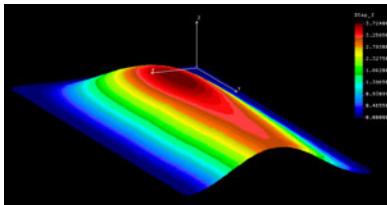
Fig. 25. Representative 3D deformations of a DP diaphragm subjected to the LPS load of 100 psig, based on the FEM analysis, half-model representation was used because of the design symmetry of the sensor.
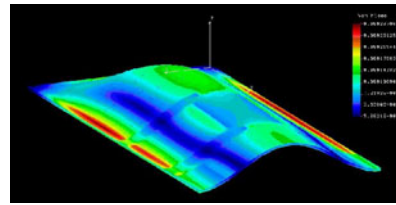
Fig. 26. Representative von Mises stress field of a multilayer DP diaphragm subjected to the pressure of +10 psig, based on the FEM analysis, half-model representation was used because of the design symmetry of the sensor.

Previous results, determined along the longitudinal lines through the center of the diaphragm, indicate that the deformations at rest range from –20 nm to +90 nm, for the PPSs considered [40]. Furthermore, at the positive and the negative differential pressures of the magnitude of 10 psig, these deformations are +813 nm and –792 nm, respectively, i.e., they display a 21 nm difference, although (according to the fundamental theories) they should be identical, i.e., the difference should be 0. This data is essential for proper quantitative interpretation of the signals produced by a MEMS PPS.

Using OELIM methodology, deformations of a PPS diaphragm can be measured as a function of increments in pressure, both, along the longitudinal and transverse lines, LL and TT, respectively, to facilitate their correlation [40].

FEM model of a MEMS PPS was developed in this study [40]. This model incorporates the multilayer structure of a diaphragm and accounts for material properties of each layer. It also incorporates the strain gages and their operational characteristics. Because of the design symmetry of the sensor, half-model of the diaphragm was used to facilitate/speed up the solution of cases considered.

The FEM model was used to determine response of a PPS to a variety of the applied pressure and temperature conditions. It was also used to study the structure of a diaphragm and the effects that the strain gauges have on its response to the applied pressure and temperature loads [41]. Comparison of the computational and experimental results on MEMS PPSs shows good correlation, well within the uncertainty limits.

4.4 Deformations of a Cantilever Microcontact

MEMS RF switches present a promising technology for high-performance reconfigurable microwave and millimeter wave circuits [42]. Low insertion loss, high isolation, and excellent linearity provided by MEMS switches offer significant improvements over an electrical performance provided by conventional p-i-n diode and metal-oxide semiconductor field-effect transistor (MOSFET) switching technologies. These superior electrical characteristics permit design of MEMS switched high-frequency circuits not feasible with semiconductor switches, such as high-efficiency broadband amplifiers and quasi-optic beam steering arrays. In addition, operational benefits arise from low power consumption, small size and weight, and integration capability of modern RF MEMS switches.

Effective computational simulation of an RF MEMS switch must simultaneously combine different loads including, but not limited to, the following: electromagnetic, electrostatic, thermal, mechanical, and aeroelastic [19]. A representative result of such computational multiphysics modeling is shown in Fig. 27, which indicates damping effects of air "surrounding" a microswitch in its package.

In some applications, the damping effects displayed in Fig. 27 help control switch dynamics and enhance tribological characteristics of the microcontacts; in others, they adversely affect performance of the microcontacts [23].
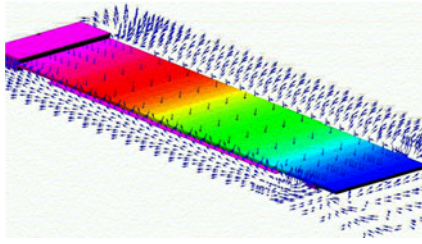
Fig. 27. Computational multiphysics simulation of an RF MEMS contact closure at atmospheric conditions: 3D representation of air damping.

Prototype microcantilever beams were fabricated and their dynamic characteristics were determined in real-time using optoelectronic methodology [22]. For example, results were obtained for the 350 μm long microcantilevers. Representative fringe patterns, corresponding to the first three flexure/bending modes are shown in parts (a) displayed in Figs 28 to 30, respectively; these figures exhibit maximum deformations ranging from about 3 μm down to 870 nm as frequency increases from 14.57 kHz to 261.4 kHz; however using different samples deformations of picometer (pm) magnitudes were recorded in a previous study [24].
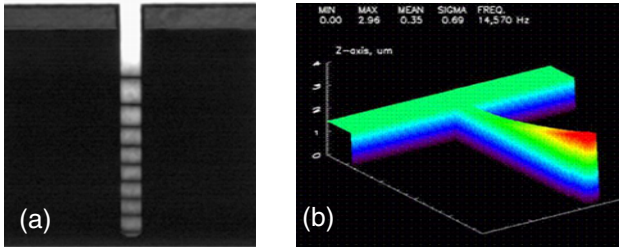
Fig. 28. OELIM measurements of a vibrating MEMS cantilever – resonating at 14,570 Hz corresponding to the first flexure mode: (a) time-average fringe pattern, (b) mode shape based on the fringe pattern of part (a) exhibiting maximum deformation of 2.96 μm.
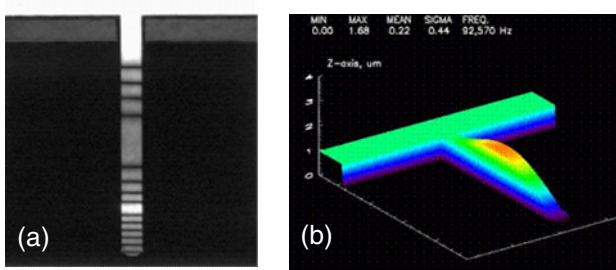
Fig. 29. OELIM measurements of a vibrating MEMS cantilever – resonating at 92,570 Hz corresponding to the second flexure mode: (a) time-average fringe pattern, (b) mode shape based on the fringe pattern of part (a) exhibiting maximum deformation of 1.68 μm.
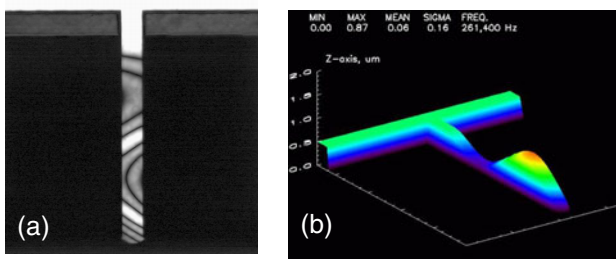
Fig. 30. OELIM measurements of a vibrating MEMS cantilever – resonating at 261,400 Hz corresponding to a complex third flexure mode: (a) time-average fringe pattern, (b) mode shape based on the fringe pattern of part (a) exhibiting maximum deformation of 870 nm.

Quantitative interpretation of these fringe patterns shows mode shapes included as part (b) of Figs 28 to 30. The corresponding frequencies of the three modes displayed show good correlation with the frequencies determined analytically, well within the uncertainty limits [43]. More specifically, fundamental resonance frequencies for the first three bending modes of the microcantilevers considered herein can be expressed as 14.57±1.72 kHz, 92.57±10.72 kHz, and 261.40±30.02 kHz, for the results displayed in Figs 28 to 30, respectively.

Following procedures used to obtain representative results shown in this Section, displacements, deformations, and motions of other MEMS and structures can be determined.

5   Conclusions and Future Work

An *optoelectronic methodology for micro- and nano-scale measurements* was presented. Suitability of this methodology in experimental mechanics on the micro/nanoscale was demonstrated by applications to representative MEMS [23,44], deformations of the maximum magnitude ranging from pm to hundreds of μm were measured on MEMS samples that were considered.

The methodology is applicable under static and dynamic conditions. In this paper, its applicability was illustrated by use of four representative MEMS samples: microengine, microgyroscope, pressure sensor, and a cantilever-type Ohmic-microswitch. Deformations of these representative MEMS samples were from picometers to a few hundred μm, depending on the specific operating conditions and nature of the MEMS considered. Theoretical results correlated with the experimental results well within the criteria specified by the *uncertainty analysis*. Validated correlations will lead to establishment of "design by analysis" *methodology for efficient and effective developments of structures*, which is becoming more and more necessary especially as consequences of MEMS reliability assessments are being considered/resolved [45,46].

All in all, representative results presented in this paper indicate that the *optoelectronic methodology* is a viable tool for micro- and nano-scale measurements,

as such it is particularly useful for *development of MEMS*, especially while considering MEMS reliability assessment. In fact, this author strongly believes that this methodology may become a *differentiating factor* in developments of reliable and durable MEMS for *high-performance applications* to satisfy ever increasing requirements especially those relating to the *Q-factor* [21] *discrimination*.

Based on a recent publication [47] we should expect to witness an increasing activity in the field of microsystems technology. More specifically, MEMS-based products made in 2005 had an estimated value of about $8 billion, 40% of which was in microsensors while the balance was for products that include micromachined features such as ink jet printers, catheters, and RF IC chips. Currently, the MEMS related activities, judging by global distribution of MEMS fabrication facilities, shown in Fig. 31, are approximately 40% in North America, 40% in Europe, and about 20% in Asia.
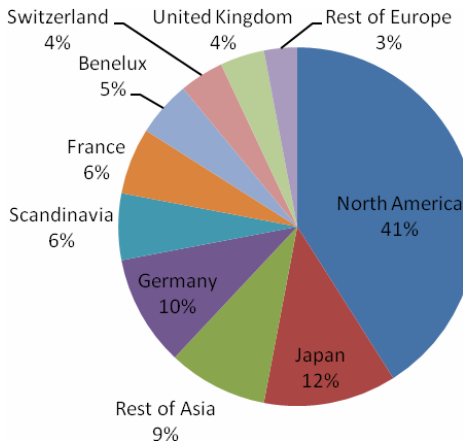
Fig. 31. Global distribution of MEMS fabrication facilities.

Growth projections for MEMS-based products follow an exponential curve [47] with value of products rising to $40 billion in 2015 and to $200 billion in 2025. This is a projected 25-fold growth of MEMS products during the 20-year period from 2005 to 2025!

Acknowledgments

References

1. Pryputniewicz, R.J.: Integrated approach to teaching of design, analysis, and characterization in micromechatronics. In: Paper No. IMECE2000/DE-13, ASME - Am. Soc. Mech. Eng., New York, NY (2000)
2. Pryputniewicz, R.J.: MEMS design education by case studies, Paper No. IMECE2001/DE-23292, ASME - Am. Soc. Mech. Eng., New York, NY (2001)
3. Pryputniewicz, R.J.: Progress in MEMS. Strain 43, 1–13 (2007)
4. Pryputniewicz, D.R.: ACES approach to the development of microcomponents, MS Thesis, Worcester Polytechnic Institute, Worcester, MA (1997)
5. Pryputniewicz, R.J.: A hybrid approach to deformation analysis. In: Proc. SPIE, vol. 2342, pp. 282–296 (1994)
6. Furlong, C., Pryputniewicz, R.J.: Hybrid computational and experimental approach for the study and optimization of mechanical components. Opt. Eng. 37, 1448–1455 (1998)
7. Furlong, C.: Hybrid, experimental and computational, approach for the efficient study and optimization of mechanical and electro-mechanical components, Ph.D. Dissertation, Worcester Polytechnic Institute, Worcester, MA (1999)
8. Pryputniewicz, E.J.: ACES approach to the study of electrostatically driven MEMS microengines, MS Thesis, Worcester Polytechnic Institute, Worcester, MA (2000)
9. Pryputniewicz, R.J., Galambos, P., Brown, G.C., Furlong, C., Pryputniewicz, E.J.: ACES characterization of surface micromachined microfluidic devices. Internat. J. of Microelectronics and Electronic Packaging (IJMEP) 24, 30–36 (2001)
10. Pryputniewicz, D. R., Furlong, and Pryputniewicz, R. J. (2001) "ACES approach to the study of material properties of MEMS," *Proc. Internat. Symp. on MEMS: Mechanics and Measurements*, Portland, OR, pp. 80-83.
11. Pryputniewicz, R.J.: Engineering experimentation, Worcester Polytechnic Institute, Worcester, MA (1993)
12. Pryputniewicz, R.J., Furlong, C., Pryputniewicz, E.J.: Optimization of contact dynamics for an RF MEMS switch. In: Paper No. IMECE2002-39504, Am. Soc. Mech. Eng., New York, NY (2002)
13. Pryputniewicz, R.J., Furlong, C.: Novel optoelectronic methodology for testing of MOEMS. In: Proc. Internat. Symp. on MOEMS and Miniaturized Systems III. SPIE, vol. 4983, pp. 11–25 (2003)
14. Rogers, M.S., Miller, S.L., Sniegowski, J.J., LaVigne, G.F.: Designing and operating electrostatically driven microengines. In: Proc. 44th Internat. Instrumentation Symp., Reno, NV, pp. 56–65 (1998)
15. Pryputniewicz, R.J., Tan, X.G., Przekwas, A.J.: Modeling and measurements of MEMS gyroscopes. In: Proc. IEEE-PLANS 2004, Monterey, CA, pp. 111–119 (2004)
16. Rowe, J.R.: Advanced sensor technology key to new multivariable transmitter. In: Proc. Instr. Soc. Am.
17. Pryputniewicz, R.J., Angelosanto, J.P., Furlong, C., Brown, G.C., Pryputniewicz, E.J.: Analysis and measurements of high pressure response of MEMS sensors. In: Proc. Internat. Symp. on MEMS: Mechanics and Measurements, Portland, OR, pp. 76–79 (2001)
18. Pryputniewicz, R.J.: Thermal management in RF MEMS Ohmic switches. In: Paper No. IPACK 2007-33502, ASME – Am. Soc. Mech. Eng., New York, NY (2007)

19. Pryputniewicz, R.J., Wilkerson, P.W., Przekwas, A.J., Furlong, C.: RF MEMS: modeling and simulation of switch dynamics. In: Proc. 35th Internat. Symp. on Microelectronics, Denver, CO, pp. 267–272 (2002)

20. Furlong, C., Pryputniewicz, R.J.: Integrated approach to development of microelectronic contacts. In: Paper No. IPACK 2007-33345, ASME – Am. Soc. Mech. Eng., New York, NY (2007)

21. Pryputniewicz, R.J., Pryputniewicz, D.R., Pryputniewicz, E.J.: Effect of process parameters on TED-based Q-factor of MEMS. In: Paper No. IPACK 2007-33094, ASME – Am. Soc. Mech. Eng., New York, NY (2007)

22. Klempner, A.R., Marinis, R.T., Hefti, P., Pryputniewicz, R.J.: Experimental determination of the Q-factors of microcantilevers coated with thin metal films. Strain 45, 295–300 (2009)

23. Pryputniewicz, R.J., Furlong, C.: MEMS and nanotechnology, Worcester Polytechnic Institute, Worcester, MA (2002)

24. Pryputniewicz, R.J.: Recent advances in optoelectronic methodologies: from milli- through micro- to even ...smaller applications. In: Proc. Workshop on Optical Methodology, Worpswede, Germany (2007)

25. Stout, P.: CFD-ACE+ a CAD system for simulation and modeling of MEMS. In: Proc. SPIE, Paris, France (1999)

26. Wilkerson, P.W., Kranz, M., Przekwas, A.J.: Flip-chip hermetic packaging of RF MEMS. In: MEMS4 Conference, Berkeley, CA, August 24-26 (2001)

27. Przekwas, A.J., Turowski, M., Furmanczyk, M., Hieke, A., Pryputniewicz, R.J.: Multiphysics design and simulation environment for microelectromechanical systems. In: Proc. Symp. on MEMS: Mechanics and Measurements, Portland, OR, pp. 84–89 (2001)

28. CFDRC, "CFD-ACE+ Multiphysics software" (2004), `http://www.cfdrc.com`

29. SRAC, "COSMOS/M user's guide", Structural Research and Analysis Corporation, Santa Monica, CA (1998)

30. Brown, G.C.: Laser interferometric methodologies for characterizing static and dynamic behavior of MEMS, Ph.D. Dissertation, Worcester Polytechnic Institute, Worcester, MA (1999)

31. Pryputniewicz, R.J.: Quantitative determination of displacements and strains from holograms. In: Holographic interferometry. Springer Series in Sciences, ch. 3, vol. 68, pp. 33–72. Springer, Berlin (1995)

32. Pryputniewicz, R.J.: High precision hologrammetry. Internat. Arch. Photogramm. 24, 377–386 (1981)

33. Pryputniewicz, E.J., Miller, S.L., de Boer, M.P., Brown, G.C., Biederman, R.R., Pryputniewicz, R.J.: Experimental and analytical characterization of dynamic effects in electrostatic microengines. In: Proc. Internat. Symp. on Microscale Systems, Orlando, FL, pp. 80–83 (2000)

34. Pryputniewicz, R.J.: Hologram interferometry from silver halide to silicon and ...beyond. In: Proc. SPIE, vol. 2545, pp. 405–427 (1995)

35. Pryputniewicz, R.J., Shepherd, E., Allen, J.J., Furlong, C.: University – National Laboratory alliance for MEMS education. In: Proc. 4th Internat. Symp. on MEMS and Nanotechnology (4th-ISMAN), Charlotte, NC, pp. 364–371 (2003)

36. Brown, G.C., Pryputniewicz, R.J.: Holographic microscope for measuring displacements of vibrating microbeams using time-average electro-optic holography. Opt. Eng. 37, 1398–1405 (1998)

37. Klempner, A.R., Hefti, P., Marinis, R.T., Pryputniewicz, R.J.: Development of a high stability optoelectronic laser interferometric microscope for characterization and optimization of MEMS. In: Proc. 15th Internat. Invitational UACEM Symp., Springfield, MA, pp. 275–285 (2004)

38. Pryputniewicz, R.J., Marinis, R.T., Klempner, A.R., Hefti, P.: Hybrid methodology for development of MEMS. In: Proc. IEEE-PLANS 2004, San Diego, CA, vol. 6 (2006)

39. Marinis, T.F., Soucy, J.W., Hanson, D.S., Pryputniewicz, R.J., Marinis, R.T., Klempner, A.R.: Isolation of MEMS devices from package stresses by use of compliant metal interposers. In: Proc. 56th IEEE Electronic Components & Technology Conf (56th-IEEE-ECTC), paper No. P1S25-MEMS, San Diego, CA (2006)

40. Pryputniewicz, R.J., Champagne, R.P., Angelosanto, J.P., Brown, G.C., Furlong, C., Pryputniewicz, E.J.: Multivariable MEMS polysilicon piezoresistive sensor: analysis and measurements. In: Proc. Internat. Symp. on Microscale Systems, Orlando, FL, pp. 72–75 (2000)

41. Pryputniewicz, R.J.: Thermomechanics of high-pressure MEMS sensors. In: Paper No. IPACK 2007-33507, ASME – Am. Soc. Mech. Eng., New York, NY (2007)

42. Mihailovich, R.E., Kim, M., Hacker, J.B.H., Sovero, A., Studer, J., Higgins, J.A., DeNatale, J.F.: MEM relay for reconfigurable RF circuits. IEEE Microwave Wireless Components Lett. 11, 53–55 (2001)

43. Pryputniewicz, R.J., Pryputniewicz, E.J.: Quantitative characterization of microsystem dynamics. In: Paper No. IPACK 2007-33503, ASME – Am. Soc. Mech. Eng., New York, NY (2007)

44. Pryputniewicz, R.J.: Advances in optoelectronic metrology: from milliscale to nanoscale applications. In: Proc. 7th Internat. Symp. on MEMS and Nanotechnology (7-ISAMAN), St. Louis, MO, pp. 1–17 (2006)

45. Zunino III, J.L., Skelton, D.R., Han, W., Pryputniewicz, R.J.: Hybrid approach to MEMS reliability assessment. In: Paper No. SPIE6563-03, Proc. Internat. Symp., on MOEMS-MEMS 2007: Reliability, Packaging, and Characterization of MEMS, San Jose, CA (2007)

46. Skelton, D.R., Zunino III, J.L., Han, W., Pryputniewicz, R.J.: MEMS reliability assessment: preliminary results. In: Paper No. 318, Proc.8th Internat. Symp., on MEMS and Nanotechnology (8-ISMAN), Springfield, MA (2007)

47. Marinis, T.F.: The future of microelectromechanical systems (MEMS). Strain 45, 208–220 (2009)

Experimental Mechanics in Nano-engineering

Cesar A. Sciammarella[1], Federico M. Sciammarella[1], and Luciano Lamberti[2]

[1] College of Engineering & Engineering Technology
 Northern Illinois University, DeKalb, USA
[2] Dipartimento di Ingegneria Meccanica e Gestionale,
 Politecnico di Bari, Bari, Italy
 `csciammarella@niu.edu, sciammarella@niu.edu,`
 `lamberti@poliba.it`

Abstract. A new renaissance in the field of Experimental Mechanics is well underway because of the recent technologies developed for Nano-Engineering. There are many challenges to face and overcome when going from the macro world to the manipulation of nano-objects. In the macro world, with the experience gained in the last century and the development of numerical techniques, Experimental Mechanics has changed its initial role of an analogical tool to solve difficult differential equations to a complementary methodology to support numerical techniques in handling complex boundary condition effects in static or dynamic problems. Experimental Mechanics is also a very important tool in materials science research. With the introduction of Nano-Engineering, Experimental Mechanics has experienced a vast expansion in its applications to understand an almost completely new field where both basic physical properties that have a well established statistical meaning in the macro world and fundamental formulations require a revision and in many cases new theoretical developments.

Since theories must be supported by experimental evidence, Experimental Mechanics represents a necessary basic tool to lay the foundations to understanding properties and behavior of materials at the nano-level. There are well established tools that allow events at the nano-level to be observed: for example, X-rays with new developments in holographic interferometry done with X-rays. Electron microscopy also has been extended to the field of holographic interferometry. Optics with its versatile photons appears also as a promising tool in many cases where X-rays or electron microscopy become difficult or impossible to apply. However, the classical resolution limitations confined for a long while optics to be used in the range of hundreds of nanometers. New recent developments have opened a new window of opportunity for optical techniques to be applied in the nano-range. This chapter will cover these recent developments. The essential theoretical aspects that make it possible to go beyond the classical resolution limits as well as their application in engineering problems such as metrology, surface topography and strain determinations will be presented.

1 Introduction and Theoretical Background

This paper is devoted to the description of methods developed to apply visible radiation optics at the nanometric level and to the procedures of data analysis to retrieve the information contained in the images. Classical optics has limitations on the resolution that can be achieved utilizing optical microscopy in the observation of events taking place at the sub-micron level, i.e. to a few hundreds of nanometers. To overcome this limitation, a new methodology was developed. The adopted solution is to apply non conventional methods of illumination. These new methods are made possible by the emission of coherent light by the objects that are under analysis. This is done through the phenomenon of light generation produced by electromagnetic resonance. Object self-luminosity is the consequence of electromagnetic resonance. Why self-luminosity may help us to increase resolution? The light generated in this way has particular properties that are not present in the light sent by an object that results from external illumination. The produced wave fronts can travel long distances or go through an optical system without the diffraction changes experienced by ordinary wave fronts [1-3].

1.1 Properties of Evanescent Waves

The self generation of light is achieved through the use of total internal reflection (TIR). At the interface between two media such that the index of refraction of medium 1 is larger than the index of refraction of medium 2 (i.e. $n_1 > n_2$), if a light beam is incident with an angle $\theta_i > \theta_{i,crit}$, a total reflection of the beam, in which essentially all of the light is reflected back into the first medium, takes place (Fig. 1a). Even though the light no longer propagates into the second medium, there is a small amount of penetration of the electromagnetic field across the interface between the two media. In the vector form solution of the Maxwell equations, it is possible to show that under the condition of total reflection the electromagnetic field does not disappear in the second medium [4]. However, there is no energy exchange with the second medium. The components of the electromagnetic field transmitted in the second medium, vectors **E** and **H**, depend on [4]:

$$\exp\left[-i\frac{2\pi}{\lambda}z\sqrt{\frac{\sin^2\theta_i}{n_{12}^2}-1}\right] \tag{1}$$

where the relative index of refraction is defined as $n_{12}=n_2/n_1$.

The intensity of the field decays by 1/e at the distance from the interface equal to:

$$z=\frac{\lambda}{2\pi\sqrt{\frac{\sin^2\theta_i}{n_{12}^2}-1}} \tag{2}$$

Under this condition a particular type of waves are produced in the interface (Fig. 1a). These waves are called evanescent waves and travel at the interface decaying exponentially in the second medium at a depth that is a fraction of the wavelength of the utilized light as shown by Eq. (2). The decay of electromagnetic field is sketched in Fig. 1a.

$$\theta_{i,crit} = \arcsin \frac{n_2}{n_1}$$
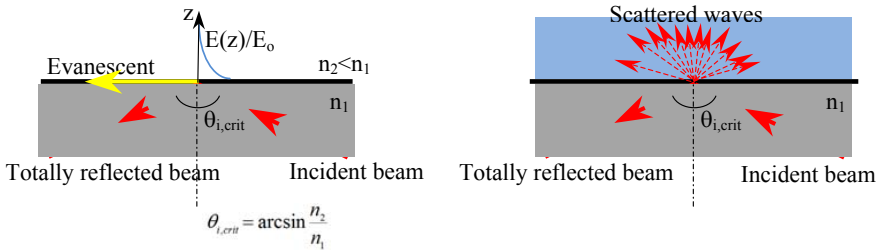
Fig. 1. a) Principle of formation and characteristics of evanescent waves; b) Propagation in a dielectric medium.

As was said before, the electromagnetic field of the evanescent waves does not propagate light in the second medium. However, if a dielectric medium or a conducting medium comes in contact with the evanescent field, light is emitted by the medium itself. This interaction depends on the properties, size and geometry of the medium. In the case of a dielectric medium, through Rayleigh molecular scattering, light is emitted in all directions as illustrated in Fig. 1b. The light emission is a function of the electronic configuration of the medium. If the medium is a metal, the Fermi's layer electrons produce resonances called plasmons. The effect is reversible, photons can generate plasmons, and the decaying plasmons generate photons. In the case of very small dielectric objects, the resonance takes place at the level of the bound electrons. The actual dimensions of the crystal determine the different resonances and light at frequencies different from the frequency of illuminating light is generated.

According to the Quantum Mechanics principle of preservation of momentum for the photons, some of the energy of the incident beam continues in the second medium (the direction indicated by the blue arrow in Fig. 1b).

1.2 Super-Resolution

In the preceding paragraphs there were outlined the basic physical processes required for light generation in an object that is within the region of influence of evanescent fields. Now the effect of self illumination in the generation of super-resolution images has to be considered. In general, the possibility of getting higher resolutions depends on the energy available and on the detector spatial frequency capability. This result was foreseen by Toraldo di Francia [5] when he postulated that the resolution of an optical system could be increased almost continuously beyond the classical Rayleigh's diffraction limit, provided that the necessary energy to achieve these results is available. When Toraldo di Francia [6] presented

this original work it was argued that his proposed super-resolution approach violated the Heisenberg uncertainty principle. In the discussion presented in [6] the arguments using the Heisenberg principle, arguments that are included in many text books of Optics, can be easily dismissed because they are based on the wave function of a single photon while one is dealing with the wave function of millions of photons. The question can be summarized in the following way [7]. If ΔE is the amount of energy invested in an observation and Δx is a distance to be measured, the Heisenberg principle can be stated as follows:

$$\Delta E \, \Delta x \geq \frac{hc}{2} \qquad (3)$$

where h is the Planck's constant, c is the speed of light. This equation tells us that by increasing the energy there is no limit to the smallness of the distance that can be measured. From the practical point of view, it implies that increases in smallness of the distance that one wants to obtain will require enormous increases in the energy that has to be invested. This is because in Eq. (3) there is a large factor: the speed of the light c. From a more direct type of approach, one can say that information is encoded in the interference patterns of the evanescent wave fronts transformed into propagating wave fronts. Whatever signal can be recovered above the noise level, it will contain some type of information that may be extracted within certain practical limits that have been analyzed. This is a general argument that applies to all types of electromagnetic radiation.

There is another important application of the Heisenberg principle that is more relevant to the topic of this chapter and has been pointed out by Vigoureux [8]. This relationship is:

$$\Delta x \, \Delta k_x > 2\pi \qquad (4)$$

The wave propagation vector has two components $\vec{k_x}$ and $\vec{k_y}$. In Eq. (4), $\vec{k_x}$ is the wave vector component in the x-direction. Vigoureux shows that for waves propagating in the vacuum Eq. (4) leads to the Rayleigh limit of λ/2. In order to go beyond the λ/2 limit, one must have values of $\vec{k_x}$ falling in the field of evanescent waves. Therefore, to capture evanescent waves is an effective approach to getting super-resolution. This conclusion is in agreement with the conjecture made by Toraldo di Francia in 1952.

A further mathematical argument can be made by resorting to a Fourier expansion of the solution of Maxwell equations. In the classical optics scheme of plane-wave solutions of the Maxwell equations, monochromatic waves with definite frequencies and wave numbers are considered. This idealized condition does not apply in the present case. One can start from the Fourier solution of the Maxwell equations in the vector field (time-space):

$$E(x, \tau) = \frac{1}{\sqrt{2\pi}} \int_{-\infty}^{+\infty} A(k) e^{ikx - i\omega(k)\tau} \, dk \qquad (5)$$

where: $E(x,\tau)$ is the scalar representation of the propagating electromagnetic field, x is the direction of propagation of the field, τ is the time, $A(k)$ is the amplitude of the field, k is the wave number $2\pi/\lambda$, $\omega(k)$ is the angular frequency. $A(k)$ provides the linear superposition of the different waves that propagate and can be expressed as:

$$A(k) = \sqrt{2\pi} \ \delta(k\text{-}k_o) \tag{6}$$

where $\delta(k\text{-}k_o)$ is the Dirac's delta function. This amplitude corresponds to a monochromatic wave, that is: $E(x,\tau) = e^{ikx-i\omega(k)\tau}$. If one considers a spatial pulse of finite length (see Fig. 2a), at the time $\tau=0$, $E(x,0)$ represents (see Fig. 2c) a finite wave-train of length L_{wt} where $A(k)$ is not a delta function but a function that spreads a certain length Δk (Fig. 2b). The dimension of L_{wt} depends on the analyzed object size. In the present case, objects are smaller than the wavelength of the light.
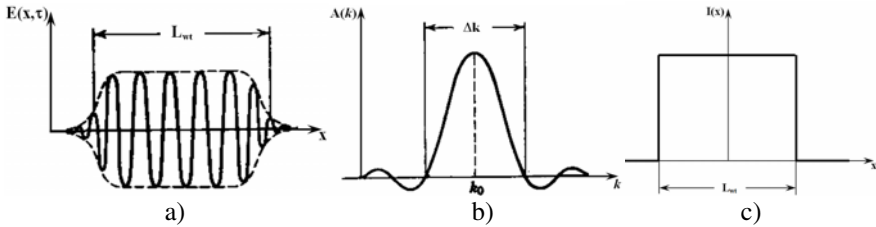
Fig. 2. a) Harmonic wave train of finite extent L_{wt}; b) Corresponding Fourier spectrum in wave numbers k; c) Representation of a spatial pulse of light whose amplitude is described by the rect(x) function.

In Ref. [9], it is stated that if L_{wt} and Δk are defined as the RMS deviations from the average values of L_{wt} and Δk evaluated in terms of the intensities $|E(x,0)|^2$ and $|A(k)|^2$, then it follows:

$$L_{wt}\Delta k \geq \frac{1}{2} \tag{7}$$

Since L_{wt} is very small, the spread of wave numbers of monochromatic waves must be large. Hence there is a quite different scenario with respect to the classical context in which the length L_{wt} is large when compared to the wavelength of light.

In order to simplify the notation, one can reason in one dimension without loss of generality. The spatial pulse of light represented in Fig. 2c is defined as follows:

$$A(x) = A_o \text{rect}(x) \tag{8}$$

where:

$$
\mathrm{rect}(x) = \begin{cases} 1 & |x| < \dfrac{1}{2} \\[2mm] \dfrac{1}{2} & |x| = \dfrac{1}{2} \\[2mm] 0 & \mathrm{elsewhere} \end{cases} \tag{9}
$$

The Fourier transform of $A(x)$ is equal to $\mathrm{sinc}(x)$. The Fourier transform of the light intensity $[A(x)]^2$ is hence $[\mathrm{sinc}(x)]^2$. To the order 0 it is necessary to add the shifted orders ± 1. The function $A(x \pm \Delta x)$ can be represented through the convolution relationship:

$$
A(x \pm \Delta x) = \int_{-\infty}^{+\infty} A(x') \cdot \delta(x \pm \Delta x) \cdot dx' \tag{10}
$$

where $x' = x \pm \Delta x$. The Fourier transform of the function $A(x \pm \Delta x)$ will be:

$$
\mathrm{FT}[A(x \pm \Delta x)] = A(f_x) \cdot e^{i[2\pi f_x(\mp \Delta x/2)]x} \tag{11}
$$

where f_x is the spatial frequency. The real part of Eq. (11) is:

$$
\mathrm{Re}\left\{\mathrm{FT}[A(x \pm \Delta x]\right\} = A(f_x) \cdot \cos\left\{[2\pi f_x(\mp \Delta x/2)]x\right\} \tag{12}
$$

By taking the Fourier transform of Eq. (12), one can return back to Eq. (10).

For the sake of simplicity, the above derivations have been done in one dimension but can be extended to 3-D. Brillouin [10] has shown that for a cubic crystal the electromagnetic field can be represented as the summation of plane wave fronts with constant amplitude as it has been assumed in Eq. (5). In such circumstances the above derivation can be extended to 3-D and can be applied to the components of the field in the different coordinates.

2 Applications to Nanometrology

The initial approach to the utilization of evanescent field properties was the creation of near-field techniques. In the near-field techniques, a probe with dimensions in the nano-range detects the local evanescent field generated in the vicinity of the objects that are observed. The following alternative approach to the classical near-field techniques has been utilized in this paper:

a) Using diffraction through the equivalent of a diffraction grating or to generate directly an ample spectrum of k vectors by means of a diffraction grating;
b) Creating a Fabry-Perot type cavity;
c) Exciting the objects to be observed with the evanescent fields so that the objects become self-luminous.

The light generated in this way has the particular property of propagating through space and optical instruments without the common diffraction effects experienced by ordinary wave fronts [1-3].

The self generation of light by small single crystals of sodium chloride has been utilized to produce the equivalent of Fourier type holograms [11].

2.1 Observation of Nano-crystals and Nano-spheres

Figure 3 shows the schematic representation of the experimental setup. Following the classical arrangement of TIR, a helium-neon (He-Ne) laser beam with nominal wavelength 632.8 nm impinges normally to the face of a prism designed to produce limit angle illumination on the interface between a microscope slide (supported by the prism itself) and a saline solution of sodium-chloride contained in a small cell supported by the slide. Consequently, evanescent light is generated inside the saline solution.

The objects observed with the optical microscope are supported by the upper face of the microscope slide. Inside the cell filled with the NaCl solution there is a polystyrene microsphere of 6 μm diameter. The microsphere is fixed to the face of the slide through chemical treatment of the contact surface in order to avoid Brownian motions. The polystyrene sphere acts as a relay lens which collects the light wave fronts generated by the nano-sized crystals of NaCl resting on the microscope slide. More details on the polystyrene sphere and the saline solution properties are given in Table 1.
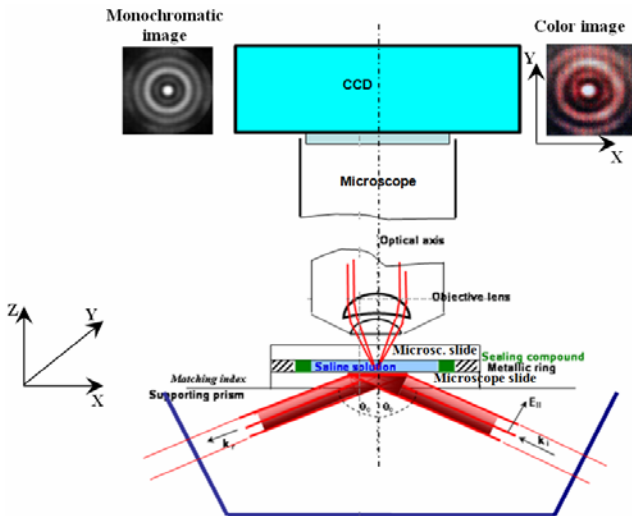
Fig. 3. Experimental setup to image nano-size objects using evanescent illumination. Two CCD cameras are attached to a microscope in order to record images: monochromatic, color.

The observed image is focused by an optical microscope with NA=0.95 and registered by a monochromatic CCD attached to the microscope. At a second port, a color camera records color images. The CCD is a square pixel camera with 1600x1152 pixels. The analysis of the image recorded in the experiment has been performed with the Holo Moiré Strain Analyzer software (HoloStrain™), Ref. [12].

Table 1. Details on polystyrene microsphere and saline solution

Parameter	Value	Note
Polystyrene microsphere diameter D_{sph}	6 ± 0.042 μm	Tolerance specified by the manufacturer
Polystyrene microsphere refraction index n_p	1.57 ± 0.01	Value specified by the manufacturer
Saline solution refraction index n_s	1.36	Computed from NaCl concentration for the nominal wavelength of λ=590 nm

2.2 Generation of Multi-k Vector Fields

Figure 4 shows the process of generation of the evanescent beams that provide the energy required for the formation of the images. The optical setup providing the illumination is similar to the setup originally developed by Toraldo di Francia to prove the existence of evanescent waves and described in Ref. [6]. A grating is illuminated by a light beam at the limit angle of incidence θ_c. A matching index layer is interposed between the illuminated surface and a prism which is used for observing the propagating beams originated on the prism face by the evanescent waves. In the original experiment conducted by Toraldo di Francia, the diffraction orders of the grating produced multiple beams that by interference generated the fringes observed with a telescope. In the present case, the interposed layer corresponds to the microscope slide. Although the microscope slide does not have exactly the same index of refraction of the prism, it is close enough to fulfill its role.

The diffraction effect is produced by the residual stresses developed in the outer layers of the prism. The multiple illumination beams are the result of residual stresses in the outer layers of the prism. In Ref. [13], there is a detailed analysis of the formation of interference fringes originated by evanescent illumination in presence of residual stresses on glass surfaces. The glass in the neighborhood of the surface can be treated as a layered medium and the fringe orders depend on the gradients of the index of refraction. In Ref. [14], there is a more extensive analysis of the role played by birefringence in the present example.

Figure 4 provides a schematic representation of the process of illumination of the observed nano-objects. The laser beam, after entering the prism, impinges on the prism-microscope slide interface, symbolically represented by a grating, where it experiences diffraction. The different diffraction orders enter the microscope slide and continue approximately along the same trajectories determined by the

diffraction process. The slight change in trajectory is due to the fact that the indices of refraction of the prism and the microscope slide are slightly different. As the different orders reach the interface between the microscope slide and the saline solution, total reflection takes place and evanescent wave fronts emerge into the solution in a limited depth that is a function of the wavelength of the light as shown in Eq. (2).
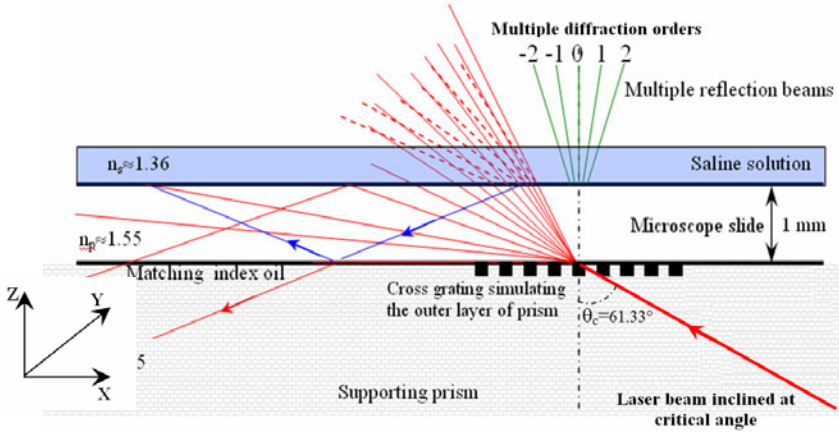
Fig. 4. Model of the interface between the supporting prism and the microscope slide as a diffraction grating causing the impinging laser beam to split into different diffraction orders.

Since the wave fronts have been originated by artificial birefringence, for each order of diffraction there are two wave fronts: the p-polarized and the s-polarized wave fronts. Upon entering the saline solution these wave fronts originate propagating wave fronts that produce interference fringes.
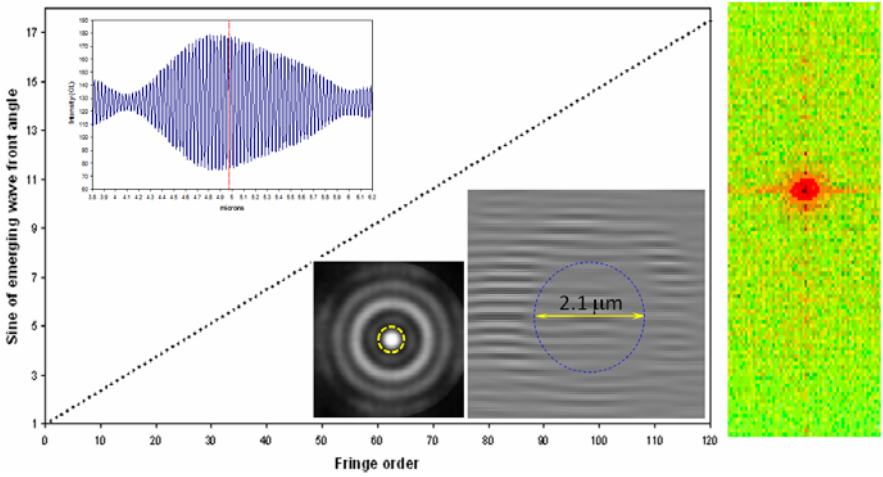
Fig. 5. System of fringes observed in the image of the 6 μm diameter polystyrene sphere. Dotted circle represents the first dark ring in the particle diffraction pattern

Figure 5 shows the diffraction orders corresponding to one family of fringes that were extracted from the FT of the image captured by the optical system and contains the diffraction pattern of the microsphere that acts as a relay lens. Since these wave fronts come from the evanescent wave fronts, their sine is a complex number taking values greater than 1. Figure 5 includes also the image extracted from the FT of the central region of the diffraction pattern of the microsphere (the first dark fringe of the microsphere diffraction pattern is shown in the figure) and shows the presence of the families of fringes that were mentioned previously. The fringes form moiré patterns that are modulated in amplitude in correspondence of the loci of the interference fringes of the microsphere. A total of 120 orders have been detected for this particular family [15]. These wave fronts play a role in the observation of the sodium-chloride nano-crystals contained in the saline solution.

Figure 6 shows the schematic representation of the optical circuit bringing the images to the CCD detector. The observed patterns are not images in the classical sense. Therefore, the meaning of the concept of "super-resolution" must be explained with respect to the present context.
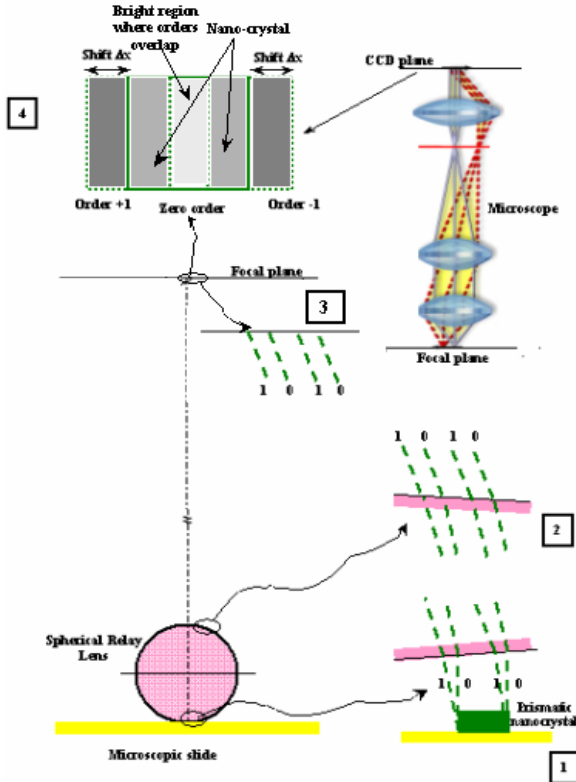
Fig. 6. Schematic representation of the optical system leading to the formation of lens hologram: 1) Prismatic nano-crystal; 2) Wave fronts entering and emerging from the polystyrene micro-sphere acting as a relay lens; 3) Wave fronts arriving at the focal plane of the spherical lens; 4) Wave fronts arriving at the image plane of the CCD. The simulation of the overlapping of orders 0, +1 and -1 in the image plane of the CCD is also shown.

It can be seen that different diffraction orders emerge from the interfaces of the crystals and the supporting microscope slide. These emerging wave fronts act as multiplexers creating successive shifted images of the object. Let us assume that we look at a prism (Fig. 6, Part 1) approximately parallel to the recording CCD image plane. Successive shifted luminous images of the prism are then recorded.

It is possible to prove that the main energy is concentrated in the zero order and the first order [11]. These orders overlap in an area that depends on the process of formation of the image (see Fig. 6). The order 0 produces an image on the image plane of the optical system, that is centered at a value x of the horizontal coordinate. Let us call S(x) this image. The order +1 will create a shifted image of the particle, S(x-Δx). The shift implies a change of the optical path between corresponding points of the surface. In the present case, the trajectories of the beams inside the prismatic crystals are straight lines and the resulting phase changes are proportional to the observed image shifts. Therefore, the phase change can be written as:

$$\Delta\phi(x, \Delta x) = K_p \left[S(x) - S(x - \Delta x) \right] \tag{13}$$

where K_p is a coefficient of proportionality. Equation (13) corresponds to a shift of the image of the amount Δx. If the FT of the image is computed numerically, one can apply the shift theorem of the Fourier transform. For a function $f(x)$ shifted by the amount Δx, the Fourier spectrum remains the same but the linear term $\omega_{sp} \Delta x$ is added to the phase: ω_{sp} is the angular frequency of the FT. It is necessary to evaluate this phase change. The shift can be measured on the image by determining the number of pixels representing the displacement between corresponding points of the image (see Fig. 6, Part 4). Through this analysis and using the Fourier Transform it is possible to compute the thickness t of the prism in an alternative way to the procedure that will be described in the following. These developments are a verification of the mechanism of the formation of the images as well as of the methods to determine prism thickness [11].

2.3   Formation of Holograms at the Nano-scale

Let us now consider the quasi-monochromatic coherent wave emitted by a nano-sized prismatic crystal. The actual formation of the image is similar to a typical lens hologram of a phase object illuminated by a phase grating [16]. The Fourier Transform of the image of the nano-crystal extended to the complex plane is an analytical function. If the FT is known in a region, then, by analytic continuation, $F(\omega_{sp})$ can be extended to the entire domain. The resolution obtained in this process is determined by the frequency ω_{sp} captured in the image. The image can be reconstructed by a combination of phase retrieval and suitable algorithms. The image can be reconstructed from a $F(\omega_{sp})$ such that $\omega_{sp} < \omega_{sp,max}$, where $\omega_{sp,max}$ is determined by the wave fronts captured by the sensor.

The fringes generated by the different diffraction orders experience phase changes that provide depth information. These fringes are carrier fringes that can be utilized to extract optical path changes. This type of setup to observe phase

objects was used in phase hologram interferometry as a variant of the original setup proposed by Burch and Gates[17,18]. When the index of refraction in the medium is constant, the rays going through the object are straight lines. If a prismatic object is illuminated with a beam normal to its surface, the optical path s_{op} through the object is given by the integral:

$$s_{op}(x, y) = \int n_i(x, y, z)dz \tag{14}$$

where the direction of propagation of the illuminating beam is the z-coordinate and the analyzed plane wave front is the plane x-y; $n_i(x,y,z)$ is the index of refraction of the object through which light propagates.

The change experienced by the optical path is given by:

$$\Delta s_{op}(x, y) = \int_0^t \left[n_i(x, y, z) - n_o \right] dz \tag{15}$$

where t is the thickness of the medium. By assuming that:

$$n_i(x, y, z) = n_c \tag{16}$$

where n_c is the index of refraction of the observed nano-crystals, Eq. (15) then becomes:

$$\Delta s_{op}(x, y) = \int_0^t \left[n_i(x, y, z) - n_o \right] dz = (n_c - n_o)t \tag{17}$$

By transforming Eq. (17) into phase differences and making $n_o = n_s$, where n_s is the index of refraction of the saline solution containing the nano-crystals, one can write:

$$\Delta\phi = \frac{2\pi}{p}(n_c - n_s)t \tag{18}$$

where p is the pitch of the fringes generated by the thickness t of the specimen. In general, the change of optical path is small and no fringes can be observed. In order to solve this problem, carrier fringes can be added. An alternative procedure is the introduction of a grating in the illumination path [16]. In the case of the nano-crystals, the carrier fringes can be obtained from the FT of the lens hologram of the analyzed crystals. In the holography of transparent objects, one can start with recording an image without the transparent object of interest. In a second stage, one can add the object and then superimpose both holograms in order to detect the phase changes introduced by the object of interest. In the present application, reference fringes can be obtained from the background field away from the observed objects. This procedure presupposes that the systems of carrier fringes are present in the field independently of the self-luminous objects. This assumption is verified in the present case since one can observe fringes that are in the background and enter the nano-crystals experiencing a shift.
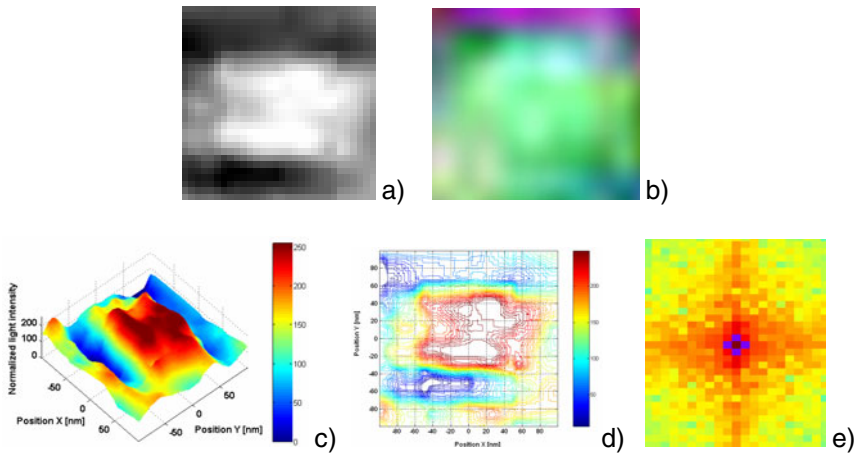
Fig. 7. NaCl prismatic nano-crystal of length 86 nm: a) Gray-level image (1024 x 1024 pixels); b) Image of the crystal captured by a colour camera; c) 3-D distribution of light intensity; d) Isophote lines; e) FT pattern.

Figure 7 illustrates the case of a square cross-section crystal of length 86 nm. Figure 7b is an image of the crystal recorded by a color camera; the crystal has a light green tone. The monochromatic image and the color image have different pixel structures. However, by using features of the images clearly identifiable, a correspondence between the images could be established and the image of the nano-crystal located. The figure indicates that the image color is the result of an electromagnetic resonance and not an emission of light at the same wavelength as the wavelength of the impinging light.

Figure 8a shows the numerical reconstruction of this crystal which is consistent with the theoretical structure 5×4×4 [19]; Fig. 8c shows the level lines of the top face of the crystal; Fig. 8d shows a cross section where each horizontal line corresponds to five elementary cells of NaCl. The theoretical structure has one step in the depth dimension (Fig. 8b). It is unlikely that the upper face of the nano-crystal can be exactly parallel to the camera plane. Hence, the crystal shows an inclination which can be corrected by means of an infinitesimal rotation. This allows the actual thickness jump in the upper face of the crystal (see the theoretical structure in Fig. 8b) to be obtained. The jump in thickness is 26 nm out of a side length of 86 nm: this corresponds to a ratio of 0.313 which is very close to theory. In fact, the theoretical structure predicts a jump in thickness of one atomic distance vs. three atomic distances in the transverse direction: that is, a ratio of 0.333.

Similarly to the case of quantum dots, nano-crystals of different sizes emit light of different frequencies. The physical reason for this is called quantum confinement effect. Smaller crystal emit higher energies and therefore their sizes determine the energy and finally the color. For example, this crystal emits light at 500 nm, in the blue-green range. An explanation of the process of light generation is given in [11].
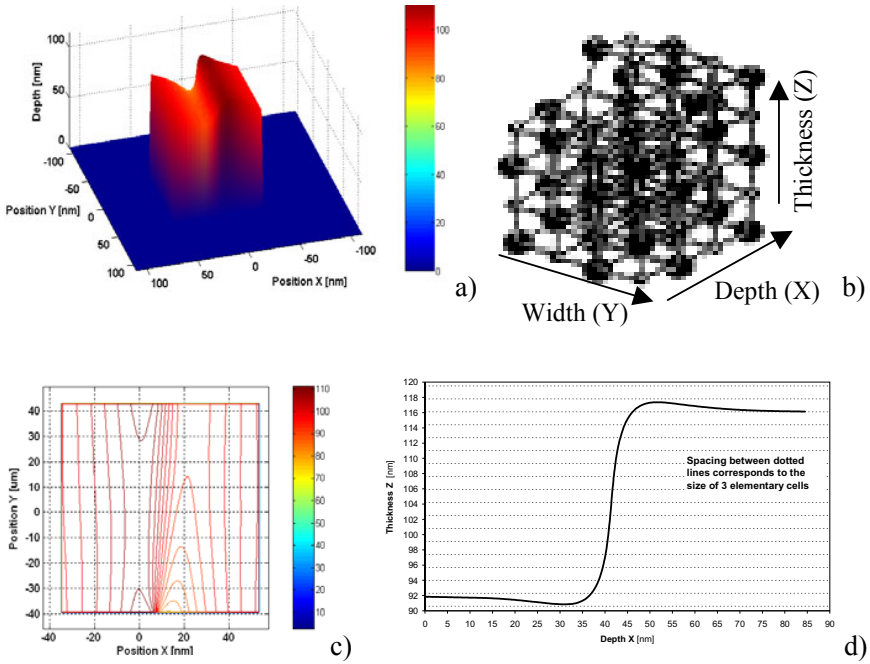
Fig. 8. a) Numerical reconstruction of a NaCl nano-crystal of length 86 nm, the crystal is inclined with respect to the image plane; b) Schematic of the theoretical structure 5x4x4; c) Level lines; d) Rotated cross section of the upper face of the nano-crystal: the spacing between dotted lines corresponds to the size of three elementary cells.

Table 2 shows the experimental aspect ratios measured for some nano-crystals: these values are compared with the theoretical aspect ratios. The table also provides the error analysis of these results. Thicknesses reported in Table 3 are the average values shown in Table 2.

Table 2. Aspect ratio of the observed nano-crystals: experiments vs. theory

Nano-crystal length (nm)	Experimental dimensions (nm)	Experimental aspect ratio	Theoretical aspect ratio
54	72 x 54 x 53	5.43 x 4.08 x 4	5 x 4 x 4
55	55 x 45 x 33.5	4.93 x 4.03 x 3	5 x 5 x 3
86	104 x 86 x 86	4.84 x 4 x 4	5 x 4 x 4
120	120 x 46 x 46	7.83 x 3 x 3	8 x 3 x 3

Mean error on aspect ratios = 4.59%; Standard deviation on aspect ratios = ± 6.57%.

Table 3, on the basis of the expected aspect ratios, gives the theoretical dimensions of the sides of the nano-crystals and compares them with the measured values. Results of statistical analysis of probable errors in measurements are also presented in the table. A conservative assumption to estimate the accuracy of the measurements was made by adopting the smallest dimensions of the crystals as given quantities from which the other dimensions are then estimated. The smallest dimensions are the ones that will have the larger absolute errors.

Table 3. Main dimensions of the observed nano-crystals: experiments vs. theory

Nano-crystal length (nm)	Dimensions Measured	Dimensions Theoretical	Difference (nm)
	72	66.3	+5.7
54	54	53	+1
	53	53	-----
	55	55.8	-0.8
55	45	55.8	-10.8
	33.5	33.5	-----
	104	107.5	-3.5
86	86	86	0
	86	86	-----
	120	122.7	-2.7
120	46	46	0
	46	46	-----

Mean absolute error = 3.06 nm; Mean error = -1.39 nm.
Standard deviation of absolute error = ± 3.69 nm.

2.4 Analysis of the Polystyrene Nano-spheres

A similar analysis can also be performed for the resonant modes of polystyrene nano-spheres injected in the saline solution. Micro-spheres and nano-spheres made of transparent dielectric media are excellent optical resonators. Unlike the NaCl nano-crystals whose resonant modes have not been previously studied in the literature, both theoretical and experimental studies on the resonant modes of micro-spheres and nano-spheres can be found in the literature. Among the resonance modes of these spheres, of particular interest are the modes localized at the surface, along a thin equatorial ring. These modes are called whispering-gallery modes (WGM)**.** The WG modes are within the Mie's family of solutions for resonant modes in light scattering by dielectric spheres. The WG modes can be also derived from Maxwell's equations by imposing adequate boundary conditions. They can also be obtained as solutions of the Quantum Mechanics Schrodinger-like equation that describes the evolution of a complex angular-momentum of a particle in a potential well.

Figure 9 shows the image of a spherical particle of diameter 150 nm. This image presents the typical whispering gallery intensity distribution. Waves are propagating around the diameter in opposite directions thus producing a standing wave with 7 nodes and 6 maxima. The light is trapped inside the particle and there is basically a surface wave that only penetrates a small amount into the radial direction. The signal recorded for this particle is noisier compared with the signal recorded for the prismatic crystals. The noise increase is probably due to the Brownian motion of the spherical particles. While the NaCl nano-crystals seem to grow attached the supporting surface, the nano-spheres are not in the same condition. Of all resonant geometries a sphere has the capability of storing and confining energy in a small volume.
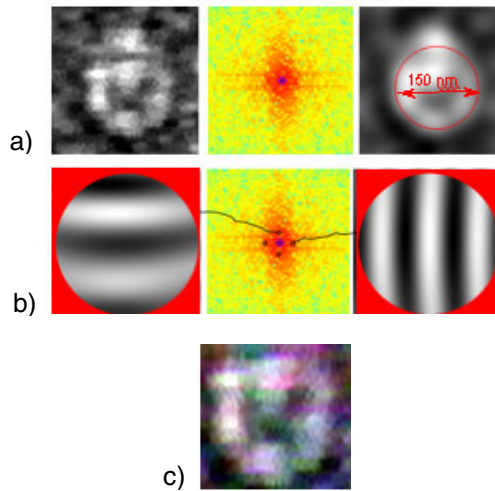
Fig. 9. Spherical nano-particle of estimated diameter 150 nm: a) Gray-level image of the particle, FT pattern and 0-order filtered pattern; b) Systems of fringes modulated by the particle; c) Color image of the particle.

The method of depth determination utilized for the nano-crystals can be applied also to the nano-spheres. While in prismatic bodies made out of plane surfaces the pattern interpretation is straightforward, in the case of curved surfaces the analysis of the patterns is more complex since light beams experience changes in trajectories determined by the laws of refraction. In the case of a sphere, the analysis of the patterns can be performed in a way similar to what is done in the analysis of the Ronchi test for lens aberrations. Figure 9 shows the distortion of a grating of pitch p=83.4 nm as it goes through a nano-sphere of estimated diameter, on the base of the edge light gradient method, D_e=150 nm. The appearance of the observed fringes is similar to that observed in a Ronchi test. The detailed description of this process is not included in this chapter for the sake of brevity.

Figure 10 shows another spherical particle of diameter 187 nm while Fig. 10b shows the average intensity. Figure 10c is extracted from Ref. [20] and shows the

numerical solution for the WGM of a polystyrene sphere of diameter 1.4 µm while Fig. 10d shows the average intensity.
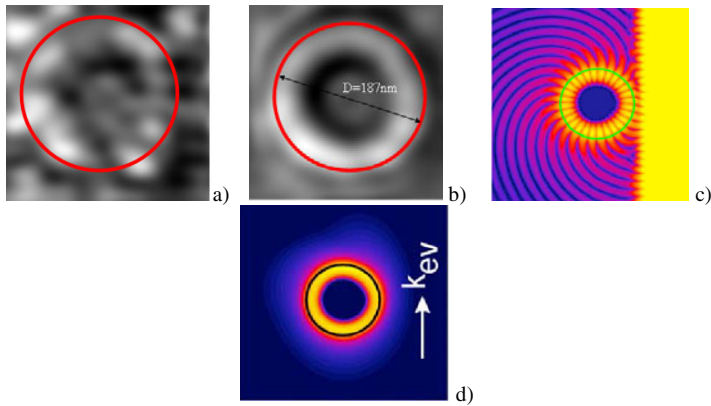
Fig. 10. Spherical nano-particle of estimated diameter 187 nm: experimentally recorded images and numerical simulations. a) Original image; b) Average intensity image; c) Numerical simulation of whispering modes; d) Average intensity of numerical simulation.

It is possible to see the correspondence between experimental results and numerical simulations. The electromagnetic resonance occurs at the wavelength $\lambda=386$ nm which corresponds to UV radiation. The color camera is sensitive to this frequency and Fig. 9c shows the color picture of the $D_e=150$ nm nano-sphere: the observed color corresponds approximately to the above mentioned resonance wavelength.

3   Application of Surface Plasmon Resonance to Surface Roughness Topography

The previous examples illustrated the utilization of evanescent waves in the analysis of nano-size dielectric objects. The next application to be described is the utilization of evanescent waves to study the topography and deformation of surfaces. In the case of the nano-objects the interaction of the evanescent waves with the objects takes place by resonance phenomena with bound electrons. When a plane wave front impinges the surface separating two media such that the index of refraction of medium 1, glass, is higher than the index of refraction of medium 2, air, at the limit angle total reflection takes place (see Fig. 1). Under these circumstances a very interesting phenomenon occurs. At the interface (glass-air) evanescent waves are produced. At the same time, scattered waves emanate from the medium 1 (glass). If a third medium, a conducting material, for example a metal, is close enough to interact with this field the energy from this field interacts with the metal's surface free electrons to generate plasmons (dark orange area in Fig. 11) that by decaying cause the metal surface to emit light.
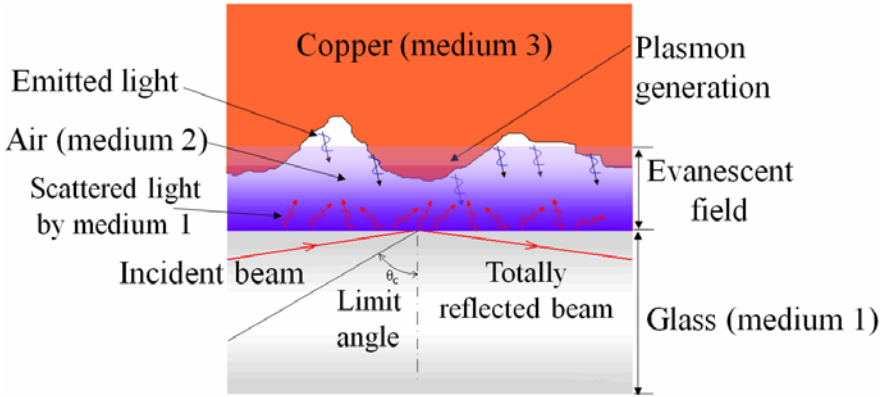
Fig. 11. Generation of the evanescent field and surface plasmon resonance in the cavity between a glass plate and a rough copper surface.

Between the copper and the glass surface there is an optical cavity or optical resonator that produces standing waves. The electromagnetic field confined in the cavity is reflected multiple times inside the cavity producing standing waves for certain resonance frequencies that depend on the geometry of cavity. The standing wave patterns thus generated are called modes: each mode is characterized by a frequency f_n, where the subscript n is an integer. Optical cavities are characterized by the quality factor, or Q factor. The Q factor is a dimensionless parameter that defines the resonator's bandwidth relatively to its center frequency. Low values of Q indicate high losses of energy in the cavity and a wide bandwidth. High values of Q indicate a low rate of energy loss in the cavity with respect to the stored energy of the oscillator and a narrow bandwidth. In general, Q is defined in terms of the ratio of the energy stored in the resonator to the energy being lost in one cycle:

$$Q = 2\pi \frac{\text{Energy Stored}}{\text{Energy loss per cycle}} \tag{19}$$

It can be proven that the maximum energy is concentrated in the direction of the normal to the face of the glass medium.

3.1 Generation of a Wide Spectrum of Frequencies due to Interaction between Evanescent Waves and Rough Surfaces

In the classical Fabry-Perot cavity analysis the two interacting surfaces are mirror-like surfaces. In the present case one of the surfaces is a mirror-like surface (the glass) while the other (the metal) is an optically rough surface. Therefore, many different spatial frequencies can be observed experimentally. At this point it is important to describe the phenomenon leading to the generation of the emitted light with different spatial frequencies on rough metallic surfaces. A rough surface can be thought of as the superposition of many gratings of different periodicities.

Kretschmann analyzed this problem in the following fashion [21]. A rough surface can be defined through the following statistical correlation function:

$$G(x,y) = \frac{1}{A} \int_A z(x',y')\, z(x'-x, y'-y)\, dx'dy' \qquad (20)$$

where $z(x,y)$ is the Monge's representation of the surface height and A is the area of integration.

Under the assumption that the height distribution is a random function, as it is usually done in the analysis of random surfaces, a Gaussian distribution can be utilized. The correlation function becomes:

$$G(x,y) = R_q^2 \exp\left(-\frac{r^2}{\sigma_i^2} \right) \qquad (21)$$

where: R_q^2 is the root-mean-square value of the surface heights assumed to be random variables with a correlation length σ_t; r is the distance from the generic point $P(x,y)$ of the object surface.

From the Fourier transform (FT) of Eq. (21) the spectrum s of spatial frequencies present in the surface can be obtained.

From the point of view of plasmon excitation, one can prove that in order to excite a plasmon resonance it is necessary that the exciting frequency coincides with a frequency in the Fermi's electromagnetic state. Hence, the larger is the spectrum of the frequencies the greater will be the amount of energy available for producing coupling of plasmons within the metallic surface. The spatial frequency spectrum is described by the following equation:

$$s\big(\|k\|_{surf}\big) = \frac{1}{4\pi} \sigma_i^2\, R_q^2 \exp\left[-\frac{\sigma_i^2\, \|k\|_{surf}^2}{4} \right] \qquad (22)$$

The above equation shows that the spectrum of light emitted by the surface consists of multiple wave vectors that are related directly with surface topography properties. Each wave vector corresponds to an equivalent pitch p_{gr} defined as:

$$\|k\|_{surf} = \frac{2\pi}{p_{gr.}} \qquad (23)$$

If the surface has only one Fourier component of roughness (i.e. the surface profile is sinusoidal), then the s function is discrete and exists only at $\|k\|_{surf} = 2\pi/p_{gr}$ where p_{gr} is the pitch of the equivalent sinusoidal grating. However, most surfaces of practical interest have a definite structure and cannot be considered random surfaces. Surfaces of technical interests manufactured industrially present a periodic structure. For this reason finished surfaces are more similar to a deterministic diffraction grating than to a random grating.

Any plasmon propagating on a rough surface with the appropriate $\mathbf{k}_{surf}$ can generate the emission of a photon [22]. Since $\mathbf{k}_{surf}$ can be a random quantity, even if the light has a defined direction it is possible to generate plasmons in all directions. This phenomenon was verified experimentally by Teng and Stern [23].

3.2   Application of the Model to the Analysis of Surface Topography

The above model gives an explanation of the interaction of evanescent waves at a glass-air-metal interface. This explanation has provided insight into how it is possible to make the experimental observations due to the ability of evanescent illumination to interact with the metal surface creating plasmons that upon decay can emit light. Since the experimental setup has a double interface (glass-air and air-metal) a cavity is created: this cavity acts as a passive optical resonator and hence resonances can be observed from the emitted light.
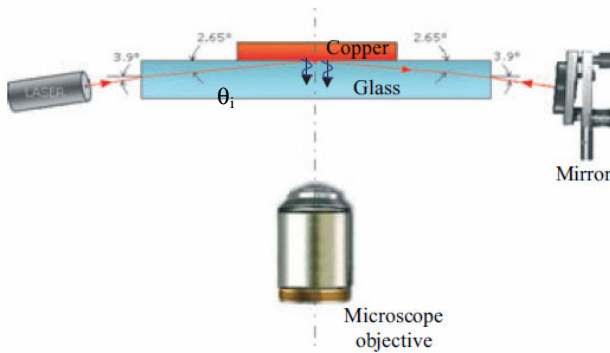
Fig. 12. Experimental setup for the SPR analysis of metallic specimens.

The original setup utilized to perform surface topography measurements on metallic specimens [24] is shown in Fig. 12. An incident laser beam is totally reflected at the glass-air interface and returned by the mirror shown in the figure. The metal-air-glass interface is observed with an optical microscope and an image is recorded by a CCD camera.
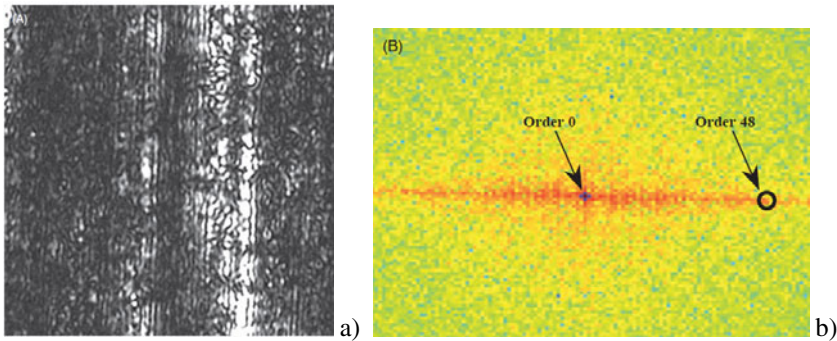
Fig. 13. a) Enlarged portion of the image of the copper plate surface; interference fringes on the metal surface are clearly visible; b) FT of the image (225 x 225 µm).

Figure 13a shows the recorded image of the copper surface. A system of fringes can be seen in this image. This system of fringes is localized on the surface since the focused image captures the surface features as well as the fringes. The spatial frequency of the fringes (pitch) can be determined by analyzing the FT of the image (see Fig. 13b). In the FT it is possible to identify the fundamental harmonic corresponding to the fringe's image. From the analysis of the fringes it was concluded that the fundamental harmonic has a pitch of 4.69 microns.

The wave vector of the emitted field corresponds to a spatial frequency of order 48 that, translated to fringe spacing in the physical space, gives a value of 4.69 μm (i.e. from the size of the region of 225 microns, one obtains 225/48=4.69 μm). In Ref. [24], it was proven that the diffracted order of the equivalent grating resulting from the electromagnetic resonance is:

$$p_{egr} = \frac{\lambda}{2 \sin \theta_i} \tag{24}$$

where θ_i is the angle made by the illumination beam with the glass surface (see Fig. 12).

By entering p_{egr}=4.69 μm into Eq. (24), a value of θ_i=3.87^o is obtained. This result is in very good agreement with the initial experimentally set value of 3.9^o.
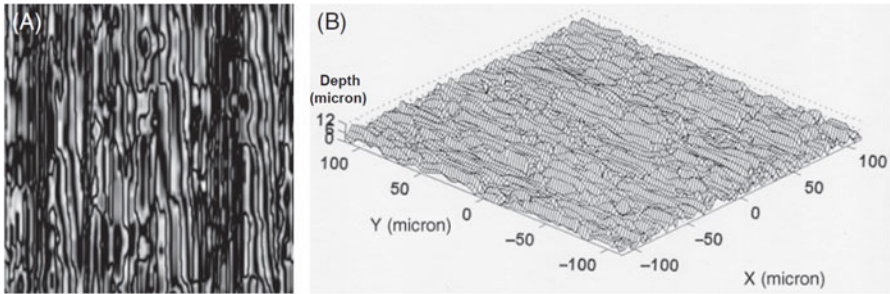
Fig. 14. a) Top view of the depth information in gray levels of a region of 225x225 μm; b) 3-D view of the same region (the same scale for all the 3 coordinates was taken).

Figure 14 shows the surface profile obtained from the fringe pattern of Fig. 13. In Ref. [24], it is shown that the model of the process to convert fringe pattern into topographic data is exactly the same that corresponds to reflection moiré when the grating is in the vicinity of the surface and the observation is made by focusing the plane of the grating. This model was originally analyzed by Ebbeni [25] by utilizing the Fresnel-Kirchhoff integral for the grating-based contouring of very large curvature radii reflecting surfaces. Sciammarella and Combel [26] also analyzed this problem. While in [25] only the first harmonic was considered, in [26] following the method introduced by Guild [27], all the harmonics that emerge with the same angle of inclination were considered thus obtaining multiple interference fringes.

The profile of the surface in terms of the surface depth h can be obtained from the equation:

$$h = \frac{np_{gr0}}{2\sin(90^{\circ} - \theta_i)} \qquad (25)$$

where n is the fringe order corresponding to the fact that an equivalent grating of pitch p_{gr0} is modulated by the surface. This relationship is similar to the equation of shadow-projection moiré except for the factor 2 that comes from the reflection effect.

In order to verify the reliability of the experimental data gathered with the above described model, other independent measurements were carried out with a Surtronic S25 profilometer (Taylor Hobson Ltd.). The ten-point height of the surface S_z was chosen as the reference parameter [28,29]. Ten transversal sections (i.e. in the direction orthogonal to grooves) and ten longitudinal sections (i.e., in the direction of the furrows present in the surface) were analyzed and the corresponding ten-point heights were computed. For the profilometer measurements, two sections of length 8 mm were analyzed both in the longitudinal (i.e. parallel to the furrows) and transversal direction (i.e., perpendicular to the furrows). Optical and mechanical measurements were in good agreement. The test of significance for small samples revealed that both optical and mechanical data belong to the same statistical population within 95% level of confidence.

In the second set of experimental tests, gratings of different pitches were utilized in order to obtain the surface topography of standard samples. The values of the roughness average parameter R_a were determined [28,29]. Surface roughness measurements carried out for the different calibrated samples were again in good agreement with profilometer measurements.

3.3 High Accuracy Measurements of Surface Topography

In order to determine the accuracy of the method of surface contouring outlined in Section 3.2, measurements of the roughness were carried out on an HQC226 precision reference standard certified by NIST according to ANSI B46.1. Figure 15 shows a schematic of the experimental setup. Some modifications have been introduced with respect to the original setup of Fig. 12. A grating has been added to the surface of the glass plate. In this way it is possible to obtain more than one fundamental frequency by utilizing the different frequencies produced by the grating.

The previous picture shows the interface between the glass surface and the metallic surface. The surface consists of a saw tooth profile of nominal pitch L_t=100 μm and depth h_t=6 μm. The resultant R_a (average depth) is 3 μm. This standard is used to calibrate devices based on the use of stylus probes.

Figure 15 provides a model for the process of contouring that can be also applied to other surfaces that are not deterministic. The figure illustrates the case of double illumination but only one illumination beam is analyzed here for the sake of simplicity.
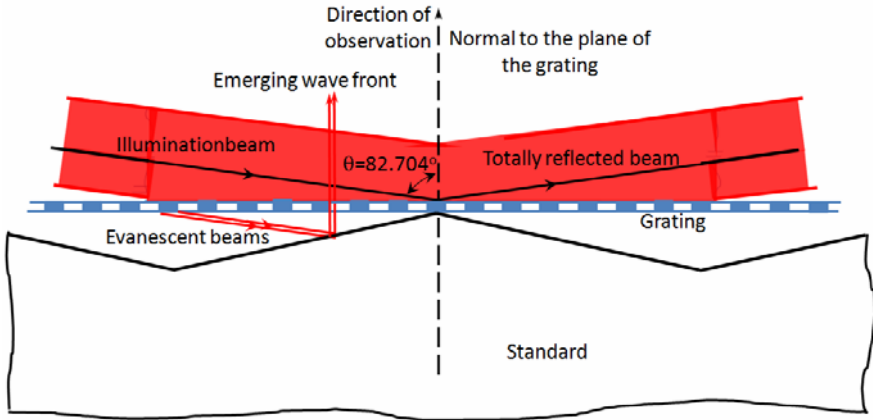
Fig. 15. Experimental setup for surface topography analysis including a grating.

The inclination of the beam is larger than the critical angle and therefore the light is totally reflected at the glass-air interface. However, as it was indicated previously, the electromagnetic field penetrates a cavity. Schematically, the figure shows the trajectory of the photons that enter the cavity and, according to the preservation of momentum, continue their trajectory. Photons finally emerge along the direction approximately perpendicular to the grating surface as it is clarified by the detailed schematic of Fig. 16.
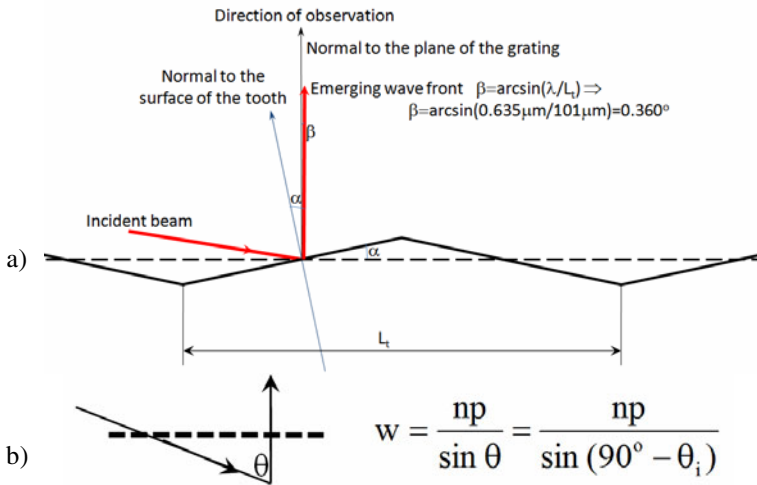
Fig. 16. Detail of the optical path of the beams diffracted by the grating (a) and equivalent shadow/projection moiré scheme (b).

Figure 16 is a schematic representation to explain the contouring model although from the theoretical point of view of optics the process is very complicated. The figure shows the beam arriving at the inclination θ_i with respect to the standard surface which is now described as a blazed diffraction grating. According to the equation of diffraction for a blazed grating, the angle of emergence β with respect to the normal to the middle surface of the grating is:

$$\beta = \arcsin\left(\frac{\lambda}{L_t}\right) \tag{26}$$

In this particular case, the wavelength of light λ is 635 nm and the spacing of the grating is $L_t = 101$ μm (i.e. the saw tooth pitch). By replacing this value in Eq. (26), the angle β of the emerging wave front is 0.360^o. Hence, the beam emerges practically orthogonal to the grating surface.

As is shown in Fig. 16, one can now apply the classical shadow-projection moiré equation:

$$w = \frac{np}{\sin \theta} = \frac{np}{\sin (90^o - \theta_i)} \tag{27}$$

This is in agreement with the formulation developed in Ref. [24].
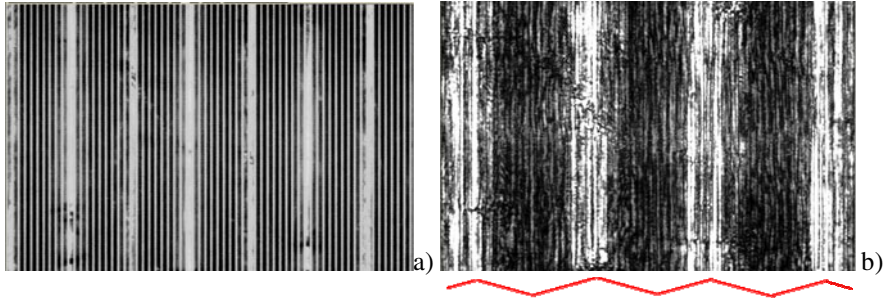
Fig. 17. a) White light image of the HQC226 standard (5 μm grating superimposed on the specimen); b) Coherent illumination image (5 μm grating superimposed on the standard). The profile of the standard is sketched in red in Fig. 17b.

Figure 17 shows the image of the standard with the superimposed 5 μm pitch grating. Figure 17a corresponds to white light while Fig. 17b corresponds to coherent illumination. It is interesting to point out that, while the white light illumination that is normal to the plane of the grating shows peaks and valleys, the evanescent illumination creates the higher intensity in the region of contact with the grating since the evanescent field dies out within a fraction of the wavelength of light. By measuring the horizontal size (i.e. in the direction normal to fringes) of the bright region, the value of 11.81 μm is obtained. This means that the local depth at the end of the bright region is $11.81 \times \tan[h_t/(L_t/2)]$, that gives 1.42 μm.
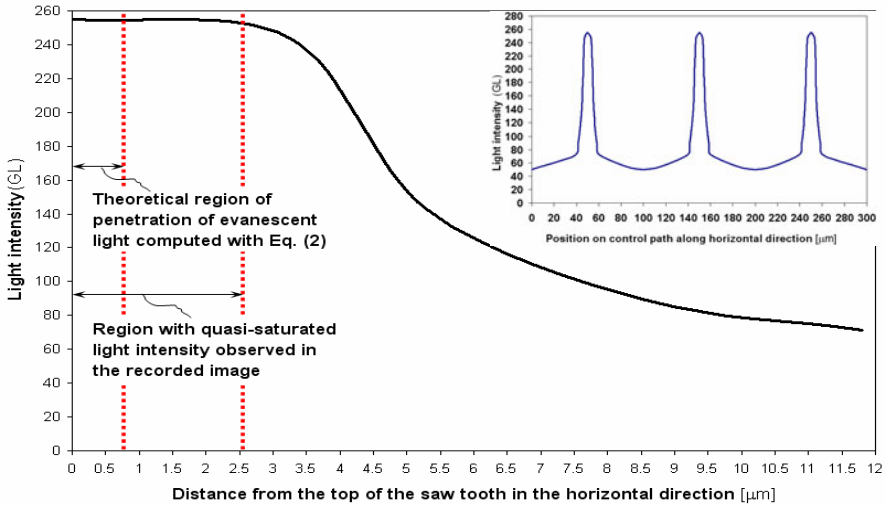
Fig. 18. Intensity distribution received by the CCD camera sensor observing in the direction normal to the plane of the grating.

The corresponding depth of penetration of the evanescent field computed with Eq. (2) is 89.6 nm. Consequently, the size of the region of illumination caused by the evanescent field is 750 nm.

Figure 18 shows in the insert the distribution of light intensity in the image as a function of the coordinates of the field of view. It can be seen that the bright illumination corresponds to a very small region of the saw tooth surface. The figure shows the intensity distribution in the brightest area. It is indicated the region where the direct influence of the evanescent field manifests itself. In this region, there is saturation of the sensor. At about 3.5 times the theoretical distance computed with Eq. (2) the intensity begins to decay reaching a minimum of about 20% of the maximum intensity in the central valley. Figure 18 indicates that the main source of light energy in the Fabry-Perot cavity is the evanescent field.
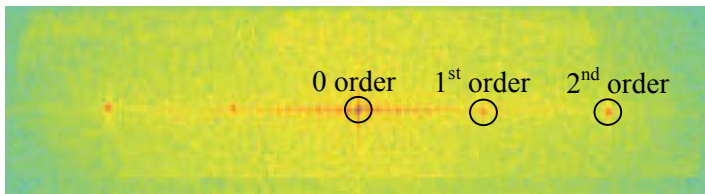
Fig. 19. FT pattern of the 5 μm pitch grating imaged by the CCD. The first harmonic (corresponding to the pitch of 5 μm) and the second harmonic (corresponding to the pitch of 2.5 μm) are visible in the FT spectrum.

Figure 19 shows the diffraction orders for the 5 µm pitch grating. The third order (1.25 µm pitch) is not present in the FT pattern because the numerical aperture of the utilized microscope objective limited the angular spectrum to the first two orders. However, by utilizing double illumination it is possible to carry out measurements with sensitivity corresponding to the 1.25 µm pitch.

3.3.1 Determination of the Size of the Field of View

In order to perform the measurement of the geometric parameters defining the tooth shape one needs to know precisely the size of the field of view. The following procedure has been applied. The grating superimposed on the top of the standard is focused and the corresponding order n_g of the grating is determined from the FT pattern. Then, it can be written:

$$L_w = n_g p \tag{28}$$

where p is the pitch of the grating. The field of view is hence known with an accuracy determined by the pitch of the grating. In order to increase the accuracy it is possible to utilize several orders of one grating and proceed to apply the method that will be explained later in the paper.

3.3.2 Determination of the Saw Tooth Geometry

The determination of geometric dimensions of the tooth includes two different steps. First, the pitch of the saw tooth is determined from the FT pattern of the image: the order n_p corresponding to the number of saw teeth included in the field of view is extracted. Then, m harmonics of the order n_p are considered.

The pitch of the tooth L_t can be obtained by dividing the size of the field of view L_w by the order corresponding to the number of teeth included in the image. Hence, one must interpolate the fraction of pixels that will correspond to the actual tooth pitch. For the first harmonic, the pitch of the tooth is given by the equation:

$$L_t = n_p p \tag{29}$$

The number of teeth N_t included in the recorded image is equal to the ratio:

$$N_t = L_w / L_t \tag{30}$$

By replacing in Eq. (30) the expressions (28) and (29) written for L_w and L_t, it follows:

$$N_t = \frac{L_w}{L_t} = \frac{n_g \cdot p}{n_p \cdot p} = \frac{n_g}{n_p} \tag{31}$$

In order to determine precisely the ratio n_g/n_p, the higher harmonics of the order n_p available in the FT pattern must be considered. In Fig. 20, the multiple values of the tooth pitch are plotted as a function of the corresponding order. By utilizing the minimum least square regression of the computed values, a line going through the origin of coordinates is obtained. The slope of this line is the most accurate value of the saw tooth pitch. Thus the quantization in pixels of the coordinates of the space can be compensated.
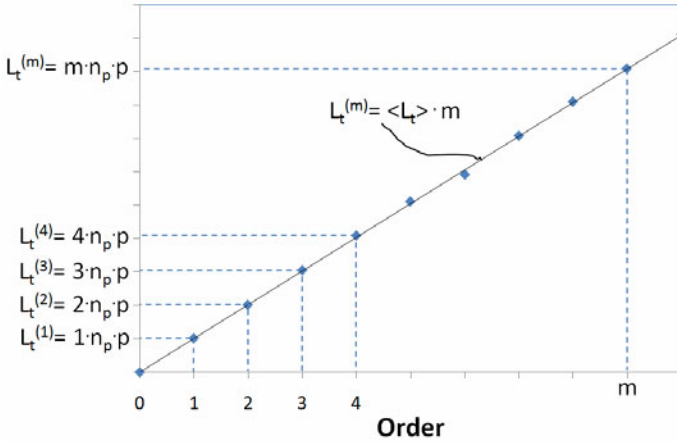
Fig. 20. Determination of the pitch of the saw tooth

The height h_t of the saw tooth (Figure 21a) is determined by considering that the equivalent grating formed in the process of illumination and projected onto the standard is modulated by the slope of the surface.
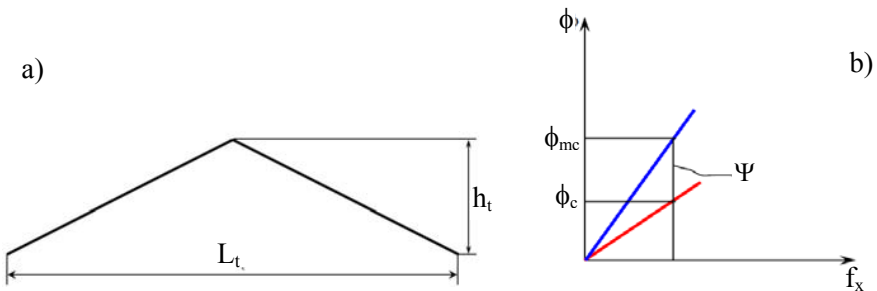
Fig. 21. a) Main geometric dimensions of the saw tooth; b) Relationship between total phase, carrier phase and modulation function.

The intensity distribution of the modulated carrier is (see [30,31] and the references cited in the former paper):

$$I_c(x, y) = I_{oc} + I_{lc} \cos\left[\frac{2\pi}{p}x + \Psi(x, y)\right] \tag{32}$$

The phase of the moiré fringes thus formed can be determined as [30,31]:

$$\Psi(x, y) = \phi_{mc}(x, y) - \phi_c(x, y) \tag{33}$$

where the different quantities entering in the above relationship are represented in Fig. 21b. The phase of the carrier is:

$$\phi_c = \frac{2\pi}{p}x \tag{34}$$

The modulation function can be expressed as:

$$\Psi(x) = \sin\theta \cdot \frac{2\pi}{p} \cdot (cx) \tag{35}$$

where θ is the illumination angle of the projection moiré equivalent scheme (see Fig. 16). In the present case, c corresponds to the constant slope of the tooth surface.

The total phase of the modulated carrier for one saw tooth hence is:

$$\phi_{mc,1tooth}(x) = \sin\theta \cdot \frac{2\pi}{p} \cdot (2h_t) + \frac{2\pi}{p} \cdot L_t \tag{36}$$

The term $2h_t$ must be introduced in Eq. (36) in order to account for the fact that each tooth is comprised of two sides with positive and negative slopes respectively.

For the entire field of view containing N_t saw teeth, the total phase is:

$$\phi_{TOT}(x) = N_t \cdot \phi_{mc,1tooth}(x) = \sin\theta \cdot \frac{2\pi}{p} \cdot (N_t \cdot 2h) + N_t \cdot \frac{2\pi}{p}L_t \tag{37}$$

In order to compute precisely the phase modulation term $\left[\sin\theta \cdot \frac{2\pi}{p} \cdot (N_t \cdot 2h)\right]$ for the entire field of view, one can use a process similar to that described previously for the tooth pitch.

Figure 22 shows the FT of the image containing the carrier frequency f_c and the modulated carrier frequency f_{mc} for the first three harmonics. The difference between the phase of the modulated carrier and the phase of the carrier can be determined for each harmonic in the whole field of view.
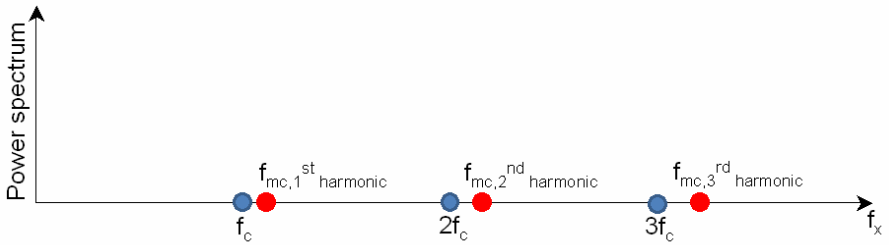
Fig. 22. Schematic representation of the different harmonics extracted from the FT spectrum. The carrier frequency f_c is a known quantity. The frequency of the modulated carrier f_{mc} is close to the carrier frequency.

In Fig. 23, the multiple values of the modulated phase are plotted as a function of the corresponding order. By fitting data of Fig. 23 in the least square sense, a line going through the origin of coordinates is obtained. The slope of this line represents the most accurate value of the average change in phase per order $<\Psi>$ that can be computed for the recorded image. From this value, it is possible to determine the height of the saw tooth pitch as follows:

$$h_t = \left(\frac{<\Psi>}{2\pi} \right) \cdot \left(\frac{p}{\sin\theta} \right) \cdot \frac{1}{2N_t} \qquad (38)$$
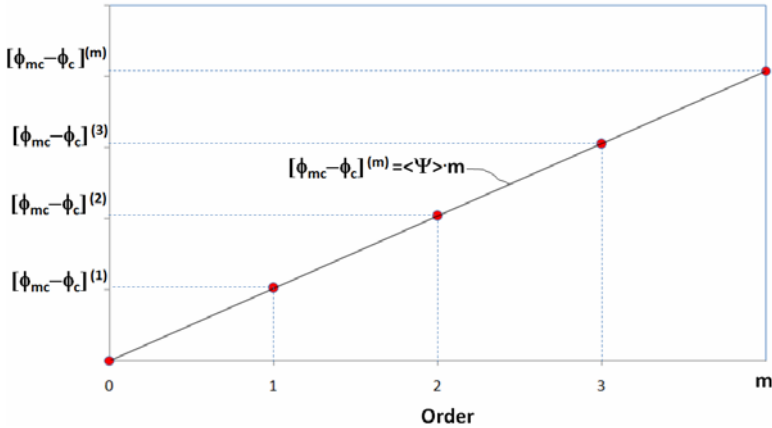
Fig. 23. Determination of the height of the saw tooth

The value of R_a evaluated, accordingly to ANSI B46.1, from the experimental data gathered with the present advanced digital moiré contouring technique falls in the $3.0175 \div 3.0784$ μm range certified by NIST. The average measured pitch is 101.24 μm with a standard deviation of ± 0.322 μm. The average measured depth is 6.078 μm: the average value of Ra is hence 3.039 μm, well within the range of

NIST's measurements. The difference between the value of roughness measured optically and the average value of roughness indicated by NIST is only 0.231% (i.e. 3.039 μm vs. 3.032 μm).
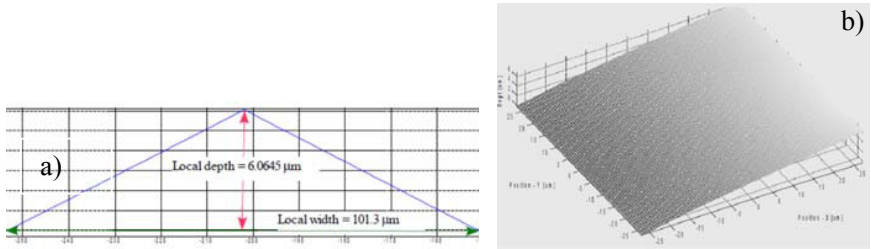
Fig. 24. a) Detail of one tooth; b) 3D MATLAB representation of the reconstructed surface of half of one tooth.

Finally, a square area has been extracted from the image and resized to 2048×2048 pixels in order to precisely reconstruct the profile of one saw tooth. Figure 24 shows the tooth profile and the reconstructed 3D shape of the tooth. The local height of the tooth profile measured in this region is 6.0645 μm, practically the same as the nominal height of 6 μm. The local length of the tooth is 101.3 μm, very close to nominal length of 100 μm. The average R_a is 3.0505 μm and oscillates between 3.0175 μm and 3.0785 μm. By extracting different profiles it is possible to make an estimate of the average surface finish of the standard. The average depth thus determined is 6.035±0.1367 μm. Therefore, the finish of surface standard can be estimated as 0.1367 μm / 0.635 μm, that is about λ/5.

4 Determination of Contact Strains

The analyzed metallic surface is made of copper and presents a system of furrows that contain some frequencies that can be utilized as carrier fringes. In preceding papers, this procedure was referred to as holographic moiré. Although there is not a physical carrier (i.e. a grating), the frequency of the reference grating can be extracted from the FT spectrum of the image. The in-plane strains can be directly derived from the basic equation of holographic moiré [32-38]:

$$u = \frac{\lambda}{2\sin(90° - \theta_i)} \qquad (39)$$

This is the fundamental equation of holographic moiré to get in-plane displacements. It corresponds to the double illumination setup that makes the sensitivity vector $\vec{S}$ equal to:

$$\vec{S} = (\vec{k}_1 - \vec{k}_2) \bullet \vec{d} \tag{40}$$

where $\vec{k}_1$ and $\vec{k}_2$ are the two symmetrical illumination vectors with respect to the normal to the observed surface and $\vec{d}$ is the displacement vector.

The strains in the contact surface can be computed through direct differentiation in the Fourier space of the unwrapped phase of the displacement field. This procedure was successfully applied to measurements in the micron range in a number of cases [38,39].

4.1 Determination of the Contact Strains of a Small Cylinder

In this work, the contact strains of a small cylinder of 10 mm in diameter and 8 mm in thickness were measured using an SPR based optical setup. The specimen was made of copper and the contact surface was finished with grooves created by scratching the surface with sandpaper. The same procedures of calibration of the pixel values and of the field of view applied in the contouring experiments described in Section 3.3 were utilized also in the strain determination experiments. The modulus of elasticity of the copper specimen is 117 GPa while the Poisson's ratio is 0.3. The yield limit is 48 MPa.
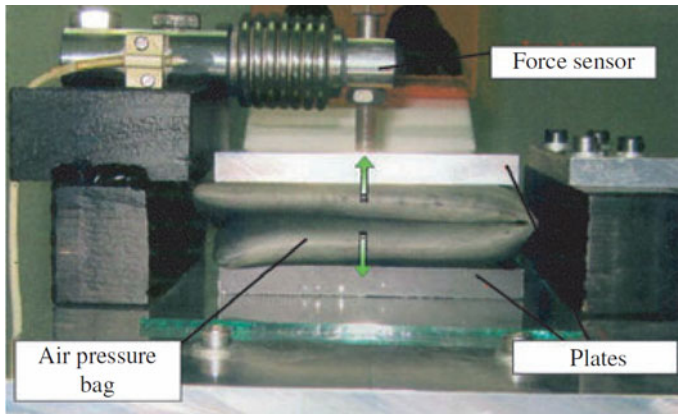
Fig. 25. Loading device with the cantilever load measuring system used in the strain determination experiments. The specimen, a small cylinder, is compressed between the aluminum plate shown in the picture and the glass surface. The specimen is not visible.

Figure 25 shows the loading device built for the strain determination experiments. A rubber bag is inflated to compress the specimen between an aluminum plate and a glass plate. The cantilever beam shown in the figure is part of a sensor that has a strain gage (Wheastone bridge) to measure the strain level.

The sensor was calibrated utilizing dead weights resulting in a linear function load in N vs. the readings in µε of the bridge. Three cycles of loading were applied. The "unloaded" images for the specimens contact stress were taken with an initial small load to eliminate rigid body motions.

Equation (39) allowed in-plane displacements of the loaded copper cylinder to be computed. Images from the central portion of the specimen (35 x 35 µm) were recorded for the unloaded state and then for the successive loads. The changes in the surface shape caused by the presence of contact loads were determined by subtracting the phase of the "loaded" image from the phase of the "unloaded" image. Then, strains were obtained by the direct differentiation of the unwrapped phase pattern. Figure 26a shows the recorded pattern corresponding to the "unloaded" state while Fig. 26b shows the recorded pattern corresponding to the contact load of 286 N. The Fourier transforms of those images are shown in Fig. 27a and Fig. 27b, respectively.
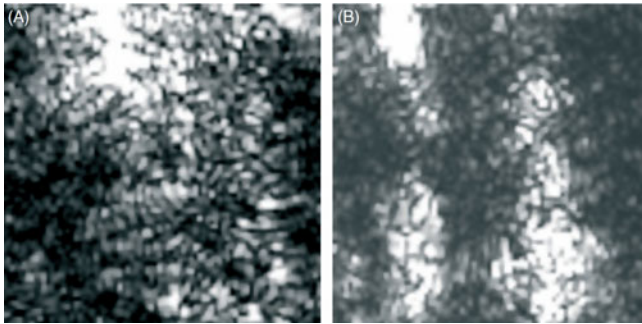
Fig. 26. Portion of contact region (35 x 35 µm) in the central part of the cylindrical specimen (diameter 10 mm and thickness 8 mm): a) pattern corresponding to zero loading; b) pattern corresponding to the load of 286 N.
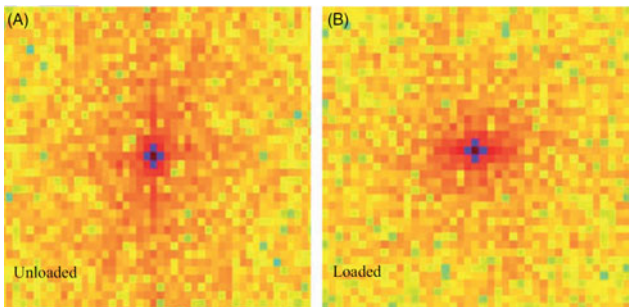
Fig. 27. a) Fourier transform of Fig. 26a; b) Fourier transform of Fig. 26b.

After the specimen was loaded, the changes in the reflectivity experienced by the specimen surface made it possible to observe the contact area between the glass and the copper cylinder. The contact area is an ellipse of major axis 5 mm and minor axis 3.5 mm. As a first approximation, one can assume that the maximum Hertzian pressure is 1.5 times the average contact pressure of 20.8 MPa (i.e. $286\,N/\pi(2.5\,mm\,x\,1.75mm)$. Therefore, the expected maximum value of stress at the center of the contact area should be $\sigma_{max}=31.2$ MPa. From the stress-strain curve of the copper plotted in Fig. 28, the corresponding deformation of the surface in the point of maximum contact pressure would be approximately 500 $\mu\varepsilon$. Such a value is well below than the 0.2% (i.e. 2000 $\mu\varepsilon$) off-set yield strain.
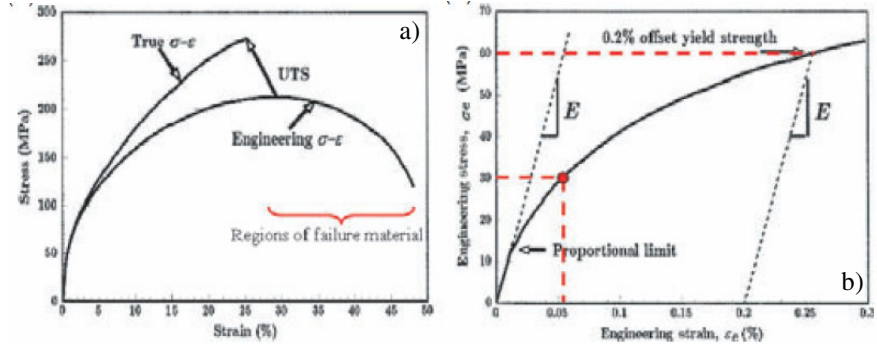
Fig. 28. Typical constitutive behavior of copper under tension: a) Engineering and true σ-ε curves; b) Enlarged view of the initial region where yield strain is defined.

However, it can be seen from Fig. 29 that the strain values in the central region of the specimen are much higher than 200 $\mu\varepsilon$. This fact indicates the presence of a local strain field produced by the contact between the asperities of the copper surface and the glass surface. At the edges of the circular region shown in Fig. 29
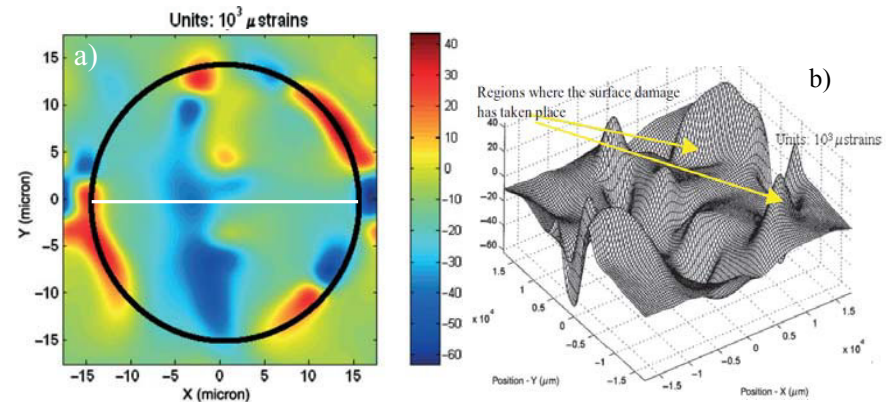
Fig. 29. a) Map of the strain ε_x obtained for the contact load of 286 N; b) 3-D view of the same map.

strains are mostly tensile and very high. The order of magnitude reached by the strain in this region corresponds to the part of the stress-strain curve limited by the red parenthesis in Fig. 28a. The region where high tensile stresses take place is outside of the contact area while the central part of contact area is under compressive stresses.

The strain distribution along the horizontal cross-section corresponding to the X-axis is plotted in Fig. 30. Since strain peaks are located at the path edges, micro-cracking may occur at the corresponding points. In order to verify this hypothesis, the topography of the contact region was analyzed in detail.
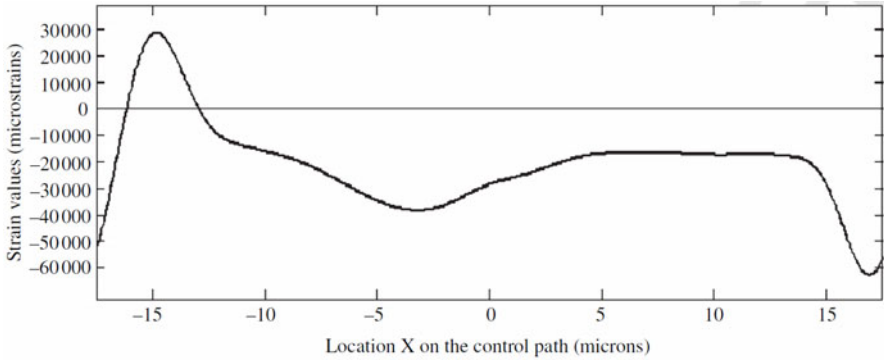
Fig. 30. Distribution of strain ε_x along the horizontal diameter of Fig. 29 (white line control path).

Figure 31a shows the surface profile before loading: depth values ranged from 1 to 3 μm. Figure 31b shows the final configuration taken by contact surface when the 286 N load was applied. It can be seen that depth values changed significantly as they go from 0.2 μm to a maximum of 1.4 μm. The differences of depth between the initial and the final surface configurations are shown in Fig. 31c: these values were obtained by simply subtracting the data of Fig. 31b from the data of Fig. 31a. The contact area indeed experienced large plastic deformations. It was flattened in agreement with the results of the strain analysis of the surface.

The results of the present experiments are another verification of the model introduced by Johnson in Contact Mechanics to explain the wear mechanism of rolling surfaces [40]. Modeling this mechanism was proven to be a very difficult challenge. The resulting wear particles are platelets that lie parallel, or nearly so, to the rolling surface, on the planes of maximum compressive stress. The large plastic strains measured in this experiment confirm the hypothesis that the resulting cracks are ductile fractures, driven by plastic strain rather than the elastic stress intensity instability and that these severe plastic strains are the consequence of the contact between asperities. In the present experiment one of the contacting surfaces, the glass plate, is very smooth. Therefore, the operating mechanism is one of flattening the copper asperities against the supporting glass plate. The results presented in this
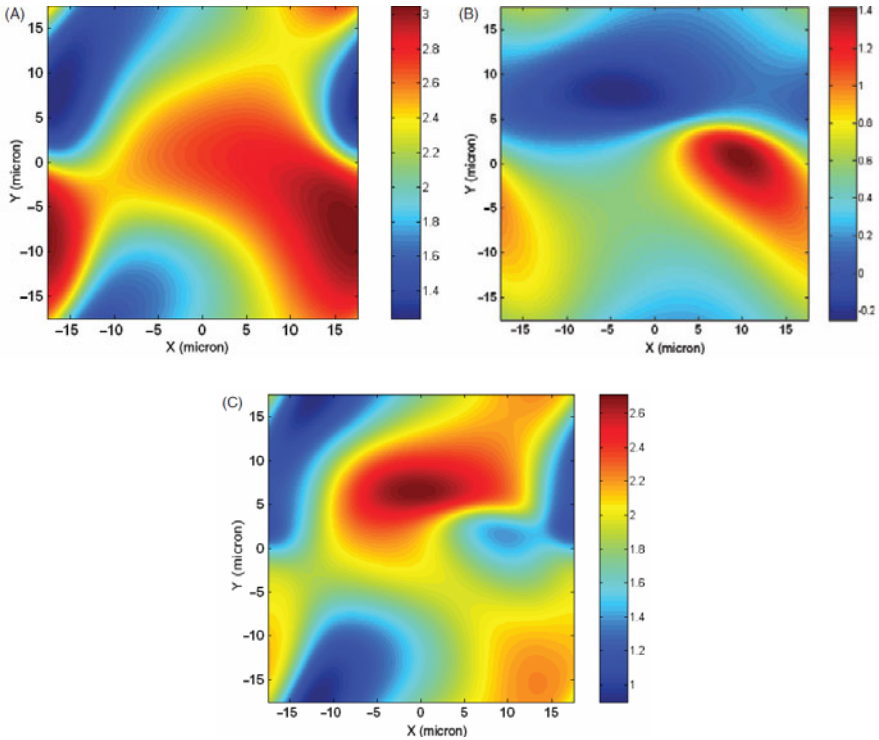
Fig. 31. Surface topography measured with the proposed SPR experimental setup: a) Unloaded specimen; b) Loaded specimen; c) Changes in surface depth after the application of the contact load.

paper are a first effort in an area that requires additional work to make the proposed techniques standard tools for engineering measurements.

5 Summary and Conclusions

This chapter presented a new approach to investigations at the nano-scale based on the use of evanescent illumination. The proposed methodology provided the means of measuring topography of nano-sized simple objects such as prismatic crystals and spherical particles. The evanescent illumination was also applied to the analysis of the topography of rough surfaces, yielding reliable values of the parameters that characterize the properties of rough surfaces with accuracies in the range of nanometers.

A great deal of theoretical developments is required to substantiate the experimentally observed properties of the light illumination resulting from evanescent waves. However, it can be said that from the point of view of direct application of these properties it is possible to access the nano-range utilizing far-field observations. The results presented in this chapter provide a very powerful

approach to the study of problems in the nano-field using light in cases where the use of other electromagnetic radiations such as X-rays or electron beam sources is very difficult or even impossible.

Furthermore, it was shown that strains can be determined in the micron-range with a great deal of accuracy and this type of application can be extended to the nano-range by introducing scale changes in the setups utilized in the experiments. For example, gratings with nano-pitches can be used in order to produce suitable $\vec{k}$ wave vectors.

The in-plane strain analysis was utilized many times in the technical literature but following a different approach: the direct illumination of the surface. Remarkably, both contouring and strain determination that work with direct illumination can also work very efficiently via the coupling of the metal surface with the energy existing in the surface evanescent field. It is extremely difficult to come with an alternative method that allows at the same time contouring and strain determination at a contact surface.

In view of the results presented in the paper, it can be concluded that the evanescent illumination plays a unique role in the measurements of dimensions and shapes of objects, surface topography, roughness and strains allowing us to precisely detect information at the nano-scale. Evanescent illumination is the key to making Experimental Mechanics methodologies well suitable for nano-engineering applications. Remarkably, nanometer resolutions were achieved by using experimental setups that included a conventional optical microscope.

References

1. Bouchal, Z.: Non diffracting optical beams: physical properties, experiments, and applications. Czechoslovak Journal of Physics 53, 537–578 (2003)
2. Gutiérrez-Vega, J.C., Iturbe-Castillo, M.D., Ramirez, G.A., Tepichin, E., Rodriguez-Dagnino, R.M., Chávez-Cerda, S., New, G.H.C.: Experimental demonstration of optical Mathieu beams. Optics Communications 195, 35–40 (2001)
3. Hernandez-Aranda, R.I., Guizar-Sicairos, M., Bandres, M.A.: Propagation of generalized vector Helmholtz–Gauss beams through paraxial optical systems. Optics Express 14, 8974–8988 (2006)
4. Born, M., Wolf, E.: Principles of Optics. VII Edition. Cambridge University Press, Cambridge (1999)
5. Toraldo di Francia, G.: Super-gain antennas and optical resolving power. Nuovo Cimento S9, 426–435 (1952)
6. Toraldo di Francia, G.: La Diffrazione della Luce. Edizioni Scientifiche Einaudi, Torino (1958)
7. Yu, F.T.S.: Entropy and Information Optics. Marcel Dekker, New York (2000)
8. Vigoureux, J.M.: De l'onde évanescente de Fresnel au champ proche optique. Annales de la Fondation Luis de Broglie 28, 525–547 (2003)
9. Jackson, J.D.: Classical Electrodynamics, 3rd edn. John Wiley & Sons, New York (2001)

10. Brillouin, L.: Les électrons dans les métaux et le classement des ondes de de Broglie correspondantes. Comptes Rendus Hebdomadaires des Séances de l'Académie des Sciences 191, 292–294 (1930)
11. Sciammarella, C.A., Lamberti, L., Sciammarella, F.M.: The equivalent of Fourier holography at the nanoscale. Experimental Mechanics 49, 747–773 (2009)
12. General Stress Optics Inc. (2008), Holo-Moiré Strain Analyzer Version 2.0., Chicago (USA), http://www.stressoptics.com
13. Guillemet, C.: L'intérférometrie à ondes multiples appliquée à détermination de la répartition de l'indice de réfraction dans un milieu stratifié. Ph.D. Dissertation, Faculté de Sciences, University of Paris, Imprimerie Jouve, Paris, France (1970)
14. Sciammarella, C.A., Lamberti, L.: Observation of fundamental variables of optical techniques in nanometric range. In: Gdoutos, E.E. (ed.) ICEM13 International Conference on Experimental Mechanics, Alexandroupolis, Greece. Springer, Dordrecht (August 2007)
15. Sciammarella, C.A., Lamberti, L., Sciammarella, F.M.: Light generation at the nano scale, key to interferometry at the nano scale. In: 2010 SEM Annual Conference & Exposition on Experimental and Applied Mechanics, Indianapolis, USA (June 2010)
16. Tanner, L.H.: The scope and limitations of three-dimensional holography of phase objects. Journal of Scientific Instrument 7, 774–776 (1974)
17. Burch, J.W., Gates, C., Hall, R.G.N., Tanner, L.H.: Holography with a scatter-plate as a beam splitter and a pulsed ruby laser as light source. Nature 212, 1347–1348 (1966)
18. Spencer, R.C., Anthony, S.A.: Real time holographic moiré patterns for flow visualization. Applied Optics 7, 561 (1968)
19. Hudgins, R.R., Dugourd, P., Tenenbaum, J.N., Jarrold, M.F.: Structural transitions of sodium nanocrystals. Physical Review Letters 78, 4213–4216 (1997)
20. Pack, A.: Current Topics in Nano-Optics. PhD Dissertation. Chemnitz Technical University, Germany (2001)
21. Kretschmann, E.: Die Bestimmung der Oberflächenrauhigkeit dünner schichten durch Messung der Winkelabhängigkeit der Streustrahlung von Oberflächen Plasma Schwingungen. Optics Communications 10, 353–356 (1974)
22. Heitmann, D.: Radiative decay of surface plasmons excited by fast electrons on periodically modulated silver surfaces. Journal of Physics C: Solid State Physics 10, 397–405 (1977)
23. Teng, Y.Y., Stern, E.A.: Plasmon radiation from metal gratings. Physical Review Letters 19, 511–514 (1967)
24. Sciammarella, C.A., Lamberti, L., Sciammarella, F.M., Demelio, G.P., Dicuonzo, A., Boccaccio, A.: Application of plasmons to the determination of surface profile and contact strain distribution. Strain 46, 307–323 (2010)
25. Ebbeni, J.: Etude du phénomène de moirure par réflexion d'un réseau plan sur une surface gauchie et de son application en analyse des contraintes et des déformations. VDI Experimentelle Spannung Analyse Berichte 102, 75–81 (1966)
26. Sciammarella, C.A., Combel, O.: Interferometric reflection moiré. In: Pryputniewicz, R.J., et al. (eds.) Proceedings of SPIE 2545, International Society for Optical Engineering, Bellingham, WA, USA, pp. 72–85 (1995)
27. Guild, J.: The interference systems of crossed diffraction gratings. Clarendon Press, Oxford (1956)
28. Stout, K.F., Blunt, L.: Three-dimensional surface topography, 2nd edn. Penton Press, London (2000)

29. International Organization for Standardization, Surface texture: Profile method – Terms, definitions and surface texture parameters. ISO Specification 4287 (1997)

30. Sciammarella, C.A.: Overview of optical techniques that measure displacements: Murray Lecture. Experimental Mechanics 43, 1–19 (2003)

31. Sciammarella, C.A., Lamberti, L., Sciammarella, F.M.: High accuracy contouring with projection moiré. Optical Engineering 44 (Paper No. 093606), 1–12 (2005)

32. Sciammarella, C.A., Gilbert, J.A.: A holographic moiré to obtain separate patterns for components of displacement. Experimental Mechanics 16, 215–220 (1976)

33. Gilbert, J.A., Sciammarella, C.A., Chawla, S.K.: Extension to 3-D of a holographic-moiré technique to separate patterns corresponding to components of displacement. Experimental Mechanics 18, 321–327 (1978)

34. Sciammarella, C.A., Chawla, S.K.: A lens holographic-moiré technique to obtain components of displacements and derivatives. Experimental Mechanics 18, 373–381 (1978)

35. Sciammarella, C.A., Rastogi, P.K., Jacquot, P.: Holographic moiré in real time. Experimental Mechanics 22, 52–63 (1982)

36. Sciammarella, C.A.: Holographic moiré. In: Lagarde, A. (ed.) Proceedings of the 1979 IUTAM Symposium on Optical Methods in Mechanics of Solids, pp. 147–176. Sijhoff and Noordhoff, The Netherlands (1981)

37. Sciammarella, C.A.: Holographic-Moiré, an optical tool for the determination of displacements, strains, contours and slopes of surfaces. Optical Engineering 21, 447–457 (1982)

38. Sciammarella, C.A., Bhat, G., Longinow, N., Zhao, M.: A high accuracy micromechanics displacement measurement optical technique. In: Sharpe, W.N. (ed.) Micromechanics: Experimental Techniques. AMD 102, The American Society of Mechanical Engineers, New York, USA, pp. 121–132 (1989)

39. Sciammarella, C.A., Sciammarella, F.M.: Measuring mechanical properties of materials in the micron range. Optical Engineering 42, 1215–1222 (2003)

40. Johnson, K.L.: Contact Mechanics. Cambridge University Press, Cambridge (1987)

Advanced Cement Based Nanocomposites

S.P. Shah[1], M.S. Konsta-Gdoutos[2], and Z.S. Metaxa[2]

[1] ACBM Center, Northwestern University, 2145 Sheridan Road,
  Suite A130, Evanston, IL 60208, USA
  `s-shah@northwestern.edu`

[2] School of Engineering, Democritus University of Thrace, GR-67100, Xanthi, Greece
  `mkonsta@civil.duth`, `zmetaxa@civil.duth.gr`

Abstract. Considerable research and development efforts have been directed towards high strength/high performance concrete with engineered properties, using three main concepts: a low water to binder ratio (w/b), and the partial replacement of cement by fine supplementary cementitious or pozzolanic materials and/or fibers. To better understand how material composition and microstructural modifications determine the concrete structural performance, and to develop new materials with specific properties, researchers at ACBM have taken a materials science approach with an application to nanotechnology to optimize the processing and micro/nanoscale structure of cement based materials. In particular, due to their exceptional mechanical properties, the reinforcing effect of highly dispersed multiwall carbon nanotubes (MWCNTs) and carbon nanofibers (CNFs) in cement paste matrix was investigated. The major challenge however, associated with the incorporation of MWCNTs and CNFs in cement based materials is poor dispersion. In this study, effective dispersion of different length MWCNTs in water was achieved by applying ultrasonic energy and with the use of a surfactant. The excellent reinforcing capabilities of the MWCNTs are demonstrated by the enhanced fracture resistance properties of the cementitious matrix. Additionally, nanoindentation results suggest that the use of MWCNTs can increase the amount of high stiffness C-S-H and decrease the porosity. Besides the benefits of the reinforcing effect, autogenous shrinkage test results indicate that MWCNTs can also have a beneficial effect on the early strain capacity of the cementitious matrix, improving this way the early age and long term durability of the cementitious nanocomposites.

1 Introduction

Although cementitious construction materials are primarily used in a large scale basis and in enormous quantities, fundamental properties of these materials such as strength, ductility, early age rheology, creep and shrinkage, fracture behavior, durability depend to a great extent on structural elements and phenomena which are effective at micro- but most important at nanoscale.

Cementitious composites typically exhibit extremely brittle failure, low tensile capacity and are susceptible to cracking. These characteristics of cement based materials are serious shortcomings that not only impose constraints in structural design, but also affect the long term durability of structures. Classical examples in infrastructure include the cracking of bridge decks, deterioration of retaining walls and degradation of bridge piers, all of which costs billions of dollars to replace or repair. To overcome the aforementioned disadvantages, reinforcement of cementitious materials is typically provided at the millimeter and/or the micro scale using macrofibers and microfibers, respectively. Fibers influence the fracture behavior of cementitious composites by interacting with the matrix they reinforce. To understand which shapes, sizes and types of fibers are most effective, one must consider the mechanism through which the fibers interact with the cementitious matrix. Fibers in general bridge cracks and transfer the load, delaying the coalescence of cracks. Crack formation and development are affected by the shape, size, type and volume of fiber reinforcement, thus influencing the mechanical performance of the structure. As Fig. 1 demonstrates, the influence of fibers in reinforcing quasi-brittle cementitious materials, such as concrete, depends on the scale of reinforcement.

Fiber size plays a significant role in the time at which the fiber acts during loading. Macrofibers (typically defined as fibers with diameters greater than 500µm) can improve post-peak toughness by bridging macrocracks. The coalescence of the first macrocrack coincides with the peak load and initiates localization, where subsequent deformation is concentrated in the opening of the crack (Fig. 1(a)). Upon further material deformation, the widening of the microcrack is resisted by the macrofibers, which bridge the localized cracks. The postpeak degradation of the concrete is prolonged and the toughness of the material is increased as these macrofibers, which carry nearly all the load on the cracked composite, either pull out or break [1]. Fine microfibers (typically defined as fibers with diameter less

Crack development in concrete

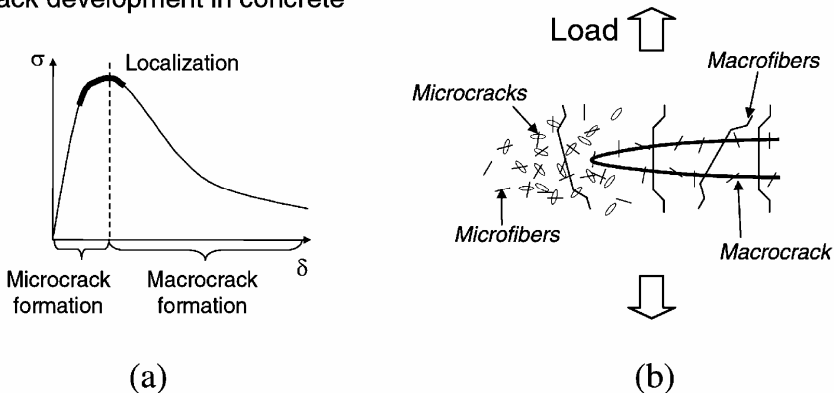(a)   (b)

Fig. 1. Relationship between (a) the mechanical response and crack development; and (b) relative scale of the crack at which fiber interaction occurs (from [1]).

than 50 µm) bridge the microcracks and delay the process by which the microcracks coalesce to form macrocracks. During the early stages of loading, microfibers provide the material with the capacity to carry a higher load for a given crack opening than macrofibers do. Thereby, they increase the elastic limit and tensile strength of the composites that they reinforce [2].

One of the most advantageous nanomaterials for nano-reinforcement is carbon nanotubes (CNTs). The unique mechanical, electrical and chemical properties of carbon nanotubes make them attractive candidates for reinforcement of composite materials. The Young's modulus of an individual nanotube should be around 1 TPa while its density is about 1.33 g/cm [3]. Molecular mechanics simulations suggested that CNT fracture strains were between 10% and 15%, with corresponding tensile stresses on the order of 65 to 93 GPa [4]. Their aspect ratios are generally beyond 1000 and their diameters range from 1 nm to 80 nm. Similarly, carbon nanofibers (CNFs), are described as an ultrahigh-strength material characterized by a high tensile modulus, tensile strength, electrical and thermal conductivity and corrosion resistance. CNFs have a unique hybrid graphene sheet structure based on both conical and tubular elements. They exhibit diameters ranging from 50 nm to 200 nm. Nanoscale three-point bending tests have shown that the Young's modulus of individual nanofibers range from 25 to 200 GPa depending on the nanofiber's diameter [5].

Both CNTs and CNFs present several distinct advantages as a reinforcing material for high strength/performance cementitious composites as compared to more traditional fibers. First, they exhibit significant greater strength and stiffness than conventional fibers, which should improve overall mechanical behavior. Second, their higher aspect ratio is expected to effectively arrest the nanocracks and demand significantly higher energy for crack propagation. Thirdly, provided that CNTs are uniformly dispersed, and due to their nanoscale diameter, fiber spacing is reduced. Both CNTs and CNFs exhibit unique electromechanical properties. They are both highly conductive and when subject to stress/strain, their electrical properties change, expressing a linear and reversible piezoresistive response [6-7].

Characterization of cementitious materials at the nanoscale will provide better understanding and lead to the development of new materials based on nanomodification. This involves use of advanced experimental tools, such as atomic force microscopy, AFM, and nanoindentation, to probe the nano/microstructure.

In this study, the development of high-performance nanocomposites reinforced with multiwall carbon nanotubes (MWCNTs) was investigated. Effective dispersion of MWCNTs in water was achieved by applying ultrasonic energy and with the use of a surfactant. The effect of ultrasonic energy on the dispersion of MWCNTs was investigated measuring the rheological properties (viscosity) of cement paste samples reinforced with MWCNTs. The effect of the surfactant concentration on the fracture properties and the microstructure of nanocomposites reinforced with 0.08wt% of cement MWCNTs was studied. Moreover, the influence of the MWCNT type (short versus long) and the effect of the concentration of MWCNTs on the fracture properties of nanocomposite specimens were studied. SEM was employed to study the morphology and the microstructure of the cementitious nanocomposites. A determination of the nanomechanical properties and

the porosity of the composites was carried out through nanoindentation experiments. Finally, since nanoindentation results implied significant changes in the nanostructure of the composites, autogenous shrinkage experiments were conducted to determine the effect of the MWCNTs on the early strain capacity of the cementitious matrix.

2   Applications of Nanotechnology in Cement Based Materials

Research on investigating the changes in nanoscale properties with the addition of different chemicals, mineral admixtures and nanofibers/CNTs is in progress at ACBM. The ultimate goal of this research is to develop nano-engineered materials with improved properties and to investigate the changes in the nanostructure, fracture properties, transport properties and durability of cement based nanocomposites reinforced with highly dispersed carbon nanotubes and nanofibers.

2.1   Dispersion

Few attempts have been made to add CNTs in cementitious matrices at an amount ranging from 0.5 to 2.0% by weight of cement. Previous studies have focused on the dispersion of CNTs in liquids by pre-treatment of the nanotube's surface via chemical modification [8-11]. The two major challenges related with the addition of CNTs in cement based materials are poor dispersion and cost. Typically, CNTs adhere together due to Van der Waal forces, and are particularly difficult to disperse. Preliminary research has shown that small amounts of CNTs can be effectively dispersed in cementitious matrices [12]. A simple one step technique, involving the application of ultrasonic energy and the use of a commercially available surfactant, commonly used in the development of advanced high performance cement based materials, was developed to effectively disperse CNTs in the mixing water.

2.1.1   Effect of Ultrasonic Energy

Ultrasonication is a common physical technique used to disperse CNTs into base fluids [13-14]. Ultrasonic processors convert line voltage to mechanical vibrations. These mechanical vibrations are transferred into the liquid by the probe creating pressure waves. This action causes the formation and violent collapse of microscopic bubbles. This phenomenon, referred to as cavitation, creates millions of shock waves, increasing the temperature in the liquid. The cavitational collapse lasts only a few microseconds. Although the amount of energy released by each individual bubble is small, the cumulative effect causes extremely high levels of energy to be released, resulting in dispersion of objects and surfaces within the cavitation field [14].

The effect of ultrasonic energy on the dispersion of the CNTs was investigated measuring the rheological properties of cement paste samples reinforced with MWCNTs under steady shear stress. Rheology is a method commonly used to study the dispersion of CNTs suspensions. Under low shear stress, CNT agglomerates control the viscosity of the suspensions. Therefore, suspensions with larger scale agglomerates exhibit higher viscosity [15].

The rheological characteristics of the samples with the sonicated dispersions were measured using a Haake Rheostress 150 rheometer with a 20 mm concentric cylinder measurement system. A steady stress protocol similar to the one proposed by Yang et al. [15] was applied to determine the viscosity dependence on stress. Cement paste was placed in the rheometer immediately after mixing. Each sample was presheared at 100 s^{-1} for 200 s, and then allowed to rest for 200 s. A low stress of 4.5 Pa was applied to the sample, and the stress was increased stepwise using the protocol shown in Fig. 2. Initial stresses were chosen to be higher than the yield stress of the material. The samples were held at each stress condition for 40 s. The holding time was necessary to ensure that an equilibrium flow had been reached. Apparent viscosity (η) as well as shear rate (γ') as a function of time was monitored and recorded during the test. The viscosity at each shear stress was obtained by averaging the values in the last 10 seconds that corresponded to the equilibrium region.

Four different MWCNT aqueous-surfactant suspensions were studied with surfactant to MWCNTs weight ratios of 1.5, 4.0, 5.0 and 6.25. The MWCNTs content was kept constant in the solution at an amount of 0.16 wt% of water. Two mixes were prepared for each surfactant to MWCNTs ratio, one with the use of ultrasonic energy and one without. Then the suspensions were mixed with cement and the rheological properties of the cementitious composite samples were investigated using the mixing and measuring protocol described previously.

Fig. 3 shows the behavior of cementitious nanocomposites (w/c=0.5) reinforced with MWCNTs with a surfactant to CNTs ratio of 6.25. Dispersions of MWCNTs were treated with (CP+SFC+CNTs sonicated) and without (CP+SFC+CNTs) the use of ultrasonic energy. The results are compared to the plain cement paste containing the same amount of surfactant (CP+SFC).
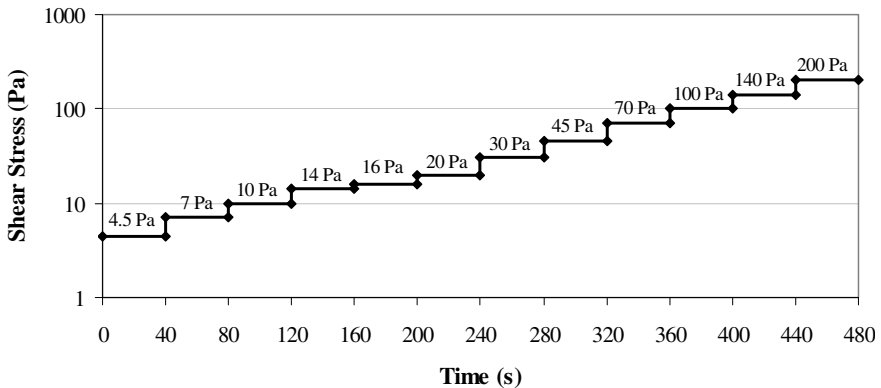
Fig. 2. Rheology measuring protocol

All samples exhibit the typical shear thinning response of cement paste. At low shear stress the viscosity is high while at high shear stress (>70 Pa) the viscosity is decreasing and reaches a "plateau" region in which the fluid seems to have a

constant viscosity. It is observed that the dispersions without sonication exhibit viscosity at low stress (14 Pa) of up to 0.13 Pas while the sonicated dispersions exhibit viscosity of 0.09 Pas which is very close to the viscosity of plain cement paste (0.07 Pas). As expected, at low stress conditions the application of ultrasonic energy controls the dispersion of the CNTs. Under high shear stress (>70 Pa) the agglomerates can be broken down by the fluid motions so the viscosities of the suspensions with and without sonication are similar. Analogous results were obtained with a surfactant to CNTs ratio of 1.5, 4.0 and 5.0. Based on those results it can be concluded that for proper dispersion the application of ultrasonic energy is required.

2.1.2 Effect of Surfactant Concentration

The morphology and the microstructure of the fracture surface of MWCNT reinforced nanocomposites were examined using an ultra-high resolution field emission scanning electron microscope operated at 3 to 5 kV. Secondary electron (SE) imaging was employed to obtain clear images at medium to high magnifications (10,000× to 150,000×). Specimens of 25.4×6.35×6.35mm were prepared for each mix. After 18 hours of curing, specimens were demolded and kept in acetone to stop the hydration. Prior to their observation, the fracture surface of the specimens was sputter-coated using a 20nm thick layer of gold-palladium (Au/Pd) to eliminate charging effects caused by insufficient coating.

The effects of surfactant concentration and ultrasonic energy were investigated in detail. Results from SEM images at 1 μm scale of fracture surfaces of cement paste samples (w/c=0.5), reinforced with 0.08 wt% CNTs, are presented in Fig. 4. The CNTs suspensions were prepared with surfactant to CNTs weight ratios of 0, 1.5, 4.0, 5.0 and 6.25.
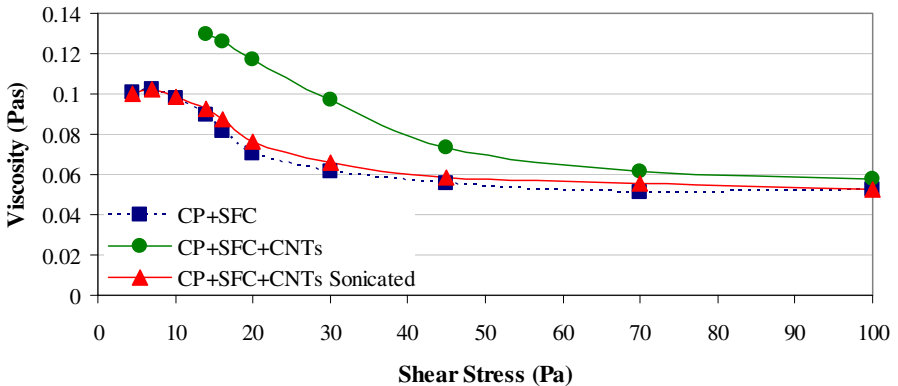
Fig. 3. Steady shear viscosity of cement paste (w/c=0.5) reinforced with CNTs. CNTs suspensions dispersed at a surfactant to CNTs weight ratio of 6.25
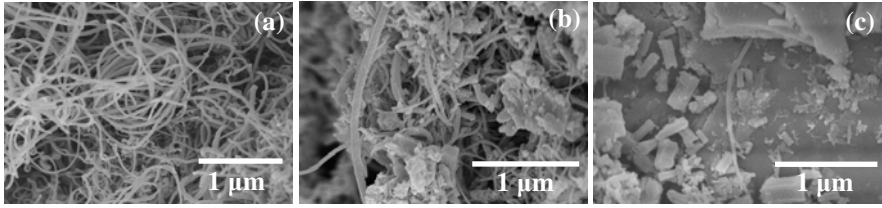
Fig. 4. Dispersant concentration effect on CNT dispersion: (a)-(c) represent a dispersant to CNTs weight ratio of 0, 1.5, and 6.25 respectively

As expected, in samples where dispersion was achieved without the use of surfactant (Fig. 4(a)), CNTs appear poorly dispersed in cement paste, forming large agglomerates and bundles. In the case where dispersion was achieved with a surfactant to CNT weight ratio of 1.5 (Fig. 4(b)), it is observed that CNTs mainly remain as large agglomerates entangled in the cement paste hydration products and only a small amount of CNTs was dispersed. Only individual CNTs were identified on the fracture surfaces of samples where the surfactant to CNT weight ratio lies within the range from 4.0 to 6.25 (Fig. 4(c)).

The mechanical performance of the CNTs nanocomposites was evaluated by fracture mechanics tests. Notched specimens of 20×20×80 mm were tested at the age of 3, 7 and 28 days, by three-point bending. The tests were performed with a closed-loop testing machine with a 89 kN capacity. The feedback control signal for running the test was the crack mouth opening displacement (CMOD) at the notch, which was advanced at a rate of 0.12 mm/min. The load and the CMOD were recorded during the test. A typical load-CMOD curve is shown in Fig. 5.
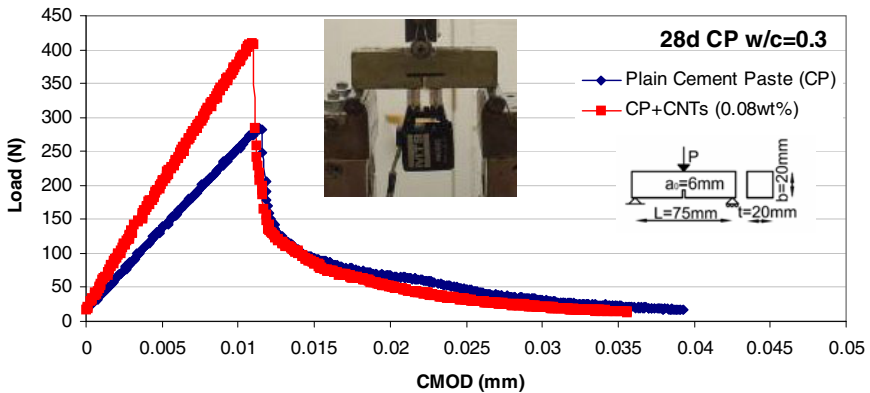
Fig. 5. CMOD-Fracture load of 28 day w/c=0.5 cement paste reinforced with CNTs (0.08wt% by weight of cement)

The results of the 28-day maximum load for the cementitious nanocomposites with different surfactant to CNTs weight ratio are plotted in Fig. 6. It is observed that samples treated with different amounts of surfactant exhibit higher fracture load than plain cement paste. Samples where dispersion was achieved without the use of surfactant exhibit lower fracture load. This decrease in strength indicates that CNTs are poorly dispersed in cement matrix and that in order to achieve proper dispersion the use of a surfactant is absolutely required. The samples with surfactant to CNT weight ratio of 4.0 give a higher average fracture load increase at all ages. Specimens where dispersion was achieved at surfactant to CNTs weight ratios either lower or higher than 4.0 exhibit lower fracture load. A possible explanation could be that at lower surfactant to CNT weight ratios, less surfactant molecules are absorbed to the carbon surface and the protection from agglomeration is reduced. At higher surfactant to CNT weight ratios, bridging flocculation can occur between the surfactant molecules. Too large amount of surfactant in the aqueous solution is causing the reduction of the electrostatic repulsion forces between the CNTs. Based on those results and the SEM imaging of the fractured surfaces it was concluded that for effective dispersion there exist an optimum weight ratio of surfactant to CNTs close to 4.0.
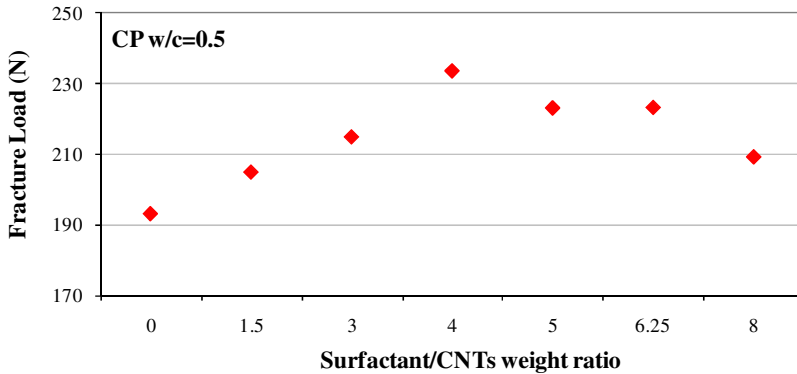
Fig. 6. Fracture load of 28 days w/c=0.5 cement paste reinforced with CNTs (0.08wt% by weight of cement)

2.2   Effect of CNTs/CNFs Type and Concentration

Current research is focused on exploring different processing methods (e.g. coating fibers with additives, varying the rheological properties of the matrix, mixing procedure, etc) and on the optimization of the amount of the CNTs and CNFs used to make the product cost effective. Moreover, the influence of CNT type (short versus long) and the effect of the concentration of CNTs on the fracture properties of nanocomposite samples were studied for a constant weight ratio of surfactant to CNTs.
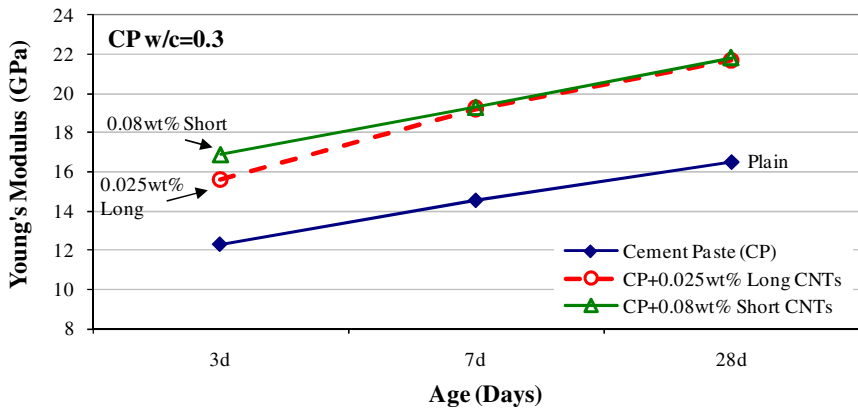
The fracture mechanics test results of the average Young's modulus of the nanocomposites which demonstrate the best mechanical performance for water to

cement ratios of 0.5 and 0.3 are illustrated in Figs 7(a) and 7(b), respectively. When compared to the OPC paste the samples reinforced with CNTs clearly exhibit improved mechanical performance. It is also noticed that, independently from the water to cement ratio, specimens reinforced with either short CNTs at an amount of 0.08 wt% or long CNTs at an amount of 0.025 wt% exhibit the same level of mechanical performance. In general, it can be concluded that the optimum concentration of CNTs depends on the aspect ratio of CNTs.

When CNTs with a low aspect ratio are used (short CNTs), a higher amount close to 0.08wt% by weight of cement is needed to achieve effective reinforcement. When CNTs with higher aspect ratio (long CNTs) are used, amounts less
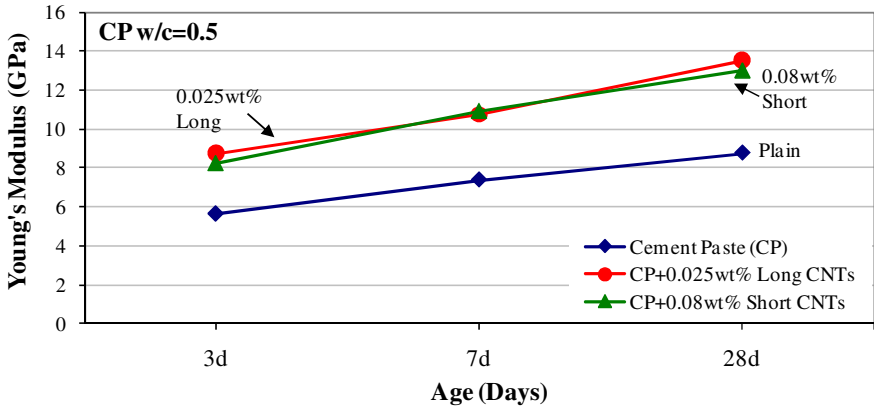
(a)

(b)

Fig. 7. Fracture mechanics test results of the Young's modulus of cement paste nanocomposites with water to cement ratio of (a) w/c=0.5 and (b) w/c=0.3

than 0.048 wt% are needed to achieve a similar level of mechanical performance. These differences are attributed to the degree of dispersion of the CNTs. Comparing similar amounts of CNTs in the mixes, long CNTs exhibit a lower degree of dispersion due to their higher aspect ratio. Consequently, adequate dispersion can be achieved at lower amounts. Short CNTs exhibit a higher degree of dispersion however, because they are shorter, a higher concentration in cement paste matrix is needed to reduce the fiber free area and arrest the nanocracks.

2.3 Nanomechanical Properties

For the characterization at the nanoscale and the determination of local mechanical properties, a nanoindenter with unique advantage of in-situ AFM like imaging that allows pre and post-test observation of the cementitious samples, is being used [16]. In any indentation technique, one material of known properties is used to indent the material with unknown mechanical properties such as elastic modulus and hardness. This technique has its origins in Mohs hardness scale developed in 1822, in which one material is considered to be harder if it can leave a permanent scratch on another material. In nanoindentation, a small indenter is pushed into a sample. Load applied by the indenter is plotted continuously with the displacement of the indenter into the sample. This kind of plot is commonly known as load-indentation or simply p-h plot (Fig. 8). The data obtained is then analyzed to estimate elastic modulus, E and hardness, H of the sample.

The nanomechanical properties of the CNTs nanocomposites were investigated using a Hysitron Triboindenter (Fig. 9) following the technique described in [17]. Before testing, thin slides of approximately 5 mm were cut out of the specimens. The surfaces were polished with silicon carbide paper discs and diamond lapping films in order to obtain a very smooth and flat surface. Nanoindentation was performed in a 12×12 grid (10 μm between adjacent grid points). This procedure was repeated in at least two different areas on each sample.
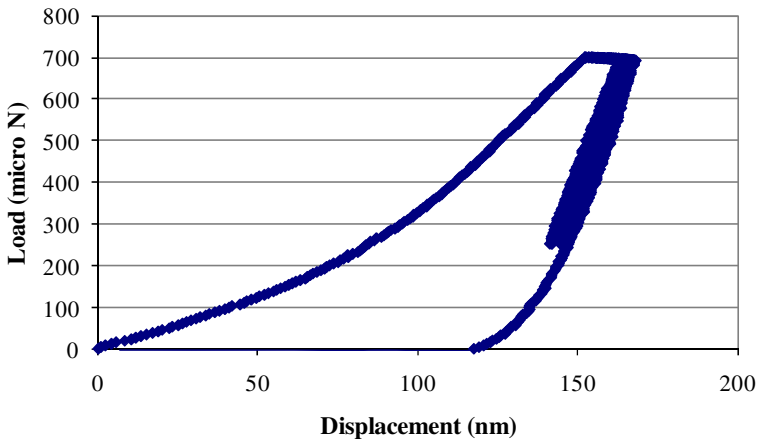

Fig. 8. Force-displacement plot from nanoindentation data
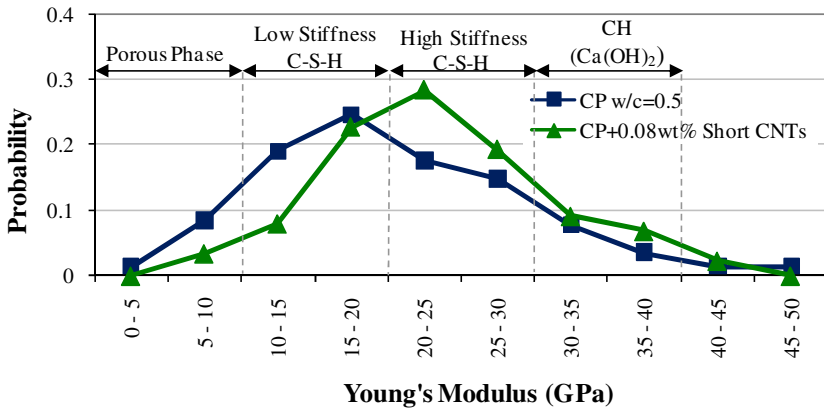
Fig. 9. Hysitron Triboindenter

Fig. 10. Probability plots of the Young's modulus of 28 day cement paste and cement paste reinforced with 0.08wt% short CNTs with w/c=0.5

The structure of cement paste at the nanoscale is dominated by the calcium-silicate-hydrate (C-S-H) phase. Fundamental properties such as strength, fracture behavior, shrinkage and durability are basically controlled by the properties of the C-S-H and the porosity.

The effects of 0.08wt% short, 0.025wt% and 0.048wt% long CNTs on the nanomechanical properties of cement paste with w/c=0.3 and 0.5 were investigated. Similar results were obtained for both water to cement ratios. Fig. 10 shows the probability plot of the 28 days Young's modulus of plain cement paste and cement paste reinforced with 0.08wt% short CNTs for w/c of 0.5. The probability plots are in good agreement with results from the literature [16, 18-19]. Values of the Young's modulus less than 50 GPa represent four different phases of cement paste corresponding to the porous phase, low stiffness C-S-H, high stiffness C-S-H and calcium hydroxide phase, while values greater than 50 GPa are attributed to nanoindentation on unhydrated particles (clinker phases) presented in the material [16, 18-19]. The different phases have been found to exhibit properties that

considered as distinct material properties and are independent of the mix proportions. As expected, the peak of the probability plots of plain cement paste falls in the area of the low stiffness C-S-H, which is the dominant phase of cement nanostructure. On the other hand, the peaks of the probability plots of the nanocomposites are in the area of 20 to 25 GPa which corresponds to the high stiffness C-S-H, suggesting that the addition of CNTs results to a stronger material with increased amount of high stiffness C-S-H. Moreover, it is observed that the probability of Young's modulus below 10 GPa is significantly reduced for the samples with CNTs for both water to cement ratios. The nanoindentation results provide an indirect method of estimating the volume fraction of the capillary pores [18] indicating that the CNTs reduce the amount of fine pores by filling the area between the C-S-H gel.
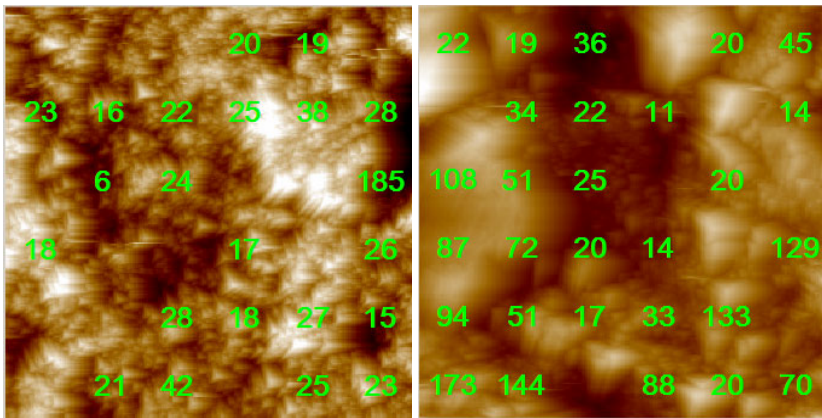
Fig. 11. Typical 60 × 60 µm AFM images of cement paste with (a) w/c=0.5 and (b) w/c=0.3 reinforced with CNTs (0.08 wt% short) showing indentation modulus in GPa

Nanoindentation of the phases of Portland cement (C3S and alite, C2S and belite, C3A, C4AF) have shown that the Young's modulus of the clinker phases range between 125 and 145 GPa [20]. In addition, in a previous study [19] using the same type of cement and testing procedure, values of the Young's modulus of cement unhydrated particles close to 110 GPa (16,000 ksi) have been reported. Fig. 11 shows typical 60×60 µm AFM images, captured using the nanoindenter tip, of the nanostructure of cement paste with w/c=0.5 and w/c=0.3 reinforced with 0.08 wt% short MWCNTs prior to nanoindentation. The values of Young's modulus calculated from the grid indentation are reported on the images in GPa at the respective indent locations. It is observed that the stiffness varies reaching values as high as 185 GPa which are attributed to the presence of unhydrated particles. The high values obtained from the nanocomposites indentation can be possibly attributed to the presence of CNTs in the vicinity of the unhydrated particles. Please note that the nanoindentation tip is in the order of 100 nm and indentation on individual MWCNTs can not be distinguished. These results suggest that

MWCNTs appear to alter the nanostructure of the cement matrix resulting in a stiffer and stronger material.

2.4 Autogenous Shrinkage

Typically, changes in the nanostructure affect the transport properties (properties that are related with the movement of the water in the pores). Recently, it has been increasingly recognized that high strength and high performance concrete is sensitive to the microcracking that occurs at early ages, as a result of the volumetric changes due to the development of high autogenous shrinkage stresses.

The autogenous shrinkage of cement nanocomposites was studied using a modified version of ASTM C 341 and ASTM C 490. Cement paste specimens of 20x20x80 mm were cast following the procedure described above. Immediately after setting (~6 hours after casting) specimens were demolded and sealed using plastic wrap. Stainless steel gage studs were glued directly to the surface of the specimens maintaining a 50.8 mm gage length, using a five minutes epoxy resin. A length comparator was used to measure the distance between the stubs from the time of final setting up to 96 hours after casting.

Fig. 12 shows the autogenous shrinkage results of plain cement paste and cement paste reinforced with 0.025% and 0.048wt% long CNTs. It is observed that the samples reinforced with CNTs exhibit lower shrinkage than the plain cement paste. Also, the samples reinforced with a higher amount of CNTs demonstrate lower autogenous shrinkage. The shrinkage development is known to be proportional to the amount of the fine pores (pores with diameter < 20 nm) in the binder at early ages [21-22]. Higher percentage of the volume fraction of small pores in a cementitious system at early ages leads to the increase of autogenous shrinkage. Due to their small diameters (20 to 40 nm) CNTs appear to reduce the amount of fine pores and also reinforce the nanostructure of cement paste, which leads to the reduction of the capillary stresses, resulting in lower autogenous strains.
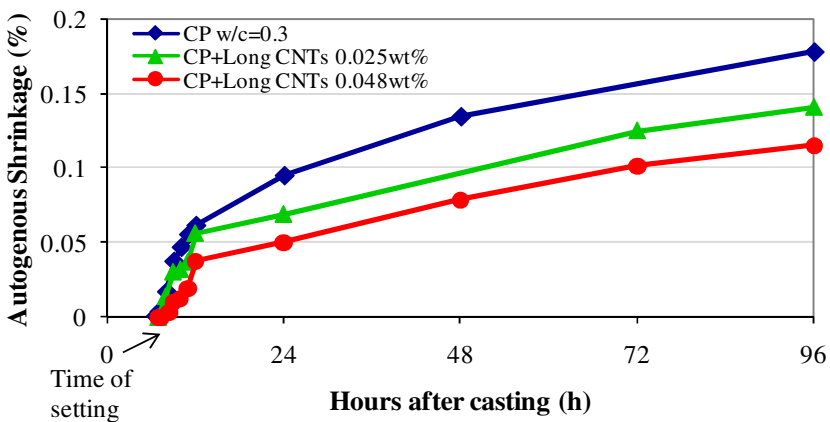

Fig. 12. Autogenous shrinkage of cement paste (w/c=0.3) and cement paste reinforced with 0.025wt% and 0.048wt% long CNTs

3 A New Generation of Cement Based Materials-Conclusions

The development of high-performance cementitious nanocomposites reinforced with multiwall carbon nanotubes was studied. Effective dispersion was achieved by applying ultrasonic energy and with the use of a surfactant. Results have shown that for proper dispersion, the application of ultrasonic energy is required. The combination of the SEM and fracture mechanics test results suggests that for effective dispersion, a weight ratio of surfactant to CNTs close to 4.0 is required. The fracture mechanics test results indicate that the fracture properties of cement matrix increased through proper dispersion of small amounts of CNTs (0.025wt% and 0.08wt%). In particular, higher concentrations of short CNTs are required to achieve effective reinforcement, while lower amounts of longer CNTs are needed to achieve the same level of mechanical performance. The nanoindentation results suggest that CNTs can modify and reinforce the cement paste matrix at the nano-scale by increasing the amount of high stiffness C-S-H and decreasing the porosity, which leads to the reduction of the autogenous shrinkage. The autogenous shrinkage results indicate that CNTs, except for the reinforcement effect, can also have beneficial effect on other properties such as the transport properties of cementitious materials.

Acknowledgements

References

1. Lawler, J.S.: Hybrid fiber-reinforced in mortar and concrete. PhD thesis, Northwestern University (2001)
2. Akkaya, Y., Shah, S.P., Ghandehari, M.: Influence of fiber dispersion on the performance of microfiber reinforced cement composites. ACI Special Publications 216: Innovations in Fiber-Reinforced Concrete for Value, SP-216-1, 1-18 (2003)
3. Salvetat, J.P., Bonard, J.M., Thomson, N.H., Kulik, A.J., Forro, L., Benoit, W., et al.: Mechanical properties of carbon nanotubes. Appl. Phys. 69, 225–260 (1999)
4. Belytschko, T., Xiao, S.P., Schatz, G.C., Ruoff, R.: Atomistic Simulations of Nanotubes Fracture. Phys. Rev. B 65, 235430–235437 (2002)
5. Lawrence, J.G., Berhan, L.M., Nadarajah, A.: Elastic Properties and Morphology of Individual Carbon Nanofibers. ACS Nano 2, 1230–1236 (2008)
6. Cao, J., Wang, Q., Dai, H.: Electromechanical Properties of Metallic, Quasimetallic, and Semiconducting Carbon Nanotubes under Stretching. Phys. Rev. Lett. 90, 157601–157604 (2003)

7. Tombler, T.W., Zhou, C., Alexseyev, L., Kong, H., Dai, H., Liu, L., Jayanthi, C.S., Tang, M., Wu, S.Y.: Reversible electromechanical characteristics of carbon nanotubes under local-probe manipulation. Nature 405, 769–772 (2000)

8. Makar, J.M., Beaudoin, J.J.: Carbon Nanotubes and Their Applications in the Construction Industry. In: Bartos, P.J.M., Hughes, J.J., Trtik, P., Zhu, W. (eds.) in Nanotechnology in Construction Proceedings of the 1st International Symposium on Nanotechnology in Construction, pp. 331–341. Royal Society of Chemistry (2004)

9. Makar, J.M., Margeson, J., Luh, J.: Carbon nanotube/cement composites – Early results and potential applications. In: Proceedings of the 3rd International Conference on Construction Materials: Performance, Innovations and Structural Implication, Vancouver, B.C., Canada, pp. 1–10 (2005)

10. Li, G.Y., Wang, P.M., Zhao, X.: Mechanical behavior and microstructure of cement com-posites incorporating surface-treated multi-walled carbon nanotubes. Carbon 43, 1239–1245 (2005)

11. Li, G.Y., Wang, P.M., Zhao, X.: Pressure-sensitive and microstructure of carbon nano-tube reinforced cement composites. Cem. Concr. Comp. 29, 377–382 (2007)

12. Konsta-Gdoutos, M.S., Metaxa, Z.S., Shah, S.P.: Nanoimaging of highly dispersed carbon nanotube reinforced cement based materials. In: Gettu, R. (ed.) Proceedings of the Seventh International RILEM Symposium on Fiber Reinforced Concrete: Design and Applications, pp. 125–131. RILEM Publications S.A.R.L. (2008)

13. Junrong, Y., Grossiord, N., Koning, C.E., Loos, J.: Controlling the dispersion o multi-wall carbon nanotubes in aqueous surfactant solution. Carbon 45, 618–623 (2007)

14. Hielscher, T.: Ultrasonic production of nano-size dispersions and emulsions. In: Proceedings of 1st Workshop on NanoTechnology Transfer in Europe, TIMA Editions, Grenoble, France, pp. 138–143 (2006)

15. Yang, Y., Grulke, A., Zhang, G.Z., Wu, G.: Thermal and rheological properties of carbon nanotube-in-oil dispersions. J. Appl. Phys. 99, 114307 (2006)

16. Mondal, P., Shah, S.P., Marks, L.D.: Nanoscale characterization of cementitious materials. ACI Mater. J. 105, 174–179 (2008)

17. Konsta-Gdoutos, M.S., Metaxa, Z.S., Shah, S.P.: Multi-scale mechanical and fracture characteristics and early-age strain capacity of high performance carbon nanotube/cement nanocomposites. Cem. Con. Com. 32, 110–115 (2010)

18. Constantinides, G., Ulm, F.J.: The nanogranular nature of C-S-H. J. Mech. Phys. Solids 55, 64–90 (2007)

19. Mondal, P.: Nanomechanical properties of cementitious materials. PhD thesis, Evanston, Northwestern University (2008)

20. Velez, K., Maximilien, S., Damidot, D., Fantozzi, G., Sorrentino, F.: Determination by nanoindentation of elastic modulus and hardness of pure constituents of Portland cement clinker. Cem. Concr. Res. 31, 555–561 (2001)

21. Tazawa, E. (ed.): Autogenous shrinkage of concrete. E&FN Spon, London (1999)

22. Konsta-Gdoutos, M.S., Shah, S.P., Dattatraya, D.J.: Relationships between engineering characteristics and material properties of high strength-high performance concrete. In: Dhir, R.V., Newlands, M.D., Csetenvi, L.J. (eds.) Proceedings of International Symposia Celebrating Concrete: People and Practice, in Role of Cement Science in Sustainable Development, pp. 37–46. Tomas Telford Limited (2003)

Application of Digital Speckle Pattern Interferometry (DSPI) in Determination of Elastic Modulus Using Plate Vibration

Chandra Shakher[1] and Rajesh Kumar[2]

[1] Laser Applications and Holography Laboratory,
  Instrument Design Development Centre,
  Indian Institute of Technology, Delhi
  New Delhi – 110 016, India
  Tel.: +91-11-2659-1432; Fax: +91-11-2686-2037
  `cshakher@iddc.iitd.ac.in, cshakher1949@hotmail.com`
[2] Department of Mechanical Engineering,
  Sant Longowal Institute of Engineering and Technology,
  (Deemed to be University; established by Government of India)
  Longowal – 148 106 (Punjab), India

Abstract. Elastic material properties critically affect the vibration behavior of structures. The value of natural frequencies changes due to change in the plate constants/plate stiffness which is a function of elastic modulus. At each natural frequency, the plate has a unique mode shape of vibration which can be easily differentiated from mode shapes at other natural frequencies. In this paper, a technique for the evaluation of the elastic modulus is proposed which is based on the vibration analysis of the plate using digital speckle pattern interferometry (DSPI) and Rayleigh method. Large numbers of experiments were conducted on square aluminium plate for the boundary condition; one edge is fixed and other edges free. The experimental result reveals that a single observation of frequency at first torsional mode is sufficient to evaluate the elastic modulus for all practical purposes. The evaluated experimental error was found to be less than 1%. Ease in sample preparation, simplicity in evaluation, non destructive nature of the DSPI and speed of DSPI has good prospect to evaluate elastic modulus of a material.

1 Introduction

Tensile test and bending test have been well established for determination of mechanical properties of material [1]. But these methods are of destructive type and suitable for bulk film materials. Optical techniques can be used to evaluate

elastic modulus for both bulk film and thin film materials [2-6]. Seebacher et al. in their work used digital holography in evaluation of elastic modulus of silicon microbeams. In their experiment, the cantilever beam was mechanically loaded by a defined force in static manner at free end. The 3D-surface displacements were measured and used in calculating elastic modulus [4]. Viotti et al. have proposed an optical system which uses a spherical tip to introduce a permanent displacement field to locally evaluate the elastic moduli of solid materials [5]. As vibration behavior of structures is critically affected by elastic material properties, hence the same can be used for estimation of elastic modulus in a non-destructive manner. Recently, in 2007, evaluation of elastic modulus of cantilever beam using ESPI and Euler–Bernoulli equation was demonstrated by Kang et al. [6]. The specimens used for the elastic modulus experiment were of pure copper beam and cold rolled carbon steel cantilever beams (ratio of length and width, a/b ≥10). But for the cantilever beam only bending modes are observed. The fringes in bending modes are straight and directed in the direction parallel to the fixed edge at every resonance frequency. This may lead to ambiguity in identifying the specific mode of vibration. Fringes generated due to the environmental perturbations may also create ambiguity in measurement. Investigation of plate vibration has received considerable attention for academic research due to its wide range engineering applications. Speed of digital speckle pattern interferometry (DSPI) made it a powerful tool for scanning and recording mode shape of vibration of plate [7-10]. Mode shapes of vibration for square, rectangular and many more shapes under different boundary conditions using DSPI were studied in detail by many investigators [9, 11-13]. Results from DSPI reveal that for different torsional and plate modes of vibration, at each natural frequency, the plate has a unique mode shape of vibration and the fringes are not unidirectionally parallel to the fixed edge of the plate (as in the bending modes). This reduces chance of ambiguity due to environmental perturbation and human error in identifying specific mode shape.

A technique for evaluation of elastic modulus has been proposed in this paper which is based on vibration analysis of plate using DSPI and Rayleigh's method. At resonance frequencies the harmonically vibrating plate has zero displacement along nodal line and higher displacement at other points. In time-average sequential subtraction DSPI, the brightest fringe represents the nodal line. A large number of experiments were conducted on square aluminum plates for the boundary condition one edge fixed and other edges free. The evaluation of elastic modulus is compared with the supplied data. Ease of sample preparation, simplicity in evaluation, nondestructive nature of experimentations, and speed of DSPI has high prospective in evaluation of elastic modulus of a material.

2   Principle

2.1   Determination of Elastic Modulus Using the Concept of Plate Vibration

The study is based on transverse/out-of-plane vibration of the plate. Normal and shear forces in the plane of the flat plate of uniform thickness are shown in Fig.1.
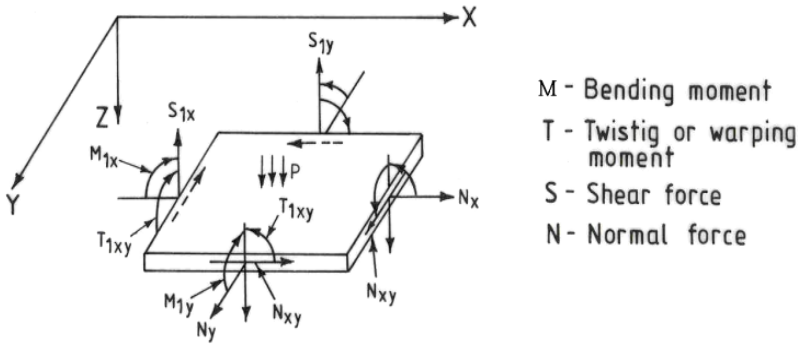
Fig. 1. An element of plate showing bending moments, normal and shear forces

Following equation relates the lateral deflection w to the loading on the plate made of homogeneous isotropic material [14]:

$$D\nabla^4 w = D(\frac{\partial^4 w}{\partial x^4} + 2\frac{\partial^4 w}{\partial x^2 \partial y^2} + \frac{\partial^4 w}{\partial y^4}) = P + N_x \frac{\partial^2 w}{\partial x^2} + 2N_{xy}\frac{\partial^2 w}{\partial x \partial y} + N_y \frac{\partial^2 w}{\partial y^2}$$

(1)

where, $D = \dfrac{Eh^3}{12(1-v^2)}$ is the plate stiffness, E is modulus of elasticity, h is the thickness of the plate and v is Poisson's ratio of the material of the plate and x and y are spatial variable for the plate. The parameter P is the loading intensity, N_x is normal (in-plane) loading in the X-direction per unit length, N_y (in-plane) is normal loading in Y-direction per unit length, and N_{xy} the shear load parallel to the plate surface in the X- and Y-directions, per unit length.

The equation of free vibration of plate is more complicated to solve than one governing the vibration of beam. By using an admissible mode function in Rayleigh's method, an approximate expression for natural frequency is obtained. This can be improved by using Ritz's method [15] in which the natural mode shape function is assumed in series form. For the mass density of the plate ρ, the Rayleigh's method gives the following frequency equation:

$$\omega_n^2 = \frac{V_{max}}{\dfrac{\rho h}{2}\iint\limits_A \overset{o}{W}{}^2 dxdy}$$

(2)

where 'V' is strain energy and is given by [14]

$$V = \frac{D}{2}\iint\limits_S \{(\frac{d^2 w}{dx^2} + \frac{d^2 w}{dy^2})^2 - 2(1-v)[\frac{\partial^2 w}{\partial x^2}\frac{\partial^2 w}{\partial y^2} - (\frac{\partial^2 w}{\partial x \partial y})^2]\}dxdy \qquad (3)$$

The Ritz method involves assuming $\overset{o}{W}$, which is a function of x and y satisfying the necessary boundary conditions, to be of the form $\overset{o}{W} = a_1 \overset{o}{W_1}(x,y) + a_2 \overset{o}{W_2}(x,y) + \ldots$ In which $\overset{o}{W_1}, \overset{o}{W_2}, \ldots$ all satisfy at least the geometric boundary conditions, and $a_1, a_2, \ldots$ are adjusted to give a minimum frequency. The first few natural frequencies obtained using these functions for a square plate under different boundary conditions are given in literature in terms of non-dimensional frequency parameters [14-16].

The non-dimensional frequency parameter is expressed as

$$\varpi = \omega_n / \sqrt{D / \rho h a^4} \tag{4}$$

where, a is the side of the plate.

Putting the value of frequency in Hz (as $f_n = \omega_n / (2\pi)$), and plate stiffness, D in the above equation, the modulus of elasticity can be written as

$$E = \frac{12(1 - v^2)\rho a^4}{h^2} \times \left(\frac{2\pi f_n}{\varpi} \right)^2 \tag{5}$$

Hence elastic modulus of a plate can easily be evaluated if the value of natural frequency and corresponding mode shape of vibration are obtained from experiments.

3   Theoretical Background of Time-Averaged Specklegrams

The time-averaged processing is an extension of addition method. When object is vibrating at a natural frequency much higher than the CCD frame refreshing time, the resulting image is the superposition of the different position of the vibration. It is called a time averaged specklegram and the modes of vibration corresponding to brightest fringes. This is due to the modulation of intensity by the function J_o^2 (0th order Bessel function) resulting from the integration of the vibration mode along the frame time of the CCD

$$\frac{1}{t} \int_0^t \exp(i\Delta\phi)dt$$

In this case contrast is really poor. To enhance the fringe contrast, it is worth subtracting from this the steady state specklegram or another time averaged specklegram. The results given above by different method are still noisy.

3.1   Interferogram Formation

In DSPI, the primary interference between a speckle object beam and specular reference beam is recorded by CCD camera.

The specular reference beam has a complex amplitude

$$A_r = \left|A_r\right| e^{i\phi_R}$$

The speckle object beam has an amplitude

$$A_o = \left|A_o\right| e^{i(\phi_o + \psi_o)}$$

In the above equation the total phase shift is splitted into two parts, ϕ_o is slowly varying function of position across the object and ψ_o is spatially rapidly varying function corresponding to randomly added phase of each speckle upon.

The phase is split into two parts so that high frequency speckles can be ensemble averaged fringes. When the object and reference beam are combined in interferometer, the resulting slowly varying phase difference is defined as $\phi = \phi_o - \phi_r$.

These amplitudes and phases are the functions of x and y, the position across the image of the speckle producing effect. When the deformations are observed, the phase of the speckle field after perturbation of object is changed by $\Delta\phi(x, y)$ and the object field complex amplitude becomes

$$A_o^{'} = \left|A_o\right| \exp(i(\psi_o + \phi_0 + \Delta\phi)) \tag{6}$$

$$I(x, y, t) = I_o + I_r + 2\sqrt{I_o I_r}\, \cos[\psi(x, y) + \phi(x, y, t)] \tag{7}$$

$$\phi(x, y, t) = \phi_o(x, y, t) - \phi_R(x, y, t) \tag{8}$$

It is assumed that beams are mutually coherent and have same state of polarization.

The phase $\phi_o(x, y, t)$ describes the optical path difference $d(x, y)$ between the object and reference beams.

$$\phi_o(x, y) = \frac{2\pi}{\lambda} 2d(x, y) \tag{9}$$

'λ' is the wavelength of light.

For rough surface 'd' varies with position by an amplitude which is much greater than the wavelength of light. Thus 'I' takes the form of "speckle pattern".

The instantaneous intensity 'I' is recorded by the detector, which measures the total energy (proportional to the intensity) incident at each detector point during the exposure period 'T' is given by

$$I_1(x, y) = I(x, y)\left\{1 + V(x, y)\frac{1}{T}\int_t^{t+T}\cos[\psi(x, y) + \phi(t)]\, dt\right\} \tag{10}$$

Where

$$I(x, y) = I_o(x, y) + I_r(x, y)$$

$$V \approx \frac{2\sqrt{I_o I_r}}{I_o + I_r}$$

The form of the integral in eq. (10) depends on the type of illumination and surface motion. We assume that during the exposure illumination is constant and that a complete number of cycles of the harmonics surface motion, occur during the exposure, 'T'. Eq. 10 can be re-written as

$$I_1(x, y) = I(x, y)\left[1 + V(x, y)\cos\psi(x, y)J_o\left(\frac{2\pi}{\lambda}2d\right)\right] \qquad (11)$$

In the above equation the time-averaged interference pattern consist of a speckle pattern in which visibility is modulated by Bessel function. Vibration nodes are defined as loci of zero amplitude of vibration while anti-nodes describe the loci of maximum amplitude of vibration. Antinodes occur between the nodes. Subsequent maxima and minima of the zero order Bessel function are much lower and the variation in the contrast of the speckles is very difficult to determine visually. Thus, it is difficult to determine the vibration amplitude. To improve the fringe contrast is essential to measure amplitude of vibration, which can be done by subtraction fringe formation.

3.2 Subtraction Fringe Formation

The term $J_o\left(\frac{2\pi}{\lambda}2d\right)$ contains useful information regarding amplitude of

vibration.

Consider acquiring two frames, each recorded when object is vibrating. The first is represented by eq. 11 and the second with a 'α' phase change introduced between the frames.

For α = π

$$I_2(x, y) = I\left[1 + V\cos(\psi + \pi)J_o\left(\frac{2\pi}{\lambda}2d\right)\right] \qquad (12)$$

Thus, the intensity difference is –

$$I_1 - I_2 \propto I.V\cos\psi\, J_o\left(\frac{2\pi}{\lambda}2d\right) \qquad (13)$$

The subtraction of two speckle patterns, corresponding to the states of the object, will generally produce negative intensity values. It is usual to assign positive intensity values at these points so that they do not appear black on monitor. Therefore, intensity differences are squared and displaced on the monitor.

$$\Delta I = \left| I_1 - I_2 \right|^2 = I^2 V^2 J_o^{\;2}\left(\frac{2\pi}{\lambda} 2d \right) \tag{14}$$

The second option is to record first interferogram when vibration amplitude is zero and other when vibration amplitude is non-zero. In this case, the intensity difference is,

$$\Delta I = I^2 V \left[1 - J_0\left(\frac{2\pi}{\lambda} \right) 2d \right]^2 \tag{15}$$

Equations 14 and 15 show that time averaged fringes are very different in appearances. No longer they follow periodic form.

$J_0^{\;2}$ function indicates that brightest fringe corresponds to an argument zero (zero vibration amplitude). That is the brightest time averaged fringe corresponds to a node of the motion. The fringes decline in brightness with the amplitude of vibration. Thus making it difficult to measure higher amplitudes where the depth of modulation is poor.

$(1 - J_0)^2$ function indicates that zero-argument fringe now corresponds to a black fringe, and fringe sensitivity is halved as compared to $J_0^{\;2}$ fringes. $(1 - J_0)^2$ method enable rapid frequency scan, during which vibration modes can be identified as no new reference image required to be recorded during the scan. Once the frequencies of interest have been identified, the high visibility $J_0^{\;2}$ fringes can be observed. To enhance the accuracy of the frequency measurement, it is better to make fast scan nearby the resonance. This method shows its capability to accurately measure vibration modes of plates and detect natural frequency with a good accuracy.

4   Experiments and Results

Schematic of the DSPI set-up used for recording the fringe patterns of out-of-plane/ transverse vibration of the plate is shown in Fig.2. The plate was excited by a shaker (model number: EX 6 / 6.4, make: Prodera, France). A beam of 30 mW He-Ne laser of wavelength 632.8 nm is split into two beams by a beam splitter BS1. One of the beams illuminates the surface of the plate under study and the other beam is used as the reference beam. The value of γ for our experimental setup is 1.938. The object beam is combined with the reference beam to form a speckle interferogram that is converted into a video signal by a CCD camera. The video analog output from HTC-550B/W CCIR CCD camera is fed to the PC-based
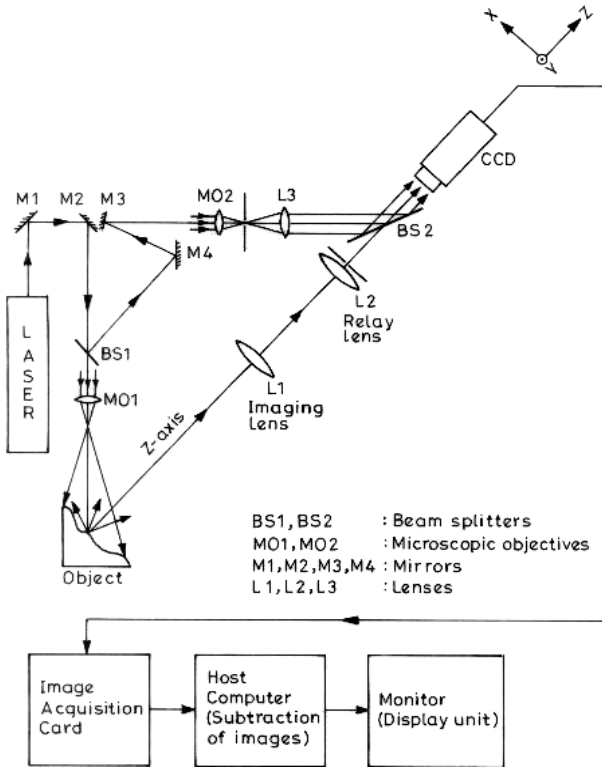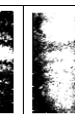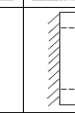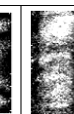
Fig. 2. Schematic of DSPI setup for measurement of out-of-plane vibrations**.**

image-processing system developed using National Instrument's IMAQ PCI-1408 card. LabVIEW 5.0 based program [20] in graphical programming language was developed to acquire, process and display the interferogram. To improve the contrast, the program implements accumulated linear histogram equalization after subtraction of the interferograms. The time-average interferogram of the vibrating plate over the frame acquisition period (1/30 second) is grabbed and subtracted from the just previous time-average inteferogram in sequential subtraction manner. The subtracted interferogram so obtained is displayed continuously on the computer screen. Experiments were conducted on square plates made of aluminium (physical properties as per the available data: Young's modulus = 70 GPa, Density = 2700 kg/m^3, and Poisson's ratio = 0.3). The plates were polished on optical grinding machine to get the required flatness and smoothness of the surface. To make the edge fixed, the plate was tightened with the help of strip and bolt to have uniformly distributed stress at the edge of the plate. For the experiments carried out with different objectives of vibration studies, to make an edge fixed, the

torque applied to tighten the plate was kept around an optimum value of 3Nm for the setup [13]. There may be possibility of shift in natural frequencies as it is difficult to meet the boundary condition perfectly fixed at the edge of the plate. Function generator (model number: HP 33120A) was set to generate the sinusoidal signal and regulates the frequency and magnitude of the force of the exciter. A large number of mode shapes according to change in excitation frequency were recorded. Some typical speckle interferograms after noise removal showing the 1st torsion, 1st plate and higher plate mode shapes for a square plate (50 mm × 50 mm × 0.8 mm) fixed at one edge and other edges being free are shown in table 1.

Table 1. Evaluation of elastic modulus based on data of first torsional and plate modes of vibration for a square plate (50 mm × 50 mm × 0.8 mm) fixed at one edge and other edges being free. Red is maximum deflection in positive direction, green is zero displacement (nodal line) and blue is maximum deflection in opposite direction i.e. negative direction.

Observed mode shape by DSPI			
Corresponding classical mode shape			
Range of observed natural frequency while reproducing the mode shape	665 Hz - 675 Hz	2.07 kHz –2.15 kHz	4.95 kHz – 5.08 kHz
Mean of observed natural frequency f_n by DSPI	670 Hz	2.110 kHz	5.015 kHz
Mode shape analyzed for the supplied material data using FEA			
Natural frequency analyzed using FEA for the supplied material data	669.61 Hz	2.141 kHz	5.069 kHz
Frequency parameter, $\overline{\omega}$ corresponding to the observed mode shape [14,15]	8.547	27.46	- (64.62 as analyzed using FEA)
E (in GPa) as evaluated from the f_n observed for DSPI and the theoretical $\overline{\omega}$	69.906	67.167	68.517
Deviation of E with respect to supplied material data	-0.134 %	-4.047 %	-2.118 %
Remark on observed mode shapes	First torsional mode (m/n = 1/1)	First plate mode (m/n = 2/1)	Higher plate mode (m/n = 3/1)

Evaluation of elastic modulus corresponding to the mode shapes are also tabulated and shown in the same table. It was observed that for specific tightening (3Nm torque) at edge of the plate, the mode shapes and corresponding frequencies are reproducible. During each set of frequency scan for mode shapes, the band width of frequency for a mode shape is approximately ±10Hz. After this band width of frequency, symmetry of the mode shape is lost. Keeping other conditions same, if the tightening at the edge is changed and frequency scan for mode shapes is made, there is shift in natural frequencies but again for this tightening condition, the natural frequencies are reproducible. Experiments were conducted time and again by applying torques to tighten the plate close to 3Nm. It was observed that the least variation (±5Hz) from the mean was for the first torsional mode. The second least variation of around ±20Hz from the mean natural frequency was observed for the first plate mode. Hence, for practical purposes, to evaluate elastic modulus, data corresponding to the first torsional mode is more reliable and reproducible.
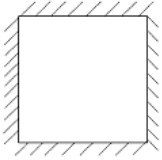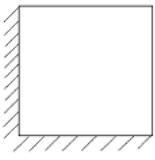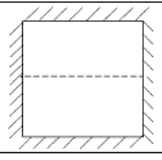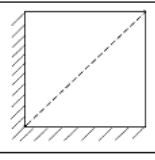
The results were also verified using finite element analysis (FEA) package (ANSYS 10.0). Natural frequency obtained using the FEA package corresponding to the 1st torsional mode is 669.61 Hz. The variation of the mean value of the experimentally obtained frequency for 1st torsional mode with that of the FEA result is only 0.04%. Although the data corresponding to the 1st torsional mode is sufficient for evaluation of elastic constant as the variation in frequency for this case is least (less than 1%), one can be interested in evaluations based on two or three least varying natural frequencies to have an average E. In these cases, the deviation in E with respect to the supplied material data was -2.090% and -2.099% respectively. Few more studies with different boundary condition are in process. The preliminary results reveal that the method can be effectively used in determination of elastic modulus of the plate. Some typical observations under different boundary conditions are shown in Table 2.

If we refer eq.5, for same material, computation of E is function of following variables

$$E = f(a, h, f_n, \varpi)$$

(16)

Hence care must be taken while measuring dimensions of the plate along the edges and locations for measurement of thickness of the plate. To have a uniform thickness of plate, flatness is required to be maintained while polishing the plate. Care during observing natural frequency, and maintaining plate clamping conditions (it influences frequency parameter, ϖ) closer to the ideal one (which can be achieved either by optimum tightening of strip and bolts, constraining more number of edges or by precisely controlled welding process) are also required to have least absolute error in measurement.

Table 2. Evaluation of elastic modulus based on data of vibrating square plate under different boundary conditions.

Boundary condition and size of the plate		
	(50mm×50mm×0.527mm)	(62mm×62mm×0.986mm)
Observed mode shape by DSPI		
Corresponding classical mode shape		
Mean of observed natural frequency f_n by DSPI	3.835 kHz	1.51 kHz
Frequency parameter, $\overline{\omega}$ corresponding to the observed mode shape [14,15]	73.41	24.08
E (in GPa) as evaluated from the f_n observed for DSPI and the theoretical $\overline{\omega}$	71.544	69.622
Deviation of E with respect to supplied material data	+ 2.206%	- 0.539%

5 Conclusion

DSPI and vibration analysis of plate can be effectively utilized to evaluate the elastic modulus. Plate has unique mode shape of vibration and there is no ambiguity in identifying these mode shapes when observed by DSPI. To establish the method a large number of experiments were conducted on square aluminum plates fixed at one edge and keeping other edges free. Experimental results reveal that if preformed carefully, a single observation is sufficient to determine the elastic modulus of the plate material. Applying the boundary condition one edge fixed and other edges free is relatively easier. It was observed that for the boundary condition, one edge fixed and other edges free, the frequencies corresponding to first torsional mode obtained from DSPI are almost same when calculated using classical theory or by the FEA. So the single observation of frequency at first

torsional mode is sufficient to evaluate the elastic modulus for all practical purposes with measurement error less than 1%. Preliminary results with other boundary conditions also reveal that this technique can effectively be used for the purpose.

References

1. ASTM Standard E132-97, Standard test method for Young's modulus, tangent modulus and chord modulus. In: Annual Book of ASTM Standards. Am. Soc. Test Mater 03.01, pp. 244–250 (2002)
2. Gascón, F., Salazar, F.: A procedure for calculating through laser speckle interferometry the elastic constants of isotropic materials. Opt. Commun. 123(4-6), 734–742 (1996)
3. Kang, X., Tay, C.J., Quan, C.: Evaluation of Young's modulus of a vibrating beam by optical method. Opt. Eng. 42(10), 3053–3058 (2003)
4. Seebacher, S., Osten, W., Baumbach, T., Jüptner, W.: The determination of material parameters of microcomponents using digital holography. Opt. Laser Eng. 36(2), 103–126 (2001)
5. Viotti, M.R., Kaufmann, G.H., Galizzi, G.E.: Measurement of elastic moduli using spherical indentation and digital speckle pattern interferometrywith automated data processing. Opt. Laser Eng. 44(6), 495–508 (2006)
6. Kang, K., Kim, K., Lee, H.: Evaluation of elastic modulus of cantilever beam by TA-ESPI. Opt. Laser Technol. 39(3), 449–452 (2007)
7. Moore, A.J., Jones, J.D.C., Valera, J.D.R.: Dynamic measurements. In: Rastogi, P.K. (ed.) Digital speckle pattern interferometry and related techniques, pp. 225–288. Wiley, Chichester (2001)
8. Wang, W.C., Hwang, C.H., Lin, S.Y.: Vibration measurement by the time-averaged electronic speckle pattern interferometry. Appl. Opt. 35, 4502–4509 (1996)
9. Huang, C.H.: Experimental measurements by an optical method of resonance frequencies and mode shapes for square plates with rounded corners and chamfers. J. Sound Vib. 253(3), 571–583 (2002)
10. Shakher, C., Kumar, R.: System and method for real time monitoring of vibrations and large deformation in diffused material using sequential subtraction and image enhancement. Indian Patent office application no.: 925/DEL/2002. September 12 (2002)
11. Kumar, R., Shakher, C.: Application of digital speckle pattern interferometry and wavelet transform in measurement of transverse vibrations in square plate. Opt. Laser Eng. 42(5), 585–602 (2004)
12. Kumar, R., Singh, I.P., Shakher, C.: Measurement of out-of-plane static and dy-namic deformations by processing digital speckle pattern interferometry fringes using wavelet transform. Opt. Laser Eng. 41(1), 81–93 (2004)
13. Mirza, S., Singh, P., Kumar, R., Vyas, A.L., Shakher, C.: Measurement of transverse vibrations/ visualization of mode shapes in square plate by using digital speckle pattern interferometry and wavelet transform. Opt. Laser Eng. 44(1), 41–55 (2006)
14. Stokey, W.F.: Vibrations of systems having distributed mass and elasticity. In: Harris, C.M. (ed.) Shock and vibration handbook, pp. 7.1–7.37. McGraw-Hill Book Comp., New York (1961)

15. Young, D.: Vibration of rectangular plates by the Ritz method. J. Appl. Mech. 17, 448–453 (1950)
16. Leissa, A.W.: The free vibration of rectangular plates. J. Sound Vib. 31(2), 257–293 (1973)
17. Lu, B., Yang, X., Abendroth, H., Eggers, H.: Time-average subtraction method in electronic speckle pattern interferometry. Opt. Commun. 70(3), 177–180 (1989)
18. Lu, B., Hu, Z., Abendroth, H., Eggers, H., Ziolkowski, E.: Improvement of time-average subtraction technique applied to vibration analysis with TV-holography. Opt. Commun. 78(3-4), 217–221 (1990)
19. Moore, A.J., Jones, J.D.C., Valera, J.D.R.: Dynamic measurements. In: Rastogi, P.K. (ed.) A Book on Digital Speckle Pattern Interferometry and Related Techniques, pp. 225–288. John Wiley & Sons Ltd., England (2001)
20. IMAQ^{TM} Vision for G Reference Manual. National Instrum Corp., Austin (1997)

The Development and Applications of Amplitude Fluctuation Electronic Speckle Pattern Interferometry Method

Wei-Chung Wang[1] and Chi-Hung Hwang[2]

[1] Department of Power Mechanical Engineering, National Tsing Hua University,
Taiwan, Republic of China
`wcwang@pme.nthu.edu.tw`
[2] Instrument Technology Research Center, National Applied Research Laboratories,
Taiwan, Republic of China
`chhwang@itrc.org.tw`

Abstract. In vibration measurement, traditional time averaged (TA) electronic speckle pattern interferometry (ESPI) method was essentially used for obtaining modal shapes rather for quantitative analysis. In 1996, the authors first reported that the driving force acting on the specimen would be fluctuated due to environmental disturbances and vibration fringe patterns obtained by TA ESPI method can be significantly improved if both the reference and object images were captured under vibration load. This new TA ESPI method was named as amplitude fluctuation (AF) ESPI method. In this paper, the development and successive improvement of the AF ESPI method was first introduced. The effects of environmental noise and vibration characteristics on the ESPI fringe pattern were then investigated. Theoretical derivation on the effect of environmental noise was performed and the time varying brightness of the traditional time averaged (TA) ESPI fringe patterns was successfully explained. In addition, applications of the AF ESPI method were briefly reviewed.

1 Introduction

In 1992, during the execution period of an investigation project of applications of composite materials of Taiwan's bicycle and motorcycle industries, the authors were aware that the inlet springs of the inlet valve of a 4-stoke motorcycle engine were made of carbon fiber reinforced plastic (CFRP) [0/90] plates as shown in Fig. 1 [1]. In practice, the engine of a motorcycle completes 3000~6000 combustion cycles per minute, i.e. the springs are forced to vibrate at about 50~100 Hz. To achieve the best efficiency of the engine, the inlet valve should be completely

closed. If the combustion frequency is happened to be the same as the modal frequency of inlet springs, the inlet valve may not be closed completely and the efficiency of the engine will be decreased. Moreover, the free ends of the inlet springs will impact on the head of the inlet valve and cracks may be produced in the springs. Besides, the inlet valve is mounted on the top of the combustion chamber and therefore the inlet springs are operated under high temperature, surface defects may also be produced on the plate springs. While defects were introduced, the dynamic properties of damaged plate springs are changed and the associated modal modes will also be different from defect-free ones. Structures may be failed because of crack propagation and large displacement introduced by crack-induced free surfaces.
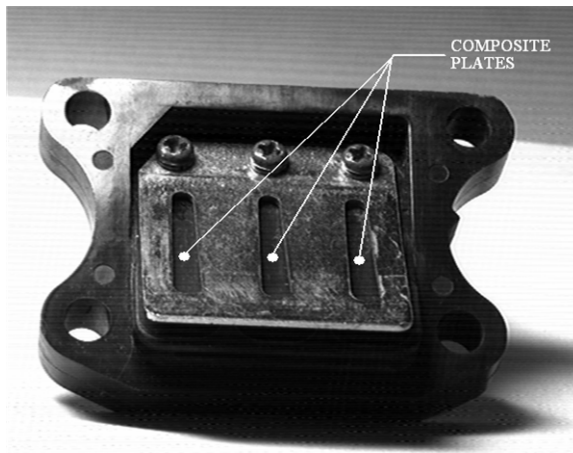

Fig. 1. An inlet-valve cover consists of three CFRP plates was used on a 4-stoke motorcycle engine [1]

Many experimental methods can be employed for vibration measurement, such as holography, modal testing method, shadow moiré method, laser Doppler vibrometer, shearography, electronic speckle pattern interferometry (ESPI), etc. Among all, the ESPI is an optical method which can provide real-time, whole-field and non-contact measurement with no special surface treatment required. The ESPI can be used for static and dynamic displacement measurement ranges within 5~100μm [2], the measurement sensitivity is as good as holography and no chemical development required. Besides, orthogonal displacement information can be obtained individually by proper optical setup.

The ESPI is also known as the TV-holography and the "Digital Speckle Pattern Interferometry" (DSPI) as video sensor and image processing hardware are utilized respectively. In 1971, Butters and Leendertz [3] demonstrated ESPI with some engineering applications including the vibration of a disc. However, detail analysis was not well described in their paper. In fact, vibration measurement is

one of the important applications of the ESPI method. The ESPI has been applied on vibration measurement in corporation with time-averaged (TA) method [4], stroboscopic method [4], the use of a pulsed laser [5] and TA based reference wave modulation method [6-8]. Because of the lower cost and simpler measurement system set up, the TA method is the easiest method to be implemented for vibration measurement. Theoretically, the absolute displacement field can be obtained by the TA ESPI method; however, the quality of the fringe patterns obtained is not good enough for accurate quantitative analysis.

In the past, many research works have been done to improve the quality of TA ESPI fringe pattern. Kerr and Tyrer [9] summarized that there are five different methods which were proposed to solve the problem of poor quality of the ESPI fringe patterns. The proposed methods are fringe tracking, spatial synchronous detection, frequency heterodyning, digital transformation and phase-steeping method. In 1989, Vikhagen [10] adopted two digital image processing methods, the max–min scanning method and the normalized max–min scanning method, to optimize fringe contrast and quality of vibration fringe patterns. It was found that the contrast of a fringe pattern can be improved by the normalized max–min scanning method by eliminating the speckle noise. Joenathan [11] adapted phase-step method with TA ESPI method and showed that the fringe patterns can be improved; in his paper, the associated S/N ratios were all developed for various phase-step methods.

In 1996, the major author and his research group [1, 12] proposed a new TA ESPI method, i.e. amplitude fluctuation (AF) ESPI method for the vibration measurement. Distinct from the conventional TA ESPI methods, the reference image of the AF ESPI method need not be obtained from the static condition but of the same nominal driving force level as the object image. In addition, higher resolution and better contrast of ESPI fringe patterns can be obtained by the AF ESPI method. The AF ESPI method is easy to implement, no extra hardware required, higher fringe density and better fringe pattern contrast can be obtained. It can be applied for quantitative displacement analysis and has been successfully applied in many engineering applications, however, how environmental disturbances and vibration characteristics affect the quality of the ESPI fringe patterns are still need to be investigated [13-15]. Besides, thanks to the improvement of computation speed, the obtained fringe patterns can be displayed in video frame rate (i.e. at least 24 images per second). Since the resolution of the ESPI is the same as the holography and the real-time fringe patterns can be taken by the ESPI, the ESPI is thus an excellent tool to investigate the fundamental problems of the TA method.

In this paper, with proper mathematical modeling and experimental design, the effect of environmental noise on the test specimen and the ESPI optical system were formulated as a function of zero order Bessel function. The formulation provides rational explanation on the time varying phenomenon of the TA ESPI images and the superiority of the AF ESPI method on the vibration measurement. The vibration characteristics were also experimentally and numerically studied.

2 Principle of Time-Averaged ESPI Method

2.1 The Traditional TA ESPI Method

A typical out-of-plane ESPI setup is shown in Fig. 1. When the specimen is under periodic motion, the light intensity detected by a CCD camera at time t can be expressed as [2]

$$I(x, y, t) = I_o + I_r + 2\sqrt{I_o I_r}\,\cos[\varphi(x, y) + \Delta(x, y, t)] \tag{1}$$

where I_o is the light intensity of the object light beam; I_r is the light intensity of the reference light beam; $\Delta = 2\pi(1 + \cos\theta)(A\cos\omega t)/\lambda$; λ is the wavelength of the light source; A is the vibration amplitude; ω is the vibration frequency; θ is the illumination angle of the object light beam; and $\varphi(x, y)$ is the random phase resulting from the surface roughness. Since a CCD camera itself accumulates the incoming light during each shutter opening time interval, τ, the output voltage, which was converted from the light intensity detected by the CCD camera, becomes

$$V_{vib} = \alpha \int_0^\tau \left[I_o + I_r + 2\sqrt{I_o I_r}\,\cos(\varphi + \Delta) \right] dt \tag{2}$$

where α is the slope of the CCD camera's sensitivity curve. Assuming τ is set to be a complete integral vibration period to avoid possible mismatch between the observed fringe patterns and the output voltage signal [1, 12], then

$$V_{vib} = \alpha\tau \left[I_o + I_r + 2\sqrt{I_o I_r}\, J_o(kA) \cos\varphi \right] \tag{3}$$

where $k = 2\pi(1 + \cos\theta)/\lambda$.

For traditional TA ESPI method, the image of the still object is taken as the reference image. Then from Eqn. (1), the reference image captured by the CCD can be expressed as

$$V_{reference} = \alpha\tau \left[I_o + I_r + 2\sqrt{I_o I_r}\,\cos\varphi \right] \tag{4}$$

In order to eliminate the background brightness, the image subtraction method is utilized. That is, the fringe patterns can be described by the following equation

$$V_{output} = \left| V_{vib} - V_{reference} \right| = 2\alpha\tau\sqrt{I_o I_r}\left[J_o(kA) - 1 \right] \cos\varphi \tag{5}$$
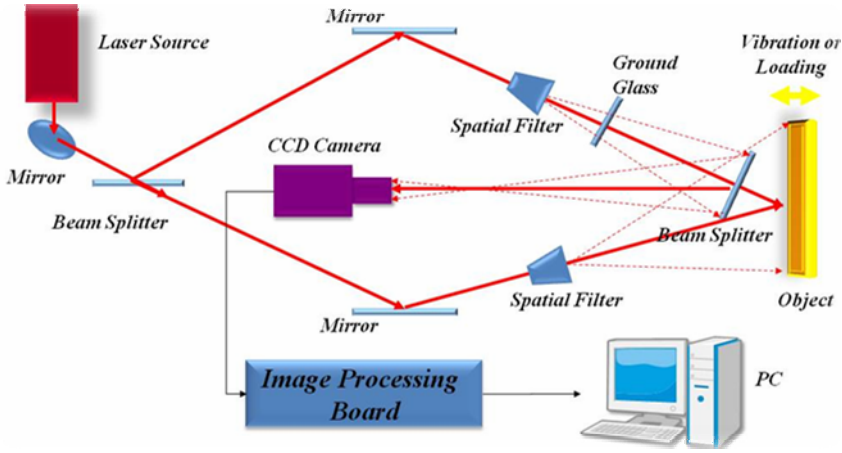
Fig. 2. Typical out-of-plane ESPI optical setup

2.2 The AF ESPI Method

The AF ESPI method for vibration measurement is also based on the traditional signal subtraction method. The essential feature of the AF ESPI lies on that both reference and object images are captured under the same nominal vibration force level. In other words, to execute the AF ESPI method, two images both subject to the vibration loading are captured. The first image is taken as the reference image and the voltage converted from the total light intensity recorded by the CCD camera is also expressed as Eqn. (3).

Since the environmental and electronic noises do exist all the time, it is appropriate to assume that the input driving force changes during each cycle. This assumption was experimentally proved [1, 12] and shown in Fig. 3 for a typical time history record of the excited force (expressed by voltage) versus time. Note that the desired input exciting force is a periodic function. However, owing to external noises, the input to the structure to be vibrated is not exactly periodic during the whole vibration period. Therefore, the amplitude of second image can be assumed to change from A into $A + \Delta A$. The output video signal of the second image now becomes

$$(V_{vib})_{disturbed} = \alpha\tau\left[I_o + I_r + 2\sqrt{I_oI_r}J_o\left(\frac{2\pi}{\lambda}(A + \Delta A)(1 + \cos\theta)\right)\cos\varphi\right] \qquad (6)$$

By using the image processing system, the resulting voltage signal $V_{output} = (V_{vib})_{disturbed} - V_{vib}$ can be expressed as

$$V_{output} = \alpha\tau\left[2\sqrt{I_o I_r}\left(J_o(k(A+\Delta A)) - J_o(kA)\right)\cos\varphi\right] \qquad (7)$$

In fact, ΔA is one of the undetermined parameters. As indicated in Eqn. (7), the output voltage V_{output} is expressed by the zero-order Bessel function. It is impossible to express concisely the relationship between the output voltage signal and the undisturbed vibration amplitude A. Hence, additional mathematical modification must be used. Considering ΔA is rather small, dividing each side of Eqn. (7) by ΔA, and evaluating the limits of both sides, Eqn. (7) is then simplified and expressed as a function of vibration amplitude only, i.e.

$$\frac{dV_{output}}{dA} = -2\alpha\tau\left[\sqrt{I_o I_r}\,J_1(kA)\cos\varphi\right] \qquad (8)$$

Eqn. (8) can be interpreted as the video-signal sensitivity of the vibration amplitude. To avoid all possible mistakes introduced when signal is transformed into the gray level; the negative voltage value must be rectified into the positive value, then the output signal becomes

$$V_{AFESPI} = 2\alpha\tau\sqrt{I_o I_r}\left[J_1^2(kA)\cos^2\varphi\right]^{1/2} \qquad (9)$$
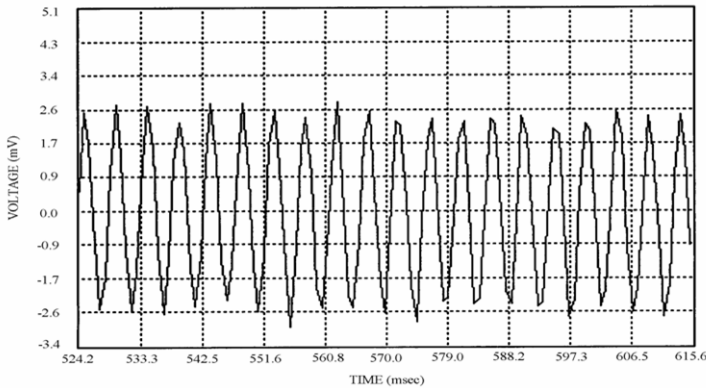

Fig. 3. Typical excited force-time histogram recorded by a force sensor attached to the driving rod with input sinusoidal exciting force. The diagram shows that the driving force fluctuates about the nominal value [1, 12].

Based on Eqn. (9), the vibration amplitude of the specimen can be obtained by a set of $kA = \zeta_i^*$, which can null Eqn. (9); then the amplitude is determined by

$$A = \frac{\lambda \zeta_i^*}{2\pi(1+\cos\theta)} \tag{10}$$

3 Experiments and Discussions

To perform the experiments, a self-assembled ESPI system as shown in Fig. 1 was used. The system is composed of two parts, the out-of-plane optical setup and the image processing system. As for the ESPI out-of-plane optical setup, a 35 mW He-Ne laser of wavelength 632.8 nm was used as the light source. Regarding the image processing subsystem, the commercial software Intelliwave [16] was utilized for image capturing and analysis. To excite the specimen with a sinusoidal force, a shaker (LDS Co., U.K.) was used. The exciting force was detected by a force sensor (PCB Co., U.S.A.) and the force history was monitored and recorded by a Signal Doctor Spectrum Analyzer (ProWave Co., Taiwan, R.O.C). As for the test specimen, an aluminum alloy plate of length 220 mm, width 130 mm and thickness 2.2 mm was used. As shown in Fig. 4, 40 mm of the specimen along the longitudinal direction is fastened by a vise to simulate clamped edge boundary condition.
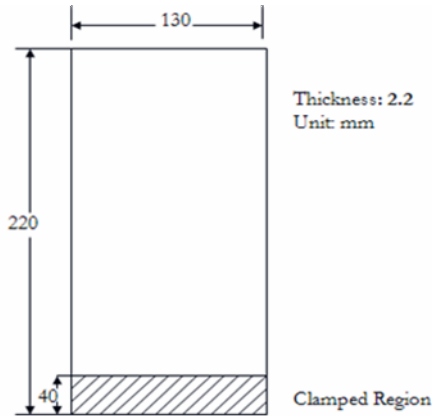

Fig. 4. An aluminum plate with described geometrical dimensions was used as the specimen to evaluate TA ESPI vibration measurement [15]

As described in Eqn. (5), the TA ESPI displacement and fringes can be determined by the function $[J_o(kA)-1]$. The TA ESPI fringe patterns show bright fringes when $[J_o(kA)-1]$ are local maximums and become dark ones as $[J_o(kA)-1]$

are local minimums. According to Eqn. (3), the dark fringes can be observed along the nodal lines, the nodal points and fixed edges where the associated displacements are zero and should be time invariant. With improvements of the image processing system, ESPI method can be performed in frame rate and fringe patterns can be recorded continuously. To re-examine the match between Eqn. (3) and experimental results, in this paper, TA was used with the out-of-plane ESPI optical setup. Since nodal lines of both 2nd and 4th resonant modes are easily determined, a video recording system was also used to record the 2nd and the 4th resonant mode fringe patterns of the aluminum plate. As observed from the recorded images, the TA ESPI fringe patterns vary with time. In fact, this time varying phenomenon cannot be easily observed without the frame rate image processing and/or continuously image recording aperture is adopted for image processing. For discussion purpose, as shown respectively in Fig. 5 and Fig. 6, five images were extracted from each of the recorded images of the 2nd and 4th modes without denotative time.
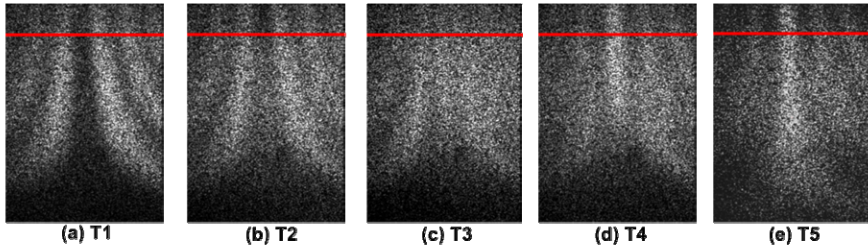

Fig. 5. The time variation of TA ESPI fringe patterns of the 2nd mode. The red line is used to highlight the area for gray level analysis.

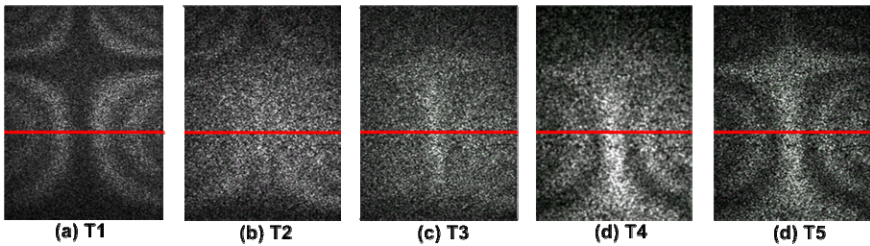**Fig. 6.** The time variation of TA ESPI fringe patterns of the 4th mode. The red line is used to highlight the area for gray level analysis

In Fig. 5, two phenomena can be observed. Firstly, the visibility of the fringe patterns is lower in images captured at time intervals T2, T3 and T4 with respect to images captured at time intervals T1 and T5. Secondly, the nodal line of the

2nd mode is a dark band in image captured at time interval T1 and becomes a bright one at time interval T5. In addition, fringe pattern at clamped edge of the specimen also turns bright. Similar results can also be observed for 4th mode (Fig. 6), i.e. the visibility of fringe patterns first becomes lower (time intervals T2 and T3) and then recovers as time increases (time intervals T4 and T5), and in particular, the nodal lines and clamped edge become bright.

To identify the variation of gray levels with time, the gray levels along the red line across the fringe patterns of Figs. 5 and 6 were processed by fast Fourier transform (FFT) and low pass filter was utilized to filter out speckle noises [13]. The associated speckle-free normalized gray levels are plotted in Figs. 7 and 8 for the 2nd and 4th modes, respectively. According to the obtained normalized gray level distributions, without any doubt, images captured at time intervals T1 and T5 give better fringe visibility than the other extracted images. Besides, from the geometrical symmetry of the specimen and the normalized gray level plots, the nodal lines of 2nd mode and 4th mode should be located at around 150th pixels counting from the left edge of the specimen. From the normalized gray level plots, the gray levels at 150th pixels of both images extracted at time interval T1 are lowest, and the normalized gray levels changes into the highest ones for both images captured at time interval T5. In short, the gray levels of fringe patterns extracted at time intervals T1 and T5 are opposite to each other, i.e. the bright bands in images of time interval T1 become dark bands for images of time interval T5. Even though the gray levels of the two fringe patterns at time intervals T1 and T5 are opposite to each other, the extreme values of gray levels at time intervals T1 and T5 occur almost at the same location.
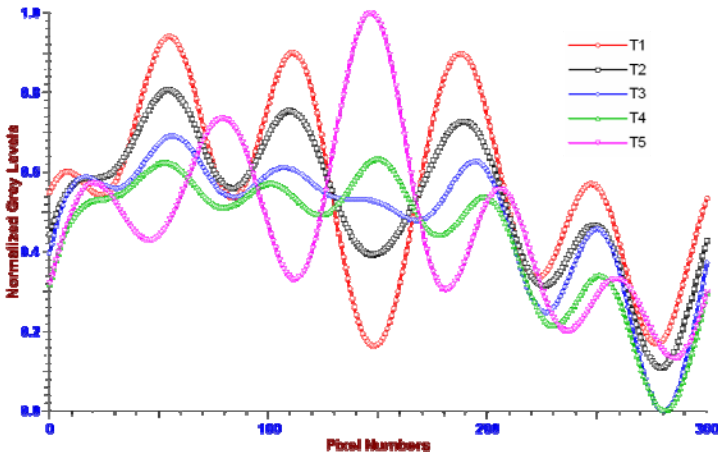

Fig. 7. The distribution of normalized gray levels of TA ESPI fringe patterns of the aluminum plate excited at 2nd mode at different time intervals
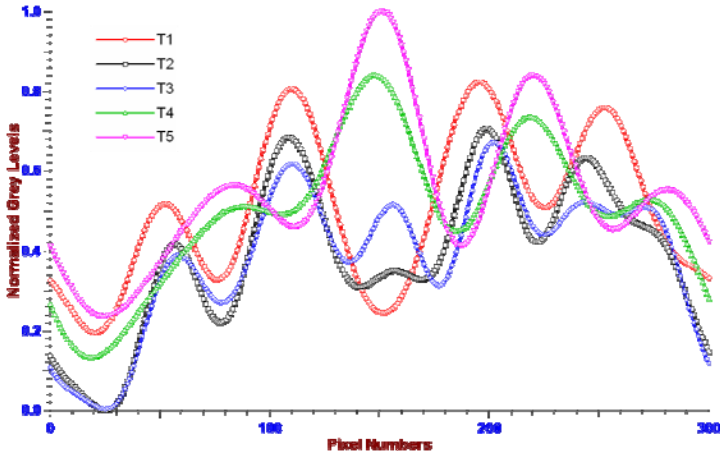
Fig. 8. The distribution of normalized gray levels of TA ESPI fringe patterns of the aluminum plate excited at 4th mode at different time intervals

As for the AF ESPI, the fringe patterns were also processed in frame rate and recorded. Without extracting images at particular time, as shown in Fig. 9, the images of five different time intervals are rather consistent; however, the visibility of images extracted at time T3 and T4 are a little bit lower than those of the other three time intervals. The normalized gray levels of fringes after FFT and low pass filter operations are shown in Fig. 10. By comparing with Figs. 7 and 8, the normalized gray levels of the AF ESPI are relatively stable with respect to those of the TA ESPI.
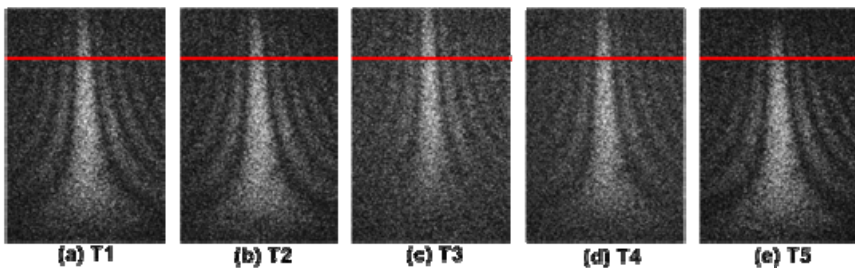

Fig. 9. The time variation of TA ESPI fringe patterns of the 2nd mode. The red line is used to highlight the area for gray level analysis
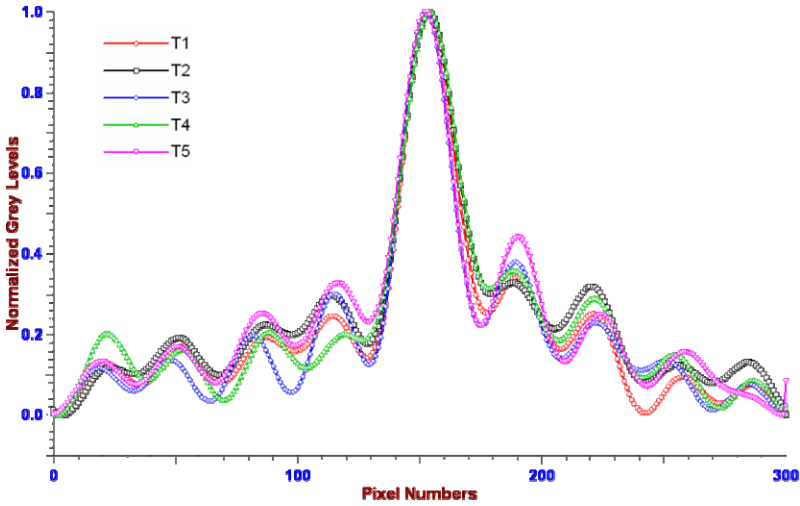
Fig. 10. The distribution of normalized gray levels of AF ESPI fringe patterns of the aluminum plate excited at 2nd mode at different time intervals

To explain why fringe patterns obtained by TA ESPI method change with time, the effect of environmental noise on the optical setup should be first considered. Assuming the environmental noise acts on the optical setup and introduces the additional phase change $\delta(x, y, t)$; Eqn. (1) can then be modified as

$$I(x, y, t) = I_o + I_r + 2\sqrt{I_o I_r} \cos[\varphi(x, y) + \Delta(x, y, t) + \delta(x, y, t)] \tag{11}$$

The environmental noise spectrum covers wide frequency ranges; however, in this paper, only low frequency environmental noise was discussed. Because of filtering or damping low frequency environmental noises cannot be done easily. As mentioned earlier, for an ESPI system, the CCD will accumulate the incoming light during each shutter opening time interval; then the general output voltages which are converted from the CCD camera detected light intensity, becomes

$$V_g = \alpha \int_0^\tau [I_o + I_r + 2\sqrt{I_o I_r} \cos(\varphi + \Delta + \delta)] dt \tag{12}$$

In the TA ESPI method, the reference image is captured from a specimen not subject to periodic driving force. The phase term, Δ introduced by the input vibration can thus be dropped, Eqn. (12) then becomes

$$V_g = \alpha \int_0^\tau [I_o + I_r + 2\sqrt{I_o I_r} \cos(\varphi + \delta)] dt \tag{13}$$

Assuming the CCD camera's frame frequency (number of frames can be captured per second) is much higher than the frequencies of environmental noise acting on

the ESPI optical system, the phase $\delta(x,y,t)$ is simplified as a linear function of time [17], i.e.

$$\delta(x,y,t) = \Phi(x,y) + \beta(x,y)t \tag{14}$$

where $\Phi(x,y)$ is the initial phase term and $\beta(x,y)$ is the time-averaged phase change. Then V_g can be approximated as

$$V_g = \alpha\tau\left[I_o + I_r + 2\sqrt{I_o I_r}\,\cos\big(\varphi + (\Phi + \beta\tau/2)\big)\right] \tag{15}$$

Similarly, the captured image of the specimen under vibration can be determined [18], i.e.

$$V_{g-vib} = \alpha\tau(I_o + I_r) +$$
$$2\alpha\sqrt{I_o I_r}\left[\cos(\varphi + \Phi*)\frac{\sin\beta*\tau}{\beta*} + \sin(\varphi + \Phi*)\frac{\cos\beta*\tau - 1}{\beta*}\right]J_o(kA) \tag{16}$$

It should be noted that that the images under vibration are captured at different time intervals with respect to the reference image, i.e. the initial phase term and the time-averaged phase change are different. In Eqn. (16), the superscript * denotes the environmental noise which is different from the reference one.

If the environmental noise does not change significantly, then both $\beta\tau$ and $\beta*\tau$ are small, Eqns. (15) and (16) can be respectively simplified into

$$V_g = \alpha\tau\left[I_o + I_r + 2\sqrt{I_o I_r}\,\cos(\varphi + \Phi)\right] \tag{17}$$

$$V_{g-vib} = \alpha\tau\left[I_o + I_r + 2\sqrt{I_o I_r}\,\cos(\varphi + \Phi*)J_o(kA)\right] \tag{18}$$

Assuming the initial phases of reference and object images are related by

$$\Phi* = \Phi + \delta\Phi \tag{19}$$

Then the traditional TA ESPI can be remodeled and the output voltage of TA ESPI method can be modified as [14]

$$V_{output} = \left|V_{g-vib} - V_g\right|$$
$$= 2\alpha\tau\sqrt{I_o I_r}\left[\left[J_o(kA)\cos(\delta\Phi) - 1\right]^2 + \left[J_o(kA)\sin(\delta\Phi)\right]^2\right]^{1/2}\left|\sin(\phi + \Phi + \varsigma)\right| \tag{20}$$

where $\varsigma = \tan^{-1}\dfrac{J_o(kA)\sin(\delta\Phi)}{\left[J_o(kA)\cos(\delta\Phi) - 1\right]}$.

The fringe patterns of TA ESPI method can be determined by the function $f(k, A, \delta\Phi)$, i.e.

$$f(k, A, \delta\Phi) = \left[\left[J_o(kA)\cos(\delta\Phi) - 1 \right]^2 + \left[J_o(kA)\sin(\delta\Phi) \right]^2 \right]^{1/2}. \tag{21}$$

The fringe patterns are not only determined by vibration amplitude and ESPI optical setup but also determined by the environmental noise introduced equivalent initial phase difference, $\delta\Phi$. When $\delta\Phi = 0$, Eqn. (21) becomes $f(k, A, \delta\Phi) = \left[J_o(kA) - 1 \right]$, this is the same as the traditional TA ESPI, the nodal lines and the clamped edge in the fringe patterns should appear in dark. When $\delta\Phi = \pi$, Eqn. (21) becomes $f(k, A, \delta\Phi) = \sqrt{J_o^2(kA) + 1}$. Different from the case of $\delta\Phi = 0$, the fringe patterns along nodal lines and clamped edge become the brightest ones. The normalized gray levels plot of Eqn. (21) is shown in Fig. 11. There are dark fringes along the nodal lines and clamped edge as $\delta\Phi$ increases
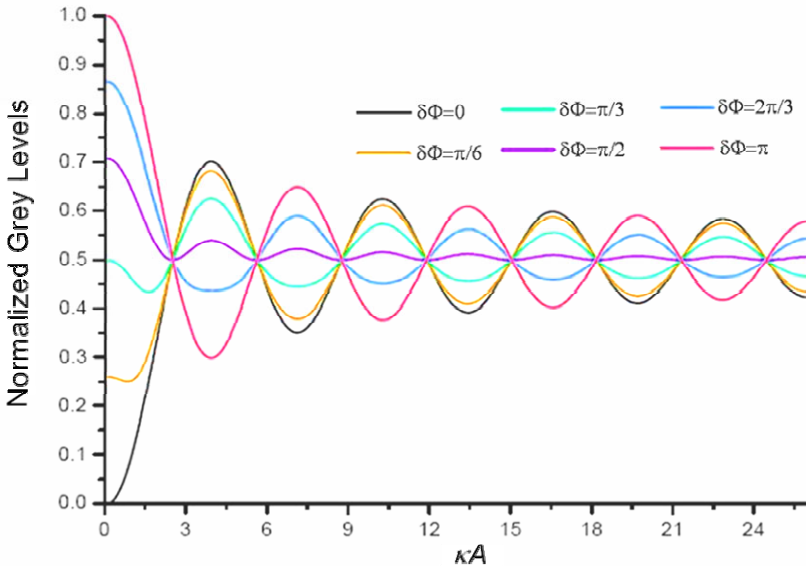

Fig. 11. Modified fringe formula with environmental noise introduced equivalent initial phase difference, $\delta\Phi$, considered

from 0 to $\pi/3$, and then the fringes become bright ones as $\delta\Phi$ increases from $\pi/3$ to π. Besides, the visibility of the fringe pattern becomes worst as $\delta\Phi$ increases from 0 up to $\pi/2$, and then the visibility increases as $\delta\Phi$ increases from $\pi/2$ to π. The above results well describe the phenomenon shown in Figs. 5 and 6, i.e. the visibility of fringe patterns first becomes lower and then recovers as time increases, and in particular, the nodal lines and clamped edge become bright.

4 Engineering Applications of the AF ESPI Method

The AF ESPI method was first used to investigate the fracture behavior of the edge-cracked composite plates [19, 20] and determine modified mode III stress intensity factors (SIFs) of different resonant frequencies. Vibration behavior was investigated for composite plates containing circular defect at different depths [21], shadow masks [22] and printed circuit boards [23]. The repair efficiency of composite patching of edge- and center-cracked aluminum and carbon fiber reinforced plastic (CFRP) plates [24, 25] was evaluated by the AF-ESPI method. In addition, nondestructive inspection of composite plates containing defects [26-28] was also performed by the AF ESPI method.

5 Conclusions

In this paper, by continuously recording TA ESPI and AF ESPI fringe patterns, the traditional time-averaged ESPI was re-examined. The recorded fringe patterns obtained by TA ESPI showed that they vary from time to time. For the extreme case, the gray levels of two fringe patterns at different time intervals are opposite to each other. No matter how the gray level changes, fortunately, the extreme values of the gray level still occur at the same location. On the contrary, AF ESPI fringe patterns remain essentially stable with almost nil visibility difference as time increases. A new mathematical model was proposed to describe the TA ESPI method. With environmental noises considered, the new model has the form $\sqrt{[J_o(kA)\cos(\delta\Phi)-1]^2 + [J_o(kA)\sin(\delta\Phi)]^2}$. Based on the proposed new model, the time variation as well as the decreasing and recovering of visibility of the fringe pattern can be well predicated by environmental noise introduced equivalent initial phase difference, $\delta\Phi$. The results indicate that the importance of $\delta\Phi$ between the reference image and the object image as TA ESPI is adopted for vibration measurement. At the end of this paper, a summary of the applications of AF ESPI method is provided.

Acknowledgement

References

1. Hwang, C.H.: Investigation of vibration characteristics of composite plates containing defect by amplitude-fluctuation ESPI, Ph. D. Dissertation. Department of Power Mechanical Engineering, National Tsing Hua University, Taiwan, Republic of China (1996)
2. Jones, R., Wykes, C.: Holographic and speckle interferometry. Cambridge University Press, Cambridge (1989)
3. Butters, J.N., Leendertz, J.A.: Holographic and video techniques applied to engineering measurement. J Measurement and Control 4, 349–354 (1971)
4. Pedersen, H.M., Løkberg, O.J., Førre, B.M.: Holographic vibration measurement using a TV speckle interferometer with silicon target vidicon. Optics Communications 12, 421–426 (1974)
5. Santoyo, F.M., Shellabear, M.C., Tyrer, J.R.: Whole field in-plane vibration analysis using pulsed phase-stepped ESPI. Applied Optics 30, 717–721 (1991)
6. Løkberg, O.J., Høgmoen, K.: Use of modulated reference wave in electronic speckle pattern interferometry. J Physics E: Scientific Instruments 9, 847–851 (1976)
7. Løkberg, O.J., Høgmoen, K.: Vibration phase mapping using electronic speckle pattern interferometry. Applied Optics 15, 2701–2704 (1976)
8. Høgmoen, K., Løkberg, O.J.: Detection and measurement of small vibrations using electronic speckle pattern interferometry. Applied Optics 16, 1869–1875 (1977)
9. Kerr, D., Jyrer, J.R.: The application of phase stepping to the analysis of ESPI fringe patterns. In: SPIE 814, Photomechanics and Speckle Metrology, pp. 379–389 (1987)
10. Vikhagen, E.: Vibration measurement using phase shifting TV-holography and digital image processing. Optics Communications 69, 214–218 (1989)
11. Joenathan, C.: Vibration fringes by phase stepping on an electronic speckle pattern interferometer: an analysis. Applied Optics 30, 4658–4665 (1991)
12. Wang, W.C., Hwang, C.H., Lin, S.Y.: Vibration measurement by the time-averaged ESPI methods. Applied Optics 35, 4502–4509 (1996)
13. Wang, W.C., Hwang, C.H., Hsu, T.W.: The intrinsic characteristics of the ESPI fringe patterns. In: Proc. SEM Annual Conf. on Exp. and App. Mech., OR, USA (2001)
14. Chang, Y.L.: Theoretical and experimental re-examination of the vibration measurement using time-averaged electronic speckle pattern interferometry. MS Thesis, Department of Power Mechanical Engineering, National Tsing Hua University, Taiwan, R. O. C (2008) (in Chinese)
15. Wang, W.C., Hwang, C.H., Chang, Y.L.: Re-examination of the time-averaged electronic speckle pattern interferometry method on vibration measurement. In: Proc. SEM Fall Int Symposium to Commemorate the 60th Anniversary of the Invention of Holography, MA, USA, pp. 228–237 (2008)

16. "Intelliwave", Version 5.008, Engineering Synthesis Design, Inc., Tucson, AZ, USA (2006)
17. Hwang, C.H., Wang, W.C.: On the vibration measurement by using electronic speckle metrologies with different driving force levels. In: Proc. Int. Conf. on Advanced Tech. in Exp. Mech., Ube, Japan (1999)
18. Hsu, T.W.: Theoretical and Experimental Investigation of the Modified Electronic Speckle Metrologies. MS Thesis, Department of Power Mechanical Engineering, National Tsing Hua University, Taiwan, Republic of China (2000) (in Chinese)
19. Wang, W.C., Hwang, C.H., Lin, S.Y.: Vibration measurement of composite plates containing defect at different depths by amplitude fluctuation ESPI method. Proc. VIII Int. Congress on Exp. Mech., TN, USA (1996)
20. Wang, W.C., Hwang, C.H.: Vibration measurement of an edge-cracked composite plate by amplitude fluctuation ESPI method. In: Proc. 9th Int Congress on Frac., Sydney, Australia (1997)
21. Wang, W.C., Hwang, C.H.: Experimental analysis of vibration characteristics of an edge-cracked composite plate by ESPI method. Int. J. Frac. Mech. 91, 311–321 (1998)
22. Wang, W.C., Tsai, Y.H.: Experimental vibration analysis of the shadow mask. Optics and Lasers in Eng. 30, 539–550 (1998)
23. Wang, W.C., Lai, K.H.: Experimental investigation of vibration of the shadow mask with different assembly conditions. IEEE Consumer Electronics 45, 1046–1056 (1999)
24. Wang, W.C., Hsu, J.S.: Investigation of the size effect of composite patching repaired on edge-cracked plates. Comp. Struct. 49, 415–423 (2000)
25. Wang, W.C., Chen, C.H.: Investigation of vibration behavior of patched edge-cracked composite plates. J Reinforced Plastics and Comp. 21, 533–557 (2002)
26. Lai, K.H.: Investigation of Vibration Behavior of Perforated Components on Elastic Supports by Hybrid Method. Ph. D. Dissertation, Department of Power Mechanical Engineering, National Tsing Hua University, Taiwan, Republic of China (2002)
27. Yang, C.C.: Investigation of Dynamic Behavior of Composite Plates Containing Defects. MS Thesis, Department of Power Mechanical Engineering, National Tsing Hua University, Taiwan, Republic of China (2002) (in Chinese)
28. Su, C.W.: Nondestructive Inspection and Vibration Analysis of Composite Plates Containing Defects. MS Thesis, Department of Power Mechanical Engineering, National Tsing Hua University, Taiwan, Republic of China (2003) (in Chinese)

Part III
Fracture Mechanics

Piezonuclear Transmutations in Brittle Rocks under Mechanical Loading: Microchemical Analysis and Geological Confirmations

A. Carpinteri[1], G. Lacidogna[1], A. Manuello[1], and O. Borla[1,2]

[1] Politecnico di Torino, Department of Structural Engineering & Geotechnics
  Corso Duca degli Abruzzi 24 – 10129 Torino, Italy
[2] Istituto Nazionale di Fisica Nucleare, INFN sez. Torino
  Via Pietro Giuria 1 – 10125 Torino, Italy
  `alberto.carpinteri@polito.it, giuseppe.lacidogna@polito.it,`
  `amedeo.manuellobertetto@polito.it, oscar.borla@polito.it`

Abstract. Neutron emission measurements, by means of ^{3}He devices and bubble detectors, were performed during three different kinds of compression tests on brittle rocks: (i) under monotonic displacement control, (ii) under cyclic loading, and (iii) by ultrasonic vibration. The material used for the tests was Green Luserna Granite. Since the analyzed material contains iron, our conjecture is that piezonuclear reactions involving fission of iron into aluminium, or into magnesium and silicon, should have occurred during compression damage and failure. This hypothesis is confirmed by Energy Dispersive X-ray Spectroscopy (EDS) tests conducted on Luserna Granite specimens. It is also interesting to emphasize that the present natural abundances of aluminum (~8%), and silicon (28%) and scarcity of iron (~4%) in the continental Earth's crust should be possibly due to the piezonuclear fission reactions considered above.

Keywords: Neutron emission, Piezonuclear reactions, Rocks crushing failure, Energy Dispersive X-ray Spectroscopy, Plate tectonics, Element evolution.

1 Introduction

We deal with a new topic in the scientific literature: piezonuclear neutron emissions from brittle rock specimens under mechanical loading. The phenomenon is analyzed from an experimental point of view. In the scientific community some studies have been already conducted on the different forms of energy emitted during the failure of brittle materials. They are based on the signals captured by the acoustic emission measurement systems, or on the detection of the electromagnetic charge. On the other hand, only very recently piezonuclear neutron emissions from very brittle rock specimens in compression have been discovered [1-3].

In this paper, after summarizing the preliminary results already presented in [1-3], involving compression tests on prismatic specimens of Carrara Marble and Green Luserna Granite, we present new experiments, using ^{3}He neutron detectors and bubble type BD thermodynamic neutron detectors, performed on brittle rock test specimens. We carried out three different kinds of compression tests: (i) under monotonic displacement control, (ii) under cyclic loading, and (iii) by ultrasonic solicitations. The material used for the compression tests was non-radioactive Green Luserna Granite, with different specimen size and shape and consequently with different brittleness numbers. The compression tests were performed at the Fracture Mechanics Laboratory of the Politecnico of Torino, while the ultrasonic test at the Medical and Environmental Physics Laboratory of the University of Torino.

For specimens of larger dimensions, neutron emissions, detected by ^{3}He, were found to be of about one order of magnitude higher than the ordinary natural background level at the time of the catastrophic failure. As regards test specimens with more ductile behaviour, neutron emissions significantly higher than the background level were found. These piezonuclear reactions are due to the different modalities of energy release during the tests. For specimens with sufficiently large size and slenderness, relatively large energy release is expected, and hence a higher probability of neutron emissions at the time of failure. Furthermore, during compression tests under cyclic loading, an equivalent neutron dose, analysed by neutron bubble detectors, about two times higher than the ordinary background level was found at the end of the test.

Finally, by using an ultrasonic horn suitably joined with the specimen, an ultrasonic test was carried out on a Green Luserna Granite specimen in order to produce continuing vibration at 20 kHz. Three hours after the beginning of the test, an equivalent neutron dose about three times higher than the background level was found.

Moreover, Energy Dispersive X-ray Spectroscopy (EDS) was performed on different samples of external or fracture surfaces belonging to specimens used in the preliminary piezonuclear tests [4]. For each sample, different measurements of the same crystalline phases (phengite or biotite) were performed in order to get averaged information of the chemical composition and to detect possible piezonuclear transmutations from iron to lighter elements. The samples were carefully chosen to investigate and compare the same minerals before and after the crushing failure. Phengite and biotite, that are rather common in the Luserna Granite (20% and 2%, respectively), were considered owing to the high iron concentration in their chemical compositions. The results of EDS analyses show that, on the fracture surface samples, a considerable reduction in the iron content (~25%) is counterbalanced by a nearly equal increase in Al, Si, and Mg concentrations.

Our conjecture is that piezonuclear reactions involving fission of iron into aluminum, or into magnesium and silicon, should have occurred during compression on the tested specimens. The present natural abundances of aluminum (~8%), and silicon (28%) and scarcity of iron (~4%) in the continental Earth's crust are possibly due to the piezonuclear fission reactions considered above. This reaction

would be activated where the environment conditions (pressure and temperature) are particularly severe, and mechanical phenomena of fracture, crushing, fragmentation, comminution, erosion, friction, etc., may occur. If we consider the evolution of the percentages of the most abundant elements in the Earth crust during the last 4.5 billion years, we realize that iron and nickel have drastically diminished, whereas aluminum, silicon and magnesium have as much increased. It is also interesting to realize that such increases have developed mainly in the tectonic regions, where frictional phenomena between the continental plates occurred [1-3, 5].

2   Neutron Emission Detection Techniques

Since neutrons are electrically neutral particles, they cannot directly produce ionization in a detector, and therefore cannot be directly detected. This means that neutron detectors must rely upon a conversion process where an incident neutron interacts with a nucleus to produce a secondary charged particle. These charged particles are then detected, and from them the neutrons presence is deduced. For an accurate neutron evaluation, a ^{3}He proportional counter and a set of passive neutron detectors, based on superheated bubble detection technique, insensitive to electromagnetic noise, were employed.

2.1 ^{3}He Proportional Counter

The ^{3}He detector used in the tests is a ^{3}He type (Xeram, France) with electronics of preamplification, amplification, and discrimination directly connected to the detector tube. The detector is powered with high voltage power supply (about 1.3 kV) via NIM (Nuclear Instrument Module) module. The logic output producing the TTL (through the lens) pulses is connected to a NIM counter. The logic output of the detector is enabled for analog signals exceeding 300 mV. This discrimination threshold is a consequence of the sensitivity of the ^{3}He detector to the gamma rays ensuing neutron emission in ordinary nuclear processes. This value has been determined by measuring the analog signal of the detector by means of a Co-60 gamma source. The detector is also calibrated for the measurement of thermal neutrons; its sensitivity is 65 cps/$n_{thermal}$, i.e., the flux of thermal neutrons was 1 thermal neutron/s cm^2, corresponding to a count rate of 65 cps.

2.2   Neutron Bubble Detectors

A set of passive neutron detectors insensitive to electromagnetic noise and with zero gamma sensitivity was used. The dosimeters, based on superheated bubble detectors (BTI, Ontario, Canada) (BUBBLE TECHNOLOGY INDUSTRIES (1992)) [6], are calibrated at the factory against an AmBe (Americium-Beryllium) source in terms of NCRP38 [7]. Bubble detectors are the most sensitive, accurate neutron dosimeters available that provide instant visible detection and measurement of neutron dose. Each detector is composed of a polycarbonate vial filled

with elastic tissue equivalent polymer, in which droplets of a superheated gas (Freon) are dispersed. When a neutron strikes a droplet, the latter immediately vaporizes, forming a visible gas bubble trapped in the gel. The number of droplets provides a direct measurement of the equivalent neutron dose with an efficiency of about 20%. These detectors are suitable for neutron dose measurements, in the energy range of thermal neutrons (E = 0,025eV, BDT type) and fast neutrons (E > 100 keV, BD-PND type).

3 Preliminary Tests on Prismatic Specimens in Carrara Marble and Green Luserna Granite

Preliminary tests on prismatic specimens were presented in previous contributions, recently published [1-3], and related to piezonuclear reactions occurring in solids containing iron −samples of granite rocks− in compression. The materials selected for the compression tests were Carrara Marble (calcite) and Green Luserna Granite (gneiss). This choice was prompted by the consideration that, test specimen dimensions being the same, different brittleness numbers [8] would cause catastrophic failure in granite, not in marble. The test specimens were subjected to uniaxial compression to assess scale effects on brittleness [9].

Four test specimens were used, two made of Carrara Marble and two made of Luserna Granite (Fig. 1). All of them were of the same size and shape, measuring $6 \times 6 \times 10$ cm^3. The same testing machine was used on all the test specimens: a standard servo-hydraulic press with a maximum capacity of 500 kN, equipped with control electronics. This machine makes it possible to carry out tests in either load control or displacement control. The tests were performed in piston travel displacement control by setting, for all the test specimens, a velocity of 0.001 mm/s during compression. Neutron emission measurements were made by means of a ^{3}He detector placed at a distance of 10 cm from the test specimen and enclosed in a polystyrene case, to prevent the results from being altered by impacts or vibrations.

The measurements of neutron emissions obtained on marble yielded values comparable with the background, even at the time of test specimen failure. The neutron measurements obtained on the two granite test specimens, instead, exceeded the background value by about one order of magnitude when catastrophic failure occurred. The first granite test specimen reached at time T = 32 min a peak load of ca 400 kN, corresponding to an average pressure on the bases of 111.1 MPa. When failure occurred, the count rate was found to be: $(28.3\pm0.2)\cdot10^{-2}$ cps corresponding to an equivalent flux of thermal neutrons of: $(43.6\pm0.3)\cdot10^{-4}$ $n_{thermal}$ cm^{-2}s^{-1}. The second granite test specimen reached at time T = 29 min a peak load of ca 340 kN, corresponding to an average pressure on the bases of 94.4 MPa. When failure occurred, the count rate was found to be: $(27.2\pm0.2)\cdot10^{-2}$ cps corresponding to an equivalent flux of thermal neutrons of $(41.9\pm0.3)\cdot10^{-4}$ $n_{thermal}$ cm^{-2}s^{-1}.
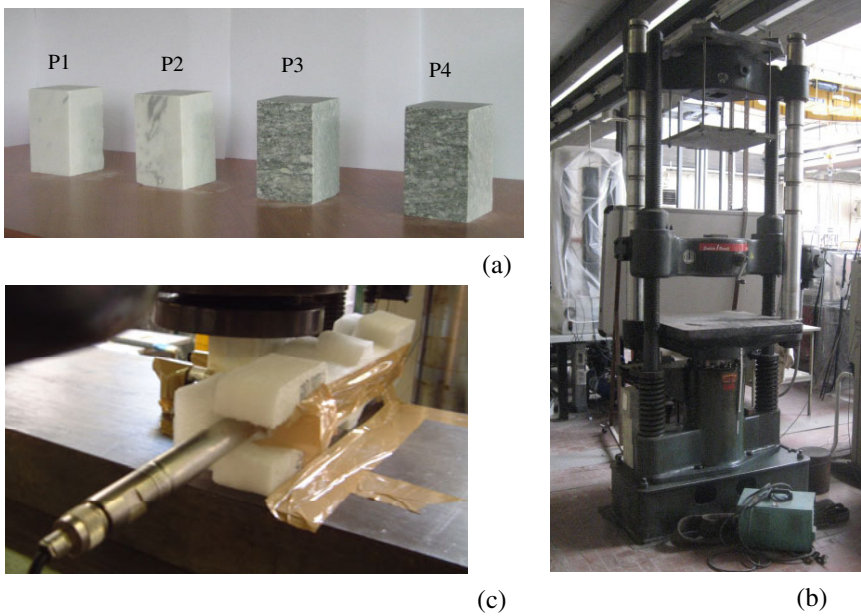
Fig. 1. The test specimens analysed, two in Carrara Marble (P1, P2) and two in Luserna Granite (P3, P4), measured 6x6x10 cm^3 (a). Baldwin servo-controlled press used for the compression tests (b). ^{3}He neutron detector placed in the proximity of test specimen P1 during the test. The detector is enclosed in a polystyrene case for protection against possible impacts due to test specimen failure (c)

These phenomena could be caused by piezonuclear reactions, that occurred in the granite, but did not in the marble. Moreover, granite contains iron, which appears to be the most favourable element for the production of piezonuclear reactions [1-3]. More particularly, the Carrara Marble used in the piezonuclear tests [1-3] contains only iron impurities (not more than 0.07% of Fe_2O_3 as total Fe), Luserna Granite instead contains a considerable amount of iron oxides (~3% of Fe_2O_3 as total Fe). For these reasons the iron content of the Luserna Granite used in the piezonuclear experiments could contribute to the phenomenon in question. These experimental evidences induced the authors to carry out further tests on cylindrical Green Luserna Granite specimens of different size and shape.

4   Experimental Set-Up

4.1   Compression Tests under Monotonic Displacement Control

Neutron emissions were measured on nine Green Luserna Granite cylindrical specimens, of different size and shape (Fig. 2, Table 1), denoted with P1, P2,…, P9.

The tests were carried out by means of a servo-hydraulic press, with a maximum capacity of 1800 kN, working by a digital type electronic control unit. The management software was TESTXPERTII by Zwick/Roel (Zwick/Roel Group, Ulm, Germany), while the mechanical parts are manufactured by Baldwin (Instron Industrial Products Group, Grove City, PA, USA). The force applied was determined by measuring the pressure in the loading cylinder by means of a transducer. The margin of error in the determination of the force is 1%, which makes it a class 1 mechanical press. The specimens were arranged with the two smaller surfaces in contact with the press platens, without coupling materials in-between, according to the testing modalities known as "test by means of rigid platens with friction". The tests were performed under displacement control, with the planned displacement velocities ranging from 0.001 to 0.01 mm/s.

The ^{3}He neutron detector was switched on at least one hour before the beginning of each compression test, in order to reach the thermal equilibrium of electronics, and to make sure that the behaviour of the devices was stable with respect to intrinsic thermal effects. The detector was placed in front of the test specimen at a distance of 20 cm and it was enclosed in a polystyrene case of 10 cm of thickness in order to avoid "spurious" signals coming from impact and vibration.

A relative measurement of natural neutron background was performed in order to assess the average background affecting data acquisition in experimental room condition. The ^{3}He device was positioned in the same condition of the experimental set-up and the background measures were performed fixing at 60 s the acquisition time, during a preliminary period of more than three hours, for a total number of 200 counts. The average measured background level is ranging from $(3.17\pm0.32)\cdot10^{-2}$ to $(4.74\pm0.46)\cdot10^{-2}$ cps (see Table 2).
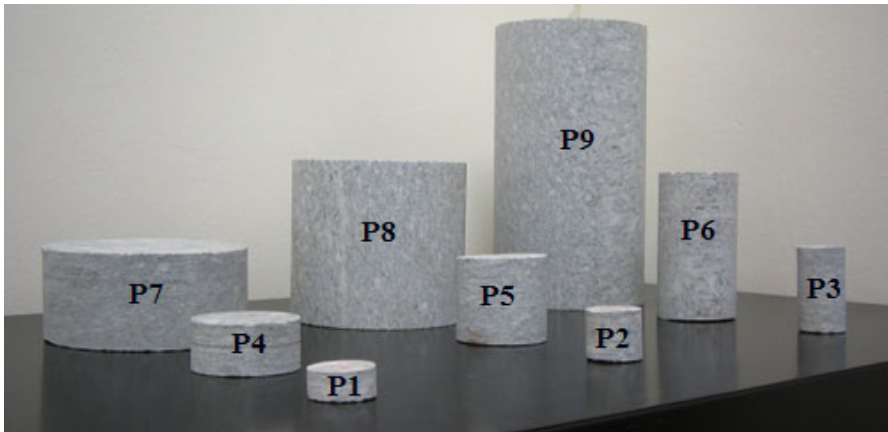

Fig. 2. Green Luserna Granite cylindrical specimens, by varing slenderness and size-scale

Table 1. Characteristics of compression tests under monotonic displacement control on Green Luserna Granite specimens

Granite Specimen	Geometry of the specimen			Displacement velocity (mm/s)	Peak Load (kN)	Time at the peak load (s)
	D (mm)	H (mm)	λ=H/D			
P1	28	14	0.5	0.001	52.19	735.0
P2	28	28	1	0.001	33.46	1239.0
P3	28	56	2	0.001	41.28	1089.0
P4	53	25	0.5	0.001	129.00	960.0
P5	53	50	1	0.001	139.10	2460.0
P6	53	101	2	0.001	206.50	1180.0
P7	112	60	0.5	0.01	1099.30	231.3
P8	112	112	1	0.01	1077.10	263.5
P9	112	224	2	0.01	897.80	218.6

4.2   Compression Test under Cyclic Loading

A Green Luserna Granite specimen (D=53mm, H=53mm, λ=1) was used. The cyclic loading was programmed at a frequency of 2 Hz and with a load excursion from a minimum load of 10 kN to a maximum of 60 kN. With respect to the tests performed under monotonic displacement control, neutron emissions from compression test under cyclic loading were performed by using neutron bubble detectors. Due to their isotropic angular response, three BDT and three BD-PND detectors were positioned at a distance of about 5 cm, all around the specimen. The detectors were previously activated, unscrewing the protection cap, in order to reach the suitable thermal equilibrium, and they were kept active for all the test duration. Furthermore, a BDT and a BD-PND detector were used as background control during the test.

4.3   Ultrasonic Test

A Green Luserna Granite specimen (D=53mm, H=100mm, λ=2) was connected to the ultrasonic horn by a glued screw inserted in a 5 mm deep hole (Fig. 3). This kind of connection was made in order to achieve a resonance condition, considering the speed of sound in Luserna stone, and the length of the specimen. Ultrasonic irradiation of the specimen was carried out for 3 hours. After the switching on of the transducer, 10% of the maximum power was reached in 20 min. Successively, the transducer power increased to 20% after one hour, and next reached a maximum level of about 30% after 2 hours. Then, the transducer worked in the same power condition up to the end of the test.
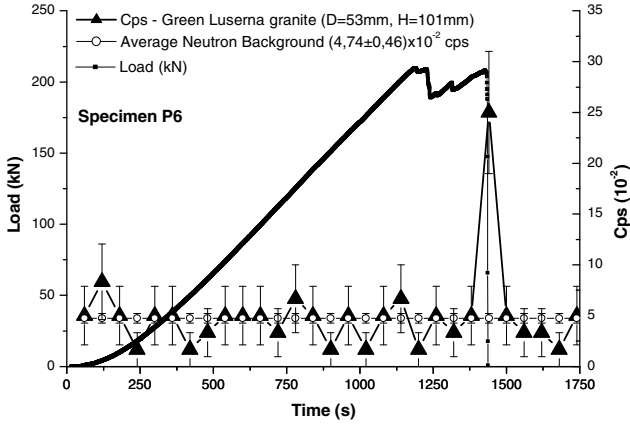
Fig. 3. The Green Luserna Granite specimen connected to the ultrasonic horn. The ultrasonic apparatus (Bandelin HD 2200) consists of a generator that converts electrical energy to 20 kHz ultrasound, and of a transducer that switches this energy into mechanical longitudinal vibration of the same frequency

5 Experimental Results

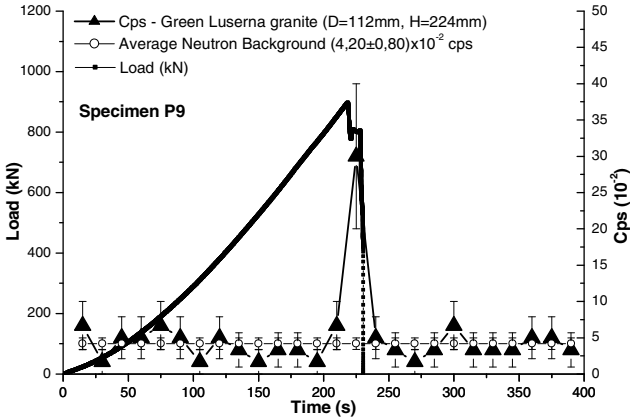### 5.1 Compression Tests under Monotonic Displacement Control

The ^{3}He device was switched on at least one hour before the beginning of each test, in order to reach a suitable electronic thermal equilibrium. Additional background measurements were repeated before each test, fixing an acquisition time of 60 s in order to check possible variation of natural background. Neutron measurements of specimens P2, P3, P4, P7 yielded values comparable with the ordinary natural background, while in specimens P1 and P5 the experimental data exceeded the background value by about four times. Instead, for specimen P6, P8 and P9, the neutron emissions achieved values higher than one order of magnitude with respect to ordinary background. In Fig. 4, for specimens P6, P8, and P9, the load vs. time diagram, and the neutron count rate evolution are shown. In Table 2, experimental data concerning compression tests on the nine Green Luserna Granite specimens are synthesized. The experimental results seem to demonstrate that neutron emissions follow an anisotropical distribution with an impulsive release from a specific zone of the specimen. Moreover, it is a matter of fact that the detected neutron flux, and consequently neutron dose, are inversely proportional to the square of the distance from the source. For these reasons, ^{3}He device could have underestimated neutron flux intensity, in any specimen. A possible solution to avoid underestimated data acquisition is an experimental measurement by using more than one ^{3}He detector and more bubble dosimeters placed around the test specimens.
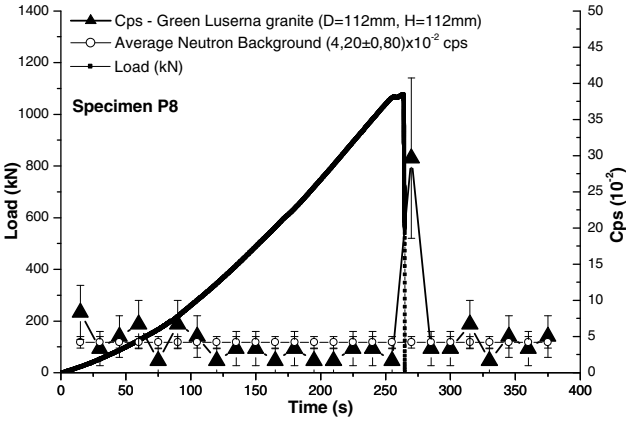
Fig. 4. Specimens P6, P8, P9. Load vs. time diagrams, and neutron emissions count rate

Table 2. Compression tests under monotonic displacement control. Neutron emissions experimental data on Green Luserna Granite specimens

Granite Specimen	D (mm)	$\lambda=H/D$	Average neutron background $(10^{-2}$ cps$)$	Count rate at the neutron emission $(10^{-2}$ cps$)$
P1	28	0.5	3.17±0.32	8.33±3.73
P2	28	1	3.17±0.32	background
P3	28	2	3.17±0.32	background
P4	53	0.5	3.83±0.37	background
P5	53	1	3.84±0.37	11.67±4.08
P6	53	2	4.74±0.46	25.00±6.01
P7	112	0.5	4.20±0.80	background
P8	112	1	4.20±0.80	30.00±11.10
P9	112	2	4.20±0.80	30.00±10.00

5.2 Compression Test under Cyclic Loading

Droplets counting was performed every 12 hours and the equivalent neutron dose was calculated. In the same way, the natural background was estimated by means of the two bubble dosimeters used for assessment. The ordinary background was found to be (13.98±2.76) nSv/h.

In Fig. 5 neutron equivalent dose variation, evaluated during the cyclic compression test, is reported. An increment of more than twice with respect to the background level was detected at specimen failure. No significant variations in neutron emissions were observed before the failure. The equivalent neutron dose, at the end of the test, was (28.74±5.75) nSv/h.
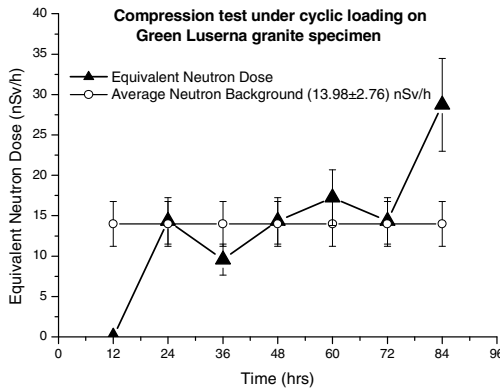
Fig. 5. Compression test under cyclic loading. Equivalent neutron dose variation on Green Luserna Granite specimen

5.3 Ultrasonic Test

Ultrasonic oscillation was generated by an high intensity ultrasonic horn (Bandelin HD 2200) working at 20 kHz. The device guarantees a constant amplitude (ranging from 10% to 100%) independently of changing conditions within the sample. The apparatus consists of a generator that converts electrical energy to 20 kHz ultrasounds, and of a transducer that switches this energy into mechanical longitudinal vibration at the same frequency.

The ultrasonic test on Green Luserna Granite specimen (D=53mm, H=100mm, λ=2) was carried out at the Medical and Environmental Physics Laboratory of Experimental Physics Department of the University of Torino. A relative natural background measurement was performed by means of the ^{3}He detector for more than 6 hours. The average natural background was of $(6.50\pm0.85)\cdot10^{-3}$ cps, for a corresponding thermal neutron flux of $(1.00\pm0.13)\cdot10^{-4}$ $n_{thermal}cm^{-2}s^{-1}$. This natural background level, lower than the one calculated during the compression tests at the Fracture Mechanics Laboratory of the Politecnico of Torino, is in agreement with the location of the experimental Physics Laboratory, which is three floors below the ground level.

During the ultrasonic test, the specimen temperature was monitored by using a multimeter/thermometer (Tektronix mod. S3910). The temperature reached 50°C after 20 min, and then increased up to a maximum level of 100°C at the end of the ultrasonic test. In Fig. 6, the neutron emissions detected are compared with the transducer power trend and the specimen temperature. A significant increment in neutron activity after 130 min from the beginning of the test was measured. At this time, the transducer power reached 30% of the maximum, with a specimen temperature of about 90°C. Some neutron variations were detected during the first hour of the test, but they may be due to ordinary fluctuations of natural background. At the switching off of the sonotrode, the neutron activity decreased to the typical background value.
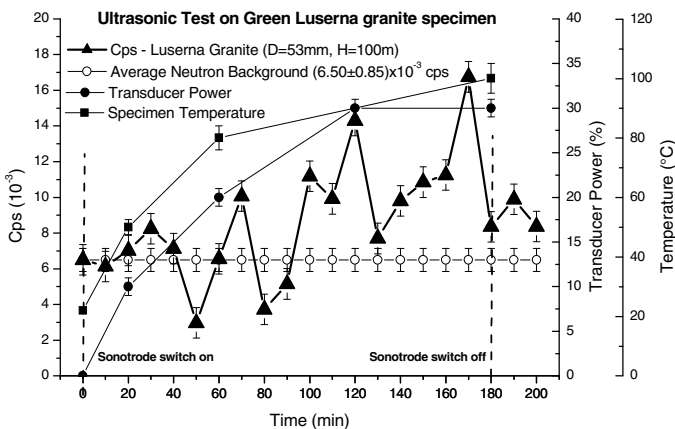

Fig. 6. Ultrasonic test. Neutron emissions compared with the specimen temperature, and with the transducer power trend

6 Compositional and Microchemical Evidence of Piezonuclear Fission Reactions in the Rock Specimens

Energy Dispersive X-ray Spectroscopy (EDS) was performed on different samples of external or fracture surfaces, belonging to the same specimens in Green Luserna Granite used in the preliminary piezonuclear tests by Carpinteri et al. [1-3]. The tests were conducted in order to correlate the neutron emission from the Luserna Granite with the variations in rock composition due to brittle failure of the granitic gneiss specimens. These analyses lead to get averaged information of the mineral chemical composition and to detect possible piezonuclear transmutations from iron to lighter elements. The quantitative elemental analyses were performed by a ZEISS Supra 40 Field Emission Scanning Electron Microscope (FESEM) equipped with an Oxford X-rays microanalysis. The samples were carefully chosen to investigate and compare the same crystalline phases both before and after the crushing failure. In particular, two crystalline phases, phengite and biotite, were considered due to their high iron content and relative abundances in the Luserna Granite (20% and 2%, respectively) [10].

Luserna "stone" is a leucogranitic orthogneiss, probably from the Lower Permian Age, that outcrops in the Luserna-Infernotto basin (Cottian Alps, Piedmont) at the border between the Turin and Cuneo provinces (North-western Italy) [11]. Characterized by a micro "Augen" texture, it is grey-greenish or locally pale blue in colour. Geologically, Luserna stone pertains to the Dora-Maira Massif [9,11], that represents a part of the ancient European margin annexed to the Cottian Alps during Alpine orogenesis. From a petrographic point of view, it is the metamorphic result of a late-Ercinian leucogranitic rock transformation [10,12] The Luserna stone has a sub-horizontal attitude, with a marked fine-grained foliation that is mostly associated with visible lineation. The mineralogical composition includes K-feldspar (10-25 Wt. %), quartz (30-40 Wt. %), albite (15-25 Wt. %) and phengite (10-20 Wt. %); subordinated biotite, chlorite, zoisite and/or clinozoisite/epidote (less then 5%). In addition to common accessory phases (ores, titanite, apatite and zircon), tourmaline, carbonates, rare axinite and frequent fluorite are present [10,13].

In consequence of Luserna stone being a very heterogeneous rock, and in order to assess mass percentage variations in chemical elements such as Fe, Al, Si and Mg, the EDS analyses have been focused on two crystalline phases: phengite and biotite. These two minerals of granitic gneiss, that are quite common in the Luserna stone (20% and 2%, respectively), show a mineral chemistry in which the iron content is largely diffused (see Figs. 7a and 7b).
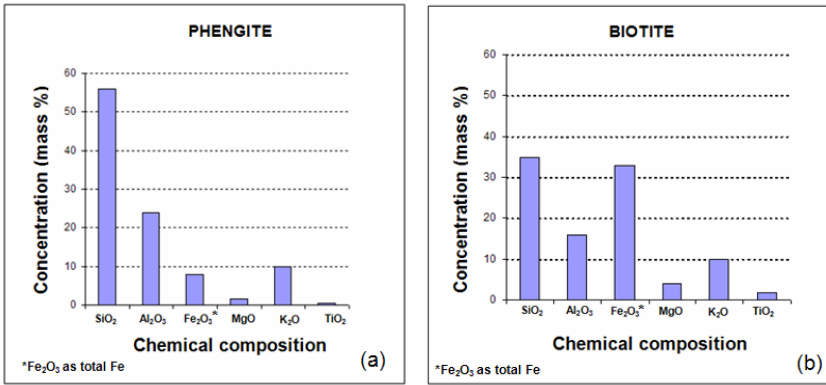
Fig. 7. (a) The chemical composition of phengite includes: SiO_2 (~56%), Al_2O_3 (~24%), Fe_2O_3 and FeO (~8%) MgO (~1.5%), Na_2O (~0.2%) and K_2O (~10%). (b) The chemical composition of biotite includes: SiO_2 (~35%), Al_2O_3 (~16%), Fe_2O_3 and FeO (~33%), MgO (~3.5%), TiO_2 (~1.5%), and K_2O (~10%)

In Fig. 8a, two thin sections obtained from the external surfaces of an integer and uncracked portion of one of the tested specimens are shown. The thin sections, finished with a standard petrographic polishing procedures, present a rectangular geometry (45×27 mm) and are 30 μm thick. In Fig. 8b, two portions of fracture surfaces taken from the tested specimen are shown. For the EDS analyses, several phengite and biotite sites were localized on the surface of the thin sections and on the fracture surfaces. Sixty measurements of phengite crystalline phase, and thirty of biotite were selected and analysed. In Figs. 9a and 9b, two electron microscope images of phengite and biotite sites, the first in the external sample (thin section 1) and the second on the fracture surface (fracture surface 2), are shown.
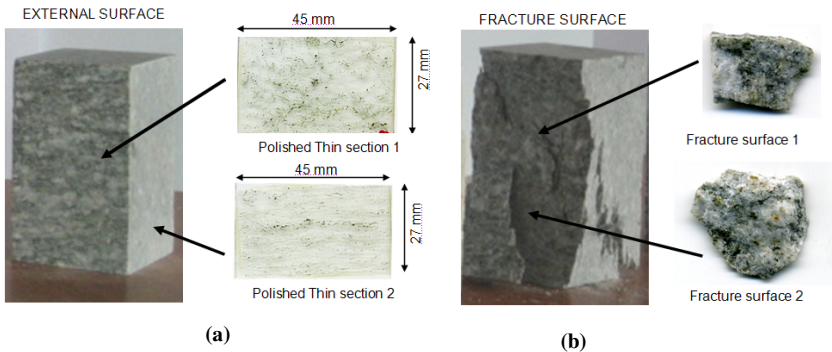

Fig. 8. (a) Polished thin sections obtained by the external surface of an integer and not fractured portion of the tested specimens [1,3]. (b) Fracture surface belonging to the tested specimens [1-3]
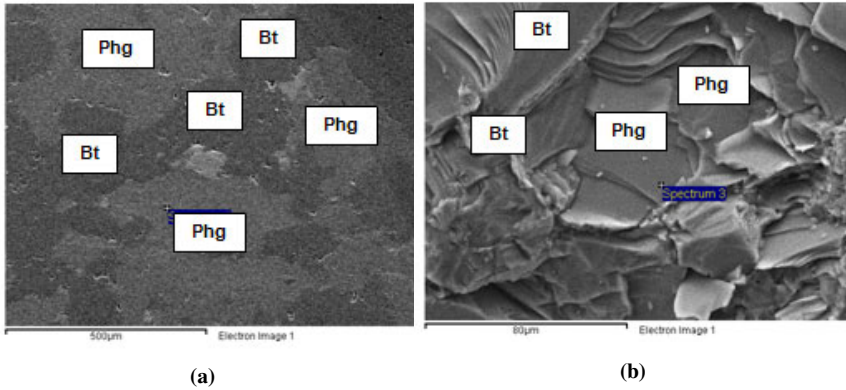
(a)   (b)

Fig. 9. FESEM images of phengite and biotite in the case of (a) external and (b) fracture sample

6.1 EDS Results for Phengite

In Fig. 10a and 10b, the results for the Fe concentrations obtained from the measurements on phengite crystalline phase are shown. Thirty of these measurements were carried out on the polished thin sections as representatives of the external surface samples, whereas the other thirty measurements were carried out on fracture surfaces. It can be observed that the distribution of Fe concentrations for the external surfaces, represented in the graph by squares, show an average value of the distribution (calculated as the arithmetic mean value) equal to 6.20%. In the same graph the distribution of Fe concentrations on the fracture samples (indicated by triangles) shows significant variations. It can be seen that the mean value of the distribution of measurements performed on fracture surfaces is equal to 4.0% and it is considerably lower than the mean value of external surface measurements (6.20%). It is also interesting to note that the two Fe value distributions are separated by at least two standard deviations ($\sigma = 0.37$ in the case of external surfaces and $\sigma = 0.52$ in the case of fracture surfaces).

The iron decrease, considering the mean values of the distributions of phengite composition, is about 2.20%. This iron content reduction corresponds to a relative decrease of 35% with respect to the previous Fe content (6.20% in phengite). Similarly to Fig. 10a, in Fig 10b the Al mass percentage concentrations are considered in both the cases of external and fracture surfaces. For Al contents, the observed variations show a mass percentage increase approximately equal to that of Fe (compare Fig. 10a and 10b). The average increase in the distribution, corresponding to the fracture surfaces (indicated by triangles), is about 2.00% of the phengite composition. The average value of Al concentrations changes from 12.50% on the external surface to 14.50% on the fracture surface. The relative increase in Al content is equal to 16%.

The evidence emerging from the EDS analyses, that the two values for the iron decrease (-2.20%) and for the Al increase ($+2.0\%$) are approximately equal, is really impressive. This fact is even more evident considering the trends of the

other chemical elements constituting the mineral chemistry (excluding H and O) in phengite, because no appreciable variations can be recognized between the average values [4].
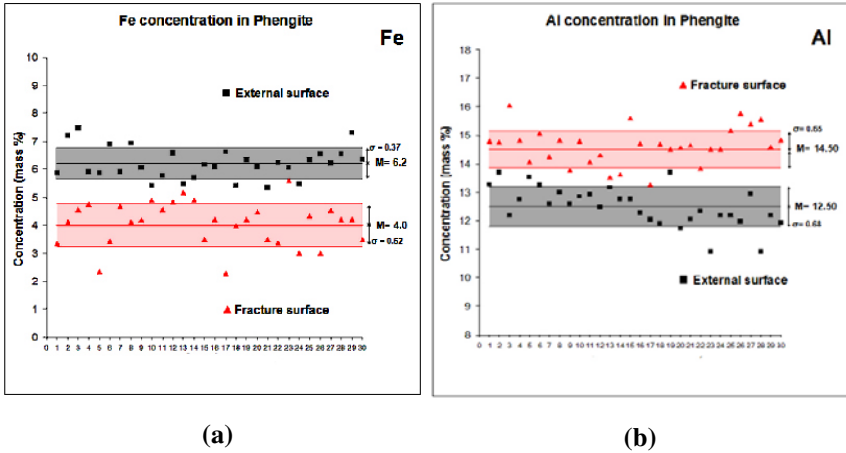

(a) **(b)**

Fig. 10. Fe and Al concentrations in phengite: (a) Fe concentrations on external surfaces (squares) and on fracture surfaces (triangles). The Fe decrease considering the two mean values of the distributions is equal to 2.20%. (b) Al concentrations on external surfaces (squares) and on fracture surfaces (triangles). The Al increase, considering the two mean values of the distributions, is equal to 2.0%

6.2 EDS Results for Biotite

In the Figs. 11a-d the results for Fe, Al, Si and Mg concentrations measured on 30 acquisition points of biotite crystalline phase are shown. These measurements were selected on the polished thin sections as representatives of the uncracked material samples (15 measurements) and of fracture surfaces (15 measurements). It can be observed that the distribution of Fe concentrations for the external surfaces, represented in Fig. 11a by squares, shows an average value of the distribution (calculated as the arithmetic mean value) equal to 21.20%. On the other hand, considering in the same graph the distribution of Fe concentrations on fracture samples (indicated by triangles), it can be seen that the mean value drops to 18.20%. In this case, the iron decrease, considering the mean values of the distributions of biotite composition, is about 3.00%. This iron content reduction (−3.00%) corresponds to a relative decrease of 14% with respect to the previous Fe content (21.20% in biotite). Similarly to Fig. 11a, in Fig. 11b the Al mass percentage concentrations are considered in both cases of external and fracture samples. For Al contents the observed variations show an average increase of about 1.50% in the biotite composition. The average value of Al concentrations changes from 8.10% on the external surface to 9.60% on the fracture surface, with a relative increase in Al content equal to 18%. In Fig. 11c and 11d it is shown that, in the case of biotite, also Si and Mg contents present considerable variations.

Figure. 11c shows that the mass percentage concentration of Si changes from a mean value of 18.4% (external surface) to a mean value of 19.60% (fracture surface) with an increase of 1.20%. Similarly, in Fig. 11d the Mg concentration distributions show that the mean value of Mg content changes from 1.50% (external surface) to 2.20% (fracture surface). Therefore, the iron decrease (−3.00%) in biotite is counterbalanced by an increase in aluminum (+1.50%), silicon (+1.20%), and magnesium (+0.70%) [4].
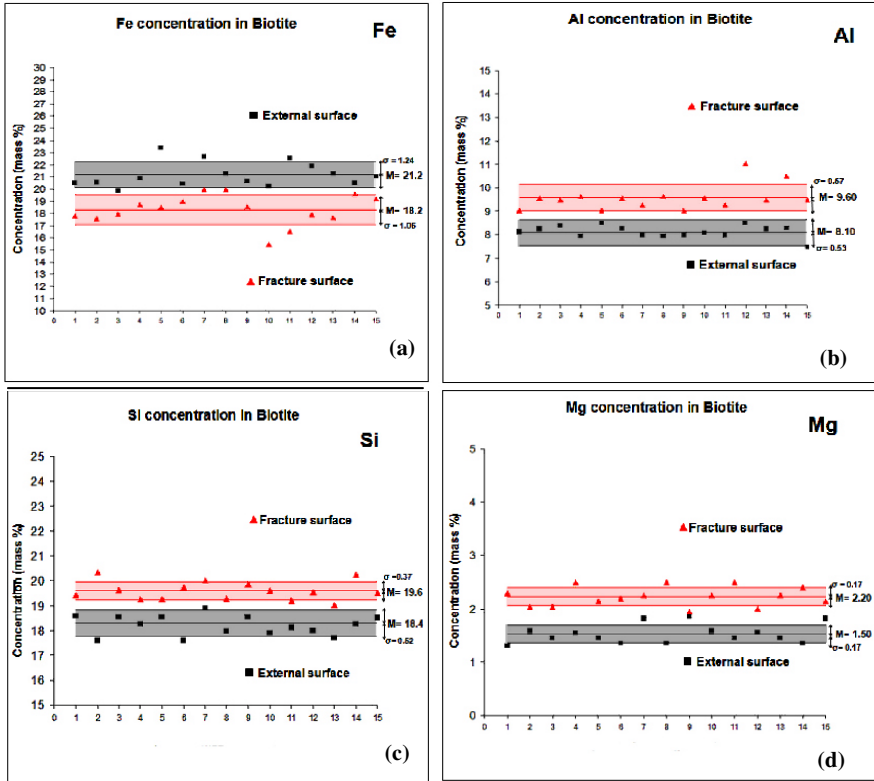
Fig. 11. Fe (a), Al (b), Si (c) and Mg (d) concentrations in biotite are reported for external and fracture surfaces. The iron decrease (−3.00%) in biotite is counterbalanced by an increase in aluminum (+1.50%), silicon (+1.20%), and magnesium (+0.70%). In the case of the other elements no appreciable variations can be recognized between the external and the fracture samples [4]

7 Piezonuclear Reactions: From the Laboratory to the Earth Scale

From the results shown in the previous sections and the experimental evidence reported in recent papers [1-3,4], it can be clearly seen that piezonuclear reactions are possible in inert non-radioactive solids.

From the EDS results on fracture samples, the evidences of Fe and Al variations on phengite (Fig. 10) lead to the conclusion that the piezonuclear reaction:

$$Fe_{26}^{56} \rightarrow 2\,Al_{13}^{27} + 2 \text{ neutrons}\,, \tag{1}$$
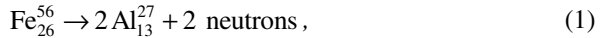
should have occurred [1-3, 4]. Moreover, considering the evidences for the biotite content variations in Fe, Al, Si, and Mg (Fig. 11), it is possible to conjecture that another piezonuclear reaction, in addition to (1), should have occurred during the piezonuclear tests [1-3,4]:

$$Fe_{26}^{56} \rightarrow Mg_{12}^{24} + Si_{14}^{28} + 4 \text{ neutrons}\,. \tag{2}$$

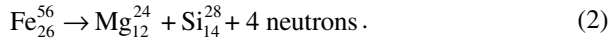Taking into account that granite is a common and widely occurring type of intrusive, Sialic, igneous rock, and that it is characterized by an extensive concentration in the rocks that make up the Earth's crust (~60% of the Earth's crust), the piezonuclear fission reactions expressed above can be generalized from the laboratory to the Earth's crust scale, where mechanical phenomena of brittle fracture, due to fault collision and subduction, take place continuously in the most seismic areas. This hypothesis seems to find surprising evidence and confirmation from both the geomechanical and the geochemical points of view. The neutron emissions involved in piezonuclear reactions can be detected not only in laboratory experiments, as shown in this paper, and in [1-3], but also at the Earth's crust scale. Recent neutron emission detections by Kuzhevskij et al. [14,15] have led to consider also the Earth's crust, in addition to cosmic rays, as being a relevant source of neutron flux variations. Neutron emissions measured near the Earth's surface exceeded the neutron background by about one order of magnitude in correspondence to seismic activity and rather appreciable earthquakes [16]. This relationship between the processes in the Earth's crust and neutron flux variations has allowed increasing tectonic activity to be detected and methods for short-term prediction and monitoring of earthquakes to be developed [14,15]. Neutron flux variations, in correspondence to seismic activity, may be evidence of changes in the chemical composition of the crust, as a result of piezonuclear reactions. The present natural abundances of aluminum (~8%), and silicon (28%) and scarcity of iron (~4%) in the continental Earth's crust are possibly due to the piezonuclear fission reactions considered above.

8 Heterogeneity in the Composition of the Earth's Crust: Fe and Al Reservoir Locations

The location of Al and Fe mineral reservoirs seems to be closely connected to the geological periods when different continental zones were formed [17-23]. This fact would seem to suggest that our planet has undergone a continuous evolution from the most ancient geological regions, which currently reflect the continental cores that are rich in Fe reservoirs, to more recent or contemporary areas of the Earth's crust where the concentrations of Si and Al oxides present very high mass percentages [17]. The main iron reservoir locations (Magnetite and Hematite

mines) are reported in Fig. 12a. The main concentrations of Al-oxides and rocky andesitic formations (the Rocky Mountains and the Andes, with a strong concentration of Al_2O_3 minerals) are shown in Fig. 12b together with the most important subduction lines, plate tectonic trenches and rifts [17,21]. The geographical locations of main bauxite mines show that the largest concentrations of Al reservoirs can be found in correspondence to the most seismic areas of the Earth (Fig.12b). The main iron mines are instead exclusively located in the oldest and interior parts of continents (formed through the eruptive activity of the proto-Earth), in geographic areas with a reduced seismic risk and always far from the main fault lines. From this point of view, the close correlation between bauxite and andesitic reservoirs and the subduction and most seismic areas of the Earth's crust provides very impressive evidence of piezonuclear effects at the planetary scale.

9   Geochemical Evidence of Piezonuclear Reactions in the Evolution of the Earth's Crust

Evidence of piezonuclear reactions can be also recognized considering the Earth's composition and its way of evolving throughout the geologic eras. In this way, plate tectonics and the connected plate collision and subduction phenomena are useful to understand not only the morphology of our planet, but also its compositional evolution [5].

From 4.0 to 2.0 Gyrs ago, Fe could be considered one of the most common bio-essential elements required for the metabolic action of all living organisms. Today, the deficiency of this nutrient suggests it as a limiting factor for the development of marine phytoplankton and life on Earth [20].

Elements such as Fe and Ni in the Earth's protocrust had higher concentrations in the Hadean (4.5−3.8 Gyr ago) and Archean (3.8−2.5 Gyr ago) periods compared to the present values. The Si and Al concentrations instead were lower than those of today [17-19]. In Fig. 13, the evolution in mass percentage concentration of Si, Al, Fe and Ni in the Earth protocrust and crust over the last 4.5 Billion years is reported.

Considering the data reported in Fig. 13, it is possible to conjecture, in addition to reactions (1) and (2), another piezonuclear fission reaction that could take place in correspondence to plate collision and subduction [5]:

$$Ni_{28}^{59} \rightarrow 2\ Si_{14}^{28} + 3\ \text{neutrons}\,, \tag{3}$$
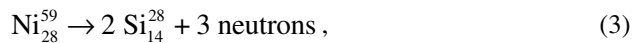
Taking into account these considerations, a clear transition from a more basaltic condition (high concentrations of Fe and Ni) to a Sialic one (high concentrations of Al and Si) can be observed during the life time of our planet [5]. The most abrupt changes in element concentrations shown in Fig. 13 appear to be intimately connected to the tectonic activity of the Earth. In particular, the abrupt transitions of 2.5 Gyrs ago coincide with the period of the Earth's largest tectonic activity [5,18,19].
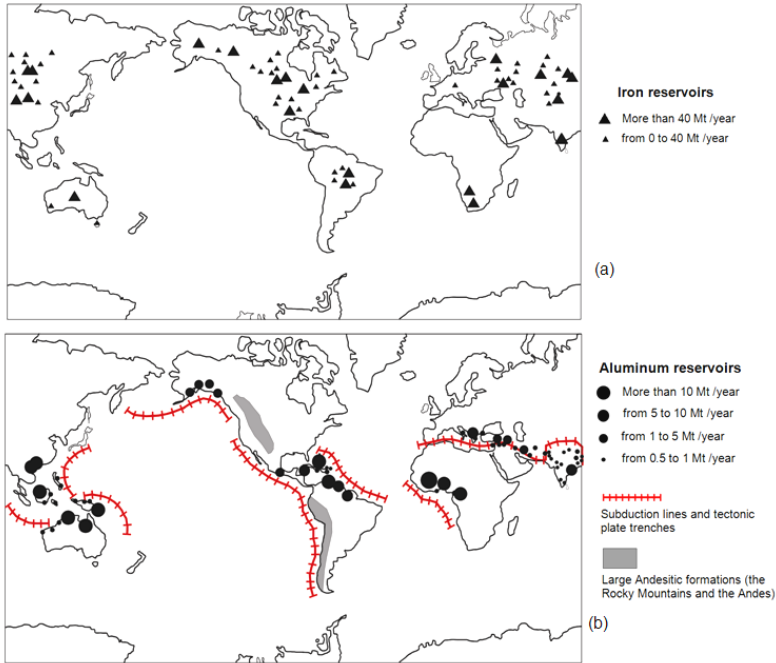
Fig. 12. (a) Locations of the largest iron mines in the world [24-27]. Iron ore reservoirs (Magnetite and Hematite mines) are located in geographic areas with reduced seismic risks and always far from fault lines. (b) The largest aluminum (bauxite) reservoirs are reported together with the main Andesitic formations and most important subduction lines and plate tectonic trenches [17]
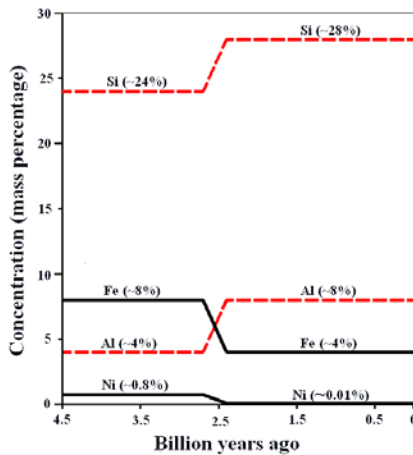
Fig. 13. The estimated mass percentage concentrations of Si, Al, Fe and Ni in the Earth crust during the last 4.5 Billion years (age of the planet Earth) [5,17-19,22, 28-34]

10 Conclusions

Neutron emission measurements were performed on Green Luserna Granite specimens during mechanical tests. From these experiments, it can be clearly seen that piezonuclear reactions giving rise to neutron emissions are possible in inert non-radioactive solids under loading. In particular, during compression tests of specimens with sufficiently large size, the neutron flux was found to be of about one order of magnitude higher than the background level at the time of catastrophic failure. For test specimens with more ductile behaviour, neutron emissions significantly higher than the background were found. Neutron detection is also confirmed in compression test under cyclic loading and during ultrasonic vibration.

Our conjecture, also confirmed by the Energy Dispersive X-ray Spectroscopy (EDS) tests, is that piezonuclear reactions involving fission of iron into aluminum, or into magnesium and silicon, should have occurred during compression on the tested specimens.

This hypothesis seems to find surprising evidence and confirmation also at the Earth crust scale from both geomechanical and geochemical points of view. In this way, the piezonuclear reactions have been considered in order to interpret the most significant geophysical and geological transformations, today still unexplained.

Finally, through experimental and theoretical studies of neutron emission and piezonuclear fission reactions from brittle fracture, it will also be possible to explore new and fascinating application fields, such as short-term prediction and monitoring of earthquakes, production of neutrons for medical use in cancer therapy, disposal of radioactive waste, and even the hypothetical production of clean nuclear energy.

Acknowledgements

References

1. Carpinteri, A., Cardone, F., Lacidogna, G.: Piezonuclear neutrons from brittle fracture: Early results of mechanical compression tests. Strain 45, 332–339 (2009); Presented at the Turin Academy of Sciences on December 10, 2008. Proc. of the Turin Academy of Sciences. Ser. vol. 33, pp. 27–42 (2010)
2. Cardone, F., Carpinteri, A., Lacidogna, G.: Piezonuclear neutrons from fracturing of inert solids. Physics Letters A 373, 4158–4163 (2009)

3. Carpinteri, A., Cardone, F., Lacidogna, G.: Energy emissions from failure phenomena: Mechanical, electromagnetic, nuclear. Exp. Mech. (2010), doi:10.1007/s11340-009-9325-7
4. Carpinteri, A., Chiodoni, A., Manuello A., Sandrone, R.: Compositional and micro-chemical evidence of piezonuclear fission reactions in rock specimens subjected to compression tests. Strain. doi: 10.1111/j.1475-1305.2010.00767.x
5. Carpinteri, A., Manuello, A.: Geomechanical and geochemical evidence of piezonuclear fission reactions in the Earth's crust. Strain, doi:10.1111/j.1475-1305.2010.00766.x
6. Bubble Technology Industries, Instruction manual for the Bubble detector, Chalk River, Ontario, Canada (1992)
7. National Council on Radiation Protection and Measurements Protection Against Neutron Radiation, NCRP Report 38 (1971)
8. Carpinteri, A.: Cusp catastrophe interpretation of fracture instability. J. of the Mech. and Physics of Solids 37, 567–582 (1989)
9. Carpinteri, A.: A catastrophe theory approach to fracture mechanics. Int. J. of Fracture 44, 57–69 (1990)
10. Vola, G., Marchi, M.: Mineralogical and petrographic quantitative analysis of a recycled aggregate from quarry wastes. The Luserna stone case-study. In: Proc. of the 12th Euroseminar on Microscopy Appl. to Building Materials, Dortmund, Germany, September 15-19 (2009)
11. Sandrone, R., Cadoppi, P., Sacchi, R., Vialon, P.: The Dora-Maira Massif. In: Von Raumer, J.F., Neubauer, F. (eds.) Pre-Mesozoic geology in the Alps, pp. 317–325. Springer, Berlin (1993)
12. Compagnoni, R., Crisci, G.M., Sandrone, R.: Caratterizzazione chimica e petrografica degli "gneiss di Luserna" (Massiccio cristallino Dora-Maira, Alpi Occidentali). Rend. Soc. It. Min. Petr. 38, 498 (1982-1983)
13. Sandrone, R.: La Pietra di Luserna nella letteratura tecnico-scientifica. Semimario Internazionale, Le Pietre Ornamentali della Montagna Europea, Luserna San Giovanni-Torre Pellice (TO), pp. 333–339 (2001)
14. Kuzhevskij, B.M., Nechaev, O.Y., Sigaeva, E.: Neutron flux variations near the Earth's crust. A possible tectonic activity detection. Nat. Haz. and Earth System Sciences 3, 637–645 (2003)
15. Kuzhevskij, B.M., Nechaev, O.Y., Sigaeva, E.A.: Distribution of neutrons near the Earth's surface. Nat. Haz. and Earth System Sciences 3, 255–262 (2003)
16. Volodichev, N.N., Kuzhevskij, B.M., Nechaev, O.Y., Panasyuk, M.I., Podorolsky, A.N., Shavrin, P.I.: Sun-Moon-Earth connections: The neutron intensity splashes and seismic activity. Astron. Vestnik 34(2), 188–190 (2000)
17. Favero, G., Jobstraibizer, P.: The distribution of aluminum in the Earth: from cosmogenesis to Sial evolution. Coord. Chem. Rev. 149, 367–400 (1996)
18. Taylor, S.R., McLennan, S.M.: The geochemical evolution of the continental crust. Rev. of Geophys. 33(2), 241–265 (1995)
19. Taylor, S.R., McLennan, S.M.: Planetary Crusts: Their Composition, Origin and Evolution. Cambridge University Press, Cambridge (2009)
20. Anbar, A.D.: Elements and evolution. Science 322, 1481–1482 (2008)
21. Lunine, J.I.E.: Earth: Evolution of a Habitable World. Cambridge University Press, Cambridge (1998)
22. Hazen, R.M., et al.: Mineral evolution. American Mineralogist 93, 1693–1720 (2008)
23. Condie, K.C.: Plate Tectonics and crustal evolution. Pergamon Press, Elmsford (1976)

24. Roy, I., Sarkar, B.C., Chattopadhyay, A.: MINFO-a prototype mineral information database for iron ore resourcers of India. Comp. and Geosci. 27, 357–361 (2001)
25. World Iron Ore producers, `http://www.mapsofworld.com/minerals/world-iron-ore-producers.html` (last accessed October 2009)
26. World Mineral Resources Map, `http://www.mapsofworld.com/world-mineral-map.htm` (last accessed October 2009)
27. Key Iron Deposits of the World, `http://www.portergeo.com.au/tours/iron2002/-iron2002depm2b.asp` (last accessed October 2009)
28. Konhauser, K.O., et al.: Oceanic nickel depletion and a methanogen famine before the Great Oxidation Event. Nature 458, 750–754 (2009)
29. Saito, M.A.: Less nickel for more oxygen. Nature 458, 714–715 (2009)
30. Rudnick, R.L., Fountain, D.M.: Nature and composition of the continental crust: A lower crustal perspective. Rev. of Geophys. 33(3), 267–309 (1995)
31. Egami, F.: Minor elements and evolution. Journal of Molecular Evolution 4(2), 113–120 (1975)
32. National Academy of Sciences, Nickel Committee on Medical and Biological Effects of Environmental Pollutants – Nickel, National Academy of Sciences, Washington, DC (1975)
33. Doglioni, C.: Interno della Terra, Treccani. Enciclopedia Scienza e Tecnica, 595–605 (2007)
34. Foing, B.: Earth's childhood attic. Astrobiological Magazine: Retrospection (on-line), February 23 (2005)

Stress Triaxiality at Crack Tips Studied by Caustics

Emmanuel E. Gdoutos

Office of Theoretical and Applied Mechanics of the Academy of Athens
School of Engineering, Democritus University of Thrace
GR-671 00 Xanthi, Greece
egdoutos@civil.duth.gr

Abstract. The optical method of caustics constitutes a powerful tool in the hands of the experimentalist for the solution of fracture mechanics problems. According to the method, the area in the vicinity of the crack tip is illuminated by a light beam and the reflected or transmitted light rays form an envelope in space. When this envelope is cut by a screen a highly illuminated curve, the so-called caustic, is formed. By measuring characteristic dimensions of the caustic the stress intensity factor is determined. The method has been based on the assumption that plane stress conditions dominate in the vicinity of the crack tip. However, experimental evidence has shown that the state of stress is not pure plane stress. It changes from plane strain near the crack tip to plane stress at a critical distance away from the tip through a three-dimensional region. In order the caustic to be generated from the light rays reflected or transmitted through the specimen from the plane stress region certain conditions among the dimensions of the optical arrangement, the specimen properties and specimen thickness need to be satisfied. These conditions are investigated in this work so that the method of caustics can safely be used for determination of stress intensity factors in fracture mechanics problems.

1 Introduction

The optical method of caustics has extensively been used for the determination of stress intensity factors in crack problems under static and dynamic conditions [1-7]. According to this method, the area in the vicinity of the crack tip is illuminated by a light beam and the reflected or transmitted light rays form an envelope in space. When this envelope is cut by a screen a highly illuminated curve, the so-called caustic, is formed. By measuring characteristic dimensions of the caustic the stress intensity factor is determined. For linear elastic crack problems the caustic is the image of the circumference of a circle surrounding the crack tip, called the initial curve, on the reference screen, and is directly related to the state of affairs along the initial curve. For the determination of stress intensity factors, the

state of stress along the initial curve must be known. This state changes with the distance from the crack tip [8, 9]. Very near to the tip the state of stress is plane strain, while after a critical distance from the tip it becomes plane stress. In the area between the two regions the state of stress is three-dimensional. An investigation of the three-dimensional effects and the limits of applicability of the method of caustics in crack problems was performed in [10-15]. An extension of the method caustics in conjunction with the method of birefringent coatings for the study of crack problems in opaque materials was performed in [16-20].

The condition that the initial curve of the caustic lays in the region where plane stress conditions dominate imposes certain restrictions on the values of the applied load, specimen dimensions and characteristic lengths of the optical arrangement. In the present work, the limiting values of these quantities are defined when the specimen is illuminated by a parallel, divergent or convergent light beam. It is shown that for the correct application of the method certain conditions among the above quantities need to be satisfied. Thus, the experimentalist can safely apply the method of caustics for the determination of stress intensity factors in fracture mechanics problems.

2 Stress-Optical Equations

The stress optical equations governing the variation of the optical path of a light ray traversing a transparent specimen or reflected from the front or the rear face of the specimen are derived. The cases of plane stress and plane strain are considered separately.

2.1 Plane Stress

The variation of the optical path $\Delta s_{t1,2}$ of a light ray normally traversing a specimen along the directions of the principal stresses σ_1 or σ_2 is due to the variation of the index of refraction and the thickness of the specimen, and is given by

$$\Delta s_{t_{1,2}} = d\Delta n_{1,2} + (n - n_0)\Delta d \tag{1}$$

where d is the thickness of the specimen, $n_{1,2}$ is the index of refraction along the directions of the principal stress $\sigma_{1,2}$, n the index of refraction of the specimen under no load, and n_0 is the index of refraction of the surrounding medium. Δ denotes the variation of the respective quantity.

According to Neumann-Maxwell stress-optical law for linear elastic behavior of the material, the variation of the refractive index $\Delta n_{1,2}$ due to loading along the direction of the principal stress $\sigma_{1,2}$ is given by

$$\Delta n_{1,2} = n_{1,2} - n = b_1\varepsilon_{1,2} + b_2(\varepsilon_{2,1} + \varepsilon_3) \tag{2}$$

where b_1 and b_2 are the strain optical constants and ε_1, ε_2, ε_3 are the principal strains.

For generalized plane stress conditions ($\sigma_3 = 0$) introducing Hooke's law into eq. (2) we obtain

$$\Delta n_{1,2} = C_1 \sigma_{1,2} + C_2 \sigma_{2,1} \tag{3}$$

where

$$C_1 = \frac{1}{E}(b_1 - 2\nu b_2), \quad C_2 = \frac{1}{E}[b_2 - \nu(b_1 + b_2)], \tag{4}$$

with ν representing Poisson's ratio.

From eqs (1) to (4) it is obtained that

$$\Delta s_{t_{1,2}} = (a_t \sigma_{1,2} + b_t \sigma_{2,1})d \tag{5}$$

where

$$a_t = C_1 - \frac{\nu}{E}(n - n_0), \quad b_t = C_2 - \frac{\nu}{E}(n - n_0) \tag{6}$$

Equation (5) can be put in the form

$$\Delta s_{t_{1,2}} = c_t [(\sigma_1 + \sigma_2) \pm \xi_t (\sigma_1 - \sigma_2)]d \tag{7}$$

where

$$c_t = \frac{a_t + b_t}{2}, \quad \xi_t = \frac{a_t - b_t}{a_t + b_t} \tag{8}$$

For optically isotropic materials for which the index of refraction does not change along the principal stress directions ($b_1 = b_2 = b$, $\xi_t = 0$), eq. (7) takes the form

$$\Delta s_{t_1} = \Delta s_{t_2} = c_t (\sigma_1 + \sigma_2)d \tag{9}$$

where

$$\alpha_t = b_t = c_t = \frac{1}{E}[(1 - 2\nu)b - \nu(n - n_0)] \tag{10}$$

Consider now the case of a light ray normally incident on the specimen, passing through it and reflected from its rear face. The variation of the optical path of the light ray along the directions of the principal stresses σ_1 and σ_1 is given by

$$\Delta s_{r_{1,2}} = 2\left[d\Delta n_{1,2} + \left(n - \frac{n_0}{2}\right)\Delta d \right] \tag{11}$$

For generalized plane stress conditions ($\sigma_3 = 0$), the Neumann-Maxwell and Hooke's law can be applied to eq. (11) rendering

$$\Delta s_{r_{1,2}} = 2\left(a_r \sigma_{1,2} + b_r \sigma_{2,1}\right)d \tag{12}$$

where

$$a_r = C_1 - \frac{v}{E}\left(n - \frac{n_0}{2}\right), \quad b_r = C_2 - \frac{v}{E}\left(n - \frac{n_0}{2}\right) \tag{13}$$

Equation (12) can be put in the form

$$\Delta s_{r_{1,2}} = 2c_r\left[\left(\sigma_1 + \sigma_2\right) + \xi_r\left(\sigma_1 - \sigma_2\right)\right]d \tag{14}$$

where

$$c_r = \frac{a_r + b_r}{2}, \quad \xi_r = \frac{a_r - b_r}{a_r + b_r} \tag{15}$$

For optically isotropic materials ($b_1 = b_2 = b$, $\xi_r = 0$), eq. (14) takes the form

$$\Delta s_{r_1} = \Delta s_{r_2} = 2c_r\left(\sigma_1 + \sigma_2\right)d \tag{16}$$

where

$$a_r = b_r = c_r = \frac{1}{E}\left[\left(1 - 2v\right)b - v\left(n - \frac{n_0}{2}\right)\right] \tag{17}$$

Finally, consider the case of a light ray normally incident on the specimen and reflected from its front face. The variation of the optical path of the light ray along the directions of the principal stresses σ_1 and σ_2 for generalized plane stress conditions is due to the thickness variation only and is given by

$$\Delta s_{r_1} = \Delta s_{r_2} = c_r\left(\sigma_1 + \sigma_2\right)d \tag{18}$$

where

$$c_r = -\frac{v}{E} \tag{19}$$

2.2 Plane Strain

The variation of the optical path of a light ray normally traversing a specimen along the directions of the principal stresses σ_1 and σ_2 under plane strain conditions ($\varepsilon_3 = 0$, $\sigma_3 = v(\sigma_1 + \sigma_2)$) is obtained from eqs (1), (2) and Hooke' law, i.e.,

$$\Delta s_{t1,2} = \left(a_t \sigma_{1,2} + b_t \sigma_{2,1}\right)d \tag{20}$$

where

$$a_t = \frac{1}{E}\left[\left(1-v^2\right)b_1 - v\left(1+v\right)b_2\right] \tag{21a}$$

$$b_t = \frac{1}{E}\left[-v\left(1+v\right)b_1 + \left(1-v^2\right)b_2\right] \tag{21b}$$

For a light ray normally incident on the specimen, and passing through its thickness and reflected from the rear face of the specimen, the variation of the optical path is given by

$$\Delta s_{r1,2} = \left(a_r \sigma_{1,2} + b_r \sigma_{2,1}\right)d \tag{22}$$

where

$$a_r = 2a_t, \quad b_r = 2b_t \tag{23}$$

Finally, the variation of the optical path of a light ray reflected from the front face of the specimen under plane strain conditions is zero.

3 The Optical Method of Caustics

In the optical method of caustics a specimen is illuminated by a light beam (Fig. 1) and the reflected or transmitted rays undergo a change of their optical path caused by the variation of the thickness and refractive index of the specimen. At stress gradients resulting at crack tips, the light rays generate a highly illuminated three-dimensional surface in space. When this surface is intersected by a reference screen, a bright curve, the so-called caustic curve, is formed. The dimensions of the caustic are related to the state of stress near the crack tip. An optical arrangement for the method of caustics is shown in Fig. 2. For the case of a mode-I through-the-thickness crack the stress intensity factor K_{exp} is given by [1]

$$K_{exp} = 0.0934 \frac{D^{5/2}}{z_0 c d m^{3/2}} \tag{24}$$

where z_0 is the distance between the specimen and the viewing screen where the caustic is formed, c is the stress optical constant of the specimen under conditions of plane stress, d is the specimen thickness, m is the magnification factor of the optical arrangement defined as the ratio of a length on the reference screen where the caustic is formed divided by the corresponding length on the specimen and D is the transverse diameter of the caustic at the crack tip (Fig. 3). The above equation is valid when the state of stress in the vicinity of the crack tip is plane stress.
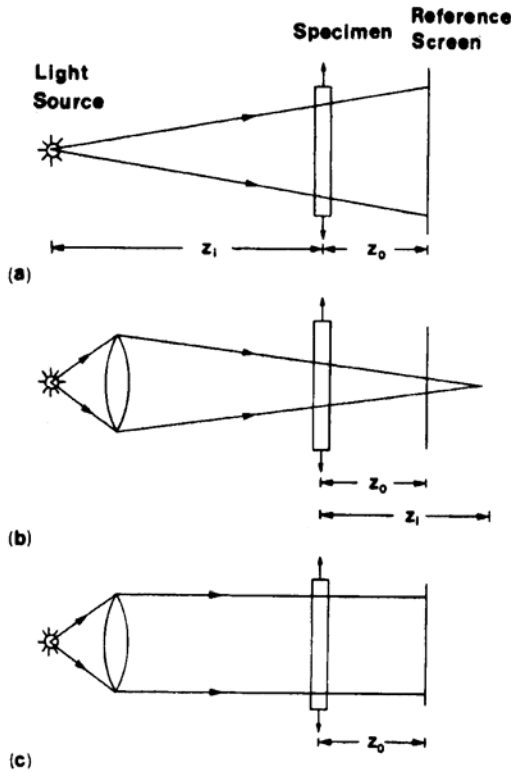
Fig. 1. Optical arrangement for divergent (a), convergent (b) and parallel (c) light

The magnification factor of the optical arrangement for divergent light is given by

$$m = \frac{z_0 + z_i}{z_i} \tag{25}$$

where z_i is the distance between the light source and the specimen.

For convergent light, where z_i is the distance between the focus of the imping-ing light beam and the specimen m is given by

$$m = \pm \frac{z_0 - z_i}{z_i} \tag{26}$$

m = 1 for parallel light.

The caustic is created by the light rays reflected from the circumference of a circle, the so-called initial curve, which surrounds the crack tip. The radius r_0 of the initial curve is given by

$$r_0 = \left(\frac{0.5984 z_0 c d K_I}{m} \right)^{2/5} \tag{27}$$

Fig. 2. Optical setup of the method of caustics

Fig. 3. Caustic under mode-I loading

Form eqs (24) and (27) it is obtained that

$$r_0 = 0.316 \, D \tag{28}$$

4 Experimental

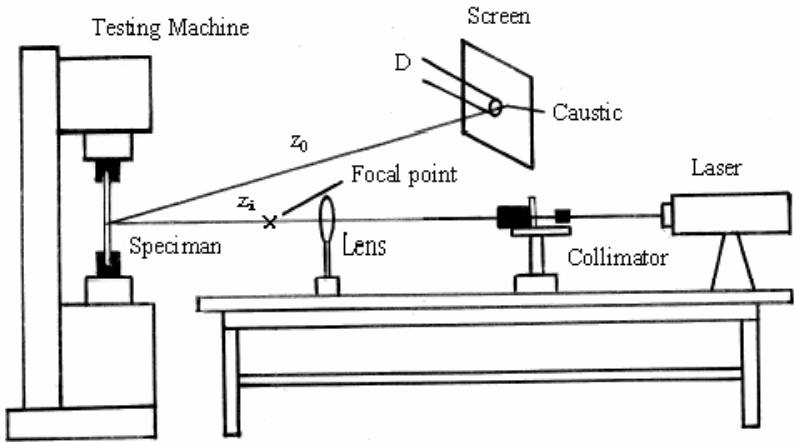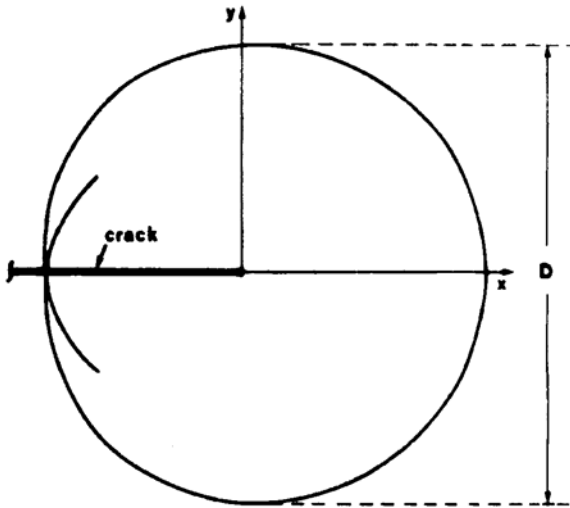Specimens made of Plexiglas of thickness d = 3.0, 4.5, 9.5 and 12.5 mm and width w = 42.4, 47.5, 51.5 and 63.5 mm, with an edge notch of length a = 15.5 mm were subjected to a progressively increasing tensile loading in an Instron testing machine. The specimens were illuminated by a convergent, divergent or parallel monochromatic light beam produced by a Ne-He laser (Fig. 2). The caustic curves obtained from the light rays reflected from the front or rear faces of the specimen, or those transmitted through the specimen were recorded on a viewing screen placed at a distance z_0 from the specimen (Fig. 2). Caustics were obtained at different load levels for various values of the magnification factor of the optical arrangement and the distance z_0. In this way, a host of caustics were obtained from different values r_0 of the radius of the initial curve from the crack tip.

Experimental values of stress intensity factor, K_{exp}, were obtained. These values were compared with theoretical values of stress intensity factor K_{th} for an edge-cracked specimen given by [21, 22]

$$K_{th} = \sigma\sqrt{\pi a}\left[1.12 - 0.23\left(\frac{a}{w}\right) + 10.55\left(\frac{a}{w}\right)^2 - 21.72\left(\frac{a}{w}\right)^3 + 30.95\left(\frac{a}{w}\right)^4\right] \quad (29)$$

Note that the experimental values of stress intensity factor are obtained under the assumption that the initial curve of the caustic lays in the region near the crack tip where plane stress conditions dominate. Thus, if the values of K_{exp} and K_{th} coincide, this means that the initial curve of the caustic lays in the region where the state of stress is plane stress. In case the values of K_{exp} and K_{th} do not coincide, this implies that the initial curve lies in the region where the state of stress is three-dimensional.

Fig. 4 presents the variation of K_{exp}/K_{th} versus r/d for specimen thickness d = 4.5 mm, crack length a = 15.5 mm and two values of specimen width w = 47.5 and 63.5 mm. Points in the figure correspond to different values of the applied load, P, the magnification factor of the optical arrangement, m, the distance between the specimen and the viewing screen where the caustic is formed, z_0, and the specimen thickness, d. Note form figure that for all specimen thicknesses the ratio K_{exp}/K_{th} increases with r/d and reaches a plateau value equal to one as the radius of the initial curve takes a limiting value r_c. At that value of $r = r_c$ the state of stress in the neighborhood of the crack tip becomes plane stress. For distances r smaller than r_c the state of stress is three-dimensional, while for values of r larger than r_c plane stress conditions dominate. From Fig. 4 and analogous figures the critical value of r_c can be determined. We obtained that r_c = d for d = 3 mm, r_c = 0.9d for d = 4.5 mm, r_c = 0.5d for d = 9.5 mm and r_c = 0.4d for d = 12.5 mm. Thus the critical value of r for which the state of stress becomes plane stress depends on d and the geometrical characteristics of the cracked plate, especially the ratio of crack length to specimen thickness.
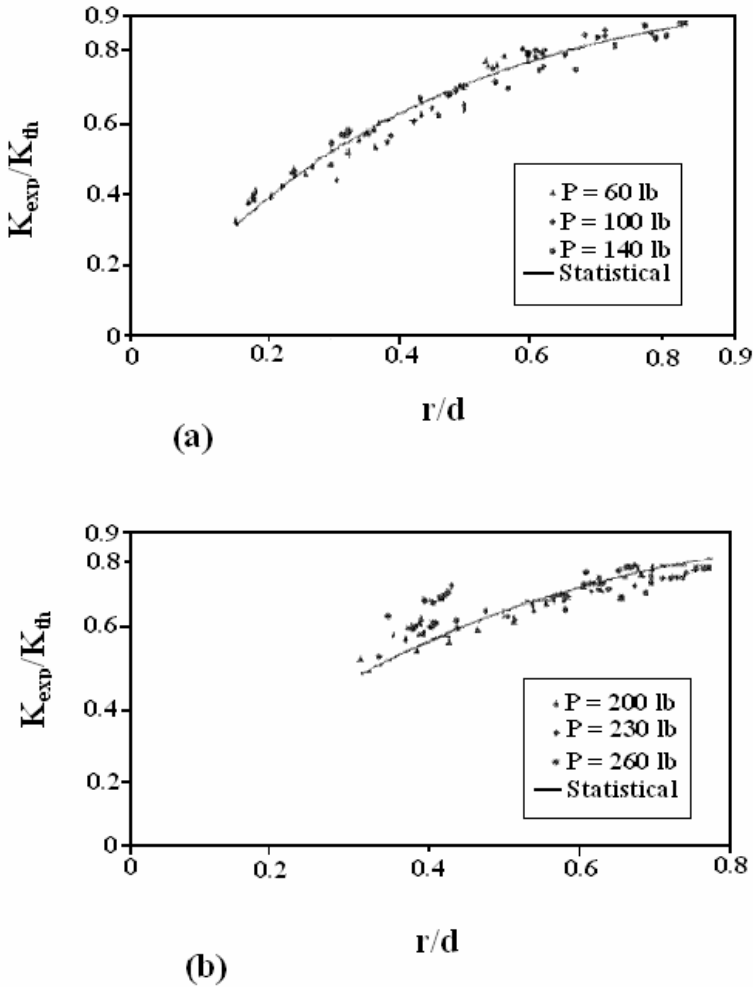
Fig. 4. Variation of K_{exp}/K_{th} versus r/d for a = 15.5 mm, d = 4.5 mm and w = 47.5 mm (a) and w = 63.5 mm (b)

From the above results it is shown that plane stress conditions prevail at distances from the crack tip larger than a specimen fraction. Analogous results obtained by finite elements have concluded that plane stress conditions dominate at distances away from the crack tip equal to half the specimen thickness [8]. This result was verified experimentally in [9]. Thus in order to obtain caustics

generated from the region of plane stress the radius of the initial curve of the caustic should be larger than a fraction of the specimen thickness. By taking it half the specimen thickness we obtain

$$\left(\frac{3.385 z_0 cK}{m} \right)^{2/3} > d \tag{30}$$

Inequality (30) establishes a condition the quantities, z_0, c, K, m, d should satisfy in order to obtain caustics generated by an initial curve that lies in the plane stress region in the neighborhood of the crack tip.

5 Limits of Applicability of the Method of Caustics

Based on the above, results are presented for the limits of validity of the method of caustics under conditions of plane stress for the determination of stress intensity factors for opening-mode loading. Fig. 5 presents the variation of the critical (maximum) value of specimen thickness, d_c, versus K_I for $z_i = 0.8$ m for a divergent light beam illuminating a notched Plexiglas specimen. z_i represents the distance between the point light source and the specimen. Observe that the critical thickness d_c increases as K_I and z_0 increase.

Fig. 6 presents the variation of r_0 versus stress intensity factor K_I for a Plexiglas specimen of thickness d = 10 mm illuminated by a parallel light beam. The caustic is created by transmitted light rays ($c_t = 1.08 \times 10^{-10} m^2 N^{-1}$) and the reference screen is placed at distances $z_0 = 0.1, 1$ and 10 m from the specimen. K_I varies up to 1 MPa√m corresponding to the value of fracture toughness of Plexiglas. In the same figure the line $r_0 = d/2$ is drawn. Observe that r_0 increases as K_I and z_0 are also increased. Only for the part of curves above the line $r_0 = d/2$, does the radius of the initial curve lay in the region of plane stress. It is observed that the realm of validity of the method of caustics under conditions of plane stress increases with K_I and z_0.

For convergent light the lower and upper bounds of validity of plane stress caustics are drawn in Fig. 7 versus K_I for $z_i = 10$ cm. The specimen thickness d takes the values 0.5 and 1 mm. The shaded areas in the figure represent the region (combination of K_I for z_0 values) where plane stress caustics are obtained. Note that the upper limit tends to infinity for $K_I = 0.31$ MPa√m. From Fig. 7 it is shown that the region of validity of plane stress caustics diminishes as the specimen thickness increases.
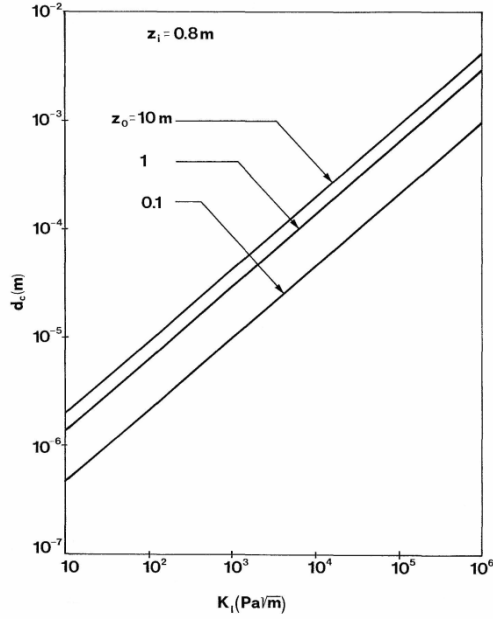
Fig. 5. Variation of maximum value of d (d_c) versus K_I for divergent light. z_i = 0.8 m, and z_0 = 0.1, 1 and 10 m.
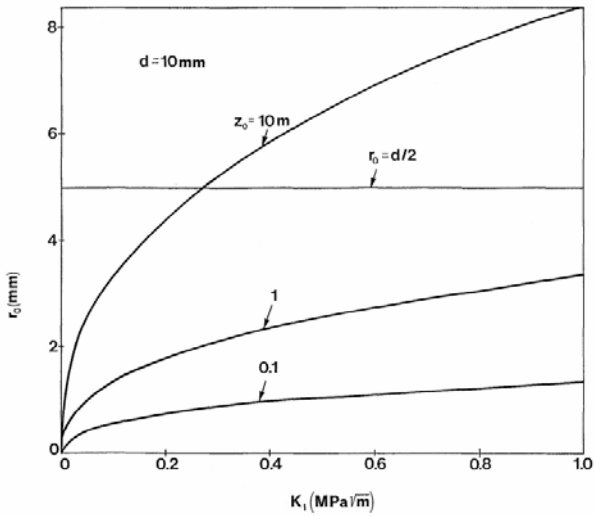
Fig. 6. Variation of r_0 versus K_I for parallel light. d = 10 mm, z_0 = 0.1, 1 and 10 m
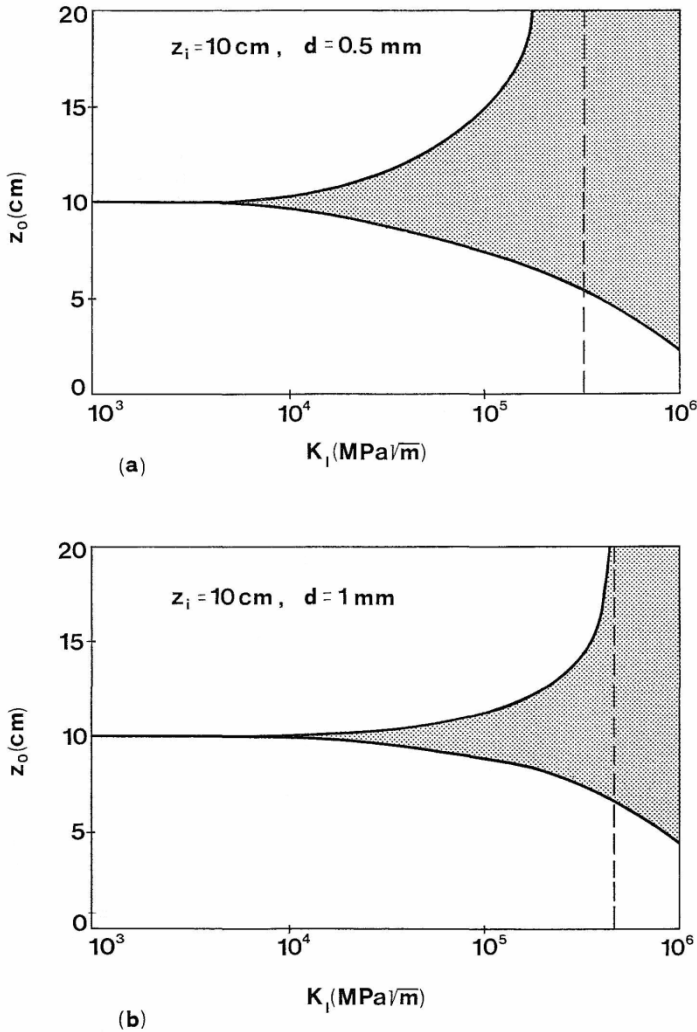
Fig. 7. Limits of applicability of plane stress caustics for convergent light. $z_i = 10$ cm, and (a) d = 0.5 mm and (b) d = 1 mm.

6 Conclusions

The basic principles of the optical method of caustics were presented. It is shown that special precautions should be taken when applying the method to determine stress intensity factors in crack problems. The applied loads, the specimen dimensions and the characteristic lengths of the optical arrangement should be properly selected for the correct application of the method. Otherwise, erroneous results may be obtained. A thorough investigation of the limits of validity of the method of caustics under conditions of plane stress was undertaken. The cases of a parallel, divergent or

convergent light beam illuminating the specimen were studied. The main results of the present study may be summarized as:

(1) The state of stress in the neighborhood of the crack tip changes from plane strain at the tip to plane stress at a critical distance from the tip. Between the two regions the state of stress is three-dimensional.

(2) The critical distance from the crack tip at which the state of stress becomes plane stress depends mainly on the thickness of the plate, and secondary on its geometrical characteristics, especially the ratio of crack length to specimen thickness.

(3) For the correct determination of K_I by the optical method of caustics certain conditions must be satisfied.

(4) The experimentalist should properly choose the geometry of the optical arrangement, the plate thickness and the applied load.

(5)The specimen thickness should be smaller than a critical value dictated by the geometry of the optical arrangement, the material of the specimen and the applied load.

(6) The maximum permissible plate thickness increases with the applied load and the distance between the specimen and the reference screen and decreases with the magnification factor.

(7) For certain materials and optical arrangements plates of very small thickness are required. Such small thicknesses may introduce difficulties in the execution of the experiment.

(8) Reflected caustics allow larger plate thicknesses to be used than transmitted caustics (the stress-optical constant for reflected light is larger than for transmitted light).

Dedication

This paper is dedicated to the memory of P.S. Theocaris, pioneer of the optical method of caustics and optical methods of stress analysis in appreciation of his mentorship, guidance and support during the first years of my academic life.

References

1. Theocaris, P.S.: Local yielding around a crack-tip in plexiglas. J. Appl. Mech. Trans. ASME 37, 409–415 (1970)
2. Theocaris, P.S.: Elastic stress intensity factors evaluated by caustics. In: Sih, G.C. (ed.) Mechanics of Fracture, vol. 7, pp. 189–252. Martinus Nijhoff Publishers (1981)
3. Theocaris, P.S., Gdoutos, E.E.: An optical method for determining opening-mode and edge sliding-mode stress intensity factors. J. Appl. Mech. Trans. ASME 39, 91–97 (1972)
4. Theocaris, P.S., Gdoutos, E.E.: The modified Dugdale-Barenblatt model adapted to various fracture configurations in metals. Int. J. Fract. 10, 549–564 (1974)
5. Theocaris, P.S., Gdoutos, E.E.: Verification of the validity of the Dugdale-Barenblatt model by the method of caustics. Engng. Fract. Mech. 6, 523–535 (1974)

6. Theocaris, P.S.: The method of caustics applied to elasticity problems. In: Holister, G. (ed.) Developments in Stress Analysis, pp. 27–63. Applied Science Publishers (1979)
7. Theocaris, P.S.: Complex stress intensity factors evaluated by pseudocaustics. Engng. Fract. Mech. 41, 707–720 (1992)
8. Levy, N., Marcal, P.V., Rice, J.R.: Progress in three-dimensional elastic-plastic stress analysis for fracture mechanics. Nucl. Engng. Design 17, 64–75 (1971)
9. Rosakis, A.J., Ravi-Chandar, K.: On crack tip stress state: an experimental evaluation of three-dimensional effects. Int. J. Sol. Struct. 22, 121–134 (1986)
10. Meletis, E.I., Huang, W., Gdoutos, E.E.: A study of the three-dimensional region at crack tips by the method of caustics. Engng. Fract. Mech. 39, 875–885 (1991)
11. Konsta-Gdoutos, M., Gdoutos, E.E.: Guidelines for applying the method of caustics in crack problems. Exp. Tech. 16, 25–28 (1992)
12. Konsta-Gdoutos, M., Gdoutos, E.E.: Some remarks on caustics in mode I stress intensity factor evaluation. Theor. Appl. Fract. Mech. 17, 47–60 (1992)
13. Konsta-Gdoutos, M., Gdoutos, E.E.: Limits of applicability of the method of caustics in crack problems. Engng. Fract. Mech. 42, 251–263 (1992)
14. Konsta-Gdoutos, M., Gdoutos, E.E., Meletis, E.I.: The state of stress at a crack tip studied by caustics. In: Proc. VII Int. Congr. Exp. Mech., Las Vegas, U.S.A., June 8-11, vol. 1, pp. 797–801. SEM (1992)
15. Konsta-Gdoutos, M., Gdoutos, E.E.: A New outlook in the evaluation of stress intensity factors by caustics. In: Proc. 1995 SEM Spring Conf. Exp. Mech., Grand Rapids, Michigan, U.S.A., June 12-14, pp. 158–161 (1995)
16. Raftopoulos, D.D., Zugang Huang, M., Konsta-Gdoutos, M., Gdoutos, E.E.: Evaluation of the three-dimensional region around a crack tip by caustics. Int. J. Fract. 98, 343–350 (1999)
17. Raftopoulos, D.D., Meissner, J., Konsta-Gdoutos, M., Gdoutos, E.E.: The method of caustics in conjunction with the method of birefringent coatings for the solution of fracture mechanics problems. Int. J. Fract. 74, R39–R43 (1996)
18. Konsta-Gdoutos, M., Gdoutos, E.E., Raftopoulos, D.D., Meissner, J.: Evaluation of stress intensity factors in metals by photoelastic coatings and caustics. J. Mech. Behav. Mats 6, 135–145 (1996)
19. Raftopoulos, D.D., Meissner, J., Konsta-Gdoutos, M., Gdoutos, E.E.: Fracture mechanics study of human bone by birefringent coatings and caustics. Int. J. Fract. 91, R51–R54 (1998)
20. Konsta-Gdoutos, M., Gdoutos, E.E., Raftopoulos, D.D., Meissner, J.: Stress intensity factors in human bones by optical methods. J. Mech. Behav. Mats 9, 17–22 (1998)
21. Gdoutos, E.E.: Fracture Mechanics Criteria and Applications. Kluwer Academic Publishers, Dordrecht (1990)
22. Gdoutos, E.E.: Fracture Mechanics – An Introduction, 2nd edn. Springer, Heidelberg (2005)

Reinforcement of a Cracked Infinite Elastic Plate with Defects

S.M. Mkhitaryan[1] and D.I. Bardzokas[2]

[1] Institute of Mechanics of NAS RA, Armenia – Yerevan
[2] National Technical University of Athens, School of Applied Mathematical
  and Physical Sciences, Department of Mechanics, Greece – Athens
  smkhitaryan@mechins.sci.am

Abstract. We study a series of problems involving multiple connected and cracked bodies. Based on the boundary conditions, we derive the equations describing the stress – strain field of the body. A case of special interest is the one when mixed boundary conditions apply on the crack lips. Specifically, either we can place thin inclusions on the crack lips near its edges or in its central part; these inclusions can be modeled as linearly deformable springs of certain stiffness, based on Winkler's model. We also examine the case when the central part of the crack is reinforced with a stringer while on the edges of the crack elastic springs are placed in specific distances. On the areas where there are no stringers or thin inclusions, the normal and shear stresses are considered as known. An infinite plate is loaded at infinity with normal and shear strains. We study the interaction of the reinforcements and the weakening of the composite plate by calculating the stress intensity factor (SIF) on the crack lips, as well as the stress – strain field of the composite cracked plate.

1 Introduction

Thin plates in structures are always reinforced with stringers especially in light constructions used in aircrafts. Hence, there has been a big interest in studying the influence of the stress distribution of the stringer on the stress field of plates. Sheremetiev, Savin, Melan, Buell, Sanders, Brown and Koiter were some of the most important researchers of the problem up to now. Since the theoretical study of the problem presents serious difficulties, many assumptions and simplifications were introduced in the previous papers. Thus, Buell, Koiter and Kalandiya assumed as a stringer an infinite or semi-infinite elastic bar whose only possible deformation was along its longitudinal axis and there was no possibility of bending the stringer. A similar study of the stress distribution in a thin flat plate cemented on a straight bar under simple tension was studied by Theocaris and Dafermos who also evaluated the singular field at the corner of the plate cemented with the stringer. Sheremetiev, as well as Muki and Sternberg, have studied the

influence of rigidity of stringers on the stress distribution of the plate embedding the stringer, whereas Sheremetiev in another paper observed that if the rigidity of the stringer is reduced to a negligible amount the state of stress of the plate in influenced considerably.

Most of the papers mentioned up to now considered the plate as uniform, not containing any discontinuity, holes or cracks. The problem becomes much more difficult when the plate is considered to have some kind of discontinuity in the form of holes and cracks. However, the problem of the cracked plate containing a stringer has an obvious importance for practical means. Greif, Sanders and Kaladiya have studied the influence of a rectilinear stringer on the stress distribution around a stationary crack contained in the plate whose form and position where given in advance. Those types of problems are of special theoretical as well as practical importance (due to their application in composite materials technology, new materials, soil and rock mechanics, navigation, biomechanics etc) so efficient methods, either analytical or numerical, are needed to treat them. Those methods enable us to study both qualitatively and quantitavely the behavior of the area where the stresses are concentrated. This is very useful in avoiding crack propagation. Due to the novelty and the complexity of the above mentioned mixed problems (when considering the boundary values) many researchers (see for example [1-4]) have focused their efforts in solving cases such as the geometry and the action of different physical or mechanical fields.

2   Reinforcement of a Cracked Plate with Stringers

In the process of reinforcing a plate, it is a common practice to adjust the position of the reinforcements according to the position and the geometry of the flaw. In this part of the paper we will examine the reinforcement of a cracked plate with straight and curvilinear stringers. Let us consider an infinite and isotropic plate of thickness h and elastic constants E, v, κ, μ, that is weakened by two cracks ℓ_1 and ℓ_2 but a also reinforced with a straight stringer L_1 and a stringer L_2 of circular shape and radius R. The thickness, the cross section area and the elastic constants of the two stringers are $h_1 = h_2 = h$, S_1, S_2, E_1, E_2 respectively. The tensions of the plate at infinity, referring to the main coordinate system are N_1, N_2. On the cracks, the following boundary conditions apply:

a) On the lips of ℓ_1 crack the stresses are given:

$$\sigma_n^\pm - i\sigma_t^\pm \tag{1}$$

b) On the lips of ℓ_2 cracks the displacements are given:

$$u^\pm + iv^\pm \tag{2}$$

c) On boundary L_1 between the plate and the straight stringer we have the following combination of boundary conditions:

$$\begin{cases} \sigma_n^+ = \sigma_n^- \\ u_n^+ + iu_t^+ = u_n^- + iu_t^- \quad t \in L_1 \\ \varepsilon_0^{str_1} = \dfrac{du_t^+}{dx} = \dfrac{du_t^-}{dx} \end{cases} \tag{3}$$

where $t = d_1 e^{i\beta_1} + x e^{i\theta_1}$, d_1 is the distance from the center of the system until the middle of L_1, β_1 is the corner between the two centers and θ_1 is the corner between the x-axis and the direction of L_1.

d) On the boundary L_2 between the plate and the curvilinear stringer we will have the following relations:

$$\begin{cases} -\dfrac{T(\theta)}{R} + h(\sigma_n^+ - \sigma_n^-) = 0 \\ \dfrac{1}{R} \dfrac{dT(\theta)}{d\theta} + h(\sigma_t^+ - \sigma_t^-) = 0 \quad t \in L_2 \\ u_n^+ + iu_t^+ = u_n^- + iu_t^- \\ T(\theta) = E_2 S_2 \varepsilon_0^{str_2} \end{cases} \tag{4}$$

where $t = d_2 e^{i\beta_2} + t_2$ and $t_2 = Re^{i\theta_2}$.

In order to deduce the state equations we will use the following complex potentials:

$$\Phi_0(z) = \Gamma + \frac{1}{2\pi i} \int_{\ell_1} \frac{\phi_1(\tau)}{\tau - z} d\tau + \frac{1}{2\pi i} \int_{\ell_2} \frac{\phi_2(\tau)}{\tau - z} d\tau + \frac{1}{2\pi i} \int_{L_1} \frac{\mu_1(\tau)}{\tau - z} d\tau + \frac{1}{2\pi i} \int_{L_2} \frac{\mu_2(\tau)}{\tau - z} d\tau \tag{5}$$

$$\Psi_0(z) = \Gamma' + \frac{1}{2\pi i} \int_{\ell_1} \frac{y_1(\tau)}{\tau - z} d\tau + \frac{1}{2\pi i} \int_{\ell_2} \frac{y_2(\tau)}{\tau - z} d\tau + \frac{1}{2\pi i} \int_{L_1} \frac{G_1(\tau)}{\tau - z} d\tau + \frac{1}{2\pi i} \int_{L_2} \frac{G_2(\tau)}{\tau - z} d\tau \tag{6}$$

where $\Gamma = \dfrac{1}{4}(N_1 + N_2)$ and $\Gamma' = -\dfrac{1}{2}(N_1 - N_2)$.

Based on the boundary values of the complex potential the boundary conditions (1) and (2) we take the following form:

$$t \in \ell_1: \quad \sigma_n^{\pm} - i\sigma_t^{\pm} = \Phi_0^{\pm}(t_1) + \overline{\Phi_0^{\pm}(t)} + \frac{dt}{dt}\left[\overline{t\Phi_0'^{\pm}(t) + \Psi_0^{\pm}(t)} \right] \tag{7}$$

$$t \in \ell_2: \quad 2\mu\left[-\frac{\overline{du^{\pm}}}{dt} + i\frac{\overline{dv^{\pm}}}{dt} \right] = \Phi_0^{\pm}(t) - \kappa\overline{\Phi_0^{\pm}(t)} + \left[\overline{t\Phi_0'^{\pm}(t) + \Psi_0^{\pm}(t)} \right] \tag{8}$$

The combination of relations (3) and (4) will yield the next relations:

$$t \in L_1: \quad ih\left[\left(\sigma_n^+ - i\sigma_t^+\right) - \left(\sigma_n^- - i\sigma_t^-\right)\right] + \frac{E_1 S_1}{E} ie^{i\theta_1} \frac{d}{dt}\left[\left(\sigma_n^+ + \sigma_t^+\right) - (1+v)\sigma_n^+\right] = 0$$

(9)

$$t \in L_2: \quad ERh\left[\left(\sigma_n^+ - i\sigma_t^-\right) - \left(\sigma_n^- - i\sigma_t^-\right)\right] - E_2 S_2\left[1 - \left(t - d_2 e^{i\beta_2}\right)\frac{d}{dt}\right] \times \left[\left(\sigma_n^+ + \sigma_s^+\right) - (1+v)\sigma_n^+\right] = 0$$

(10)

Boundary conditions (9) and (10) based on the boundary values of the complex potential will take the following form:

$$ih\left[\Phi^+(t) - \Phi^-(t)\right] + \left(\overline{\Phi^+(t)} - \overline{\Phi^-(t)}\right) + \frac{\overline{dt}}{dt}\left[\overline{t}\left(\Phi'^+(t) - \Phi'^-(t)\right) + \Psi^+(t) - \Psi^-(t)\right] +$$

$$+ \frac{E_1 S_1}{E} ie^{i\theta_1} \frac{d}{dt}\left\{(1-v)\left(\Phi^+(t) + \overline{\Phi^+(t)}\right) - \left[\operatorname{Re}\frac{dt}{dt}\left[\overline{t}\Phi'^+(t) + \Psi^+(t)\right]\right] +$$

$$+ 2(1-v)\Gamma - (1-v)\operatorname{Re}\left(\frac{\overline{dt}}{dt}\Gamma'\right)\right\}, \qquad t \in L_1$$

(11)

$$ERh\left[\left(\Phi^+(t) - \Phi^-(t)\right) + \left(\overline{\Phi^+(t)} - \overline{\Phi^-(t)}\right) + \frac{\overline{dt}}{dt}\left[\overline{t}\left(\Phi^+(t) - \Phi^-(t)\right) + + \Psi^+(t) - \Psi^-(t)\right]\right] -$$

$$- E_2 S_2\left(1 - \left(t - d_2 e^{i\beta_2}\right)\frac{d}{dt}\right)\left\{(1-v)\left(\Phi^+(t) + \overline{\Phi^+(t)}\right) - \left[\operatorname{Re}\frac{d}{dt}\left[\overline{t}\Phi'^+(t) + \Psi^+(t)\right]\right] +$$

$$+ 2(1-v)\Gamma - (1-v)\operatorname{Re}\left(\frac{d}{dt}\Gamma'\right)\right\}, \qquad t \in L_2$$

(12)

By subtraction of the reciprocal relations in (7) and (8), and taking into account relations (3) and (4) as well as the Sohotsky – Plemely formulas for the boundary values of the complex potentials relation (6) will take the following form:

$$\Psi_0(z) = \Gamma' + \frac{1}{2\pi i}\int_{\ell_1}\frac{q_1(\tau)}{\tau - z}\overline{d\tau} - \frac{1}{2\pi i}\int_{\ell_1}\frac{\overline{\phi_1(\tau)}}{\tau - z}\overline{d\tau} - \frac{1}{2\pi i}\int_{\ell_1}\frac{\overline{\tau\phi_1(\tau)}}{(\tau - z)^2}d\tau +$$

$$+ \frac{1}{2\pi i}\int_{\ell_2}\frac{g_1(\tau)}{\tau - z}d\tau + \frac{\kappa}{2\pi i}\int_{\ell_2}\frac{\overline{\varphi_2(\tau)}}{\tau - z}\overline{d\tau} - \frac{1}{2\pi i}\int_{\ell_2}\frac{\overline{\tau\varphi_2(\tau)}}{(\tau - z)^2}d\tau +$$

(13)

$$+ \frac{\kappa}{2\pi i}\int_{L_1}\frac{\overline{\mu_1(\tau)}}{\tau - z}\overline{d\tau} - \frac{1}{2\pi i}\int_{L_1}\frac{\overline{\tau\mu_1(\tau)}}{(\tau - z)^2}d\tau + \frac{\kappa}{2\pi i}\int_{L_2}\frac{\overline{\mu_1(\tau)}}{\tau - z}\overline{d\tau} - \frac{1}{2\pi i}\int_{L_2}\frac{\overline{\tau\mu_2(\tau)}}{(\tau - z)^2}d\tau$$

where $q_1(t) = \left(\sigma_n^+ - \sigma_n^-\right) - i\left(\sigma_t^+ - \sigma_t^-\right)$, $g(t) = 2\mu\left[-\frac{d}{dt}\left(u^+ - u^-\right) + i\frac{d}{dt}\left(v^+ - v^-\right)\right]$

Taking into consideration the reciprocal Sohotsky – Plemely formulas for the complex potentials (5) and (13) in relations $(7_1)+(7_2)$, $(8_1)+(8_2)$, (11), (12) we will get a system of four singular integral equations with respect to densities $\phi_1(t), \phi_2(t), \mu_1(t), \mu_2(t)$. The system must be augmented with the condition of uniqueness of displacements for the crack ℓ_1. The above system fully describes the stress – strain field of the cracked plate that is reinforced by stringers.

3 Reinforcement of a Plate with a Patch

Let us consider the case when we put a circular patch S_1 to reinforce a crack that exists in an infinite and isotropic plate S. The infinite plate is loaded at infinity with prime stresses N_1, N_2, the stresses $(\sigma_n^\pm - i\sigma_t^\pm)$ or displacements $(u^\pm + iv^\pm)$ on the crack lips are considered known. On the boundary γ between the plate S and the patch S_1 the following boundary relations for the unknown deformations and stresses hold true:

$$
\begin{cases}
\dfrac{d}{dt}(u+iv) = \dfrac{d}{dt}(u_1+iv_1), & t \in \gamma \\[2mm]
(\sigma_n + i\sigma_t)\big|_{t \in \gamma \in S} = -(\sigma_n + i\sigma_t)\big|_{t \in \gamma \in S_1} = f(t)
\end{cases}
\tag{14}
$$

The elastic constants of the two bodies S and S_1 will be κ, μ and κ_1, μ_1 reciprocally. For the description of the stress – strain field of the composite body we will need two pair of complex potentials.

For the plate:

$$
\begin{cases}
\Phi(z) = \Gamma + \dfrac{1}{2\pi i}\displaystyle\int_\ell \dfrac{\phi(\tau)}{\tau - z}d\tau + \dfrac{1}{2\pi(1+\kappa)}\oint_\gamma \dfrac{f(z)}{\tau - z}d\tau \\[4mm]
\Psi(z) = \Gamma' + \dfrac{1}{2\pi i}\displaystyle\int_\ell \dfrac{y(\tau)}{\tau - z}d\tau - \dfrac{\kappa}{2\pi(1+\kappa)}\oint_\gamma \dfrac{\overline{f(\tau)}}{\tau - z}\overline{d\tau} + \dfrac{1}{2\pi(1+\kappa)}\oint_\gamma \dfrac{\overline{\tau}f(\tau)}{(\tau - z)^2}d\tau
\end{cases}
\tag{15}
$$

for the circular patch

$$
\Phi_1(z) =
\begin{cases}
\dfrac{1}{2\pi i}\displaystyle\oint_\gamma \dfrac{G(\tau)}{\tau - z}d\tau, & z \in S_1 \\[4mm]
0, & z \notin S_1
\end{cases}
$$

$$
\Psi_1(z) =
\begin{cases}
\dfrac{1}{2\pi i}\displaystyle\oint_\gamma \dfrac{Q(\tau)}{\tau - z}d\tau, & z \in S_1 \\[4mm]
0, & z \notin S_1
\end{cases}
\tag{16}
$$

The boundary conditions on the crack lips will be written as follows, if we consider the complex potential (15):

$$\sigma_n^\pm - i\sigma_t^\pm = \Phi^\pm(t) + \overline{\Phi^\pm(t)} + \frac{dt}{d\bar{t}}\Big[\bar{t}\overline{\Phi}'^\pm(t) + \overline{\Psi^\pm(t)}\Big], \quad t \in \ell \tag{17}$$

or

$$2\mu\left[-\frac{d}{dt}u^\pm + i\frac{d}{dt}v^\pm\right] = \Phi^\pm(t) - \kappa\overline{\Phi^\pm(t)} + \frac{dt}{d\bar{t}}\Big[\bar{t}\overline{\Phi}'^\pm(t) + \overline{\Psi^\pm(t)}\Big], \quad t \in \ell$$

Based on conditions (14) and the expressions for the stresses and the displacements through the complex potentials (15) and (16):

$$t \in \gamma \qquad \frac{\kappa+1}{\mu}\Phi(t) + \frac{f(t)}{\mu} = \frac{\kappa_1+1}{\mu_1}G(t) - \frac{f(t)}{\mu_1} \tag{18}$$

or

$$G(t) = \frac{\mu_1}{\mu}\frac{\kappa+1}{\kappa_1+1}\Phi(t) + \frac{\mu+\mu_1}{\mu(\kappa_1+1)}f(t) \tag{19}$$

Following the know process we analyzed in the previous section we will get two integral equations on ℓ and the boundary γ of the patch S_1.

$$\frac{1}{\pi i}\int_\ell \frac{\phi(\tau)}{\tau - t}d\tau + \frac{\lambda}{\pi i}\int_\ell \frac{\overline{\phi(\tau)}}{\overline{\tau} - \overline{t}}\overline{d\tau} - \frac{dt}{d\bar{t}}\left[-\frac{\lambda}{\pi i}\int_\ell \frac{\overline{\phi(\tau)}}{\overline{\tau} - \overline{t}}\overline{d\tau} + \frac{1}{\pi i}\int_\ell \frac{\overline{\tau} - \overline{t}}{(\tau - t)^2}\phi(\tau)d\tau\right] +$$

$$+\left[\frac{1}{\pi(1+\kappa)}\oint_\gamma \frac{f(\tau)}{\tau - t}d\tau + \frac{\lambda}{\pi(1+\kappa)}\oint_\gamma \frac{\overline{f(\tau)}}{\overline{\tau} - \overline{t}}\overline{d\tau} - \frac{dt}{d\bar{t}}\left[-\frac{\kappa}{\pi(1+\kappa)}\oint_\gamma \frac{\overline{f(\tau)}}{\overline{\tau} - \overline{t}}\overline{d\tau} + \tag{20}\right.$$

$$\left.+\frac{1}{\pi(1+\kappa)}\oint_\gamma \frac{\overline{\tau} - \overline{t}}{(\tau - t)^2}f(\tau)d\tau\right] = q_2(t) - \frac{dt}{d\bar{t}}\int_\ell \frac{\overline{q_1(\tau)}}{\overline{\tau} - \overline{t}}\overline{d\tau}, \qquad t \in \ell$$

where

a) when the stresses on the crack lips are given

$$\lambda = -1, \quad q_1(t) = \left(\sigma_n^+ - \sigma_n^-\right) - i\left(\sigma_t^+ - \sigma_t^-\right), \quad q_2(t) = \left(\sigma_n^+ + \sigma_n^-\right) - i\left(\sigma_t^+ + \sigma_t^-\right) - 2\left(\Gamma + \overline{\Gamma} + \frac{dt}{d\bar{t}}\Gamma'\right)$$

b) when the displacements on the crack lips are given

$$\lambda = \kappa, \quad q_1(t) = 2\mu\left[-\frac{d}{dt}\left(u^+ - u^-\right) + i\frac{d}{dt}\left(v^+ - v^-\right)\right],$$

$$q_2(t) = 2\mu\left[-\frac{d}{dt}\left(u^+ + u^-\right) + i\frac{d}{dt}\left(v^+ + v^-\right)\right] - 2\left(\Gamma - \kappa\overline{\Gamma} + \frac{dt}{d\bar{t}}\Gamma'\right)$$

The integral equation on the boundary γ has the following form, $t \in \gamma$:

$$\frac{1}{\pi i}\oint_\gamma \frac{G(\tau)}{\tau-t}d\tau - \frac{1}{\pi i}\oint_\gamma \frac{\overline{G(z)}}{\overline{\tau}-\overline{t}}\overline{d\tau} - \frac{dt}{d\overline{t}}\left[\frac{1}{\pi i}\oint_\gamma \frac{\overline{G(\tau)}}{\tau-t}\overline{d\tau} + \frac{1}{\pi i}\oint_\gamma \frac{\overline{\tau}-\overline{t}}{(\tau-t)^2}G(\tau)d\tau\right] = -\overline{f(t)} + \frac{dt}{d\overline{t}}\frac{1}{\pi i}\oint_\gamma \frac{\overline{f(\tau)}}{\tau-t}\overline{d\tau}$$

$$(21)$$

also relation (19) can be written as an integral equation

$$\frac{\mu_1}{\mu}\frac{\kappa+1}{\kappa_1+1}\left[\Gamma + \frac{1}{2\pi i}\int_\ell \frac{\phi(\tau)}{\tau-t}d\tau + \frac{1}{2\pi i}\oint_\gamma \frac{f(\tau)}{\tau-t}d\tau\right] + \frac{\mu+\mu_1}{\mu(\kappa_1+1)}f(t) = G(t), \quad t \in \gamma \quad (22)$$

The system of equations (20) – (22) augmented with the condition of uniqueness of displacements on the crack, when the stresses are given, can fully describe the stress – strain field of the composite cracked plate.

4   Linear Crack of Finite Size, the Lips of Which Are Connected with Elastic Springs

Let us consider, in the framework of generalized plain strain an infinite isotropic and elastic plate of height h, and elastic constants E, v. We will use the Cartesian system of coordinates Oxy to describe the plate. On Ox-axis a mathematical crack exists in the space $[-a, a]$. In this section, we will examine two problems. In the first problem the lips of the crack in the extreme points $(-a, -b) \cup (b, a)$, where $b < a$ are connected between them with equally dispersed linear elastic springs with stiffness Ek, while on the rest part of the crack $(-b, b)$ act perpendicular tensions, the intensity of which is $p_\pm(x)$ (the signs refer to each of the crack lips). The plate is subjected to an equally dispersed and perpendicular to the crack tension σ at infinity. In the second problem, the springs and the loading are switched between each other.

Using the known processes, we transfer the tension σ from infinity on the crack lips. This will be achieved by drawing an imaginary incision of the plate in the direction of Ox-axis thus separating it in to two half-planes symbolized as $\pm$. For the first problem, under the assumption that the springs behave linearly we will have:

$$\sigma_{yy}\Big|_{y=\pm0} = -\Sigma_\pm(x) = \begin{cases} -\sigma - p_\pm(x), & |x| < b \\ -\sigma \pm Ekv_\pm(x), & b < x < a \\ -\sigma(x), & |x| > a \end{cases} \quad (23)$$

$$\sigma_{xy}\Big|_{y=\pm0} = -T_\pm(x) = \begin{cases} 0, & |x| < a \\ -\tau(x), & |x| > a \end{cases} \quad (24)$$

For the second problem we will have

$$\sigma_{yy}\Big|_{y=\pm 0} = -\Sigma_{\pm}(x) = \begin{cases} -\sigma \pm Ekv_{\pm}(x), & |x| < b \\ -\sigma - p_{\pm}(x), & b < |x| < a \\ -\sigma(x), & |x| > a \end{cases} \tag{25}$$

while the boundary condition $\sigma_{xy}\Big|_{y=\pm 0}$ will be the same as (24)

In the above $\sigma_{yy}(x,y)$ and $\sigma_{xy}(x,y)$ are the perpendicular and shear stresses with respect to the height h of the plate, $\sigma(x)$ and $\tau(x)$ with the opposite sign the perpendicular and shear stresses outside of the crack and along the Ox-axis. Also $v_{\pm}(x)$ are the components of the perpendicular displacements of the boundary points of the upper and lower half-plate reciprocally. We notice that the shear stresses $\sigma_{xy} = -\tau(x)$ outside of the crack and on its direction appear due to the existence of perpendicular loading $p_{\pm}(x)$ that acts on the crack.

In order to deduce the state equations of the above boundary problems we will express the two components of the displacements $u_{\pm}(x), v_{\pm}(x)$ of the boundary points of the upper and lower half-planes as a functions if the perpendicular and shear loadings (23) – (25), which will take the form $-\infty < x < +\infty$:

$$u_{\pm}(x) = \pm \frac{2}{\pi E} \int_{-\infty}^{\infty} \ln \frac{1}{|x-s|} T_{\pm}(s)ds - \frac{1-v}{2E} \int_{-\infty}^{\infty} sign(x-s)\Sigma_{\pm}(s)ds + C_{1} \tag{26}$$

$$v_{\pm}(x) = \pm \frac{2}{\pi E} \int_{-\infty}^{\infty} \ln \frac{1}{|x-s|} \Sigma_{\pm}(s)ds + \frac{1-v}{2E} \int_{-\infty}^{\infty} sign(x-s)T_{\pm}(s)ds + C_{2} \tag{27}$$

Consequently, we introduce the following two functions of the displacement jumps on the crack lips:

$$v_{+}(x) - v_{-}(x) = \Phi(x) = \begin{cases} \varphi(x), & |x| < a \\ 0, & |x| > a \end{cases} \tag{28}$$

$$u_{+}(x) - u_{-}(x) = \Psi(x) = \begin{cases} \psi(x), & |x| < a \\ 0, & |x| > a \end{cases} \tag{29}$$

Based on the methods described in works [2,9,10] and relations (26) – (29) for the first problem we will have the next singular integral state equations:

$$\frac{1}{\pi} \int_{-1}^{1} \frac{\chi'(\eta)}{\eta - \xi} d\eta = \begin{cases} -\sigma_{0} - p_{0}(\xi), & |\xi| < \rho \\ -\sigma_{0} + \lambda\chi(\xi), & \rho < |\xi| < 1 \end{cases} \tag{30}$$

$$\chi(-1) = \chi(1) = 0 \tag{31}$$

$$\int_{-1}^{1}\frac{\psi'_0(\eta)}{\eta-\xi}d\eta = 2v_0\lambda\left(\int_{-1}^{-\rho}+\int_{\rho}^{1}\right)\frac{v_0(\eta)}{\eta-\xi}d\eta - v_0\int_{-\rho}^{\rho}\frac{q_0(\eta)}{\eta-\xi}d\eta, \quad |\xi|<1 \qquad (32)$$

$$\psi_0(-1)=\psi_0(1)=0 \qquad (33)$$

$$v_0(\xi)+\frac{\lambda}{\pi}\left(\int_{-1}^{-\rho}+\int_{\rho}^{1}\right)\ln\frac{1}{|\xi-\eta|}v_0(\eta)d\eta = \frac{1}{2\pi}\int_{-\rho}^{\rho}\ln\frac{1}{|\xi-\eta|}q_0(\eta)d\eta \qquad (34)$$

$$\rho<|\xi|<1$$

In the above equations are used some dimensionless quantities and coordinates

$$\xi=\frac{x}{\alpha}, \eta=\frac{s}{\alpha}, \rho=\frac{b}{\alpha}, \lambda=2\alpha k, \sigma_0=4\sigma/E, v_0=(1-v)/4, \sigma_0(\xi)=4\sigma(\alpha\xi)/E, \tau_0(\xi)=4\tau(\alpha,\xi)/E$$

$$\chi(\xi)=\varphi(a\xi)/a, p_0^{\pm}(\xi)=4p_{\pm}(a\xi)/E, p_0(\xi)=\frac{1}{2}\left[p_0^{+}(\xi)+p_0^{-}(\xi)\right]$$

$$q_0(\xi)=p_0^{+}(\xi)-p_0^{-}(\xi), \psi_0(\xi)=\psi(a\xi)/a, v_0(\xi)=v(a\xi)/a=\left[v_+(a\xi)+v_-(a\xi)\right]/a$$

Equations (30) and (32) that enable us to calculate the unknown normalized densities of the dislocations of the displacement components on the crack lips should be examined in combination with conditions (31) and (33) reciprocally. Those relations express the continuity of the displacement components in the crack lips.

It is obvious that the combination of (30)-(31) can be separated from relations (32)-(33), which means that those systems can be examined undependably. System (30)-(31) contains the basic information of the first problem, while for the second problem equation (30) will become:

$$\frac{1}{\pi}\int_{-1}^{1}\frac{\chi'(\eta)}{\eta-\xi}d\eta = \begin{cases} -\sigma_0+\lambda\chi(\xi), & |\xi|<\rho \\ -\sigma_0-p_0(\xi), & \rho<|\xi|<1 \end{cases} \qquad (35)$$

when (31) as well as the rest of the equations (32)-(34) while remain almost the same, with a just some simple modifications.

We have to note here that for $\rho=0$ the system (30)-(31), as well as (35) are transformed in the known integro-differential equation Prandtl [1]. In the case that $\rho=1$ and $\rho=0$, the above equations will result to the known equation for the crack [2,9,10].

After the solving the system (30)-(34) the perpendicular and shear dimensionless stresses outside the crack, on the direction of Ox-axis are given by:

$$\sigma_0(\xi)=-\frac{1}{\pi}\int_{-1}^{1}\frac{\chi'(\eta)}{\eta-\xi}d\eta, \quad |\xi|>1 \qquad (36)$$

$$\tau_0(\xi)=-\frac{1}{\pi}\int_{-1}^{1}\frac{\psi'_0(\eta)}{\eta-\xi}d\eta-\frac{v_0}{\pi}\int_{-\rho}^{\rho}\frac{q_0(\eta)}{\eta-\xi}d\eta+\frac{2v_0\lambda}{\pi}\left(\int_{-1}^{\rho}+\int_{\rho}^{1}\right)\frac{v_0(\eta)}{\eta-\xi}d\eta, \quad |\xi|>1 \qquad (37)$$

To solve the system (30)-(31) we will use an infinite series:

$$\chi'(\xi) = \frac{1}{\sqrt{1-\xi^2}} \sum_{n=0}^{\infty} x_n T_n(\xi), \quad |\xi| < 1 \tag{38}$$

with unknown factors x_n $(n = 0,1,2,...)$ where $T_n(\xi)$ is the Chebysev polynomial of the first type. By integration of (38) on $(-1,\xi)$ and taking into consideration relation (31), we note that $x_0 = 0$ and $\chi(\xi)$ become:

$$\chi(\xi) = -\sqrt{1-\xi^2} \sum_{n=1}^{\infty} \frac{x_n}{n} U_{n-1}(\xi), \quad |\xi| \le 1 \tag{39}$$

where $U_{n-1}(\xi)$ is the Chebyshev polynomial of the second type. Consequently, we note that equation (30) based on (38), (39) and the known relation:

$$\frac{1}{\pi} \int_{-1}^{1} \frac{T_n(\eta)}{(\eta-\xi)\sqrt{1-\eta^2}} d\eta = U_{n-1}(\xi), \quad |\xi| < 1, n = 1,2,...$$

can be reduced to an infinite system of algebraic equations, with respect to the unknown constants x_n $(n = 0,1,2,...)$:

$$x_n + \lambda \sum_{n=1}^{\infty} K_{k,n} x_n = a_k, \quad (k = 1,2,...) \tag{40}$$

where:

$$K_{k,n} = \begin{cases} -\dfrac{2\left[1+(-1)^{k+n}\right]}{\pi n \left[n^2-(k-1)^2\right]\left[n^2-(k+1)^2\right]} \Big[n\left(n^2-k^2-1\right)\sin\alpha \cdot \sin k\alpha \cdot \cos n\alpha + \\ +k\left(k^2-n^2-1\right)\sin\alpha \cdot \cos k\alpha \cdot \sin\alpha - \left(k^2+n^2-1\right)\cos\alpha \cdot \sin k\alpha \cdot \sin n\alpha + \\ +2kn\left(1-\cos\alpha \cdot \cos k\alpha \cdot \cos n\alpha\right) \Big], \quad n \ne k-1, n \ne k+1 \\ 0, \quad n = k-1, n = k+1, k,n = 1,2,... \end{cases}$$

$$a_k = -\sigma_0 a_k^{(1)} - a_k^{(2)}, \quad a_k^{(1)} = \begin{cases} 1, & k=1 \\ 0, & k=2,3,... \end{cases}, a_k^{(2)} = \frac{2}{\pi} \int_{-\rho}^{\rho} p_0(\xi)\sqrt{1-\xi^2} U_{k-1}(\xi) d\xi, \quad \alpha = \arccos\rho$$

In the same way, we can deduce a similar infinite and linear algebraic system of equations for the second problem. The non-singularity and the uniqueness of the solution of the system (40) is proven in [1], so the issue of solving this problem is fully covered.

For the stress intensity factors (SIF) on the edges of the crack we will have, based on (38) and known expressions from [5,6]:

$$K_{\pm\alpha} = \mp \frac{E}{4} \lim_{x \to \pm\alpha \mp 0} \left[\sqrt{2\pi(\alpha \mp x)} \varphi'(x) \right]$$

If we introduce the dimensionless quantities of the SIFs and putting $x = a\xi$, we will have:

$$K^0_{\pm a} = \mp \lim_{\xi \to \pm 1 \mp 0} \left[\sqrt{2\pi (1 \mp \xi)} \chi'(\xi) \right]$$

$$K^0_{\pm a} = 4K_{\pm a} / E\sqrt{a}$$

and taking into consideration expression (38) we have:

$$K^0_a = -\sqrt{\pi} \sum_{n=1}^{\infty} x_\eta, \quad K^0_{-a} = \sqrt{\pi} \sum_{n=1}^{\infty} (-1)^n x_n \tag{41}$$

Based on (37) with a similar process we will get expressions for the SIFs that are analogous to (41).

With the help of mathematical tools of the Chebyshev polynomials, the system of equations (32)-(33) can be also reduced to an infinite system of linear equations, while equation (34) can be transformed to a system of second type Fredholm integral equations with logarithmic kernels, and on that system method [12] can be applied. On equations (30)-(31) and (32)-(33) we can use the known arithmetic-analytic method of solving singular integral equations that is presented in [7,8].

5 Linear Crack of Finite Size, with Transverse Loading, the Lips of Which Are Connected with Thin Inclusions

As before, let us consider an infinite elastic plate with the same geometrical and elastic characteristics. Using a Cartesian system of coordinates Oxy, we will have a crack $(-a, a)$ on Ox-axis. On the edges of the crack $(-a, -b) \cup (b, a)$ where $b < a$, the crack is reinforced with thin inclusions that are described by Winker's model when in shear loading. On the rest part $(-b, b)$, and on the upper and lower part of the crack act equally distributed shear loadings with intensity $\tau_\pm(x)$, reciprocally. We also assume that there is a equally distributed load at infinity, the intensity of which is q.

We divide the plate in two half-planes by making an imaginary cut along the Ox-axis and, as we did on part 3, we will transfer the loading from infinity on the crack lips, taking into consideration the linear relation between shear stresses and horizontal displacements that the Winkers model suggests. We will have the next boundary conditions:

$$\sigma_{xy}\big|_{y=\pm 0} = -T_\pm(x) = \begin{cases} -q - \tau_\pm(x), & |x| < b \\ -q \pm Gku_\pm(x), & b < |x| < a \\ -\tau(x), & |x| > a \end{cases} \tag{42}$$

$$\sigma_{yy}\big|_{y=\pm 0} = -\Sigma_{\pm}(x) = \begin{cases} 0, & |x| < a \\ -\sigma(x), & |x| > a \end{cases} \tag{43}$$

here Gk is the coating coefficient of the Winkers' model, expressed through the shear modulus $G = E/2(1+v)$ of the plate. Begging form (42)-(43) and following the process of part 4 we can deduce the necessary state equations. If we apply the arithmetical method we described before on them, we will get in an infinite linear algebraic system of equations, the solution of which gives us the stress-strain field of the composite cracked plate.

6   Reinforcement of the Crack Lips with Stringers and Elastic Springs

Let us again consider the case when a linear crack $(-a, a)$ exists on Ox-axis. On the center part of the crack $(-b, b)$ the crack lips are connected with a thin elastic stringer, parts $(-c, -b) \cup (b, c)$ are free of stresses, while on the edges of the crack $(-a, -c) \cup (c, a)$ the crack lips are connected to each other via elastic springs of Ek -stifness. It is $0 < b < c < a$. We also consider that at infinity and along Oy-axis there is an equally distributed tension σ , when on Ox-axis pressure p is applied.

The stringer will be described by the one-dimensional elastic continuous medium [1,6,13]. On the edges of the stringer $x = \pm b$ tensile concentrated and horizontal forces $Q_{\pm}$ are applied. The elasticity modulus of the stringer is E_s and the height of its orthogonal cross section is $\delta\,(\delta << b)$, the width is d and as a special case we have $d = h$. From the assumptions above, the axial deformation of the stringer will be expressed as in [1]:

$$\varepsilon_{xx} = \frac{1}{E_s A_s}\left[Q_- + 2d \int_{-b}^{x} \tau(s)ds \right], \quad \left(-b \le x \le b,\, A_s = 2d\delta\right) \tag{44}$$

where $\tau(x)$ is the distribution function of the unknown shear contact stresses on the crack lips at the part that the stringer exists. Those stresses are the same due to symmetry with respect to Ox-axis.

The equilibrium equation of the stringer has the form:

$$2d \int_{-b}^{b} \tau(s)ds = Q_+ - Q_- \tag{45}$$

If we take into consideration the contact condition of the stringer and the plate we have [1,6]:

$$\frac{du_+}{dx} = \frac{du_-}{dx} = \varepsilon_{xx}$$

$$\frac{dv_+}{dx} = \frac{dv_-}{dx} = 0 \quad -b < x < b \tag{46}$$

using the expressions (26)-(27) and the known method [1,13] we will have the following singular integral and integro-differential equations that describe the problem (state equations):

$$\frac{1}{\pi}\left(\int_{-1}^{-\rho} + \int_{\rho}^{1}\right)\frac{\chi'(\eta)d\eta}{\eta-\xi} - \frac{2v_0}{\pi}\int_{-\rho}^{\rho}\frac{\tau_0(\eta)}{\eta-\xi}d\eta = \begin{cases} -\sigma_0 - p_0(\xi), & 1\xi|<\rho \\ -\sigma_0, & \rho<|\xi|<r \\ -\sigma_0 + \lambda\chi(\xi), & r<|\xi|<1 \end{cases} \tag{47}$$

$$\chi(-1) = \chi(1) = 0 \tag{48}$$

$$\frac{1}{\pi}\int_{-\rho}^{\rho}\frac{\chi_0(\eta)}{\eta-\xi}d\eta + 2iv_0\chi_0(\xi) = -\frac{\chi_*}{2}\int_{-\rho}^{\xi}\left[\overline{\chi_0(\eta)} - \chi_0(\eta)\right]d\eta +$$

$$+\frac{\lambda}{\pi}\left(\int_{-1}^{-r} + \int_{r}^{1}\right)\frac{\chi(\eta)d\eta}{\eta-\xi} - \frac{1}{\pi^2}\left(\int_{-1}^{-\rho} + \int_{\rho}^{1}\right)\frac{\ell(\eta) - \ell(\xi)}{\eta-\xi}\chi'(\eta)d\eta - \tag{49}$$

$$-\frac{iv_0}{\pi^2}\int_{-\rho}^{\rho}\frac{\ell(\eta)-\ell(\xi)}{\eta-\xi}\left[\overline{\chi_0(\eta)} - \chi_0(\eta)\right]d\eta + f_0(\xi), \quad 1\xi|<\rho$$

Definitions of the quantities, dimensionless or not, that were used in the above:

$$\chi_0(\xi) = p_0(\xi) - i\tau_0(\xi), \quad f_0(\xi) = -i\left(q_- + \frac{\sigma_0 + p_0}{2}\right) + \frac{\sigma_0}{\pi}\ln\frac{1-\xi}{1+\xi}$$

$$p_0(\xi) = 4p(\alpha\xi)/E, \tau_0(\xi) = 4\tau(\alpha\xi)/E, r = c/a, \rho = b/a$$

$$\chi_* = \frac{aE}{2\delta E_s}, p_0 = \frac{4}{E}p, q_\pm = \frac{Q_\pm}{d\delta E_s}, \ell(\xi) = \ln\frac{1+\xi}{1-\xi}, \quad 1\xi|<\rho<1$$

Here, we have to note that function $p(x)\,(|x|<b)$ expresses the unknown distribution of the perpendicular stresses on the contact boundary of the stringer and the plate. The equilibrium equation of the stringer will take the following form:

$$\int_{-\rho}^{\rho}\left[\overline{\chi_0(\eta)} - \chi_0(\eta)\right]d\eta = 2iq_0, \quad \left(q_0 = \frac{q_+ - q_-}{\chi_*}\right) \tag{50}$$

the maximum opening of the edges of the springs is given by:

$$\delta_{\max} = \chi(\pm r), \quad (r = c/a)$$

therefore the density of the normal displacements dislocation on the crack lips and the dimensionless contact stresses $p_0(\xi)$ and $\tau_0(\xi)$ are defined by the system of equations (47) and (49) as well as relations (48) and (50) where $\chi(\pm\rho) = 2\delta_0$, $(\delta_0 = \delta/\alpha)$. After solving that system, the dimensionless normal stresses outside the crack and on Ox-axis are given by:

$$\sigma_0(\xi) = -\frac{1}{\pi}\left(\int_{-1}^{\rho} + \int_{\rho}^{1}\right)\frac{\chi'(\eta)}{\eta-\xi}d\eta + \frac{2v_0}{\pi}\int_{-\rho}^{\rho}\frac{\tau_0(\eta)}{\eta-\xi}d\eta, \quad |\xi|>1$$

As examples one can study some special cases of the examined here problem. First, the case when a total rigid inclusion partially covers the plate $(E_s = \infty, b < a)$, or secondly a totally rigid inclusion that covers the plate $(E_s = \infty, b = a)$. In the last case we will get the known result of [14] (for $\sigma = 0$).

7 Conclusions

In this work a series of problems of the linear elasticity for cracked bodies with reinforcements, that are classified as contact problems, are treated with the help of Complex Analysis and the Theory of Singular Integral Equations. With this work we can chose the optimal position of the reinforcement, so that we can achieve lower stress intensity factors (SIF) in the edges of the crack; but also to calculate the distribution of stresses outside and on the crack lips.

References

1. Alexandrov, V.M., Mkhitaryan, S.M.: Contact problems for bodies with thin covers and layers. Moscow, Nauka (1983) (in Russian)
2. Gevorgyan, S.K., Manukyan, E.H., Mkhitaryan, S.M., Mkrtchyan, M.S.: The mixed problem for anisotropic compound wedge with a crack. In: Modern problems of deformable bodies. Mechanics, Collection of papers, Yerevan, Armenia. Dedicated to the memory of Prof. P.S. Theocaris, vol. 1, pp. 98–113 (2005)
3. Bardzokas, D., Parton, V.Z., Theocaris, P.S.: Integral equations of elasticity for a multiconnected domain with inclusion. Journal of Appl. Math. and Mech. (P.M.M.) 53(3), 375–384 (1989)
4. Bardzokas, D.I., Filshtinsky, M.L., Filshtinsky, L.A.: Mathematical methods in electromagnetoelasticity. Springer, Heidelberg (2007)
5. Rose, L.R.F.: Crack reinforcement by distributed springs. J. Mech. Phys. Solids 35(4), 383–405 (1987)
6. Melan, E.: Ein beitrag zur theorie geschweisster verbindungen. Ingr-Arch 3(2), 123–129 (1932)
7. Thecoaris, P.S.: Numerical solution of singular integral equations: Methods. J. Eng. Mech. Div. ASCE 107, 733–752 (1981)
8. Theocaris, P.S.: Numerical solution of singular integral equations: Applications. J.Eng.Mech. Div. ASCE 107, 753–771 (1981)

9. Bardzokas, D.I., Gevorgyan, J.K., Mkhitaryan, S.M.: About a stress deformation condition of piecewise-uniform wedge with a system of collinear cracks at an antiplane deformation. Mathematical Problems in Engineering 2, 245–268 (2005)

10. Bardzokas, D.I., Mkhitaryan, S.M.: About an interaction of stress concentrators of various types. In: Proceedings if Int. Conf. dedicated to the 95th Anniversary of Academician N.K. Arutyunyan, Yerevan, pp. 91–96 (2007)

11. Savruk, M.P.: Stress intensity factors in cracked bodies. Mechanics, fraction and endurance of materials. In: Panasynk, A.V.V. (ed.), vol. 2 (1998) (in Russian)

12. Shtaernan, I.Y.: Contact problems of theory of elasticity. Moscow – Leningrad, Gostehigdat (1949) (in Russian)

13. Buffler, M.: Sceibe mit endlisher elastischer versteilung. VDI-Fossehung Sheft 485, Ausgabe B., Bd 27, S 44 (1961)

14. Cherepanov, G.P.: "Mechanics of brittle fracture". Moscow-Nauka (1974) (in Russian)

Some Actual Problems of Fracture Mechanics of Materials and Structures

Volodymyr Panasyuk and Ihor Dmytrakh

Karpenko Physico-Mechanical Institute of National Academy of Sciences of Ukraine
5 Naukova Street, 79601, Lviv, Ukraine
panasyuk@ipm.lviv.ua, dmtr@ipm.lviv.ua

Abstract. Some theoretical and experimental results on fracture mechanics of materials and durability of structural elements are presented. Conceptual bases (statements) of fracture mechanics and strength of cracked materials as well as urgent problems of prospective investigations in this field of science about materials and their strength are formulated. The actual problems of fracture mechanics and strength of materials in service environments are considered.

1 Introduction

Development of new machines, structures and means of transport as well as goods production require design of new materials and data on their physicomechanical characteristics (strength, plasticity, hardness, resistance to aggressive media effect, the influence of constant or time variable external loadings, etc). For a long time have people paid much importance to accumulation of data on such properties. As a result the science about physicochemical properties of materials, strength in particular, their integrity, fracture and durability under given service conditions have been created, methods of these properties prediction have also been developed.

In the first half of the 20th century in the engineering practice there were already a number of physicomechanical statements (hypotheses, experimental generalisations, and postulates) for the assessment of the serviceability of the material under loading. These theoretical and experimental data, and also methods based on these methods for assessment of materials strength and fracture form the „classical approaches" of fracture mechanics and structural integrity.

In the frames of classical approaches the methods for assessment of structural elements strength and durability have been developed; methods for determination of basic physicomechanical characteristics for macrovolumes of structural elements have been created too. The size of the specimen of this material is by an order or two larger than the typical size of the material microstructure. These approaches are widely used in engineering practice, but in many cases they can be used for the assessment of structural elements serviceability under the non-extreme service

conditions. But under severe conditions, in particular when structural elements contain sharp stress notches or cracks, classical criteria are insufficient. For such cases it is necessary to expand the basic statements of the classical mechanics of materials and to formulate new, physically sound schemes-models for such problems solution. As a result of theoretical and experimental researches into this problem in the middle of the 20th century a new direction in the science on materials strength and fracture – fracture mechanics and strength of bodies with cracks (or abbreviated as materials fracture mechanics (MFM)) was created. Materials fracture mechanics formulated new approaches – new paradigm – for the strength assessment.

2 Classical and Non-classical Approaches

Let us formulate in short the main postulates of classical and non-classical approaches. In classical approaches and phenomenological criteria, when evaluating the strength of materials and structures, a structural element was considered as a continuum (solid) with given rheological properties (e.g. an elastic continuum).
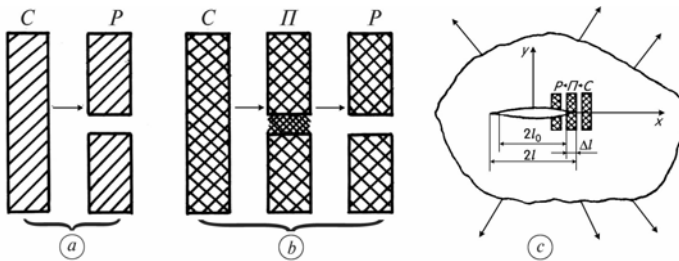

Fig. 1. Material fracture: classical (*a*) and non-classical (*b*) charts; non-classical chart of fracture at the crack tip (*c*)

It is assumed [1, 2] that the element of the deformed body is in one of such states (see Fig. 1a): continuous state (C-state) or fractured state (P-state). Transition of the element from state C to state P (fracture process) occurs instantaneously, if only the stress-state state calculated by the assumed rheological model attains some critical level (e.g. if tensile stresses at least at one point of a body reach the material macrovolumes (σ_B) strength under its tension).

Application of the classical approach to the bodies (materials) with cracks does not allow estimating their strength. For example, if one uses such an approach during the assessment of the tensioned plate with an elliptical hole, when the elliptical hole transforms into a crack-cut, then one would receive a physically non-sound result – such an approach, according to the postulate formed above states out that in this case the plate strength equals zero. In reality experimental data show that strength of such a plate does not equal zero but depends on the crack length and physical characteristics of the plate material. This is related with the fact that in the classical approach the special stress-strain state at the tip of a sharp defect-crack is not taken into account during deformation of a body.

The main idea of the non-classical approach (fracture mechanics) is the following: it is assumed that during the transition of the deformed body element from *C*-state to *P*-state a certain intermediate *Π*-state is formed (Fig. 1*b*), which should be considered when solving the problem on strength of materials with crack-like defects [1, 2].

An important feature of the deformed solid regions, where *P*-states (regions of the material prefracture) appear, is the fact that the material here is always deformed beyond the stress limit. Just in these regions of the material occur the intensive processes of plastic yield, interaction with the environment, diffusion processes, material damaging etc. All this causes local fracture of the material, i.e. *C*→*Π*→*P*-transitions.

Thus, non-classical fracture chart (Fig. 1*b*), put into the basis of the modern fracture mechanics, takes into account the *Π*-state of the material in deformed solids (such states arise mainly at the tips of crack-like defects, Fig. 1*c*).

In the second half of the 20th century fracture mechanics of materials as a modern science on strength and structural integrity intensively developed in different countries of the world: in Great Britain, China, Italy, Germany, Poland, Russia, USA, Ukraine, Hungary, France, Japan and other. Speaking about the scientists who founded the basis of fracture mechanics and who were the first to implement the ideas of non-classical approach to the assessment of the deformation of the solid with sharp stress concentrators we must mention A. Griffith, G. Irwin, K. Weighard [1–8]). (In [3] one can find publications about the history of fracture mechanics development).

3 Griffith–Irwin Concept

A. Griffith (1920, 1924) was the first to consider the presence of *Π*-states in the stress-strained body (material) at the crack tip and to formulate the criterion (condition) of crack growth and formation of new surface (fracture) of a body, using not a classical approach but a generalized energy balance of a deformed solid with a crack and the energy that is spent for the formation of new surface during crack propagation. He was also first who formulated a known energetic criterion of crack propagation in a deformed body [9]. The establishment of the structure of stress field asymptotic and displacements at the crack–cut in the deformed solid (see ref. in [1–3]) was a very important stage in fracture mechanics development. Thus it was shown that the stress tensor components (σ_{ij}, Fig. 2) near the crack tip can be written as:

$$\sigma_{ij} = \frac{1}{\sqrt{2\pi r}}\left\{K_{I0}f_{1ij}(\theta) + K_{II0}f_{2ij}(\theta) + K_{III0}f_{3ij}(\theta)\right\} + 0(1), \qquad (1)$$

where $i, j = x, y, z$ in Cartesian coordinate system or $i, j = r, \theta, z$ in polar (cylindrical) coordinate system; $K_{I0} = K_{I0}(p,l)$, $K_{II0} = K_{II0}(p,l)$, $K_{III0} = K_{III0}(p,l)$ are the stress intensity factors (SIF) that are the functions of the body configuration,

crack dimensions (l) and loading p; $\int_{kij}(\theta)$ are known functions (k = 1, 2, 3); $0(1)$ is a limited value at $r \to 0$.
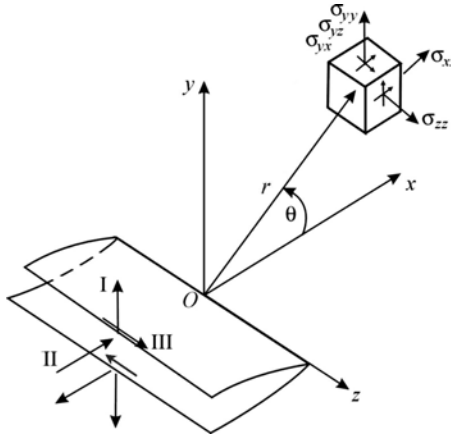

Fig. 2. Local system of coordinates at the crack front (line 0z) and components (I, II, III) of the vector of crack edges displacements

Considering dependences (1) in 1957 G. Irwin formulated [10] a new criterion of limiting-equilibrium state for a cracked body under quasistatic loading for the case when mode I fracture (Fig. 2) occurs in a body, i.e. when $K_{I0} \neq 0$, and $K_{II0} = 0$; $K_{III0} = 0$. This criterion is based on the statement that the external loading p will be limiting equilibrium $(p = p_*)$ when for a deformed cracked body the stress intensity factor $K_{I0}(p,l)$ is equal to K_{Ic} – some constant for the given material, i.e.

$$K_{I0}^* = K_{I0}(p_*,l) = K_{Ic} \ , \ \ K_{II} = 0, \ K_{III} = 0. \tag{2}$$

Under the brittle fracture conditions that is when $\Delta l \leq l_0$ (see Fig. 1c), G. Irwin proved the equivalency of criterion (2) and A. Griffith energy concept.

4 Linear Fracture Mechanics

The Griffith–Irwin calculation models form the basis of the so-called linear fracture mechanics of solids**.** The main peculiarity of this part of fracture mechanics is that the typical dimensions of the region near the crack tip (Π-state) where material is deformed beyond the elastic limit, are considered to be small in comparison with the crack sizes and the body itself. The stress-strain state in this body is determined by solving the corresponding problems of linear theory of elasticity for bodies containing cracks-cuts (that's why this part is called linear fracture mechanics, LFM). Using the obtained solutions the SIF values ($K_{i0}(p,l)$, i = I, II, III) are calculated, and

criteria (2) is used. Crack growth resistance values (K_{Ic}, K_{IIc}, K_{IIIc}) are determined experimentally [14–15].

In the cases when the cracked solid is under the complex loading, i.e. when all SIFs do not equal zero ($K_{I\theta}\neq 0$, $K_{II\theta}\neq 0$, $K_{III\theta}\neq 0$) for the estimation of limiting loading value ($p = p_*$) the following criteria equation (as a phenomenological generalization of Griffith–Irwin criteria) is used:

$$\left(\frac{K_{I\theta}^*}{K_{Ic}}\right)^{n_1} + \left(\frac{K_{II\theta}^*}{K_{IIc}}\right)^{n_2} + \left(\frac{K_{III\theta}^*}{K_{IIIc}}\right)^{n_3} = 1, \tag{3}$$

where n_1, n_2, n_3, K_{Ic}, K_{IIc}, K_{IIIc} are characteristics obtained experimentally (see references in [14–16]).

Relatively criteria equation (3) it is necessary to mention that for all possible SIFs it requires yet experimental approbation and theoretical development, in particular the estimation of such a criteria not by phenomenological generalization but by formulation of the certain calculation model, and construction on this base of certain criteria, in particular when some SIFs are negative. Some experimental results on this problem are published in [16–18]. These and other problems of LFM are important nowadays too.

For practical realization of LFM according to criteria (1)–(3) it is necessary to know the value of the material crack growth resistance, that is the characteristics K_{Ic}, K_{IIc}, K_{IIIc}, and parameters n_1, n_2, n_3. Today [19, 20] methods for experimental determination of the materials resistance to crack growth (K_{Ic}) have already been developed and standardized. Concerning the establishment of the material crack growth resistance characteristics under mode II (Fig. 2) displacement of crack faces (displacement perpendicular to the line of the crack front) K_{IIc}, i.e. when $K_I = 0$, $K_{II} \neq 0$, $K_{III} = 0$, and also under the mode III (Fig. 2) displacement of the crack faces (displacement parallel to the line of the crack front) K_{IIIc}, i.e. when $K_I = 0$, $K_{II} = 0$, $K_{III} \neq 0$, we have no yet unified methods (standards) for the experimental determination of mentioned characteristics and there is no the appropriate data base of these characteristics for different structural materials. Preparation of reference books on these characteristics is a very important task for engineers and scientists.

Factors n_1, n_2, n_3 are determined using the experimental results or modelling of the crack process zone under complex loading. The known investigations [21] show (in the frames of the generalized δ_c-model of the crack propagation) that these factors can be considered as being equal $n_1 = n_2 = n_3 = 4$ or equal $n_1 = n_2 = n_3 = 2$ on the basis of approximate phenomenological approach.

Thus, we know factors $K_i\,(i = I,II,III)$ and parameters $n_i\,(i = 1,2,3)$ for practical use of equation (3) of the limiting-equilibrium state of the deformed cracked body under complex loading. It is necessary for each concrete case to set up K_{Ic},

$K_{\mathrm{II}c}$ and $K_{\mathrm{III}c}$ values. The value of $K_{\mathrm{I}c}$ is found in the reference book or is determined according to known standard [19, 20].

Test methods for the determination of factors $K_{\mathrm{II}c}$ and $K_{\mathrm{III}c}$ are developed [23, 24] for a tubular specimen with a circular crack (Fig. 3).
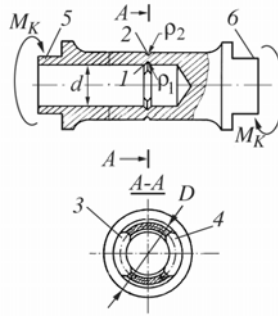

Fig. 3. Specimen for crack growth resistance of material ($K_{\mathrm{II}c}$, $K_{\mathrm{III}c}$) determination: *1, 2* – circular concentrator; *3, 4* – symmetrical cracks; *5, 6* – places of specimen gripping during torsion ($K_{\mathrm{III}c}$) or tension ($K_{\mathrm{II}c}$)

Experimental verification of criteria equation (3) was done in works [23, 24] under investigation of the limiting-equilibrium state of materials under the complex loading of cracked specimens. The fracture of these specimen occurred under the mixed-mode fracture macro-mechanisms, that is: mode I–mode II, and mode I–mode III.
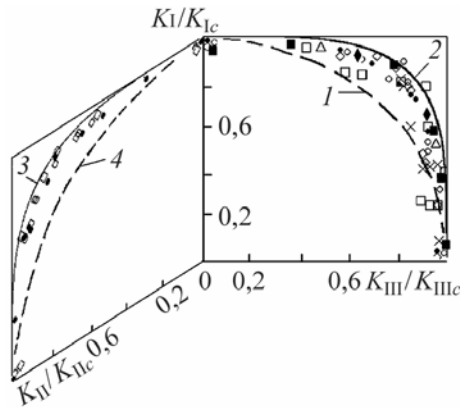

Fig. 4. Diagram of limiting-equilibrium state of a deformed cracked solid under complex loading and realization of fracture macro-mechanism (I + II) (*a*) and (I + III) (*b*) (curve *1* – according to formula (3) when $n_i = 4$, and curve *2* – according to formula (3) when $n_i = 2$): ○ – 40XH steel, quenching in oil at 1123 K, tempering at 833 K; ◇ – 30XHГCHA steel, normalized; ● – 40X steel, quenching in oil at 1133 K, tempering at 773 K (results of Ya. Ivanytskyi); *b*: □ – 4340 steel (results of A.Chyzhyk); aluminium allow 2219 (E87) (results of A. Chyzhyk); × – 9XФ steel: ◆ – quenching in oil at 1133 K, tempering at 873 K; ■ – tempering at 773 K; △ – tempering at 673 K (results of Ya. Ivanytskyi)

It is stated that criteria (3) agrees well with experimental data for deformed-strengthened materials ($\sigma_B/\sigma_T > 1,4$), when $n_i = 4$, and for deformed-softened materials ($\sigma_B/\sigma_T < 1,4$) when $n_i = 2$. All experimental data are situated in the region bounded by curves *1* and *2* (Fig. 4).

Thus it is possible to plot diagrams of limiting-equilibrium state of structural elements with available cracks or sharp stress concentrators under complex loading of the structure in the frames of LFM. But we still have no appropriate approbation of criteria (3) for cases when one of SIFs is negative.

5 Non-linear Fracture Mechanics

It is known that prior to failure of real structural materials, first of all metals, the plastic zones at the stress concentrators, in particular crack-like defects, are formed. The typical linear dimensions of such zones (*Π*-states) can be commensurable with the defect size or the typical linear size of the deformed body. In such cases the application of the Griffith-Irwin concept (LFM) without additional refinements is not correct.

To solve these problems different deformation criteria, in particular the criterion of critical crack tip opening displacement (CTOD criterion) and also the concept of the δ_c-model for evaluation of crack opening displacement near its tip, proposed in [22-24] (1959,1960), are used. The given concept was the beginning of the investigations in non-linear fracture mechanics of materials, i.e. when the typical linear dimension of the region of plastically deformed material at the sharp stress concentrator-crack (*Π*, Fig. 1) is commensurable with the typical size of a defect or a body ($\Delta l \approx l_0$, Fig. 5).
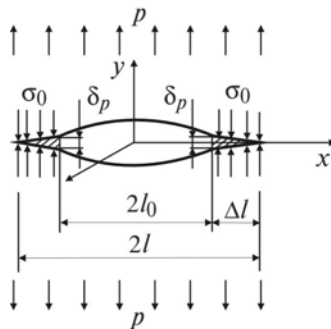

Fig. 5. A plate with a central crack ($2l_0$) and model plastic zones (Δl); δ_p – displacement of the initial crack edges in the deformed body under loading *p*

According to the δ_c-model the regions of the body (Fig. 5) where plastic zones have appeared, are modelled by a cut (cuts) opposite sides of which are attracted with stresses σ_0, which are the averaged local stresses arising in the plastic zone of the material (for materials without hardening we can assume that $\sigma_0 \approx \sigma_T$, where σ_T is yield stress of the material). At all points of the deformed body (outside the cuts) the deformations are elastic. Crack opening δ_p near the initial crack tip (mutual displacement of edges) at the moment of the crack start is equal to constant (δ_c) of the material (Fig. 5). Within the framework of the accepted model for elasoplastic material there exists the equality $\sigma_0 \delta_c = 2\gamma$ between values δ_c, σ_0 and density of material fracture γ, where γ is the average value of the energy necessary for formation of the surface unity in the given material.

Similar approaches, however partial and developed somewhat later, were proposed by D.S. Dugdale [26] (1960) and A.A. Wells [27].

The concept of the δ_c-model was realized for the first time by M.Ya. Leonov and V.V. Panasyuk, M.Ya. Leonov and P.V. Vytvytskyi on the example of the generalized problem of A.A. Griffith and M.Ya. Leonov and V.V. Panasyuk using the Sack's generalized problem (see ref. in [25]).

For the generalized Griffith problem i.e. for the cracked plate under tension (Fig. 5) when the value of plastic zone (Δl) is commensurable with l_0 ($\Delta l \approx l_0$) in the frames of the δ_c-model the value of the limiting loading $p = p_*$ and δ_p value was established for the first time (1960) as

$$p_* = \left(\frac{2}{\pi}\right)\sigma_0 \arccos \exp\left(-\frac{d_*}{l_0}\right), \qquad \delta_p = -\frac{8l_0\sigma_0}{\pi E}\ln\left(\cos\frac{\pi p}{2\sigma_0}\right), \qquad (4)$$

where $d_* = \left(\pi E \delta_c\right)/\left(8\sigma_0\right)$; E is Young's modular, δ_c is material constant.

The size of the area of inelastic (plastic) deformations in the crack plane (the value of the zone Π) in this case is determined by the equality

$$d_p = l - l_0 = l_0\left[\sec\frac{\pi p}{2\sigma_0} - 1\right]. \qquad (5)$$

Formula (4) can be used for the crack of any initial length $l_0 \left(0 \leq l_0 \triangleleft \infty\right)$. According to this formula the critical loading p_* is always finite and (when $l_0 \to 0$) tends to σ_0. This physically sound result is not obtained in the Griffith–Irwin theory (Fig. 6).
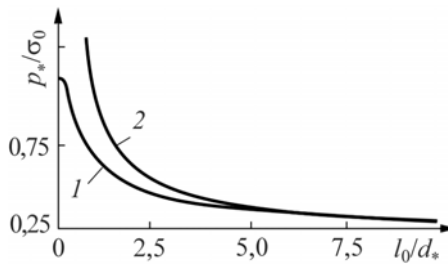
Fig. 6. Specimen for crack growth resistance of material (K_{IIc}, K_{IIIc}) determination: *1, 2* – circular concentrator; *3, 4* – symmetrical cracks; *5, 6* – places of specimen gripping during torsion (K_{IIIc}) or tension (K_{IIc})

In the 80s of the last century (see references in [5]) the δ_c-model concept was generalized for mode II and mode III cracks, and the methods of experimental determination of critical opening displacement (δ_{Ic}) and critical displacement (δ_{IIc}, δ_{IIIc}) of the crack edges were proposed.

At the beginning of the 90ies M.P. Savruk et al. [28] used the δ_c-model for plastic bands, initiating from the crack tip at arbitrary angle.

It should be noted that the effective and reliable experimental methods for the estimation of deformation characteristics of crack growth resistance (δ_{Ic}) have not been developed yet. Here we meet difficulties presented in [29]. The precise analysis of elastic-plastic deformation of the material near the crack tip in the tensioned plate basing on the approach that is grounded on the correlation of speckle-images of the surface in the prefracture zone (Fig. 7) has been done in the above paper. Here the value of deformation in this zone was assessed at the different measurement bases $b(b_1, b_2, b_3)$. Specimens of Д16АТ alloy were tested. As a result the distribution of deformations in the process zone in the loaded and unloaded plates was established. This distribution is presented in Fig. 7 (curves *1–3* for different measurement bases $b(b_1, b_2, b_3)$ and $p = \text{const}$, and curves *1'–3'* after unloading of the plate accordingly). The received results show that the experimental determination of critical crack opening displacement (δ_{Ic}) between the crack edges near its tip is not constant, i.e. these displacements are different depending on measurement base (b). At the same time experimental results in Fig. 9 illustrate that the size of the process zone d_p dose not depend on the measurement base. It remains constant for the given material. This can be used for the modification of the δ_c-model [25], and of the experimental method for δ_{Ic} characteristics determination.

Taking into account the above-mentioned let us consider that the critical length of the process zone (d_*) to be the material constant. Than using formulas (4)–(5)
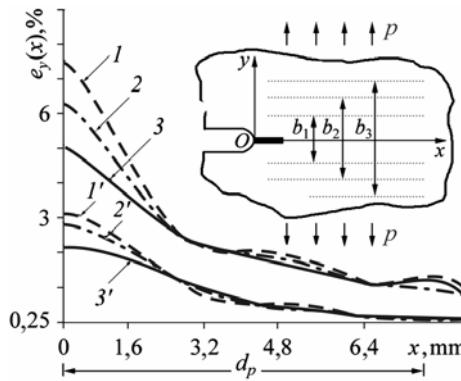
Fig. 7. Distribution of deformations $e_y(x)$ near the crack tip under different measurement bases b ($1 - b_1 = 1.28$ mm; $2 - b_2 = 2.56$ mm; $3 - b_3 = 3.08$ mm) in loaded ($1–3$) and unloaded ($1'–3'$) Д16АТ alloy specimen; $p = $ const

for the macrocrack in the plate under tension (Fig. 5) one receives such dependence between the averaged value of the deformational crack growth resistance ($\tilde{\delta}_{Ic}^*$) and (d_*) – value of the structural material:

$$\tilde{\delta}_{Ic}^* = 8\sigma_0 d_*/(\pi E), \quad (d_* << l_0). \tag{6}$$

Using formula (6) for experimental determination of $\tilde{\delta}_{Ic}^*$ one can avoid difficulties arising in its direct evaluation, and also those concerning loading amplitudes of the materials specimen when the incoming macrocrack initiates in it.

The following important task is the experimental approbation of the $\tilde{\delta}_{Ic}^*$ characteristics evaluation according to formula (6) and application of this approach to establishing $\tilde{\delta}_{IIc}^*$, $\tilde{\delta}_{IIIc}^*$.

6 Fatigue Crack Nucleation and Growth (Fatigue of Materials)

The problem of materials fatigue is one of the central problems of fracture mechanics and prediction of structural elements lifetime (durability). Great efforts have been spent by scientists and engineers for this problem solution since the 19th century, when this phenomenon was considered for the first time. The concepts of fracture mechanics, that is the concepts of cracks initiation and growth in the cyclically deformed body, are very important for the solution of this problem. If the initiation period (N_i) of the minimum macrocrack in the given material and its propagation period (N_p) are known, the total life time (N_*) is determined by formula:

$$N_* = N_i + N_p, \tag{7}$$

where N_i and N_p are determined using corresponding theoretical and experimental approaches of fracture mechanics [30], in particular using corresponding characteristics on materials crack growth resistance.

It is known [30, 31] that the material ability to resist crack initiation (resistance to macrocrack propagation in it) represents the dependence of crack growth rate (v) on the stress intensity factor (K_I) or deformation amplitude of the material at the crack tip (Fig. 8).

As a result of experimental investigations it was shown that such diagrams ((v–K)-diagrams) are of S-shape and on a certain region 2 (Fig. 8) they can be considered rectilinear and can be described ([5] volumes 3 and 4) by Paris equation

$$v = CK_I^n \quad \text{or} \quad v = 10^{-7}\left(K_I/K^*\right)^m, \tag{8}$$

where K^* is the value of K_I at which the crack growth rate in the given material is 10^{-7} m/cycle (Fig. 8); C, K^*, m, and n are material constants. To construct the (v–K)-diagrams the range of the stress intensity factor ΔK_I ($\Delta K_I = K_{Imax} - K_{Imin}$ and $\Delta K_I = K_{Imax}$ when $K_{Imin} = 0$) is used instead of the value of $K_I = K_{Imax}$. Every (v–K)-diagram is bounded on the left by the threshold value of K_{Ith} i.e. by such a value of K_I or ΔK_I that for $K_{Imax} < K_{Ith}$ (or $\Delta K_{Imax} < \Delta K_{Ith}$) the crack does not propagate. On the right this diagram is bounded by the value of K_{Ifc} i.e. by such a SIF value at which spontaneous failure occurs ($v \to \infty$).
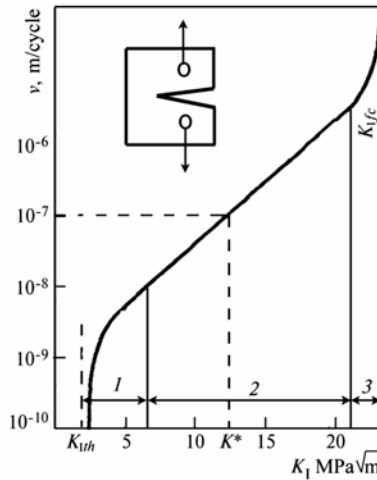

Fig. 8. Diagram of fatigue crack growth resistance of the material (or (v–K)-diagram): 1 is the region close to threshold K_{th}; 2 is practically rectilinear region; 3 is the region of rapid crack growth and entire failure under condition $K_{Imax} = K_{Ifc.}$

So for fatigue fracture of the material we have the following basic fatigue crack growth resistance characteristics: C, K_{Ith}, K^*, K_{Ifc}, m, n .

For description of complete (v–K)-diagram such formula was proposed in [31]:

$$v = v_0\left[(K_I - K_{Ith})/(K_{Ifc} - K_I)\right]^q, \tag{9}$$

where v_0, K_{Ith}, K_{fc}, q are material constants, obtained experimentally.

If one takes into consideration that the plastic deformations zone at the fatigue crack tip is small to compare with the crack length, i.e. in case of macrocrack ($\Delta l \ll l_0$) it is possible to establish [1] the relationship between K_{Imax} and $\delta_p^{(\text{max})}$ where δ_p is the distance between the opposite crack edged at its tip under the loading of the body by the force p (Fig. 5).

Using the diagram, of fatigue crack growth resistance (Fig. 8), in particular formula (9), N_p value is calculated from the formula:

$$N_p = \int_{l_*}^{l_c} \frac{dl}{v[K_{\text{I}}(l)]}, \quad ,$$

$$K_{\text{I}}(l_c) = K_{\text{Ifc}}, \tag{10}$$

where l_* is the minimum length of the macrocrack for this material.

The construction of the minimum macrocrack (l_*) initiation period depending on the cyclic loading amplitude is a more complicated problem and still has been no effectively solved. At the same time a certain progress in this direction of investigations was noticed [30].
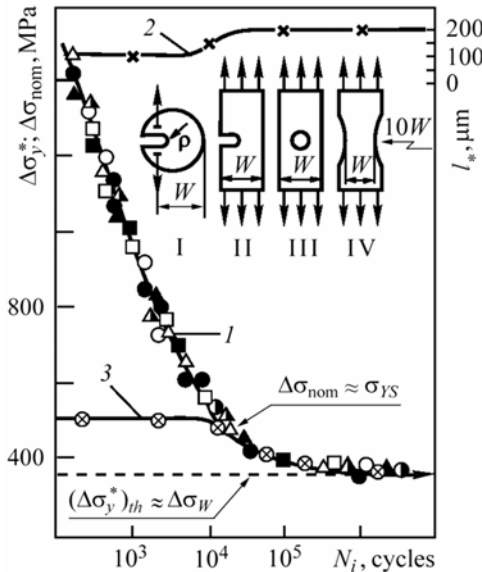

Fig. 9. Dependences of $\Delta\sigma_{\text{nom}} \sim N_i$, (curve *1*) and $l_* \sim N_i$ (curve *2*) for notched specimens and $\Delta\sigma_{\text{nom}} \sim N_i$ (curve *3*) for smooth specimens of aluminium Д16чАТ alloy; specimen types: I – $W = 64$ mm; $\rho = 0{,}75$ and $6{,}5$ mm ($\triangle$,$\bigcirc$); II – $W = 64$ mm; $\rho = 0{,}75$ and $6{,}5$ mm ($\blacktriangle$, $\bullet$); $W = 30$ mm; $\rho = 0{,}75$ and $2{,}0$ mm ($\blacktriangle$, $\leftmoon$); III – $W = 30$ mm; $\rho = 0{,}75$ mm ($\square$); $W = 20$ mm; $\rho = 0{,}75$ mm ($\blacksquare$); IV – $W = 10$ mm ($\otimes$)

Special investigations on the dependence of the period (N_i) of the minimum macrocrack initiation in the plates with concentrators on cyclic loading amplitude ($\Delta\sigma_y^*$) for the Д16чAT alloy specimens (Fig. 9) were done [30, 32–34]. The value of the macrocrack was measured by microscope.

On the basis of dependences $\Delta\sigma_y^* = f_1(N_i)$ it is also possible to establish the threshold value of $\Delta\sigma_y^*$ for the given material, i.e. the value of $(\Delta\sigma_y^*)_{th}$ below which the crack does not initiate. Let us denote this value $\Delta\sigma_y^*$ (threshold) by $(\Delta\sigma_y^*)_{th}$ (see Fig. 9). It equals the ordinate asymptote to the curve $\Delta\sigma_y^* = f_1(N_i)$ when $N_i \to \infty$. The value of $(\Delta\sigma_y^*)_{th}$ is an analogue to fatigue limit ($\Delta\sigma_R$) of the material for smooth macrospecimens (without concentrator). That is why (by analogue to $\Delta\sigma_R$) it can be stated that for amplitude of cyclic loading $\Delta\sigma_y^* < (\Delta\sigma_y^*)_{th}$ the initiation of the macrocrack near the stress concentrator will not occur and the fatigue of the material will be not realized.

Ostash O.P. et al [35, 36] established the dependence between the characteristics of macrospecimens fatigue fracture mechanics and characteristics of the macrocrack propagation in the deformed body, and also between the amplitude cyclic loading ($\Delta\sigma_y^*$) and minimum value of the crack (l_*), that is

$$\Delta K_{Ieff} = 0{,}886\Delta\sigma_y^* \sqrt{l_*} \ , \ l_* = \eta\left(\Delta K_{Itheff}/\Delta\sigma_R\right)^2, \ (\eta \sim 1{,}25), \qquad (11)$$

where $\Delta K_{Ieff} = \Delta K_I - \Delta K_{Iop}$, ΔK_{Iop} is SIF at which the crack opens; η is the numerical factor close to unit; $\Delta\sigma_R$ is the fatigue limit of the material on smooth standard specimens.

Using these correlations, the diagram ($v \approx K_{eff}$) can be changed by the diagram ($\Delta\sigma_y^* \sim N_i$) or vice versa. This procedure is shown in Fig. 10. It consists of such operations.

Let us consider a certain point on the ($v \sim K_{Ieff}$) diagram. For example, this is a point A_1 on the diagram *3* (Fig. 10*b*). For this point abscissa ΔK_{Ieff} is connected with values $\Delta\sigma_y^*$ (amplitude of cyclic loading near the stress concentrator or crack tip) by formula (11). Using this formula one can calculate the value $\Delta\sigma_y^*$ and fix it as an ordinate of the point A_1' on the diagram *1* (Fig. 10*a*). Further consider the macrocrack growth to be step-wise (as it is shown in [35]). In means that each time the macrocrack in the cyclically deformed body grows by a step l_*. So, the average macrocrack growth rate on diagram *3* (Fig. 10*b*) is evaluated by formula

$$v_i = l_* / N_i , \qquad (12)$$

where N_i is the period of the macrocrack l_* formation, this period depends on the loading amplitude ($\Delta\sigma_y^*$ or ΔK_{Ieff}).

Thus, for the point A_1 on the diagram *3* (Fig. 10*b*) we have the value $N_1 = l_* / v_1$. Let us fix this value as abscissa of the point A_1' on the diagram *1* (Fig. 10*a*). Continue this procedure for points A_2, A_3 ... of the diagram *1* (Fig. 10*b*) and receive corresponding points A_2', A_3' ... of the diagram *1* (Fig. 10*a*). In such a way we receive the diagram for the determination of the period (N_i) of the minimum macrocrack initiation for the given material near the stress concentrator. Diagram *2* in Fig. 10*a* is constructed by formula (11).
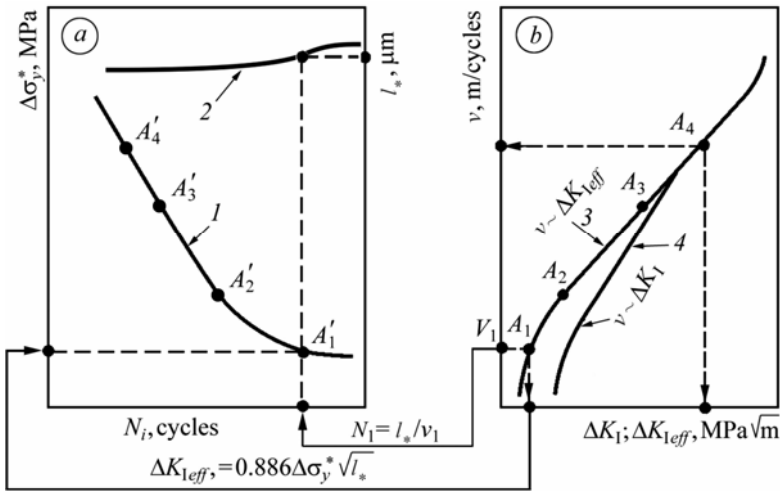

Fig. 10. A scheme of construction of the initiation (N_i) of the minimum length (l_*) macrocrack when the amplitude ($\Delta\sigma_y^*$) of cyclic loading of the body near the stress concentrator on the bases of $v \sim K_{\text{Ieff}}$ diagram is known

Construction of diagrams *1* and *2* for the evaluation of period (N_i) of the l_* length crack initiation (Fig. 10*a*) on the basis of the diagram ($v \sim \Delta K_{\text{Ieff}}$) for the evaluation of the structural elements durability becomes very important for engineering practice. Tables 1 and 2 illustrate the application of this approach.

Table 1. Experimental and calculated values of the process zone [30, 36, 37]

Material	Characteristics			Value l_*, µm		Formula (11)
				Experiment		
	σ_T, MPa	σ_B, MPa	δ, %	Low-cycle fatigue ($N_i = 10^3 \div 10^4$)	High-cycle fatigue ($N_i = 10^5 \div 10^6$)	
Aluminium alloy						
Д16Т	350	460	15	100	100	135
Д16чАТ1	442	475	10	40	180	159
Д16чАТН	417	533	17	60	80	100
Д16очТ	330	454	22	160	200	237
В95pchТ2	456	510	12	100	100	180
В95pчТ3	432	498	14	80	80	78
1420Т1	282	431	19	110	110	97
1201Т1	340	442	10	130	130	154
Steels						
08кп	190	270	48	200	250	208
35ХС2Н3МФ	1700	1950	10	5	10	7
Cast irons						
ВЧ50	310	510	14	200	200	158
ВЧ90	850	980	3	50	150	208

Table 2. Experimental and calculation characteristics N_i, N_p, N_* for specimens-bands with a central hole [36]

Hole diameter, mm	Loading range ΔP, kN	Experiment, cycles $\cdot 10^{-3}$			Calculation, cycles $\cdot 10^{-3}$		
		Ni	Np	N*	Ni	Np	N*
3.2	9.0	135	15	150	132.3	10.3	142.6
	12.6	25.2	6	32.2	17.2	4.5	21.7
5.0	9.0	118	5	123	100.9	6.6	107.5
	13.5	15.3	3.3	18.6	10.1	2.2	12.3

Thus the proposed concept of the evaluation for structural elements durability under long-term cyclic loading has a certain experimental confirmation and can be recommended for engineering practice to determine their life time. Theoretical and experimental investigations should be continued in order to develop the most effective and simple procedures for the evaluation of the structural elements durability in the given service conditions.

7 Interaction between Environments and Deformed Metal

In the mid 50's of the 20th century H.V. Karpenko was the first [37] who discovered the phenomenon of the steels fatigue limit decrease (approximately by 10–15%) in

surface-active environments (Fig. 11). However, tests on the static tension of steel cylindrical specimens 10 mm in diameter in the same surface-active environments showed no influence on the changes of static strength of the steel. This contradiction was explained by the short-time action of the environment and, as a result, it was considered that the adsorption effect was not apparent. Such interpretation of the adsorption effect cannot be convincing.
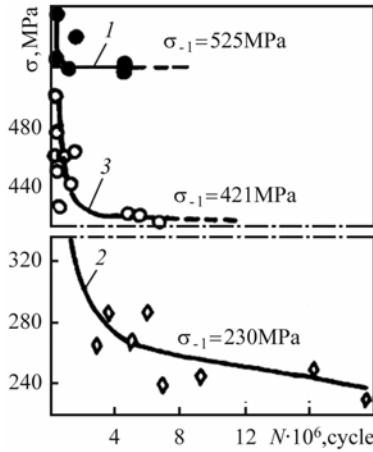

Fig. 11. Fatigue curves under the circular tension of $d = 7,62$ mm in diameter cylindrical specimen (40 X steel, structure – sorbite) under different test conditions: *1* – air; *2* – water; *3* – machine (liquid paraffin) oil, activated by 0.3% of oleic acid [37]

Within the frames of the deformed bodies fracture mechanics concept the following experiment was made [38] taking into account that the fatigue fracture occurs by the crack formation and propagation. A plate with the concentrated forces *P* was tensioned as it is shown in Fig. 12.
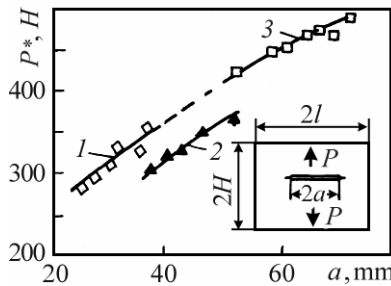

Fig. 12. Critical loading $P = P^*$ dependence on the crack length under the tension of glass plates in dry air (*1*, *3*) and water (*3*)

Such loading provides the gradual propagation of the crack. The dependence of critical value of force P^* on the crack length l is shown in Fig. 12 by dashed line *1–3*. The plate was tensioned step-wise: *1* – in the dry air; *2* – in the surface-active environment (for glass plate, for example, in the water); *3* – the same plate (after environment removal) was again tensioned in the air. The experimental results (glass, metal) showed that the surface-active environment decreases the static fatigue loading by 10–15% as under cyclic loading. Thus the contradiction between cyclic and static strength was removed for surface-active environment on one hand, and on the other it was shown that the most important material characteristics is its resistance to crack propagation in it, i.e. its crack growth resistance. It is typical of macrovolumes and not of mesovolumes. Just the surface-active environment changes the value of crack growth resistance, i.e. the characteristics of mesovolumes and not the macrovolumes of the material as a whole. The present-day fracture mechanics differs from the classical concepts of fracture mechanics. It includes the characteristics of mesovolumes during the estimation of materials strength. The change of these characteristics under the interaction with the surface-active environment can substantially influence the static and cyclic durability.

Evaluation of the environment effect on structural materials strength in terms of the change of their crack growth resistance is an important problem of engineering practice for assessment of durable-operation structural elements lifetime.

Within the frames of fracture mechanics concept the residual cyclic durability of the materials is determined by using ($v - K_I$) diagram according to formula (10). As it is known, at first the crack growth rate (v) diagrams versus the SIF values (ΔK_I, K_I) in the environment and in the dry air were constructed. Already at the beginning of 80s of the 20th century in the science on materials strength a disturbance appeared concerning the invariance of ($v - K_I$) diagrams constructed like this in the given surface-active environment. If the diagrams are constructed as in the case of dry (neutral) air, not in the air – but in the given surface-active environment, in particular corrosive environment, one can get different ($v \sim K_I$) diagrams if their construction begins from different SIF values (Fig. 13). Using such an approach one will receive different ($v \sim K_I$) diagrams. So they are not invariant, that is they are not characteristic of the system „deformed metal–environment".

In the mid 80s of the 20th century in was stated by I.M. Dmytrakh, L.V. Ratych and V.V. Panasyuk [40] that non-invariance of such diagrams is stipulated by: the crack growth rate (v) in metals under loading and environments influence, in particular corrosive environment, depends not only on SIF ($K_{I max}$) but also on the physico-chemical properties of the environment itself and the metal near the crack tip. It does not depend on their properties on the smooth surface. If, for example, it is considered that physicochemical properties of the system „metal–environment" are characterized by the hydrogen factor (pH) and electrode potential (φ), these values for the given system on the surface of the body $\left[(pH)_s, \varphi_s \right]$ and near the crack tip $\left[(pH)_t, \varphi_t \right]$ are not equal.
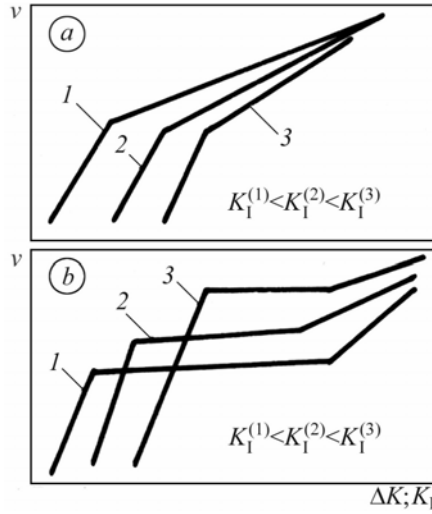
Fig. 13. Dependence of ((v–K_I)-diagrams) of crack growth (v) on K_I under the simultaneous action of loading and environment, constructed using different initial $K_I^{(i)}$: a – cyclic loading; b – static loading [39]

Based on these facts a new model [40] of the physicochemical situation at the corrosion crack tip in metal materials was proposed. This situation supposes that the crack growth rate (v) depends on $K_I, (pH)_t$ and ϕ_t (Fig. 14).
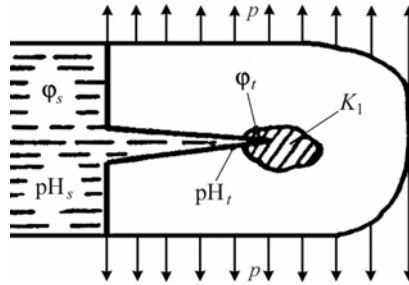

Fig. 14. Scheme of the physicochemical situation near the crack tip

According to this model the ($v - K$)-diagram of the corrosive crack growth is determined as a certain function of parameters, which characterise the stress-strain state and physicochemical situation of the system „material–environment" at the crack tip, that is:

$$v = f\left(K_I; (pH)_t; \phi_t\right),$$
(13)

where K_I is the stress intensity factor for the cracked body; $(\mathrm{pH})_t$ and φ_t are the hydrogen factor and electrode potential in the vicinity of the crack tip in the system „material–environment".

It follows from formula (13) that to receive the invariant ($v-K$) diagram it is necessary to provide such conditions:

$$(\mathrm{pH})_t = \mathrm{const} \text{ and } \varphi_t = \mathrm{const} . \qquad (14)$$

Experiments show [40, 41] that the maximum rate ($v_{\max}$) in the system „metal–corrosive environment" will be when parameters φ_t and $(\mathrm{pH})_t$ reach minimum values, that is

$$v_{\max} = f\left(K_I; (\mathrm{pH})_t^{\min}; \varphi_t^{\min}\right). \qquad (15)$$

Thus, diagram (15) becomes the basic diagram for estimation of the durability of cracked structural elements in the given service environments.

The original methods for experimental investigations of metal local corrosive fracture with the account of electrochemical processes parameters in the crack are developed for the proposed model scheme [40, 41]. The methods of direct electrochemical measurements in corrosive cracks are based on the application of special minielectrodes of different construction [41], which are placed in special holes of the tested cracked specimen.

Such an approach was a principally new tool for the determination of the influence of surface-active and corrosive-aggressive environments on the materials physicomechanical characteristics. These methods are effective and agree well with well-known (but low effective) approaches of American scientists [42]. In accordance with these approaches the enveloping curve of a great deal of experimental data received under different test conditions is used as a basic (calculation diagram ($v \sim K_I$)-diagram). The ($v \sim K_I$) diagram received by equation (15) practically coincides with this curve (see Fig. 15).

At the end the problem of hydrogen (or hydrogen-containing environments) interaction with metals should be mentioned. This problem needs a special attention. It is a many-sided problem of the present-day material science, and is concerned with the phenomena of hydrogen embrittlement (or plasticization) of metals under their deformation in the hydrogen or hydrogen-containing environments. In whole this problem includes the following aspects:

– development of materials resistant to hydrogen embrittlement and development of reliable criteria for estimation of the given materials service ability in hydrogen environment to use them in engineering structures, in particular for hydrogen storage and transportation;

– use of hydrogen as a technological media for effective treatment of materials and improvement of their functional properties.

Currently the main task for researchers in the field of fracture mechanics and materials strength in hydrogen-containing environments is the consolidation of their efforts
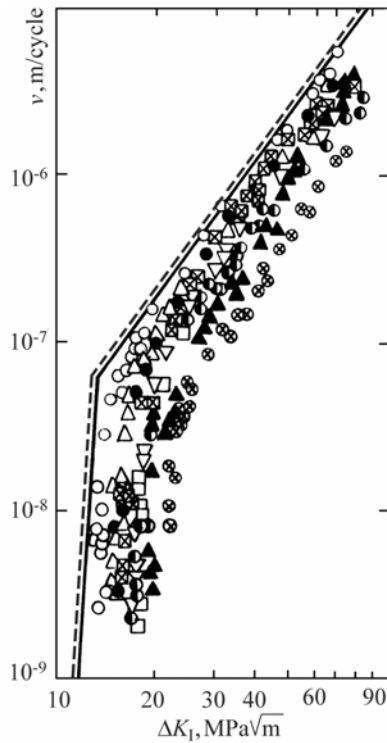
Fig. 15. Basic diagram of the cyclic corrosion cracking of the weld material (10ХМФТ steel) constructed using traditional [42] approaches (doted line) and in the frames of the proposed concept [41] (firm line) in the reactor water of boron regulation (1% H_3BO_3+KOH up to pH 8): ▲ – 0.017 Hz, 80°C; ⊗ – 0.017 Hz, 25°C; ⊠ – 0.1 Hz, 80°C; ◑ – 0.1 Hz, 25°C; △ – 0.33 Hz, 80°C; ▽ – 0.33 Hz, 25°C; ● – 1.0 Hz, 80°C; □ – 1.0 Hz, 25°C; ○ – 0.33 Hz, 25°C, $pH=pH_t^{min}=6$. $R = K_{Imin}/K_{Imax}$ – asymmetry of the loading cycle

on the studies, which concerned to the development of future hydrogen energy infrastructure. As typical sample of such research the recent works [43-45] can be mentioned where the hydrogen influence on low-alloyed pipeline steels was considered. Here the existence of some critical hydrogen concentration in metal, which causes the significant loss of local fracture resistance of material, was shown. For assessment of local strength in presence of hydrogen the diagram "work of local fracture – hydrogen concentration" has been proposed and verified [43].

References

1. Panasyuk, V.V.: Mechanics of Materials Quasibrittle Fracture. Naukova Dumka, Kyiv (1991) (in Russian)
2. Panasyuk, V.V.: An outline of the development of fracture mechanics and strength of materials investigations. In: Investigations on Fracture, Strength and Integrity of Materials and Structures. Physico-Mechanical Institute, Lviv (1993)

3. Rossmanith, H.P.: The Struggle for Recognition of Engineering Fracture Mechanics. Fracture Research in Retrospect. In: An anniversary volume in honour of G. R. Irwin's 90th Birthday. A.A. Balkema, Rotterdam (1997)

4. Panasyuk, V.V.: Fracture mechanics of material – new research area. In: Po-hodnya, I.K. (ed.) Advanced materials and technologies, Adademknyha, Kyiv, vol. 2 (2003) (in Ukrainian)

5. Panasyuk, V.V. (ed.): Fracture Mechanics and Materials Strength, Naukova Dumka, Kyiv, vol. 4 (1988-1990) (in Russian)

6. Ya, Y.S., Vitvitskii, P.M., Datsyshyn, A.P.: First All-Union Conference Fracture mechanics of materials. Physicochemical Mechanics of Materials 1, 124–126 (1988) (in Russian)

7. Panasyuk V.V., Andreykiv A. Ye., Lobanov L.M., Taplin D.M., Kuzniak N.V. Fracture Me-chanics: Advances and Problems. Review of ICF8 (1994) Physico-Mechanical Institute, Lviv (in Ukrainian)

8. Panasyuk, V.V.: Deformation criteria in fracture mechanics of materials. Physico-Mechanical Institute, Lviv (1993)

9. Griffith, A.A.: The theory of rapture. In: Proc. 1st Int. Conf. Appl. Mech., Delft (1924)

10. Irwin, G.R.: Analysis of stresses and strains near the end of a crack, traversing a plate. J. Appl. Mech. 24, 361–364 (1957)

11. Panasyuk, V.V., Andreykiv, A.Ye., Kovchyk, S.Ye.: Methods of Evaluation of the Crack Growth Resistance of Structural Materials. Naukova Dumka, Kyiv, in Russian (1977)

12. Frolov, K.V. (ed.): Mechanics of catastrophes. Determination of characteristics of crack growth resistance of structural materials. Methodical guidelines, CODAS, Moscow (1995) (in Russian)

13. Yarema, S.Ya.: Test Method for the Determination of Crack Growth Rates and Crack Extension Resistance under Cyclic Loading. Materials Science 3, 384–402 (1994) 4, 512–530; 6, 706–717; 1, 140–152 (1995)

14. Kovchyk, S.Ye., Morozov, Ye.M.: Characteristics of short time crack growth resistance of materials and methods of their determination. In: Panasyuk, V.V. (ed.) Fracture Mechanics and Materials Strength, vol. 4 ,3 (1988-1990) Naukova Dumka, Kyiv (in Russian)

15. ASTM Standard No. 399, Standard test method for plane-strain fracture toughness of metallic materials. Annual book of ASTM standards, vol. 11.03 (1974)

16. Panasyuk, V.V., Berezhnyts'kyi, L.T.: Determination of limiting forces under tension of plate with arched crack. Questions of mechanics of real solid 3, 3–19 (1964) (in Russian)

17. Panasyuk, V.V., Berezhnyts'kyi, L.T., Kovchyk, S.Y.: On propagation of arbitrary oriented rectilinear crack. Applied Mechanics 1(2), 48–55 (1965) (in Russian)

18. Andreykiv, O.Y.: Spatial problems of theory of cracks. Naukova Dumka, Kyiv (1982) (in Russian)

19. Makhutov, N.A., Panasyuk, V.V., Yarema, S.: Calculation and testing on strength. Methods of mechani-cal testing of materials. Determination of characteristics of crack growth resistance (fracture toughness) under static loading. Publishing House of State Committee for Standards of USSR, Moscow (1985) Standard USSR 25.506-85 (in Russian)

20. Brown, W., Srowley, J.: Fracture toughness tests of high-strength materials in plane strain. ASTM, Philadelphia (1971)

21. Panasyuk, V.V., Ivanyts'kyi, Y.L., Andreykiv, O.Y.: Methods of assessment of cyclic crack growth resistance under realization of mixed macromechanisms of fracture. In: Proceedings of International conference Assessment and ground of lifetime extension of structural elements. Institute of Applied Problems of Mechanics and Mathematics of NASU, Lviv, pp. 43-56 (2000) (in Ukrainian)

22. Panasyuk, V.V.: Some problems of fracture mechanics and strength of materials. In: Panasyuk, V.V. (ed.) Proceedings of the 2nd International conference "Fracture mechanics of materials and strength of structures" in 3 volumes, vol. 1 (1999) (in Ukrainian)

23. Ivanyts'kyi, Y.L., Shtayura, S.T.: Methodical guidelines. Determination of crack growth resistance of structural materials under complex loading. In: Panasyuk, V.V. (ed.) Fracture mechanics of materials and strength of structures. Karpenko Physico-Mechanical Institute of National Academy of Sciences, Lviv (2004) (in Ukrainian)

24. Ivanyts'kyi, Y. L.: Methods of assessments of crack growth resistance of structural materials under complex loading. ScD Thesis, Karpenko Physico-Mechanical Institute of National Academy of Sciences, Lviv (2005) (in Ukrainian)

25. Panasyuk, V.V.: Limiting Equilibrium of Brittle Solids with Cracks. Naukova Dumka, Kyiv (1974) (in Russian); Michigan Manag. Inform. Ser., Detroit (1968) (in English)

26. Dugdale, D.-S.: Yielding of steel sheets containing slits. J. Mech. And Phys. Solids. 8(2), 100–108 (1960)

27. Wells, A.-A.: Critical tip opening displacement as fracture criterion. Proceedings of Crack Propagation Symposium (Crangield) 1, 210-221 (1961)

28. Panasyuk, V.V., Savruk, M.P.: Plastic strip model in elastic-plastic problems of fracture mechanics. Adv. Mech. 15(3), 123–147 (1992)

29. Panasyuk, V.V., Ivanyts'kyi, Y.L., Maksymenko, O.P.: Analysis of the Elasoplastic Deformation of the Material in the Process Zone. Materials Science 5, 648–655 (2004)

30. Ostash, O.P., Panasyuk, V.V.: Fatigue process zone at notches. Int. J. Fatigue 23(7), 1115–1120 (2001)

31. Yarema, S.Y., Mykytyshyn, S.I.: Analytical description of fatigue fracture diagram of materials. Soviet Materials Science 6, 47–54 (1975)

32. Ostash, O.P., Panasyuk, V.V.: Theory of initiation and propagation of fatigue cracks. Material Science 24(1), 10–17 (1988)

33. Panasyuk, V.V., Ostash, O.P., Kostyk, Y.M.: Relationship of cyclic cracking resistance characteristic of crack initiation and growth stages. Materials Science 22(6), 584–589 (1986)

34. Ostash, O.P., Panasyuk, V.V.: A unified approach to fatigue macrocrack initiation and propagation. Inter. J. Fatigue. 25, 703–708 (2003)

35. Ostash, O.P.: New Approaches in Fatigue Fracture Mechanics. Materials Science 1, 5–19 (2006)

36. Ostash, O.P., Chepil', R.V., Vira, V.V., Zhmur-Klymenko, V.T.: Prediction of the Durability of Cyclically Loaded Structural Elements. Materials Science 4, 479–485 (2005)

37. Karpenko, H.V.: Influence of active liquid media on endurance of steel. Publishing House of UkrSSR Acad. Sci., Kiev (1955) (in Russian)

38. Panasyuk, V.V., Kovchyk, S.Y.: Influence of surface-active medium on surface energy of brittle fracture of body. Proc. USSR Acad. Sci. 146(1), 82–85 (1962) (in Russian)

39. Romaniv, O.M., Nykyforchyn, H.M.: Mechanics of corrosion fracture of structural alloys. Melallurgia, Moscow (1986) (in Russian)

40. Panasyuk, V.V., Ratych, L.V., Dmytrakh, I.N.: Fatigue crack growth in corrosive environments. Fatigue Fract. Eng. Mater. and Struct. 7(1), 1–11 (1984)
41. Dmytrakh, I.M., Panasyuk, V.V.: Influence of Corrosive Environments on Local Fracture of Metals near Stress Concentrators. National Academy of Sciences of Ukraine, Karpenko Physico-Mechanical Institute, Lviv, in Ukrainian (1999)
42. Bamford, W.H.: Application of corrosion fatigue growth rate data to integrity analyses of nuclear reactor vessels. J. Eng. Mater. and Technol. 101(3), 182–190 (1979)
43. Capelle, J., Gilgert, J., Dmytrakh, I., Pluvinage, G.: Sensitivity of Pipelines with Steel API X52 to Hydrogen Embrittlement. International Journal of Hydrogen Energy 33(24), 7630–7641 (2008)
44. Capelle, J., Dmytrakh, I., Pluvinage, G.: Electrochemical Hydrogen Absorption of API X52 Steel and its Effect on Local Fracture Emanating from Notches. Structural Integrity and Life 9(1), 3–8 (2009)
45. Capelle, J., Dmytrakh, I., Pluvinage, G.: Comparative assessment of electro-chemical hydrogen absorption by pipeline steels with different strength. Corrosion Science 52, 1554–1559 (2010)

Cyclic Plasticity with an Application to Extremly Low Cycle Fatigue of Structural Steel

Dragoslav Šumarac[1] and Zoran Petrašković[2]

[1] Faculty of Civil Engineering, University of Belgrade, Serbia
[2] Research-productive Centre System DC 90, 11000 Belgrade, Serbia
 `sumi@eunet.rs, dc90@eunet.rs`

Abstract. In the present paper the Preisach model of hysteresis is applied to model cyclic behavior of elasto-plastic material. The problem of axial loading of rectangular cross section will be studied in details. Hysteretic stress-strain loop for prescribed history of stress change is plotted for material modeled by series connection of three unite element. All obtained results clearly show advantages of the Preisach model for describing cyclic behavior of so called stable plastic material. Other effects such are racheting and creep will be studied elsewhere. In this paper extremly low cycle fatigue will also be examined. Extremly low cycle fatigue stands for number of cycles to failure in between 10 and 20. The stress level is larger than the yield stress and the plastic strain is of the same magnitude as the elastic strain. In this paper it is shown that this case is of importance to dampers applied for reconstruction of earthquake damaged structures.

1 Introduction

In the present paper the model of elasto-plastic behavior for quasy static cyclic loading will be explained. Special attention will be made to hysteretic behavior and mathematical models applied for their description. In this paper stress-strain loops will be constructed for cyclic axial loading. From this examples it is obvious that suggested (Preisach) model is simple enough and very appropriate to describe hysteretic behavior of elasto-plastic material. In the case of racheting, cyclic creep and fatigue some aditional improvements of Preisach model should be applied. An interesting proposal for Very low cycle fatigue has been done by Dufailly and Lemaitre [7]. In this case number of cycles to failure is of the order of 10 to 20. Plastic strain is much larger than the elastic one as well as the dissipative work to the elastic power. In this paper it will be show that this case is of importance to dampers applied for reconstruction of earthquake damaged structures.

2   The Preisach Model of Hysteresis

The Preisach model of hysteresis, dealing with the problem of magnetism, is described thoroughly in the monograph of Mayergoyz [6]. The phenomenon of hysteresis occurs in various branches of physics: mechanics, magnetism, optics, adsorption etc. Application of the Preisach model to cyclic behavior of elasto-plastic material is shown in (Lubarda et al., [3]) and extended to cyclic bending by (Sumarac and Stosic, [5]). In this paper short outline of Preisach model of hysteresis will be presented. According to Mazergoyz [6], the Preisach model implies the mapping of an input of strain ε (t) on the output of stress σ (t) in the integral form:

$$\sigma(t) = \iint P(\alpha,\beta) G_{\alpha,\beta} \varepsilon(t) \, d\alpha \, d\beta \tag{1}$$
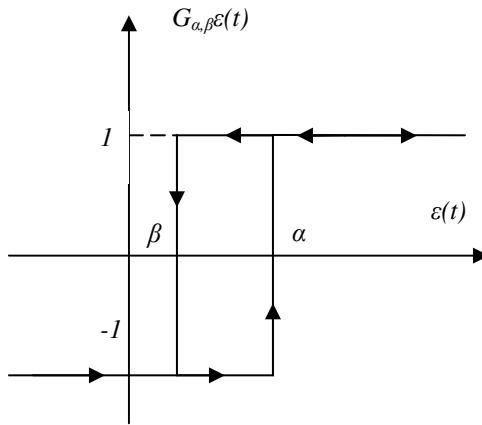
Fig. 1. Elementary hysteresis operator

where $G_{\alpha,\beta}$ is an elementary hysteresis operator given in Figure 1. Parameters α and β are up and down switching values of the input, while P (α, β) is the Preisach function. i.e. a weight (Green′s) function of the hysteresis nonlinearity to be represented by the Preisach model. The domain of integration of integral (1) is right triangle in the α, β plane, with $\alpha=\beta$ being the hypotenuse and $(\alpha_0, \beta_0 = -\alpha_0)$ being the triangular vertex (Fig.2). History of loading corresponds to staircase line L (t) which divides triangle into two parts (Lubarda et al., [2]). Maxima or minima of loading history are represented by the vertices with coordinates (α, β) on staircase line L(t) in such a way if the input at a previous instant of time is increased, the final link of L(t) is horizontal, and vise versa if it is decreased it is vertical. Therefore, the triangle is divided into two parts with the positive and negative values of $G_{\alpha,\beta}$ by the interface staircase line L(t). From formula (1) it is than obtained:

$$\sigma(t) = \iint_{A^+(t)} P(\alpha,\beta) G_{\alpha,\beta} \varepsilon(t) \, d\alpha \, d\beta - \iint_{A^-(t)} P(\alpha,\beta) G_{\alpha,\beta} \varepsilon(t) \, d\alpha \, d\beta \tag{2}$$

Denoting the output value at $\varepsilon = \beta$ by $f_{\alpha,\beta}$ from the limiting triangle, it follows that

$$f_{\alpha,\beta} - f_\alpha = -2 \int_\beta^\alpha \left(\int_{\beta'}^\alpha P(\alpha',\beta')\,d\alpha' \right) d\beta' \tag{3}$$
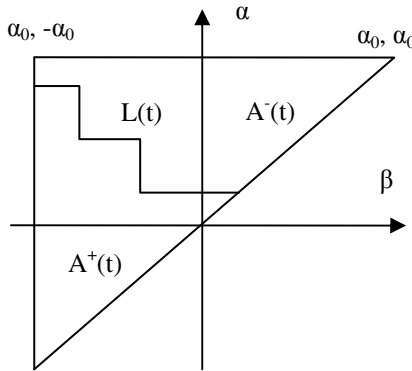

Fig. 2. Limiting triangle with the interface staircase line L(t)

By differentiating expression (3) twice, with respect to α and β, the Preisach weight function is derived in the form

$$P(\alpha,\beta) = \frac{1}{2} \frac{\partial^2 f_{\alpha,\beta}}{\partial\alpha\partial\beta} \tag{4}$$

The Preisach model explained above possesses two properties: wiping out and congruency properties. Those properties and much more about Preisach model is explained in the (Lubarda et al., [2]) and (Lubarda et al., [3]).
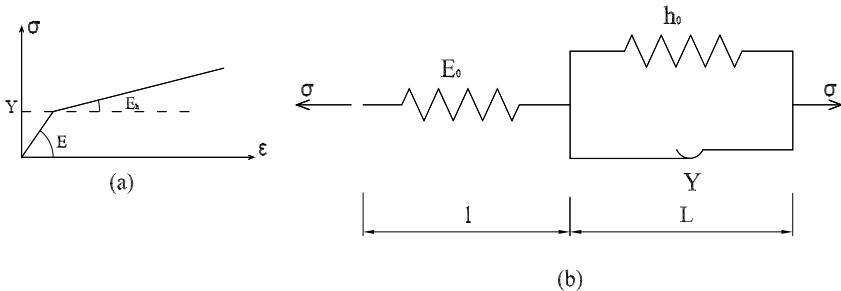
Fig. 3. (a)Elastic-linearly hardening stress-strain behaviour with elastic modulus E, initial yield stress Y and hardening modulus E_h (b) Three-element unit reproducing the stress-strain behaviour in (a)

3 The Preisach Model for Cyclic Behaviour of Ductile Materials

One dimensional hysteretic behavior of elasto-plastic material can be successfully described by the Preisach model. Ductile material is represented in various ways by a series or parallel connections of elastic (spring) and plastic (slip) elements (Lubarda, at al., [2]). These results have advantage in comparison with classically obtained (Iwan, [4]) because of simplicity and strict mathematical rigorous procedure. Parallel Connection of elastic and slip elements, Series connection of elastic and slip elements are discussed elsewhere (Sumarac and Stosic, [5]), (Lubarda, at al., [2]). Here we will consider a three element unit.
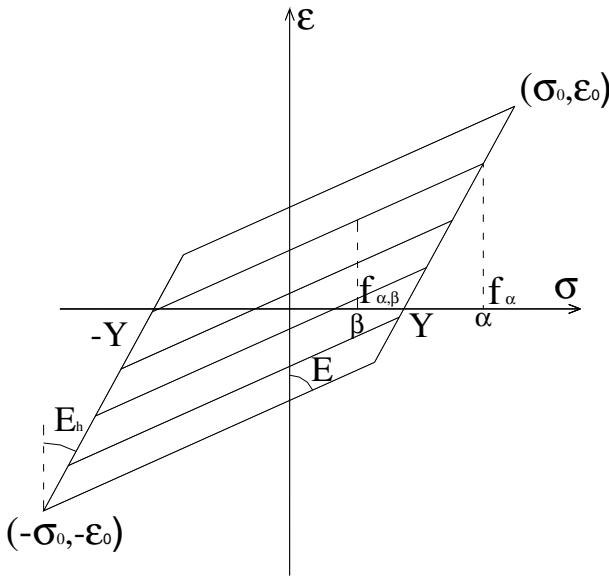
Fig. 4. Major hysteresis loop and several transition lines, corresponding to the material model in Fig. 3

3.1 A Three-Element Unit

Elastic-linearly hardening material behavior, characterized by the stress-strain curve shown in Fig. 3a. (E and E_h are elastic and hardening moduli), can be modeled by a three-element unit shown in Fig. 3b. Elastic element of length l and modules E_0 is connected in a series with a parallel connection of elastic and slip element, of length L modulus h_0 and yield strength Y. It then follows that $E = E_0\,(l + L)/l$ and $E_h = Eh(E + h)$, where $h = h_0\,(l + L)/L$ .The Preisach function can be determined from the hysteresis nonlinearity shown in Fig. 4,

which relates the stress input to strain output. The Preisach function in this case has support along the lines $\alpha - \beta = 0$ and $\alpha - \beta = 2Y$, i.e. it is given by

$$P(\alpha,\beta) = \frac{1}{2E}\left[\delta(\alpha-\beta) + \frac{E-E_h}{E_h}\delta(\alpha-\beta-2Y)\right]. \tag{5}$$

The expression for strain as a function of applied stress is, consequently,

$$\varepsilon(t) = \frac{1}{2E}\left[\int_{-\sigma_0}^{\sigma_0} G_{\alpha,\alpha}\sigma(t)d\alpha + \frac{E-E_h}{E_h}\int_{2Y-\sigma_0}^{\sigma_0} G_{\alpha,\alpha-2Y}\sigma(t)d\alpha\right], \tag{6}$$

The first and second term on the right-hand side of (6) are elastic and plastic strain, respectively. For a system consisting of infinitely many of three-element units, connected in a series and with uniform yield strength distribution within the range $Y_{min} \leq Y \leq Y_{max}$, the total strain is

$$\varepsilon(t) = \frac{1}{2E}\left[\int_{-\sigma_0}^{\sigma_0} G_{\alpha,\alpha}\sigma(t)d\alpha + \frac{E-E_h}{2E_h}\frac{1}{Y_{max}-Y_{min}}\iint_A G_{\alpha,\beta}\sigma(t)d\alpha d\beta\right]. \tag{7}$$

In (7) the integration domain A is the area of the band contained between the lines $\alpha - \beta = 2Y_{min}$ and $\alpha - \beta = 2Y_{max}$ in the limiting triangle, shown in Fig. 5. The first term on the right-hand side of (7) is the elastic strain, which can be written as $\sigma(t)/E$.
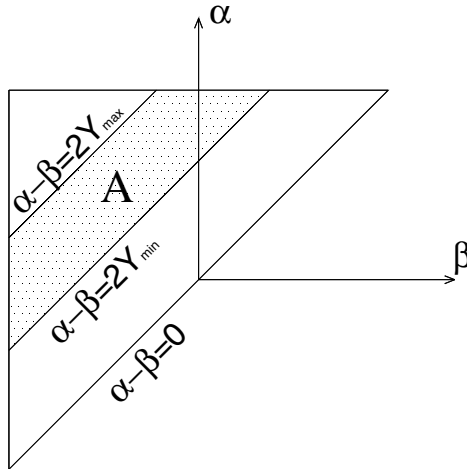

Fig. 5. The Preisach function corresponding to series connection of infinitely many three element units

In the case when the strain is the input and stress output, the Preisach function becomes

$$P(\alpha, \beta) = \frac{E}{2}\delta(\alpha - \beta) - \frac{1}{2}(E - E_h)\delta\left(\alpha - \beta - 2\frac{Y}{E}\right).$$ (8)

The stress expression is form (1)

$$\sigma(t) = \frac{E}{2}\int_{-\varepsilon_0}^{\varepsilon_0} G_{\alpha,\alpha}\varepsilon(t)d\alpha - \frac{1}{2}(E - E_h)\int_{2\frac{Y}{E}-\varepsilon_0}^{\varepsilon_0} G_{\alpha,\alpha-2\frac{Y}{E}}\varepsilon(t)d\alpha.$$ (9)

3.2 Ilustrative Example

To illustrate the application of the Preisach model the stress-strain hysteretic curve is determined for material model of series connection of three unite element introduced in the previous subsection. In the calculation it is used $E_h = E/9$ and $Y_{max} = 2Y_{min}$. The loading history of stress change is shown in Fig.6. From the procedure explained above the strain in the first portion $-4Y_{min} < \sigma < -2Y_{min}$ is linear:
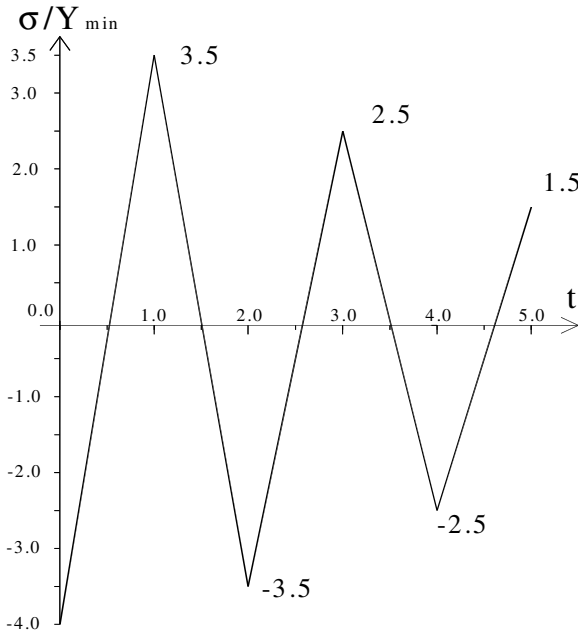

Fig. 6. History of stress input

$$\frac{\varepsilon E}{Y_{min}} = -20 + \frac{\sigma}{Y_{min}} \qquad (10)$$

For further increase of stresses in the region $-2Y_{min} < \sigma < 0$, staircase line L falls into the band are A shown in Fig.5 and consequently response is nonlinear:

$$\frac{\varepsilon E}{Y_{min}} = -22 + \left(\frac{\sigma}{Y_{min}} + 2 \right)\left(5 + 2\frac{\sigma}{Y_{min}} \right) \qquad (11)$$

At the stress level $\sigma=0$ the strongest element Y_{max} starts to yield. Saturation occurs and the system responds elastically with the Young's modulus $E_h=E/9$, i.e. in the region $0 < \sigma < 3.5Y_{min}$:

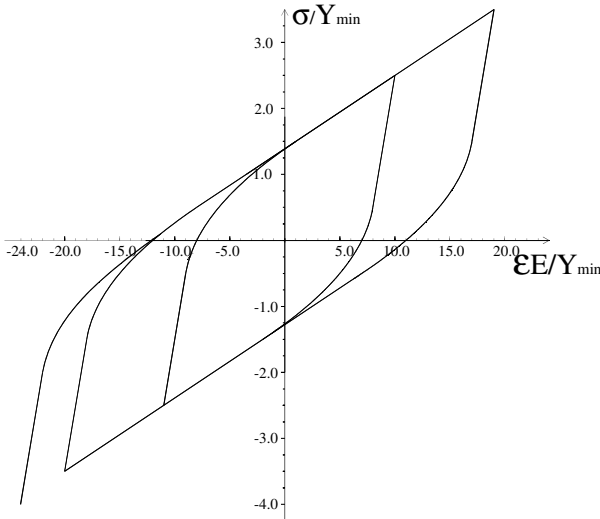$$\frac{\varepsilon E}{Y_{min}} = 9\frac{\sigma}{Y_{min}} - 12.5 \qquad (12)$$

Fig. 7. Stress-strain loop

In the region $1.5\ Y_{min} < \sigma < 3.5\ Y_{min}$ response is linear with the Young's modulus E:

$$\frac{\varepsilon E}{Y_{min}} = 15.5 + \frac{\sigma}{Y_{min}} \qquad (13)$$

Further decrease of stresses, $-0.5Y_{min} < \sigma < 1.5Y_{min}$, leads to nonlinear response with the quadratic parabola:

$$\frac{\varepsilon E}{Y_{min}} = 17 - \left(1.5 - \frac{\sigma}{Y_{min}} \right)\left(4 - 2\frac{\sigma}{Y_{min}} \right) \qquad (14)$$

In the region, $-3.5Y_{min} < \sigma < -0.5Y_{min}$, saturation again occurs and the system responds as elastic with the Young's modulus of E_h:

$$\frac{\varepsilon E}{Y_{\min}} = 11.5 + 9\frac{\sigma}{Y_{\min}} \tag{15}$$

The further procedure is obvious, and the stress-strain loop is presented in Fig 7.

4 Extremly Low Cycle Fatigue

In the literature the Manson-Coffin law is widely used to explain cyclic fatigue of materials:

$$N_f = \left(\Delta\varepsilon_p / C\right)^{\gamma} \tag{16}$$

Where N_f is number of cycles to failure, $\Delta\varepsilon_p$ is plastic strain amplitude and C and γ are material constants [8], [9] and [10]. This diagram in Log-Log graph is represented by linear lines. However experimentally it is shown that eq. (16) overestimates number of cycles in the case of very low cycle fatigue. An atempt to model extremly low cycle fatigue is given in [7]. Application of Preisach model to solve this problem will be disscused elsewere. Here, experimental verification of low cycle fatigue on example of Dampers DC 90 will be shortly explained.

5 Application and Testing of DC90 Dampers

Earthquakes are very dangerous impacts on civil engineering structures. Specially this is the case of masonry structures. It is well known that those structures have large mass, and consequently, because of bad cohesion between bricks (stones) and mortar they crack and suffer damage when exposed to earthquakes. In Fig. 8. typical masonry structure in the western part of Serbia, after Kolubara earthquake, 4.8 Richter scale is shown. The cracks and damage, due to alternating loading is along diagonals. Strong need and desire to find a new effective object protection from seismic loads and realization of the tougher masonry and even concrete constructions resulted a new, DC 90 Construction System and associate devices [11], presented briefly in this article.

Fig. 8. Damage of two store building

Produced dampers for DC 90 system (Fig. 9) were tested by variable loading on MTS servo-hydraulic closed-loop machine (Fig. 10) at Faculty of Civil Engineering and Geodesy in Ljubljana. The test was performed on 18 specimens and obtained hysterezis loop and force-number of cycles to rupture diagram is given in Fig. 11 for 1mm displacement.

Fig. 9. Typical dampers of DC 90 system

Fig. 10. Damper testing

After conducting the serial tests of twelve specimens we demonstrate the tests for three typical specimens.

Fig. 11. Hysteresis loop diagram and force - number of cycles diagram, for cycle loading at constant displacement range ± 1 mm.

It is shown that number of cycles before rupture is les than 150 for ±1 mm of displacement range. With increasing displacement range number of cycles even decreased, which clearly shows that DC 90 dampers behaves under the earthquakes according to very low cycle fatigue.

6 Conclusions

In the present paper it is shown, that Preisach model has several advantages when it is applied to the problem of so called cyclic stable plasticity of axially loaded members. Mathematical rigor and a closed form analytical solutions makes the Preisach model very competitive with the other methods of solution. Application

of the Preisach model to extremely low cycle fatigue is obvious. Extremely low cycle fatigue happens in the case of 10 to 20 cycles before rupture, followed by large plastic strain and maximum stresses much larger than the yield stress. This case is very important for design of dampers applied for reconstruction of seismically damaged structures, because Manson-Coffin Law overestimates the number of cycles before failure.

References

 [1] Preisach, F.: Uber die magnetishe Nachwirkung. Z. Phys. 94, 277–302 (1936)
 [2] Lubarda, A.V., Sumarac, D., Krajcinovic, D.: Hysteretic response of ductile materials subjected to cyclic loads. In: Ju, J.W. (ed.) Recent Advances in damage Mechanics and Plasticity, vol. 123, pp. 145–157. ASME Publication, AMD (1992)
 [3] Lubarda, A.V., Sumarac, D., Krajcinovic, D.: Preisach model and hysteretic behaviour of ductile materials. Eur. J. Mech., A/Solids 12(4), 145–157 (1993)
 [4] Iwan, W.D.: On a class of models for the yielding behaviour of con-tinuous and composite systems. J. Appl. Mech. 34, 612–617 (1967)
 [5] Sumarac, D., Stosic, S.: The Preisach model for the cyclic bending of elasto-plastic beams. Eur. J. Mech., A/Solids 15(1), 155–172 (1996)
 [6] Mayergoyz, I.D.: Mathematical Models of Hysteresis, pp. 1–140. Springer, NY (1991)
 [7] Dufailly, J., Lemaitre, J.: Modeling Very Low Cycle Fatigue. Int. J. Damage Mechanics 4, 153–170 (1995)
 [8] Manson, S.S.: Behaviour of Materials under Conditions of Thermal Stresses, N.A.C.A. Tech. Note, 2933 (1954)
 [9] Coffin, L.F.: A Study of the Effects of Cyclic Thermal Stresses in a Ductile Metal. Transactions of the A.S.M.E. 931, 76 (1954)
[10] Šumarac, D., Krajčinović, D.: Elements of Fracture Mechanics. Scientific Book, Belgrade (1990) (in Serbian)
[11] Petraskovic, Z.: System of Seismic Strengthening of Structure, Unitet States Patent and Trademark Office, Pub. No. US 2006/0207196 A1, Serial No. 10/555,131, September 21 (2006)

The Fracture Toughness of a Highly Filled Polymer Composite

O.A. Stapountzi[1], M.N. Charalambides[1], and J.G. Williams[1,2]

[1] Mechanical Engineering Department, Imperial College London, UK
[2] School of Aerospace, Mechanical & Mechatronic Engineering,
   University of Sydney, Australia

Abstract. Fracture toughness values are given for an ATH-PMMA composite for filler volume fractions ranging from 0.35 to 0.49 and tested over the temperature range from 0 to 90 °C. The toughness decreased with increasing filler content contrary to expectations. A toughness model based on debonding, and subsequent plastic void growth was extended from a low volume fraction form to accommodate interaction between particles. From the fitted data it was possible to calculate the adhesion energy of the particles and the average particle size. The former was somewhat less than the matrix toughness and the latter agreed quite well with the sizes found from particle size measurements on the filler and surface roughness measurements on the fracture surfaces.

1 Introduction

Two recent papers have reported results on this ATH (alumina trihydrate) – PMMA composite containing up to 50% filler content by volume [1, 2].   A high filler content is used to achieve a high elastic modulus (≈12 GPa) whilst maintaining a sufficient fracture toughness. [1] reported data on fatigue crack resistance for a single volume fraction over a range of temperatures since this aspect of performance is important practically. In [2] the study was extended to a set of materials with a range of volume fractions (0.33 – 0.49) in which Young's modulus was measured over a range of temperatures [0 - 90°C]. This presented an interesting opportunity to compare the predictions of a range of modulus models since the temperature variations resulted in the matrix properties changing while the filler properties remained constant. It was demonstrated that such stiffness properties could be accurately predicted by several models [2].

   This work reports fracture toughness data on a similar set of materials tested over the same temperature range. This data presents an opportunity to explore

toughness models of composites since, again, the matrix properties change with temperature whilst the filler properties do not. The fatigue data [1] showed a peak in fatigue crack growth rate ($\mathrm{d}a/\mathrm{d}N$) at around $50°\mathrm{C}$ which was attributed to thermal stresses around the particles.

Some recent work on modelling the toughening mechanism in particle filled composites as plastic void growth resulting from the debonding of the particles [3] will also be explored here. It has been necessary to extend the earlier, low volume fraction analyses, to account for the high values used here.

2 Materials and Experiments

Nine materials were used with volume fractions ranging from 0.35 to 0.49. These were supplied by Du Pont as 12.5 mm thick sheets and prepared by casting the filled monomer syrup in moulds. The curing process is exothermic so that the moulds are cooled leading to thermal stresses both in the bulk and on an inter particle range. The lowest volume fraction was the practical limit for the process and the upper is close to the theoretical maximum of 0.52 (see section 4).

The fracture toughness tests were performed in accordance to ISO 13586, the linear elastic fracture mechanics standard for polymers and using three point bend tests. A specimen thickness of around 5 mm was used and this gave valid results over the whole temperature range. Notching such materials was a challenge. Razor tapping was employed but the particles often gave damage around the crack tip which led to considerable scatter in some of the data. At each temperature a minimum of five specimens was tested.

The matrix material is a lightly cross linked PMMA but, as in previous papers, we have assumed that it behaves in a similar manner to normal PMMA. Fracture tests were performed in the range 20-90^{0}C and compression tests using cylindrical samples tests were employed to determine the yield stress. The loading times of all the tests was kept approximately constant. Talysurf measurements were made on fracture surfaces of samples taken from all the test temperatures to determine the average roughness values.

3 Experimental Results

Table 1 gives the fracture data for all the composite tests; the data are also plotted in Fig. 1. The standard deviations are generally less than 10% which is low for this type of test. The G_c values increase somewhat with temperature but the most notable feature is the decrease with volume fraction. In most cases this decrease is about 30% over the volume fraction range. This is contrary to expectations and an increase would be predicted [3].

Table 2 shows the experimental data for the matrix (PMMA). No tests were performed at 0^0C and so these values are extrapolated. The modulus values are taken from the fracture tests and the yield stresses were obtained in compression. A value of 0.4 is assumed for the Poisson's ratio, V, in subsequent calculations [2].

The G_m values presented some difficulties. At 22, 40 and 65°C the data showed little evidence of ductility and a small decrease in G_m was observed at 65°C. At 90°C, however, a value of 1.10 kJ/m^2 was obtained and the very low yield stress led to crack blunting although the results were valid. Again the standard deviations are about 10%.

Table 1. Fracture Toughness Data, (*S* is standard deviation).

| $T\,°C$	0	22	40	65	90
ϕ		$G_c \pm S$	(kJ/m^2)		
0.35	0.54±0.08	0.54±0.07	0.69±0.06	0.68±0.06	0.77±0.14
0.37	0.48± 0.05	0.44±0.05	0.61±0.04	0.62±0.09	0.62±0.05
0.38	0.56± 0.06	0.55±0.10	0.56±0.06	0.59±0.03	0.61±0.05
0.40	0.48±0.06	0.44±0.07	0.51±0.07	0.54±0.02	0.56±0.03
0.42	0.47±0.03	0.41±0.10	0.51±0.07	0.55±0.09	0.62±0.07
0.42	0.45± 0.02	0.39±0.06	0.47±0.07	0.50±0.06	0.59±0.17
0.45	0.45±0.03	0.35±0.08	0.47±0.06	0.48±0.06	0.59±0.06
0.47	0.43±0.05	0.37±0.06	0.43±0.04	0.45±0.05	0.49±0.09
0.49	0.36±0.02	0.26±0.04	0.40±0.06	0.41±0.02	0.44±0.06
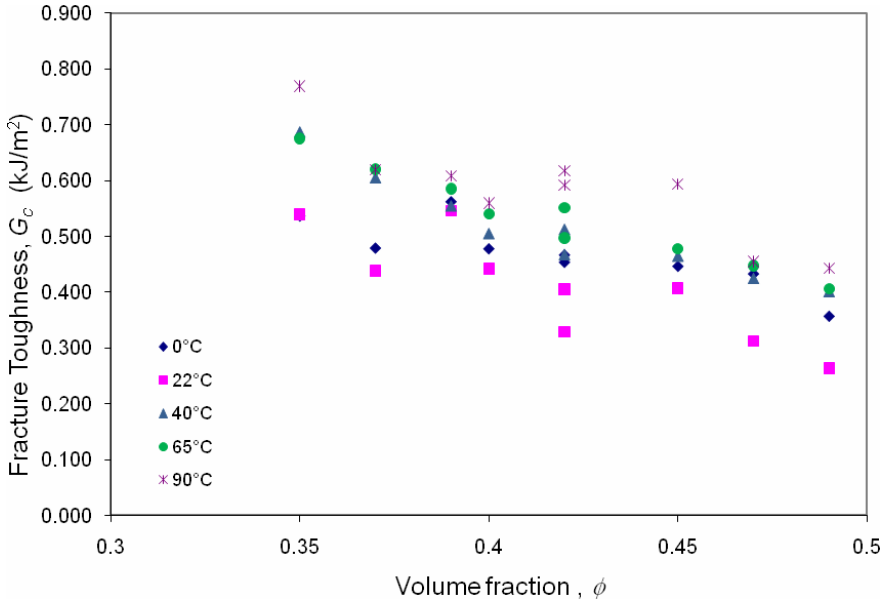
Fig. 1. Composite Fracture Toughness Data versus filler volume fraction at various temperatures.

Table 2. PMMA Matrix Property Data, ( ) indicate extrapolated values.

$T\,°C$	σ_y (MPa)	E (GPa)	$G_m \pm S$ (kJ/m^2)
0	(150)	(3·5)	(0·45)
22	125	3·4	0·45 ±·03
40	100	3·2	0·45 ±·03
65	71	2·6	0·35 ±·03
90	39	1·4	1·10 ±·07

4   Toughness Model

A model to describe these high volume fraction data is based on that given in [3]. In the model the toughening is assumed to arise from a single mechanism is which particles around the crack tip are subjected to sufficient hydrostatic stress to cause debonding. This freeing of the particle interface gives rise to plastic work being dissipated in a zone surrounding the particle.

The model is based on a cell of side length l containing a spherical particle of radius $r_\circ$ as shown in Fig. 2. The volume fraction of particles, ϕ, is given by,

$$\phi = \frac{4\pi}{3}\left(\frac{r_\circ}{l}\right)^3 \tag{1}$$

(The upper limit for the particles to touch is $r_o = \dfrac{l}{2}$ and $\phi = \dfrac{\pi}{6} = 0.52$).
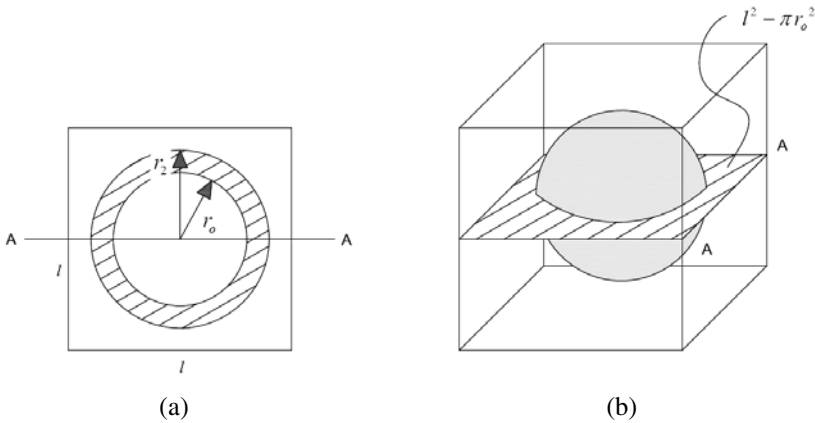
Fig. 2. Particle unit cell and fracture area.

The area fraction of matrix on a plane through the equator of the particle, AA in Fig 2.a and shown in Fig 2.b, is

$$\phi_a = 1 - \pi\left(\frac{r_o}{l}\right)^2 = 1 - \pi\left(\frac{3\phi}{4\pi}\right)^{2/3} = 1 - 1.21\phi^{2/3} \tag{2}$$

The rigid particle is assumed to be subjected to a surface radial stress of σ_c and that, prior to yielding, the matrix is elastic and debonding occurs when [3],

$$\sigma_c^2 = \frac{4}{1+v}\frac{EG_a}{r_o} \tag{3}$$

On debonding this gives rise to plastic work being performed, via a constant yield stress σ_y in a zone of radius r_2 also shown in Fig 2a. r_2 is given by [3]:

$$\ln R^3 = \frac{1}{2}\left(\frac{1+v}{1-v}\right)\frac{\sigma_c}{\sigma_y} - 1 \tag{4}$$

where $R = \dfrac{r_2}{r_o}$.

This gives rise to a plastic energy dissipation per unit of particle surface area, $4\pi r_o^2$ of

$$G_p = \frac{2}{3}(1-v)\frac{\sigma_y^2 r_o}{E}x^2\left(\frac{R^3}{x}-1\right) \tag{5}$$

where

$$x = \frac{1}{2}\left(\frac{1+v}{1-v}\right)\frac{\sigma_c}{\sigma_y}$$

For micron scale particles only those in the fracture plane are involved [3] and so the measured G_c is given by,

$$l^2 G_c = \left(l^2 - \pi r_o^2\right)G_m + 4\pi r_o^2\left(G_p + G_a\right)$$

i.e.

$$\frac{G_c}{G_m} = \phi_a + 4\left(\frac{G_p}{G_m} + \frac{G_a}{G_m}\right)(1-\phi_a) \tag{6}$$

where G_m is the matrix toughness. If we now introduce a matrix plastic zone size

$$r_m = \frac{EG_m}{2\pi\sigma_y^2}$$

then from equation (5) we have,

$$\frac{G_p}{G_m} = \frac{(1-v)}{3\pi}\left(\frac{r_0}{r_m}\right)x^2\left(\frac{R^3}{x}-1\right)$$

Equation (3) gives

$$\frac{G_a}{G_m} = \frac{(1-v)^2}{2\pi(1+v)}\left(\frac{r_0}{r_m}\right)x^2$$

and hence

$$4\left(\frac{G_p}{G_m} + \frac{G_c}{G_m}\right) = \frac{4(1-v)}{3\pi}\left(\frac{r_0}{r_m}\right)x^2\left(\frac{e^{x-1}}{x} - \left(\frac{5v-1}{2(1+v)}\right)\right)$$

since $R^3 = e^{x-1}$ from equation (4).

From equation (6) we may write,

$$\frac{\dfrac{G_c}{G_m}-\phi_a}{1-\phi_a}=\frac{4(1-v)}{3\pi}\cdot\left(\frac{r_0}{r_m}\right)x^2\left(\frac{e^{x-1}}{x}-\left(\frac{5v-1}{2(1+v)}\right)\right) \tag{7}$$

This is the relationship explored in [3] and it was shown that for micron scale particles for $\phi<0.20$ the right hand side of equation (7) did remain constant so that $\dfrac{G_c}{G_m}$ increased with ϕ (i.e. with $1-\phi_a=1.21\phi^{2/3}$) with x approximately 3.1 for $V=1/3$ and for G_a being a substantial proportion of G_m, i.e. 0.2-0.4 G_m. The analysis assumes that there is no inter-particle interaction and so would be appropriate for low volume fractions. Here we are considering cases where $0.3<\phi<0.5$ and $\dfrac{G_c}{G_m}$ decreases with increasing ϕ.

To accommodate inter-particle effects it will be assumed that r_2 is constrained by adjacent particles. This is taken as when r_2 encompasses the whole unit cell and

$$\frac{4\pi}{3}\hat{r}_2^{\,3}=l^3, \quad i.e. \quad \hat{r}_2=\left(\frac{3}{4\pi}\right)^{1/3}l=0.62l$$

as illustrated in Fig 3 and

$$\hat{R}^3=\left(\frac{\hat{r}_2}{r_0}\right)^3=\left(\frac{3}{4\pi}\right)\left(\frac{l}{r_0}\right)^3=\frac{1}{\phi} \tag{8}$$
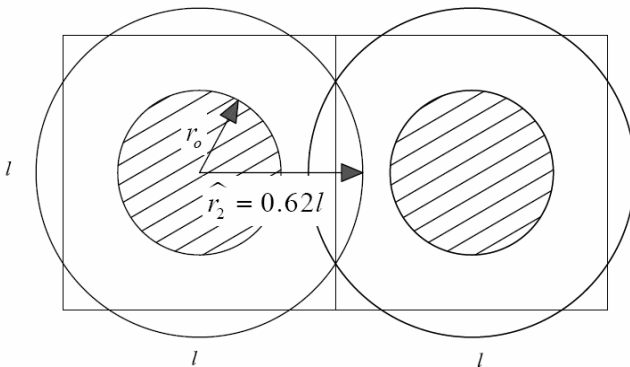

Fig. 3. Upper limit of plastic radius $\hat{r}_2$.

Thus we now have,

$$\frac{G_p}{G_m} = \frac{(1-v)}{3\pi}\left(\frac{r_0}{r_m}\right)x^2\left(\frac{1}{x\phi}-1\right)$$

and

$$\frac{G_a}{G_m} = \frac{(1-v)^2}{2\pi(1+v)}\left(\frac{r_0}{r_m}\right)x^2$$

The equivalent relationship to equation [7] becomes,

$$Y = \frac{\dfrac{G_a}{G_m}-\phi_a}{1-\phi_a} = \frac{4(1-v)}{3\pi}\left(\frac{r_0}{r_m}\right)x^2\left(\frac{1}{x\phi}-\left(\frac{5v-1}{2(1+v)}\right)\right) \tag{9}$$

The transition from constant Y occurs when

$$\frac{1}{\phi} = e^{x-1}$$

and for $x \approx 3.1$, $\overline{\phi} \approx 0.12$.

The various parameters may be found by plotting Y versus ϕ^{-1} and fitting a best straight line,

$$Y = m\phi^{-1} + c$$

and for $v=0.4$ for PMMA [2]:

$$m = 0.25\left(\frac{r_0}{r_m}\right)x \quad \text{and} \quad -c = .089\left(\frac{r_0}{r_m}\right)x^2$$

$$\text{i.e.} \quad x = 2.81\left(\frac{-c}{m}\right), \quad \left(\frac{r_0}{r_m}\right)=1.42\left(\frac{m^2}{-c}\right)$$

$$\text{and} \quad \frac{G_a}{G_m} = 0.46(-c)$$

The standard deviations of these parameters may be found from a best fit line which determines m, c and R^2, the correlation coefficient. The necessary formulae are given in the Appendix.

5 Analysis of Results

Table 3 gives the results of plotting the fracture data in Table 1 according to equation [9], i.e. Y versus ϕ^{-1}. The values of R^2, the correlation coefficient, indicate

that the data at 40 and 65°C are a good linear fit with $R^2 > 0.9$ and with standard deviations in both m and c of about 10% and 20% respectively. That for 0 and 22°C shows considerably more scatter with $R \approx 0.7$ and standard deviations of about double the 40 and 65°C values. The 90°C labelled (1) used $G_m = 1.1$ kJ/m^2 which made Y small and gave a very poor correlation with $R^2 \approx 0.5$. The high value of G_m is open to some doubt since there is some plastic blunting involved in the bend specimens which would probably not be present in the highly constrained layers between particles. With this in mind $G_m = 0.55$ kJ/m^2 was used in 90(2) which gave $R^2 \approx 0.8$ and standard deviation similar to those at 0 and 22°C.

Table 3. Derived parameters.

T °C	$m \pm S_m$	$-c \pm S_c$	R^2	$x \pm 2.81\ S_{c/m}$	$r_0/r_m \pm 1.42\ S_{m^2/c}$	$G_a/G_m \pm 0.46\ S_c$
0	0.62±0.15	0.43±0.36	0.72	1.95±0.85	1.27±1.69	0.20±0.16
22	1.00±0.23	1.54±0.56	0.73	4.33±2.53	0.92±0.78	0.71±0.26
40	1.17±0.12	1.60±0.30	0.93	3.84±1.12	1.21±0.48	0.74±0.14
65	1.57±0.10	2.00±0.25	0.97	3.58±0.96	1.75±0.45	0.92±0.12
90(1)	0.25±0.10	0.28±0.23	0.51	3.15±3.71	0.32±0.53	0.13±0.11
90(2)	0.90±0.18	1.08±0.43	0.79	3.73±2.00	1.07±0.85	0.50±0.20

Also shown in Table 3 are the derived values of x, $\dfrac{r_o}{r_m}$ and $\dfrac{G_a}{G_m}$. The nature of these derivations increases the standard deviations and so the possible variation in these sets, other than the 40 and 65°C data, is quite large. However x is generally greater than three as expected from [3] and $\dfrac{r_o}{r_m}$ is around unity. $\dfrac{G_a}{G_m}$ is less than unity, as expected.

6 Discussion

In [3] all the toughness data analysed increased with volume fraction and the right hand side of equation (7) was constant. Thus to determine x and hence G_a, r_0 had to be known. Values were taken from particle size distributions but there was some uncertainty about the effects of agglomeration. In this case equation (9) pertains and from m and c it is possible to find x, and hence σ_c, $\dfrac{r_o}{r_m}$ hence r_o and $\dfrac{G_a}{G_m}$ and hence G_a. G_a comes directly from c and G_m and has the least scatter. The values deduced are given in Table 4 and are somewhat less than G_m but a substantial proportion as would be expected for particles treated to enhance bonding as used here.

Table 4. Surface energy, particle radius and interfacial stress values.

$T°C$	$G_a \pm S$ (kJ/m^2)	$r_m \pm S$ (µm)	$r_0 \pm S$ (µm)	$\sigma_c \pm S$ (MPa)
0	0.09±0.07	11	14±19	250±240
22	0.32±0.12	16	15±19	476±270
40	0.33±0.06	23	28±11	330±96
65	0.32±0.04	29	51±11	220±60
90(1)	0.14±0.11	160	51±85	110±120
90(2)	0.28±0.11	80	86±68	110±70

The values of σ_c are determined by G_a and r_0 via equation (3). The variations in both are substantial and arise from the derivations from equation (9). Since x does not change greatly the changes in σ_c with temperature arise mostly from changes in σ_y. One would expect r_0 to be independent of temperature since it is a measure of the effective particle size. Again the variations are large but r_o does show some evidence of varying with temperature. The average value is 39 μm. Particle size analysis of the filler gave a minimum of 10 μm with agglomerates up to 100 μm. The Talysurf roughness measurements of the fracture surfaces gave an average of 37 μm over the temperature range with no evidence of a trend. However the agreement is acceptable but the trend persists.

The quality of the data limits how far one can pursue the cause of this apparent trend in r_o. In [1] some effects were attributed to thermal stresses which were estimated at about 40 MPa. These would change σ_c but are not sufficient to account for the changes to r_o. Such stresses may be the cause of the high scatter at 0°C and 22°C though they would not for 90°C where the low modulus greatly reduces their value. A further possibility is that at the lower temperatures crazing occurs rather than shear yielding [4]. This would reduce the effective yield stresses to about 100 MPa and so increase r_m to about 25 μm and thus increase r_o to about 30 μm and greatly reduce the increasing trend in r_0. The presence of crazing is another possible cause of the increased scatter at 0 and 22°C.

Fig. 4 and Fig. 5 show micro graphs of the fracture surfaces for two temperatures. At the higher temperature there is clear evidence of plastic deformation and debonding of the particles as postulated in the toughness model. At the lower temperatures this is less and may indicate the onset of crazing.
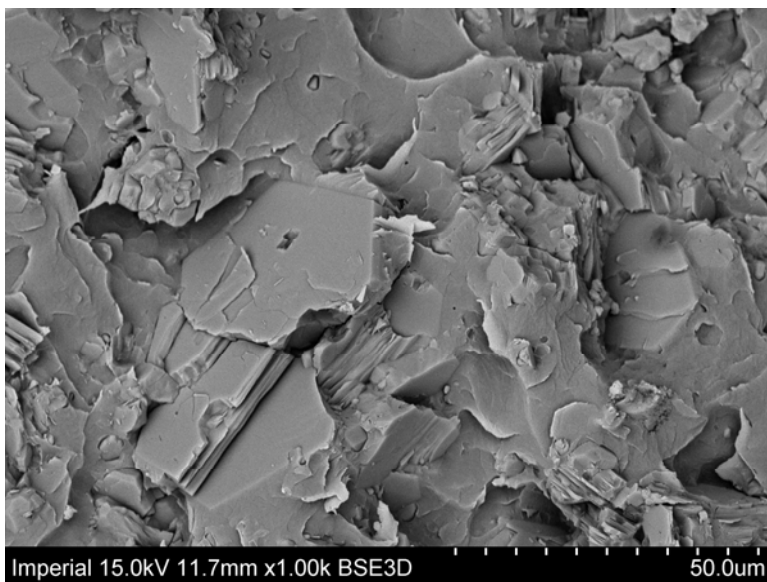

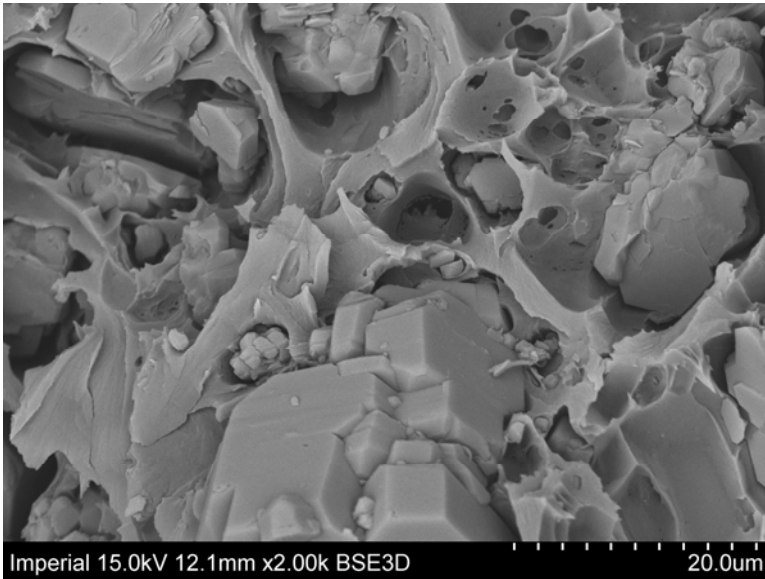**Fig. 4.** SEM micrograph of fracture surface for 35% volume fraction sample fractured at 22°C.

Imperial 15.0kV 12.1mm x2.00k BSE3D   20.0um

Fig. 5. SEM micrograph of fracture surface for 35% volume fraction sample fractured at 90°C.

7   Conclusions

It is difficult to achieve consistent fracture data with this type of material particularly when sharp cracks are needed as in these tests. However the data described do show clear trends with both volume fraction and temperature. The latter effectively give composites of different matrix behaviour with large variations in modulus and yield and/or craze stress.

The notion that the toughness arises from the debonding of the particles followed by plastic deformation is confirmed by the description of the data by the model and the micrographs. The values of G_a are sensible as is the predicted particle size when compared to direct measurements such as surface roughness and size distributions. The assumption that the plastic deformation is limited by $\hat{R}^3 = \phi^{-1}$ is, to some extent, arbitrary but is justified by the fit to the data. More evidence is needed to confirm this extension to the model.

Unlike the fatigue behaviour described in [1] there was no evidence here of residual or thermal stresses. It is possible that this is due to low cooling rates in the moulding process.

Acknowledgments

References

1. Obakponovwe, O., Williams, J.G.: Temperature Effects on the Fatigue of Highly Filled PMMA. J. Mat. Sci. 41, 4976–4986 (2006)
2. Stapountzi, O.A., Charalambides, M.N., Williams, J.G.: Micromechanical models for stiffness prediction of alumna trihydrate (ATH) reinforced PMMA: effect of volume fraction and temperature. Comp. Sci. & Tech. 69, 2015–2023 (2009)
3. Williams, J.G.: Particle toughening of Polymers by Plastic Void Growth. Comp. Sci. & Tech. 70, 885–891 (2010)
4. Morgan, G.P., Ward, I.M.: Temperature dependence of craze shape and fracture in Poly (methyl methacrylate). Polymer 18, 87–91 (1977)

Appendix: Statistical Parameters

The data is analysed via a linear regression of,

$$Y = m\phi^{-1} + c$$

which may be written as $y = mx + c$. Each set of data (at each temperature) are y_i and x_i. The parameters used are

$$\bar{x} = \frac{1}{n}\sum_1^n x_i \quad \text{and} \quad \hat{x}^2 = \frac{1}{n}\sum_1^n x_i^2$$

From a best fit analysis we may find m, c and R^2, the correlation coefficient. The standard deviations for the various parameters are.

For m,

$$S_m^2 = \frac{m^2}{n-2}\left(\frac{1}{R^2}-1\right)$$

$-c$,

$$S_c^2 = \hat{x}^2 S_m^2$$

$-c/m$,

$$\frac{S_c^2}{m} = \frac{S_m^2}{m^2}\left[\hat{x}^2 + \left(\frac{c}{m}\right)^2 + 2\bar{x}\left(\frac{c}{m}\right)\right]$$

$m^2/-c$,

$$\frac{S_{m^2}^2}{c} = \left(\frac{m}{c}\right)^2 S_m^2\left[\left(\frac{m}{c}\right)^2 \hat{x}^2\left(1+\frac{S_m^2}{m^2}\right)^2 + 4\left(\frac{m}{c}\right)\bar{x}\left(1+\frac{S_m^2}{m^2}\right)+4\right]$$

For all the sets used

$$\bar{x} = 2.42, \quad \hat{x} = 2.43, \quad \text{and } n = 9.$$

Author Index